Investigations into the use of continuous shear wave measurements in geotechnical engineering

by

Mark Anthony Styler

B.Sc. Computer Engineering, Purdue University, 2003

M.A.Sc. Civil Engineering, University of Florida, 2006

A THESIS SUBMITTED IN PARTIAL FULFILLMENT
OF THE REQUIREMENTS FOR THE DEGREE OF

Doctor of Philosophy

in

THE FACULTY OF GRADUATE AND POSTDOCTORAL STUDIES

(Civil Engineering)

The University Of British Columbia

(Vancouver)

October 2014

© Mark Anthony Styler, 2014

Abstract

The research presented within this thesis covers the development of a means to continuously monitor shear waves in a laboratory triaxial apparatus and down-hole during seismic cone penetration. This work resulted from an investigation of ageing of Fraser River Sand using a bender element triaxial apparatus.

Shear wave propagation times from bender elements were interpreted using published time domain and frequency domain techniques. These techniques provided similar results, but the variability exceeded the effect of ageing. The frequency domain and time domain techniques had different shortcomings. The two techniques could be combined to converge on a single frequency-dependent propagation time that was independent of the trigger signal waveform. This contribution was capable of resolving the small increase in shear wave velocity with age duration.

The frequency domain component of the combined bender element technique could run continuously during an experiment. With this further contribution, it was possible to track the change in shear wave propagation time throughout an experiment. The continuous bender element testing was not observed to influence the effect of ageing.

It was found that in Fraser River Sand ageing had a small effect on the shear wave velocity, no effect on the ultimate strength, and a significant effect on the shear stiffness over the intermediate small-strain range (observed from 0.01 to 1%). The normalized shear stiffness curve shifts to larger strains and becomes more brittle with ageing.

The concepts of the developed continuous bender element method are

not restricted to this equipment or even to just bender element testing. The continuous bender element method was adapted to down-hole seismic testing in the field. This contribution resulted in a continuous profile of the shear wave velocity during seismic cone penetration testing that is obtained without stopping the cone penetration.

The developments in this thesis provide a continuous measure of the shear wave velocity through a laboratory experiment and a continuous profile with down-hole penetration depth, i.e. the shear wave velocity is measured every time the other parameters are taken.

Preface

This dissertation is based mostly on original work by the author M.A. Styler.

My contributions included re-developing the laboratory equipment, performing the laboratory experiments, developing and investigating new techniques in the laboratory, and analysis of the results. The bender element equipment was constructed and installed by Scott Jackson. The worked presented in Chapter 6 combined my laboratory program with selected experimental results from T.A. Shozen and K. Lam, two previous graduate students at the University of British Columbia. For the work in Chapter 7, I specified the requirements for the perpetual source testing, but the equipment was constructed by ConeTec Investigations. I was responsible for the in-situ testing program and analysis of the results.

Chapter 4 was adapted for publication in the ASTM Geotechnical Testing Journal [Styler, M.A., and Howie, J.A., 2013, "Measuring the phase velocity with bender elements by combining time and frequency domain approaches," *ASTM Geotechnical Testing Journal*, Vol. 36, No. 5]. Chapter 5 was adapted for publication in the ASTM Geotechnical Testing Journal [Styler, M.A., and Howie, J.A., 2014, "Continuous monitoring of Bender Element shear wave velocities in triaxial specimens of Fraser River Sand," *ASTM Geotechnical Testing Journal*, Vol. 37, No. 2, pp. 218-229]. The results presented in Chapter 7 have also been used in three conference papers: at GeoManitoba [Styler, M.A., Howie, J.A., Woeller, D., 2012, "Perpetual Source Seismic Piezocone Penetration Testing: A new method for down-hole shear wave velocity profiling," *GeoManitoba*, Winnipeg, Manitoba, September 2012], at GeoMontreal [Styler, M.A., Howie, J.A., Woeller, D., 2013,

"Measuring down-hole shear waves from a vibrating perpetual source during Cone Penetration Testing," *GeoMontreal*, Montreal, Quebec, September 2013], and at CPT'14 [Styler, M.A., Howie, J.A., Sharp, J.T., 2014, "Perpetual source SCPTu: Signal stacking shear waves during continuous penetration," *CPT 14*, Las Vegas, NV.].

Table of Contents

List of Tables

List of Figures

Acknowledgements

I'd like to first thank my research supervisor, Dr. John A. Howie, for his enthusiasm, breadth of geotechnical knowledge, and support. He helped drive my work by linking the small details to the larger picture. He has been instrumental in developing my ability to get my ideas on to paper through numerous collaborations on journal and conference papers. His comments on practice runs through my presentations were also incredibly valuable. I'd also like to thank my committee members in alphabetical order: Dr. Alex Sy, Dr. Mahdi Taiebat, and Dr. Dharma Wijewickreme. It was very useful to obtain a different perspective on my work. My thesis is improved through their contributions.

I am grateful to have been a part of the Geotechnical Research Group at the University of British Columbia during my studies. They have been both my colleagues and friends throughout my years at UBC. We have worked through courses together, commiserated over marking assignments, and celebrated each other's graduations. I am grateful to have had the opportunity to share ideas during seminars and informally in the lab and field.

My work in the geotechnical laboratory would not have succeeded without the technical support provided from Scott Jackson, Harold Schrempp, and Bill Leung. If you knew what you wanted, they were very helpful. Additionally, meeting with Dr. Yogi Vaid in the lab was instrumental to my successful research program. He quickly identified many improvements for the equipment and in my procedure.

I'd like to thank ConeTec Investigations, Ltd. for their financial support

of my research. I'd also like to thank them for supporting the Perpetual Source testing and equipment. Specifically, I'd like to thank David Woeller, Ron Dolling, Jamie Sharp, and James Greig. We have collaborated on various conference papers and they have provided constructive feedback on practice runs of my presentation.

I'd like to thank my parents for their continued support through my time at the University of British Columbia. They always believed me when I told them that I was almost finished.

I'd also like to thank Dr. Kaley Crawford-Flett. She showed me what it takes to finish a PhD and how great it is to be done.

Chapter 1

Introduction

This thesis covers continuous shear wave velocity measurements in laboratory triaxial tests and during seismic cone penetration. Continuous measurements are an alternative to the conventional discrete measurements. A discrete bender element test uses a finite length trigger signal, obtains a response wave, and determines the shear wave velocity at a single point in the experiment. The continuous technique was developed during this research. It uses a perpetual bender element trigger signal and tracks the change in propagation time through-out the experiment. This technique was then adapted to down-hole seismic testing during a cone penetration test.

These developments occurred during an investigation of the effect of ageing on the small-strain stiffness of Fraser River Sand. Ageing is poorly understood despite significant observed effects in the field. The deformation and performance of non-failing geotechnical structures is dependent on the soil stiffness, not soil strength. The stiffness over small strains less than 1 % governs the behaviour for most applied stresses in actual geotechnical designs (Atkinson, 2000; Burland, 1989). Clayton (2011) recently reviewed research and practice for small strain stiffness applications. His motivation was the increasing importance of consideration of deformation for design of substructures. This is a pressing concern for inner city redevelopment in order to evaluate the effects on buried infrastructure and adjacent buildings and roads.

Stiffness is the ratio of the change in stress against strain. The stiffness can be quantified as either the secant stiffness or the tangent stiffness. These two related values are depicted in Figure 1.1. The secant shear stiffness, G_{sec}, is the slope of a line from the origin to a point on the shear-stress shear-strain curve. The tangent shear stiffness, G_{tan}, is the local slope of the shear-stress shear-strain curve at a point. The secant shear stiffness is non-linear and usually decreases with increasing shear strain.

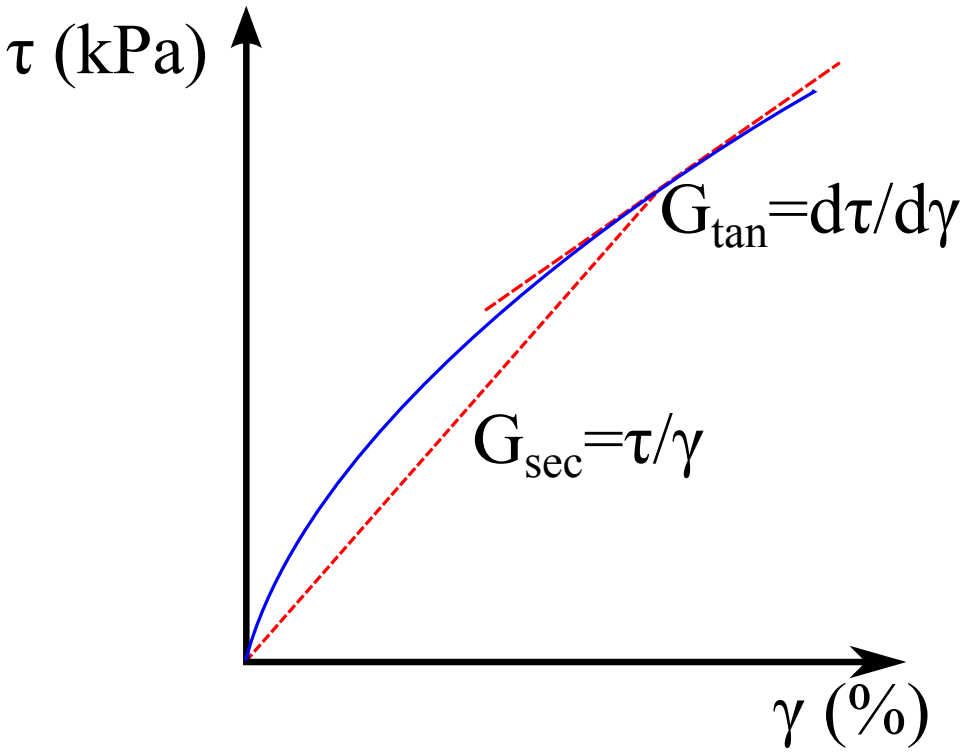

Figure 1.1: Definition of secant and tangent shear stiffness on a stress-strain curve

As implied by Figure 1.1, a single stiffness value does not describe soil behaviour. Figure 1.2 shows a conceptual illustration of non-linear shear stiffness for soil. Atkinson (2000) divided the non-linear stiffness degradation curve into three regions. The "very small strain" region has a constant high

stiffness plateau up to a threshold shear strain. The "small strain" region covers the stiffness from this threshold strain up to 0.1 %. The "large strain" region is shear strain greater than 0.1 %.

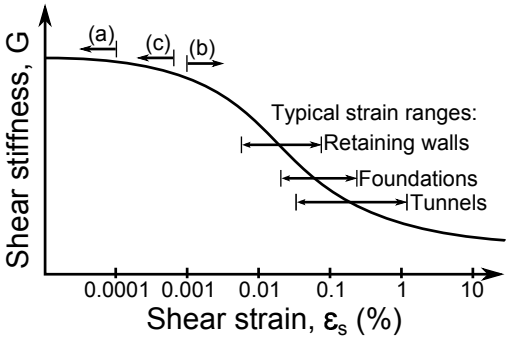

(a) Bender element testing < 0.0001% (Jovicic and Coop 1997, Kuwano and Jardine 2002)

(b) Non-linear beyond 0.001% (Afifi and Richart 1973, Kuwano and Jardine 2002, Muir Wood 2007)

(c) Mean elastic threshold strain in sand 0.0007% (Oztoprak and Bolton 2013)

Figure 1.2: Conceptual non-linear equivalent elastic shear stiffness behaviour for soils, underlying curve adapted from Atkinson (2000) with referenced annotations

The stress-strain curve and soil stiffness are very sensitive to the soil state. In-situ sands cannot be routinely sampled undisturbed for careful laboratory testing. Therefore, stiffness characterization in sands is challenging. This problem has led to the empirical characterization of the influence of various factors affecting the stiffness of sands.

Previous research at the University of British Columbia (UBC) investigated the effect of ageing, initial stress ratio, and stress path on the secant stiffness of reconstituted specimens of Fraser River Sand (Lam, 2003; Shozen, 2001). These previous investigations observed a large effect of age on the secant shear stiffness at strains from 0.03 % up to failure, with the effect being much more significant at low strains. These research projects were unable to resolve the secant shear stiffness below 0.03%. The trends suggested that the effect of ageing should be even more pronounced at smaller strains.

Both of these investigations recommended the addition of bender elements to link the effect of ageing from the small strain range to the very-small strain range. Bender elements are used to measure shear waves and determine the shear wave velocity, V_S. The shear wave velocity can be used

to calculate the very small strain stiffness, G_0. The first objective of the current research project is to install bender elements into the UBC triaxial apparatus.

There is no standard for bender element installation, operation, or interpretation. Figure 1.3 depicts the scatter in interpreted G_0 stiffness from parallel bender element tests on Toyoura sand from different labs under the same stress state. Different bender element installation details, trigger waveforms, signal processing, and interpretation methods result in a wide range of V_S for a given soil at a given density and stress state. Robertson et al. (1995b) also observed that an additional source of variation may have been due to differences in specimen preparation. The second objective of this research project is to investigate the application of bender elements for studying ageing of Fraser River Sand.

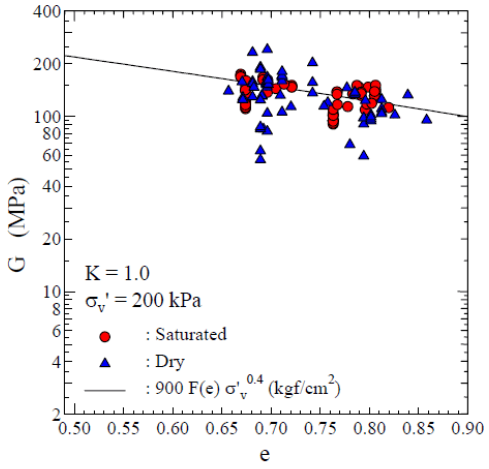

Figure 1.3: Scatter of $G_0 = \rho V_S^2$ in specimens of Toyoura sand under hydrostatic consolidation in an international parallel bender element test (Yamashita et al., 2009). Used with permission from Satoshi Yamashita. This material may be downloaded for personal use only.

Normalizing the laboratory G_{sec} stiffness curves by G_0 permits the re-

sults to be compared to recent published stiffness degradation curves from Wichtmann and Triantafyllidis (2013) and Oztoprak and Bolton (2013). These published stiffness degradation curves do not account for the effect of ageing, despite the huge effect observed by previous investigations at UBC. The third objective of this research is to integrate the bender element characterized G_0 values into a small strain stiffness investigation of Fraser River Sand.

1.1 Research objectives

To reiterate, the following research objectives have been identified:

1. Install bender elements into the UBC triaxial apparatus,
2. Investigate the use of bender elements for an investigation of ageing of Fraser River Sand,
3. Integrate the bender element determined G_0 into a laboratory study of Fraser River Sand stiffness,

1.2 Thesis organization

Chapter 2 reviews the background for this research work, including triaxial testing(Section 2.1), bender element equipment and signal interpretation (Section 2.2), factors affecting V_S and G_0(Section 2.3), and empirically modelling normalized shear stiffness degradation curves (Section 2.4).

Chapter 3 describes the improvements in UBC's triaxial equipment, compares preliminary triaxial results to previous studies, and illustrates the challenge of using prevalent and state of the art bender element techniques to observe the effect of ageing of Fraser River Sand on G_0. The results of Chapter 3 met the first research objective and demonstrated that the second objective cannot be achieved with the interpretation techniques described in Section 2.2.

Chapter 4 and Chapter 5 investigate the use of bender elements. In Chapter 4 a technique that combined a suite of signals in the time and

frequency domains was developed. This technique converged on a single frequency dependent phase velocity solution. In Chapter 5 this technique was further developed to provide continuous bender element signal monitoring during a triaxial test. The results from these two chapters achieved the second research objective.

Chapter 6 presents the integration of bender element determined G_0 values into a laboratory investigation of the stiffness of Fraser River Sand. Normalized G_{sec}/G_0 stiffness degradation curves were characterized. This achieved the third objective of this research.

Chapter 7 switches from the laboratory setting to the field. It was realized that the continuous bender element technique developed and described in Chapter 5 could be adapted to in-situ measurements. This adaptation of the continuous V_S technique to down-hole seismic testing during cone penetration, and preliminary results, are presented. A continuous depth-profile of V_S was successfully obtained. This technique has the potential to increase the depth resolution of in-situ V_S measurements. Measuring V_S in-situ and calculating G_0 could permit the laboratory characterized normalized stiffness curves to be scaled to in-situ conditions.

Chapter 8 contains a summary of the implications, conclusions, contributions, unresolved issues, and identifies future research topics.

The appendices contain details necessary for reproducing the triaxial results and data from each laboratory test. Appendix A contains the equipment sensor and systematic error calibrations. Appendix B details the triaxial testing procedure using the UBC triaxial apparatus - including sample preparation, specimen preparation, and testing. Appendix C contains the equations used to reduce the raw sensor measurements to soil state properties. Appendix D contains the reduced laboratory results.

Chapter 2

Measurement of soil stiffness

This work continues from previous research performed at UBC (Howie et al., 2002; Lam, 2003; Shozen, 2001). The previous work used triaxial testing to interpret the secant shear stiffness above 0.03 % shear strain. The tests were performed on Fraser River Sand, a major foundation soil unit and building material in the lower mainland of British Columbia. The previous work did not include bender elements. Shear waves were not measured. The previous researchers were unable to normalize the secant shear stiffness degradation curves with a very small strain G_0 value. This made it difficult to compare the effect of the testing variables on the shape of the stiffness degradation curve. The previous research projects recommended the addition of bender elements to be able to measure shear waves and obtain normalized secant stiffness, G_{sec}/G_0, degradation curves. Normalized curves are useful as they can be scaled to in-situ measured V_S and G_0 values.

Bender element applications can be a challenge. There are no standards for manufacture, installation, operation, or data reduction. The reported results from various researchers are highly variable (Yamashita et al., 2009). This chapter contains a literature review covering the use of bender elements and interpretation of the shear wave velocity.

Bender elements are used in order to obtain G_0 from V_S. The simplest and most widely used model for shear wave propagation is through an infinite homogeneous isotropic linear elastic continuum. Under these assumptions,

Equation 2.1 can be derived from Cauchy's momentum transport equation. A derivation can be found in most text books covering elasticity or wave propagation, including Slawinski (2003).

$$G_0 = \rho V_S^2 \tag{2.1}$$

In this equation ρ is the bulk density of the medium and G_0 is the very small strain shear stiffness. The first application of this equation to investigate laboratory sand specimens was by Iida (1938). His justification was that elastic waves propagated through sand, and therefore that sand should possess elastic constants. He acknowledged that the assumption that elastic theory can be applied to sand behaviour required further experimental support.

A bender element equipped triaxial apparatus should be able to obtain both G_{sec} and G_0 in order to obtain normalized secant stiffness degradation curves. This can be used to investigate the influence of soil variables on the shape of the curve. Wichtmann and Triantafyllidis (2013) and Oztoprak and Bolton (2013) empirically characterized the effect of the uniformity coefficient, mean stress, and density on the shape of the normalized stiffness degradation curves. The significance of their work, for this thesis, is the technique by which this empirical characterization was carried out. They fit hyperbolic functions to the normalized stiffness degradation curves. These hyperbolic functions reduced the entire curve to two (Wichtmann and Triantafyllidis, 2013) or three (Oztoprak and Bolton, 2013) parameters. They then fit equations between the soil properties of interest to these hyperbolic coefficients. This is relevant to this thesis as the previous work by Shozen (2001) and Lam (2003) investigated various factors affecting G_{sec} degradation. With this empirical characterization procedure, the influence of these factors can be quantified.

The normalized curves have additional value due to the use of G_0. Shear waves can be measured both in-situ and in laboratory soil specimens. In-situ shear waves are measured during seismic cone penetration testing (SCPTu), down-hole seismic testing, from cross-hole testing with multiple bore holes,

and inferred from the frequency dispersion of non-invasive surface Rayleigh wave velocities (SASW, MASW). The laboratory or empirical characterized normalized curves may be applicable in field applications.

The purpose of this chapter is to cover the background for the measurement of soil stiffness in a laboratory using a bender element equipped triaxial apparatus.

2.1 Triaxial testing

Triaxial testing is used to investigate fundamental soil behaviour (Bishop and Henkel, 1957; Saada and Townsend, 1981), including small strain behaviour (Atkinson, 2000; Kuwano and Jardine, 2002a; Negussey, 1984; Shozen, 2001). The laboratory work in this thesis acquired small strain measurements using triaxial testing due to previous experience in the UBC laboratory for similar research programs (Lam, 2003; Negussey, 1984; Shozen, 2001), availability of equipment, and intent to complement past studies with bender element results. Small strain measurements challenge the limitations of the sensors.

2.1.1 Local versus external sensors

The triaxial test is an element test and to be considered an element test, the stresses and strains should be uniformly distributed in the specimen (Saada and Townsend, 1981). Test procedures should be designed to achieve as close to uniform conditions as possible. Local sensor measurements over the middle third of the specimen have shown that conventional triaxial testing devices do not achieve uniformity (Scholey et al., 1995). It has even been suggested that the difference between laboratory and in-situ measurements is not sample disturbance, but non-uniform strain distributions (Scholey et al., 1995).

Local measurements are made on the specimen. The advantage of local measurements is that they eliminate a number of systematic corrections necessary for external measurements. The disadvantages are that they add complexities to the apparatus and experimental procedure and may limit

the radial deformations and stress paths that can be explored. Scholey et al. (1995) provide an overview of common local measurement sensors and applications for triaxial specimens. An alternative to local sensors are external sensors.

External measurements are not made on the specimen. The external sensors respond to the displacement of the top cap, the load applied to the downward ram, the pressure due to a volume of water expelled or drawn into the specimen. The advantages of external sensors are simplicity, reliability, and easier reproducibility of measurements. The disadvantages are that they assume uniform stress and strain distributions and the measurements contain a set of systematic errors that must be corrected to characterize the soil behaviour. Each of these corrections adds to the uncertainty in the calculated specimen state.

The UBC triaxial apparatus uses external sensors. Uniformity of the stress and strain within the specimen is assumed.

Enlarged frictionless end platens have been recommended to promote strain uniformity. Negussey (1984) attempted to use enlarged frictionless end platens in his research on the small strain. He found that they only promoted uniform stresses and strains in the bottom half of the specimen. Furthermore, he found that at a height to diameter ratio of 2 the effect of end restraint is insignificant for small strain investigations. The UBC triaxial specimens are prepared at a height to diameter ratio of 2 and do not use enlarged end platens.

The UBC triaxial apparatus uses polished metal end platens and concentrates on the early part of the stress-strain curve. The early part of the stress-strain curve is less influenced by barrelling of the sample.

2.1.2 Systematic error corrections for external sensor measurements

The stress state needs to be evaluated at the centre of the specimen. Since measurements are not made at the centre of the specimen, the measured values need to be corrected.

The systematic corrections for the axial stress include the weight of the

top cap, half the weight of the soil, ram friction, uplift from cell pressure on unequal end areas, and membrane elasticity. The uplift from unequal end area is due to the pore water pressure acting on the cross-sectional area of the specimen and the chamber pressure acting on the specimen cross-section area minus the driving ram area. Kuerbis and Vaid (1990) presented the corrections necessary to adjust for the systematic errors due to membrane elasticity on the axial and radial stresses.

A systematic error in the volume measurement results from the elastic membrane penetrating into the pore space on the surface of the specimen. This changes the volume of the water within the membrane enclosed specimen without a corresponding change in the soil skeleton volume. A simple procedure to approximately characterize this correction was presented by Vaid and Negussey (1984). This procedure compares the volumetric strains developed during hydrostatic unloading to an assumed isotropic strain response. The difference between these volumetric strains is approximately the membrane penetration into the cylindrical soil surface.

2.1.3 Previous UBC triaxial testing research on ageing of Fraser River Sand

Shozen (2001) investigated the effect of age on the small strain secant shear stiffness, G_{sec}, of drained triaxial specimens of Fraser River Sand. The motivation for his research came from the published significant effect of age in-situ (Mitchell and Solymar, 1984; Schmertmann, 1991) on the CPT response in man-made hydraulic deposits, the focus of laboratory resonant column investigations on the very small strain (Anderson and Stokoe, 1978), and the working strains of less than 0.5 % imposed by typical geotechnical designs (Burland, 1989). The desired knowledge was the effect of age on secant shear stiffness over the small strain range from 0.001 % to 1 %. Triaxial tests that accounted for the small-strain measurement considerations developed by previous UBC research (Kuerbis and Vaid, 1990; Negussey, 1984; Vaid and Negussey, 1984) were performed on reproducible and homogeneous water pluviated specimens (Vaid and Negussey, 1988). Shozen (2001) investigated the effect of ageing under different stress-ratios on the

subsequent shearing along various stress paths to failure. The stress ratio is the ratio of axial to radial effective stress during ageing. The shear stress paths are the stress paths followed to failure after the ageing phase. He observed that the increase in the secant shear stiffness with age was significantly greater at shear strains of 0.03 % than at 0.15 %. He was unable to confidently measure G_{sec} at strains below 0.03 %. He noted that the percentage increase in G_{sec} with age increased with the imposed axial to radial stress ratio. He confirmed published observations that ageing has no effect on the ultimate strength of the soil. His work, and subsequent work at UBC, showed the importance of uniform ageing to get reproducible small-strain soil behaviour. He pointed out that empirical relationships derived from calibration chamber tests may not work very well on geological aged in-situ soil. He concluded with a recommendation to add the measurement of the very small strain stiffness using bender elements to allow the investigation of the effect of ageing from the very small strain through the small strain range.

Lam (2003) complemented the work of Shozen (2001) with tests at additional stress ratios and stress paths. Lam (2003) also recommended the inclusion of bender elements to measure the stiffness at very small strains to investigate G_{sec}/G_0 attenuation.

2.2 Laboratory measurement of V_S by bender element testing

Adding bender elements to a triaxial apparatus adds the capability of measuring shear waves. Measured shear waves can be interpreted to obtain V_S and calculate G_0. This section covers background for the bender element instrumentation, data acquisition, and interpretation.

Piezoceramic bender elements are used to both generate and measure shear waves through soil specimens. They comprise a conductive centre shim sandwiched between two piezoceramic plates, as shown in Figure 2.1a. Figure 2.1b shows a bender element cantilever beam. It is installed into a recess, as shown in Figure 2.1c, such that only a few millimetres of the free

end penetrates into the soil specimen. These cantilever beams will bend due to an applied voltage or generate a small voltage due to an applied mechanical disturbance. To exploit this behaviour, bender elements are installed on opposite ends of a specimen to both trigger and receive a shear wave through the soil.

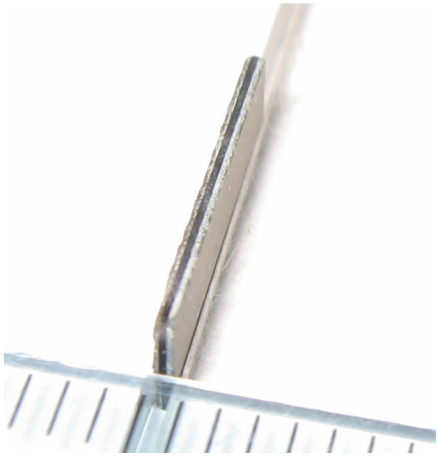

(a) Pizeoceramic plates sandwiching conductive centre shim

(b) Bender element

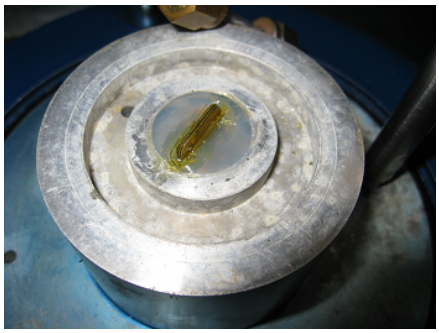

(c) Bender element installed in triaxial end platen

Figure 2.1: Photographs of a a bender element

Piezoceramics have a long history of use for measuring shear waves in soil specimens. The first published application using piezoceramics to acquire V_S in soil specimens was by Lawrence Jr (1965). Shirley (1978) introduced modern cantilever beam bender elements that penetrate into the soil speci-

men. Since then, a significant body of research has been created to address the various encountered difficulties and applications.

Alternatively, the shear stiffness, G_0, can be obtained using a laboratory resonant column (Drnevich et al., 1978) or torsional shear device (Woods, 1994). These techniques are briefly described here as they were used in many of the investigations covered later in Section 2.3. This subsequent section covers some of the soil properties that influence G_0 and the shear wave velocity.

Resonant column testing identifies the first resonant frequency due to an oscillating torsional driving force. The system is comprised of a cylindrical soil specimen capped with an active end platen and passive end platen. The active end platen is driven with an adjustable frequency sinusoidal torsional force. This results in a set of peak resonant frequencies. The peak resonant frequency corresponding to the cylindrical soil specimen depends on the conditions of the passive end platen. The passive end platen can be fixed or free with an associated mass. In resonant column testing, the shear modulus is found by solving an equation for an idealized system with the same resonant frequency. This system includes the mass and inertia of the end platens and a cylindrical, uniform, linear elastic material with the same mass and dimensions as the soil specimen. Additional information on resonant column testing can be found in the ASTM Standard (D4105-07) and in Drnevich et al. (1978).

A torsional shear test is a result of instrumenting the resonant column device to measure the applied torque and resulting rotation of the active platen. Similar to resonant column testing, this information is interpreted assuming an idealized elastic cylindrical specimen (Isenhower et al., 1987). The shear modulus is calculated for the measured rotation angle and applied torque. d'Onofrio et al. (1999) designed a torsional shear apparatus that could perform dynamic testing over a frequency range from 0.1 to 100 Hz.

Compared to resonant column testing, bender element testing has the following disadvantages: it is unable to measure the degradation of the shear modulus at higher strains (Thomann and Hryciw, 1990), V_S is measured at frequencies above 1000 Hz, while in-situ measurements are typically made

below 100 Hz; and V_S interpretation methods are inconsistent (Yamashita et al., 2009). It has the following advantages: bender elements are small, versatile, economical; the test is fast (Thomann and Hryciw, 1990); and it is less destructive than resonant column testing (Thomann and Hryciw, 1990). Another disadvantage of bender elements stated by Thomann and Hryciw (1990) was that they cannot be used to measure soil damping. However, Brocanelli and Rinaldi (1998) subsequently developed a method to measure damping using bender elements.

Bender elements have become the prevalent means to characterize the shear wave velocity in laboratory soil specimens. Bender elements are most commonly installed in conventional geotechnical laboratory equipment such as triaxial cells (i.e. Kuwano and Jardine (2002b)) and oedometers (i.e. Lee et al. (2008), Thomann and Hryciw (1990)). The versatility of bender elements has also permitted their inclusion in more unconventional laboratory equipment (Comina et al., 2008), and even in-situ tools (Jang et al., 2010).

2.2.1 Installation

The research covered in this thesis used a triaxial apparatus that was modified to include bender elements. There is no standard for the manufacture or installation of bender elements. This makes bender element testing both versatile and potentially variable.

The bender elements themselves are a cantilever beam. This beam is as thick as the piezoceramic plates, but has a variable length and width. A fraction of the cantilever beam penetrates into the soil specimen. In a comparison of 23 different bender element systems (Yamashita et al., 2009), the cantilever length was 12-20 mm, the width was 10-12 mm, and the average specimen penetration length was 4.7 mm. For comparison, even though it is out of place in this literature review chapter, the installed UBC bender elements were 14 mm long, 10 mm wide, and penetrated 4.5 mm and 4.6 mm into the specimen. More installation details are provided in Section 3.3.2.

Figure 2.2 depicts three published examples of installed bender elements.

This figure shows some common features to all bender element installations. They are installed in a recess such that only a fraction of the length penetrates into the soil specimen. If this recess is a thin slot the bender element can be glued in place, as illustrated in Figure 2.2a and Figure 2.2b. Bender elements have also been mounted onto the surface of latex membranes as depicted in Figure 2.2c. Figure 2.2a also shows how two bender elements are mounted opposite to each other in an apparatus.

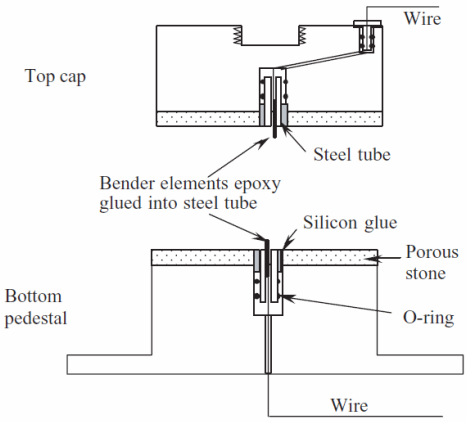

(a) Pedestal mounted bender element (Leong et al., 2005)

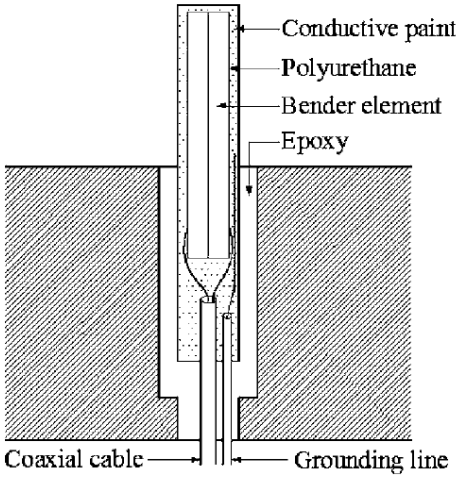

(b) Pedestal mounted bender element (Cha and Cho, 2007)

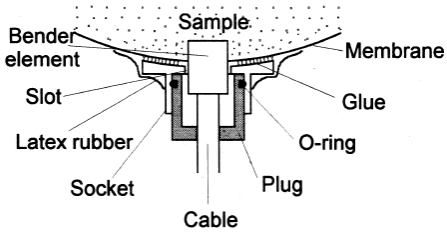

(c) Membrane mounted bender element (Kuwano et al., 2000)

Figure 2.2: Published bender element installation details. Reprinted, with permission, from Geotechnical Testing Journal, copyright ASTM International, 100 Barr Harbor Drive, West Conshohocken, PA 19428.

There are no standard design details for bender element installations. However, there are a lot of common features. They all have similar dimensions. They are all installed in a recess. They are all coated to be water proof. They all require electrical cables and wiring. Following a similar design to what has been done in the past makes a significant body of bender element research relevant.

2.2.2 Series and Parallel type bender elements

There are two different types of bender elements, series or parallel, with different wiring configurations. Different results are obtained based on the type of bender element used.

A series type element has opposing piezoceramic plate polarization directions. A series type bender element is wired by completing a circuit across the outside faces of the entire bender element. The outside edge of one plate is wired to ground, and the outside edge of the opposite plate is wired to the trigger voltage source. The electrical potential drop is in the same direction across both plates. Since the polarization is in opposite directions, this causes one plate to extend and one to contract. The result is the bending of the cantilever beam.

The polarization directions for the piezoceramic plates in a polar element are aligned. A parallel type bender element has three connecting wires. Two outside face wires are connected to ground and the centre shim is wired to the trigger voltage signal. A parallel type bender element with wiring is shown in Figure 2.3. Parallel type wiring results in the same voltage potential across both piezoceramic plates. On one of the plates, this voltage potential is aligned with the polarization direction. On the other plate, it opposes the polarization direction. This causes one plate to extend, one to contract, and the bender element to bend when a voltage is applied.

If the series or parallel bender elements are wired incorrectly they will not bend. An applied voltage would cause both piezocermaic plates to extend or contract. A shear wave will not be generated.

Parallel type elements generate more deformation than series type for

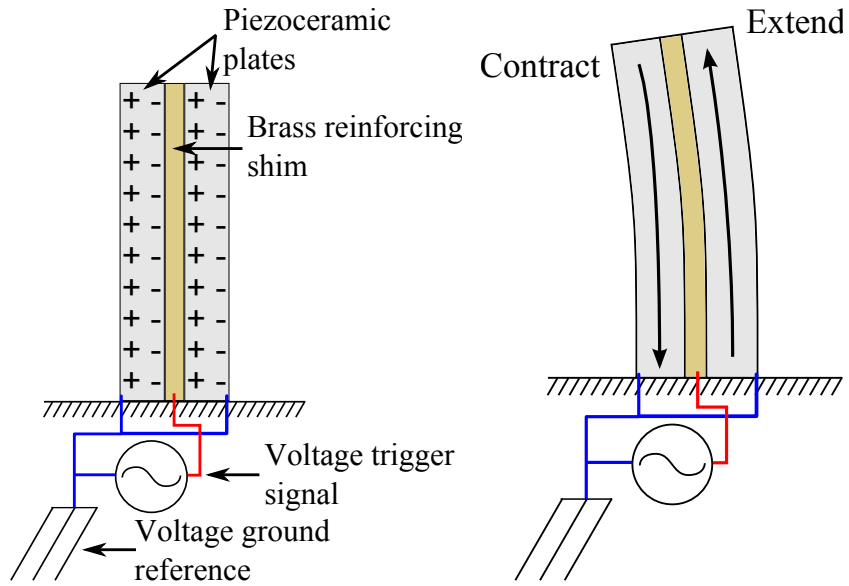

(a) Trigger bender element wired in parallel

(b) Piezoceramic plates extend and contract causing the cantilever beam to bend

Figure 2.3: Piezoceramic parallel type bender trigger element

an applied trigger voltage amplitude. Conversely, series type elements generate more voltage than parallel type for a received mechanical wave. Series type elements are easier to manufacture and install. However, parallel-type elements are self-shielding.

Lee and Santamarina (2005) present measured signals from series-series unshielded, series-series with installed shielding, parallel-series, and parallel-parallel combinations of bender element triggers and receivers. Series type bender elements can be shielded with a coating of conductive paint that is wired to ground. Parallel type elements are self shielding when the outer plate is wired to ground. The least distorted signals were provided by shielded series-series and parallel-parallel bender element systems. Shielding reduces the environmental electrical noise and cross-talk in the received signals. Cross-talk results in a systematic distortion of the received signal. A distorted version of the applied trigger signal is almost instantaneously observed in the received channel. With unshielded bender elements the

electrical signals propagate through the specimen pore fluid.

2.2.3 Signal conditioning

The signal to noise ratio (SNR) is the ratio of the amplitude of the informative signal to the amplitude of the random noise. The SNR may be increased through signal conditioning. Signal conditioning includes filtering, amplification, and signal stacking.

Amplification uses an external power source to increase the amplitude of a signal. The trigger signal can be amplified to induce stronger shear waves. The response signal can be amplified prior to analogue to digital conversion to increase the resolution of the signal.

Filtering alters features in the measured signals. A low-pass filter reduces high frequency content, a high pass filter reduces low frequency content, and a band-pass filter reduces both low and high frequency contents. Filtering may be used to reduce frequency contents outside of the bender element operating range. Filtering may increase the clarity of the measured shear wave for visual interpretation. Improper filtering can adversely affect the interpretation of the propagation time. It can distort the informative shear wave component of the received signal. Filtering cannot be used when the noise is over the same frequencies as the signal.

Signal stacking sums up the results of a series of identical tests performed back to back. Signal stacking is very useful when the frequency of the noise coincides with the frequency of the signal. In signal-stacking, random noise cancels itself out and systematic signal components are amplified. The signal to noise ratio increases with the square root of the number of stacked signals. A two-fold increase is realized by stacking only 4 signals. A 10-fold increase is realized with 100 stacked signals. Lee and Santamarina (2006) recommend signal stacking over filtering.

To use signal stacking, a period of time must elapse between repeated tests to permit any reflected waves in the specimen to dissipate. Brandenberg et al. (2008) developed a fast stacking procedure by randomizing the pause time between subsequent trigger signals. With these random wait

times, the residual signal components become random and only the main shear wave is systematic and amplified. SNR does not increase with the square root of the number of stacked signals using this fast-stacking approach.

Signal stacking only reduces random noise. There are systematic bender element distortions that are amplified through signal stacking. These include the near field effect (Section 2.2.4) and wave reflections (Section 2.2.5).

2.2.4 Near field effect

The near field effect is a phenomenon that can distort measured bender element shear waves. The near field effect is a shear-motion distortion that precedes the arrival of the main shear wave. This effect is systematic, and not random. It cannot be reduced through signal stacking. It is at a similar frequency as the shear wave. It cannot be eliminated through filtering.

The near field effect is not compression wave interference. It is interference from transverse motion at the speed of a compression wave. Cruse and Rizzo (1968) derived an equation for particle motion due to elastic waves in linear, isotropic, homogeneous, elastic materials. Sánchez-Salinero et al. (1986) applied the solution from Cruse and Rizzo (1968) to investigate analytically the response of a material to excitation from single cycles of sine pulse waves. Sánchez-Salinero et al. (1986) includes both 2D and 3D analytical solutions. The calculations for transverse motion predicted two wave arrivals. The first was an arrival of transverse motion at the speed of the compression wave. The second was the arrival of transverse motion at the speed of the shear wave.

The amplitude of the shear motion propagating at a compression wave velocity attenuates over shorter distances than the shear wave velocity component. At a large enough propagation distance, the shear motion propagating at a shear wave velocity dominates the response. This is why it is termed a near field effect, it is only observed close to the source.

The near field effect was observed in 3D numerical finite element modelling of bender element tests (Arroyo et al., 2006). Figure 2.4 depicts the

received wave after propagation through a linear elastic constitutive model. The near field effect is observed between the arrival of waves travelling at speeds of V_P and V_S.

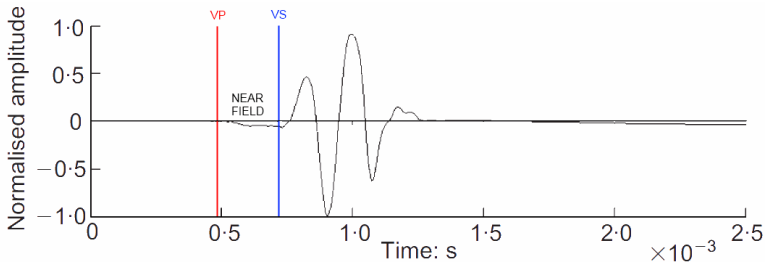

Figure 2.4: Observed near field distortion in a 3D numerical model using linear elastic constitutive elements with absorbing lateral boundaries, adapted from Arroyo et al. (2006)

Figure 2.5 shows an experimental observation of the near-field effect. This specimen had a propagation length to wavelength ratio ($L_{tt} : \lambda$) of 3.1. The near field effect was observed to be marginal above a $L_{tt} : \lambda$ ratio of 3.33 for dry sand and unsaturated residual soil (Leong et al., 2009, 2005).

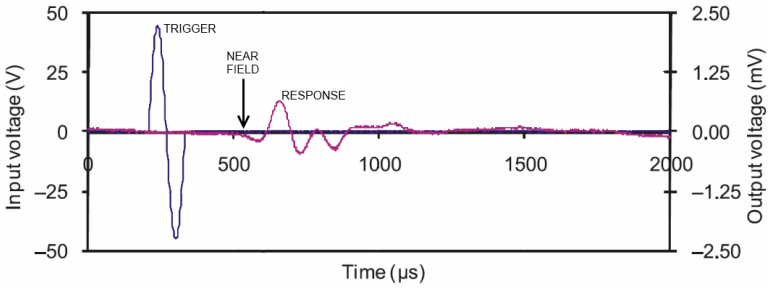

Figure 2.5: Experimentally observed near field distortion in a specimen of compacted residual soil (λ=31 mm, L_{tt}=95.57 mm), adapted from Leong et al. (2009). Adapted, with permission, from Canadian Geotechnical Journal, copyright NRC Research Press, Engineering Institute of Canada

For a fixed propagation length, the magnitude of the near field effect

decreases as the frequency of the shear wave increases. It is therefore desirable to perform bender element testing at high frequencies. However, there is an upper frequency limit for bender element testing. If the frequencies are too high the shear wave will attenuate before arriving at the receiving bender element. This frequency limit depends on the bender elements, soil coupling, soil state, and soil damping. It will change during an experiment.

Rio (2006) stated that sine pulse trigger waveforms cannot be used to control the frequency component of the shear wave. Sine pulse triggers contain a wide band of frequency contents. A single wavelength to use to evaluate the L_{tt}/λ near field criteria cannot be calculated.

The near field effect has been supported theoretically, analytically, numerically, and observed experimentally. More distortion occurs over short propagation lengths and at low frequencies. The common sine-pulse bender element trigger does not define or limit the frequencies of the generated or propagated shear wave.

2.2.5 Sample size effects

The elastic waves induced by the bender elements reflect off the end platens of the apparatus and the constrained sides of the specimen. The received mechanical wave is the direct transmitted wave with a superposition of these reflections. The dimensions of the specimen can result in a distorted shear wave signal. These distortions are systematic. They cannot be reduced through signal stacking. They are at the same frequency as the direct shear wave. They cannot be reduced through filtering.

Arulnathan et al. (1998) investigated the effects of end platen reflections for shear waves propagated in the axial direction using a 2D finite element model. They modelled the received wave as the summation of four wave paths: unreflected trigger-receiver, once reflected behind the trigger element, once reflected behind the receiver element, and twice reflected behind both the trigger and receiver elements. This model resulted in a distortion that was dependent on the bender element penetration length into the soil. These simulations resulted in signals that were qualitatively similar to

typical measurements.

Arroyo et al. (2006) investigated the effects of side reflections on bender element tests using three dimensional finite element numerical models. The cylindrical soil specimens were represented by a linear elastic constitutive model. The shear waves propagated along the cylindrical axis. The dimensions of these cylinders can be normalized by the ratio of the length to diameter - the slenderness ratio. These models explored absorbing and reflective side-wall boundary conditions with different slenderness ratios. Figure 2.6a shows the results for a shear wave propagating through a specimen with a slenderness ratio of 4.0 and absorbing side walls. The shear wave arrival corresponded to the first main pulse in the received trace. Figure 2.6b depicts the results for the same slenderness ratio, but with reflective side walls. This signal is highly distorted and the shear wave does not correspond to the first complete pulse or the first major pulse. Figures 2.6c and 2.6d show that the side wall boundary conditions have little influence when the propagation distance is short.

Marjanovic and Germaine (2013) recommend that slenderness ratios be less than 1.0 to avoid reflection interference. Rio (2006) went into more detail and recommended that the H^2/D ratio be less than 15 mm (oedometer specimens) or greater than 45 mm (triaxial specimens). These recommendations were based on a parametric investigation of sample size effects using synthetic rubber samples and FLAC3D numerical models. The behaviour was observed to depend on the H^2/D ratio, rather than H/D. Between these two dimension ratios was a transition geometry with unpredictable behaviour.

Oedometers have low slenderness ratios, so the side wall reflections are not a source of error. However, the errors due to reflected wave interference from the end caps would have increased significance (Arulnathan et al., 1998). Furthermore, Rio (2006) found some uncertainty in the actual wave propagation length. He found that it may be longer than the assumed bender tip-tip length. Such uncertainty in the propagation length will have a more significant impact on V_S determinations over short distances.

Triaxial specimens typically have slenderness ratios around two and are

bounded by an elastic latex membrane. Arroyo et al. (2006) suggested that the triaxial membrane would represent behaviour somewhere between the reflective and absorbing side wall models. Results from triaxial specimens are expected to include some reflection interference. However, the uncertainty in the propagation length is reduced.

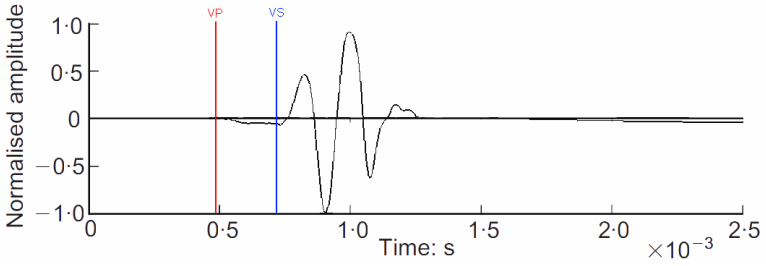

(a) Slenderness 4, absorbing side walls

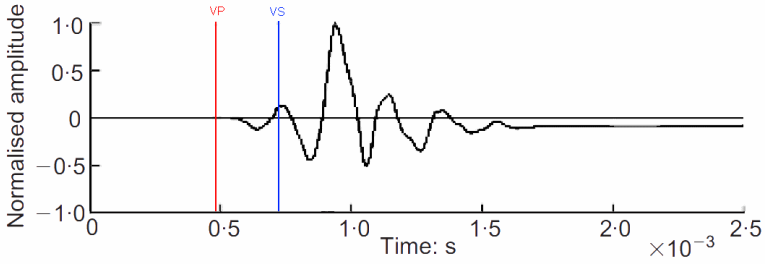

(b) Slenderness 4, reflective side walls

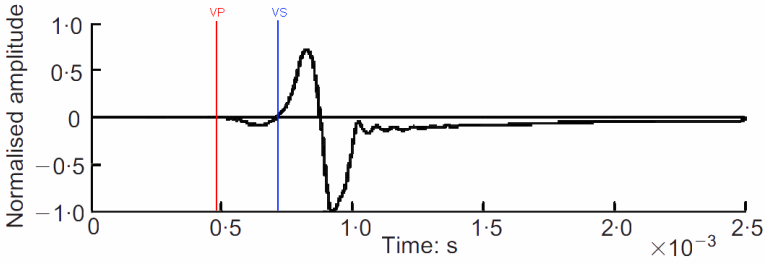

(c) Slenderness 0.25, absorbing side walls

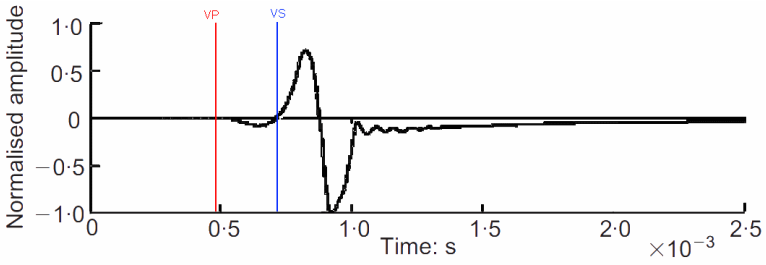

(d) Slenderness 0.25, reflective side walls

Figure 2.6: Modelled bender element signals with different slenderness ratios and boundary conditions (adapted from Arroyo et al. (2006)). Adapted with permission from Geotechnique, copyright Thomas Telford. This material may be downloaded for personal use only. Any other use requires prior permission of Thomas Telford.

2.2.6 Classification of observed bender element response signals

The distortions due to the near field effect and specimen reflections are common in bender element testing. It is possible to characterize the signals based on the type of observed distortion. Received bender element signals from sine pulse triggers can be classified into one of three waveform types (Brignoli et al., 1996). Type 1 has no pre-arrival distortion. The first pulse has the largest amplitude and the first arrival point is easy to select. Type 1 signals are rarely observed. Type 2 signals have an observed near field distortion obscuring the first arrival pick (see Figure 2.5). Type 3 signals have a small amplitude cycle prior to a major shear pulse (see Figure 2.6b). They appear to be a result of reflected wave interference. Type 3 signals have the most inconsistent propagation time interpretations.

Published bender element signals encountered during the literature review for this thesis were classified with the waveform characteristics identified by Brignoli et al. (1996). Table 2.1, Table 2.2, and Table 2.3 detail published bender element tests that depicted Type 1, 2, and 3 waves. Note that only two of the encountered signals could be classified as Type 1. These signals have a high propagation length to wavelength ratio. The specimens described in Table 2.2 generally have low propagation length to wavelength ratios. In Table 2.3, the specimens have a higher slenderness ratio - the ratio of the propagation length to specimen diameter. It is important to note that these observations of common features between the signal types are fairly weak.

Table 2.1: Type 1: clear first major pulse, first arrival is easy to select, simplest to interpret, least common to encounter (Brignoli et al., 1996)

Soil	Equip.	$L_{tt}/dia.$	L_{tt}/λ
Compacted Residual, Sat=90 % (Leong et al., 2009)	Trx.	2	6.1
Clay (Jovicic et al., 1996)	Trx.	–	8.1

Table 2.2: Type 2: apparent near field distortion, the arrival is the first strong pulse with correct polarity (Brignoli et al., 1996)

Soil	Equip.	$L_{tt}/dia.$	L_{tt}/λ
Compacted Residual, Sat=90 % (Leong et al., 2009)	Trx.	2	0.8-3.1
Sand, dry (Leong et al., 2009)	Trx.	2.4	1.2
Linear-elastic (Arroyo et al., 2006)	F.E.	0.25	3.3
Clay, Saturated (Brignoli et al., 1996)	Trx.	2.0	2.7
Clay (Bonal et al., 2012)		L_{tt}=91 mm	1.4-4.1
Clay (Chan et al., 2010)	Trx.	2.0	4.8
Sand, dry (Kumar and Madhusudhan, 2010)	RC	2.0	0.8-1.9
Sand, P.sat. (Ghayoomi and McCartney, 2011)		N/A	2-4
Clay (Jung et al., 2007)	Trx.	2.1-2.3	1.8
Silt (Karl et al., 2008)	Trx.	1.7	1.1-2.2

It will be described in Section 2.2.7 and Section 2.2.8 how the type of observed bender element signal should be considered when selecting an appropriate interpretation technique.

2.2.7 Interpreting V_S in the time domain

Bender elements trigger and receive shear wave signals. These signals must be interpreted to obtain a shear wave velocity. As previously covered, there are significant distorting factors that can affect the measured signals. This makes the interpretation of the shear wave velocity challenging.

Historically, bender element testing was performed using a square wave trigger signal. A square wave trigger signal is a sharp step in voltage applied to the trigger bender element. For square wave trigger signals, three characteristic points in the received wave have been used to identify the arrival: the first marked deflection, the first reversal, and the first polarity cross (Viggiani and Atkinson, 1995). Of the three points, Viggiani and Atkinson (1995) and Jovicic et al. (1996) recommend the first reversal. These

Table 2.3: Type 3: a small amplitude cycle prior to the main shear pulse (Brignoli et al., 1996), selected arrival times are inconsistent

Soil	Equip.	$L_{tt}/dia.$	L_{tt}/λ
Peat, $w_c = 200\%$ (Arulnathan et al., 1998)	Trx.	2.1	7.3
Linear-elastic (Arulnathan et al., 1998)	F.E.	2.0	2.0
Linear-elastic (Arroyo et al., 2006)	F.E.	2	3.3
Linear-elastic (Arroyo et al., 2006)	F.E.	4	6.7
Sand (Brandenberg et al., 2008)	Chamber	–	1.3-5.4
Clay, saturated (Landon et al., 2004)	Block sample	–	3.9
Sand, saturated (Brignoli et al., 1996)	Trx.	2.0	2, 4
Sand, dry (Kumar and Madhusudhan, 2010)	RC	2.0	3.3
Sand (Brocanelli and Rinaldi, 1998)	Trx.	0.3	N/A (Square trigger)

points are depicted in Figure 2.7 with the first reversal labelled "1". Square waveforms are now used infrequently due to added uncertainty in the determination of the arrival time (Yamashita et al., 2009).

A sine pulse trigger is a single period of a sine pulse waveform. Sine pulse triggers have replaced square wave triggers as the prevalent bender element trigger waveform. Sine pulse bender element tests can be interpreted by selecting the first arrival, measuring the time difference between characteristic points, or finding the peak cross correlation time. The rest of this time-domain section concerns the interpretation of sine pulse trigger signals.

Sine pulse triggers require the selection of the sine pulse frequency. As previously covered, high sine pulse frequencies have been suggested to reduce the near field effect. Leong et al. (2009) suggested a propagation length to wavelength ratio greater than 3.33 (see Section 2.2.4). The wavelength

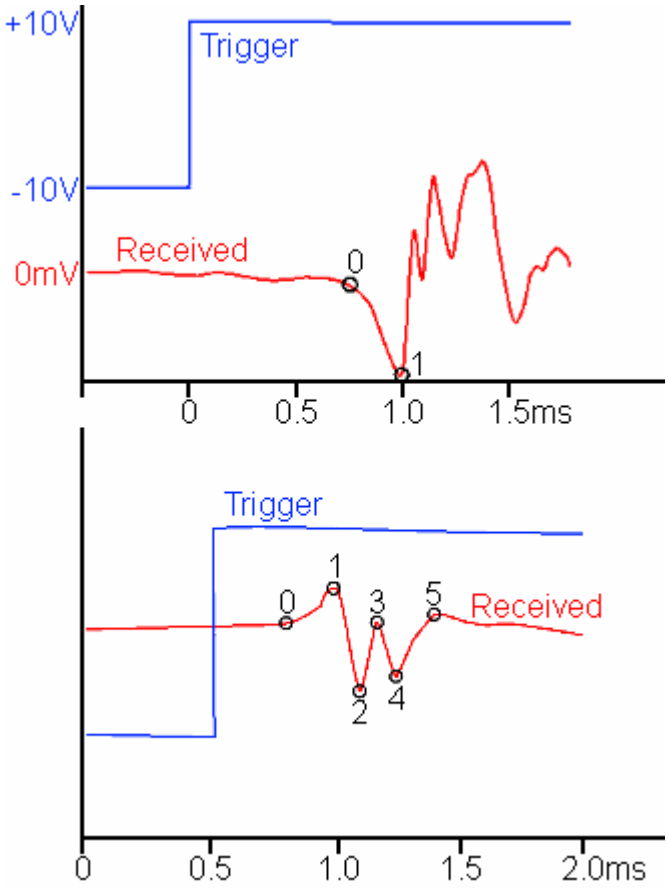

Figure 2.7: Characteristic received points from a square wave trigger: top adapted from Viggiani and Atkinson (1995), bottom adapted from Jovicic et al. (1996). Both sub-figures adapted with permission from Geotechnique, copyright Thomas Telford. This material may be downloaded for personal use only. Any other use requires prior permission of Thomas Telford.

(λ) is calculated from the selected trigger sine pulse frequency (f) and the interpreted shear wave velocity V_S using $V_S = \lambda f$. Camacho-Tauta et al. (2011) selected a sine pulse frequency that had the largest amplitude response and a propagation length to wave length ratio greater than 2.0. The selected sine pulse frequency alters the measured response wave and can

change the V_S interpretations. However, as previously stated, Rio (2006) correctly stressed that sine pulse signals should not be used to address any frequency dependent effects - including the near field. Sine pulse testing does not restrict the frequencies of the shear wave.

First arrival

The first arrival method entails picking the arrival time from a visual inspection of the received signal. This method is applicable to Type 1 signals (Table 2.1). These are the rarest signals, yet first arrival is the simplest and most common interpretation method. In Type 2 and especially Type 3 signals, the distortion will mask the first arrival. In an international parallel bender element test on Toyoura Sand, Yamashita et al. (2009) found that different laboratories measured similar waveforms but used different points as the first arrival. Type 2 signals may be incorrectly interpreted by selecting a point in the near field as the arrival or by overcompensating for an observed near field effect. On Type 3 signals, it is not clear if the first low amplitude pulse is the arrival or the first major pulse is the arrival.

Characteristic points

The response to sine pulse triggers can be interpreted by measuring the time differences between characteristic points on both signals. For example, the peak-peak points compare the peak in the trigger signal to the first peak in the response signal. The trough-trough points compare the first minimum points. Compared to the first arrival method, this is less subjective. This method can be used to interpret Type 1 or Type 2 signals. On Type 3 signals it is not clear if the first low amplitude cycle or subsequent major amplitude cycle should be used to find the characteristic points.

Arulnathan et al. (1998) found that the characteristic points difference required a wavelength to bender element penetration length ratio (λ/l_b) less than 8 for peak-peak, and less than 4 for cross correlation. If λ/l_b exceeded these limits, travel times were underestimated and V_S was overestimated.

Another problem with the characteristic points interpretation is that

the input sine pulse frequency is often different than the response pulse frequency. This systematically alters the time difference between the peak-peak and trough-trough points based on the selected trigger frequency. For example, if a 4 kHz and 6 kHz sine pulse both resulted in an equivalent 5 kHz sine pulse response, then the characteristic points on the 6 kHz test will result in a slower V_S then the 4 kHz sine pulse trigger.

Cross correlation

Viggiani and Atkinson (1995) regarded the cross correlation results as more accurate than the first arrival or time difference between characteristic points. The cross-correlation function compares the entire trigger signal to the response signal. The maximum cross correlation value occurs at the time offset for the trigger signal which results in the best overlap of the response signal. Equation 2.2 is used to calculate the cross-correlation between two signals (Bendat and Piersol, 2010). In this equation, c_{xy} is the cross correlation, r is an index from 0 to N-1, Δt is the sampling interval, N is the number of samples, x is the discrete input signal and y is the discrete output signal.

$$c_{xy}(r\Delta t) = \frac{1}{N-r}\sum_{n=1}^{N-r} x_n y_{n+r} \tag{2.2}$$

The maximum cross correlation value occurs at the time offset which results in the strongest overlap between the two signals. For sine pulse tests, the cross correlation function results in a series of peaks. Cross correlation results can be misleading when constructive and destructive interference changes the amplitudes of peaks in the received signal. The cross correlation peak corresponding to the arrival may be less than the amplitude of a subsequent peak. This was observed in a numerical model by Arroyo et al. (2006). Cross-correlation methods suffer from the same problem as characteristic points for Type 3 signals. The trigger signal and response signals are different waveforms due to the frequency dependence of the bender elements (Lee and Santamarina, 2006).

Auto-correlation

Auto-correlation is the same as cross correlation, only the response signal is compared to itself. Lee and Santamarina (2005) showed that this technique can isolate the effect of the soil from the bender elements. A bender element system is comprised of a series of components including peripheral electronics, the bender element trigger, the soil, the bender element response, and signal amplifiers. Each component of the bender element system contributes to the distortion and translation from the input trigger signal to the measured response signal. Auto-correlation requires received signals that include the arrival of the first shear wave and a subsequent arrival of the twice reflected shear wave. The time difference between these two arrivals is calculated using the auto-correlation function. The advantage of this is that both arriving shear waves have experienced the same time lag due to the bender elements and peripheral electronics. The disadvantage of this method is that it requires an observed twice reflected wave. This can be challenging in longer propagation lengths or in slender specimens. Arulnathan et al. (1998) also noted that comparing reflected signals does not account for non-1D wave travel.

Matching simulated signals

Lee and Santamarina (2005) presented a method to estimate the arrival time by matching the response to simulated received bender element signals. The bender element cantilever beams were modelled as single degree of freedom systems with a resonant frequency and damping. The soil was modelled using the analytical results from Sánchez-Salinero et al. (1986). The model parameters were adjusted until the simulated signal agreed with the response signal. This may be applicable when significant near field effects obscure the arrival of the shear wave.

Time domain summary

In summary, square wave trigger signals are no longer used in bender element research. Type 1 signals may be easily interpreted with the simplest time

domain method - the selection of the first arrival point. Type 2 signals can be interpreted with the characteristic points or cross correlation method if the measured response signal is similar to the selected trigger signal, or by matching simulated signals. Type 3 signals are challenging. They can give misleading results using the time domain methods. Type 3 signals have a leading low amplitude pulse. In a numerical model (Arroyo et al., 2006) found that no characteristic of the received signal corresponded to the shear wave arrival. Type 3 signals cannot be confidently interpreted with time domain techniques.

2.2.8 Interpreting V_S in the frequency domain

Various techniques to obtain a shear wave velocity have been developed in the frequency domain. The frequency domain may be more applicable to Type 3 signals. The frequency domain representation of a time domain signal is a summation of continuous sinusoids. Each sinusoid can be represented by $g(t) = A \times \sin(2\pi ft + \theta)$. This function is defined by three parameters: the amplitude (A), the frequency (f), and the phase angle (θ). The change in the phase angle between the trigger signal and response signal is used to calculate the shear wave propagation time.

Frequency domain methods used the Discrete Fourier Transform to convert the finite length time-based signals into a finite array of complex numbers. Each complex number corresponds to a single frequency and can be used to calculate the sinusoid magnitude and phase angle. The Fast Fourier Transform (FFT) uses the Cooley-Turkey algorithm (or variation) to perform Discrete Fourier Transforms on finite sized datasets. The FFT is not an approximation - the exact time domain signal can be recovered from the inverse Fourier Transform. No information is lost on the conversion between the time domain and frequency domain.

The change in the phase angle between the trigger and response signals is called the phase shift. For a given function of time, $g(t)$, a positive shift along the time axis results in $g(t - \Delta t)$. By substituting this into the sinusoidal function, this results in a phase shift of: $\Delta\theta = -2\pi f \Delta t$. From the variation

in phase shift and frequency the propagation time can be calculated.

Figure 2.8 shows the relationship between an example trigger signal and response signal in both the time domain and frequency domain. This signal is a single sinusoid with a frequency of 5 kHz. In the time domain the response follows the trigger. Since the signal is periodic, there is no way to know how many cycles have occurred between the trigger and response signal. More information is needed. The frequency domain is plotted in a polar plot. The phase angle for the response is behind the trigger. The signal is periodic and there is no way to know how many complete cycles behind the trigger is the response.

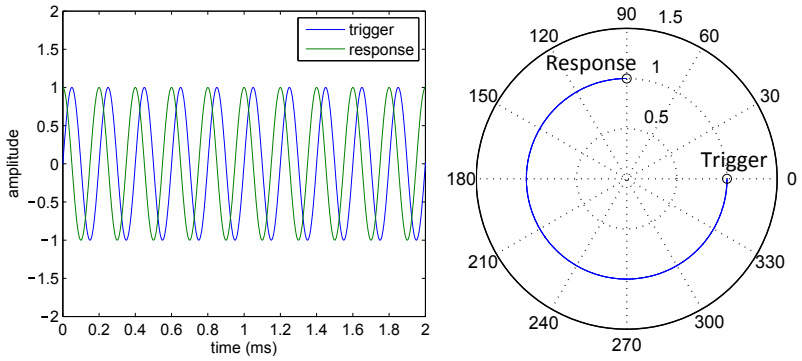

Figure 2.8: Example signals depicting the response following the trigger signal in the time domain $(-\Delta t)$ and frequency domain $(-\Delta\theta)$

There are two general approaches to adding the missing information required to interpret periodic signals in the frequency domain. The propagation time can be assumed constant and additional frequencies can be tested. A small change in the frequency will necessarily change the phase angle if δt is constant and independent of frequency. This results in a group velocity - the velocity of a band of frequencies. The second approach is to figure out how many cycles have occurred and quantify the integer n. Then the total phase shift can be calculated and used to find the propagation time for a single frequency. This results in the phase velocity. These two

velocities are further described in Section 2.2.8.

Equation 2.3 is used to calculate the phase shift between the trigger signal, $x(t)$, and response signal, $y(t)$. In this equation FFT is the Fast Fourier Transform. The $imag()$ function returns the imaginary component of the complex number and the $real()$ function returns the real component. This equation is used to calculate the phase shift between all of the sinusoid components in the trigger and response signals.

$$\Delta\theta = tan^{-1}\left(\frac{imag\left(FFT(y(t))/FFT(x(t))\right)}{real\left(FFT(y(t))/FFT(x(t))\right)}\right) \tag{2.3}$$

Frequency domain approaches use signals with a wide band of frequency contents. Early work used sine pulses (Sachse and Pao, 1978; Viggiani and Atkinson, 1995). Modern work employs linear swept sine waves (Greening and Nash, 2004; Viana da Fonseca et al., 2009). A linear swept sine signal increases the frequency with time over the duration of the trigger signal. A typical signal would increase the frequency from 0 to 10 kHz over 20 ms, $g(t) = \sin(2\pi(500000t)t)$, where $f(t) = 500000t$ (Hz) and t is in seconds.

An advantage of frequency domain interpretations is the quantification of the bender element operating frequency range. It can be characterized by the coherence between the trigger and response signals. The coherence is a function of frequency that ranges between 0 and 1 depending on the linearity of the relationship between the trigger and response. Coherence values less than 1.0 are due to noise, a non-linear relationship between the trigger and response, and/or the response being a function of additional input signals (Bendat and Piersol, 2010). Greening and Nash (2004) found the coherence between bender element trigger and response waves dropped off rapidly below 0.5 kHz. Viana da Fonseca et al. (2009) calculated coherence functions where the low frequency drop off depended on the applied stress and ranged from 1 kHz for a mean stress of 100 kPa to 8 kHz under a mean stress of 800 kPa. Bender elements cannot measure low-frequency shear waves. Only a small fraction of the mechanical signal is linearly converted to a voltage and it is obscured by noise. The additional information provided by the coherence function is not typically obtained with time-domain

interpretations.

The challenge in all frequency domain approaches is due to uncertainty in the phase degeneracy. Only the relative phase shift is calculated with Equation 2.3. The absolute phase shift, the total shift in the phase angle between the trigger and response signals, is not known.

Phase degeneracy

The phase angle in a sinusoidal signal can only be calculated between $-\pi$ and $+\pi$. For bender element applications this range is too small to directly calculate the propagation time. For example, a hypothetical specimen with a shear wave velocity of 200m/s and a propagation length of 120 mm has a propagation time of 0.6 ms. This propagation time would result in a 5 kHz sinusoid having an absolute phase shift of -18.85 radians ($\Delta\theta = -2\pi f \Delta t$). However, the measured relative phase shift would be 0 radians. The unobtainable phase degeneracy is $-3 \times 2\pi$.

The phase shift calculated with Equation 2.3 results in discontinuities at frequencies where the the phase shift changes from $-\pi$ to $+\pi$ and vice versa. An unwrapping algorithm is used to remove these discontinuities. This is possible because the phase-shift against frequency is a continuous curve. Any observed discontinuities are always equal to 2π. They are easily corrected by incrementing or decrementing the remainder of the signal by 2π.

The unwrapping procedure may not correct all of the phase degeneracy between the trigger and response signals. Bender elements do not operate at low frequencies. An integer (non-fraction) number of phase degeneracy discontinuities may occur over frequencies below the bender element operating range. Therefore, the unwrapped phase shift is still a relative phase shift between the trigger and response frequency components. It cannot be used directly to calculate the propagation time. The difference between the unwrapped relative phase shift and the unknown absolute phase shift is the phase offset or phase degeneracy.

The way the phase degeneracy is addressed leads to two possible fre-

quency domain velocities: the group velocity or the phase velocity.

Group versus phase velocity

The group velocity refers to the propagation speed of a band of frequencies. The phase velocity is the speed of a single frequency component. In a non-dispersive linear elastic continuum, these two velocities must be equal. In dispersive media the velocity is a function of frequency and the group and phase velocities will be different.

The cross spectrum technique solves for the propagation time using the slope of the phase shift against frequency, $\Delta t = (-1/(2\pi))(\Delta\theta/\Delta f)$. This slope is calculated from the unwrapped relative phase shift using linear regression over the frequency range observed to have high coherence. Cross-spectrum techniques have been found to result in slower velocities than Time Domain results (Greening and Nash, 2004; Viana da Fonseca et al., 2009; Yamashita et al., 2009). The cross-spectrum technique and the time domain methods determine the group velocity.

Viana da Fonseca et al. (2009) found that the best fit lines over the range of frequencies corresponding to high coherence values gave inconsistent results over different frequency windows. They calculated the best fit line for a moving frequency window over the unwrapped phase shift. Each best fit line has a corresponding squared correlation coefficient (r^2) indicating how linear the phase shift is within the moving frequency window. They found that for frequency windows of 4 and 6 kHz, the arrival time corresponding to the slope ($\Delta\theta/\Delta f$) with the maximum r^2 appeared to agree with the selected first arrival from time domain results.

Greening and Nash (2004) presented a different variation on the cross-spectrum technique for calculating the phase offset. They solved for the phase offset that resulted in the minimum variance in the resulting velocity over the coherent frequency range. This method does not use a best fit line over the phase shift. Using the calculated phase offset to correct the unwrapped phase shift, they were then able to estimate a phase velocity over the bender element frequency operating range. However, it is not clear

if they are actually calculating the absolute relative phase shift using this technique.

Boonyatee et al. (2009) presented a variable path length method which measured the phase velocity using a continuous sine wave. This method calculated the change in phase shift between the trigger and receiver as the receiver element is penetrated from 5 to 11 mm into the specimen. This resulted in a plot of the change in propagation time against the change in propagation length, which led to a determination of the phase velocity at the selected continuous sine wave frequency. An advantage of this system is that any time lag due to the receiver element transfer function or peripheral electronics is absolute and does not change the measured phase velocity. The disadvantages are the requirement of a bender element that can penetrate into the specimen during an experiment, it is a destructive measure of the phase velocity. It also results in a single measured phase velocity instead of measurements over the bender element frequency range.

Blewett et al. (1999) measured the phase velocity by comparing the response due to a square wave trigger to the response due to a continuous sine trigger. This also resulted in a measured phase velocity at a single frequency, instead of over the operating range of the bender elements. The square wave trigger response was used to figure out which cycle in the response was due to the absolute phase shift from the trigger.

In dispersive systems, the response signal experiences additional distortion. In dispersive systems, the velocity is a function of frequency and the group and phase velocities are different. Sachse and Pao (1978) identified different origins of dispersion as geometric, material, scattering, dissipative, and non-linear. Geometric dispersion has been demonstrated by Arroyo et al. (2006) in a numerical solution for a propagating pulse wave under various sample sizes and boundary conditions. Material dispersion includes the frequency dependence described by the Biot theory for shear wave propagation in saturated soils (Biot, 1956a,b). Scattering dispersion is due to inhomogeneities in the specimen. It can occur when the wavelength approaches the size of the particles or specimen features. Dissipative dispersion is the frequency dependent attenuation of the waves. Non-linear dispersion is the

possible dependence of the shear wave on the amplitude. All of these dispersion effects add to the distortion of the trigger signal as it propagates through real soils. Additionally, the conversion between electrical and mechanical signals and vice-versa by the bender elements is not linear. The bender elements themselves contribute to the frequency dispersion of the measuring system.

In non-dispersive systems the group and phase velocities are identical. This means that the phase shift against frequency is a perfect straight line that intercepts the origin. In the time domain, the response signal is a time shifted and amplitude scaled version of the trigger signal. In a non-dispersive system, the response signal waveform is identical to the trigger signal waveform.

Frequency domain summary

Frequency Domain methods provide an alternative to Time Domain methods. The Frequency Domain methods interpret the shear wave velocity from the phase shift of the frequency components. The challenge in Frequency Domain methods is accounting for the phase degeneracy, also known as the phase offset, between the absolute phase shift and the measured relative phase shift. Cross-spectrum techniques address this challenge by calculating the slope of the phase-shift. This slope is independent of the phase offset. However, cross-spectrum techniques result in a group velocity that is sensitive to dispersion. Therefore, the measured V_S will vary depending on the method of interpretation and the frequency window used in the cross-spectrum technique.

2.2.9 Summary

Interpreting the shear wave propagation time with bender elements can be challenging due to numerous factors that contribute to the measured response signal. The bender elements should be shielded to avoid electronic cross-talk interference from the trigger element. Series type elements can be shielded with a coating of electrically grounded conductive paint. Parallel

type elements are inherently shielded if the outer plates are wired to ground. Signal stacking is a simple procedure to amplify the systematic features in the collected signals. The systematic features include the shear wave and interference from the near field and reflections. Bender element signals can be classified according to the observed interference.

Bender element testing can be interpreted in the time domain and frequency domain. The selection of the first-arrival point is subjective and variable between labs with qualitatively similar signals (Yamashita et al., 2009). The difference between characteristic points is affected by the frequency contents in the trigger and response signals. The problem with the cross-correlation method is that the peak corresponding to the arrival is not clear. The applicable interpretation method depends on type of observed signal. Type 3 signals have reflected wave interference and include an apparent low amplitude pre-arrival cycle. No characteristic point in a received Type 3 signal corresponds to the shear wave arrival (Arroyo et al., 2006). Frequency domain interpretations may be more applicable to Type 3 signals. However, existing Frequency Domain methods are sensitive to dispersion and bender element transform functions are dispersive (Alvarado and Coop, 2012).

Significant differences in shear wave velocity measurements can occur due to variations in the installation of the bender elements, types of signal distortion, and interpretation technique. Bender element testing to confidently acquire V_S is not a simple exercise.

2.3 Factors influencing shear wave propagation in soil

The shear wave velocity is affected by many soil factors, some of these include the fabric, effective stress state, void ratio, and even ageing. Some of the later work reported in this thesis involves the development of an empirical relationship for G_0. The functional form of this empirical relationship has a theoretical underpinning established from micro-mechanical derivations. This section covers the factors that influence G_0 and hence, V_S.

Soil behaviour is governed by the physical interaction of many particles of many different shapes, sizes, orientations, and contacts. To understand the propagation of elastic waves, the soil can be idealized, such as a linear elastic continuum or a particulate material where the particle contact interaction is assumed to follow Hertz-Mindlin contact behaviour between perfect mono-sized elastic spheres. These models can be used to predict the effect of changes in the medium stiffness, density, effective stress, void ratio, and particle contact behaviour. The factors that govern shear wave propagation velocity through soil have both theoretical and empirical support.

2.3.1 Saturation

The shear wave velocity is faster in dry soil than saturated soil. However, the change in V_S between dry and saturated can be calculated assuming that G_0 is constant. At a lower bulk density in dry soil, V_S must increase to maintain a constant G_0. Youn et al. (2008) published shear wave velocities measured from dry and saturated specimens of Toyoura and Silica Sand from bender elements and resonant column testing. At the same effective stress and similar void ratios, the dry soil had a significantly higher G_0 than the saturated soil. A similar observation was make by Hardin and Richart Jr (1963). They observed a 15 % reduction in G_0 with as little as 1.4 % moisture content compared to the dry specimen. A similar observation on Ottawa Sand was made by Velea et al. (2000). The source of this drop in G_0 with small initial moisture changes was attributed to matrix suction and surface tension by Cho and Santamarina (2001). After this drastic reduction, Hardin and Richart Jr (1963) observed little additional decrease in G_0 with saturation; the change in V_S with bulk density could be predicted with Equation 2.1.

Therefore, saturation does not affect G_0 except when suction increases the effective stress. Saturation does affect V_S by changing the bulk density.

2.3.2 Micro-mechanical G_0 characterization

The functional form of successful empirical relationships for G_0 follows theoretical micro-mechanical derivations. An underlying theory is an important aspect for empirical relationships (Wroth, 1984). The additional significance of this is that it provides a theoretical meaning for the characterized empirical coefficients.

G_0 depends on the soil particle interactions. A micro-mechanical approach to soil behaviour estimates macro-scale soil properties by averaging micro-scale particle interactions. Closed-form solutions for the macro-scale G_0 have been published (Chang et al., 1991; Petrakis and Dobry, 1989; Yimsiri and Soga, 2000) that account for the applied macro-scale effective stress, the soil particle fabric, and the soil particle interaction behaviour.

Petrakis and Dobry (1989) presented solutions for G_0 for symmetric idealized fabrics under hydrostatic stress with Hertz-Mindlin contact behaviour. These idealized fabrics included Simple Cubic Array, Body Centered Cubic Array, and Face Centered Cubic Array. Hertz-Mindlin theory is a complete contact model that describes the response between two deformable perfectly linear-elastic uniform spheres. It only requires two elastic constants for the soil particles. Petrakis and Dobry (1989) observed that the theoretical micro-mechanical G_0 was dependent on the number of contacts per particle, C_N, and that C_N can change significantly with the void ratio remaining essentially constant.

Chang et al. (1991) presented a closed form solution for G_0 for isotropic fabric, hydrostatic stress, and with Hertz-Mindlin particle contact behaviour. Their equation has been reformulated into three terms in Equation 2.4.

$$G_0 = \frac{5-4\nu_p}{10-5\nu_p}\left(\frac{G_p\sqrt{3}}{\sqrt{2\pi(1-\nu_p)}}\right)^{2/3}\left(\frac{C_N}{1+e}\right)^{2/3}\left(\sigma_0'\right)^{1/3} \tag{2.4}$$

The first term, $\frac{5-4\nu_p}{10-5\nu_p}\left(\frac{G_p\sqrt{3}}{\sqrt{2\pi(1-\nu_p)}}\right)^{2/3}$, is constant and is defined by the linear elastic properties of the material forming the soil particles: G_p and ν_p (elastic shear modulus and Poisson's ratio). The second term, $\left(\frac{C_N}{1+e}\right)^{2/3}$,

represents the fabric. The last term contains the dependence of the Hertz-Mindlin inter-particle contact behaviour on the hydrostatic effective stress.

Emeriault and Chang (1997) observed that this equation over predicts the stiffness measured for quartz and attributes it to the averaging process to convert micro to macro behaviour. For a sample of spherical quartz particles with a void ratio of 0.8 under 100 kPa of effective hydrostatic stress, Equation 2.4 results in an unrealistically large estimated shear stiffness of 579 MPa. This value was calculated using the elastic properties of natural quartz: $G_p = 46.91$ GPa and $\nu_p = 0.0600$ (Heyliger et al., 2003). This stiffness calculation used an estimated C_N of 6.88 from a relationship presented by Chang et al. (1991), $C_N = 13.28 - 8e$. Assuming the soil is dry and Quartz has a specific gravity of 2.647, this void ratio results in a bulk density of 1470 kg/m^3. The shear wave velocity for this material using Equation 2.1 is then 627 m/s. This stiffness and velocity exceed the range of values typically measured in soil.

Therefore, Equation 2.4 is not directly applicable to real soil measurements. If the particle properties and fabric were measured, it would not be able to predict the shear wave velocity or G_0. However, it does provide an informative analogue for soil behaviour. A stiffer G_0 would be expected in soils comprised of stiffer particles, in closely packed soils with higher coordination numbers, and in solids under higher effective stresses.

Much of the early development of empirical G_0 relationships involved B.O. Hardin and his colleagues performing resonant column testing. The form of the early empirical relationship for G_0 is Equation 2.5:

$$G_0 = Af(e)\sigma_0^{'n} \tag{2.5}$$

This equation includes two empirical coefficients (A and n) and a function of the void ratio, f(e). The comparison of this equation and Equation 2.4 suggests that the leading A coefficient depends on the particle properties, f(e) is a function of the fabric, and the n exponent is 1/3 for Hertz-Mindlin contact behaviour.

Fam et al. (2002) presented an experimental study that changed the co-

ordination number without changing the effective stress. They prepared dry specimens of sand with salt grains. These dry specimens were consolidated and then saturated. The saturation caused the salt particles to dissolve. This increased the void ratio and transferred more load to the soil particle force chains. They observed a 25 % drop in the shear wave velocity once the salt was removed. By accounting for the effect of the change in mass and void ratio, they concluded that 10 % of this V_S drop was due to a change in soil fabric. Therefore, a reduction in the coordination number has a larger effect on V_S than an increase in the strength of the force chains. This was confirmed in a DEM model by Somfai et al. (2005). They observed that the strength of the force chains affected the amplitude of the propagating shear wave, but did not affect the velocity.

Hardin and Richart Jr (1963) demonstrated that V_S was not related to the relative density, just the void ratio. For a single soil, there will be a relationship between V_S and the relative density. However, this relationship will not be applicable to other soils. Relative density relationships are not applicable beyond the immediate context over which it was developed. V_S cannot be used directly to estimate the relative density of a soil.

Hardin and Black (1966) proposed three equations for f(e). The first two f(e) equations were for round grained Ottawa sand at low stresses, Equation 2.6, and high stresses, Equation 2.7. The high-stress f(e) equation is very similar to Equation 2.6 and was never used again. The third equation, Equation 2.8, was for angular crushed quartz silt. These equations imply that V_S and C_N are more sensitive to void ratio changes in angular soils than in round grained soil. These equations did not work with high void ratio soils. Hardin and Blandford (1989) proposed Equation 2.9, which did not have this shortcoming.

$$f(e) = \frac{(2.17 - e)^2}{1 + e} \tag{2.6}$$

$$f(e) = \frac{(2.12 - e)^2}{1 + e} \tag{2.7}$$

$$f(e) = \frac{(2.97 - e)^2}{1 + e} \tag{2.8}$$

$$f(e) = \frac{1}{0.3 + 0.7e^2} \tag{2.9}$$

Hardin and Black (1968) investigated the application of forms of Equation 2.5 in normally consolidated clays. They found that Equation 2.8 was applicable for clays if the void ratio did not approach 2.97. They further validated this f(e) application with more clay soils in a discussion of this article (Hardin and Black, 1969).

Using the proposed f(e) equations, this early empirical relationship (Equation 2.5) was found to be broadly applicable from clays through sands (Hardin and Drnevich, 1972). The form of this empirical equation is similar to the micro-mechanical solution. One drawback is that this relationship is in terms of hydrostatic effective stress, i.e. $K_0 = 1.0$, which is rarely encountered in-situ.

2.3.3 Anisotropic effective stress state

The anisotropic stress state can be completely described by three principal stresses and an orientation. Principal stress directions are normal to planes with zero shear stress. Principal stresses are given the symbols σ_1, σ_2, and σ_3. A shear wave propagates in one direction with particle motion in the perpendicular direction. It has been found that the shear wave propagation velocity only depends on the effective stresses in the directions of wave propagation and particle motion (Bellotti et al., 1996; Hardin, 1980; Roesler, 1979; Wang and Mok, 2008). It is independent of the out-of-plane effective stress. Therefore, it is incorrect to use the mean effective stress, p, in empirical G_0 and V_S equations.

Roesler (1979) developed the experimental programme and results to demonstrate this independence on the intermediate stresses. It was experimentally demonstrated on a $30cm^3$ specimen of dry sand. This specimen had one internal excitation source and two internal transducers to measure

the shear wave velocity propagating in one direction. A vacuum pressure was used to apply an average effective stress to the soil. The top of the cubic specimen was loaded to increase one principal effective stress. The specimen was rotated to align the shear wave propagation direction and particle motion with each of the three principal stresses. Figure 2.9a shows the effect of increasing the stress aligned with the shear wave propagation direction. Figure 2.9b shows the effect of increasing the stress in the direction of shear wave particle motion. Figure 2.9c shows the effect of increasing the out-of-plane effective stress. In Figure 2.9c the mean effective stress $(\sigma_1+\sigma_2+\sigma_3)/3$ is increasing and the shear wave velocity is constant. Therefore, any empirical formulation for V_S or G_0 in terms of the mean stress is fundamentally flawed, even though it would work if two of the principal stresses are the same.

The results by Roesler (1979) depicted in Figure 2.9c are conclusive. They were immediately supported by Hardin (1980) and further confirmation was provided in a later study by Bellotti et al. (1996) and then by Wang and Mok (2008). All of these investigations confirmed the independence of V_S on the out-of-plane effective stress.

Hardin and Blandford (1989) reformulated their empirical equation for G_0 to account for the observations by Roesler (1979).

2.3.4 Age and Stiffness

Ageing affects G_0. Ageing is observed in reconstituted laboratory specimens over a short time frame. Natural deposits continue to age for much longer geological-scale durations. G_0 increases with time have been measured with resonant column testing (Afifi and Richart, 1973; Anderson and Stokoe, 1978; Hardin and Richart Jr, 1963) and bender elements (Baxter and Mitchell, 2004) in the laboratory.

Hardin and Richart Jr (1963) observed a strong time-dependence in V_S for crushed quartz silt. Once they recognized that age duration was a variable, they kept it constant between experiments. They were able to develop an empirical relationship for G_0 in terms of stress and void ratio by perform-

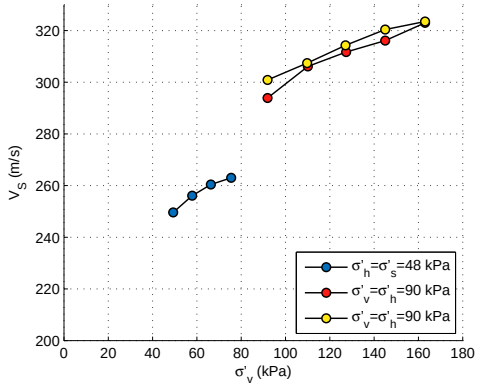

(a) V_S dependence on σ'_v

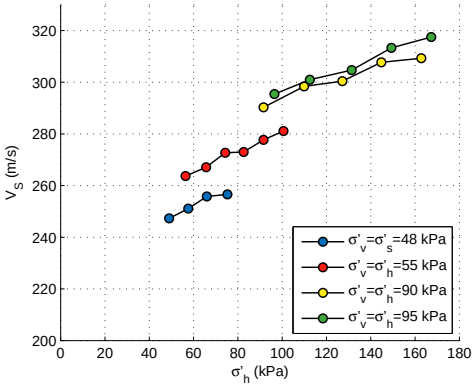

(b) V_S dependence on σ'_h

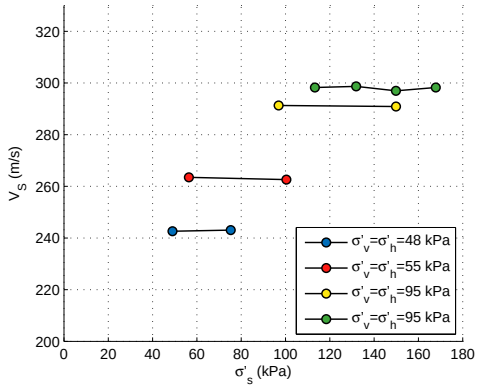

(c) V_S dependence on σ'_s

Figure 2.9: Dependence of V_S on anisotropic stresses with σ'_v equal to the stress in the wave propagation direction, σ'_h the stress in the particle motion direction, and σ'_s the stress orthogonal to both the wave direction and particle motion, adapted from Roesler (1979). Adapted with permission from the American Society of Civil Engineers. This material may be downloaded for personal use only. Any other use requires prior permission of the American Society of Civil Engineers.

ing resonant column testing after a constant amount of elapsed time at each stress state. They observed that age has less of an influence in Ottawa Sand than in quartz silt. Hardin and Black (1968) found that the increase in density from small volumetric creep changes did not account for the observed

effect of age on G_0. Hardin and Black (1969) stated that the stiffness that built up during ageing was sensitive to disturbance and could be partially or total destroyed by changes in effective stress. However, little evidence was provided for this conclusion.

Afifi and Richart (1973) further investigated the effect of time on G_0. The effect was quantified using Equation 2.10. This quantification was first used by Afifi and Richart (1973) and later termed N_G by Anderson and Stokoe (1978).

$$N_G = \frac{\Delta G_0}{G_{1000}\left(log_{10}\left(\Delta t\right)\right)} \tag{2.10}$$

Afifi and Richart (1973) and Anderson and Stokoe (1978) plotted G_0 against log-time. In kaolinite, Afifi and Richart (1973) observed a steepening of G_0 against log-time when it became log-linear. Conversely, Anderson and Stokoe (1978) observed a flattening of the rate of increase in G_0 measurements when it became log-linear. The conflict between these observations has not been resolved. The increase in G_0 with time is normalized to G_0 measured at 1000 minutes(G_{1000}) to avoid these initial G_0 effects. Anderson and Stokoe (1978) observed that in sands the behaviour was log-linear by the time they were able to acquire their first measurement. They speculated that it may not be log-linear at very short age durations due to visco-elastic effects.

Table 2.4 details the results of various experimental investigations into factors that influence N_G. The expected N_G factor for clean sands is less than 3 % (Afifi and Richart, 1973; Anderson and Stokoe, 1978). V_S measurements against time require careful interpretation to observe this small increase. The current state of bender element practice may be unable to confidently resolve the increase in V_S due to ageing.

Mitchell (2008) reviews the hypothesized mechanisms for the source of the effect of ageing on G_0. He concludes that a chemical solution-precipitation-cementation hypothesis is unlikely to account for the observed stiffness increase in many experiments. First, Baxter and Mitchell (2004) did not observe a dependence on temperature. Second, it can not account for the

Table 2.4: Experimental investigations into factors influencing the ageing effect on G_0

Property	Effect
Particle size	Fine grained: NC clay N_G=5-20 %, clean sands: N_G=1-3 % (Afifi and Richart, 1973; Anderson and Stokoe, 1978)
Saturation	Saturated kaolinite: N_G=11 %, dry kaolinite: N_G=6% (Afifi and Richart, 1973)
OCR-Clays	NC clay N_G=5-20 %, OC clay N_G=3-10 % (Afifi and Richart, 1973; Anderson and Stokoe, 1978)
OCR-Sands	N_G is higher for NC sands. However there is a measurable increase in G_0 after unloading or reloading (Jovicic and Coop, 1997)
Plasticity index	N_G increases with PI (Mitchell, 2008)
Undrained shear strength	N_G decreases with increasing s_u (Anderson and Stokoe, 1978)
Void ratio	N_G has been observed to both increase (Anderson and Stokoe, 1978) and decrease (Baxter and Mitchell, 2004) with increased void ratio
Fines content	N_G increases with fines content (Anderson and Stokoe, 1978)
Confining stress	N_G increases (Anderson and Stokoe, 1978)
Temperature	No conclusive effect in Evanston beach sand and Density sand (Baxter and Mitchell, 2004)
Pore fluid	N_G in water was higher than in ethylene glycol (Baxter and Mitchell, 2004)
Stress ratio	N_G increases with $R = \sigma'_v/\sigma'_h$ (Mitchell, 2008)

observed stiffness increase in dry sands. Additionally, Clayton (2011) noted that cementation has a huge effect on G_0 and the observed effect of ageing is small. A microbiological hypothesis may influence ageing under special environmental circumstances, but not globally as observed in almost every ageing investigation. After an examination of the observed effects of ageing, Mitchell (2008) concludes the the physical rearrangement and a stress redistribution process plays the dominant role in the ageing phenomenon. He views this process as a secondary compression for sands where the soil

skeleton adjusts to the boundary conditions. Petrakis and Dobry (1989) and Santamarina and Cascante (1996) both noted that significant changes in C_N can occur with negligible changes on the void ratio. The physical rearrangement mechanism can account for the observed ageing increase in G_0.

2.3.5 Summary

Soil models are simplifications of a complex medium. Linear elastic and Hertz-Mindlin assumptions have been used to gain theoretical insight into factors affecting small strain wave propagation. The behaviour of these simple models have empirical support. The shear wave velocity and small strain stiffness depend on in-plane effective stress state, void ratio, fabric, coordination number, and age. The shear wave velocity is a soil measure that can be obtained in-situ through seismic techniques and in the laboratory through bender element and resonant column testing.

2.4 Stiffness degradation with strain

As introduced in Chapter 1, the shear stiffness of a soil decreases as additional shear stress is applied. In soils, beyond a very small linear elastic region, the tangent stiffness and secant stiffness both depend on the shear strain. The tangent stiffness is the local slope of the shear stress against shear strain. The secant stiffness is the total change in shear stress divided by the total shear strain since the start of a shear path. The tangent stiffness is a derivative. It is very sensitive to noise and is difficult to quantify experimentally. The secant stiffness is easy to quantify once the strains exceed the measurement uncertainty. Furthermore, the secant stiffness can be used to directly convert total applied shear stress to shear strain and vice versa.

Many soil variables govern the secant stiffness curves. To investigate the effect of these variables it is useful to normalize the curves. Shozen (2001) normalized the secant stiffness degradation curves to compare different test conditions. He normalized G_{sec} using the measured secant stiffness at 0.03 % shear strain and 10 minutes of ageing along a conventional stress path, if the

comparison was between experiments at the same stress ratio. Otherwise, he normalized the secant stiffness with the mean effective stress or the mean effective stress to the power of 0.6. Lam (2003) compared different test conditions by normalizing the secant stiffness with the mean stress raised to a power of 0.7.

Measuring the shear wave velocity permits the normalization of G_{sec} with G_0. This is useful for comparing different experimental conditions and to other published observations. More importantly, V_S can be measured in-situ to acquire G_0. This can be combined with published normalized curves to estimate the in-situ deformation properties of soils. This is particularly useful in soils that cannot be routinely sampled undisturbed - such as sands and gravels.

Ageing results in a very small increase in G_0 in sands, significant increase on the secant modulus over the small strain range (Howie et al., 2002; Lam, 2003; Shozen, 2001), and large strain strength measurements are unaffected (Howie et al., 2002; Lam, 2003; Mitchell, 2008; Shozen, 2001). This suggests that the shape of the G_{sec}/G_0 versus shear strain will change with age.

Darendeli (2001) proposed a hyperbolic model describing the shape of the normalized G_{sec}/G_0 curves. His model had two parameters: a reference shear strain to 50% modulus degradation and a curvature parameter. Empirical formulas for these parameters were developed by Wichtmann and Triantafyllidis (2013) and Oztoprak and Bolton (2013). This same approach can be used to quantify the effect of ageing on the change in shape of the G_{sec}/G_0 curves.

Fitting G_{sec}/G_0 curves with hyperbolic relationships reduces the entire normalized stiffness curve to two or three variables depending on the hyperbolic model. Seed et al. (1984) and Seed et al. (1986) presented results for granular soils in terms of relative density, mean particle size, and mean effective stress. Wichtmann and Triantafyllidis (2013) characterized the effect of the uniformity coefficient and mean grain size on the degradation of G_{sec}/G_0 curves. This was accomplished using resonant column testing on a set of specimens with different particle size distributions. The specimens were created by mixing sieve-separated constituents of a natural quartz-sand. The

amplitude of the resonant column cycles was increased to measure the degradation from G_0 to 0.05 % shear strain. They fitted a hyperbolic curve to the calculated normalized stiffness degradation curves. They then empirically related the soil indices C_u and d_{50} to the hyperbolic curve coefficients. They found that the non-linear stiffness degradation was mostly independent of the mean grain size. Oztoprak and Bolton (2013) characterized the effect of mean effective stress, uniformity coefficient, relative density, and void ratio on the normalized shear stiffness curves for sands. They characterized these effects by fitting hyperbolic curves to a dataset of laboratory measurements. This dataset was developed by compiling and digitizing published stress-strain curves for sands. They then developed empirical relationships for the hyperbolic model coefficients based on these soil parameters. The properties required are frequently estimated (mean effective stress, relative density, void ratio) or measured (uniformity coefficient, mean particle size).

Equation 2.11 is the hyperbolic-strain stiffness model proposed by Oztoprak and Bolton (2013). Note that their equation was in terms of $\gamma = \varepsilon_a - \varepsilon_r$ for shear strain. The triaxial shear strain is $\varepsilon_q = 2/3\gamma$. This 2/3 scaler cancels out by taking the ratio of the shear strains and does not affect the equation or the coefficients.

$$\frac{G_{sec}}{G_0} = \frac{1}{1 + \left(\frac{\varepsilon_q - \varepsilon_{qe}}{\varepsilon_{qr}}\right)^a} \tag{2.11}$$

This hyperbolic model has three coefficients: ε_{qe}, ε_{qr}, and a. The ε_{qe} parameter is the elastic threshold strain. At strains below ε_{qe}, the secant stiffness equals the very small strain stiffness: $G_{sec} = G_0$. The ε_{qr} parameter is a reference strain that corresponds to G_{sec}/G_0=0.5. The a parameter is the curvature of the normalized secant stiffness curve. As this parameter increases, the behaviour becomes more brittle and the stiffness degradation becomes steeper. It becomes stiffer before the reference strain and softer beyond the reference strain. Figure 2.10 depicts the effect of these three variables using typical values.

Oztoprak and Bolton (2013) characterized the effect of the mean effective stress (p'), uniformity coefficient (C_u), relative density (Dr), and void

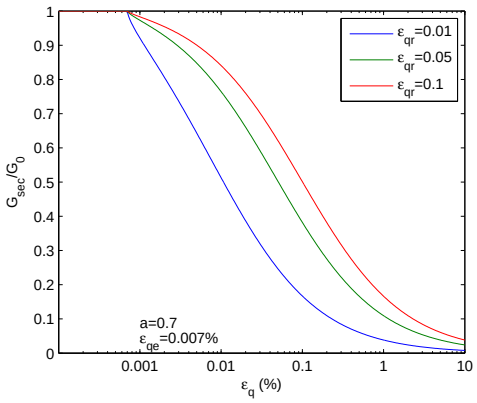

(a) Effect of reference strain

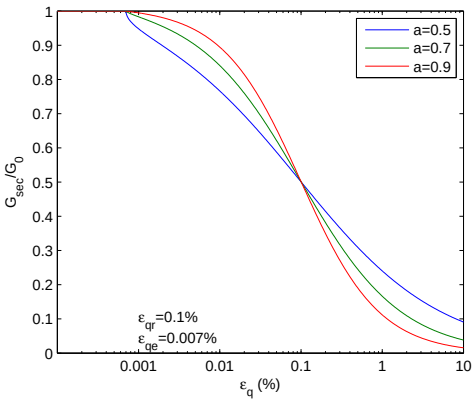

(b) Effect of curvature parameter

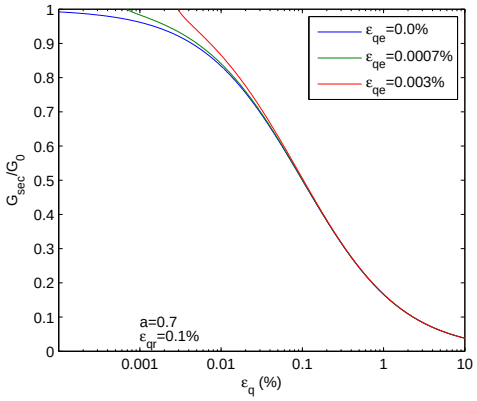

(c) Effect of elastic strain threshold parameter

Figure 2.10: Effect of parameters on modelled normalized secant shear stiffness (Equation 2.11)

ratio (e) on the hyperbolic-strain model coefficients. The threshold strain trended linearly with the reference strain, Equation 2.12. The reference strain, Equation 2.13, decreased with the uniformity coefficient, increased with mean stress, and increased with the multiple of the void ratio and relative density. They found that the curvature parameter was best estimated using only the uniformity coefficient. The C_u is an intrinsic soil property defined by the particle size distribution; it is independent of the state of the soil. Alternatively, Wichtmann and Triantafyllidis (2013) found that the

curvature was independent of the uniformity coefficient and recommended a constant value of 1.03. Wichtmann and Triantafyllidis (2013) also calibrated Equation 2.15 for the reference strain in terms of C_u and mean effective stress p. The hyperbolic model used by Wichtmann and Triantafyllidis (2013) did not include a threshold strain.

The following are from Oztoprak and Bolton (2013):

$$\varepsilon_{qe} = 0.002 + 0.012\varepsilon_{qr} \tag{2.12}$$

$$\varepsilon_{qr} = 0.01 C_u^{-0.3} \frac{p'}{p_a} + 0.08 eDr \tag{2.13}$$

$$a = C_u^{-0.075} \tag{2.14}$$

The following are from Wichtmann and Triantafyllidis (2013):

$$\varepsilon_{qr} = 0.000652 exp\left(-0.59 ln\left(C_u\right)\right) \left(\frac{p'}{p_a}\right)^{0.4} \tag{2.15}$$

$$a = 1.03 \tag{2.16}$$

Neither of these empirical formulations include the effect of ageing, initial stress ratio, or stress path. As confirmed in the current work and previous published research (Afifi and Richart, 1973; Anderson and Stokoe, 1978; Baxter and Mitchell, 2004) ageing results in a small increase in G_0, a large increase in G_{sec} (Howie et al., 2002), and has no effect on the large strain strength (Mitchell, 2008). These three observations can all occur if ageing increases both the curvature and the reference strain of the model normalized secant stiffness curve.

2.5 Proposed research

This research began as a continuation of the laboratory studies in Fraser River Sand that were performed by Shozen (2001) and Lam (2003). These

investigations did not have shear wave measurements, which precluded the normalization of the measured non-linear shear stiffness curves with G_0.

The first objective of this research program was to add bender elements to the UBC triaxial apparatus in order to obtain the capability of acquiring V_S and G_0.

Based on the preceding background section, it is clear that particular attention must be paid to the interpretation of the bender element signals in order to make consistent estimates of V_S and resolve the anticipated small increase in V_S with age expected for a clean sand.

The second objective of this research program was to investigate the application of bender elements to observe very small changes in V_S during ageing and confidently characterize both G_0 and an N_G factor.

The previous UBC research (Lam, 2003; Shozen, 2001) observed that the specimen age had a significant impact on the secant stiffness curve. Conversely, this literature review established that ageing has a small effect on the very small strain G_0. Once the first two objectives are met, the bender element equipped triaxial apparatus will be used to investigate the effect of ageing on the shape of the normalized secant stiffness degradation curves.

The third objective of this research was the integration of G_0 from bender element V_S interpretations with triaxial measurements to study the effect of age on the stiffness of Fraser River Sand.

Chapter 3

Equipment, materials, and initial results

The first objective of this research was to add bender elements to the UBC triaxial equipment. Bender elements were fabricated and installed in the triaxial apparatus used by Shozen (2001) and Lam (2003). The data acquisition system and control needed to be replaced to allow sufficient sampling rates for bender element testing.

Initial testing was performed to evaluate the installed bender elements. This was done to see if the new equipment had the capability to allow confidence in acquired G_0 and could be used to investigate the effect of ageing on Fraser River Sand stiffness.

This chapter includes these initial triaxial results. The past experiments by Shozen (2001) and Lam (2003) were replicated in order to check if the redeveloped equipment provides similar results. The purpose was to confirm that the new equipment and data reduction procedures perform as expected and that data from the previous investigations could be considered with the current one. The current study investigated Fraser River Sand. This was the same material that was tested in previous investigations. However, the tested material was from a different bulk sample with slightly different intrinsic properties. It is necessary to compare the results to past studies to check that the updated equipment provides similar results and to observe

the consequence of testing specimens from different bulk samples.

3.1 Test programme

This research project was instigated to complement and continue the previous investigations by Shozen (2001) and Lam (2003) with bender element shear wave velocity measurements. The experimental variables in this investigation include the consolidation stress ratio, age duration, and shear path to failure. Figure 3.1 depicts these variables on a p-q stress path plot.

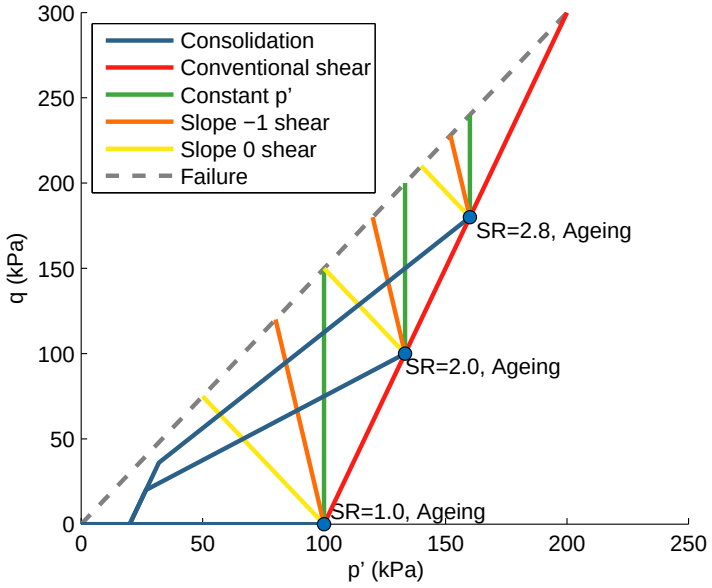

Figure 3.1: Experimental variables include consolidation stress ratio (1.0, 2.0, 2.8), age duration (10 minutes, 100 minutes, 1000 minutes), and shear path to failure (conventional, constant p, slope -1, and slope 0)

Shozen and Lam carried out tests over a range of stress paths and consolidation stress ratios. This investigation followed the same general testing procedure. The consolidation phase of testing occurs over two stages. In Figure 3.1, consolidation begins near the point $(p, q) = (20\text{kPa}, 0\text{kPa})$. The first stage of consolidation is an increase in the axial stress until the desired

stress ratio is achieved. This occurs over the blue line segment in the lower left corner of Figure 3.1. The second stage of consolidation involves increasing the radial and axial stresses simultaneously up to a radial effective stress of 100 kPa. A constant stress ratio (1.0, 2.0, 2.8) is maintained during the second stage of consolidation.

The next phase of testing involves ageing the specimen at a constant stress state for a set amount of time. In Figure 3.1, this is depicted as a blue point for each of the three stress ratios. The second experimental variable is the age duration. In this investigation, age durations were 10 minutes, 100 minutes, or 1000 minutes.

The last phase of testing is the stress path to failure. Figure 3.1 depicts four shear stress paths from each ageing point to the failure surface. The "Conventional" stress path is an increase in axial stress with no change in radial stress. The "Constant P" stress path is an increase in the axial stress and decrease in the radial stress to maintain a constant mean stress. The "Slope -1" shear path is an increase in the axial stress and decrease in the radial stress by the same amount. This maintains a constant in-plane effective stress ($\sigma'_a + \sigma'_r$) during shear. The "Slope 0" shear path is a decrease in the radial stress while maintaining a constant axial stress.

The completed test programme included significant amounts of work on testing and evaluating equipment and bender element techniques. Many experiments were repeated at the same test conditions. The test programme included two specimens at a stress ratio of 1.0, 46 specimens at a stress ratio of 2.0, and eight specimens at a stress ratio of 2.8. It included 6 specimens aged for 10 minutes, 33 specimens aged for 100 minutes, and 17 specimens aged for 1000 minutes. It included 32 specimens sheared along a conventional stress path, 17 sheared along a constant "p" stress path, five shear along a slope 0 stress path, and two sheared along a "-0.5" stress path. These experimental details are summarized in Table 3.1.

Table 3.1: Experimental details

Count	Stress ratio	Age (min)	Shear path
21	2.0	100	C
6	2.0	100	P
6	2.0	1000	P
4	2.0	10	C
3	2.0	1000	C
3	2.8	1000	P
2	1.0	100	C
2	2.0	1000	0
1	2.0	10	-0.5
1	2.0	100	0
1	2.0	10	P
1	2.0	1000	-0.5
1	2.8	100	C
1	2.8	100	0
1	2.8	1000	C
1	2.8	100	P
1	2.8	1000	0

3.2 Material tested

3.2.1 Fraser River Sand sample properties

A large sample of Fraser River Sand was sourced from Mathers E Bulldozing Co. Ltd. on October 6, 2010. Table 3.2 summarizes measured intrinsic properties from this sample. Tests were repeated multiple times to estimate the standard deviation of the mean of the intrinsic properties. Figure 3.2 depicts the measured particle size distribution. The grain shape is semi-angular. It is a finer bulk sample than what was tested previously. This sample classifies as a poorly graded sand (SP) by the USCS classification. The mineralogy of this sample was not tested. A published mineralogical result for Fraser River Sand contained 40 % quartz, 11 % feldspar, 45 % unstable rock fragments, and 4 % miscellaneous detritus (Garrison et al., 1969).

Table 3.2 presents the classification properties of the sand tested and also presents those obtained by Shozen and Lam. The characteristic particle sizes were interpolated from adjacent sieve results (as shown in Figure 3.2). In this sand the ASTM method for maximum relative density results in a lower than expected void ratio. To avoid this conflict with expectations, Shozen estimated e_{max} as the maximum void ratio achieved during water pluviation. The same technique for e_{max} is used in this thesis so that water pluviated relative densities agree with values previously measured at UBC. It is recognized that this means that the relative density calculations in this thesis are not transferable to other investigations or other sands. However, the relative density is not a good property to use to compare different sands (Hamidi et al., 2013) and the shear wave velocity depends on the void ratio not the relative density (Hardin and Richart Jr, 1963). The results for both of these techniques for estimating the maximum void ratio are included in Table 3.2. This table also shows that the current specimen D_{50} is slightly finer than the previous sample tested by Shozen.

Table 3.2: Intrinsic properties of Fraser River Sand sample, values reported by Shozen (2001) and Lam (2003) are in parentheses

Property	Average	Range
Fines content ASTM D1140-00	0.5 %	0.47 to 0.54 %
D_{10} ASTM D422-63	0.140 mm (0.161, 0.150 mm)	0.136 to 0.143 mm
D_{50} ASTM D422-63	0.214 mm (0.271, 0.270 mm)	0.207 to 0.218 mm
D_{60} ASTM D422-63	0.232 mm (NA, 0.280 mm)	0.228 to 0.238 mm
Uniformity Coefficient ASTM D422-63	1.66 (1.88, 1.87)	1.61 to 1.72
Specific Gravity ASTM D854-10	2.730 (2.719, 2.719)	2.723 to 2.736
e_{min} ASTM D4254-00	0.659 (0.627, 0.627)	0.650 to 0.679
e_{max} ASTM D4253-00	0.994 (0.955, NA)	0.977 to 1.006
e_{max} Water pluviated	1.05 (0.989, 0.989)	

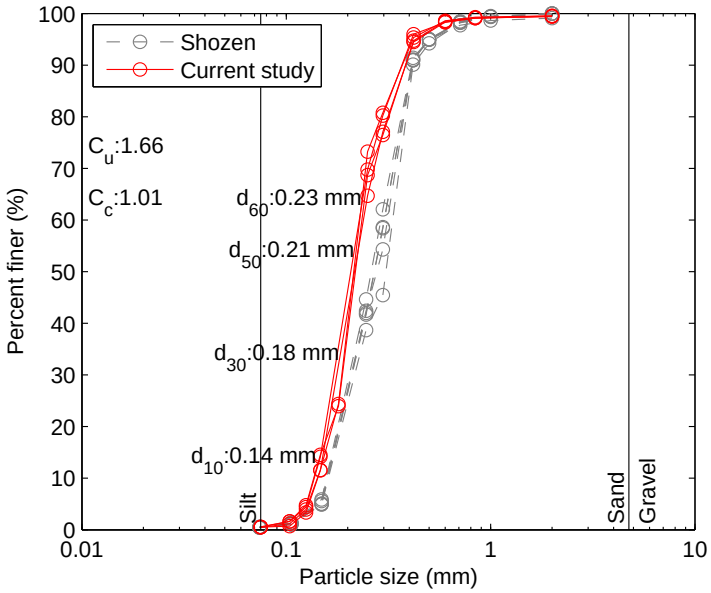

Figure 3.2: Particle size distribution for Fraser River Sand sample from the current study and from the sample used by Shozen (2001)

Smaller sub-samples were prepared from the large bulk sample prior to specimen preparation. The complete details are described in Appendix B. The sample preparation screened out the large particles, washed out the fines, and saturated the sand in boiling water to remove the air.

3.2.2 Specimen reconstitution

Vaid and Negussey (1988) demonstrated that clean sand specimens reconstituted by water pluviation were almost full saturated. Saturated specimens are necessary in order to allow the change in the specimen volume to be determined from the quantity of water expelled or admitted to the specimen voids. The water pluviation technique also produces specimens are repeatable with a homogeneous void ratio distribution. Repeatable specimens are necessary for reproducible results. Homogeneous specimens are assumed when interpreting the triaxial test as an element test. Further details for

the water pluviation procedure can be found in Appendix B.

It was noted that the void ratio at the end of water pluviation was consistently greater than the maximum void ratio determined following ASTM procedures. As previously stated, a similar observation was made by Shozen. The average void ratio obtained during loose specimen preparation is included in Table 3.2.

3.3 Improved triaxial apparatus

Figure 3.3 is a diagram of the triaxial apparatus used in this research program. This apparatus includes five external sensors. The load cell is used to measure the axial load applied through the loading ram. The LVDT responds to the displacement of the top cap. The two pressure transducers are used to measure the pore water and chamber pressure. The differential pressure transducer monitors the elevation head in a reservoir of water that changes as the specimen expels or admits water into its void volume.

A new data acquisition system was developed using a National Instruments board. This system was controlled with a custom developed program made with National Instrument's LabView software. Routines for automated back pressure saturation, stress ratio consolidation, performing suites of high sampling rate bender element tests, and testing various stress paths were developed.

Additional details for this apparatus can be found in Appendix A. The procedures for sample preparation, specimen preparation, and triaxial testing are in Appendix B. Appendix C covers the triaxial data reduction.

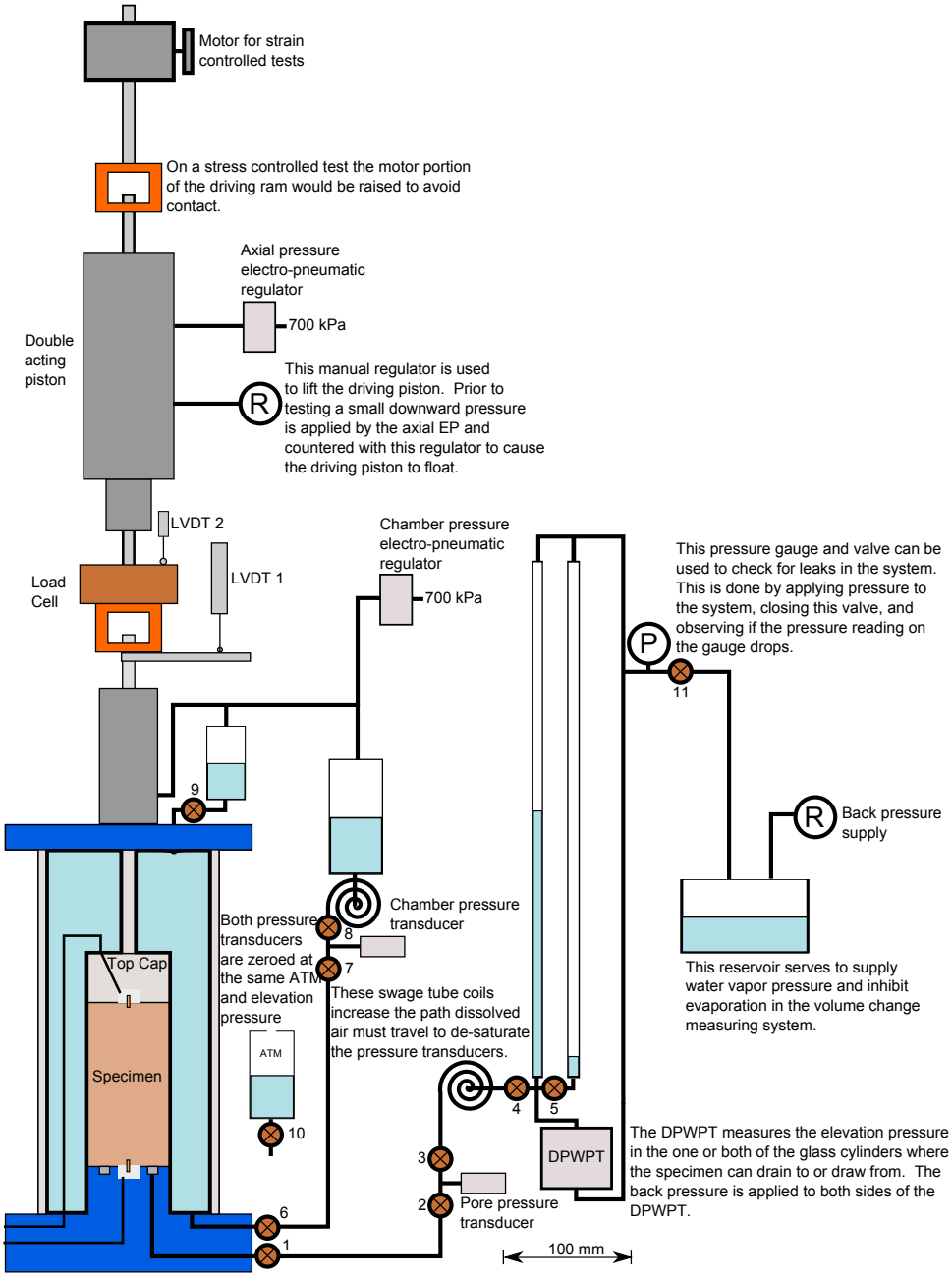

Figure 3.3: Triaxial diagram

3.3.1 Improved stress path control

The stress path for consolidation and shearing imposed during the triaxial test is computer controlled. The triaxial equipment has two electrical pressure regulators to control the downward load on the axial ram and the chamber pressure (see Figure 3.3). These devices provide indirect control of the axial and radial effective stress on the specimen. The computer control of these two regulators is based upon real-time data reduction of the triaxial sensor measurements (load cell, pressure transducers, differential pressure transducer, axial displacement). The data recorded from these sensors are used to calculate the specimen cross section area, current axial stress, and current radial stress. Software routines calculate the voltage increment to apply to each electrical pressure regulator based on the current stress state, the desired future stress state, and the past applied voltages and stresses. The change in the applied voltage increment is based on a feedback loop during back pressure saturation and consolidation. During non-conventional stress path testing, it is based on linear regression results to hit the desired stress state on the next iteration of the triaxial control program.

The stress control system includes fixed limits on the incremental change in applied voltage. These limits reduce the chance that a noise spike in the sensor measurements will result in a sudden and drastic change in the applied voltage to the electrical regulators.

Figure 3.4 compares computer controlled stress paths for the present triaxial equipment to previous experimental results. In this figure the results by Shozen (2001) and this investigation were from specimens consolidated at a stress ratio of 2.0. The results from Lam (2003) were from specimens consolidated at a stress ratio of 2.1. This figure demonstrates that the improved triaxial system has better stress control than was previously achieved. Linear shear stress paths from the start of shearing to failure are achieved. The constant "p" stress path is significantly improved.

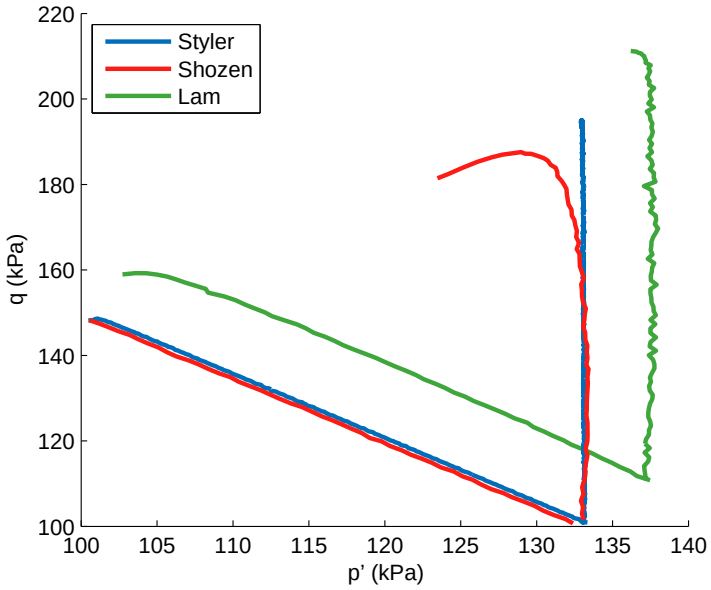

Figure 3.4: Comparing stress path control for new triaxial control system (blue) against previous results from Shozen (2001) (red) and Lam (2003) (green) for Slope 0 and Constant P shear paths

3.3.2 Addition of bender elements

The triaxial apparatus shown in Figure 3.3 was modified to include bender elements. Bender sockets have been cut into the triaxial base pedestal and top cap. The bender elements were mounted as cantilevers within these sockets.

The UBC triaxial apparatus was initially modified with two X-poled series bender elements for triggering and receiving shear waves. This system experienced significant cross talk between the elements. An attempt was made to shield these series bender elements with conductive paint. This shielding was attached to a building ground reference, but created ground loops that ruined the other triaxial sensor measurements. The bender element system was reconfigured using two Y-poled parallel type bender elements to take advantage of the inherent shielding (Lee and Santamarina, 2005).

Figure 3.5 shows details of the installed bender elements. The bender elements were fabricated from a Y-poled parallel piezoceramic sheet. This piezoceramic sheet was sourced from Piezosystems, Inc., part number T226-H4-503Y. The composition of the piezoceramic in the bender elements used in this study is lead titanate zirconate. The bender elements are approximately 14 mm long and 10 mm wide. They were mounted on a piece of printed circuit board. A lower corner of the bender element was milled off to expose the centre shim for wiring in parallel. To avoid shorting the electrical potential difference across the piezoceramic plates, five coats of polyurethane were applied for waterproofing the bender element prior to screwing the printed circuit board base into the apparatus. To protect this coating, the top cap and base pedestal must only be cleaned with flowing water. Cleaning the apparatus with pressurized air will damage the polyurethane coating and electrically short the bender elements. The recess was filled with RTV silicone. The final bender element penetration length into the sample was 4.5 mm for the base pedestal and 4.6 mm for the top cap.

The apparatus includes a signal amplifier on the bender element response. This is a battery powered 1000-fold amplifier which is applied to the signal prior to analogue to digital conversion and recording. For each bender test, the data acquisition system sampled the applied trigger signal and amplified response signal at a rate of 500 kHz for 20 ms. For discrete bender element testing, each response signal was a result of 10 stacked signals. A minimum 100 ms pause was included between stacked signals to allow reflected waves to dissipate. No filtering of the response signals was performed.

For repeatable bender element signals, the polarity of the trigger and receiver bender elements must be aligned when the top cap is placed on the soil specimen. To verify the alignment, the bender elements were placed in contact in the same plane and a trigger sine pulse was applied. Figure 3.6a depicts the measured response of in-contact bender elements. The trigger sine pulse is not inverted in the responding bender element. The resonance and damping of the receiver bender element are apparent. The resonant

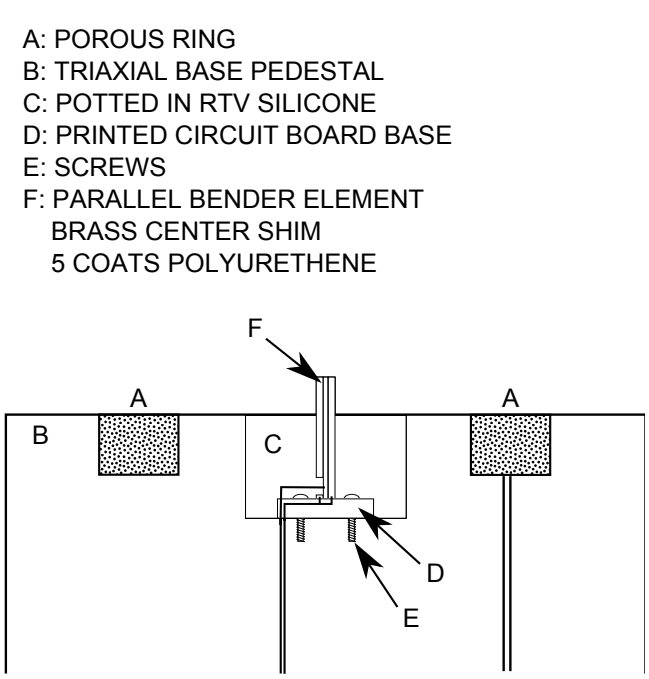

Figure 3.5: Bender element installation details

frequency is near 3.4 kHz and the system is under-damped with ζ=0.5 to 0.6. It appears that the bender elements are only in contact for the initial rise of the trigger pulse.

Figure 3.6b depicts the measured bender element response for a 100 kHz sine pulse through air and through water. Through air, the response is negligible. Through water, a clear long duration response is measured. It is believed that this is a result of the RTV silicone potting (see Figure 3.5) generating compression waves when the bender element cantilever beam bends. This same effect on the receiving end is transferring the arriving compression waves into the bender element and generating a response. This compression wave feature may be present in the measured signals.

A bender element test begins with applying a trigger signal waveform to one of the bender elements. The received signal and applied trigger signal are recorded. The test is repeated ten times and signal stacking is performed to increase the signal to noise ratio. The applied trigger signal depends

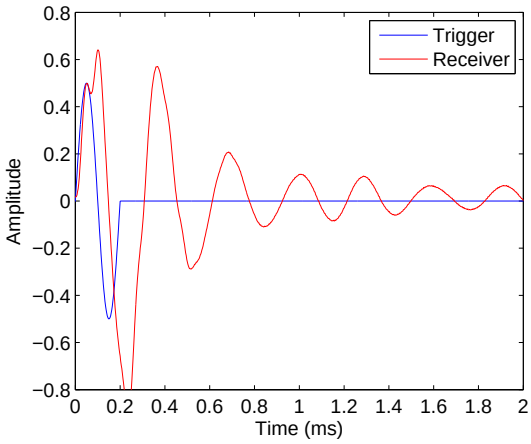

(a) Aligned polarity of the bender elements initially in contact

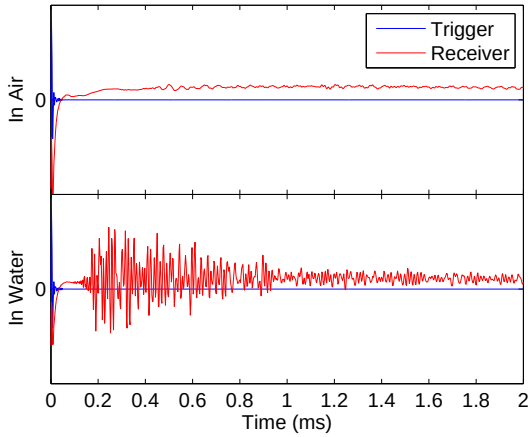

(b) Bender element response through triaxial chamber filled with air and water

Figure 3.6: Bender element response (a) in contact; and (b) through air and water

on the desired interpretation method. Sine pulses of selected frequencies are performed for time domain interpretations. Sweeping sine waves are performed for frequency domain interpretations. The height of the specimen at the time of the test is recorded with the bender element signals to calculate the bender element tip-tip separation to obtain the shear wave velocity.

Due to signal stacking, bender element testing takes a finite amount of

time. The triaxial test is paused during bender element testing. This means that the computer controlled changes in the applied stresses are suspended. Apart from suspending computer controlled changes in applied stress, the bender element system operates independently from the triaxial system.

3.4 Confirmation testing

3.4.1 Comparing to previous triaxial results

Comparing to past results is necessary to demonstrate and confirm that the equipment, procedures, and data reduction give similar results. A subset of the triaxial dataset with similar experimental parameters was compiled as detailed in Table 3.3. This subset of experiments included two from the present study (248, 262), one from Lam (25020517), and two from Shozen (rw0611-1, rw0616-2). These specimens were all prepared loose, consolidated near a stress ratio of 2.0, aged for 100 minutes, and sheared along a conventional stress path. The void ratio in Table 3.3 is from the end of consolidation. For completeness, the relative density was calculated using the e-min and e-max values for the respective soil sample. The e-max values used were estimated from the end of water pluviation soil state not the ASTM standard.

Table 3.3: Reproducing triaxial results from previous investigations from specimens aged for 100 minutes and sheared along a conventional stress path

Investigation	Specimen	Void ratio	Dr	Stress ratio
Styler	248	0.975	19 %	1.95
Styler	002	0.955	24 %	1.99
Lam	25020517	0.898	25 %	2.10
Shozen	rw0611-1	0.921	18 %	2.00
Shozen	rw0616-2	0.924	18 %	2.00

The experiment by Lam (2003) was the only one he performed under similar conditions to Specimens 248, 002, rw0611-1, and rw0616-2. Between

experimental datasets, the differences in void ratio may be due to the different intrinsic properties of the Fraser River Sand sample (Section 3.2.1).

Figure 3.7 compares the applied stress paths for each experiment in Table 3.3. The first linear segment is from the state of the specimen at the end of back pressure saturation up to a stress ratio (σ'_a/σ'_r) of 2.0, or 2.1 for Lam. The second line segment is consolidation up to a radial stress of 100 kPa, while maintaining a constant stress ratio. The third line segment is the conventional shear path to failure.

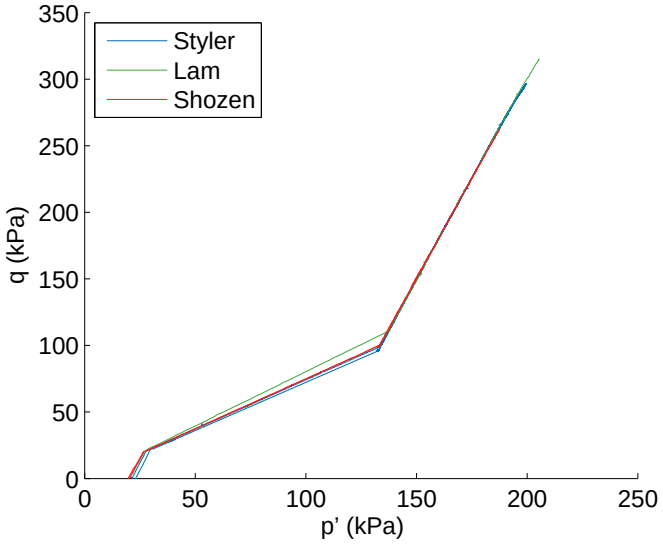

Figure 3.7: Comparing stress path control to previous experiments detailed in Table 3.3

Figure 3.8 shows the axial and volumetric strains developed during these experiments. One of the experiments by Shozen (2001) appears to have had a compliance issue at the start of the experiment. The consolidation phase is from the origin (0,0) to the circle point. As shown in Figure 3.7, this involves a change in stress path direction once a stress ratio of 2.0 is achieved. Creep strains are developed over 100 minutes of ageing between the circle and triangle points. Beyond the triangle point are strains developed during the conventional shear path. The two tests in the current study (blue lines)

appear very reproducible.

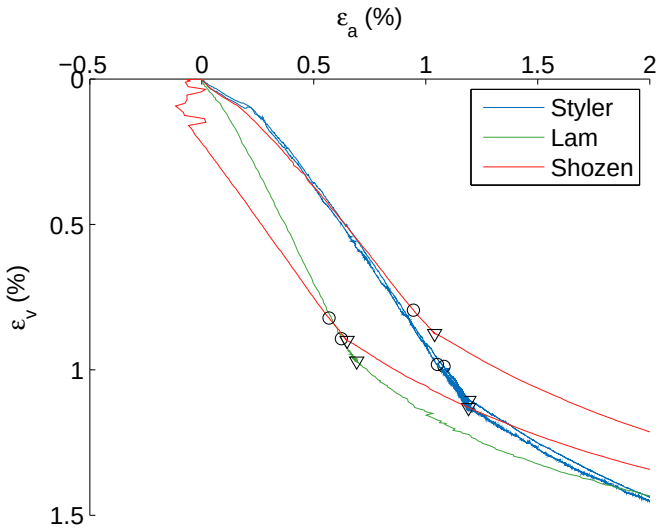

Figure 3.8: Comparing developed strains to previous experiments detailed in Table 3.3, where the circle points are the end of consolidation and the triangle points are the start of conventional shear

Figure 3.9 shows the shear stress against axial strain during shearing in the large strain region. The experiment by Lam (2003) appears to be stiffer and reaches a higher deviatoric stress at failure. The low strain details are difficult to observe on this scale.

Figure 3.10 shows the corresponding developed volumetric strains. The specimens in the current investigation experienced different amounts of contractive volumetric strain. The slightly denser specimen, 002, experienced less contractive volumetric strain than specimen 248. Another feature in this plot is a kink immediately after the transition from contractive to dilative behaviour. This kink is believed to be a result of a meniscus change in the measurement system for volumetric changes. It is observed in the two current tests and the one performed by Lam (2003). It was not observed in the two experiments by Shozen (2001) as these were terminated immediately

after the end of contraction.

Figure 3.9 and Figure 3.10 are repeated in Figure 3.11 and Figure 3.12 over the small strain region of interest to this investigation. The two experiments in the current study and the two by Shozen (2001) are very similar over the small strain range. The experiment by Lam (2003) is both stiffer and more contractive. This may be a result of his specimen being a higher density and consolidated and aged at a higher stress ratio.

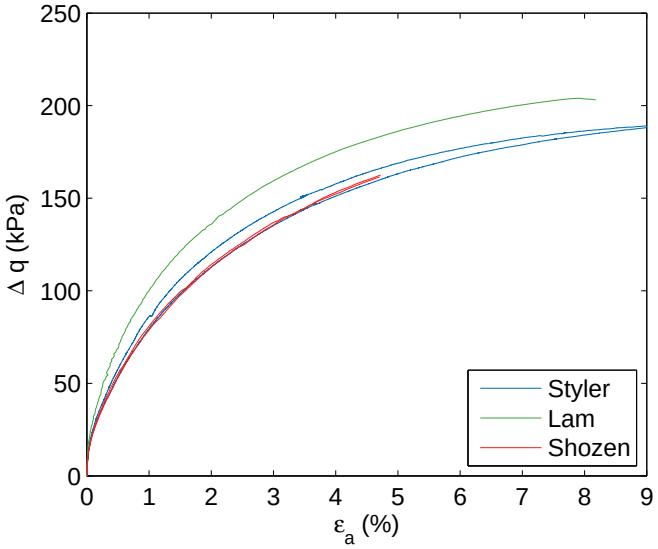

Figure 3.9: Comparing stress-strain plot during conventional shear to previous experiments detailed in Table 3.3

The improved triaxial apparatus, testing procedure, and data reduction appear to give results that are generally similar to those obtained by Shozen and Lam. The results shown by Figure 3.8 show that the current testing is very reproducible through consolidation. Furthermore, Figure 3.9 through Figure 3.12 show very good agreement over the small strain range between the current study and Shozen (2001). Despite slightly different particle size distributions, the results are very similar.

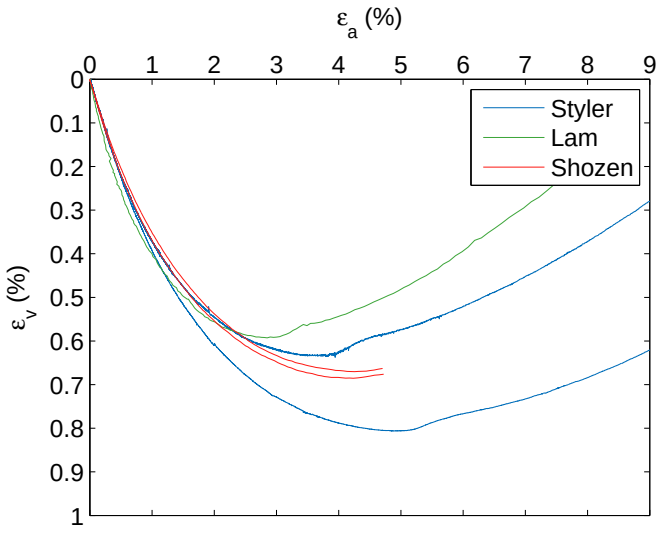

Figure 3.10: Comparing strains during conventional shear to previous experiments detailed in Table 3.3

3.4.2 Evaluation of measurement uncertainty

The evaluation of measurement uncertainty is more than just quantifying sensor resolution. It also includes the entire measurement model reducing the raw sensor voltages to the calculated small strain shear stiffness. The uncertainty for the calculated small strain shear stiffness was evaluated following the recommendations from the Joint Committee for Guides in Metrology (JCGM) in the "Guide to the expression of Uncertainty in Measurement document (GUM)" (JCGM et al., 2008a). Specifically, the approach covering the propagation of uncertainty distributions using the Monte Carlo method (JCGM et al., 2008b) was followed.

All of the sensors were calibrated using the triaxial data acquisition system. This inherently captures the contribution of signal conditioning and environmental electrical noise in the uncertainty of the calibration factor. Appendix A contains the sensor calibration factors and conditional standard deviation for each calibration. The resolution of each sensor can be taken as the conditional standard deviation value. These values are reported in Ta-

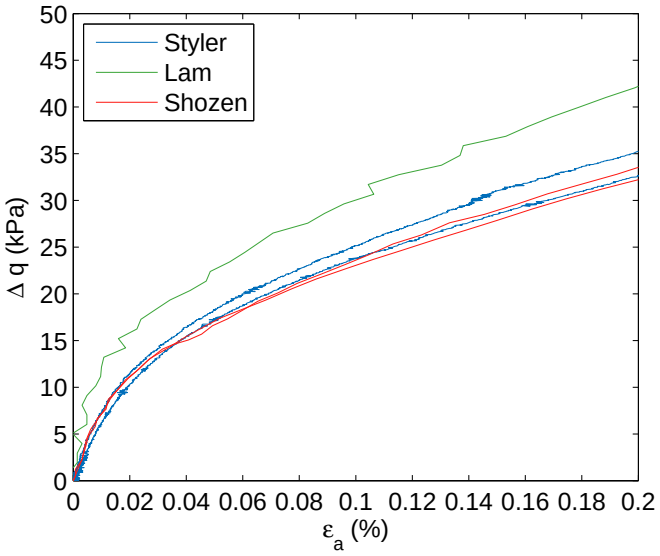

Figure 3.11: Comparing stress-strain plot at low strains during conventional shear to previous experiments detailed in Table 3.3

ble 3.4. This is in engineering units and conditional on a measured voltage.

Table 3.4: Calibration summary table

Sensor	n	Calibration factor	Conditional stdev	r^2_{xy}
Load cell	24	-13.424 kg/V	0.0566 kg	0.999987
LVDT 1	28	-3.721 mm/V	0.00386 mm	0.999999
LVDT 2	27	0.8046 mm/V	0.0166 mm	0.999075
PWPT	22	-86.0205 kPa/V	0.136 kPa	0.999999
Cell	22	-136.7504 kPa/V	0.164 kPa	0.999998
DPWPT	11	-2.833 cm^3/V	0.00735 cm^3	0.999985
DPWPT	10	-2.831 cm^3/V	0.00872 cm^3	0.999971
DPWPT*	21	-2.832 cm^3/V	0.00562 cm^3	NA
DPWPT	14	-87.3715 mm/V	1.37 mm	0.999318

A small amount of time-averaging is used to reduce the signal noise. The data acquisition system records the average of 200 voltages measured over a tenth of a second. It was found to be undesirable to decrease this averaging window time. A measurable source of electrical noise was observed at the

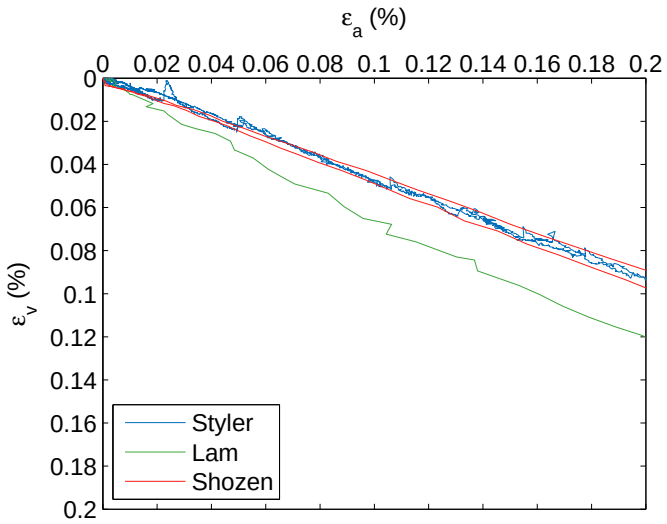

Figure 3.12: Comparing low strains during conventional shear to previous experiments detailed in Table 3.3

power supply frequency of 60 Hz (0.0167 seconds). If the averaging time window was less than 0.0167 seconds then this electrical environmental noise would contribute a noticeable amount of noise on the recorded voltages. The error in the calibration factors account for the 200-point time averaging in the conditional standard deviations for each calibration.

The sensor calibrations and apparatus measurements detailed in Appendix A were used with the data reduction equations in Appendix C to create a measurement model to propagate the uncertainties for Specimen 245. Log-normal random variables were assumed if the variable must be positive. Otherwise normal random variable distributions were used. The Monte Carlo simulation generated 100,000 sets of possible input variables for each row of triaxial sensor measurements. This is sufficient for estimating the dispersion of the results, but not the probabilities of the extreme tails of the distributions.

In this measurement model the secant shear modulus, G_{sec}, has 18 sources of error. G_{sec} is a result of all five triaxial sensors: the linear dis-

placement (LVDT), cell pressure (CELL), pore water pressure (PWP), differential pore water pressure (DPWPT), and load cell (LOAD). It includes most of the specimen preparation variables: dial gauge (DIAL), dummy specimen height (DATUM), calibrated graduated cylinder (GC), and the expanded membrane diameter (XPN DIA). It includes contributions due to the membrane penetration volume (MEM-P), elasticity of the membrane, including the initial membrane strain (MEM ϵ_i), Young's modulus (E_{mem}), the unstretched membrane thickness (T_{mem}), and the unstretched membrane diameter (DIA_{mem}). It includes contributions to the axial stress from the top cap mass (CAP MASS), ram friction (RAM), soil weight (SOIL), and an uplift pressure correction due to the driving rod diameter (ROD DIA).

The contribution to the uncertainty in G_{sec} from these variables depended on the magnitude of the developed shear strain. Table 3.5 details the sources of error at three different magnitudes of shear strain. In the small strain secant shear modulus at 0.02 % shear strain, 82 % of the uncertainty is due to the LVDT. It is clear that improvements in the LVDT have the most potential for reducing the uncertainty in the small strain secant shear modulus. However, it is unlikely that this sensor can be further improved through re-calibration. The calibration procedure is not complicated and very good results were achieved (see Table 3.4).

The value in performing this measurement uncertainty quantification is that resources in money, time, and effort can be focused on the specific area that will yield the most beneficial results. The first time the sources of measurement uncertainty were evaluated it led to two recalibrations. A significant source of error was observed due to the measurement of the expanded membrane diameter and the differential pore water pressure sensor. Both of these calibrations were repeated.

The current investigation has an improved signal resolution compared to past studies (Lam, 2003; Shozen, 2001), despite using the same sensors and signal amplifier. The main difference is the new computer and developed data acquisition and stress control program. The resolution of the sensors is slightly improved due to a reduction in random noise through more time-averaging of the recorded data. The current system also records data more

Table 3.5: Sources of error in the measured secant shear modulus from 100,000 Monte Carlo simulations for Specimen 245

G_{sec} = Source	ϵ_q=0.02 % 20 ± 5 MPa Contribution to error	ϵ_q=0.6 % 3.84 ± 0.03 MPa	ϵ_q=2.5 % 1.797 ± 0.005 MPa
LVDT	82.0 %	42.8 %	20.2 %
CELL	0.2 %	1.3 %	2.4 %
PWP	0.0 %	1.3 %	2.4 %
DPWPT	10.0 %	7.0 %	4.1 %
LOAD	6.5 %	22.1 %	21.4 %
DIAL	0.1 %	1.3 %	2.4 %
DATUM	0.0 %	0.4 %	0.8 %
GC	0.1 %	1.3 %	2.4 %
XPN DIA	0.5 %	10.4 %	18.6 %
MEM-P	0.1 %	1.5 %	2.8 %
MEM-ϵ_i	0.1 %	1.3 %	2.4 %
E_{mem}	0.1 %	1.7 %	5.0 %
T_{mem}	0.1 %	1.3 %	2.8 %
DIA_{mem}	0.1 %	1.3 %	2.5 %
CAP MASS	0.1 %	1.3 %	2.4 %
RAM	0.1 %	1.3 %	2.4 %
SOIL	0.1 %	1.2 %	2.4 %
ROD DIA	0.1 %	1.3 %	2.4 %

frequently than what was previously performed. This increases the time-resolution of the collected signals.

The triaxial system is capable of obtaining G_{sec} degradation curves. The error in G_{sec} increases at lower strains.

3.4.3 Initial bender element testing and interpretation

The developed triaxial equipment and data acquisition system were able to reproduce past experimental results and enabled the V_S and hence G_0 to be obtained. As one objective of the research was to obtain G_0 and to study the effect of ageing on stiffness, initial testing was carried out to assess the capability of the bender element system.

A set of signals collected during ageing of Specimen 261 have been interpreted using existing techniques. A suite of 12 different trigger signals were tested at 1 minute, 10 minutes, and 100 minutes of age duration.

Figure 3.13 depicts a 9 kHz sine pulse trigger (green) and response signal (red) at 10 minutes of ageing. As previously discussed (and shown in Figure 3.6b), a higher frequency compression wave signal is observed prior to the arrival of the shear wave. The first arrival characteristic points were selected where the signal first deviates under the lower shear wave frequencies. This occurred at 0.6200 ms resulting in an estimated shear wave velocity of 190.0 m/s. The peak to peak propagation time was selected using the maximum peak in the response signal. This resulted in a propagation time of 0.7200 ms and a much slower shear wave velocity of 163.6 m/s. Figure 3.14 presents the cross correlation function for this 9 kHz sine pulse test. The peak cross-correlation results in a propagation time of 0.7125 ms and velocity of 165.4 m/s.

This bender element test exhibited Type 3 signals (Table 2.3). There was an early, low amplitude, first pulse in the response. Consequently, a decision must be made on which feature in the response signal corresponds to the arriving shear wave. If the first deviation is selected, then the main shear pulse is travelling at a slower velocity or over a longer distance. If the main shear pulse is selected, then there is a pre-arrival distortion. The cross-correlation results do not provide an answer to this problem. As shown in Arroyo et al. (2006), constructive and destructive interference can change which cross-correlation peak has the maximum amplitude. The maximum peak may not be the peak that corresponds to the arrival. A peak prior to 0.7125 ms at 0.6050 ms can be selected that is close to the chosen first-arrival point. Figure 3.14 shows such a peak.

Another problem not depicted in Figure 3.13 or Figure 3.14, is that different sine pulse frequencies systematically change the measured velocity. This can be observed in Figure 3.15. This figure presents the results for all 12 tested frequencies at three times during specimen ageing. There is a range of possible velocities for each method at each suite of bender element sine pulses. There is no scientific justification for taking the average of these

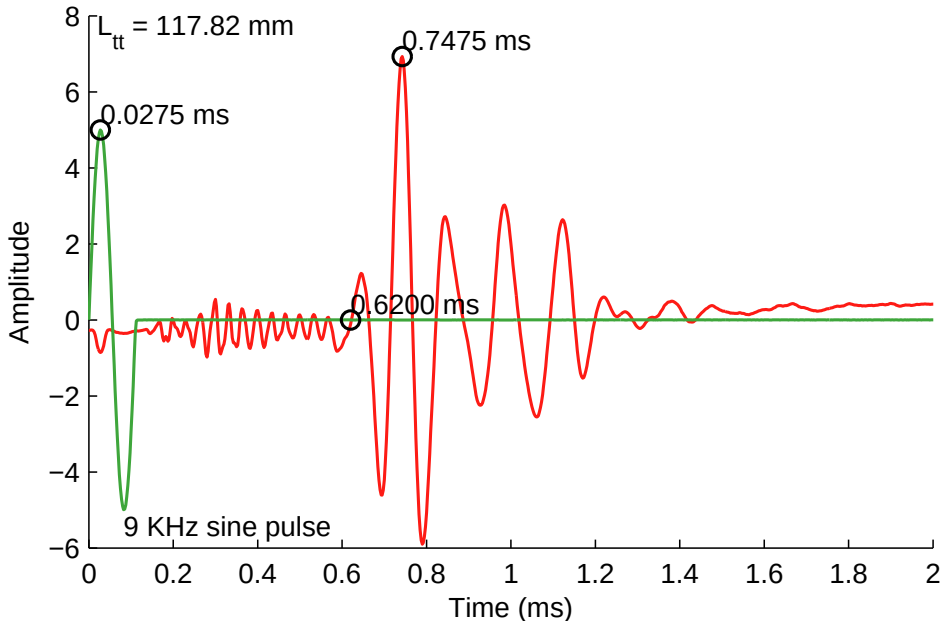

Figure 3.13: Time-domain results for specimen 261 from a 9 kHz sine pulse (green trigger, red response) at 10 minutes of ageing depicting a first arrival velocity of 190.0 m/s and a peak to peak velocity of 163.6 m/s

results. The difference in velocities is systematic, not random.

Figure 3.15 does show a general slightly increasing effect of age on V_S. An N_G factor might be estimated from this figure. However, this figure also demonstrates another problem. G_0 would vary significantly based on the technique used to select the propagation time. It is not clear if the shear wave arrival corresponds to the first distortion or to the subsequent larger amplitude cycle. This is seen in Figure 3.14. The arrival could be the preceding peak which would agree with the first-arrival results.

One of the trigger signals included in the suite of bender element tests was a sweeping sine wave. This was used to calculate the propagation time and shear wave velocity in the Frequency domain. Figure 3.16 presents the cross-spectrum method results using the approach from Viana da Fonseca

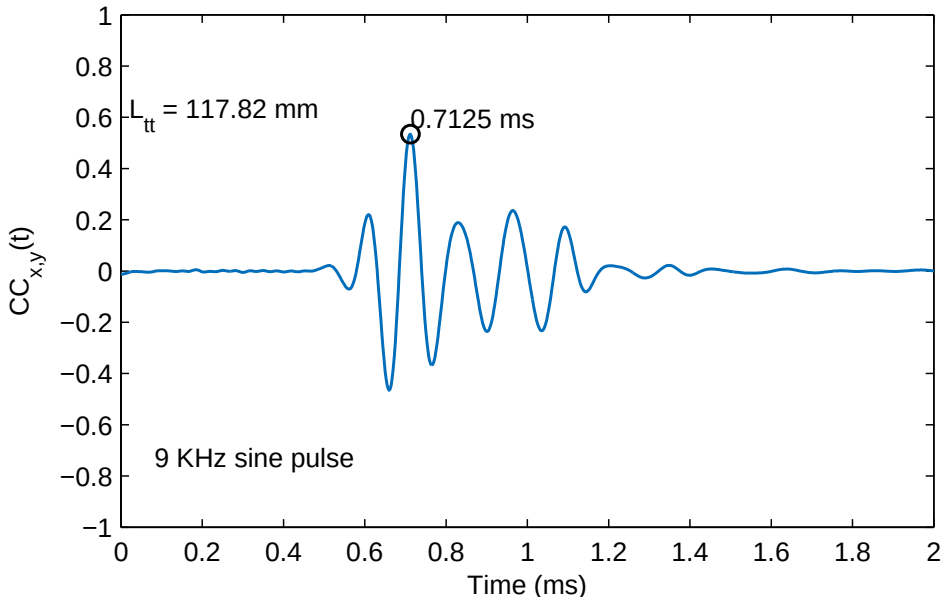

Figure 3.14: Time-domain cross-correlation result for specimen 261 from a 9 kHz sine pulse at 10 minutes of ageing depicting a velocity of 165.4 m/s

et al. (2009). This cross-spectrum technique performs linear regression over a moving 4 kHz frequency window on a plot of the unwrapped phase shift against frequency (Figure 3.16a). The propagation is calculated with $\Delta t = \frac{\Delta\theta}{\Delta f}\frac{1}{-2\pi}$. For these three age times, the cross spectrum method resulted in a V_S that was faster than the cross-correlation and peak to peak results, but slower than the first-arrival selection.

The problem is not that these different trigger signals and interpretation methods result in different shear wave velocities. The problem is that nothing in the model of a shear wave propagating through a soil specimen would indicate that there should be a difference. There is no informed or objective means to select the correct velocity. The different time domain methods should converge on the same velocity. The frequency domain interpretations should agree with this velocity.

Furthermore, there is little confidence in estimating a G_0 value using

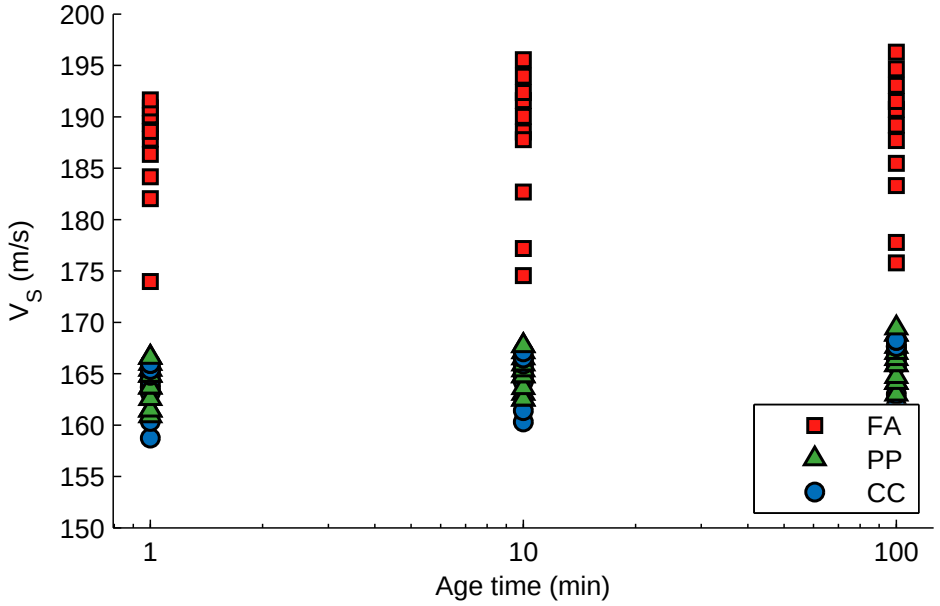

Figure 3.15: Time-domain bender element test results for Specimen 261 during ageing where FA is First Arrival, PP is peak to peak, and CC is cross correlation

ρV_S^2. At the end of ageing, Specimen 261 had a bulk density of $\rho = 1902$ kg/m^3. Assuming a representative First Arrival shear wave velocity of 187 m/s, this results in $G_0 = 67$ MPa. The cross correlation and peak-peak values may share an average shear wave velocity of 165 m/s, resulting in $G_0 = 52$ MPa. Finally, the frequency domain cross spectrum method at the peak correlation coefficient is close to 180 m/s, resulting in $G_0 = 62$ MPa. Clearly, these three values are not in agreement.

Additionally, the peak-peak and cross-correlation techniques resulted in a variation of 5m/s depending on the selected trigger signal. For a specimen with an N_G factor of 2 % and ρ of 1900 kg/m^3, V_S will increase from 165 m/s to 170 m/s over 1000 minutes of ageing. The uncertainty in state of practice time-domain bender element testing exceeds the effect of ageing in clean sands. N_G cannot confidently be determined using state-of-practice

bender element testing.

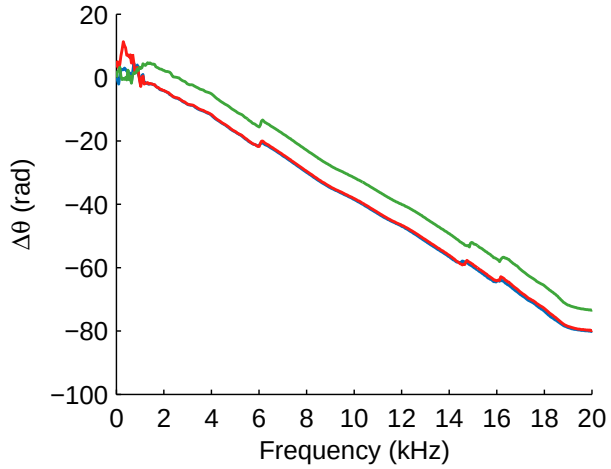

(a) Phase shift (rad)

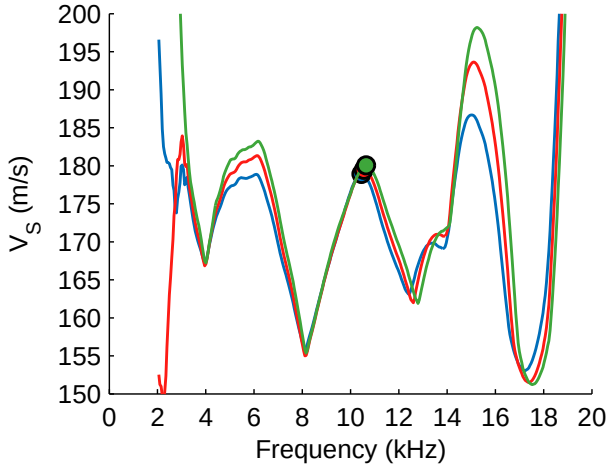

(b) V_S with moving 4 kHz window

Figure 3.16: Frequency domain interpretation following Viana da Fonseca et al. (2009) with 1 minute (blue), 10 minutes (red), and 100 minutes (green) bender element tests on Specimen 261

Type 3 signals were observed using the installed bender elements. There does not appear to be an acceptable published technique for Type 3 signals that can confidently determine a propagation time and shear wave velocity.

The second objective of this research has not been met by these initial results. Further study into the application and interpretation of bender elements is required.

3.5 Summary

The improved triaxial apparatus is capable of producing results similar to those of previous investigations (Section 3.4.1). This validates the developed data acquisition system and data reduction procedure. The equipment has at least the same capability to acquire secant shear stiffness curves as the equipment used in previous investigations. Additionally, the stress path control is improved and a higher density of data is obtained.

Bender elements were added to the UBC triaxial apparatus. This meets the first research objective outlined in Section 1.1. Bender element shear wave signals can be measured over the triaxial specimens of Fraser River Sand.

The second research objective was the evaluation of the applicability of these bender elements to perform a study of the effect of ageing on stiffness. Exploratory testing was performed with the bender elements using prevalent time domain and frequency domain interpretation techniques. It was concluded that these techniques were unable to confidently characterize G_0 or the N_G ageing factor. The use and interpretation of bender element testing requires further investigation.

Chapter 4

Development of a combined time and frequency domain bender element interpretation method

Accurate determination of the travel time increment has been the subject of considerable research since the introduction of bender element testing. Methods of interpretation have been developed in both the time and frequency domains, as covered in Chapter 2. Section 3.4.3 investigated the application of these techniques for this investigation. The effect of ageing could not be confidently determined.

This chapter presents an improved method of determining the shear wave propagation time in bender element testing. It is a combination of time and frequency domain techniques. This technique has been published by Styler and Howie (2013) in the ASTM Geotechnical Testing Journal.

This method of interpretation minimizes the subjectivity of the process and provides a consistent approach to determination of V_S. It combines the FD cross spectrum technique with an approach proposed by Blewett et al. (1999). This results in a determination of the phase velocity instead of

the group velocity over the bender element operating frequency range. The proposed method is evaluated for both synthetic and experimental signals.

4.1 Proposed method

The group velocity is distorted by frequency dependent effects while the variation of phase velocity with frequency characterizes frequency dependence. The phase velocity is a more appealing measure than the group velocity for bender element testing. The phase velocity at a given frequency can be calculated using Equation 4.1, where f is the frequency, L_{tt} is the propagation length (bender element tip to tip length), $\Delta\theta_r$ is the unwrapped phase shift, and n is the determined phase degeneracy constant.

$$V_S = \frac{-2\pi f L_{tt}}{\Delta\theta_r - 2\pi n} \tag{4.1}$$

The combined TD and FD approach described in this chapter solves for the constant integer n so that Equation 4.1 can be solved for the phase velocity. The unwrapped phase shift, $\Delta\theta_r$, is calculated from the response to a wide band trigger signal, the exact same procedure as in the cross spectrum technique. Sachse and Pao (1978) and Viggiani and Atkinson (1995) both calculated the phase shift from sine pulse triggers. Recent published investigations on frequency domain approaches have used linear swept sweeping sine triggers (Greening and Nash, 2004; Viana da Fonseca et al., 2009).

In the proposed technique, two trigger signal waveforms are used to determine the absolute phase shift at a single frequency, $\Delta\theta_a = \Delta\theta_r - 2\pi n$. These are a continuous sine wave over 20 ms and a sine pulse. The long duration continuous sine wave trigger and response have almost all of their power at a single frequency. The cross correlation of a continuous sine wave bender test results in a series of peaks, with each peak being separated by the period of the continuous trigger, T=1/f. The peak corresponding to the arrival of the shear wave is chosen based on the results of a sine pulse test. In this work, the sine pulse frequency is the same as that of the continuous sine. The propagation time for the continuous wave and the

frequency of the continuous wave are used to calculate the absolute phase shift, $\Delta\theta_a = 2\pi f \Delta t$.

The absolute phase shift, $\Delta\theta_a$, is compared to the relative phase shift from the linear sweeping sine, $\Delta\theta_r$, to determine the phase degeneracy, $-2\pi n$. The absolute and relative phase shifts are compared at multiple frequencies to confirm that they agree on the same phase degeneracy i.e. that n is constant for each unwrapped relative phase shift. Once the relative phase shift and phase degeneracy are determined, Equation 4.1 can be solved for the phase velocity.

The difference between the phase velocity and group velocity is now demonstrated using simulated signals. This demonstrates that they are different velocities and that the group velocity is distorted by frequency dependent dispersion.

4.2 Validation using simulated bender element signals

Synthetic bender element signals provide a controlled means to evaluate various methods of propagation time interpretation. The generated synthetic signals must be representative of the measured distortion that is found in experimental bender element testing. This can be achieved by characterizing a series of subsystems making up the experimental system. For this exercise, the soil subsystem for shear wave propagation is simulated using the boundary value solution by Cruse and Rizzo (1968). Lee and Santamarina (2005) and Wang et al. (2007) used the same approach. Although Alvarado and Coop (2012) found that a single degree of freedom oscillator representation of a bender element is often not reflected in real bender element systems that exhibit multiple resonance peaks, it is used to represent the receiving bender element as was done by Santamarina and Fam (1997) and Wang et al. (2007). The low frequency range is not measured in experimental bender element testing, the charge density between the piezoceramic plates dissipates and less mechanical force is generated at low frequencies. To simulate this phenomenon, a simple high pass filter was included in the

synthetic system. The high pass filter is modelled with Equation 4.2 where f_c is the corner frequency. At the corner frequency the output power is half of the input power.

$$H_T(\omega) = \frac{j\omega}{j\omega + 2\pi f_c} \tag{4.2}$$

The soil model used in the simulation had a total bulk density of $\rho = 1900 kg/m^3$, a shear wave velocity V_S = 200 m/s, a compression wave velocity V_P = 1428 m/s (Poisson's ratio equal to 0.49, simulating saturated soil), soil damping D = 0.025, and a propagation length r = 125 mm. The receiving bender element was modeled as a damped single-degree of freedom oscillator, with a resonant frequency of $\omega = 2\pi$9kHz, and damping of D_{be} = 0.2. The parameters for the soil damping and bender element damping are the same as the ones used by Wang et al. (2007). The resonant frequency was selected to match the peak energy in the experimental signals presented later. The trigger bender element is modelled as a high pass filter (Equation 4.2), with a corner frequency f_c = 2 kHz. A noise signal was added to the simulated output. This noise signal consists of random Gaussian noise with an amplitude of 5 % of the output and a 60 Hz sinusoidal wave with a random phase angle and amplitude of 10 % of the output signal. The 60 Hz sine wave noise models environmental noise due to an alternating current house power supply. The contribution of this noise is reduced by simulating signal stacking with 10 stacked signals for each simulated output signal.

Figure 4.1 depicts the synthetic bender element trigger, response, and cross correlation for a 5 kHz sine pulse and a 5 kHz continuous sine wave. The near-field effect preceding the arrival of the 5 kHz sine pulse (Figure 4.1c) is obscured by the noise in the signal. The peak cross correlation of the sine pulse occurs at 0.646 ms, resulting in an estimated V_S = 125 mm/0.646 ms = 193 m/s. The cross correlation of the continuous sine wave results in a set of peaks [0.044, 0.244, 0.444, 0.644, 0.844 ms, ...], of which 0.644 ms correlates to the sine pulse results. This propagation time is used to solve for the absolute phase shift at 5 kHz: $\Delta\theta(5\text{kHz}) = -2\pi 5\text{kHz}\Delta t = -2\pi \times 5\text{kHz} \times 0.644ms = -20.30$ radians.

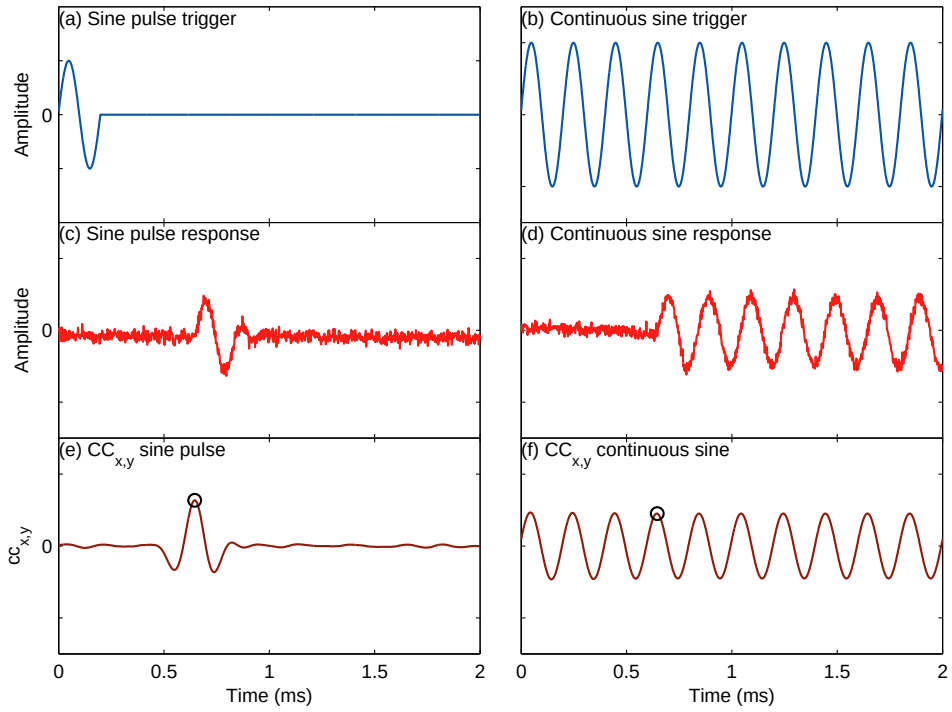

Figure 4.1: Synthetic bender element trigger and response signals: (a) 5 kHz sine pulse trigger; (b) 5 kHz continuous sine pulse trigger; (c) sine pulse response; (d) continuous sine response; (e) cross correlation of sine pulse trigger and response; and (f) cross correlation of continuous sine with circle point marking the peak cross correlation of the sine pulse

Figure 4.2 depicts a synthetic bender element linear sweeping sine trigger and response. The sweeping sine trigger frequency increases linearly from 0 to 10 kHz over 20 ms (Figure 4.2a). The simulated response to this trigger is depicted in Figure 4.2b. Unlike Figure 4.1, the sweeping sine wave response cannot be visually interpreted in the time domain. Figure 4.2c shows that the sweeping sine wave trigger has a wide band of uniform magnitude in the frequency domain. Figure 4.2c shows that the magnitude of the response wave peaked at 9 kHz, the resonant frequency of the bender element.

Ten simulated bender element signals were generated for the sweeping

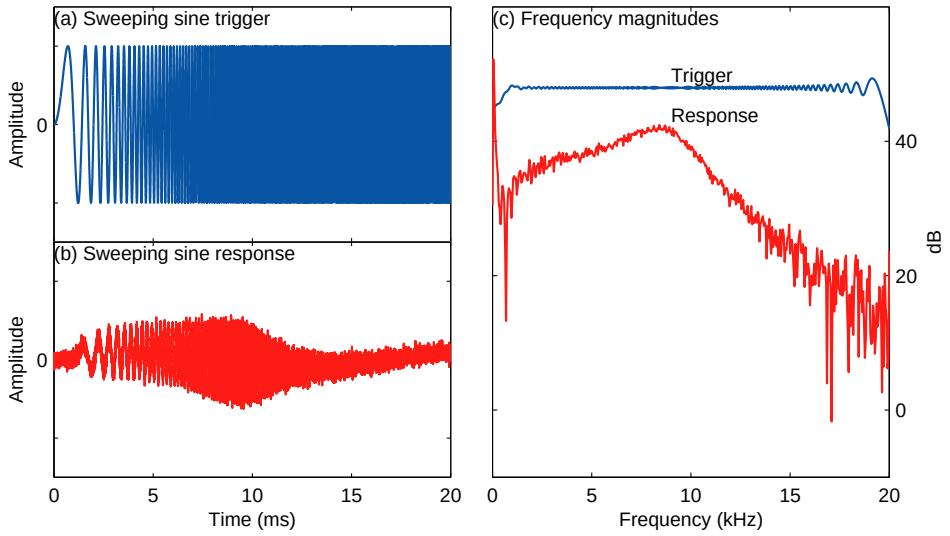

Figure 4.2: Synthetic bender element results: (a) linear sweeping sine wave trigger; (b) response; and (c) magnitude of the trigger and response signals in the frequency domain

sine response and the coherence function was calculated. This coherence function is depicted in Figure 4.3a. A drop off occurs at low frequencies and there is a gradual decline above 12 kHz. Figure 4.3b depicts the calculated phase shift between the trigger and response signals. This equation has discontinuities at $+\pi$ and π. The unwrapped phase shift is depicted in Figure 4.3c as a dashed line. At 5 kHz, the unwrapped phase shift is -13.92 radians. The absolute phase shift determined at this frequency in Figure 4.1 was -20.30 radians. The difference between these two values is the phase offset, -20.30 + 13.92 = -6.38 radians $\approx -2\pi$. The corrected phase shift is then depicted as a solid line in Figure 4.3c. Figure 4.3d shows the phase velocity, group velocity, and model velocity $V_S = 200$ m/s.

The phase velocity is calculated from the corrected phase shift with $V_S = -2\pi f L_{tt}/\Delta\theta_a$. For the range of frequencies for which the coherence was 1, it ranged between 195 m/s at frequencies from 4 to 7 kHz to 189 m/s over frequencies from 9 to 14 kHz. The group velocity was calculated from the slope of the phase shift in a moving 4 kHz frequency window. The

group velocity reached a minimum of 183 m/s as it approached the resonant frequency of the bender element.

Both the group and phase velocities underestimate the actual shear wave velocity, with the phase velocity being within 5 to 10 % of the specified velocity. This is due to the resonance model used to represent the receiver element. As the propagation length gets shorter, the bender element transfer function has a greater influence on the propagation time. This is a particular problem for short specimens (Wang et al., 2007), such as those used for consolidation testing or direct simple shear.

In general, the application of the proposed combined FD and TD approach to the synthetic signals has shown that the technique permits estimation of V_S of the soil samples but that the values obtained are influenced by the bender-soil transfer functions, tending to result in phase velocities that are less than the V_S of the soil. The group velocities are shown to be considerably more variable than the phase velocities and are affected by the resonant frequency of the bender element. The proposed technique is now demonstrated using experimental signals.

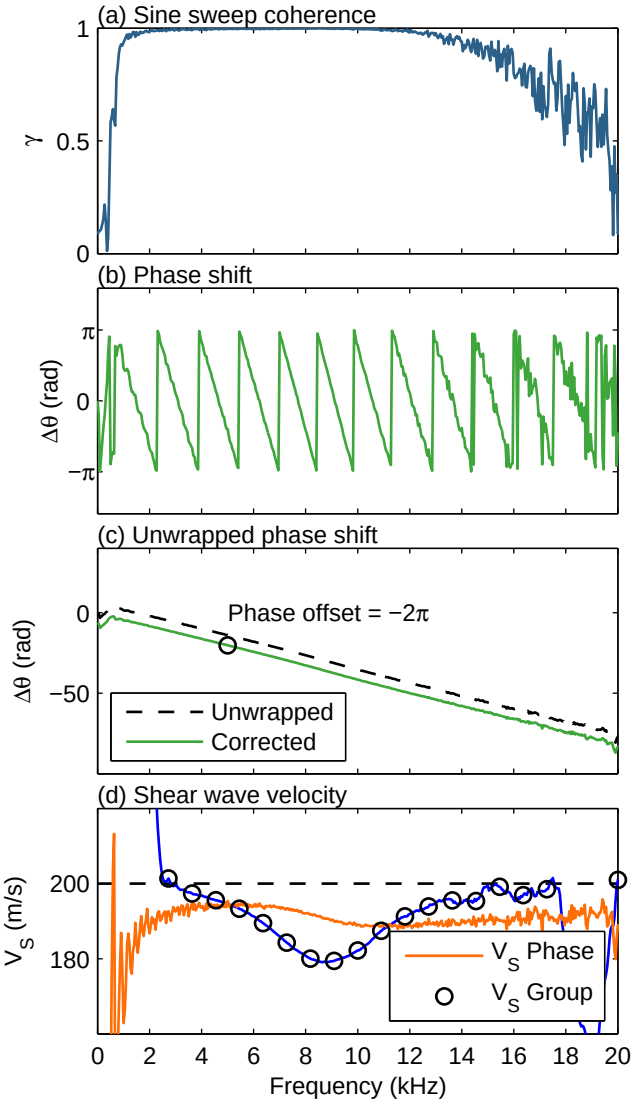

Figure 4.3: Interpreted synthetic frequency domain results: (a) coherence function; (b) calculated phase shift; (c) unwrapped and corrected phase shift; and (d) phase and group velocities

4.3 Experimental demonstration

To demonstrate that the proposed combined TD and FD method provides a reproducible measure of V_S, ten similar experiments were compared. These ten specimens of Fraser River Sand were prepared in as loose an initial state as possible using the procedures described in Chapter 3 and Appendix B.

Consolidation was performed in two stages. First, the axial stress was increased to a stress ratio of 2.0 (σ'_a/σ'_r), and then both the axial and radial stresses were increased to maintain the stress ratio constant up to the desired confining stress state. The rate of consolidation was sufficiently slow to prevent generation of excess pore pressure. The final samples had consolidated void ratios that ranged from 0.969 to 0.988.

The consolidation was temporarily paused to perform bender element testing at radial stresses of 60, 70, 80, and 90 kPa. Bender element tests were performed at an axial stress of 160 kPa and radial stress of 80 kPa. Each bender element test consisted of a suite of 10 trigger signals. These included 7, 9, 11, and 13 kHz sine pulses, 20 ms duration continuous sine waves and two linear swept sine waves from 0 to 10 kHz over 20 ms. The trigger signal amplitude was 3 volts.

Figure 4.4 presents a 9 kHz sine pulse and continuous sine trigger and response for Specimen 016 at an axial stress of 159.6 kPa, radial stress of 79.2 kPa, void ratio of 0.977, propagation length of 120.0 mm, and a propagation length to diameter ratio of 1.90. Comparing Figure 4.4 and Figure 4.1, the compression wave through water is observable prior to the shear wave arrival in both Figure 4.4c and Figure 4.4d. It was shown in Section 3.3.2 that this is interference from a compression wave. The amplitude of the arriving compression wave builds up to a peak around 0.3 ms before decaying. The peak cross correlation (Figure 4.4e) of the sine pulse occurs at 0.774 ms and corresponds to the first major shear signal in the response. This point correlates to a peak of 0.770 ms in the cross correlation of the continuous sine signal (Figure 4.4f) which leads to a determination of an absolute phase shift at 9 kHz of -41.85 radians ($-2\pi \times 9\text{kHz} \times 0.740\text{ms}$).

A low amplitude pulse in the received wave was observed immediately

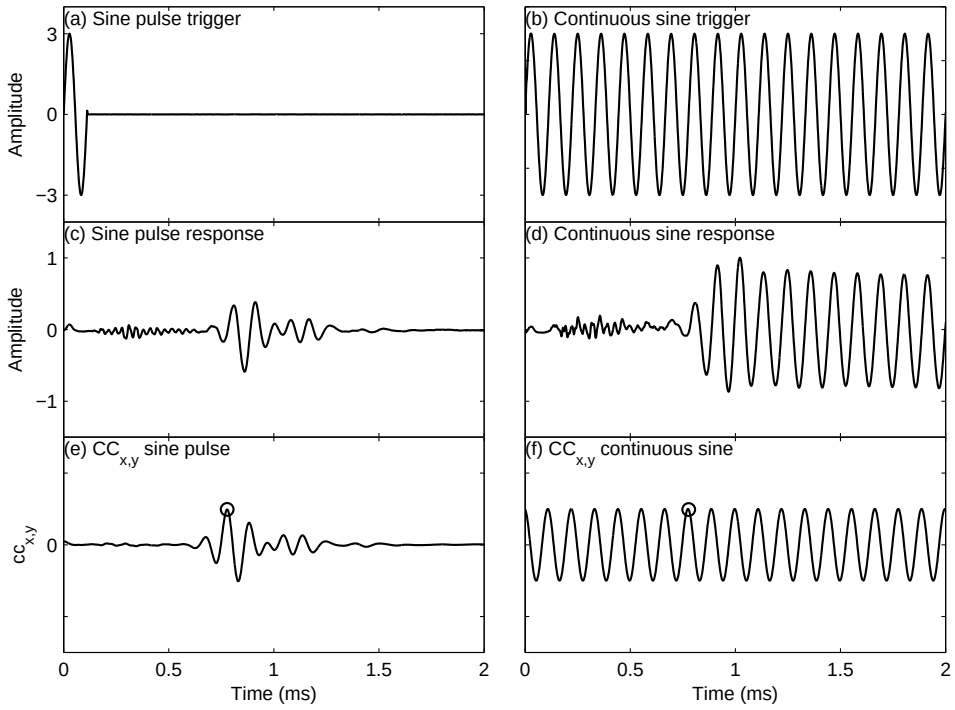

Figure 4.4: Experimental bender element signals for saturated Fraser River Sand Specimen 016, σ_a = 159.6 kPa, σ_r = 79.2 kPa, void = 0.977, l_{tt} = 120.0 mm, slenderness l_{tt}/d = 1.90: (a) 9 kHz sine pulse trigger; (b) 9 kHz continuous sine pulse trigger; (c) sine pulse response; (d) continuous sine response; (e) cross correlation of sine pulse trigger and response; and (f) cross correlation of continuous sine with circle point marking the peak cross correlation of the sine pulse

prior to the arrival of a major shear component. This characteristic has been observed by other bender element investigations (Arulnathan et al., 1998; Brandenberg et al., 2008; Brignoli et al., 1996; Landon et al., 2004). In Figure 4.4c, following the compression wave is this initial low amplitude pulse prior to a strong shear wave pulse. In a numerical model without reflective boundaries, Arroyo et al. (2006) showed the amplitude of the leading shear pulse decreasing with increasing propagation distance. Consequently,

this first low amplitude cycle may represent the shear wave arrival. In a numerical model with reflecting boundaries, Arroyo et al. (2006) observed a similar pre-arrival pulse suggesting that the experimental observation may be due to distorting reflections. The first pulse and the main shear pulse were both investigated as possible shear wave arrivals. The first pulse resulted in a phase velocity that increased without bounds with decreasing frequency. The main shear pulse resulted in a less sensitive change with frequency. Therefore, the main shear pulse is considered indicative of the shear wave arrival. This point is very important. It is why the developed method can be used to investigate Type 3 signals. Other techniques provide no guidance on the commonly observed low amplitude pre-arrival cycle.

Figure 4.5 shows the applied and measured sweeping sine wave over Specimen 016 collected in the same suite of signals in Figure 4.4. The experimental sweeping sine response signal is much more complex than the simulated result in Figure 4.2 but displays the same characteristic trends. In Figure 4.5c, the amplitude of the response rises to a peak at about 11 kHz and then drops away again with increasing frequency. It has been observed that these frequency-dependent features are systematic, but can migrate to different frequencies throughout an experiment.

Figure 4.6 illustrates the reduction of the sweeping sine wave data for Specimen 016. Figure 4.6a shows that the coherence drops off below 3 kHz. This range corresponds to a degraded phase shift in Figure 4.6b. The relative phase shift is plotted as a dashed line in Figure 4.6c. At 9 kHz, the relative phase shift is -35.34 radians. This results in an estimated phase degeneracy of -41.85 + 35.34 = -6.51 radians $\approx -2\pi$. Figure 4.6d depicts the resulting phase and group velocities. As was done for the synthetic signals, the group velocity is calculated over a moving 4 kHz window. In Figure 4.6d, the group velocity is approximately 150 m/s between 3 and 10 kHz, and then drops to 105 m/s at 14.4 kHz. The phase velocity is approximately 158 m/s between 3 and 10 kHz and drops to 142 m/s at 14 kHz.

Table 4.1 summarizes the results for Specimen 016 at 7, 9, 11, and 13 kHz. The phase degeneracy is approximately -2π, independent of the sine pulse and continuous sine frequency. Table 4.2 presents experimental results

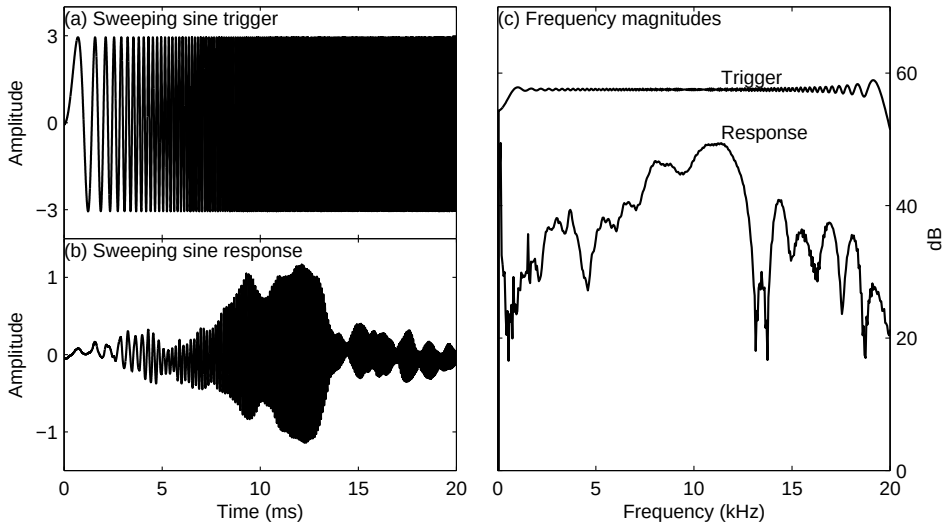

Figure 4.5: Sweeping sine was trigger and response over saturated Fraser River Sand Specimen 016: (a) linear sweeping sine wave trigger; (b) response; and (c) magnitude of the signals in the frequency domain

for all ten specimens at the similar stress and volume states. This table includes the cross correlation from a 9 kHz sine pulse, the phase velocity at 9 kHz, and a group velocity centred at 9 kHz. The phase offsets are $0, -2\pi, -4\pi, or -6\pi$. The phase and group velocities for each bender element test suite in Table 4.2 are plotted in Figure 4.7. This figure shows that the phase velocity converges between 5 and 14 kHz at about 155 $\pm$ 3 m/s, while the group velocity is much more variable.

The results in Table 4.2 correspond to the third suite of bender element tests for each specimen. This corresponds to a stress state of $\sigma'_a = 160$ kPa, $\sigma'_r = 80$ kPa at which a wide band of frequencies were propagated. The observation of test to test reproducible phase velocities and variations in group velocities was made for all four suites of bender tests. At lower stresses, the resonance peak locations are more compressed, the group velocity is more variable, and the bender element system has a smaller operating frequency range.

Table 4.1: Measured phase offsets at four different frequencies for saturated Fraser River Sand Specimen 016 at 159.6 kPa, 79.2 kPa, note that the phase offset, θ_o, is approximately constant and independent of the input frequency

Frequency (kHz)	$\Delta t^{(a)}$ (ms)		Phase (radians)		
	$SP^{(b)}$	$CS^{(c)}$	$\Delta\theta_a^{(d)}$	$\Delta\theta_r$	$\theta_o^{(e)}$
7	0.774	0.760	-33.43	-27.19	-6.24
9	0.778	0.774	-43.77	-37.60	-6.17
11	0.778	0.772	-53.36	-47.33	-6.04
13	0.778	0.786	-64.21	-58.23	-5.98

(a) Cross correlation
(b) Sine pulse
(c) Continuous sine
(d) $\Delta\theta_a = -2\pi f \Delta t$
(e) $\theta_o = \Delta\theta_a - \Delta\theta_r$

Table 4.2: Ten different bender element results at similar stress and void conditions for saturated Fraser River Sand

ID	σ'_a (kPa)	σ'_r (kPa)	void ratio	L_{tt} (mm)	$\frac{L_{tt}}{D}^{(a)}$	θ_o (rad)	$V_{S-TD}^{(b)}$ (m/s)	$V_{S-PH}^{(c)}$ (m/s)	$V_{S-GRP}^{(d)}$ (m/s)
004	159.7	80.1	0.969	118.50	1.87	-4π	152	151	157
008	161.2	80.6	0.987	118.34	1.87	-6π	151	151	161
012	160.4	80.0	0.965	119.48	1.89	0	153	153	158
015	161.2	80.9	0.965	118.67	1.87	0	155	154	161
016	159.6	79.2	0.977	119.96	1.90	-2π	155	158	149
020	160.7	80.1	0.977	118.68	1.87	-2π	156	157	151
021	160.2	79.7	0.988	119.81	1.90	-2π	157	159	150
023	160.3	79.7	0.974	120.85	1.91	0	154	156	150
024	159.8	78.9	0.969	121.55	1.92	-2π	154	155	146
027	160.6	79.7	0.974	120.76	1.90	0	151	151	153

(a) Slenderness ratio
(b) Cross correlation of a 9 kHz sine pulse
(c) Phase velocity at 9 kHz
(d) Group velocity between 7 and 11 kHz

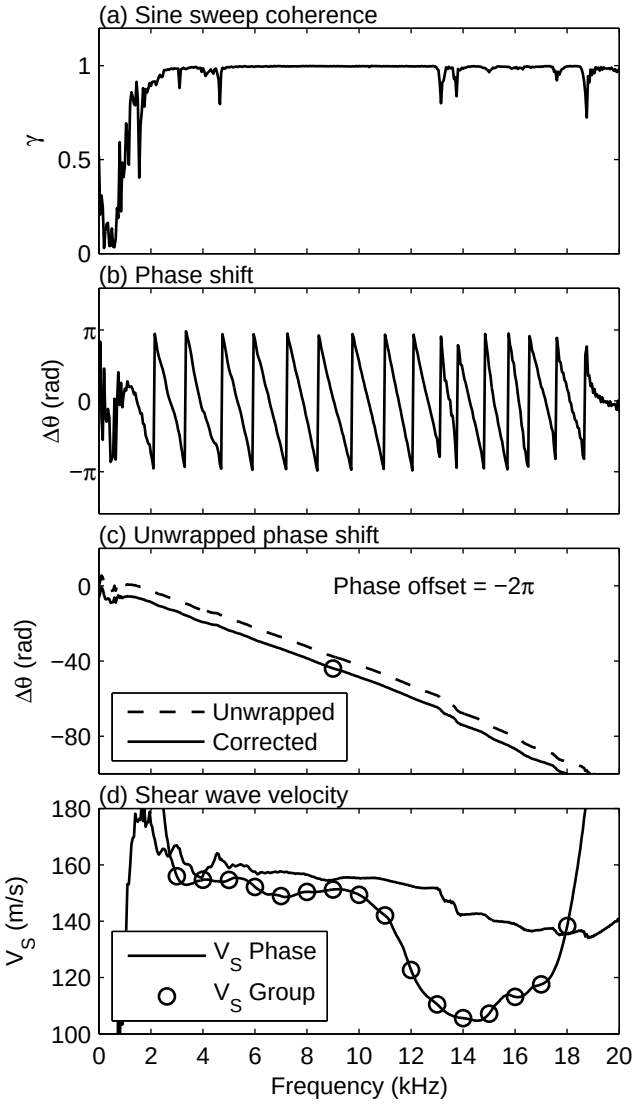

Figure 4.6: Interpreted results for specimen 016: (a) coherence function; (b) calculated phase shift; (c) unwrapped and corrected phase shift; and (d) phase and group velocities

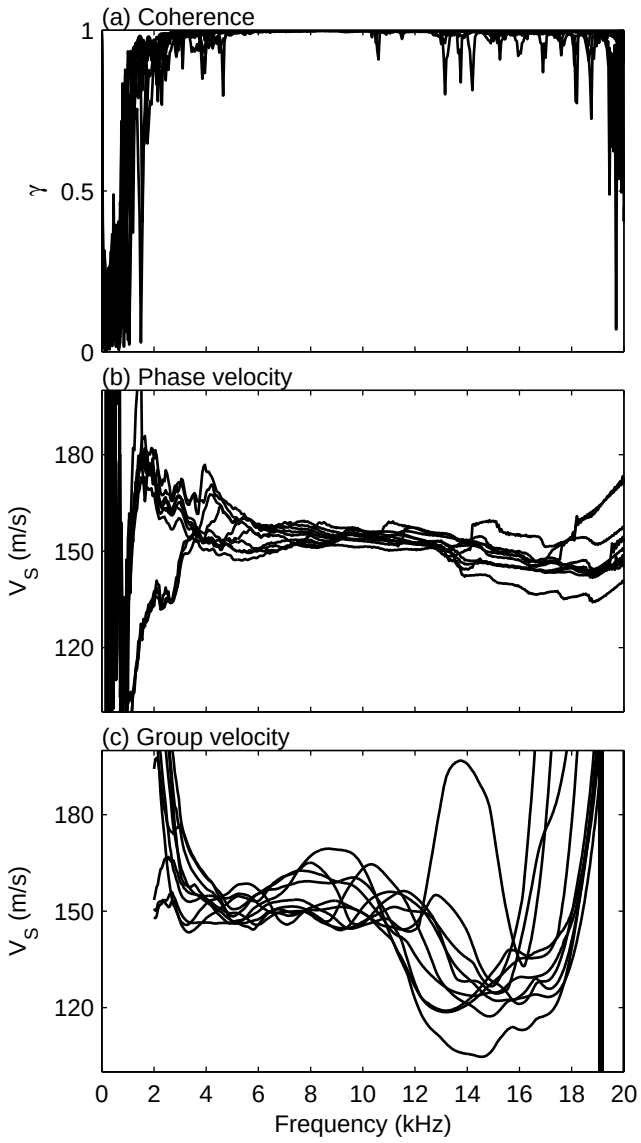

Figure 4.7: Interpreted phase and group velocities for all ten experiments of saturated Fraser River Sand specimens at stress and volume states indicated in Table 4.2

4.4 Observing the effect of ageing on V_S

As noted in Section 3.4.3, current methods of interpretation of bender results were unable to provide sufficiently consistent values of G_0 to assess the effects of ageing. Published techniques to interpret bender element tests are in the time domain (Section 2.2.7) or frequency domain (Section 2.2.8). The results were inconclusive. More troubling, a Type 3 signal (Section 2.2.6) was observed adding considerable uncertainty to the estimation of the propagation time from time domain techniques.

Figure 4.8 shows the interpretation of the bender element signals from Specimen 261 using the combined TD and FD approach. This figure demonstrates that an increase in V_S does occur during ageing. It also suggests that the increase in V_S is log-linear as the change from 1 to 10 minutes is almost equal to the change from 10 to 100 minutes. This trend may be extrapolated to explain observed differences between laboratory reconstituted specimens and aged field results.

Figure 4.8 includes some evidence that illustrates the difficulty in using conventional time domain or cross-spectrum approaches. The velocity is frequency dependent. Therefore, a phase velocity should be interpreted instead of a group velocity. There are significant frequency-features at 6 kHz and near 15 kHz. These are likely to be resonance peaks in the bender-soil system. A cross-spectrum velocity calculated over a resonance peak will not give reasonable results. The data in Figure 4.8 should be interpreted at frequencies where the V_S is stable. In this figure, this range is between 6.5 and 14 kHz.

4.5 Discussion

Based on the results obtained with simulated and experimental bender element signals, the interpreted group velocities appear to have three main problems: they appear sensitive to dispersion, the results are not reproducible test to test, and the method is contingent on unmeasured input criteria: the selection of a frequency window for linear regression.

The effect of dispersion on the group velocity is apparent in the simulated

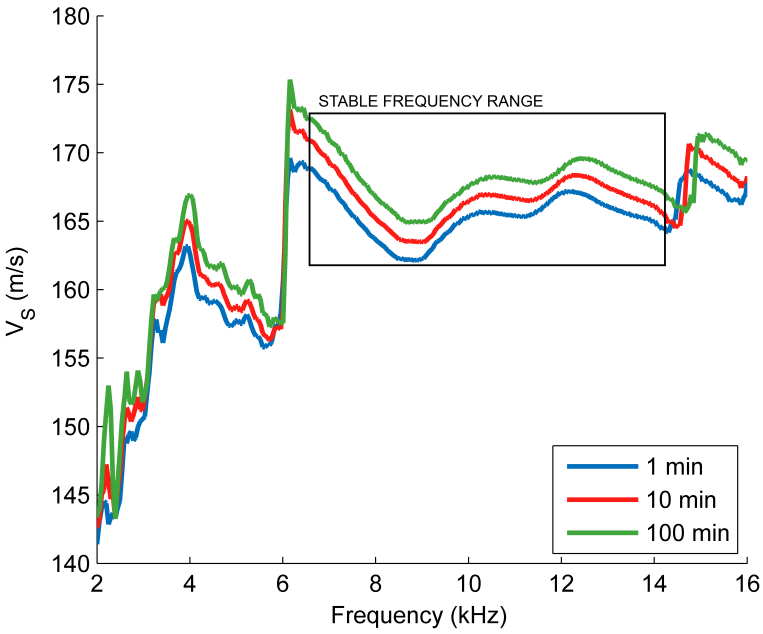

Figure 4.8: TD-FD technique on bender elements tests during ageing of Specimen 261 ($\sigma'_a/\sigma'_r = 2.0$, e=0.964-0.962) with annotated stable frequency range

signals where it is controlled by the bender element resonance model. In the simulated signals (Figure 4.3), the group velocity reaches a minimum at the simulated resonant frequency of the bender element. In the experimental signals (Figure 4.6d), the group velocity deviates from the phase velocity around 14 kHz.

Figure 4.7 depicts 9 of the 10 experimental signals exhibiting this drastic drop in V_S above 11 kHz. The group velocity measurements are not reproducible test to test. Below 11 kHz, the group velocities do not appear to converge on a single solution over any frequency range. The multiple resonance peaks result in a highly variable group velocity characterization. Small variations in the frequency dependent dispersion are exaggerated when the slope is calculated.

The final problem is that the group velocity measurements vary with

the selected frequency range. For the results presented, a 4kHz moving frequency window was used as suggested by Viana da Fonseca et al. (2009). The measured group velocity changes based on the selected frequency window size and location. Recommendations have been published for selecting the group velocity frequency window based on the coherence function or correlation coefficient (Viana da Fonseca et al., 2009; Viggiani and Atkinson, 1995). However, the resulting frequency window is still selected by the interpreter and this choice will influence the results.

The results of time domain methods are also influenced by required subjective input. This includes the selected trigger waveform, frequency, and interpretation method. For the same measured signals, different interpretations result in different velocities (Viggiani and Atkinson, 1995). The selected waveform and frequency also bias the results due to the resonant frequency of the bender element system (Lee and Santamarina, 2006). Developing objective criteria for TD bender element interpretations is difficult due to the lack of representation of influencing factors in the model of a bulk propagating elastic wave through a non-dispersive linear elastic continuum. The characterization of the phase velocity does not assume a bulk propagating elastic wave. The effects of dispersion, while not individually isolated, all influence the resulting measured phase velocity.

The proposed phase velocity method uses only measured input values. It measures the relative phase shift in the frequency domain. The absolute phase shift is measured at a point in the time domain. These two values are used to correct the unwrapped relative phase shift and calculate the phase velocity. It was demonstrated that the sine pulse trigger signal frequency is arbitrary. In this work, frequencies of 7,9,11 and 13 kHz all resulted in the same phase offset. The phase velocity approach measures the velocity and does not require any external input.

4.6 Conclusion

The time domain and frequency domain approaches can be combined in order to measure the phase velocity. The time domain cross correlation

technique was used to solve for the phase degeneracy and find the absolute phase shift. An unwrapped phase shift from a sweeping sine wave was used to find the relative phase shift over the bender element frequency range. It was shown that the same phase degeneracy and phase offset were determined for four different analysed frequencies. This makes the selected frequency arbitrary instead of subjectively influencing the results. This can lead to a consistent frequency dependent measurement of the phase velocity. Conversely, time domain results are influenced by the trigger waveform and interpretation method. Group velocity interpretations are influenced by the selected frequency window.

The combined method was demonstrated using synthetic and experimental signals. The reproducibility test to test of this method was demonstrated over ten saturated specimens of Fraser River Sand. These results were compared to cross spectrum group velocity measurements. It was found that:

- Realistic coherence functions from simulated bender element signals can be achieved using a high pass filter and noise signal, as shown by comparing Figure 4.3(a) to Figure 4.6(a).

- Group velocity methods are sensitive to dispersion, not reproducible, and contingent on subjective input, as demonstrated experimentally and depicted shown inFigure 4.6(c).

- The phase degeneracy can be determined at selected arbitrary frequencies in the bender element operating range, as detailed in Table 4.1 for four different frequencies.

- The proposed method determines the shear wave phase velocity using only measured values over the bender element frequency operating range.

- The proposed method was capable of observing the small effect of age on V_S in a clean specimen of Fraser River Sand.

The proposed method provides a more complete analysis of bender element testing than available from time domain or cross-spectrum results.

The proposed method overcomes many drawbacks of existing techniques. It acquires the phase velocity over the bender-soil system and is less subjective than other interpretation methods. One unresolved issue is the isolation of the soil response when using a two-bender element system to determine the shear wave velocity.

In Section 3.4.3 it was observed that different trigger signals and interpretation methods resulted in an unacceptable range of V_S interpretations and G_0 calculations. The proposed method systematically combines the results from a suite of trigger signals in both the time and frequency domain. It is shown that these results all converge on a single phase velocity solution. A V_S value can be selected with more confidence from the observed variations in the phase velocity. The N_G factor can be better quantified. The bender element equipped triaxial apparatus can now be used to confidently acquire G_0.

Chapter 5

Development of a continuous bender element phase velocity monitoring method

The combined TD and FD method interpreted the phase velocity from a suite of bender element trigger signals. One of the trigger signal waveforms was a 20 ms duration continuous sine wave. This was used to find the relative phase shift at a single frequency. There is no reason to stop the continuous sine wave after 20ms. It could operate continuously and the relative phase shift could be monitored in real time.

This chapter describes a procedure by which shear wave velocities can be monitored continuously throughout a triaxial test. To achieve this, the triggering element is subjected to continuous excitation at one end of the sample and the response of the bender at the opposite end is recorded and analyzed to determine the travel time. Instead of performing a bender element test at a discrete point in the test over a finite amount of time, the bender element test is running throughout the experiment. The method allows V_S to be measured during dynamic phases of the experiment, such as during changes in the stress path direction, the onset of ageing, the onset of shearing, and during the phase transformation from contractive to dilative behaviour. It does not require special equipment; it uses a typical bender

element setup.

The proposed continuous method has been accepted for publication in the ASTM Geotechnical Testing Journal (Styler and Howie, 2014).

5.1 Continuous monitoring method

Blewett et al. (1999) monitored the change in the relative phase shift of a continuous sinusoidal trigger signal. This was corrected to the absolute phase shift based on a square pulse trigger test. In the current approach, we use a multi-tonal signal to transmit multiple frequencies which is complemented by a small number of sine pulse triggers to find the constant phase offsets. The multi-tonal signal addresses the challenges posed by migrating frequency features and resonance peaks during an experiment.

The relative phase shift between the two signals $\Delta\theta_r$ is monitored for multiple frequencies in real time during an experiment. Monitoring the relative phase shift includes correcting the arc-tan discontinuities.

Continuous sinusoidal signals do not provide enough information to determine the absolute propagation time. The evolving relative phase shift can be monitored, but no information is provided for the phase offset correction. The phase offset is determined using a small set of discrete conventional bender element tests.

The absolute phase shift is determined using a suite of bender element tests as described in Chapter 4. The absolute phase shift at a single frequency is compared to the monitored relative phase shift at the same frequency to determine the constant phase offset. The phase offset is $\theta_o = \Delta\theta_a - \Delta\theta_r = n2\pi$, where n is an integer. At a minimum, a single absolute phase shift is required during an experiment to find the constant phase offset. Determining the absolute phase shift multiple times during an experiment confirms that the phase offset from the tracked relative phase shift is a constant for a single frequency.

Migrating resonance peaks can influence the monitored shear wave velocity. To address this, multiple different frequencies are monitored. These multiple frequencies will be affected differently by migrating resonance peaks.

The continuous shear wave velocity method determines the shear wave velocity at multiple frequencies throughout an experiment. This is accomplished by using a continuous sinusoidal trigger signal. The continuous multi-tonal sinusoidal trigger signal may be expressed as:

$$trg(t) = sin(2\pi f_1 t) + sin(2\pi f_2 t) + sin(2\pi f_3 t) + sin(2\pi f_4 t) \tag{5.1}$$

for four different constant frequencies f_1, f_2, f_3, and f_4. Every time the experimental sensors are sampled, the phase angles of the bender trigger and response signals are measured at the multi-tonal frequencies.

5.2 Experimental demonstration

Procedure

The bender element monitoring technique has two components: continuously measuring the relative phase shift and discrete measurements of the absolute phase shift.

Multiple phase velocities were monitored simultaneously at four frequencies: 6.25, 7.15, 8.35, and 10 kHz. These four frequencies are within the bender element frequency operating range for most of the soil states in the reported experiments. Approximately 3 times per second, the relative phase shifts for the 6.25, 7.15, 8.35, and 10 kHz frequency components were measured and recorded. This was accomplished by analysing a 20 ms window of the trigger and response bender element signals. The 20 ms windows were used in Equation 2.3 to solve for the frequency dependent relative phase shifts. The four phase shifts were recorded simultaneously with the five triaxial sensors.

The multi-tonal trigger signal was temporarily suspended to perform absolute phase shift measurements. This was performed during consolidation at σ'_r stresses of 60, 70, 80, and 90 kPa. The absolute phase shifts for the 6.25, 7.15, 8.35, and 10 kHz frequency components were determined from a

suite of bender element tests using the procedure described in Chapter 4. This suite of tests included two sweeping sine waves, four sine pulses (at the multi-tonal frequencies), and four 20 ms continuous sine triggers. Each of the trigger signal waveforms was stacked 10 times to increase the signal to noise ratio.

The absolute phase shift was measured four times at different points during consolidation. These repeated measurements demonstrated that the phase offset, $\theta_o = n2\pi$ was constant for each frequency throughout the experiment. The n parameter is a constant integer for each experiment at each frequency.

The four monitored frequencies are different than what was used in Chapter 4. A multi-tonal signal with only integer value frequencies repeats every 1ms. This does not occur with the selected fractional frequencies(6.25, 7.15, 8.35, and 10 kHz). It was thought that the relative phase shifts for these four frequencies might correspond to only one plausible absolute phase shift. Then, the absolute phase shift and phase velocity could be calculated in real time without performing discrete bender testing. This approach proved difficult to pursue due to challenges from moving resonance features. It was not further pursued in this research.

Results

In order to demonstrate the continuous monitoring method, the results from a single experiment are presented in detail. Figure 5.1 depicts the 6.25 kHz components of four discrete bender element tests performed on Specimen 040. The 6.25 kHz component consists of two trigger signals. The first was a 6.25 kHz sine pulse, and the second was a 20 ms duration 6.25 kHz continuous sine wave (only the first 2 ms are depicted). Each subfigure in Figure 5.1 contains two plots. The upper plot is the received wave from the 6.25 kHz sine pulse. The lower plot is the cross correlation of the 20 ms duration continuous wave. The cross correlation function resulted in a series of peaks. The peak corresponding to the arrival of the sine pulse was selected as the propagation time for the 6.25 kHz wave. This propagation

time was used to solve for the absolute phase shift, $\Delta\theta_a = -2\pi f \Delta t$. The bender tests depicted in Figure 5.1 were performed at different stress states during consolidation of Specimen 040. As the stress increased, the specimen consolidated and the absolute phase shift decreased, resulting in a faster propagation time.

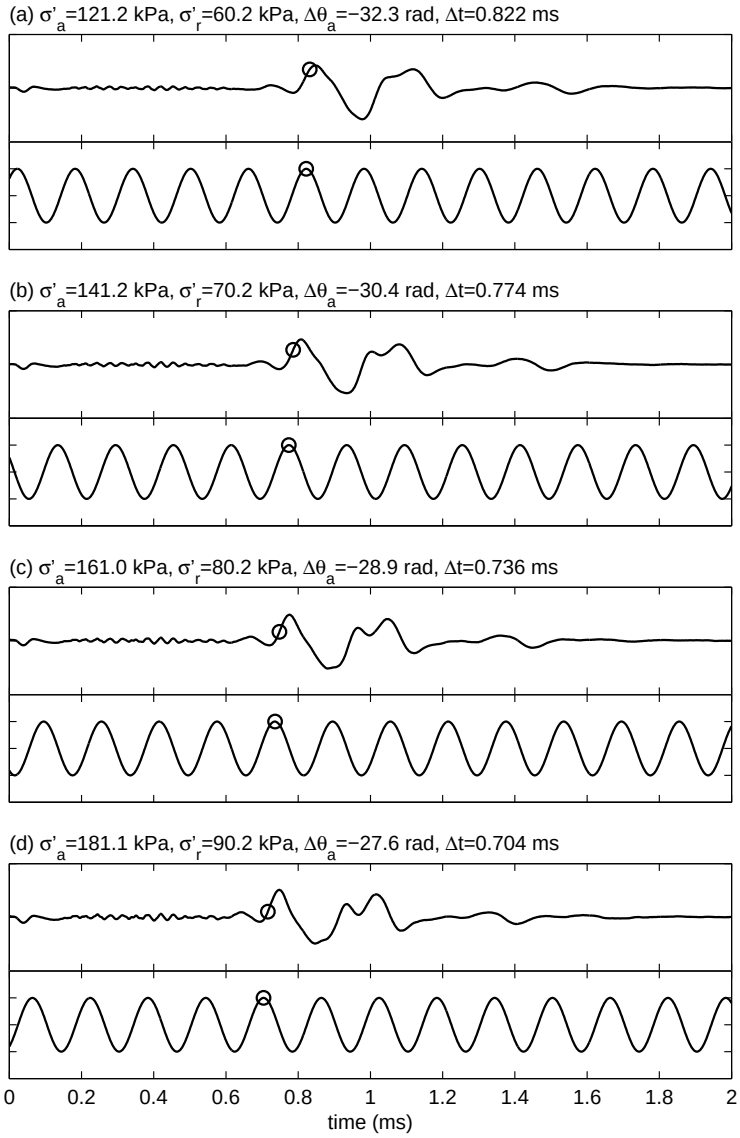

Figure 5.1: Measured 6.25 kHz sine pulse response and cross correlation of 6.25 kHz continuous sine wave during drained consolidation of loose saturated Fraser River Sand Specimen 040 to acquire absolute phase shift of a 6.25 kHz wave at multiple points during the experiment

The relative phase shift was monitored continuously at four frequencies using a multi-tonal sinusoidal trigger signal. Figure 5.2 depicts a 2 ms window of the applied and measured multi-tonal continuous trigger signal in the time domain and frequency domain immediately prior to the discrete bender element test in Figure 5.1d. In the time domain, the received signal resembled the applied signal. In the frequency domain, it is shown that these signals contained all of their energies at the four selected frequencies: 6.25, 7.15, 8.35, and 10 kHz.

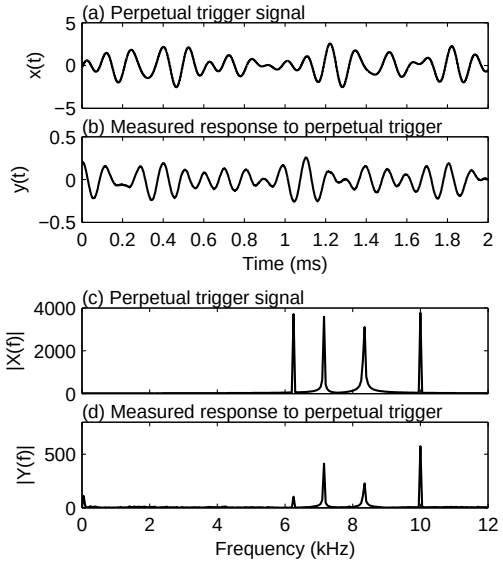

Figure 5.2: Perpetual trigger and response signals in the time domain (a,b) and frequency domain (c,d) applied to and measured over drained saturated Fraser River Sand Specimen 040 at $\sigma_a = 181.1$ kPa, $\sigma_r = 90.2$ kPa to monitor the relative phase shift ($\Delta\theta_r$) at four frequencies, 6.15, 7.15, 8.35, and 10 kHz

Figure 5.3 depicts the measured 6.25 kHz relative phase shift during the triaxial test of Specimen 040. The specimen was consolidated for 17.7 minutes at a stress ratio of σ_a/σ_r of 2.0, followed by 100 minutes of ageing. It was then sheared along a conventional stress path of increasing σ_a to failure. Figure 5.3 depicts *arc tan* discontinuities during consolidation, one

noise spike during ageing, and eight noise spikes during shearing. Figure 5.4 depicts the unwrapped 6.25 kHz relative phase shift for the first 25 minutes of the triaxial test of Specimen 040. This figure includes the four measured relative phase shifts immediately prior to the discrete bender element tests depicted in Figure 5.1.

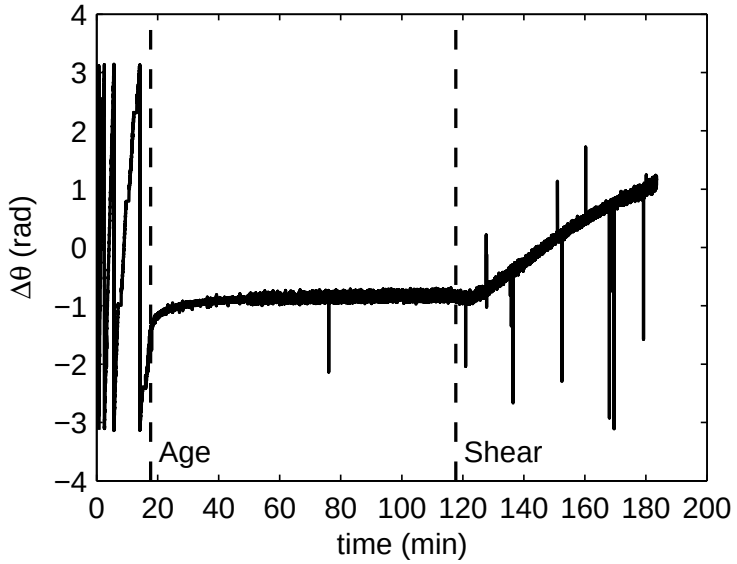

Figure 5.3: Measured relative phase shift from 6.25 kHz component of perpetual trigger and response signals over consolidation, ageing, and shearing of saturated Fraser River Sand specimen 040

The continuous method requires a constant phase offset correction between the unwrapped monitored relative phase shift and the measured discrete absolute phase shift. Table 5.1 details the calculated phase offsets for Specimen 040. The absolute phase shift was measured at four frequencies and at four different times during consolidation. Figure 5.1 depicts the 6.25 kHz absolute phase shifts at these four points.

The frequency of the bender element shear wave has a systematic effect on the resulting shear wave velocity. This was previously shown in Chapter 4 and specifically Figure 4.8. It is further shown in Table 5.1. The ultimate objective in a bender element test is to obtain a single velocity for the

propagation of a shear wave through the soil. A technique to correct the systematic effect of frequency has not been developed in this work or in other published research to date. Consequently, bender element V_S results should be reported with the wave frequency.

Figure 5.4 shows the measured relative phase shifts for the 6.25 kHz wave at four points during consolidation. The time for consolidation is due to the rate of stress increase and temporary pauses to perform suites of bender element tests to obtain the phase offsets. The consolidation test phases lasts 17 minutes. The triaxial specimen of sand does not take 17 minutes to consolidate.

The phase offset is the difference between the discrete absolute phase shift points and the monitored corrected relative phase shift. The difference between the absolute phase shift and the relative phase shift must be a multiple of 2π. For Specimen 040, the 6.25 kHz continuously monitored relative phase shift had a phase offset of $-9 * 2\pi$. Making multiple measurements of the phase offset at different points during the experiment confirmed this value.

Figure 5.5 shows the monitored phase velocity at 6.25, 7.15, 8.35, and 10 kHz for the saturated drained Fraser River Sand Specimen 040. There was a large increase in V_S during consolidation up to a 6.25 kHz phase velocity of 175 m/s. The kinks in the measured V_S during consolidation are due to pauses during the test to perform conventional bender element tests. During 100 minutes of ageing the 6.25 kHz phase velocity increased to 179 m/s. When sheared along a conventional shear path the 6.25 kHz phase velocity reached a peak of 183 m/s at $\sigma'_a = 336$ kPa. This figure contains 26319 measurements of the phase velocity for each of the four frequencies. This figure only contains measured phase velocities; it does not contain interpolated values or curve fitting. Before calculating V_S, the monitored change in specimen height was used to adjust the propagation length.

Table 5.1: Measured absolute phase shifts, phase offsets, and phase velocities for a loose saturated drained specimens of Fraser River Sand Specimen 040

Specimen state	Freq. (kHz)	Phase shift (rad) $\theta_a^{(a)}$	$\theta_r^{(b)}$	$\theta_o^{(c)}$	$n^{(d)}$	V_S (m/s)
$\sigma'_a = 121.2$ (kPa)	6.25	-32.28	24.14	-56.42	9	144.1
$\sigma'_r = 60.2$ (kPa)	7.15	-37.02	19.32	-56.35	9	143.7
$e = 0.998$	8.35	-43.44	25.13	-68.58	11	143.0
$L_{tt} = 118.426$ (mm)	10.0	-48.51	26.32	-74.84	12	153.4
$\sigma'_a = 141.2$ (kPa)	6.25	-30.40	25.93	-56.32	9	152.9
$\sigma'_r = 70.2$ (kPa)	7.15	-35.13	21.18	-56.31	9	151.3
$e = 0.996$	8.35	-41.03	27.68	-68.71	11	151.3
$L_{tt} = 118.335$ (mm)	10.0	-46.00	28.90	-74.90	12	161.6
$\sigma'_a = 161.0$ (kPa)	6.25	-28.91	27.44	-56.35	9	160.6
$\sigma'_r = 80.2$ (kPa)	7.15	-33.52	22.89	-56.40	9	158.5
$e = 0.993$	8.35	-39.14	29.64	-68.78	11	158.5
$L_{tt} = 118.250$ (mm)	10.0	-43.99	30.88	-74.87	12	168.9
$\sigma'_a = 181.1$ (kPa)	6.25	-27.65	29.03	-56.67	9	167.8
$\sigma'_r = 90.2$ (kPa)	7.15	-31.99	24.45	-56.44	9	165.9
$e = 0.991$	8.35	-37.46	31.45	-68.91	11	165.5
$L_{tt} = 118.161$ (mm)	10.0	-42.23	32.74	-74.97	12	175.8

(a) Interpreted from a suite of bender element trigger signals
(b) Monitored unwrapped relative phase shift
(c) The difference between the absolute and relative phase shifts
(d) $n = \theta_o/(-2\pi)$, constant for each frequency

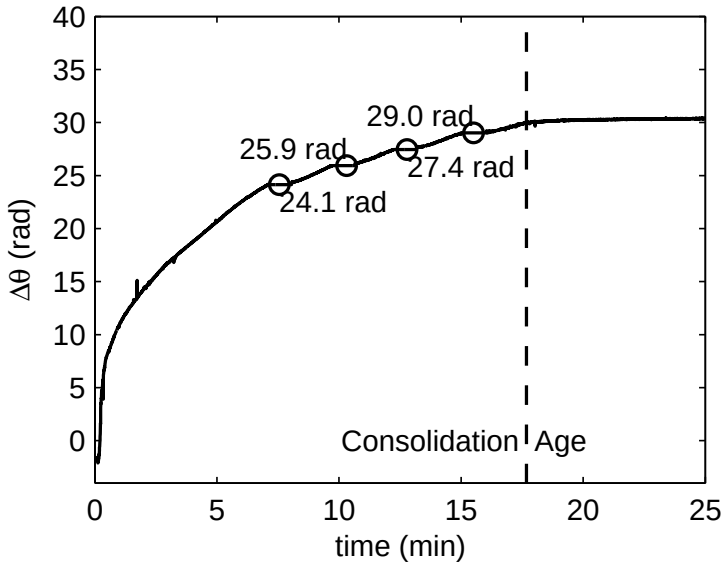

Figure 5.4: Unwrapped relative phase shift during drained consolidation of loose saturated Fraser River Sand Specimen 040

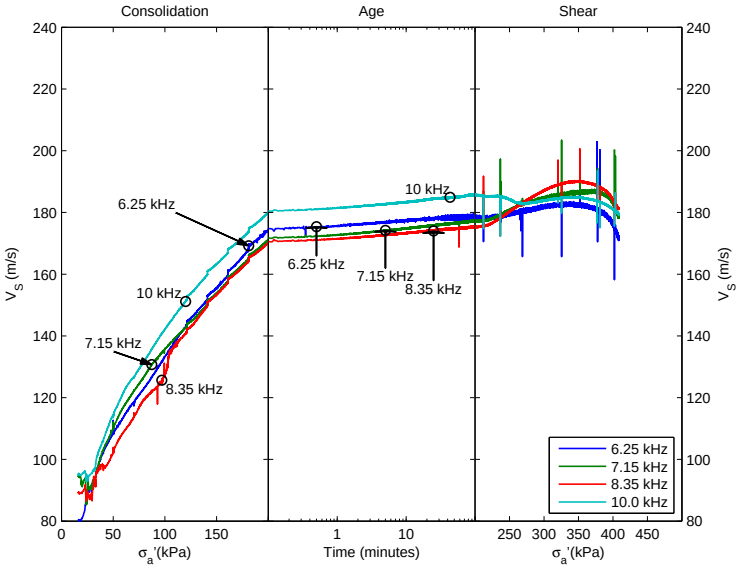

Figure 5.5: Perpetual source measured phase V_S for saturated drained Fraser River Sand Triaxial Specimen 040 with consolidation at a stress ratio of $\sigma_a/\sigma_r = 2.0$, aged for 100 minutes, and sheared along a conventional shear path

5.3 Interpretation challenges

Some noise spikes in the monitored relative phase shift are visible on Figure 5.4. Under certain circumstances, noise spikes resulted in an incorrect phase discontinuity correction. These circumstances depend on the magnitude of the noise spike and the unwrapping algorithm used to correct the discontinuities. Most noise spikes observed in these experiments did not exceed the threshold for a phase discontinuity correction or resulted in two subsequent phase discontinuity corrections that cancelled each other out. However, it was occasionally observed that a noise spike resulted in a single incorrect phase discontinuity correction. In Specimen 048 this occurred for the 8.35 kHz monitored relative phase shift during shearing, as shown in Figure 5.6. The result is an obvious discontinuity in the measured V_S. This effect is corrected by incrementing the remainder of the relative phase shift values by 2π. This inconsistency is easy to identify and easy to fix.

Another problem was observed at low stresses. The continuously monitored frequencies may not be in the bender element testing frequency range. This results in a relatively constant, but incorrect, monitored phase shift during the low stress portion of consolidation. Once a sufficient stress is achieved, the receiver bender element begins sensing the propagating shear wave and the relative phase shift is correct. This inconsistency is depicted in Figure 5.7 for the 10.0 kHz shear wave. At low stresses, the measured relative phase shift and V_S are incorrect. This is easy to identify, but can only be fixed by changing the monitoring frequency. This may be addressed by testing multiple frequencies with a multi-tonal signal as done in this investigation.

Migrating frequency features in the bender element transform function result in a phase velocity where the dominant factor causing the change in velocity is a change in the system transfer function, not a change in the shear wave propagation time. This effect is shown in Figure 5.8 during ageing for Specimens 044 and slightly in 047.

The frequency-dependent features can be observed by calculating the phase velocity over the bender element operating range. The discrete ben-

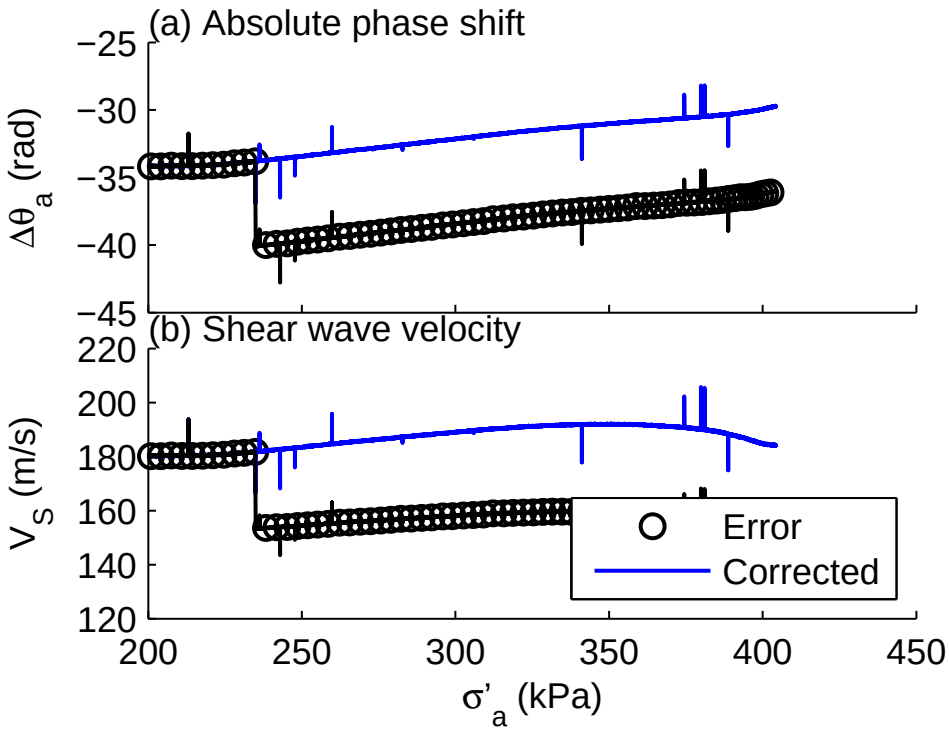

Figure 5.6: Correcting a discontinuity in the 0.835 kHz phase shift in Specimen 048 to result in a continuous measured phase velocity

der element tests consisted of a suite of bender element signals including a sweeping sine wave. Figure 5.9a depicts the magnitude of the transfer function at two different stress states for Specimen 040. The transfer function is the frequency dependent conversion from the input electrical signal, to the mechanical wave in the soil specimen, to the output voltage signal, and then through the signal amplifier. The mechanical response of the soil cannot be isolated without characterizing the transfer functions of the trigger and receiver bender elements. A method to characterize these transfer functions during an experiment has not yet been devised. They must be characterized during an experiment as the soil-coupling will change the response of the bender element cantilever beam. Figure 5.9b depicts the interpreted frequency dependent phase velocity following the method described in Chap-

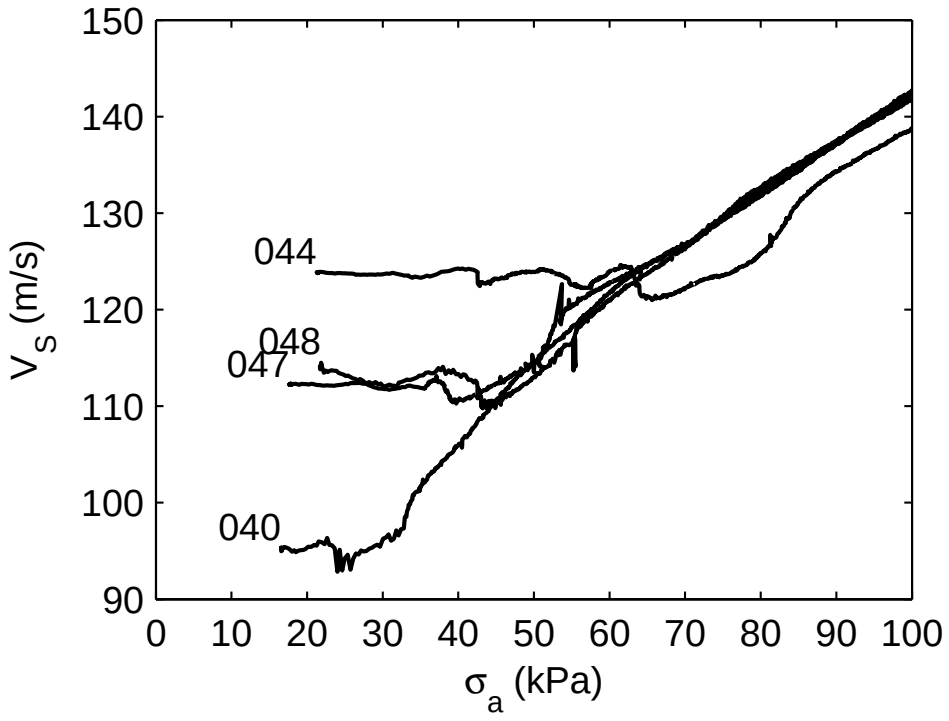

Figure 5.7: Monitored 10.0 kHz shear wave velocities during consolidation of loose saturated Fraser River Sand are not within the bender element frequency operating range at low stresses

ter 4. The frequency dependent features in the phase velocity correspond to changes in the magnitude of the transfer function. The frequency dependent features are translated to higher velocities and different frequencies as the stress increases.

The phase velocity is not constant across the bender element frequency range. This was observed in Specimen 040 as detailed in Table 5.1 and in Figure 5.5. The 10 kHz shear wave velocity was almost 10 m/s faster than the three other frequencies. This 10 m/s difference was not constant throughout the experiment. During shear, the system transfer function changes at 10 kHz. After this change, the 10 kHz signal agrees with the other three frequencies.

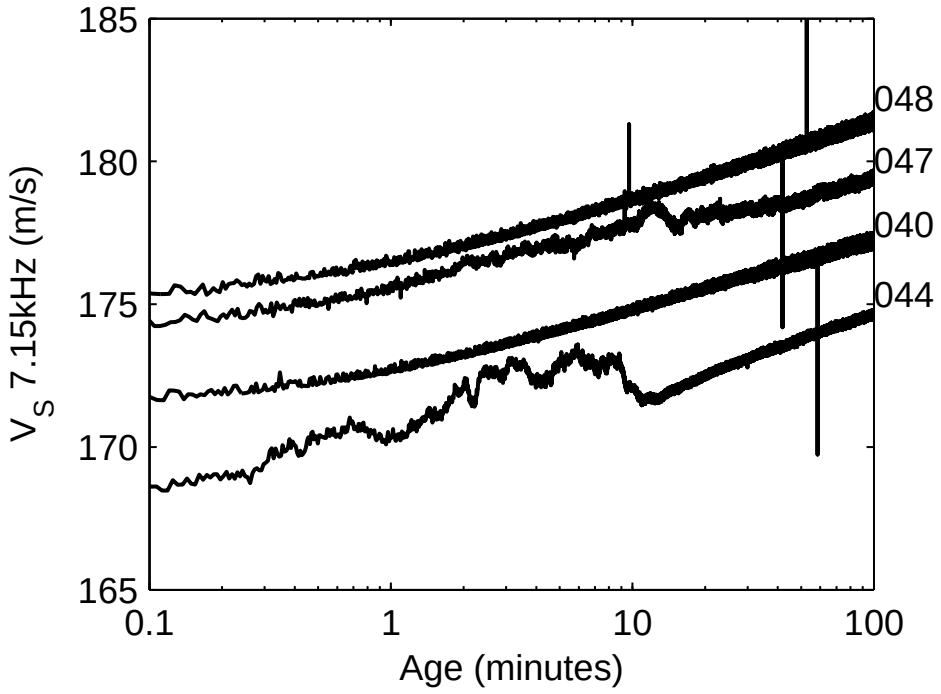

Figure 5.8: 7.15 kHz shear wave phase velocity during ageing of four loose saturated Fraser River Sand specimens at $\sigma_a = 200$, $\sigma_r = 100$ kPa

Figure 5.9b for Specimen 040 contradicts the results in Table 5.1 with the 10 kHz phase velocity being slower than the velocities at 6.25, 7.13, and 8.35 kHz. The difference in the absolute phase shift between the 10 kHz results in Figure 5.9b and Table 5.1 is 2π. The combination of the cross correlation of the sine pulse and continuous sine at 10 kHz resulted in the values in Table 5.1. The sweeping sine wave anchored at the absolute phase shifts for 3 of the 4 signals results in Figure 5.9b. The dispersive phase velocity over the bender-soil system makes it difficult to interpret the results.

It was observed that the trends in V_S with stress and void ratio are typically consistent, even if the V_S measurements at different frequencies disagree. The only time these trends deviate is when a significant frequency feature appears at the frequency being monitored, as depicted during shear

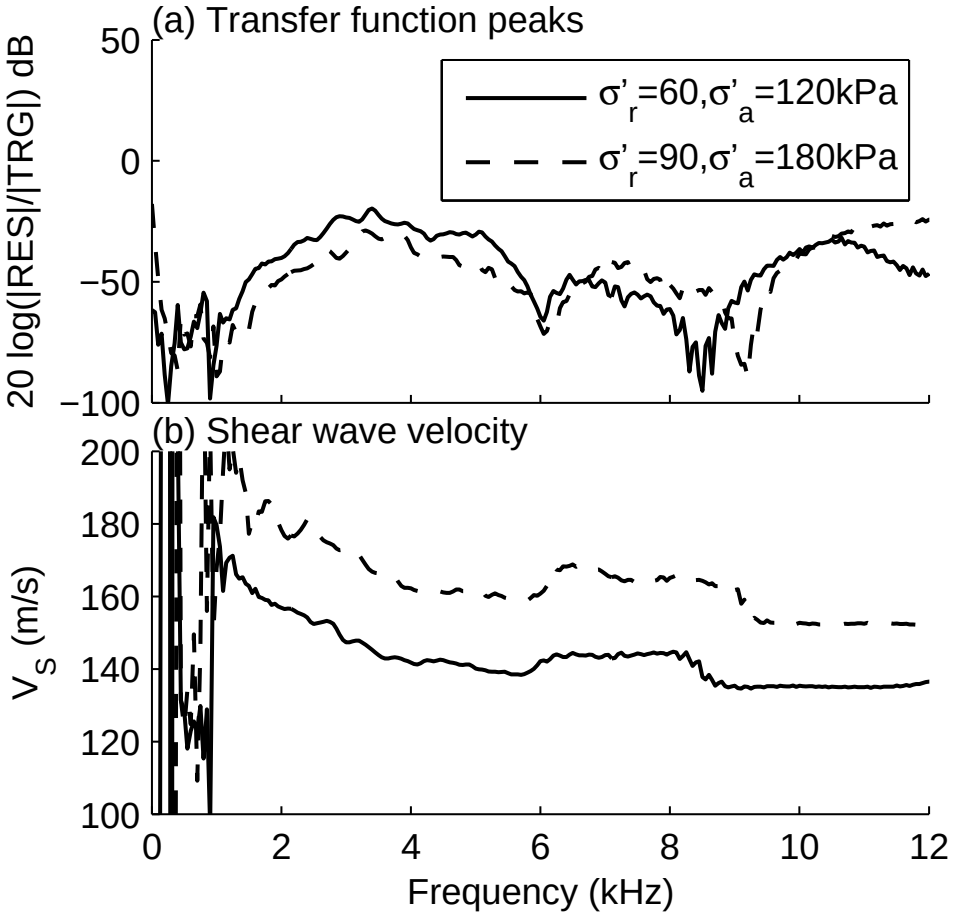

Figure 5.9: Bender element test results from Saturated Fraser River Sand specimen 040; (a) Migration of multiple resonance peaks with increasing stress, (b) Phase velocity against frequency

of Specimen 040 for 10 kHz (Figure 5.5) and during ageing of Specimens 047 and 044 (Figure 5.8). The proposed method monitors the shear wave velocity across the soil-bender system. This compares a trigger voltage signal to a received voltage signal, not the mechanical input and output waves sensed by the cantilever bender elements. The effect of the bender element electrical to mechanical transform function depends on the bender-soil coupling and

changes through-out the experiment. Until a method is devised to measure the transform function during an experiment, judgement must be used to interpret bender element V_S measurements. In order to detect changes in V_S with age, stress, and density; the observer can concentrate on signals that are not adversely affected by the system transform functions. More attention is placed on consistent V_S results than outliers.

The implementation of the continuous technique is mostly automated. In this work, the manual effort involved creating Table 5.1 in order to calculate the phase offset to apply to each monitored phase shift. The discrete bender element tests needed to be manually aligned with the continuous monitored relative phase shifts. The post-processing required in Figure 5.6, to correct discontinuities missed by the phase-unwrapping algorithm, was rarely encountered.

5.4 Evaluation of bender element induced disturbance

For the trigger bender elements, it can be shown that for excitation in air, the bender tip deflection increases with applied voltage. To investigate the potential disturbance to the specimens caused by continuous excitation of the benders and the effect of triggering voltage, the triaxial behaviour was compared between the proposed continuous bender element method and tests without bender element testing. Disturbance was evaluated by comparing axial and volumetric creep strains of loose specimens of Fraser River Sand under $\sigma_a = 200$ kPa and $\sigma_r = 100$ kPa. It was expected that if the continuous trigger signal induced disturbance then the developed creep strains would correlate to the trigger signal amplitude. The testing program, as detailed in Table 5.2, included three specimens without bender element monitoring, two specimens at ± 3 V, one at ± 6 V, and one at ± 10 V.

Creep strains were measured during ageing for all seven specimens. Figure 5.10 shows the measured volumetric strains during constant stress ratio consolidation for the seven specimens. Four of these specimens included continuous bender element trigger excitation. Figure 5.11 shows the measured volumetric creep strains against the applied trigger signal amplitude at 1, 10, and 100 minutes for each specimen. There is no obvious effect of the trigger signal amplitude on the volumetric creep strains.

Table 5.2: Experimental program and specimen properties

ID	B-Value	Void ratio		Perpetual trigger amplitude (V)	N_G
		Initial	End Consolidation		
034	0.991	0.998	0.973 (-0.025)	0	-
040	0.991	1.012	0.989 (-0.023)	± 3	2.1 %
042	0.994	1.025	0.997 (-0.028)	0	-
044	0.990	0.996	0.968 (-0.028)	± 10	2.2 %
047	0.999	0.981	0.954 (-0.027)	± 6	2.8 %
048	0.988	0.998	0.974 (-0.024)	± 3	2.3 %
049	0.992	0.994	0.969 (-0.025)	0	-

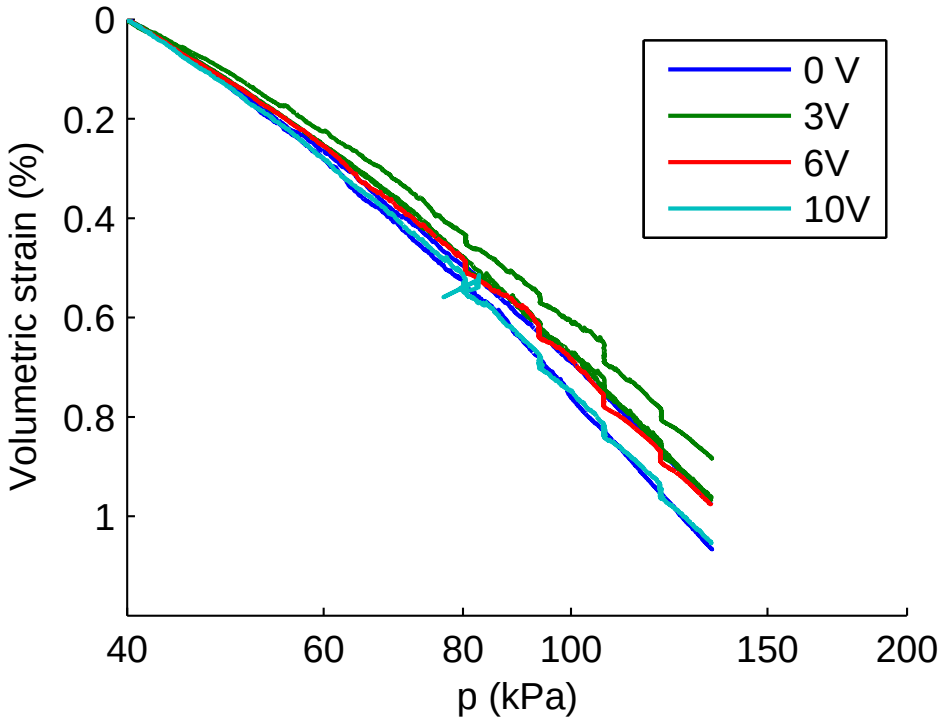

Figure 5.10: Measured volumetric strains during constant stress ratio ($\sigma_a/\sigma_r = 2.0$) consolidation of loose saturated Fraser River Sand

For the four specimens with continuous V_S measurements, the measured increase in phase velocity during ageing is presented in Figure 5.8. This increase in V_S at constant effective stress is similar to observations by Afifi and Richart (1973); Anderson and Stokoe (1978); Baxter and Mitchell (2004). The calculated N_G factors for the specimens with continuous V_S measurements are provided in Table 5.2.

The amplitude of the bender element trigger signals did not result in an observable change in the void ratio during consolidation or in the creep strain magnitudes. For the given loose samples of Fraser River Sand and sensor resolution of the triaxial equipment, the disturbance induced creep strains did not exceed experimental scatter, a function of the repeatability of

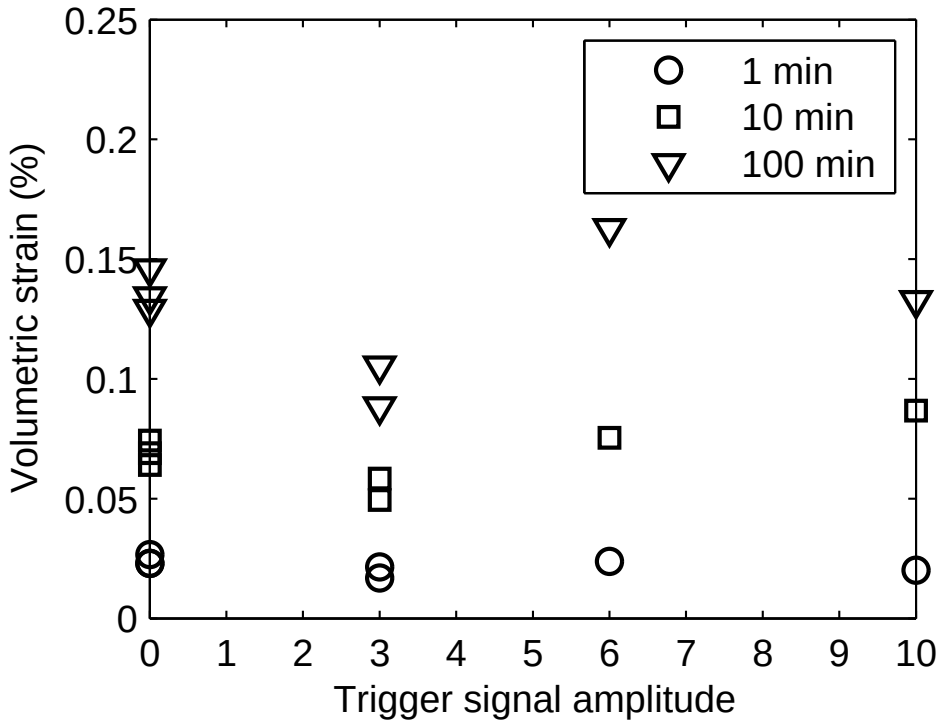

Figure 5.11: Volumetric strains during ageing of seven loose saturated Fraser River Sand specimens at $\sigma_a = 200$, $\sigma_r = 100$ kPa

the specimens and test procedure and the uncertainty of the measurements. The increase in small strain stiffness, as quantified with N_G, did not change significantly with changes in the trigger signal amplitude. The effect of age on the increase of G_0 does not depend on the bender element trigger signal amplitude, for the given equipment up to a trigger amplitude of $\pm$ 10 V. Based on the bender element equipment and soil, continuous monitoring with bender elements was judged to be non-destructive.

There will be a zone of disturbance adjacent to the trigger bender element. This will be due to the mechanical triggering of the shear wave from the bender element. The extent of this zone could not be examined with the UBC triaxial equipment. For the triaxial specimens with a propaga-

tion length around 120 mm, this zone of disturbance was unobservable. For shorter propagation lengths, such as in an oedometer cell, the proportion of disturbance caused by the continuous excitation of the trigger bender element may be significant. However, it was not examined in this study.

5.5 G_0 during ageing of Fraser River Sand

The observed G_{sec} at small strains along conventional stress paths is sensitive to specimen age duration (Lam, 2003; Shozen, 2001). There were two different expectations for the effect of ageing on G_0 in Fraser River Sand. The trend in results from Shozen (2001) showed an increased sensitivity to ageing at lower strains. This suggests a significant increase in G_{sec} at the even lower shear wave strain level. Conversely, published resonant column results found a negligible increase in stiffness during ageing for clean sands, as summarized in Section 2.3.4.

Continuously monitored bender element measurements depicted either stable or unstable behaviour. Figure 5.12 is an example of stable bender element behaviour during ageing and Figure 5.13 is an example of unstable bender element behaviour during ageing. Unstable ageing was observed without any noticeable stability issues in the creep strain measurements. It appears to be a result of the migration of resonance peaks in the bender element transducer-sensor system as the soil stiffens. An advantage of continuous bender element monitoring is that the results can be screened for stable bender element behaviour. This prevents the characterization of erroneous N_G factors that may be too high or even negative.

The N_G factor, Equation 2.10, is the normalized change in G_{vh} per log-cycle of time. The calculated N_G factors are detailed in Table 5.3. The median stable N_G factor for ageing of G_{vh} was 1.9$\pm$0.5 % for loose specimens and 1.0 $\pm$ 0.2 % for the stable denser specimens. These results agree with the published values of 1-3 % for coarse grained soil (Anderson and Stokoe, 1978).

In this chapter G_{vh} corresponds to a stiffness interpreted from a bender element shear wave velocity propagating in the vertical direction with hori-

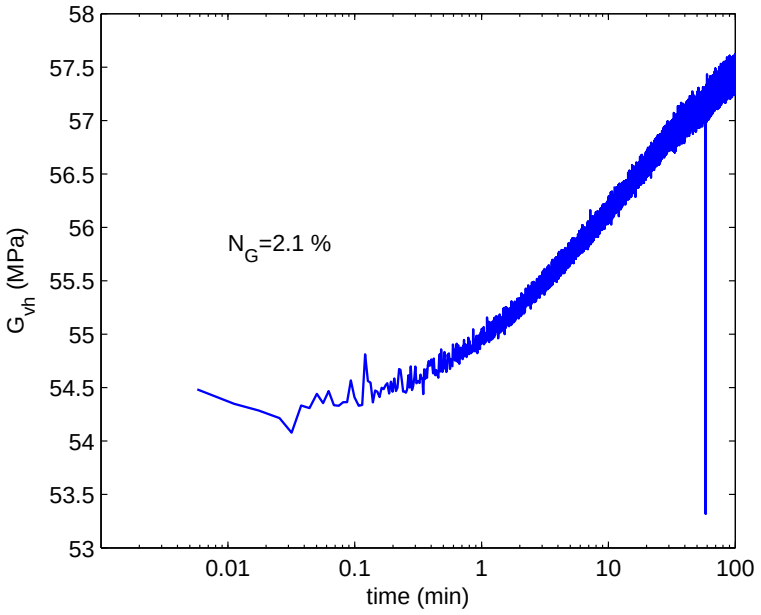

Figure 5.12: Example of stable ageing for Specimen 040 at 8.35 kHz

zontal particle motion. G_{vh} represents interpreted values from measured V_S. G_0 is used when referencing the isotropic elastic shear stiffness, when referring to theoretical equations, when discussing other publications to match their nomenclature, and when presenting normalized G_{sec}/G_0 curves.

The N_G equation is normalized by G_0 at 1000 minutes to avoid an apparent change in the log-linear behaviour for fine grained specimens (Afifi and Richart, 1973; Anderson and Stokoe, 1978). For coarse-grained specimens Anderson and Stokoe (1978) observed a log-linear increase in G_0 from the start of ageing. They speculated that it may not be initially log-linear, but were unable to make this observation using resonant column equipment. Figure 5.12 shows that the log-linear behaviour begins around 1 minute after the onset of ageing in clean Fraser River Sand.

The bender element modified triaxial equipment is capable of acquiring G_{sec} and G_{vh}. It can be used to characterize the G_{sec}/G_0 degradation with shear strain during the shear phase. It can also be used to calibrate an

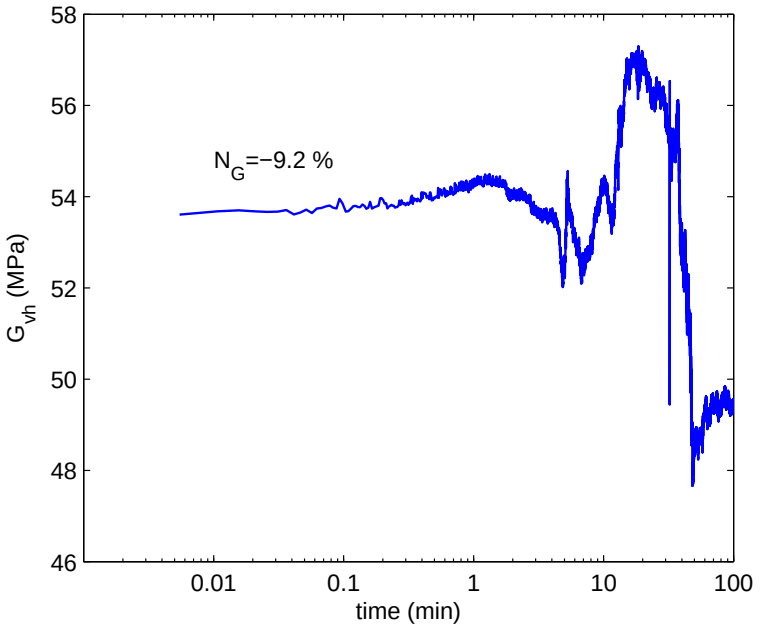

Figure 5.13: Example of unstable ageing for Specimen 015 at 9 kHz

empirical G_0 equation for Fraser River Sand.

5.6 Calibration of G_0 equation for Fraser River Sand

The form of the calibrated empirical equation is given in Equation 5.2. It has three empirical components: the leading coefficient A, the void ratio function f(e), and the in-plane effective stress exponent (n/2). The stress exponent is divided by two to match a convention by Hardin and Blandford (1989). The original work by Hardin raised the isotropic stress to the power of n. When it was found that the shear wave velocity depends only on the in-plane stresses, it required the equation to be modified. If the soil is under isotropic effective stress and σ'_0 replaces both σ'_a and σ'_r, then the original equations are obtained as the two $n/2$ exponents are added together.

Table 5.3: Calculated N_G factors(Equation 2.10) for continuously monitored bender element tests

Specimen	σ'_a	σ'_r	Void ratio	N_G	Stable
004	199.0	99.9	0.966	1.8 ± 0.2 %	Yes
008	200.1	100.1	0.984	1.7 ± 0.4 %	Yes
012	199.9	99.9	0.962	2.9 ± 0.4 %	Yes
013	100.0	100.0	0.971	-1.3 ± 2.8 %	No
014	280.3	100.2	0.937	2.0 ± 0.3 %	Yes
015	199.9	100.2	0.962	0.8 ± 10.8 %	No
016	199.6	99.7	0.973	2.0 ± 0.4 %	Yes
018	199.6	99.6	0.760	1.0 ± 0.2 %	Yes
019	198.6	99.1	0.816	0.2 ± 7.2 %	No
020	200.0	99.9	0.974	-0.3 ± 0.4 %	No
023	200.3	100.0	0.970	0.1 ± 3.2 %	No
024	200.7	100.2	0.965	-5.8 ± 4.2 %	No
026	99.9	99.9	0.952	3.3 ± 2.5 %	No
027	200.5	100.3	0.970	3.9 ± 1.4 %	No
040	200.9	100.3	0.989	2.0 ± 0.5 %	Yes
043	194.0	100.8	0.968	2.2 ± 0.7 %	Yes
044	200.5	100.0	0.968	2.7 ± 1.1 %	Yes
047	200.4	100.1	0.954	2.8 ± 0.9 %	Yes
048	200.8	100.1	0.974	2.3 ± 0.4 %	Yes

$$G_0 = Af(e)\left(\sigma'_a\sigma'_r\right)^{n/2} \tag{5.2}$$

An attempt to isolate the effect of the in-plane stresses on G_0 was made. A dataset was compiled for the measured G_0 at void ratios of 0.96, 0.97, and 0.98, at stress ratios of 2.0, without any ageing. The underlying assumption is that the void ratio term, f(e), would be approximately constant since the specimens are at the same void ratio and stress ratio. This resulted in a stress exponent $(n/2)$ of 0.31.

The stress exponent was calibrated from 18 similar experiments and resulted in $n/2 = 0.31$. This is slightly higher than the expected $n/2 = 0.25$ from Hardin and Blandford (1989). It is within the range of published

empirical relationships for many sands summarized by Cho et al. (2006), and similar to some of the crushed sand types.

Three potential published void ratio functions were investigated. The first two are from Hardin and Black (1966), the third one is from Hardin and Blandford (1989). None of these three equations clearly provided an improved empirical fit. Therefore, the most recent formulation, Equation 5.3, will be used.

$$f(e) = \frac{1}{0.3 + 0.7e^2} \tag{5.3}$$

In this study, the intrinsic particle properties are constant - Fraser River Sand is used for every experiment. The leading coefficient in the empirical equation, A, should be a constant. A value of 2440 was calibrated using the preceding f(e) function and stress exponent.

5.6.1 Evaluation of calibrated equation

Equation 5.4 is the final calibrated equation. This equation has been normalized by dividing the atmospheric pressure ($P_a^{0.38}$) out of the leading A coefficient. The stress ratio correction proposed by (Yu and Richart, 1984) was not used. The majority of these data were measured at a stress ratio of 2.0. This results in a stress ratio correction of $(1 - rK_N^2) = (1 - 0.2(1/3)^2) = 0.978$. Applying this stress-ratio correction would increase the leading coefficient from 420 to 429.

$$\left(\frac{G_0}{P_a}\right) = (420)\frac{1}{0.3 + 0.7e^2}\left(\frac{\sigma'_a}{P_a}\frac{\sigma'_r}{P_a}\right)^{0.31} \tag{5.4}$$

Hardin and Blandford (1989) proposed initial values for the leading coefficient of 680 and for $n/2$ of 0.25. The calibrated Fraser River Sand equation is softer and more stress dependent.

Figure 5.14 compares this calibrated empirical equation to the entire tested dataset with continuous bender element measurements. The standard deviation for Equation 5.4 was calculated to equal 3.3 MPa as shown in Equation 5.5. This figure includes three monitored frequencies for each

experiment. One unaccounted source of error is the frequency of the bender element testing. The bender element performance was found to be frequency dependent and this dependence could not be predicted. This effect can be seen in Figure 4.8. For example, the V_S at 8 kHz is systematically different than at 9 kHz, despite both being within the stable range between 6 and 14 kHz.

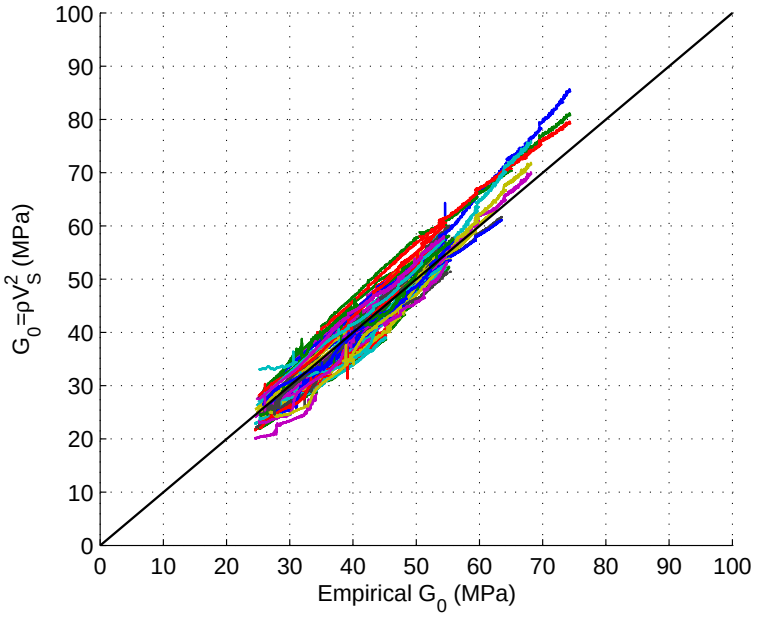

Figure 5.14: Comparing empirically estimated G_0 to the entire dataset of measured ρV_S^2

$$s = \sqrt[2]{\frac{1}{n-2}\sum (measured - predicted)^2} = \sqrt[2]{\frac{450998 MPa^2}{40720}} = 3.3 MPa \tag{5.5}$$

The empirical trends capture the effect of void ratio and in-plane effective stress on G_0. In triaxial testing, the void ratio and in-plane effective stress can be confidently determined. Conversely, bender element testing is measuring the velocity across the entire measurement system. It includes

an unknown effect due to the bender element sensors. The different tested frequencies do not agree - even within the same experiment. However, each frequency depicts the same trends with soil state. The empirical relationship and uncertainty for G_0 were developed with the multiple tested frequencies.

5.6.2 Comparing to other empirical G_0 equations for Fraser River Sand

Chillarige et al. (1997) used a laboratory calibrated V_S equation for Fraser River Sand to interpret in-situ soil state. Their empirical V_S equation was converted to G_0 using $G_0 = \rho V_S^2$, with $\rho = \frac{\gamma_w}{gravity}\left(\frac{Se+G_S}{1+e}\right)$. Converting their empirical equation for V_S to G_0 results in Equation 5.6. This equation solves for G_0 in terms of Pa units.

$$G_0 = \frac{\gamma_w}{gravity}\left(\frac{Se+G_S}{1+e}\right)(294-143e)^2\left(\frac{\sigma'_v}{P_a}\right)^{0.52}K_0^{0.25} \tag{5.6}$$

Wride et al. (2000) used an empirical equation calculated by Cunning et al. (1995) to interpret V_S measurements in Fraser River Sand at the Kidd-2 research site. They used this equation even though the coefficients calculated by Cunning et al. (1995) were for Syncrude Sand, Ottawa Sand, and Alaska Sand. This empirical equation for V_S has been reformulated to G_0 in Equation 5.7.

$$G_0 = \frac{\gamma_w}{gravity}\left(\frac{Se+G_S}{1+e}\right)(359-231e)^2\left(\frac{\sigma'_v}{P_a}\right)^{0.50}K_0^{0.25} \tag{5.7}$$

Although not Fraser River Sand, Lee et al. (2004) used an equation calibrated by Salgado et al. (2000) for a sand with no silt. The work by Salgado et al. (2000) characterized empirical coefficients for different amounts of fines content. Equation 5.8 is for a clean sand.

$$G_0 = 611P_a\frac{(2.17-e)^2}{1+e}\left(\frac{p'}{P_a}\right)^{0.44} \tag{5.8}$$

These three equations were compared to the calibrated empirical Equation 5.4 and a continuous measurement of V_S. Figure 5.15 was generated

using the measured void ratios and stresses from the consolidation of Specimen 040. A K_0 value of 0.5 was assumed for Equation 5.6 and Equation 5.7.

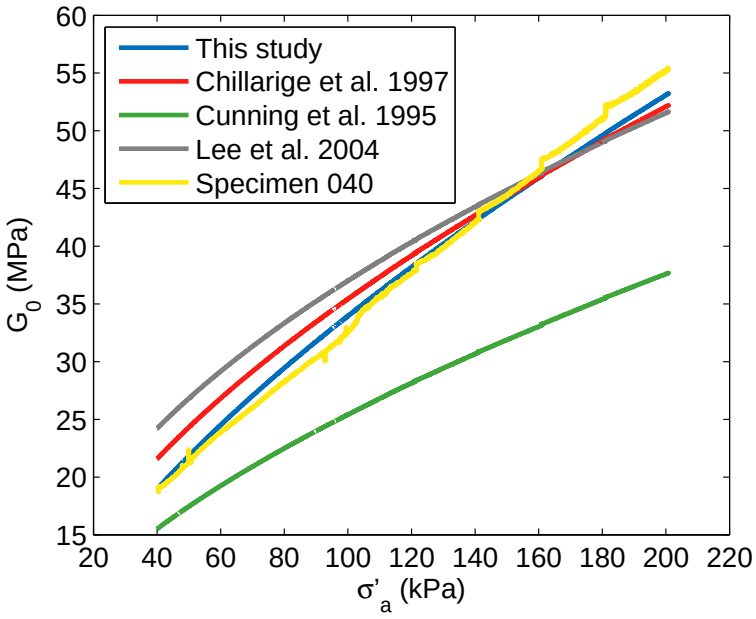

Figure 5.15: Empirical G_0 estimates during consolidation of Specimen 040 ($\sigma'_a/\sigma'_r = 2$) using Equation 5.4(blue), Equation 5.6(red), Equation 5.7(green), Equation 5.8(grey), and measured from Specimen 040 (yellow)

The calibrated empirical equation compares very well with a previous investigation by Chillarige et al. (1997). It also fits the measured dataset better. This past study used Fraser River Sand, but was not performed on the same laboratory equipment using the same laboratory techniques. The improved accuracy in the interpretation of bender element tests was necessary for evaluating the small change in G_0 during ageing, not the large change during consolidation. The comparison is poor between the current study and Cunning et al. (1995). This may entirely be a result of the different sand investigated by Cunning et al. (1995). An equation calibrated by Salgado et al. (2000) and used by Lee et al. (2004) for a sand with no

silt was too high at low stresses compared to the characterized Fraser River Sand equation and measured results.

Cho et al. (2006) compiled a set of empirical coefficients for different sand types. They fit an empirical equation with two coefficients: $V_S = \alpha\,(\sigma'_{mean}/1(kPa))^{\beta}$. The coefficients in this study can be manipulated to provide an α of 39 m/s and β equal to $n/2$ of 0.31. The Fraser River Sand α value is less than Nevada Sand ($\alpha = 56.3$) and Ticino sand ($\alpha = 70.7$). The β value is greater than Nevada Sand ($\beta = 0.242$) and Ticino Sand ($\beta = 0.231$). Based on the work by Cha et al. (2014), this implies that Fraser River Sand is slightly more compressible than these two soils.

5.6.3 Comparing effect of age on G_0 to calibrated G_0 equation

It can be seen that volumetric creep strain occurs during ageing. This results in a decrease in the void ratio. Using Equation 5.4, a decrease in the void ratio would increase G_0 and consequently increase the shear wave velocity. Therefore, it might be expected that Equation 5.4 inherently accounts for ageing and that the ageing phenomenon is just a consequence of increased density due to volumetric creep. This expectation is not supported by the data.

Equation 5.4 does not account for the observed increase in stiffness during ageing. This is demonstrated conclusively by Figure 5.16 which shows a plot of the calculated and measured stiffness against time for a specimen under a stress ratio of 2.0. Additional details for this figure are provided in Table 5.4. This observation has been made before; e.g. Figure 9 in Anderson and Stokoe (1978). The effect of age on G_0 is not due to volumetric creep changes. Therefore, an N_G factor must be used. An N_G factor for FRS was calibrated in Section 5.5.

5.7 Conclusion

This chapter presented a method to monitor V_S throughout a laboratory experiment with bender elements at multiple user selected frequencies. The

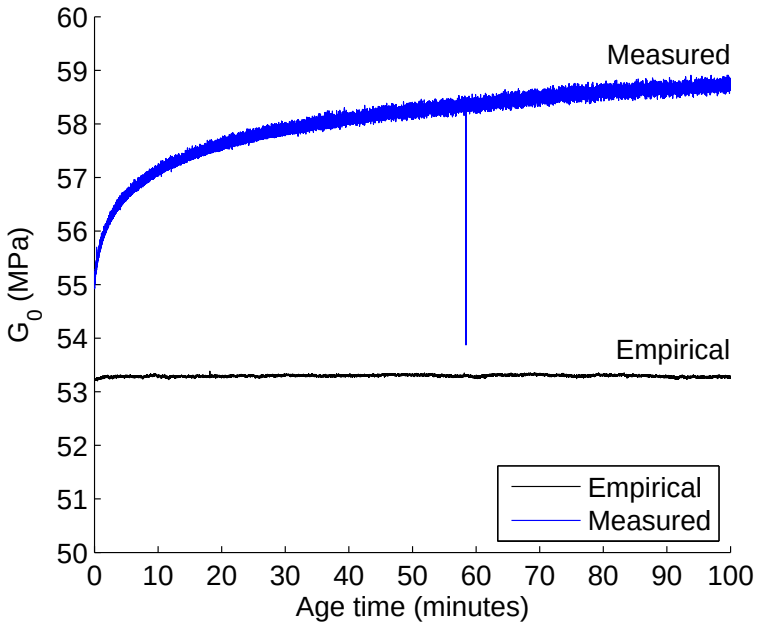

Figure 5.16: Empirical G_0 estimates during ageing for Specimen 040 compared to measured values

Table 5.4: Comparing empirical and measured G_0 (at 7.15 kHz) during ageing of Specimen 040

Time (min)	σ'_a (kPa)	σ'_r (kPa)	void	Equation 5.4 (MPa)	$G_0 = \rho V_S^2$ (MPa)
1	200.9	100.1	0.989	53.2	55.8
10	200.9	100.0	0.988	53.3	57.2
100	200.5	99.7	0.987	53.2	58.6

equipment used is a typical two element bender system. Challenges in applying the developed method were identified. Errors in the correction of discontinuities in the monitored relative phase shift are easy to fix and unrepresentative low-stress velocities are easy to identify. The migration of frequency-dependent features is more challenging. The measured propagation time across the system is correct, but it is not possible to separate the

change due to the soil from the change due to the bender element transfer function. This effect cannot be corrected without characterizing the evolving bender element transfer functions. To date, the characterization of an in-specimen bender element transfer function has not been achieved.

Monitoring multiple frequencies allows detection of anomalous results caused by changes in the bender element transform function. Frequency dependent effects may not occur on all of the monitored frequencies simultaneously, and the additional monitored frequencies still reflect the soil behaviour. Conventional discrete bender element testing does not allow easy identification of detrimental system effects. This technique permits bad data to be identified and discarded, which protects against reporting and drawing conclusions from bad results.

Monitoring the relative phase velocity throughout an experiment uses a continuous trigger signal. The value of this method would be reduced if the continuous excitation caused sample disturbance. For the given equipment details using the metric of creep strains and N_G age factor, bender element testing is considered to be non-destructive.

There is a variation in the frequency-dependent bender element results between "identical" specimens. A portion of this is due to the natural variation between identical specimens. The same exact specimen cannot be recreated. The systematic frequency dependence of the shear wave velocity is affected by differences in the geometry of the specimen and coupling of the soil-bender element. Figure 5.9 shows how frequency dependent features can migrate during a single experiment. However, as shown in Chapter 4, the phase velocity is much more consistent than group velocity measures.

The empirical G_0 Equation 5.4 can be used to estimate the small strain shear stiffness from the void ratio and effective stress state in Fraser River Sand. The equation matched the form proposed by Hardin and Blandford (1989). The calibrated equation using the continuous bender element technique was similar to other published relationships.

This technique was further developed to create a new in-situ testing technique. This development is reported in Chapter 7. Before switching to in-situ testing, the third research objective outlined in Section 1.1 is

addressed.

The research into bender element testing and interpretations reported on in this chapter and Chapter 4 will now be used to integrate V_S measurements and G_0 calculations into a laboratory investigation of the effect of age on shear stiffness of Fraser River Sand.

Chapter 6

Characterizing normalized stiffness degradation curves in the laboratory

The deformation properties of in-situ granular soils cannot be easily characterized through laboratory testing. The deformation is very sensitive to the state of the soil and free-draining soils cannot be routinely sampled undisturbed. One way to estimate the deformation properties is to measure the in-situ G_0 and select an equivalent modulus based on applicable shear strain. G_0 can be determined using in-situ V_S measurements. Its degradation with shear strain can be captured using published or empirical normalized shear stiffness degradation curves (G_{sec}/G_0 against shear strain). This chapter contains measured shear stiffness degradation curves that demonstrate the significance of specimen age, initial stress ratio, and stress path variables.

It was demonstrated in Section 3.4.1 that the triaxial equipment can be used to produce results similar to previous studies. It was shown in Section 3.4.3 that current bender element techniques were unable to confidently determine small changes in G_0, such as during ageing at constant stress. A combined time and frequency domain approach was proposed in Chapter 4. This method was shown to be reproducible for simulated and experimental bender element signals. This method was further developed into a continu-

ous technique in Chapter 5. The continuous excitation did not influence the effect of ageing. Bender element testing in this research can now be used to provide consistent values of G_0 that can be used to study G_{sec}/G_0.

Before integrating the bender element results into the stiffness investigation, this chapter first briefly covers the triaxial consolidation and creep strain measurements. The G_{sec} stiffness is then evaluated to demonstrate the need for a normalization factor, G_0, to compare different testing conditions.

This investigation complemented past studies (Lam, 2003; Shozen, 2001) by adding bender elements to the triaxial investigation of the small strain behaviour of Fraser River Sand. The test program in the current study repeated many experiments during the development of the equipment, data acquisition, stress control routines, and bender element techniques. These tests were all performed under drained conditions through the consolidation, ageing, and shear phases. Section 3.4.1 demonstrated that the small strain results in the current investigation are very similar to the past studies. Therefore, the results from the current investigation may be combined with previous results when making observations or conclusions.

6.1 Consolidation of Fraser River Sand specimens

Consolidation occurs in two phases. The effective axial stress is increased until the desired stress ratio is achieved. Then the axial stress and chamber pressure are increased simultaneously while maintaining the desired stress ratio. The effective stresses are increased up to the desired stress state.

Assuming that the specimen is a perfect cylinder, the axial and volumetric strains can be used to calculate the radial strain, $\varepsilon_r = (\varepsilon_v - \varepsilon_a)/2$, and shear strain, $\varepsilon_q = 2/3(\varepsilon_a - \varepsilon_r)$. If the developed strains are isotropic then they are the same in every direction. This means that $\varepsilon_a = \varepsilon_r$, $\varepsilon_v = 3\varepsilon_a$, and $\varepsilon_q = 0$. An isotropic soil fabric will have isotropic strains when an isotropic effective stress is applied. Zero radial strain corresponds to a K_0 stress path. Zero radial strains are typical in oedometers with a fixed radial boundary. In-situ at-rest conditions are at $K_0 = \sigma'_h/\sigma'_v$ stress.

During the second phase of consolidation, the stress path direction is constant. Figure 6.1 depicts the developed axial and radial strains during consolidation at a constant stress ratio for nine specimens. The origin of this plot is at the top centre - it corresponds to the point at which the desired stress ratio was achieved. The sign convention for axial compression is positive. The sign convention for radial compression is positive. Compressive radial strains mean that the radius of the cylindrical specimen is decreasing. The final point for each of these nine strain paths is labelled. This label contains the applied constant stress ratio (σ'_v/σ'_h) and an identifier for the dataset with TS being Takahiro Shozen, KL being Keith Lam, and MS being myself.

This figure includes two lines identifying the isotropic strain path and K_0 strain path. The hydrostatic stress paths ($\sigma'_v/\sigma'_h = 1.0$) have lower axial strains than the isotropic strain path. Therefore, water pluviated specimens do not create isotropic fabric - they are stiffer in the axial direction. This agrees with the observation by Negussey (1984) that WP pluviated specimens are anisotropic. This figure also shows that the 2.8 stress ratios result in radial extension strains and 1.6 have compressive radial strains. The 2.0 tests are near the K_0 strain path.

6.2 Developed creep strains during ageing

After consolidation, the applied axial load and chamber pressure were kept constant for an ageing duration. This ageing duration was typically 10, 100, or 1000 minutes. During the holding phase the specimen exhibits creep or secondary compression strains. The creep strain magnitudes are summarized in Appendix D.

Figure 6.2 depicts radial strain against axial strain during secondary compression. This is the same type of plot as Figure 6.1, but at much lower strain magnitudes. This shows that during ageing there is a constant strain path direction. The test by Lam at a stress ratio of 2.5 does not appear to be stable.

Figure 6.3 compares the consolidation strain path direction to the age

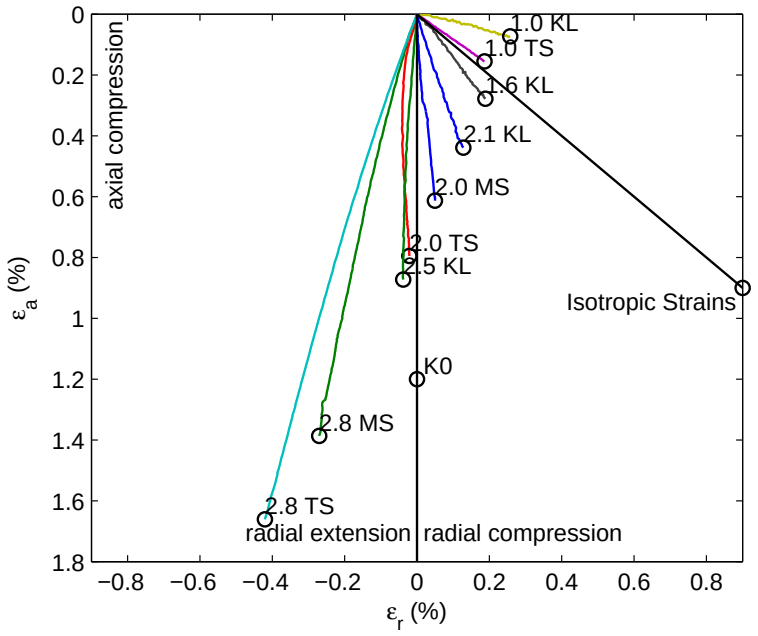

Figure 6.1: Primary compression strains for nine specimens at six different stress ratios from this study (MS), Shozen (TS), and Lam (KL)

strain path direction. Most points plots below the 1:1 line. This means that during creep there is a larger ratio of axial to radial strain than during consolidation. This implies that K_0 is lower during consolidation. This agrees with observations by Mesri and Vardhanabhuti (2009).

6.3 Secant stiffness during shearing

All imposed shear stress paths involve an increase in σ'_a/σ'_r until failure. The conventional stress path is an increase in the axial stress without changing the chamber pressure. The constant-p stress path is $\frac{\Delta\sigma'_r}{-2} = \Delta\sigma'_a$. The -1 stress path is $\frac{\Delta\sigma'_r}{-1} = \Delta\sigma'_a$. The slope 0 stress path is a decrease in confining pressure with an increase in axial load to maintain a constant σ'_a. The axial load has to be increased to compensate for the reduction in the

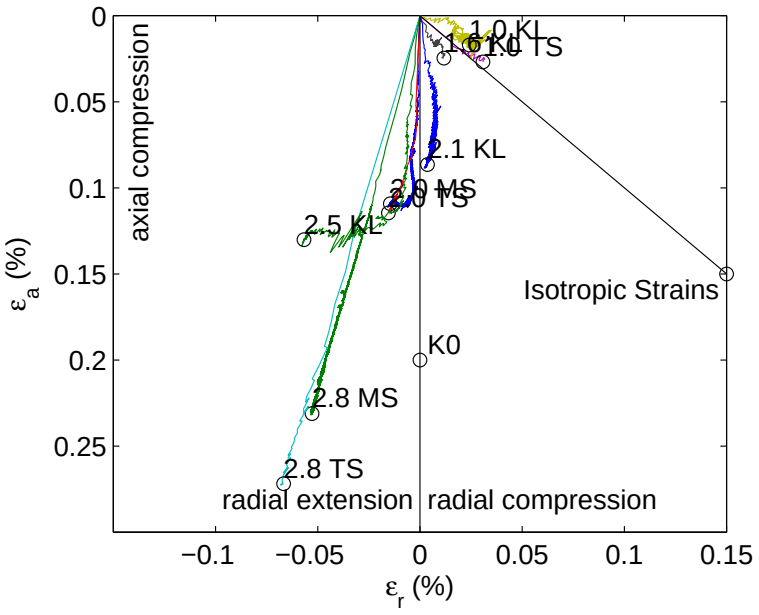

Figure 6.2: Secondary compression strains for nine specimens at six different stress ratios from this study (MS), Shozen (TS), and Lam (KL)

chamber pressure contribution to σ'_a. In the work performed by Shozen (2001) and Lam (2003), the constant-p stress path was called a -2 stress path. This naming convention identified the slope of $\Delta\sigma'_a/\Delta\sigma'_r$. In this work the -2 stress path was renamed the constant-p stress path to make it more informative in the Cambridge stress space.

Figure 6.4 compares the responses to the three different stress paths performed during this investigation. In this figure all three specimens were prepared loose, consolidated along a constant stress ratio of 2.0 up to $\sigma'_a =$ 200 kPa, $\sigma'_r = 100$ kPa, and aged for 100 minutes. The -1 stress path was not performed in this study.

Figure 6.4a shows that the three stress paths have very different ultimate shear stresses, Δq. However, it does not show that these different failure state effective stresses are on the same failure surface. The conventional

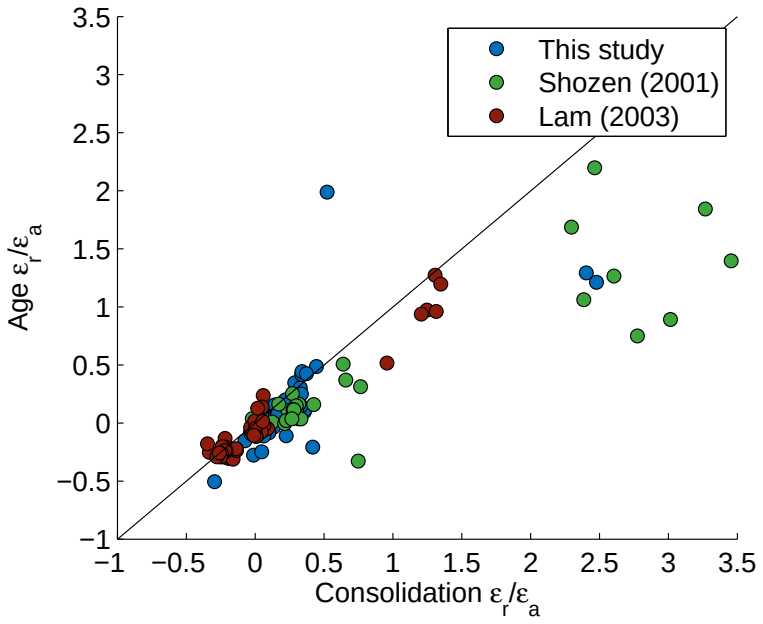

Figure 6.3: Comparing the strain ratio during consolidation to age

path reaches a maximum stress ratio (σ'_1/σ'_3) of 3.99, slope P reaches 3.92, and slope 0 reaches 3.87. Figure 6.4b shows that the different stress paths experience much different volumetric strains. The conventional stress path, which involves an increasing mean stress, results in more contractive strains. The slope-P stress path is at a constant mean stress. It shows that the increasing shear stress also results in contractive strains. The slope-0 stress path, which involves a decreasing mean stress and increasing shear stress, also shows contractive volumetric strains. The phase transformation point from contractive to dilative volumetric strain occurs at lower axial strains as the shear stress path rotates towards the failure surface. Figure 6.4c and Figure 6.4d show the secant stiffness against shear strain. The log-plot in Figure 6.4d is more informative at the small strain. The slope-0 and slope-P stress paths appear to have an initial constant stiffness plateau before degrading with strain. All of these specimens were prepared loose and the shear phases began at the same stress state and age duration. They have

different secant stiffness values above 0.01 % shear strain.

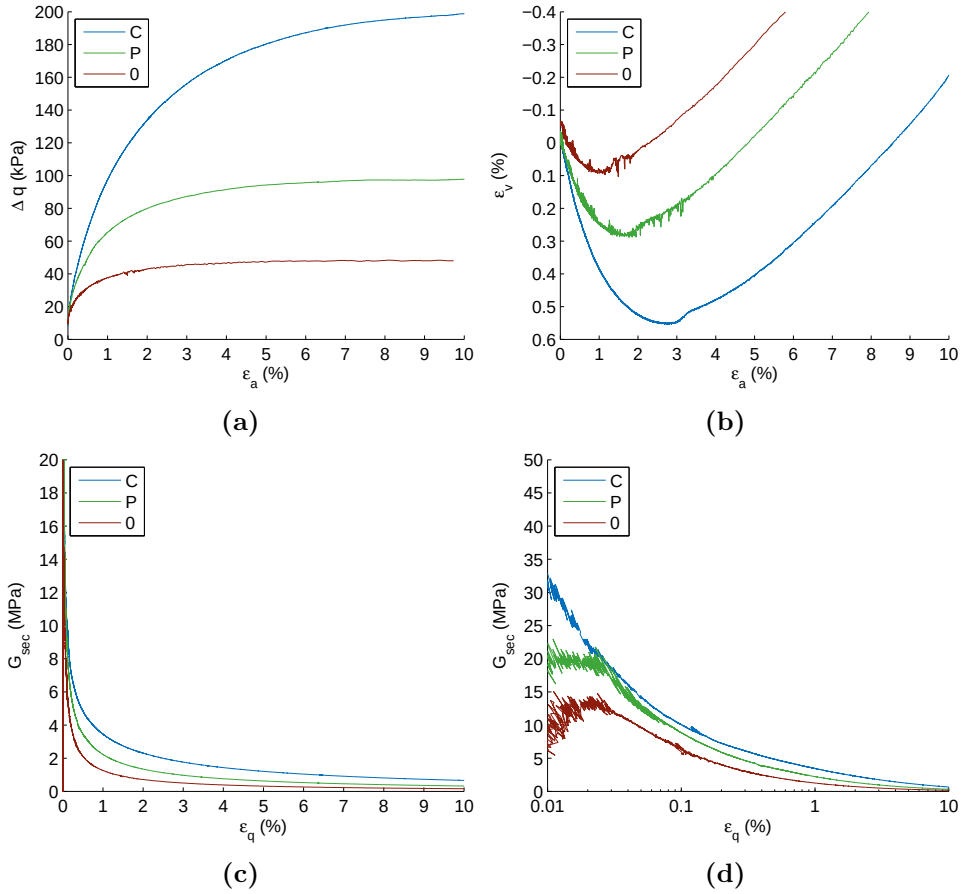

Figure 6.4: Effect of stress path for specimens 012 (e=0.960, conventional, see Figure D.36), 015 (e=0.959, constant-p, see Figure D.39), and 016 (e=0.971, slope-0, see Figure D.40); all prepared loose, consolidated at a SR 2.0 to σ'_a =200 kPa and σ'_r = 100 kPa, and aged 100 minutes

Figure 6.5 depicts a similar set of plots, but for different initial stress ratios. In this figure all three specimens were aged for 100 minutes and sheared along a conventional stress path. At higher initial stress ratios the specimen state at the onset of shearing is closer to the failure surface. Similar to Figure 6.4a, Figure 6.5a shows that for the same conventional

stress path, a different initial stress ratio results in a very different ultimate shear stress. However, they all reach the same failure surface. The ultimate stress ratio is 4.04 for a stress ratio of 1.0, 3.98 for a stress ratio of 2.0, and 4.04 for a stress ratio of 2.8. The shear path for all three tests includes an increase in both mean stress and shear stress to failure. Figure 6.4b shows that an increasing initial stress ratio results in a less contractive volumetric strain. Furthermore, the phase transformation point is reached at lower axial strains. Figure 6.4c and Figure 6.4d shows the secant stiffness against shear strain. The log-scale plot shows that the higher stress ratio specimens have a larger secant stiffness at very low strains. It also shows that the stiffness for the 1.0 stress ratio does not degrade as rapidly as the higher stress ratios.

Figure 6.6 shows the effect of the age duration on conventional stress paths from a stress ratio of 2.0. The strains have been corrected for continued creep following the observations by Shozen (2001). The void ratios are reported at the end of ageing. The differences between these void ratios is due to the challenge of reproducing identical very loose specimens. The effect of volumetric creep during the ageing phase is very minor on the void ratio.

Figure 6.6a shows that the 100 minute and 1000 minute tests reach a similar ultimate stress state. The 10 minute test was not completely sheared to failure. It has been observed elsewhere that the ageing does not affect the ultimate strength of the soil (Mitchell, 2008). Figure 6.6b shows that the developed volumetric strains for the three age durations did not depict a trend. It may be experimental scatter due to differences in specimen preparation. The secant stiffness is compared in Figure 6.6c and Figure 6.6d. Figure 6.6c is not informative. It must be a log-scale to depict the effect of ageing. This is shown in Figure 6.6d. At 0.01 % shear strain the 1000 minute test secant stiffness is more than double the 10 minute secant stiffness. Shozen (2001) normalized the stiffness results with the 10 minute test stiffness at 0.03 % shear strain. This normalization made the effect of ageing on the secant stiffness very clear.

This brief review of a subset of the investigation observed that the peak

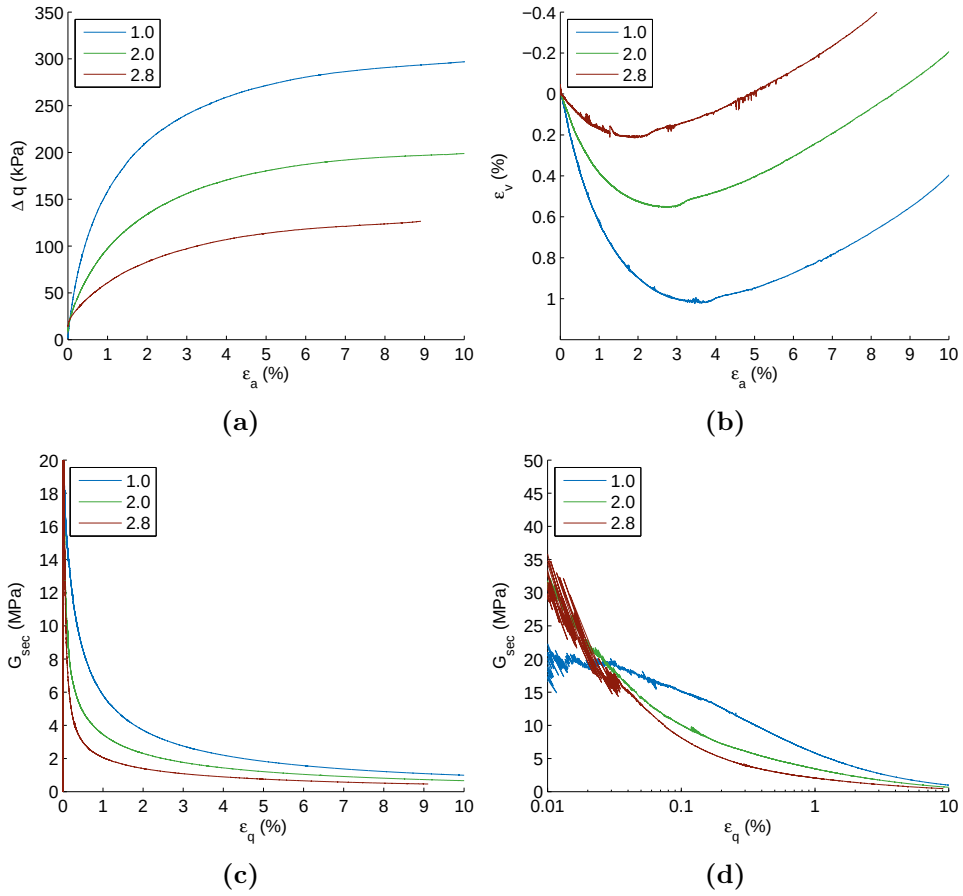

Figure 6.5: Effect of stress ratio for specimens 013 (e=0.969, SR=1.0, see Figure D.37), 012 (e=0.960, SR=2.0, see Figure D.36), and 014 (e=0.934, SR=2.8, see Figure D.38); consolidated to σ'_r = 100 kPa, aged 100 minutes, and sheared along a conventional stress path

stress ratio was independent of the shear path, initial stress ratio, and age duration. It was also observed that the deformation is dependent on these variables. Predicting the deformation of in-situ sands is very difficult. These soils will be at an in-situ stress ratio, possibly near $\sigma'_a/\sigma'_r = 2.0$ as identified by K_0 in Section 6.1 and Section 6.2, and will be aged on a geological scale. These soils cannot be routinely sampled undisturbed for careful laboratory

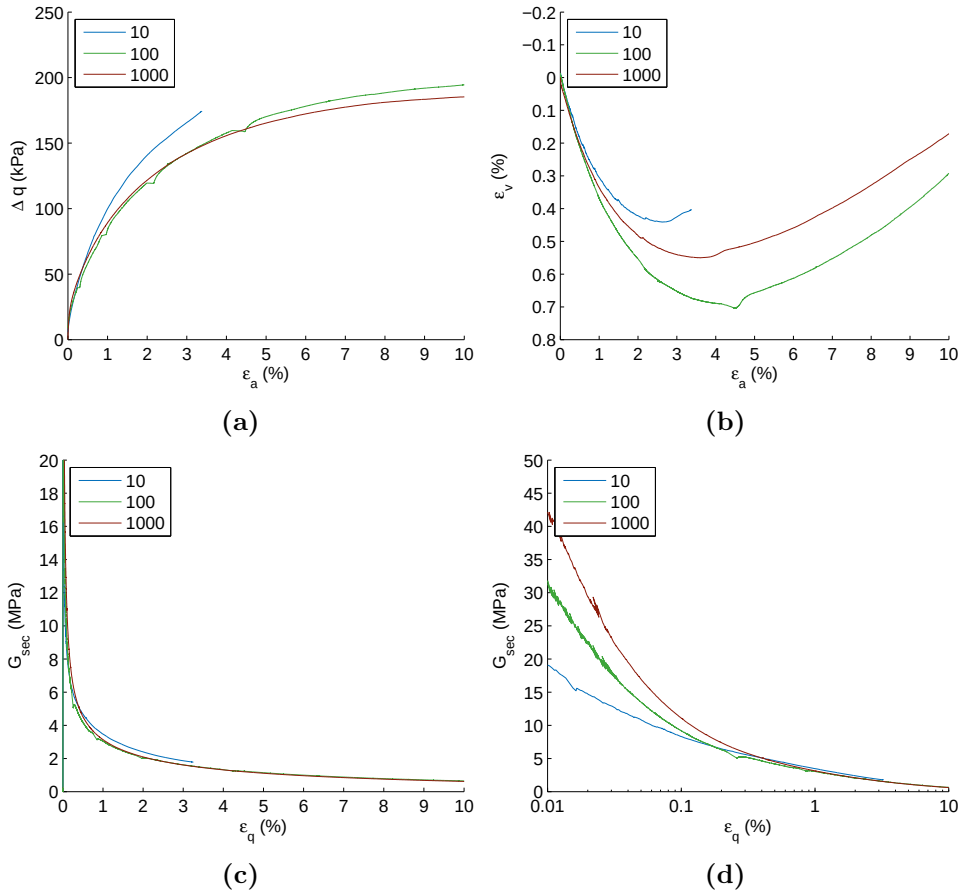

Figure 6.6: Effect of age for specimens 090 (e=0.871 at end of ageing, 10 minutes, see Figure D.8), 261 (e=0.962 at end of ageing, 100 minutes, see Figure D.28), and 108 (e=0.918 at end of ageing, 1000 minutes, see Figure D.14); all prepared loose, consolidated at a SR 2.0 to σ'_a =200 kPa and σ'_r = 100 kPa, and sheared along a conventional stress path

testing.

6.4 Normalizing G_{sec} degradation curves with G_0

Secant stiffness curves can be normalized with G_0. G_0 can be obtained from shear wave velocity measurements. The shear wave velocity can be obtained

in-situ and in the laboratory using bender elements. The shear strains for these shear waves are estimated to be below $1.0 \times 10^{-}4\%$ (Jovicic and Coop, 1997; Kuwano and Jardine, 2002b). This strain range should correspond to an elastic shear modulus. Clayton (2011) questioned the existence of an elastic zone, but it cannot be examined with this equipment as it is below the resolution of the sensors.

Normalized stiffness degradation curves can be used in practice by scaling the curve using an in-situ measured V_S. The normalized curves can be empirically estimated or measured in a laboratory.

The bender element equipped triaxial apparatus can be used to investigate the effects of stress path, initial stress ratio, and age on the normalized stiffness degradation curves. This equipment can also be used to examine recently published empirical procedures by Oztoprak and Bolton (2013) and Wichtmann and Triantafyllidis (2013) for estimating normalized stiffness degradation curves.

Figure 6.7 depicts the measured G_{sec}/G_0 stiffness degradation curves for a set of experiments consolidated to the same stress state of $\sigma'_a = 200$ kPa and $\sigma'_r = 100$ kPa, aged for 100 minutes, and sheared along a conventional stress path to failure. The specimen information for these experiments is provided in Table 6.1. The G_0 values from bender element testing have a range of 4 MPa. The reduced triaxial sensor measurements are not reproducible over the entire depicted small strain range. They deviate below 0.1 % shear strain. This deviation is explained by the measurement uncertainty quantified in Section 3.4.2. This figure also includes two predicted curves using the relationships covered in Section 2.4.

The formulation proposed by Oztoprak and Bolton (2013) fits the experimental results better than Wichtmann and Triantafyllidis (2013), but both approaches overestimate the stiffness of loose Fraser River Sand. The Oztoprak and Bolton (2013) relationship was based on a dataset compiled from published stiffness degradation curves. Only one source investigated the effect of stress ratio. The measurements may be close to the predicted curve due to the combined effects of an increase in G_{sec} due to ageing and decrease due to testing at a higher stress ratio. Both of these studies pro-

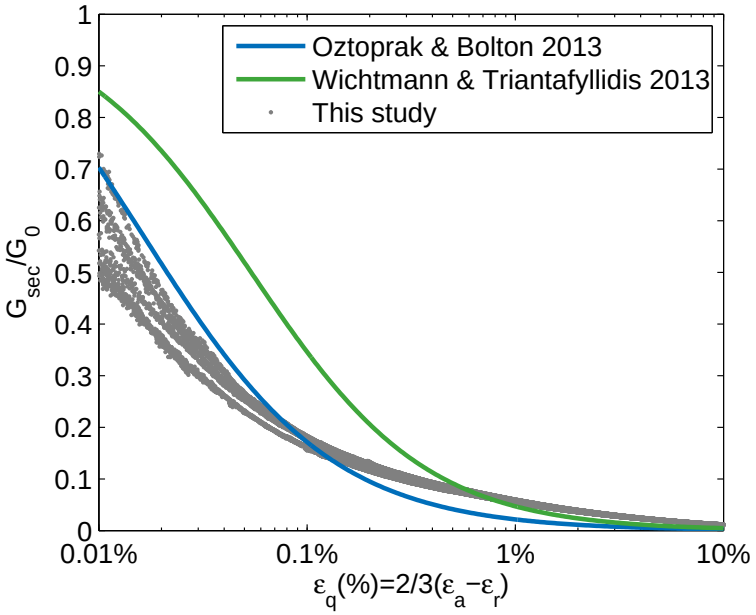

Figure 6.7: Measured and predicted normalized stiffness degradation curves for loose specimens of saturated Fraser River Sand consolidated at SR 2.0 up to $\sigma'_a = 200$ kPa and $\sigma'_r = 100$ kPa, aged for 100 minutes, and sheared conventionally where G_0 ranged from 58 to 62 MPa with specimen details in Table 6.1

vided a means to estimate a non-linear normalized shear stiffness curve from readily obtainable parameters.

The empirical equation for reference strain from Wichtmann and Triantafyllidis (2013) given in Equation 2.15 was developed using a resonant column apparatus. It was calibrated for stiffness degradation from a hydrostatic stress state, while the results in Figure 6.7 began from a stress ratio of 2.0. Wichtmann and Triantafyllidis (2013) stated that stress anisotropy would only have a significant effect near failure, based on the work by Yu and Richart (1984). However, the work by Yu and Richart (1984) was for G_0. G_{sec} degradation curves are significantly affected by the initial stress ratio - this parameter was not considered by either Wichtmann and Triantafyllidis (2013) or Oztoprak and Bolton (2013). It was demonstrated clearly

Table 6.1: Specimen variables for Figure 6.7, void ratios and G_0 measured at end of ageing

Specimen	Void ratio	G_0 (MPa)
008 (see Figure D.35)	0.982	58
012 (see Figure D.36)	0.960	62
040 (see Figure D.52)	0.987	59
043 (see Figure D.54)	0.967	59
044 (see Figure D.55)	0.965	57
047 (see Figure D.56)	0.951	61
048 (see Figure D.57)	0.972	62

in Section 6.3 that the initial stress ratio has a significant effect on G_{sec}. Wichtmann and Triantafyllidis (2013) clearly misinterpreted the results by Yu and Richart (1984). They applied the observations of the effect of stress ratio on G_0 by Yu and Richart (1984) to G_{sec}.

In this investigation, the same approach was taken to characterize the effect of ageing. For every test, the hyperbolic curve model was fitted to the dataset of measured G_{sec}/G_0. The elastic threshold strain was estimated using Equation 2.12 as it is below the observable strain range with this triaxial equipment. The laboratory triaxial apparatus is unable to observe the possible dependence of the threshold strain on age duration. It cannot be used to measure shear strains around 1e-4 %.

Better empirical relationships can be achieved using a larger dataset. A larger dataset was created by combining the results from the current investigation to the previous studies by Shozen (2001) and Lam (2003). These past studies did not include V_S measurements and G_0 calculations. These parameters need to be empirically estimated. The form and variables for a proper empirical equation for G_0 were previously covered in Section 2.3.

A shortcoming of this dataset is that it is dominated by loose, contractive, specimens. This was done to produce saturated homogeneous specimens with the water pluviation technique. Densifying the specimens through mechanical disturbance during specimen preparation may not have been as reproducible or homogeneous.

The continuous bender element measurements were used to calibrate an empirical G_0 equation and estimate an N_G ageing factor. Both of these are required to estimate G_0 for Fraser River Sand experiments performed without bender element testing. This included the investigations by Shozen (2001) and Lam (2003) as well as experiments conducted in this investigation that did not include V_S measurements. This led to the creation of a large dataset of Fraser River Sand G_{sec}/G_0 strain degradation curves (Appendix D).

6.5 Factors influencing G_{sec}/G_0 degradation curves

The empirical relationships for N_G and G_0 were calibrated. This permits every G_{sec} curve to be normalized by a measured or estimated very small strain shear stiffness. This increases the size of the dataset for making empirical observations.

6.5.1 Effect of shear stress path

As covered in Section 2.4, the empirical equations for the hyperbolic parameters proposed by Oztoprak and Bolton (2013) and Wichtmann and Triantafyllidis (2013) do not include the shear stress path as a variable. Consequently, the same normalized stiffness degradation curve is predicted for every shear stress path. A subset of the experimental results that were prepared loose, consolidated to an effective radial stress of 100 kPa, and at a consolidation stress ratio of 2.0 were compiled. This subset contained 29 triaxial experiments. The shear paths in the current program that included unloading and reloading loops were excluded. One of the 19 conventional stress path experiments is 25025017 from Lam (2003), which was at a stress ratio of 2.1 instead of 2.0.

Table 6.2 contains the average hyperbolic parameters. For comparison, the empirical prediction from Oztoprak and Bolton (2013) results in a curvature of 0.96 and reference strain of 0.026 %. The curvature parameter does not appear to have any trend with the rotating stress path direction.

The reference strain appears to decrease as the stress path is rotated toward the failure surface.

Table 6.2: Effect of stress path on curvature(a) and reference strain(ε_{qr}) for a hyperbolic model of the normalized secant stiffness curve Equation 2.11 from loose specimens consolidated at a stress ratio of 2.0 up to σ'_r=100 kPa and aged for 100 minutes

Stress path	Specimens	Curvature(a)	Reference strain (ε_{qr})
C	19	0.61	0.009 %
P	7	0.71	0.009 %
-1	1	0.73	0.007 %
0	2	0.64	0.002 %

Figure 6.8 compares predicted stiffness degradation curves, fitted hyperbolic curves using the parameters in Table 6.2, and the measured data. The predicted stiffness degradation curves from the Oztoprak and Bolton (2013) and Wichtmann and Triantafyllidis (2013) equations are identical for all four shear stress paths. The conventional test matches the hyperbolic function over the small strain range. The other three stress paths deviate from this curve at lower strains. The predicted curves overestimate the normalized shear stiffness.

It appears that the hyperbolic formulations may not fit non-conventional stress paths at low strains. This was observed in Constant-P and Slope-0 shear paths. The plateau to a shear strain beyond 0.01 % is not characterized by the hyperbolic degradation function. There is more evidence of this observation included in Appendix D for different age durations and consolidation stress ratios. The stiffness degradation of non-conventional stress paths should be investigated with an apparatus that can measure lower strains.

6.5.2 Effect of initial stress ratio

The developed hyperbolic relationships proposed by Oztoprak and Bolton (2013) and Wichtmann and Triantafyllidis (2013) do not account for the

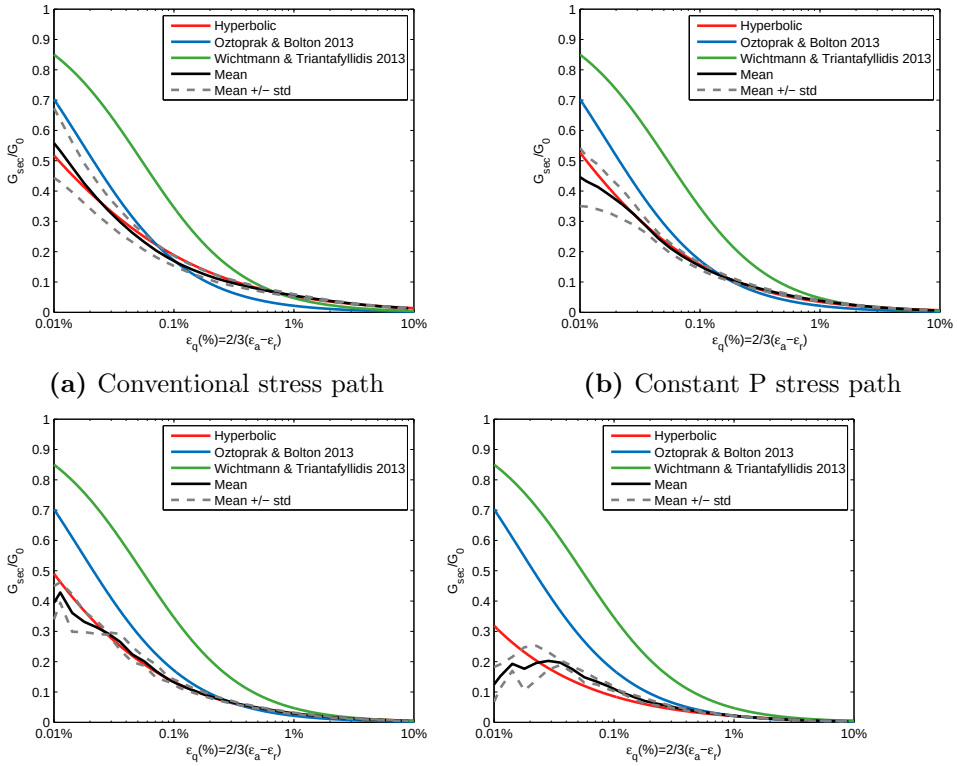

(a) Conventional stress path

(b) Constant P stress path

(c) Slope -1 stress path

(d) Slope 0 stress path

Figure 6.8: Effect of stress path on measured and hyperbolic stiffness degradation curves for loose specimens consolidated at SR 2.0 and aged for 100 minutes

effect of the initial stress ratio. The shearing of specimens consolidated at higher stress ratios begins closer to the failure surface. They require much less deviator stress to reach failure and have softer normalized stiffness degradation curves. Many of the experiments used to develop the empirical relationships in Oztoprak and Bolton (2013) and all of the specimens in Wichtmann and Triantafyllidis (2013) were on hydrostatically consolidated specimens. Shearing in-situ soil rarely begins at such a stress state.

This effect was investigated by comparing experiments that were prepared loose, consolidated to a radial effective stress of 100 kPa, aged for 100 minutes, and sheared along a conventional stress path. The stress ra-

tio is the variable that is being changed. This subset contained 27 triaxial experiments.

Table 6.3 details the effect of the consolidation stress ratio on the hyperbolic model coefficients. No conclusive trend on the curvature was observed as the stress ratio increases. The reference strain decreases as the consolidation stress ratio increases. Higher stress ratios result in an increase in G_0 and decrease in G_{sec}, resulting in a softer normalized stiffness curve.

Table 6.3: Effect of stress ratio on curvature(a) and reference strain(ε_{qr}) for a hyperbolic model of the normalized secant stiffness curve Equation 2.11 from loose specimens consolidated and aged for 100 minutes and sheared along conventional stress paths

Stress ratio	Specimens	Curvature(a)	Reference strain (ε_{qr})
1.0	4	0.64	0.046 %
1.6	1	0.78	0.026 %
2.0	19	0.61	0.009 %
2.5	1	0.62	0.005 %
2.8	2	0.64	0.004 %

Figure 6.9 compares predicted stiffness degradation curves against the fitted hyperbolic relationship and measured data. The parameters for the fitted hyperbolic relationships are in Table 6.3. The measured data and fitted hyperbolic curves are softer at higher stress ratios. The reference strain decreases as the initial stress-state of the shear path is closer to failure.

Equation 2.13 from Oztoprak and Bolton (2013) and Equation 2.15 from Wichtmann and Triantafyllidis (2013) both determine an increase in the reference strain at higher mean stress. Based on the results from this investigation, the effect of mean stress needs to be separated from the effect of stress ratio when predicting hyperbolic-strain stiffness degradation curves. Higher initial stress ratios increase the mean stress, but decrease the reference strain. The predictions from Oztoprak and Bolton (2013) and Wichtmann and Triantafyllidis (2013) disagree with this observation.

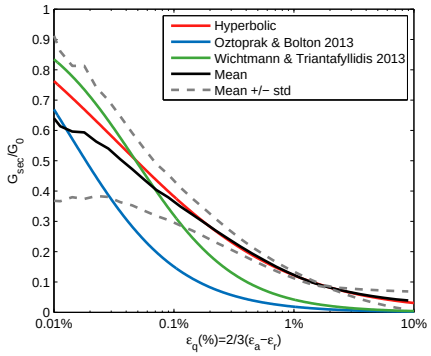

(a) Stress ratio 1.0

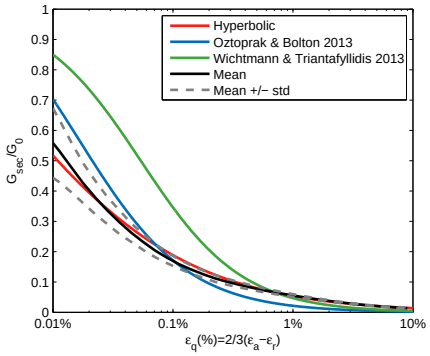

(b) Stress ratio 2.0

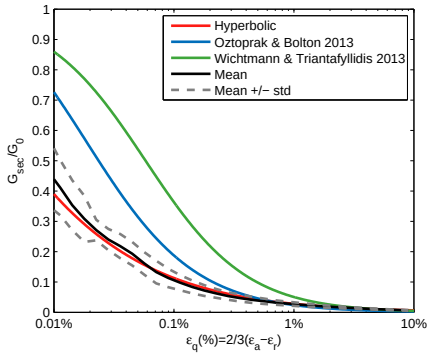

(c) Stress ratio 2.8

Figure 6.9: Effect of stress ratio on measured and hyperbolic stiffness degradation curves for loose specimens, aged for 100 minutes, and sheared along a conventional stress path

6.5.3 Effect of reconstituted specimen age

The reconstituted specimen age is not a variable in the existing methods to estimate a stiffness degradation curve. On laboratory specimens, ageing has a significant effect on the secant shear modulus (Howie et al., 2002; Lam, 2003; Shozen, 2001), no effect on the strength, and a small effect on G_0. A subset of the triaxial experiments consolidated at a stress ratio of 2.0, sheared along a conventional stress path, and aged for different durations, was compiled. This dataset contains 34 experiments.

Table 6.4 details the fitted hyperbolic coefficients. Both the brittleness

(curvature) and reference strain increase with age duration. Figure 6.10 depicts the the effect of age on the hyperbolic stiffness degradation from 1 to 1000 minutes. Ageing changes the shape of the curve. The effect of ageing is not accounted for by normalizing with G_0.

Table 6.4: Effect of age on curvature(a) and reference strain(ε_{qr}) for a hyperbolic model of the normalized secant stiffness curve Equation 2.11 from loose specimens sheared along a conventional stress path from a stress ratio of 2.0

Age(minutes)	Specimens	Curvature(a)	Reference strain (ε_{qr})
1	2	0.49	0.002 %
10	5	0.52	0.003 %
100	19	0.61	0.009 %
1000	5	0.66	0.011 %
10000	3	0.75	0.020 %

Reconstituted laboratory specimens are at a very different age than in-situ soil. To predict in-situ behaviour of Fraser River Sand, the ageing trends for G_0, the reference strain(ε_{qr}), and the curvature(a), have been extrapolated. For loose Fraser River Sand, G_0 increases with N_G equal to 1.9 %. For a stress ratio of 2.0, Figure 6.11 depicts the effect of age on the reference strain and curvature. The trend with age for these two variables appears to be log-linear up to 10000 minutes. A best-fit for these data points resulted in Equation 6.1 and Equation 6.2.

$$\varepsilon_{qr}(\%) = 0.0044 log_{10}(age\text{minutes}) + 0.004 \tag{6.1}$$

$$a = 0.0665 log_{10}(age\text{minutes}) + 0.471 \tag{6.2}$$

For σ'_a=200 kPa, σ'_r=100 kPa, and a void ratio of 0.95, G_0 according to Equation 5.4 is 56 MPa. Figure 6.12 depicts the effect of ageing on the non-linear secant stiffness curve for these initial properties. The extrapolated age effects are indicated with dashed lines. This figure also includes the stiffness degradation curve from Specimen 040. This specimen was consolidated at

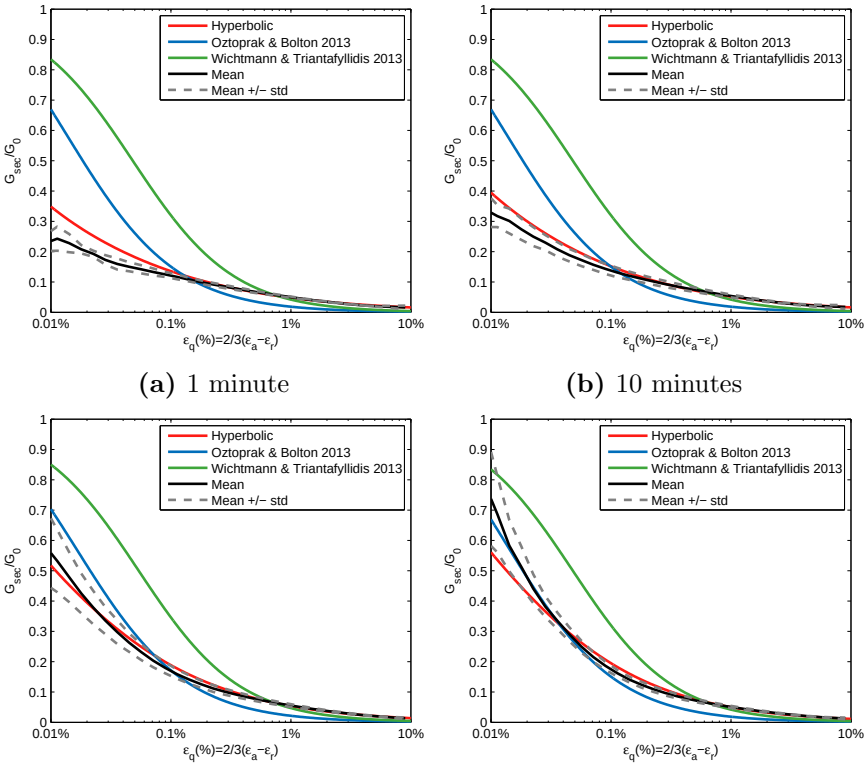

(a) 1 minute **(b)** 10 minutes

(c) 100 minutes **(d)** 1000 minutes

Figure 6.10: Effect of specimen age duration on measured and hyperbolic stiffness degradation curves for loose specimens consolidated at SR 2.0 and sheared along a conventional stress path

a stress ratio of 2.0, aged for 100 minutes, and sheared along a conventional stress path.

This approach captures the general trends in observations of the effect of ageing. It results in an increase in the reference strain (strain to G_{sec}/G_0=0.5) and an increase in the curvature (i.e. more brittle). It does not capture the independence of strength due to ageing. The hyperbolic relationships do not include a strength term and do not fit large strain measurements. The presented results are only for the conventional stress path.

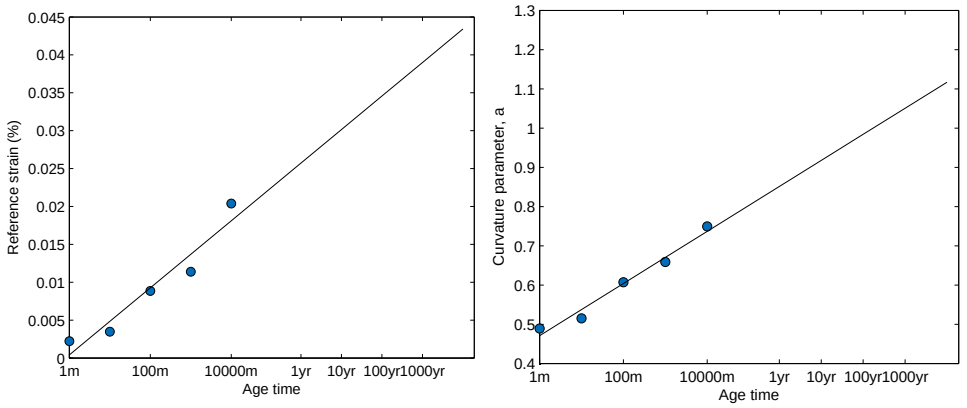

(a) Reference strain

(b) Curvature parameter

Figure 6.11: Extrapolation of normalized secant stiffness curve parameters

6.6 Discussion

The effects of age, initial stress ratio, and stress path were quantified with the same approach as Wichtmann and Triantafyllidis (2013) and Oztoprak and Bolton (2013). The average of fitted hyperbolic coefficients was calculated. The effect of ageing was extrapolated by developing empirical relationships for the empirical model coefficients from the fitted stiffness degradation curves.

The trends with age, stress ratio, and stress path can be used to modify the predicted hyperbolic reference strain and curvature. The work in this chapter was mostly based on very loose reconstituted specimens of Fraser River Sand aged for less than 1000 minutes. The values reported should not be applied to other soils or densities, but the trends may be used to estimate better stiffness degradation curves or explain differences in observed and predicted deformation behaviour.

6.7 Conclusion

The third objective of this research project was to integrate bender elements into the triaxial small strain shear stiffness investigation of Fraser River

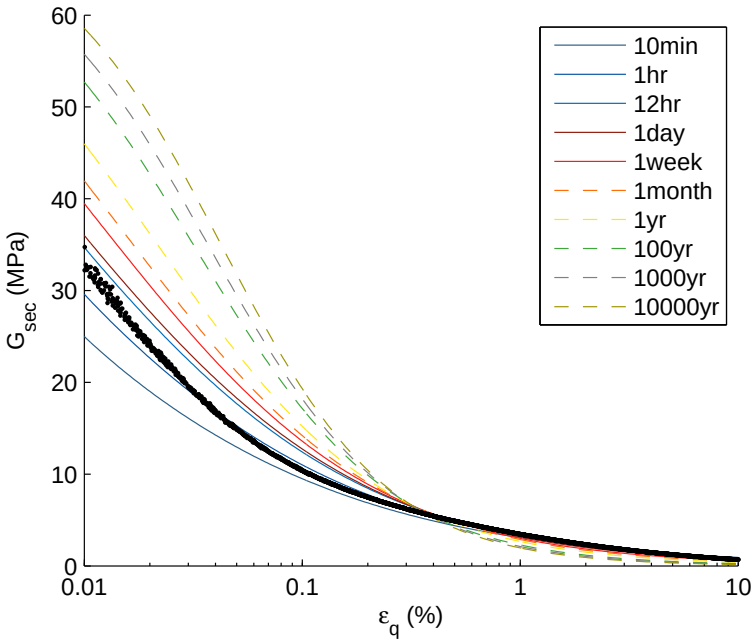

Figure 6.12: Effect of age on secant stiffness curve for σ'_a=200 kPa, σ'_r=100 kPa, G_0 according to Equation 5.4, $N_G = 1.9$ %, where solid lines are interpolated and dashed lines are extrapolated, the solid black points correspond to Specimen 040 (see Figure D.52) aged for 100 minutes

Sand. This objective has been achieved. This was accomplished by using the UBC bender element equipped triaxial apparatus (Chapter 3) with bender element techniques developed and reported in Chapter 4 and Chapter 5.

This study demonstrated the shortcomings of recently published empirical methods to estimate G_{sec}/G_0. It was found that these methods do not correctly handle the initial stress ratio. It was shown that the effect of the stress path and age duration is not removed by normalizing with G_0.

To increase the size of the dataset the results from past investigations by Shozen (2001) and Lam (2003) were included by using an empirically estimated G_0 value. The empirical equation for G_0 was developed in Section 5.6 combining the data collected in this research following the theoretical back-

ground and past empirical relationships described in Section 2.3. The results of this research were able to show that ageing can result in the observed small increase in G_0, large increase in G_{sec}, and no change in strength.

The following conclusions were drawn from the research presented in this chapter:

1. The developed triaxial apparatus is capable of acquiring G_{sec}/G_0 stiffness degradation curves above 0.01 % shear strain.

2. The effect of ageing on G_{sec} is not eliminated by normalizing with G_0 - i.e. the stiffness degradation curves do not collapse to a single reference curve.

3. The effect of ageing on the model hyperbolic-stiffness parameters was plotted (Figure 6.12). The parameters appeared to increase on a log-linear relationship with age duration. Ageing is a significant difference between reconstituted specimens and in-situ soil, particularly over the strain range experienced by most geotechnical structures.

4. The hyperbolic stiffness degradation curves did not appear to fit non-conventional stress paths, particularly slope-0 stress paths.

5. Wichtmann and Triantafyllidis (2013) and Oztoprak and Bolton (2013) proposed very simple techniques to estimate a normalized stiffness degradation curve from readily obtained granular soil properties. This work demonstrated the importance of the specimen age, stress ratio, and stress path on the measured normalized stiffness degradation curves. These variables are not accounted for in the work by Wichtmann and Triantafyllidis (2013) and Oztoprak and Bolton (2013).

As mentioned at the end of Chapter 5, the next chapter concerns in-situ measurements. It describes the adaptation and preliminary evaluation of the developed continuous monitoring method to down-hole seismic testing. V_S can be measured in-situ and used to scale the empirically predicted normalized stiffness curves to estimate deformation of sands.

Chapter 7

Development of Perpetual Source SCPTu

Shear waves are measured in both laboratory specimens and in the field. This permits empirical normalized stiffness degradation curves (Chapter 6) to be scaled to in-situ conditions. While developing the continuous laboratory bender element technique (Chapter 5), it was realized that it could be adapted to in-situ measurements. This chapter reports on this adaptation. This work has been the subject of three conference papers: Styler et al. (2012), Styler et al. (2013), and Styler et al. (2014).

Chapter 5 presented a method to continuously monitor the shear wave velocity with bender elements throughout a laboratory experiment. This method used a continuous multi-tonal shear wave signal measured at two spatial points - the bender element locations. The phase shift of the signals between these two monitoring locations were used to estimate the shear wave propagation time and V_S. This chapter presents the adaptation of this continuous bender element technique to down-hole shear wave velocity measurements. This was accomplished by creating a continuous seismic source using a vibrator at the ground surface. The shear waves propagating downward from this continuous source were monitored at multiple down-hole locations. The phase shift or cross correlation of the signals measured at these points was used to calculate the propagation time and V_S. Seismic

signals were collected concurrently with CPT measurements while the cone was advanced at the standard rate of 2 cm/sec (ASTM D5778-12). This method has been named "Perpetual Source SCPTu" (PS-SCPTu) to differentiate it from other attempts to measure a profile of V_S continuously during CPT penetration. This development provides a profile of measurements of in-situ soil response at the in-situ state. These measurements include the cone tip resistance, friction sleeve, pore water pressure, and shear wave signals. Additional details on cone testing and interpretation can be found in Lunne et al. (1997).

Figure 7.1 shows three different sources that can be used to generate shear waves at the ground surface. The conventional source is the sledge hammer and shear beam. The continuous-interval source uses a motor to prime a spring loaded pendulum. Both of these sources create a shear wave from the impact of a swinging hammer. The third source is new and is the focus of this chapter. It does not have an impact. It generates a continuous field of downward propagating shear waves.

The objective of this chapter is to demonstrate that this new technique provides a measure of the in-situ V_S. This was accomplished by comparing the results to conventional shear-beam down-hole seismic testing.

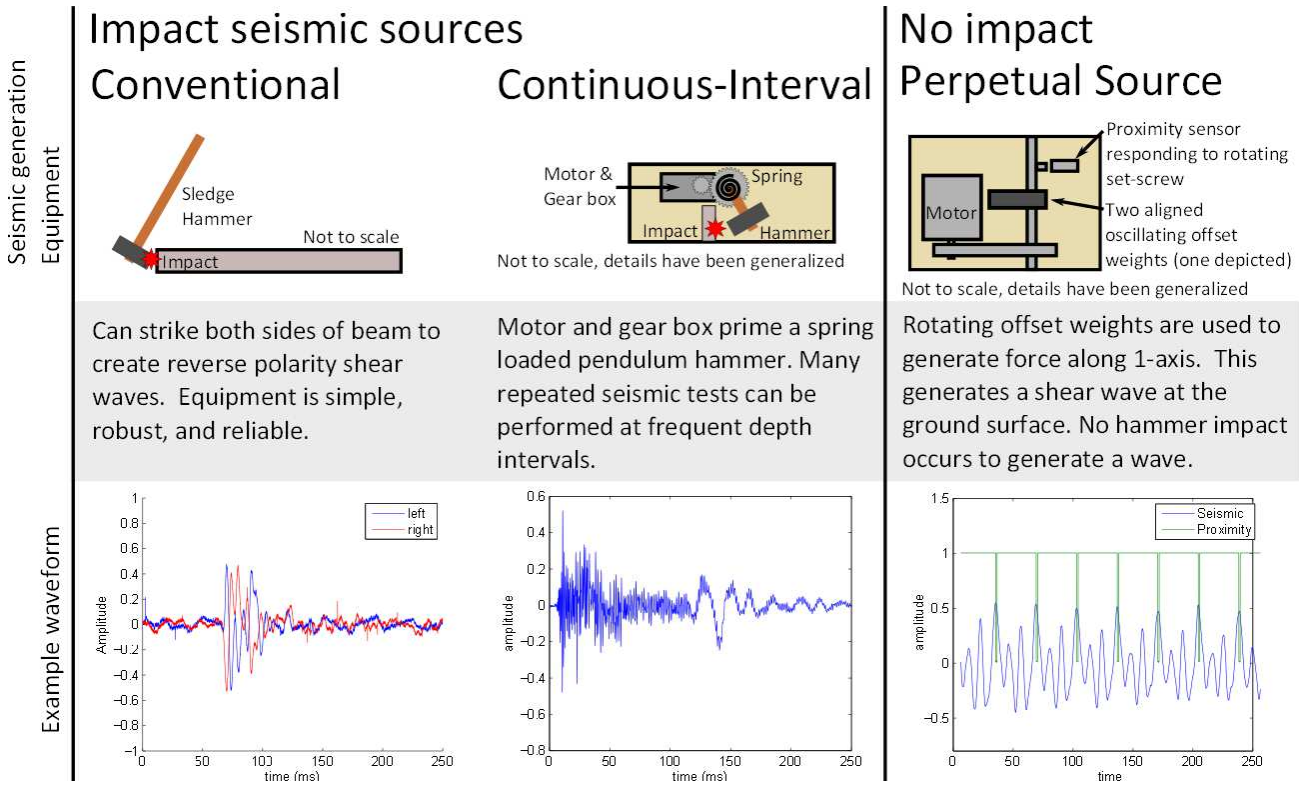

Figure 7.1: Three different shear wave sources for down-hole seismic testing during cone penetration

7.1 Existing down-hole in-situ V_S measurements

7.1.1 Conventional SCPTu

The cone penetrometer is an in-situ tool with almost 80 years of refinement in equipment, technique, and interpretation. Robertson et al. (1986) described the combination of conventional down-hole seismic testing with CPTu to provide seismic cone testing (SCPTu). A shear wave was triggered at the ground surface and a seismic sensor behind the sleeve responded to the downward propagating wave. The shear waves were generated by striking the end of a beam with a sledge hammer. Seismic signals were generated when the cone penetration was paused at 1m interval rod breaks. Adjacent down-hole seismic signals were compared to determine the shear wave velocity over the interval between measured signals. Conventional seismic testing results in a coarse step plot of V_S measurements at 1 m intervals.

True-interval testing uses one set of shear waves and two seismic sensors. The seismic sensors are spaced behind the cone tip and a single shear beam hit can be used to estimate the propagation time. Pseudo interval testing uses two sets of shear waves and one seismic sensor to estimate V_S. A set of seismic signals is collected, the cone is advanced to the next depth, and another set of seismic signals is collected. The advantages of true interval testing are that it eliminates error of the data-acquisition trigger time and seismic sensor spacing. It also reduces the need for a reproducible shear wave. This makes true interval testing a more attractive option if less controllable shear sources, i.e. shotgun shells, are used. The disadvantage of true interval testing is that it uses multiple seismic sensors. These sensors must respond identically to the shear wave to avoid introducing a bias into the signals. They must have the same frequency response and soil coupling. The advantage of pseudo-interval testing is that it only uses a single sensor. This simplifies the equipment and shortens the length of the probe. Any bias in this sensor is subtracted out when two signals, both measured from the same sensor, are compared.

7.1.2 Continuous SCPTu

Research over the past decade at Georgia Tech in Atlanta, Georgia has focused on a seismic source and interpretation procedure for a continuous profile of V_S. This method has been named Continuous Interval Seismic Cone Penetration (CiSCPTU). It involves the frequent collection of hammer strike seismic signals down-hole during cone penetration. Casey and Mayne (2002) and McGillivray and Mayne (2008) describe the development of the automatic seismic source, called a Roto-seis. It contains a motor driven geared wheel which primes a spring loaded short arm pendulum. An electronic trigger signal initiates an immediate and reproducible hammer strike. This trigger signal is wired to a depth increment measurement system to automatically trigger shear waves at frequent depths. The Roto-seis unit is compact and weighs only 35 kg.

The CiSCPTu approach creates a number of challenges for interpretation of the propagation time that are not an issue for conventional down-hole seismic testing. Many more seismic signals are collected for a single sounding. This required the development of automated signal processing routines. The measured seismic signals include noise from external disturbance, vibrations, stray signals, and seismic noise from the cone shearing the soil. The signals are collected while the cone is moving. This prevents the use of signal stacking to reduce random noise. It also prevents the use of the conventional left-hit right-hit cross over point identification. Further details on these challenges and the required post-processing can be found in Ku and Mayne (2012); Ku et al. (2013).

The developed PS-SCPTu technique described in this chapter differs from the Continuous Interval method. PS-SCPTu does not use a hammer-strike shear wave. The seismic signal is from a vibration source. This focuses the downward propagating shear wave into a small frequency window. The shear waves are continuous - they are arriving throughout the collected signal. There is no window to select for the arrival. Furthermore, the entire measured signal contains useful information. With hammer strike signals, everything before the shear wave arrival is discarded and everything after

has minimal use.

Confident interpretations of the shear wave propagation time require a sufficient signal to noise ratio (SNR). The signal strength depends on the continuous vibration source, geometric radiation damping, and soil damping. The power of the signal, and consequently the SNR, is reduced due to geometric damping as the depth of the receiver increases. Higher frequency vibrations are reduced by soil damping with depth. Noise is generated by the grinding caused by penetration of the cone tip through the soil. The signals are collected while the cone is moving, so signal stacking procedures to reduce random noise are not applicable. The source has to be strong enough to overcome the noise at depth.

As covered in Chapter 2 and will be demonstrated in Chapter 6, V_S is an informative soil parameter. Measuring profiles of V_S during cone penetration testing has implications for soil profiling and soil property interpretations. Soil behaviour charts using a normalized tip resistance and G_0 have been proposed by Robertson et al. (1995a) and Schnaid and Yu (2007). These charts provide an indication of the type of soil and soil properties including cementation, age, and compressibility. In-situ measurements of V_S provide additional information that may improve existing empirical correlations.

7.2 Perpetual source method

The perpetual source technique consists of advancing a seismic cone through a continuous field of radiating shear waves from the ground surface. Implementation of the technique required development of a suitable perpetual source, the test procedure and interpretation method, and evaluation of the profile of V_S obtained against conventional results.

7.2.1 Perpetual source

The perpetual source device consists of two motor driven rotating offset weights. The plane of rotation for these two weights is parallel to the ground surface. On this plane, the two offset weights constructively create a vibration in one direction. Perpendicular to this direction, the vibrations pro-

duced by offset weights destructively interfere to minimize any motion. The perpetual source device vibrates along a line parallel to the ground surface. This line is directed toward the CPT hole. Additionally, the CPT seismic sensors are aligned to respond to shear motion in this direction. This device vibrates at a frequency of 28 Hz. Figure 7.2a is a photo of this source during a perpetual source test at Kidd 2 in Richmond, BC.

7.2.2 True interval cone

A true interval cone with three seismic sensor locations was used to measure the continuous wave at three depths simultaneously. The first geophone was 0.3m behind the cone tip in a standard seismic cone. The second and third geophones were 0.8 and 1.3 m behind the cone tip in a true interval module. All three of these geophones are aligned in the same direction. These three geophones were reported to have a resonance frequency of 24 Hz.

Geophone measurements depend on the velocity of a coil of wire relative to a magnet (Santamarina et al., 2001). Geophones have a non-linear frequency response and amplify shear wave frequencies (Stewart and Campanella, 1993). Geophones are also rugged, inexpensive, and do not need to be filtered (Laing, 1985). Geophones perform better than accelerometers for detecting shear waves with frequencies less than 60 Hz (Hons, 2009).

Accelerometers are an alternative to geophones. Accelerometers respond to the acceleration of a seismic mass on a chip (Santamarina et al., 2001). The change in capacitance between electrodes sandwiching this seismic mass is measured (Hons, 2009). Campanella and Stewart (1992) recommended a high sensitivity, critically damped piezoresistive accelerometer with a flat response from 0 to above 350 hz. Accelerometers were not evaluated. This research employed geophones, but does not make a recommendation on the type of seismic sensor.

Figure 7.2b is a photo of the seismic cone attached to the true interval module.

(a) Perpetual shear wave source

(b) Seismic cone with true interval module

Figure 7.2: Photos of PS equipment taken at Kidd 2 in Richmond, BC

7.2.3 Procedure

The Perpetual Source technique supplements conventional cone penetration testing. ASTM standard (D5788-12) procedures for CPT were followed. This standard covers the required calibration standard, penetration rate, and data acquisition. The perpetual source device is placed on the ground surface 1-3 m from the CPT hole. It is orientated so that the active vibration axis points towards the CPT. The cone is rotated so that the three geophones are aligned with the perpetual source vibrations. The perpetual source is turned on and left on through out the PS-CPTu sounding.

During penetration, a depth-wheel rotates as the cone rods are advanced downward. This wheel has a proximity sensor that responds to small metal tags on the depth wheel every 2.5, 5.0 or 10.0 cm. This proximity sensor triggers the seismic data acquisition. At every single depth wheel trigger, the data acquisition system automatically records for 250 ms from the top, middle, and bottom geophones simultaneously at a sampling rate of 20 kHz (5000 measurements per geophone). These three signals are compared to determine the propagation time, i.e. a true interval technique.

7.2.4 Interpretation of collected signals for V_S

The large number of seismic signals collected during a PS-SCPTu sounding require an automated approach to interpretation. Ideally, the interpretation of V_S should not depend on subjective input and a general procedure applicable to any sounding needs to be developed and demonstrated. Automated interpretation is necessary to make this test a viable tool for routine site investigations.

Conventional approaches to down-hole seismic interpretations will not work. As the polarity of the signal is not inverted during testing, there is no cross-over point to identify. A single point in the 250ms signals does not correspond to the shear wave arrival. The shear wave is continuous - it is arriving at 0ms and 250ms, and at every time in between. V_S is determined by identifying the time of travel of significant features in the shear wave signal over known depth intervals.

Two methods were investigated to estimate the propagation time between two signals collected at the same time: the cross correlation function and the phase shift. It was found that when the measured perpetual source signals were dominated by a single frequency, the two approaches gave the same answer. However, the perpetual source was unable to generate a clean single frequency sine wave. The cross-correlation of the signals was used in order to compare all of the propagating frequency components.

The simplest approach to estimating the shear wave propagation distance is the difference in the shortest line to each geophone from the perpetual source. This may not be accurate if the shear wave direction changes due to refraction. This work is focused on the estimation of the propagation time from the perpetual source during cone penetration. Errors in the propagation length due to refraction are beyond the scope of the early stages of this research.

7.3 Field testing

To demonstrate that this new approach can be used to acquire in-situ V_S, it is compared to coarse, conventional, 1m interval measurements. Three PS-SCPTu soundings were performed. The first one was made adjacent to a previous conventional SCPTu profile. To reduce any potential spatial variability errors, the second sounding included concurrent conventional measurements. The perpetual source was paused every metre to trigger and record conventional hammer-test seismic shear waves. These two tests used the true-interval module and measured true-interval shear wave velocities from the Top-Middle, Middle-Bottom, and Top-Bottom geophone pairs.

In these two tests, it was observed that the top-middle geophone pair resulted in a faster velocity than the middle-bottom pair. The second sounding included concurrent seismic-hammer testing that showed the same result. The true interval cone was disassembled and the geophone locations were confirmed. The cone was placed on a vibration table and the geophones responded in phase. The source of this anomaly was investigated. A six-geophone true interval module with 25cm spacing was constructed and

tested. No trend with geophone pair location was observed. It is believed that the effect observed on the original equipment is due to a difference in mounting of one of the geophones. However, this theory has not been conclusively tested. To avoid this problem, the PS-SCPTu method was altered for pseudo-interval testing. Pseudo-interval testing uses the same geophone at different depths to acquire the propagation time, as in conventional seismic cone testing using a single geophone probe. The third PS-SCPTu sounding was performed adjacent to another conventional SCPTu and used the modified pseudo-interval technique.

7.3.1 PS-SCPTu-01: Feasibility test

The PS-SCPTu-01 sounding was performed at 12410 Vulcan Way, Richmond, BC. This test went to a depth of 45 m. Seismic data acquisition was manually triggered - an automatic interface to cone depth increment system had not yet been developed. Seismic signals were collected approximately every 10 cm of cone penetration. The perpetual source was 3.16 m from the PS-SCPTu hole.

Figure 7.3a shows the measured and recorded top, middle, and bottom geophone signals at a cone tip depth of 6 m. The top geophone is at a depth of 4.7 m, the middle geophone is at 5.2 m, and the bottom geophone is at 5.7 m. This demonstrates that the source is generating a periodic shear wave signal that propagates to 5.7 m, the location of the bottom geophone. Figure 7.3b shows the same three signals in the frequency domain. The peak in this plot is at the perpetual source frequency of 28 Hz. Some harmonics of this frequency occur near 60, 90, 120, and 150 Hz.

Figure 7.4 depicts the cross correlation of the three geophone signals shown in Figure 7.3a. The peak cross correlation corresponds to the true interval change in propagation time. For the top-middle geophone pair this occurs at 4.00 ms. For the middle-bottom geophone pair this occurs at 4.50 ms. For the top-bottom geophone pair, the largest propagation distance, this occurs at 8.75 ms. These propagation times occur with the geophone depths at 4.7 m (top), 5.2 m (middle), and 5.7 m (bottom). The ray path distances

from the source to the geophones are 5.66 m (top), 6.08 m (middle), and 6.52 m (bottom). This results in an estimated V_S of 105 m/s from the top to the middle geophones, 96 m/s from the middle to the bottom, and 98 m/s from the top to the bottom. At a cone tip depth of 6 m, the raw data was interpreted with the cross correlation technique. This did not require any subjective selection of filters, averaging, or windowing.

Figure 7.5 shows the PS-SCPTu-01 profile with an adjacent conventional SCPTu. The first column is the corrected cone tip resistance ($q_t = q_c + (1-a)u_2$). The second column is the friction ratio ($Rf = f_s/q_t(100\%)$). The third column includes the measured pore water pressure and hydrostatic pore water pressure line based on the estimated ground water table (dashed blue line). The fourth column includes the interpreted cross-correlation V_S from the top to bottom geophone pair (green line) with the adjacent conventional seismic interpretations (black step plot). The last column is the interpreted soil behaviour. There is a close agreement between the V_S interpretations in the top 15 m and in the lower silt. There are some variations in the sand layer.

One apparent advantage of the PS-SCPTu results is when the results do not agree with conventional measures. A poor quality seismic wave measurement from conventional testing may affect up to 2 metres of the seismic profile. The perpetual source technique provides so many more velocity interpretations that apparent outliers are either confirmed with immediately adjacent results or confidently ignored.

(a) Time domain signals

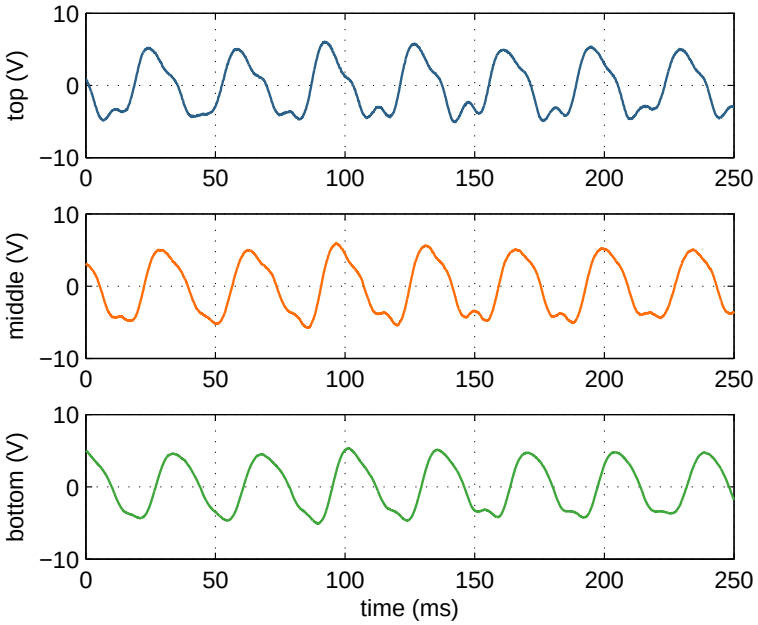

(b) Frequency domain signals

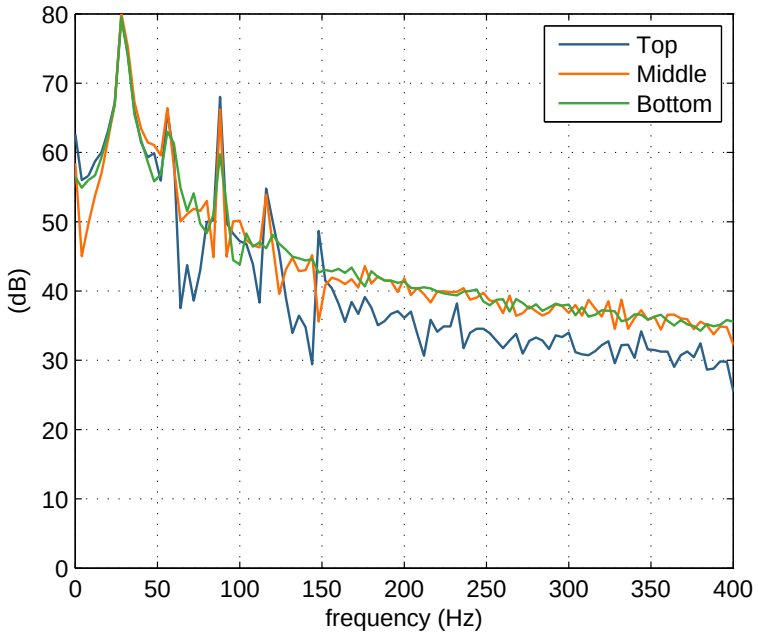

Figure 7.3: Collected signals at a cone tip depth of 6m

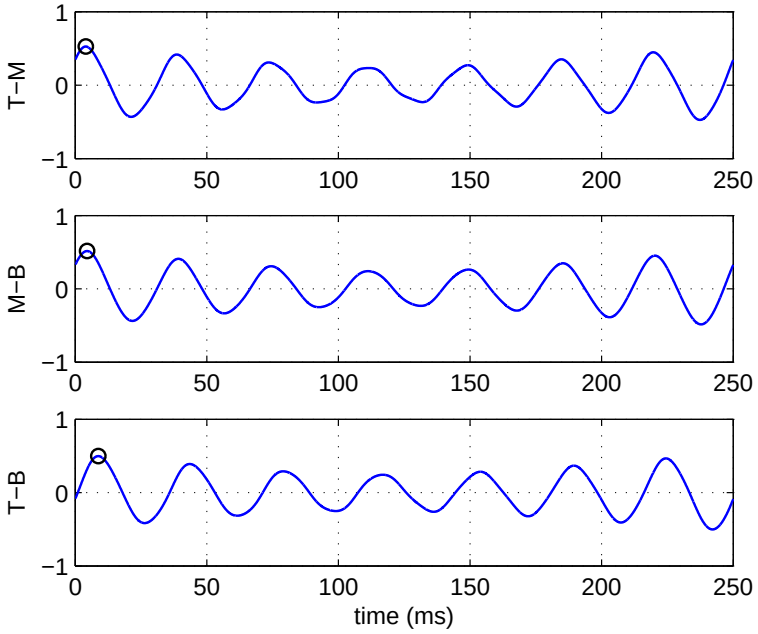

Figure 7.4: Cross correlation of measured signals shown in Figure 7.3: T-M = 4.00 ms, M-B = 4.50 ms, T-B = 8.75 ms

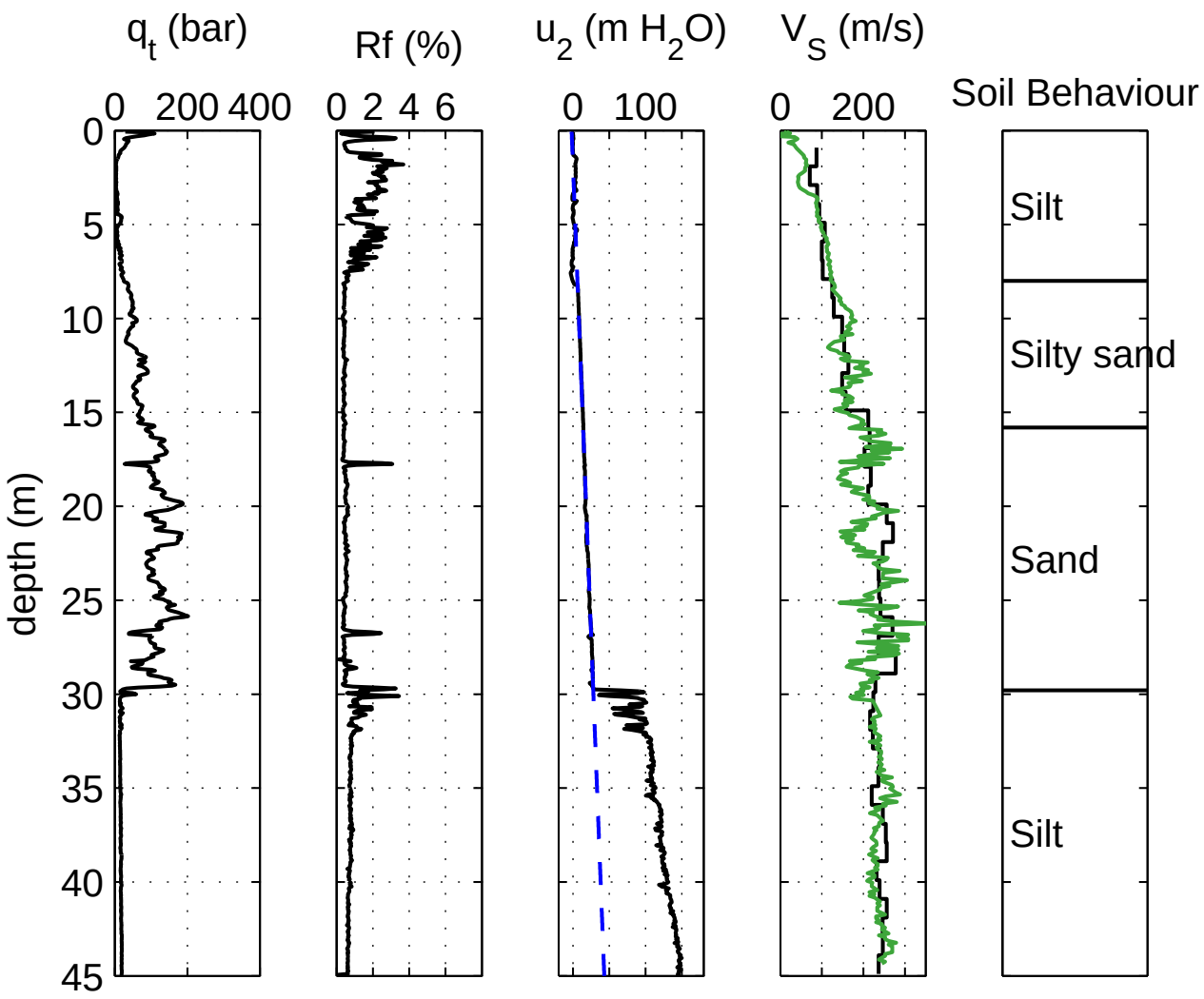

Figure 7.5: First PS-SCPTu profile collected in Richmond, BC where the green trace in the fourth column represents the perpetual source results and the black step trace is from adjacent conventional hammer beam strike tests

7.3.2 PS-SCPTu-02: Concurrent hammer testing

The second test was performed at Kidd-2, a nearby site in Richmond, BC that was part of the CANLEX liquefaction research project (Robertson et al., 2000; Wride et al., 2000). This test included concurrent hammer strike shear wave signals from 3 through 13 m. These were concurrent signals, not adjacent signals. The perpetual source was turned off at rod breaks and hammer strike shear wave data was collected. The perpetual source was then turned back on to generate continuous shear waves during penetration. The purpose of this test was to create a dataset to allow a direct comparison between the Perpetual Source V_S and the accepted conventional V_S measurements that did not include an unknown spatial variability.

Testing at this site also attempted to measure shear wave signals during rod retraction. It was expected that this would significantly reduce any seismic noise generated by cone penetration. However, this data was dominated by noise and could not be interpreted. It may be due to poor coupling between the soil and cone probe. The source of this noise was not investigated and further developments on PS-SCPTu was focused on measurements during downwards cone penetration.

The results of this second test are shown in Figure 7.6. The V_S column includes four sets of data. The black line is V_S from concurrent conventional hammer testing from 3 through 13 m. The green line is the cross correlation results of the Middle-Bottom geophone pair, the blue line is the Top-Middle, and the orange line is the Top-Bottom. The conventional hammer testing and the Top-Bottom perpetual source method are both interpreted over a 1m depth interval. The Top-Middle and Middle-Bottom geophone pairs are interpreted over a 50 cm depth interval.

Figure 7.7a compares the ratio of the geophone pair velocities against depth for the perpetual source testing. Figure 7.7b presents the same plot for the conventional hammer test velocities. Not only is the top-middle V_S significantly faster than the middle-bottom, this inconsistency increases with depth. This discrepancy was only observed due to the use of three seismic sensor locations. A typical true interval module only has two seismic

locations and this effect would not be measurable. A literature search was unsuccessful for other published data using a true-interval module with more than two geophones. It is not yet clear if the observed phenomenon is isolated to this equipment. Two possibilities are that it is a function of surface waves along the cone rod-soil interface or an amplitude dependent change in the coupling between the soil motion and geophone motion (McGillivray, 2013). Asalemi (2006) observed that the shear wave velocity increased with ageing when multiple tests were carried out without advancing the cone. At the ASTM rate of 2cm/sec, the soil around the top geophone was sheared 50 seconds before the soil around the bottom geophone. This ageing effect may explain the increase in the measured shear wave velocity over the top interval. Errors in the physical geophone locations and electronic bias were conclusively eliminated.

The hammer-strike data was collected during rod-breaks. It could be interpreted using pseudo-interval techniques instead of true-interval. The Pseudo-interval technique estimates the propagation time from signals collected from the same geophone at two different depths. Any inherent bias in the geophone will subtract out when comparing pseudo-interval signals. Figure 7.8 depicts pseudo-interval interpretations from 3m to 13m using the hammer strike signals. No systematic trends with geophones or depth were observed. Pseudo-interval testing does not suffer from the observed true-interval discrepancy.

For comparison purposes, Figure 7.9 combines the data shown in Figure 7.7b and Figure 7.8. The Pseudo-Interval results were generally slightly larger than the T-B geophone pair.

The two preceding sets of perpetual source signals cannot be interpreted with the pseudo-interval technique. The source operates independently of the data acquisition. It is only possible to compare signals that are aligned in time. The hammer strike signals are aligned in time. For every hammer strike signal, the time origin corresponds to the hammer strike. For perpetual source testing the time origin corresponds to a depth wheel event. This is asynchronous with any features in the perpetual source shear waves. The only aligned signals in the perpetual source testing are the set of three

simultaneously collected signals - top, middle, and bottom at each depth wheel trigger.

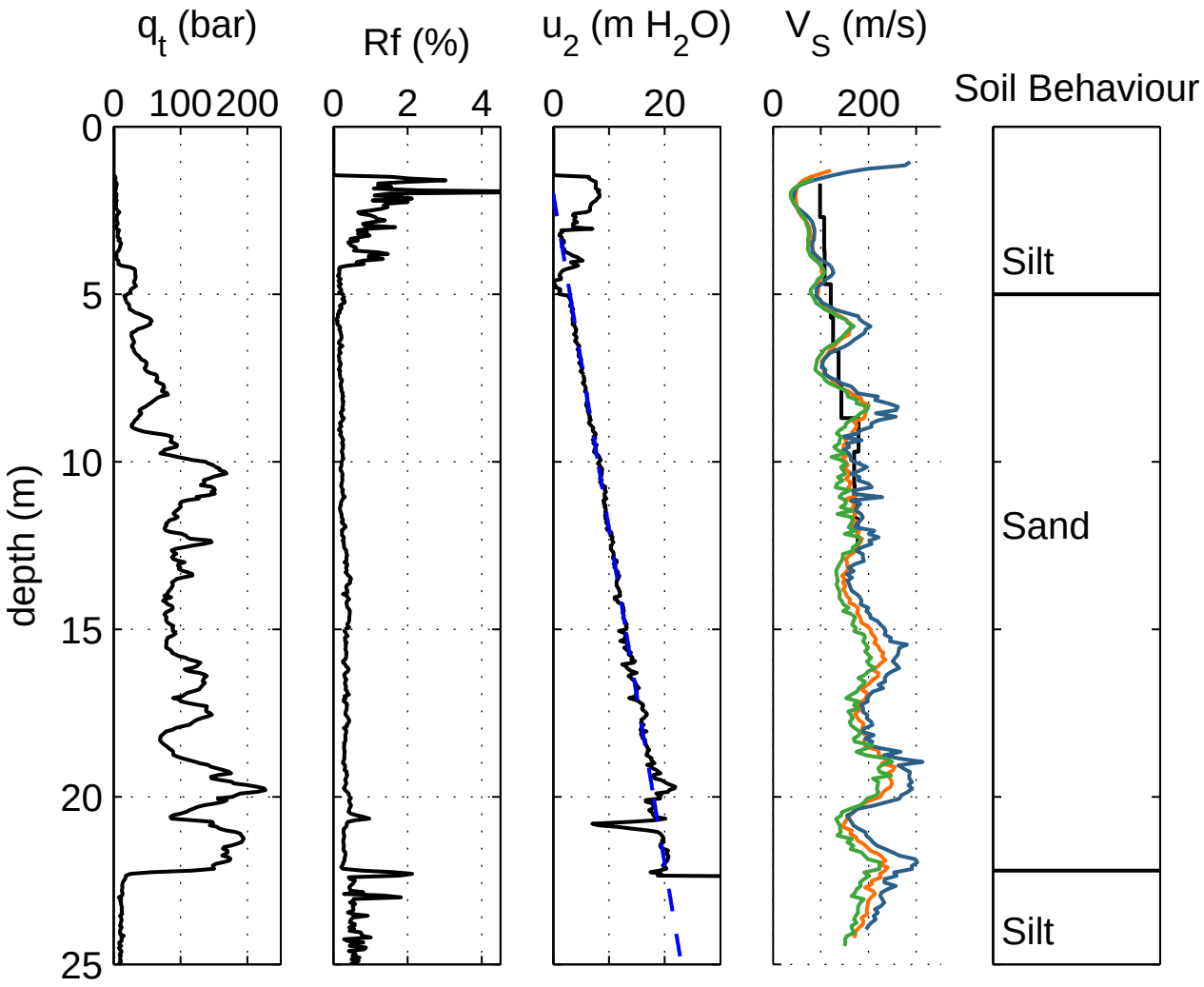

Figure 7.6: Second PS-SCPTu profile collected in Richmond, BC

(a) Ratio of measured velocities: blue points Kidd-2, green points Vulcan Way (feasibility test)

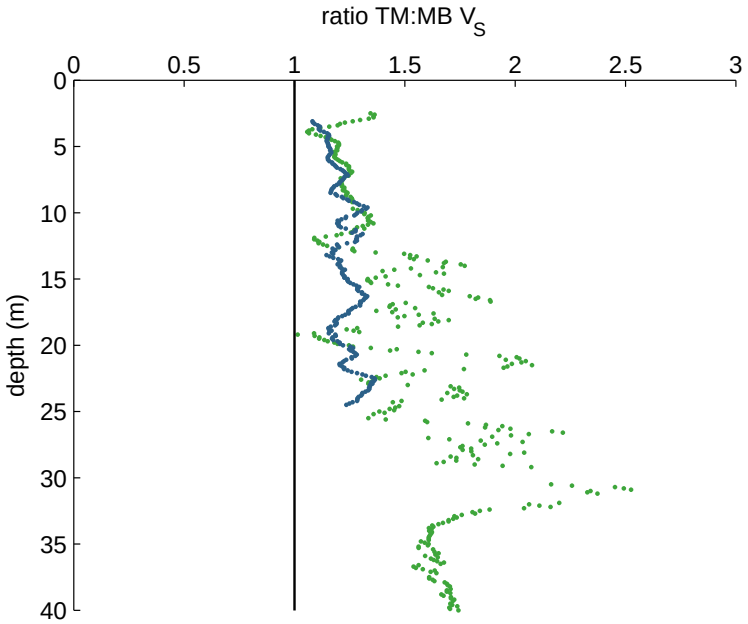

(b) Measured true interval shear wave velocities for concurrent hammer strikes at Kidd 2: blue T-M, green: M-B, orange: T-B

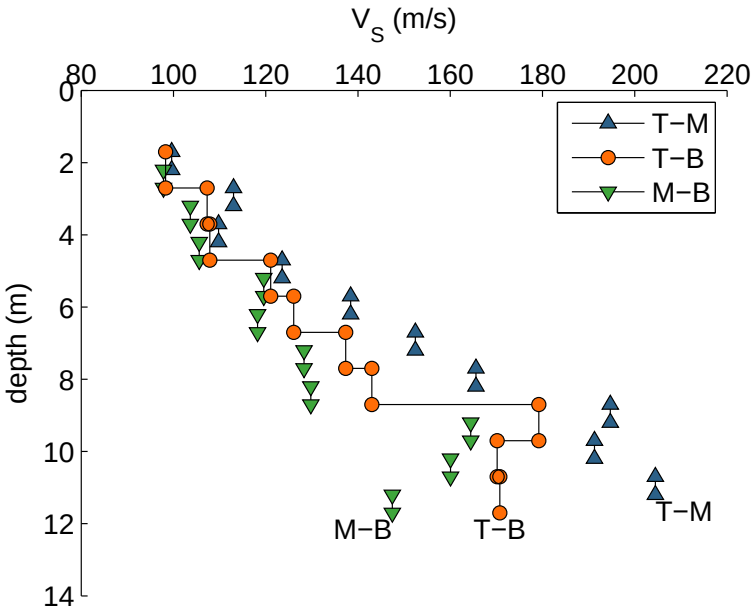

Figure 7.7: True interval discrepancy

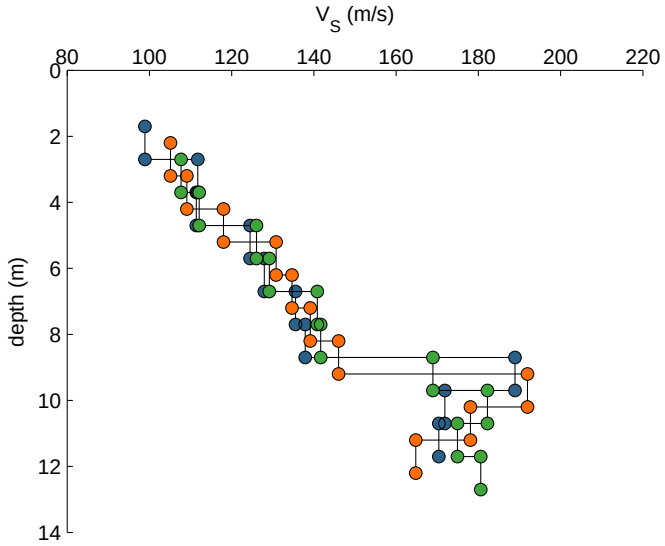

Figure 7.8: Measured pseudo-interval shear wave velocities for concurrent hammer strikes at Kidd 2: blue T, green: B, orange: M

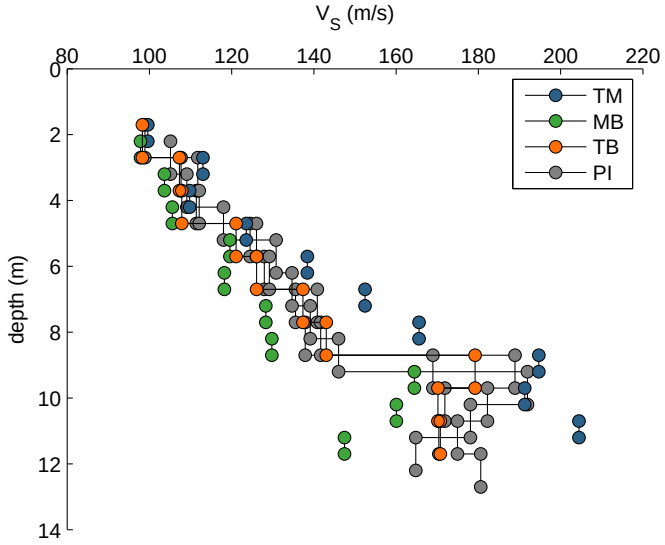

Figure 7.9: Comparing measured True Interval to Pseudo-Interval shear wave velocities for hammer-test data from a 3-geophone true interval cone

7.3.3 PS-SCPTu-03: Pseudo Interval

For psuedo-interval testing, the collected perpetual source seismic signals need to share a common time-origin. The time origin for the signals collected at a depth of 10m needs to be the same as for the signals collected at 11m. For hammer strike testing, this time origin is the initiation of the shear wave. Perpetual source testing does not have such an event. The shear wave is propagating continuously throughout the recorded signals. The perpetual source is periodic. Instead of aligning the collected signals to the time origin of the shear wave, they can be aligned to a constant phase angle of the source wave. This was accomplished by adding a proximity sensor to the perpetual source device. This sensor is fixed in place and responds to an adjustable set screw attached to one of the rotating weights. The proximity sensor signal has a sharp step in voltage when this set screw is detected. In addition to the three geophone signals (top, middle, and bottom), the proximity sensor signal is recorded at 20 khz for 250 ms. Figure 7.10 depicts all four measured channels at a depth of 6 m. These signals alone can only be interpreted with the true interval technique.

Pseudo interval testing determines the shear wave propagation time using a single geophone. To do this, the recorded signals are shifted in time so that a proximity sensor edge occurs at the time origin. Once the proximity sensor edge is aligned, two signals collected with the same geophone at different depths can be compared. Proximity sensor edges are easily identified. The cross-correlation signal comparison technique can identify the change in propagation time.

These modifications were implemented on a PS-SCPTu sounding performed at the Vulcan Way, Richmond, BC (Fraser River Delta) site. Perpetual source seismic signals were collected every 2.5 cm from all three geophones. This test included an adjacent conventional SCPTu profile.

Figure 7.11 shows two bottom geophone signals and proximity sensor signals collected at 6m and 7m cone tip depth. In this figure, the time origin corresponds to the depth-wheel data acquisition trigger. To perform pseudo-interval testing, the signals need to be shifted so that the time origin

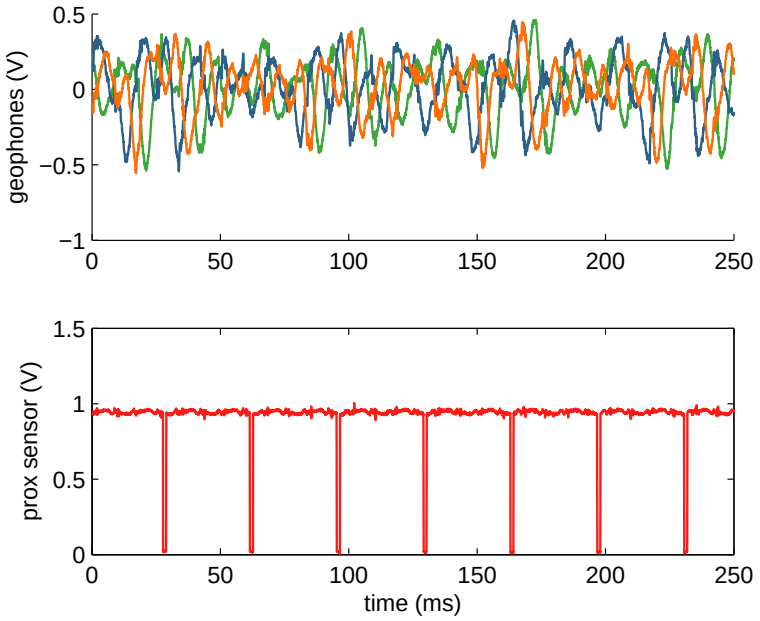

Figure 7.10: Measured PI signals with perpetual source proximity sensor: blue T, green: B, orange: M

corresponds to a step in the proximity sensor. This is shown in Figure 7.12a.

A pseudo-interval velocity can be interpreted from the proximity sensor aligned signals. The cross-correlation of the results in Figure 7.12a has a peak at 8.25 ms. This corresponds to a difference in ray path length of 0.97 m and a V_S of 118 m/s. This is the pseudo-interval velocity. It was estimated using the response of a single geophone at two different depths.

Figure 7.12b depicts the effect of shifting the 6 m bottom geophone signal by the cross correlation result of 8.25 ms. There is a high degree of overlap between the two signals. The features in the signal that propagate over 8.25 ms dominate these two signals.

Waterfall plots can be generated for pseudo-interval measured signals. A waterfall plot contains every measured signal at the depth where it was collected. For 1 m increment hammer testing to 30 m, this can result in 60 plotted signals (left hit, right hit) at each depth. Figure 7.13 shows

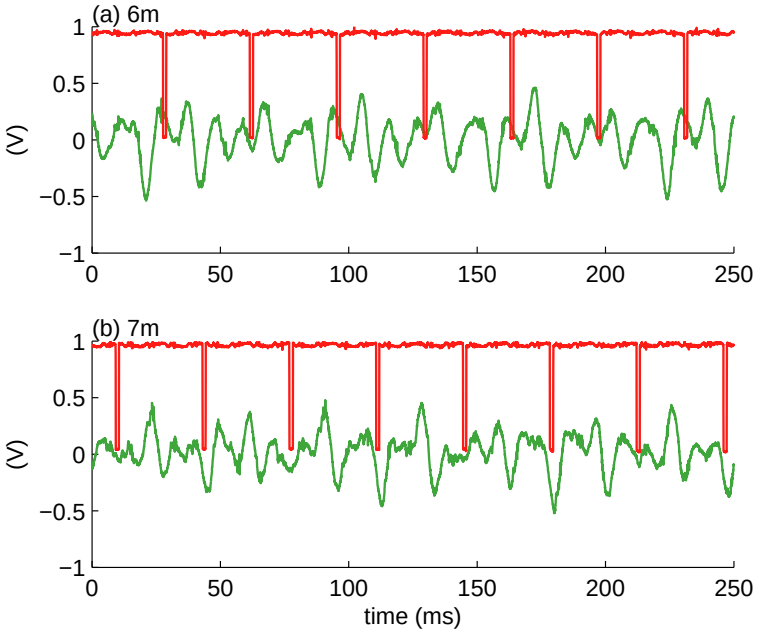

Figure 7.11: Measured bottom geophone signal and proximity sensor signal at 6 m and 7 m, where time 0 corresponds to a depth wheel data acquisition trigger

a waterfall plot from the adjacent conventional testing over-plotted onto a grey scale waterfall plot of the pseudo-interval bottom geophone. For the perpetual source data the time origin (time = 0 ms) for every signal corresponds to an edge in the proximity sensor. In this plot, the shear wave velocity is approximately equal to the slope of the seismic features. This slope is the change in propagation time against the change in geophone depth. The difference between this slope and the actual shear wave velocity is due to the difference between the change in ray path length and the change in depth. The waterfall figure depicts the aligned geophone signals. It does not directly provide an estimate of the propagation time or shear wave velocity.

The propagation time was estimated over a 1m moving window for the bottom geophone. Figure 7.14 shows the resulting PS-SCPTu profile. In

this figure the black lines correspond to the adjacent conventional SCPTu profile, the red lines correspond to the PS-SCPTu test. The V_S column shows the similarity between the perpetual source pseudo-interval V_S (bottom geophone) and the conventional seismic cross-over point interpreted V_S.

(a) Aligned 6 m and 7 m cone tip depth bottom geophone phone signals with the proximity sensor edge

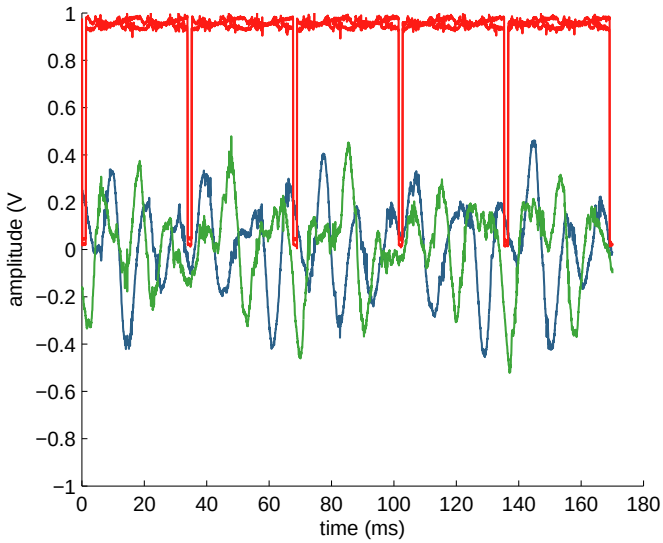

(b) Applied time shift to the 6 m cone tip bottom geophone signal by the cross correlation result of 8.25 ms

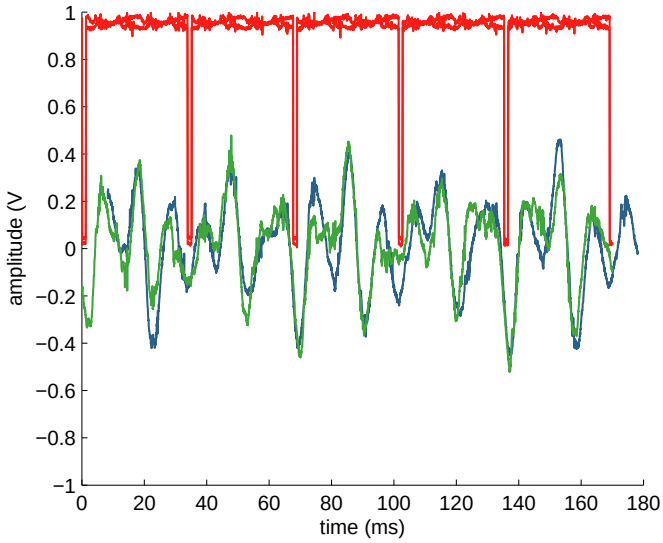

Figure 7.12: Interpreting a pseudo-interval propagation time using a single geophone with a perpetual source

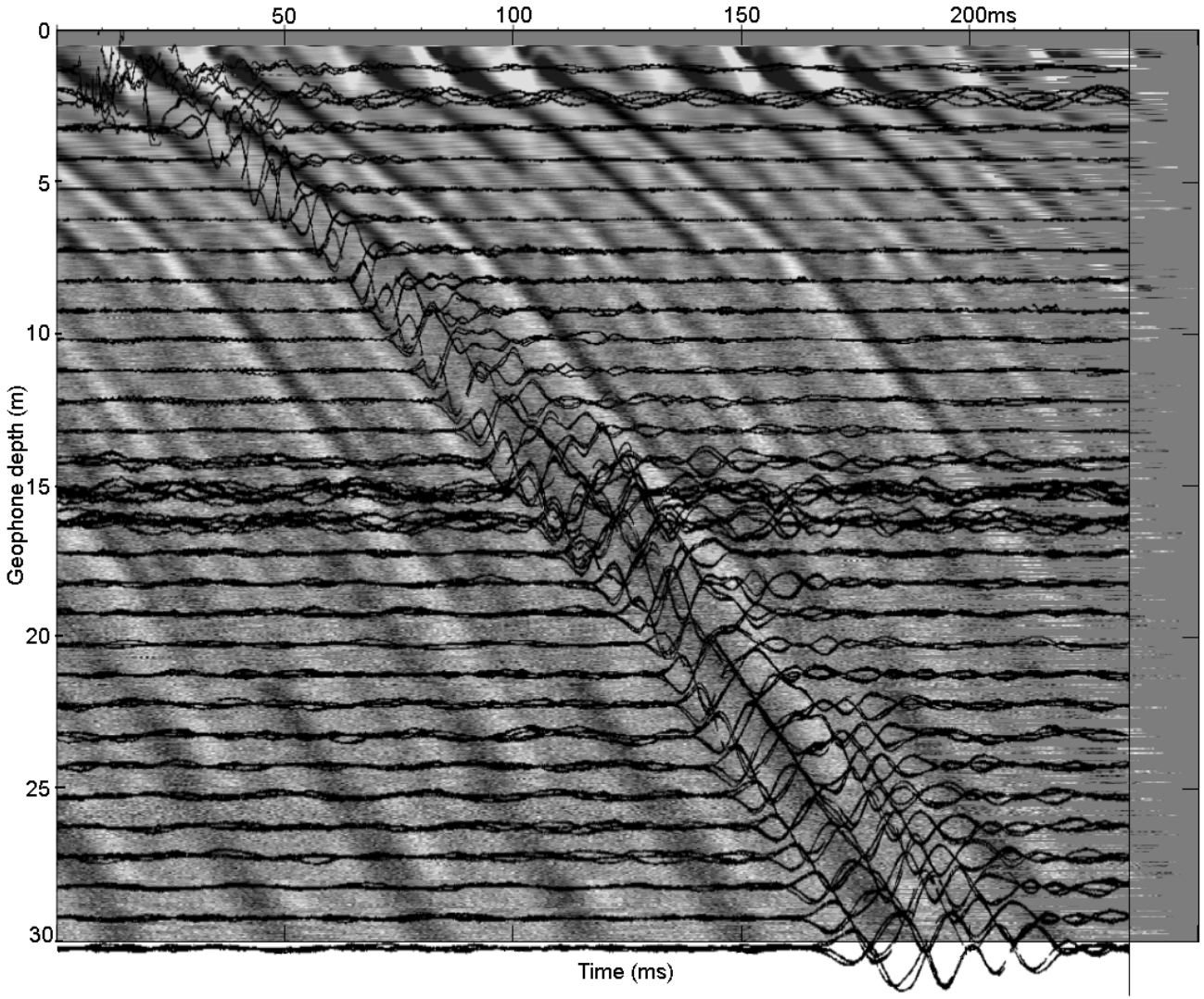

Figure 7.13: Perpetual source PI and conventional PI overlapping waterfall plots

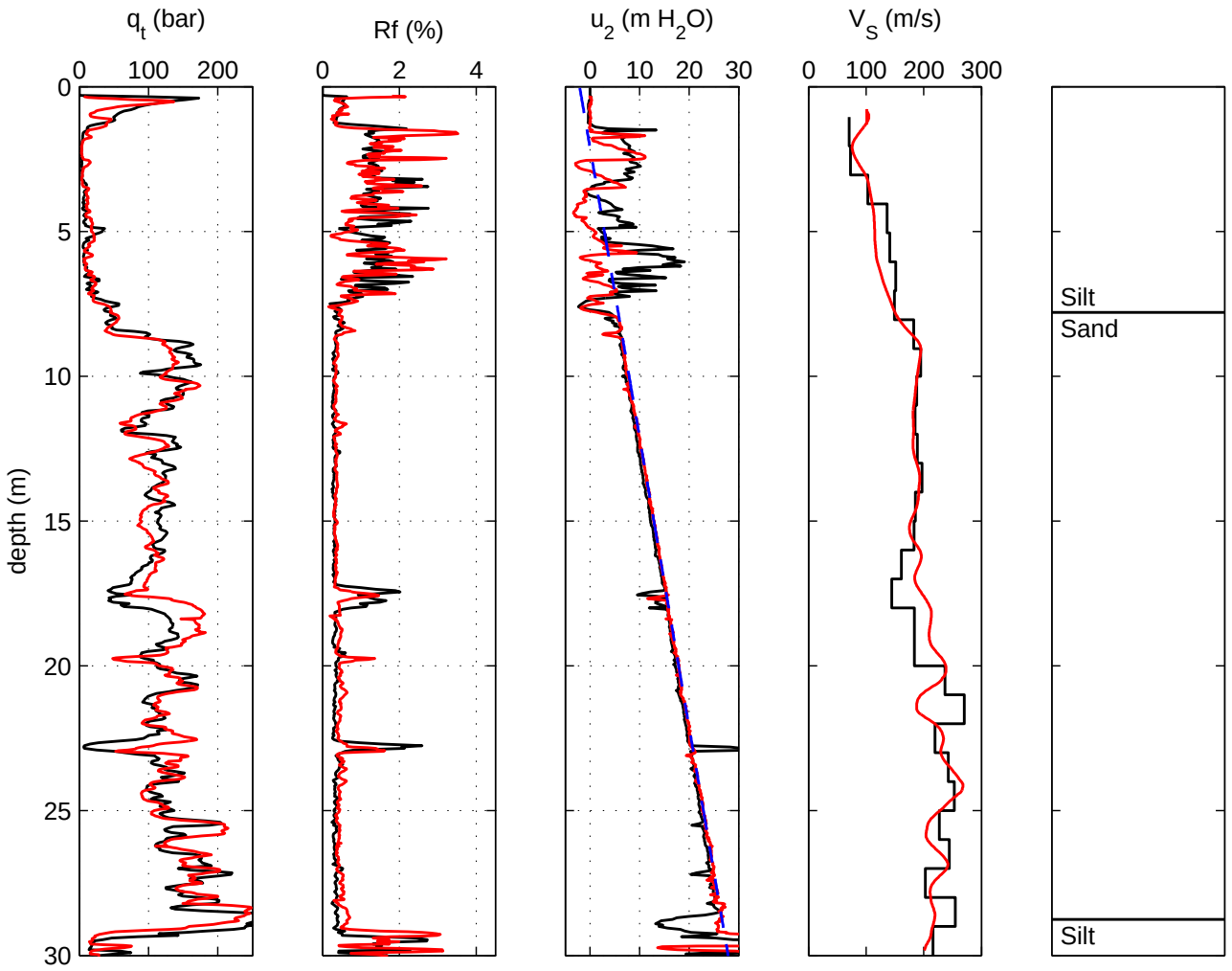

Figure 7.14: PS-SCPTu profile for pseudo-interval testing (red) with adjacent conventional SCPTu (black)

7.3.4 Comparing to conventional pseudo-interval V_S

The data presented in this chapter used two different techniques to acquire the in-situ velocity for a downward propagating shear wave. The conventional method interprets the propagation of shear waves generated from an impact-hammer source. The perpetual source method measures the velocity from continuous shear waves.

There are a few obvious differences between these types of measurements. The PS-SCPTu-01 and PS-SCPTu-03 had adjacent conventional seismic profiles. There will be some spatial variability between these measurements. PS-SCPTu-02 had concurrent measurements. However, the perpetual source and conventional seismic beam were necessarily in different location. Therefore, the ray paths for the waves in the second-hole are different. The second hole would also contain some spatial variability. The perpetual source method has most of its energy at a single frequency. The conventional hammer-testing covers a wide band of frequencies with a frequency distribution that changes with penetration due to in-situ soil damping. Any frequency-dispersion effects may cause these two measurements to differ. The perpetual source measurements also include noise from the grinding cone tip that is not present during conventional testing when the cone penetration is paused.

The interpretation of perpetual source signals is automated. It must be automated to handle the large number of signals collected during each test. The post-processing used in this work does not require subjective filter selections or windowing. It requires significantly less post-processing than described by Ku et al. (2013). Conventional testing - particularly the first-cross over technique - requires manual interpretation and has associated overhead.

Furthermore, by collecting and interpreting a large number of shear wave velocities - the outliers can be ignored. This cannot be done with conventional data without sacrificing up to 2 m of data. For example, if one set of measured signals were anomalous it would affect 2 m of interpreted conventional data. For the perpetual source results, it would affect only two points

on the moving window interpretations.

7.4 Discussion

The Perpetual Source technique that has been proposed has some advantages over conventional seismic testing. First, the test is faster. It does not require seismic testing during rod breaks. This is a minor advantage over conventional seismic testing and does not justify the additional equipment and interpretation costs. Second, a high depth resolution profile of V_S is determined. This is much more data than conventional seismic testing which results in a step plot of V_S. Empirical tools need to be developed that use V_S measurements to reduce uncertainty in soil profiling and soil properties. Once these have been developed, the additional equipment and interpretation costs associated with perpetual source measurements may be justified.

An interesting observation was made concerning the use of true interval cones. True interval measurements are taken to be more accurate than pseudo-interval (Jamiolkowski, 2012). They do not have additional random error from the differences in trigger time and depth. In true interval testing there is one trigger time and the depth-spacing of the geophones is exactly known. Conventional pseudo-interval testing may have a random error on trigger time. The zero time for the hammer strike may not be exactly the same between adjacent seismic tests. Conventional pseudo-interval testing may also have error due to the depth of the geophone. A 5cm depth resolution may be acceptable for CPT profiles, but may add considerable error when calculating the shear wave velocity over 1 metre. The exact depth spacing of the adjacent seismic tests has more uncertainty than true interval testing.

Despite these advantages of true interval testing, this work identified a potential problem. Three identical geophones resulted in a significant systematic discrepancy in V_S. The exact cause of this discrepancy has not been conclusively determined. It was not due to the geophone location or electronics. Another hypothesis is that the down-hole coupling between the

geophone and soil motion is not consistent between the three geophones. This effect is only observable with more than two geophones. With only two, as commonly used in true-interval testing, there may be an unknown error in the measurements. The only way to avoid this error is to compare signals collected from the same geophone.

Therefore, the highest quality in situ V_S measurements can be made from pseudo-interval testing with careful attention paid toward the depth increment and the repeatability of the hammer strike trigger. The Perpetual-Source testing uses a proximity sensor to ensure that the signals are aligned. The Perpetual-Source testing is triggered off a depth wheel. The depth wheel trigger encourages consistent in-situ depth separation of the recorded seismic signals used to calculate V_S.

The PS-SSCPTu method provides measurements that trend with conventional down-hole seismic measurements. This is depicted by the waterfall plot in Figure 7.13 that compares the actual data instead of the interpreted V_S results. The waterfall plot provides additional information on the exact depth where the signals qualitatively change. This may be useful for profiling and other seismic studies.

7.5 Conclusion

The new perpetual source technique was developed for down-hole seismic testing. Based on the results in this chapter it is concluded that careful pseudo-interval testing is more reliable than true-interval testing. The perpetual source technique was modified for pseudo-interval testing. Future work on the development of perpetual-source testing should explore the effect of changing the source frequency, seismic measurements during dissipation, the effect of approaching a reflective layer, and the development and implementation of a stronger and portable seismic source.

Chapter 8

Conclusion

The original intention of this research work was to examine the effect of ageing using a bender element triaxial apparatus. However, preliminary results found that the small effect of ageing could not be measured using bender elements. This led to an examination of bender element testing and interpretation. More advanced signal interpretation techniques were implemented, which led to the contribution of a combined time domain and frequency domain approach covered in Chapter 4. Further improvements in bender element V_S measurements were realized and Chapter 5 demonstrated that V_S could be monitored with bender elements continuously throughout a triaxial experiment. This technique was able to characterize the small increase in stiffness due to ageing when the bender element signals were stable. This enables the equipment to be used to investigate the effect of ageing on normalized shear secant-stiffness curves for laboratory specimens of clean Fraser River Sand using bender elements. This research project investigated only a small part of the effect of ageing on sands.

The limitation of using bender elements is that it is still a measurement over the bender-soil-bender system. The behaviour of the soil is not isolated and the bender element electrical-physical transformations may influence the results. These bender element transformations are not linear - they are strongly affected by the multiple frequency resonance peaks in the system. These resonance peaks change frequencies during a test (Alvarado and Coop,

2012). The behaviour of the bender elements can be characterized in air, but it would not be applicable to the response with soil coupling (Lee and Santamarina, 2005). This work demonstrated the significance of the systematic effect of frequency. Additional research may be able to characterize and correct the sources of these frequency effects.

One important implication of the developed continuous method is that the stability of the bender element testing can be observed. The stability of the bender elements appears to be lost when a major frequency feature - such as a resonance peak - approaches or crosses one of the monitoring points. Without monitoring the bender elements continuously it would be challenging to confidently disregard a measured bender element velocity. It is even possible to measure an incorrect negative N_G factor using bender elements when the results are influenced by the resonance peaks.

Continuous bender element monitoring was used to characterize an empirical G_0 equation and N_G ageing coefficient in Fraser River Sand (Section 5.6). This equation was used to calculate G_0 for the previous experiments (Lam, 2003; Shozen, 2001) and create a large dataset of normalized secant-stiffness (G_{sec}/G_0) curves for different age durations, consolidation stresses, and shear stress paths.

By following the same empirical technique used by Wichtmann and Triantafyllidis (2013) and Oztoprak and Bolton (2013), the effect of ageing could be quantified and extrapolated. This was done by characterizing the effect of ageing on best-fit hyperbolic function coefficients. The hyperbolic coefficients for the normalized stiffness degradation curves were found to follow log-linear trends with age duration (Section 6.5.3).

The normalized secant stiffness degradation curve is sensitive to reconstituted specimen age over the small strain range (approximately 0.01% to 1% shear strain). This may explain how ageing can result in a very small increase in G_0 and a very large increase in G_{sec}. This suggests that V_S interpretations are not very useful for investigating the consequences of ageing. However, the implications of the age induced increase in G_{sec} can be seen in the conceptual shear stiffness degradation curve given in Figure 1.2. Empirical shear stiffness degradation estimates will suffer if the difference in

ageing between laboratory reconstituted specimens and in-situ soils is not considered. Neglecting the effect of ageing may result in an overestimate of displacements. The hyperbolic models do not account for the fact that the strength is independent of ageing. They also do not explain the underlying mechanism responsible for the observed effect of ageing. There is still a need for more research into the fundamental mechanism responsible for ageing.

Chapter 7 presented the adaptation of the continuous bender element method to down-hole seismic testing. In-situ V_S measurements can be used to acquire G_0 and scale estimated normalized G_{sec}/G_0 stiffness curves. It was shown that this new in-situ method is capable of measuring a continuous profile of V_S. A continuous profile of V_S has implications for improving empirical interpretations of seismic cone testing. It may be able to increase the resolution of the V_S measurements by acquiring the propagation time over shorter intervals. An important outcome of the PS-SCPTu research was the observation that the true-interval shear wave velocities may be dependent on the geophone pair location behind the cone tip. It still needs to be confirmed if this observation is limited to the equipment used or endemic to all true-interval testing. Both possibilities have different implications. If it is related to the equipment, then a requirement for all true-interval module designs could be developed. If it is related to the true-interval technique, then an improved understanding of down-hole seismic testing could be realized.

Summary of research contributions

To reach the conclusions of this thesis, a number of contributions have been made. Most of these contributions are related to improvements in the measurements of V_S. These contributions are:

1. Development of a combined time domain and frequency domain interpretation method for bender element testing (Chapter 4). This technique eliminates the systematic effect of the selected trigger signal waveform from the resulting V_S measurement.

2. Development of a technique for continuous bender element V_S monitoring (Chapter 5). The developed technique is able to measure V_S

at dynamic phases of the experiment - including the transition from consolidation to ageing, from ageing to shear, and from contractive to dilative behaviour.

3. An empirical G_{vh} and N_G equation for clean Fraser River Sand (Section 5.6 and Section 5.5). These empirical coefficients can be used to estimate G_{vh} in reconstituted Fraser River Sand specimens. It was used in this study to complement previous investigations by Shozen (2001) and Lam (2003).

4. Extrapolation of the effect of ageing on normalized G_{sec}/G_0 curves (Section 6.5.3) for Fraser River Sand. The extrapolated curves demonstrated a significant effect of age over the small-strain stiffness range. As shown in Figure 1.2, this strain range is critical for typical geotechnical designs.

5. Development of Perpetual Source Seismic Cone Penetration Testing and the pseudo-interval modification (Chapter 7). This technique may be able to be used to increase the depth resolution of in-situ V_S measurements.

Summary of conclusions

This research developed new methods for measuring V_S with bender elements and in-situ. The laboratory and in-situ investigations led to the following primary conclusions:

1. The group velocity measured with bender elements is sensitive to dispersion and contains significant scatter (see Figure 4.6). The variation in group velocity is due to the non-linear frequency response of the bender element-soil system.

2. The phase velocity measures dispersion of the bender-soil system and is reproducible (see Figure 4.7). Phase velocity measurements are at a single frequency, and unlike group velocities they are not as strongly affected by dispersion.

3. Bender element testing is non-destructive for loose specimens of Fraser River Sand in the UBC triaxial apparatus (Section 5.4). No conclusive change in behaviour was observed with the external triaxial sensors or bender elements. Continuous bender element testing can be used to evaluate the effect of ageing.

4. Ageing increases the reference strain to 50 % G_0 and the brittleness (curvature) of the secant stiffness curve (Section 6.5.3). This increases the secant stiffness over the small strain range significantly, despite only a small increase in G_0 and negligible change in strength.

5. In-situ pseudo-interval shear wave testing is more reliable than true-interval until the observed inconsistency is resolved (Section 7.3.2). The error sources in pseudo-interval testing are known and can be controlled.

Unresolved issues

The characterization of N_G and G_0 with bender elements required a study of bender element errors. This led to improvements in bender element testing and in-situ V_S measurements. The following list summarizes some unresolved issues:

1. Characterization of the bender element electrical-mechanical transform function under evolving bender-soil coupling. Acquiring the trigger and receiver bender element transform functions would enable the measure of the shear wave across the soil specimen, instead of the current practice of measuring the shear wave across the bender-soil-bender system. Characterizing this transform function may significantly reduce the observed frequency dispersion in bender element testing and improve the understanding of the frequency evolution of the resonance peak features.

2. The secant stiffness for non-conventional shear stress paths over strains below 0.01 % is not clear. In the current investigation, these curves did

not appear to fit the hyperbolic relationships. They did not appear to trend towards G_0 with decreasing shear strain.

3. An inconsistency in true-interval measurements was observed on a 3-geophone seismic probe. This error was observed for both perpetual source testing and conventional hammer testing. The source of this error was not resolved. Therefore, it is not known if this error is isolated to the used true-interval probe or endemic to all true-interval measurements.

Further research on the effect of age is warranted. The following programs of study are suggested:

1. Create an electronically and mechanically stable triaxial apparatus for long-term age investigations. This apparatus requires constant temperature. It may require damping to eliminate mechanical vibrations. It may require a battery power supply to avoid electronic noise and power outages.

2. Measure Slope-0 stress paths at various age durations to investigate the effect of the initial volumetric expansion on the stiffness degradation.

3. It was observed that N_G for the stable denser specimens (1.0 ± 0.2 %) was less than the loose specimen dataset (1.9 ± 0.5 %). This conflicts with an increase in N_G with an increase in relative density reported by Baxter and Mitchell (2004) for Evanston Beach Sand. A test program should investigate the effect of density on N_G.

4. Perform continuous bender element monitoring on Slope -1 shear paths. These shear paths to failure are at a constant in-plane effective stress state. This investigation may provide insight into the effect of fabric, void ratio, and stress ratio on the shear wave velocity.

Closing remarks

The use of bender elements for measuring V_S in the laboratory has been investigated and improved. The continuous method can be used to charac-

terize the effect of ageing on V_S in clean sands. In practice, the effect of ageing on G_{sec} over the small strain range is much more significant in both magnitude and importance. It is more important because this strain range governs the response of many geotechnical designs.

The previous triaxial results at the University of British Columbia have been complemented with G_0 estimates. The apparent contradiction between small age-induced increases in G_0 and large age-induced increases in G_{sec} are due to a change in the shape of the non-linear shear-stiffness curve. The effect of age is insignificant over the very small strain range and at strains greater than 2 %. In the small strain range that governs soil behaviour in most geotechnical designs (Atkinson, 2000; Burland, 1989; Clayton, 2011), the effect of age cannot be ignored. Small strain behaviour is increasingly important for designs that are constrained by displacement instead of failure. Such designs include redevelopment adjacent to existing buildings and buried infrastructure. The advantage of the hyperbolic stiffness degradation curves is in predicting the small strain behaviour using readily obtained soil parameters. This is of particular importance in granular soils that cannot be routinely collected undisturbed. These hyperbolic curves can be scaled to in-situ calculated G_0 values from V_S measurements.

References

Afifi, S. and Richart, F. (1973). Stress-history effects on shear modulus of soils. *Soils and Foundations*, 13(1):77–95.

Alvarado, G. and Coop, M. (2012). On the performance of bender elements in triaxial tests. *Géotechnique*, 62(1):1–17.

Anderson, D. and Stokoe, K. (1978). Shear modulus: A time dependent soil property. *Dynamic Geotechnical Testing, ASTM STP*, 654:66–90.

Arroyo, M., Muir Wood, D., Greening, P., Medina, L., and Rio, J. (2006). Effects of sample size on bender-based axial G_0 measurements. *Géotechnique*, 56(1):39–52.

Arulnathan, R., Boulanger, R., and Riemer, M. (1998). Analysis of bender element tests. *ASTM Geotechnical Testing Journal*, 21(2):120–131.

Asalemi, A. A. (2006). *Application of seismic cone for characterization of ground improved by vibro-replacement*. PhD thesis, University of British Columbia.

Atkinson, J. (2000). Non-linear soil stiffness in routine design. *Géotechnique*, 50(5):487–508.

Baldi, G. and Nova, R. (1984). Membrane penetration effects in triaxial testing. *Journal of Geotechnical Engineering*, 110(3):403–420.

Baxter, C. D. and Mitchell, J. K. (2004). Experimental study on the aging of sands. *Journal of Geotechnical and Geoenvironmental Engineering*, 130(10):1051–1062.

Bellotti, R., Jamiolkowski, M., Lo Presti, D., and O'Neill, D. (1996). Anisotropy of small strain stiffness in ticino sand. *Géotechnique*, 46(1):115–132.

Bendat, J. and Piersol, A. (2010). *Random data: analysis and measurement procedures*. Wiley.

Biot, M. (1956a). Theory of propagation of elastic waves in a fluid-saturated porous solid. I. low-frequency range. *Journal of the Acoustical Society of America*, 28(2):168–178.

Biot, M. (1956b). Theory of propagation of elastic waves in a fluid-saturated porous solid. II. higher frequency range. *Journal of the Acoustical Society of America*, 28(2):179–191.

Bishop, A. and Henkel, D. (1957). The measurement of soil properties in the triaxial test. *Edward Arnold (Publishers) Ltd.*

Blewett, J., Blewett, I., and Woodward, P. (1999). Measurement of shear-wave velocity using phase-sensitive detection techniques. *Canadian Geotechnical Journal*, 36(5):934–939.

Bohac, J. and Feda, J. (1992). Membrane penetration in triaxial tests. *ASTM Geotechnical Testing Journal*, 15(3):288–294.

Bonal, J., Donohue, S., and McNally, C. (2012). Wavelet analysis of bender element signals. *Géotechnique*, 62(3):243–252.

Boonyatee, T., Chan, K., and Mitachi, T. (2009). Determination of shear wave velocity by bender elements using variable-path length method. *Soils and Foundations*, 49(3):489–494.

Brandenberg, S., Kutter, B., and Wilson, D. (2008). Fast stacking and phase corrections of shear wave signals in a noisy environment. *Journal of Geotechnical and Geoenvironmental Engineering*, 134(8):1154–1165.

Brignoli, E., Gotti, M., and Stokoe, K. (1996). Measurement of shear waves in laboratory specimens by means of piezoelectric transducers. *ASTM Geotechnical Testing Journal*, 19(4):384–397.

Brocanelli, D. and Rinaldi, V. (1998). Measurement of low-strain material damping and wave velocity with bender elements in the frequency domain. *Canadian Geotechnical Journal*, 35(6):1032–1040.

Burland, J. (1989). Ninth laurits bjerrum memorial lecture:" small is beautiful"-the stiffness of soils at small strains. *Canadian Geotechnical Journal*, 26(4):499–516.

Camacho-Tauta, J., Cascante, G., Santos, J., and da Fonseca, A. (2011). Measurements of shear wave velocity by resonant-column test, bender element test and miniature accelerometers. In *2011 Pan-Am Canadian Geotechnical Society Geotechnical Conference, Toronto*.

Campanella, R. and Stewart, W. (1992). Seismic cone analysis using digital signal processing for dynamic site characterization. *Canadian Geotechnical Journal*, 29(3):477–486.

Casey, T. and Mayne, P. (2002). Development of an electrically-driven automatic downhole seismic source. *Soil Dynamics and Earthquake Engineering*, 22(9-12):951–957.

Cha, M. and Cho, G. (2007). Shear strength estimation of sandy soils using shear wave velocity. *ASTM Geotechnical Testing Journal*, 30(6):484–495.

Cha, M., Santamarina, J., Kim, H.-S., and Cho, G.-C. (2014). Small-strain stiffness, shear-wave velocity, and soil compressibility. *Journal of Geotechnical and Geoenvironmental Engineering*.

Chan, K., Boonyatee, T., and Mitachi, T. (2010). Effect of bender element installation in clay samples. *Géotechnique*, 60(4):287–291.

Chang, C., Misra, A., and Sundaram, S. (1991). Properties of granular packings under low amplitude cyclic loading. *Soil Dynamics and Earthquake Engineering*, 10(4):201–211.

Chillarige, A., Robertson, P., Morgenstern, N., and Christian, H. (1997). Evaluation of the in situ state of Fraser River Sand. *Canadian Geotechnical Journal*, 34(4):510–519.

Cho, G.-C., Dodds, J., and Santamarina, J. C. (2006). Particle Shape Effects on Packing Density, Stiffness, and Strength: Natural and Crushed Sands. *Journal of Geotechnical and Geoenvironmental Engineering*, 132(5):591–602.

Cho, G. C. and Santamarina, J. C. (2001). Unsaturated particulate materials-particle-level studies. *Journal of Geotechnical and Geoenvironmental Engineering*, 127(1):84–96.

Clayton, C. (2011). Stiffness at small strain: research and practice. *Géotechnique*, 61(1):5–37.

Comina, C., Foti, S., Musso, G., and Romero, E. (2008). EIT Oedometer: an advanced cell to monitor spatial and time variability in soil with electrical and seismic measurements. *ASTM Geotechnical Testing Journal*, 31(5):404–412.

Cruse, T. and Rizzo, F. (1968). A direct formulation and numerical solution of the general transient elastodynamic problem. transient problem solution in linear elastodynamics by integral equation in laplace transform space. *Journal of Mathematical Analysis and Applications*, 22:244–259.

Cunning, J., Robertson, P., and Sego, D. (1995). Shear wave velocity to evaluate in situ state of cohesionless soils. *Canadian Geotechnical Journal*, 32(5):848–858.

Darendeli, M. B. (2001). *Development of a new family of normalized modulus reduction and material damping curves*. PhD thesis, The University of Texas at Austin.

d'Onofrio, A., Silvestri, F., and Vinale, F. (1999). A new torsional shear device. *ASTM Geotechnical Testing Journal*, 22(2):107–117.

Drnevich, V., Hardin, B., and Shippy, D. (1978). Modulus and damping of soils by the resonant-column method. *Dynamic Geotechnical Testing, ASTM STP*, 654:91–125.

Emeriault, F. and Chang, C. S. (1997). Anisotropic elastic moduli of granular assemblies from micromechanical approach. *Journal of Engineering Mechanics*, 123(12):1289–1293.

Fam, M., Cascante, G., and Dusseault, M. (2002). Large and small strain properties of sands subjected to local void increase. *Journal of Geotechnical and Geoenvironmental Engineering*, 128(12):1018–1025.

Garrison, R. E., Luternauer, J. L., Grill, E. V., MacDonald, R. D., and Murray, J. W. (1969). Early diagenetic cementation of recent sands, Fraser River Delta, British Columbia. *Sedimentology*, 12(1-2):27–46.

Ghayoomi, M. and McCartney, J. (2011). Measurement of small-strain shear moduli of partially saturated sand during infiltration in a geotechnical centrifuge. *ASTM Geotechnical Testing Journal*, 34.

Greening, P. and Nash, D. (2004). Frequency domain determination of G_0 using bender elements. *Geotechnical Testing Journal*, 27(3):288–294.

Hamidi, B., Varaksin, S., and Nikraz, H. (2013). Relative density correlations are not reliable criteria. *Proceedings of the ICE-Ground Improvement*, 166(4):196–208.

Hardin, B. (1980). Discussion: Anisotropic shear modulus due to stress anisotropy. *Journal of the Geotechnical Engineering Division*, 106(8):956–958.

Hardin, B. and Black, W. (1966). Sand stifness under various triaxial stresses. *Journal of the Soil Mechanics and Foundations Division*, 92(SM 2):27–42.

Hardin, B. and Black, W. (1968). Vibration modulus of normally consolidated clay. *Journal of the Soil Mechanics and Foundations Division*, 95(SM 2):–361.

Hardin, B. and Black, W. (1969). Closure: Vibration modulus of normally consolidated clay. *Journal of the Soil Mechanics and Foundations Division*, 95(SM 6):1531–1537.

Hardin, B. and Drnevich, V. (1972). Shear modulus and damping in soils: Measurement and parameter effects. *Journal of the Soil Mechanics and Foundations Division*, 98(SM6):603–623.

Hardin, B. and Richart Jr, F. (1963). Elastic wave velocities in granular soils. *Journal of the Soil Mechanics and Foundations Division*, 89(SM 1):33–65.

Hardin, B. O. and Blandford, G. E. (1989). Elasticity of particulate materials. *Journal of Geotechnical Engineering*, 115(6):788–805.

Heyliger, P., Ledbetter, H., and Kim, S. (2003). Elastic constants of natural quartz. *The Journal of the Acoustical Society of America*, 114:644.

Hons, M. (2009). *Seismic sensing: Comparison of geophones and accelerometers using laboratory and field data*. PhD thesis, University of Calgary.

Howie, J., Shozen, T., and Vaid, Y. (2002). Effect of ageing on stiffness of very loose sand. *Canadian Geotechnical Journal*, 39(1):149–156.

Iida, K. (1938). The velocity of elastic waves in sand.

Isenhower, W., Stokoe, K., and Allen, J. (1987). Instrumentation for torsional shear/resonant column measurements under anisotropic stresses. *ASTM Geotechnical Testing Journal*, 10(4):183–191.

Jamiolkowski, M. (2012). Role of p-waves and s-waves in geotechnical site characterization. In *Third international workshop on Modern Trends in Geomechanics IW-MTG3, 4-5 September 2012*.

Jang, I., Kwon, O., and Chung, C. (2010). A pilot study of in-hole type cptu using piezoelectric bender elements. In *2nd International Symposium on Cone Penetration Testing. Huntington Beach, California*.

JCGM, BIPM, IEC, IFCC, ILAC, ISO, IUPAC, IUPAP, and OIML (2008a). Evaluation of measurement data - guide to the expression of uncertainty in measurement - GUM 1995 with minor corrections. Technical Report JCGM 100:2008.

JCGM, BIPM, IEC, IFCC, ILAC, ISO, IUPAC, IUPAP, and OIML (2008b). Evaluation of measurement data - supplement 1 to the "Guide to the expression of uncertainty in measurement" - proagation of distributions using a monte carlo method. Technical Report JCGM 101:2008.

Jovicic, V. and Coop, M. (1997). Stiffness of coarse-grained soils at small strains. *Géotechnique*, 47(3):545–61.

Jovicic, V., Coop, M., and Simic, M. (1996). Objective criteria for determining Gmax from bender element tests. *Géotechnique*, 46(2):357–362.

Jung, Y., Cho, W., and Finno, R. (2007). Defining yield from bender element measurements in triaxial stress probe experiments. *Journal of Geotechnical and Geoenvironmental Engineering*, 133(7):841–849.

Karl, L., Haegeman, W., Degrande, G., and Dooms, D. (2008). Determination of the material damping ratio with the bender element test. *Journal of Geotechnical and Geoenvironmental Engineering*, 134(12):1743–1756.

Ku, T. and Mayne, P. (2012). Frequent-interval SDMT and continuous SCPTu for detailed shear wave velocity profiling in soils. *Geotechnical Engineering Journal of the SEAGS & AGSSEA*, 43(4):34–40.

Ku, T., Mayne, P. W., and Cargill, E. (2013). Continuous-interval shear wave velocity profiling by auto-source and seismic piezocone tests. *Canadian Geotechnical Journal*, (Online pre-print).

Kuerbis, R. H. and Vaid, Y. P. (1990). Corrections for membrane strength in the triaxial test. *ASTM Geotechnical Testing Journal*, 13(4):361–369.

Kumar, J. and Madhusudhan, B. (2010). A note on the measurement of travel times using bender and extender elements. *Soil Dynamics and Earthquake Engineering*, 30(7):630–634.

Kuwano, R., Connolly, T., and Jardine, R. (2000). Anisotropic stiffness measurements in a stress-path triaxial cell. *Geotechnical Testing Journal*, 23(2).

Kuwano, R. and Jardine, R. (2002a). On measuring creep behaviour in granular materials through triaxial testing. *Canadian Geotechnical Jounral*, 39:1061–1074.

Kuwano, R. and Jardine, R. (2002b). On the applicability of cross-anisotropic elasticity to granular materials at very small strains. *Géotechnique*, 52(10):727–749.

Laing, N. (1985). Sources and receivers with the seismic cone test. Master's thesis, University of British Columbia.

Lam, C. K. K. (2003). Effects of aging duration, stress ratio during aging and stress path on stress-strain behaviour of loose fraser river sand. Master's thesis, University of British Columbia.

Landon, M., DeGroot, D., and Jakubowski, J. (2004). Comparison of shear wave velocity measured in situ and on block samples of a marine clay. In *Proc. of the 57th Canadian Geotechnical Conference, Quebec.*

Lawrence Jr, F. V. (1965). Ultrasonic shear wave velocities in sand and clay. Technical report, DTIC Document.

Lee, C., Lee, J., Lee, W., and Cho, T. (2008). Experiment setup for shear wave and electrical resistance measurements in an oedometer. *ASTM Geotechnical Testing Journal*, 31(2):149–156.

Lee, J., Salgado, R., and Carraro, J. A. H. (2004). Stiffness degradation and shear strength of silty sands. *Canadian Geotechnical Journal*, 41(5):831–843.

Lee, J. and Santamarina, J. (2005). Bender elements: performance and signal interpretation. *Journal of Geotechnical and Geoenvironmental Engineering*, 131:1063.

Lee, J. and Santamarina, J. (2006). Discussion "Measuring Shear Wave Velocity Using Bender Elements" By Leong, EC, Yeo, SH, and Rahardjo, H. *ASTM Geotechnical Testing Journal*, 29(5):439.

Leong, E., Cahyadi, J., and Rahardjo, H. (2009). Measuring shear and compression wave velocities of soil using bender-extender elements. *Canadian Geotechnical Journal*, 46(7):792–812.

Leong, E., Yeo, S., and Rahardjo, H. (2005). Measuring shear wave velocity using bender elements. *Geotechnical Testing Journal*, 28(5):488–498.

Lunne, T., Robertson, P., and Powell, J. (1997). *Cone Penetrating Testing: In Geotechnical Practice*. Blackie Academic and Professional.

Marjanovic, J. and Germaine, J. T. (2013). Experimental study investigating the effects of setup conditions on bender element velocity results. *ASTM Geotechnical Testing Journal*, 36(2):187–197.

McGillivray, A. (2013). personal communication.

McGillivray, A. and Mayne, P. (2008). An automated seismic source for continuous-push shear wave velocity profiling with SCPT and SDMT. In *Geotechnical & Geophysical Site Characterization, ISC-3, Taipe*.

Mesri, G. and Vardhanabhuti, B. (2009). Compression of granular materials. *Canadian Geotechnical Journal*, 46(4):369–392.

Mitchell, J. K. (2008). Aging of sand - a continuing enigma? In *Sixth International Conference on Case Histories in Geotechnical Engineering and Symposium in Honor of Professor James K. Mitchell*. Missouri University of Science and Technology.

Mitchell, J. K. and Solymar, Z. V. (1984). Time-dependent strength gain in freshly deposited or densified sand. *Journal of Geotechnical Engineering*, 110(11):1559–1576.

Negussey, D. (1984). *An experimental study of the small strain response of sand*. PhD thesis, University of British Columbia.

Oztoprak, S. and Bolton, M. (2013). Stiffness of sands through a laboratory test database. *Géotechnique*, 63(1):54–70.

Petrakis, E. and Dobry, R. (1989). Micromechanical behavior and modelling of granular soil. Technical report, DTIC Document.

Rio, J. (2006). *Advances in laboratory geophysics using bender elements*. PhD thesis, University College London.

Robertson, P., Campanella, P., Gillespie, D., and Rice, A. (1986). Seismic CPT to measure in situ shear wave velocity. *Journal of Geotechnical Engineering*, 112:791.

Robertson, P., Fear, C., Woeller, D., and Weemees, I. (1995a). Estimation of sand compressibility from seismic cpt. In *48th Canadian Geotechnical Conference*.

Robertson, P., (Fear) Wride, C., List, B., Atukorala, U., Bigger, K., Byrne, P., Campanella, R., Cathro, D., Chan, D., Czajewski, K., Finn, W., Gu, W., Hammamji, Y., Hofmann, B., Howie, J., Hughes, J., Imrie, A., Konrad, J.-M., Kupper, A., Law, T., Lord, E., Monahan, P., Morgenstren, N., Phillips, R., Piche, R., Plewes, H., Scott, D., Sego, D., Sobkowicz, J., Stewart, R., Watts, B., Woeller, D., Youd, T., and Zavodni, Z. (2000). The CANLEX project: summary and conclusions. *Canadian Geotechnical Journal*, 37(3):563–591.

Robertson, P., Sasitharan, S., Cunning, J., and Sego, D. (1995b). Shear-wave velocity to evaluate in-situ state of ottawa sand. *Journal of Geotechnical Engineering*, 121(3):262–273.

Roesler, S. K. (1979). Anisotropic shear modulus due to stress anisotropy. *Journal of the Geotechnical Engineering Division*, 105(7):871–880.

Saada, A. and Townsend, F. (1981). State of the art: laboratory strength testing of soils. *Laboratory shear strength of soil, ASTM STP*, 740:7–77.

Sachse, W. and Pao, Y. (1978). On the determination of phase and group velocities of dispersive waves in solids. *Journal of Applied Physics*, 49(8):4320–4327.

Salgado, R., Bandini, P., and Karim, A. (2000). Shear strength and stiffness of silty sand. *Journal of Geotechnical and Geoenvironmental Engineering*, 126(5):451–462.

Sánchez-Salinero, I., Roesset, J., and Stokoe, K. (1986). *Analytical Studies of Body Wave Propagation and Attenuation; a Report on Research*

Sponsored by United States Air Force, Office of Scientific Research, Bolling Air Force Base. University of Texas, Geotechnical Engineering Center, Civil Engineering Dept.

Santamarina, J. and Cascante, G. (1996). Stress anisotropy and wave propagation: a micromechanical view. *Canadian Geotechnical Journal*, 33(5):770–782.

Santamarina, J. and Fam, M. (1997). Discussion: Interpretation of bender element tests. *Géotechnique*, 47(4):873–877.

Santamarina, J., Klein, K., and Fam, M. (2001). *Soils and Waves*. John Wiley, Hoboken, NJ.

Schmertmann, J. H. (1991). The mechanical aging of soils. *Journal of Geotechnical Engineering*, 117(9):1288–1330.

Schnaid, F. and Yu, H. (2007). Interpretation of the seismic cone test in granular soils. *Géotechnique*, 57(3):265–272.

Scholey, G. K., Frost, J. D., and Lo, P. (1995). A review of instrumentation for measuring small strains during triaxial testing of soil specimens. *ASTM Geotechnical Testing Journal*, 18(2):137–156.

Seed, H., Wong, R., Idriss, I., and Tokimatu, K. (1984). *Moduli and damping factors for dynamic analyses of cohesionless soils*. College of Engineering, University of California. Earthquake Engineering Research Center.

Seed, H. B., Wong, R. T., Idriss, I., and Tokimatsu, K. (1986). Moduli and damping factors for dynamic analyses of cohesionless soils. *Journal of Geotechnical Engineering*, 112(11):1016–1032.

Shirley, D. (1978). An improved shear wave transducer. *The Journal of the Acoustical Society of America*, 63:1643.

Shozen, T. (2001). Deformation under the constant stress state and its effect on stress-strain behaviour of fraser river sand. Master's thesis, University of British Columbia.

Slawinski, M. (2003). *Seismic waves and rays in elastic media*. Elsevier Science.

Somfai, E., Roux, J., Snoeijer, J., Van Hecke, M., and Van Saarloos, W. (2005). Elastic wave propagation in confined granular systems. *Physical Review E*, 72(2).

Stewart, W. and Campanella, R. (1993). Practical aspects of in situ measurements of material damping with the seismic cone penetration test. *Canadian Geotechnical Journal*, 30(2):211–219.

Styler, M. and Howie, J. (2013). A combined time and frequency domain approach to the interpretation of bender element tests. *ASTM Geotechnical Testing Journal*, 36(5).

Styler, M. and Howie, J. (2014). Continuous monitoring of bender element shear wave velocities during triaxial testing. *ASTM Geotechnical Testing Journal*, 37(2):218–229.

Styler, M., Howie, J., and Sharp, J. (2014). Perpetual source scptu: Signal stacking shear waves during continuous penetration. In *CPT́14 Las Vegas*.

Styler, M., Howie, J., and Woeller, D. (2012). Perpetual Source Seismic Piezocone Penetration Testing: A new method for down-hole shear wave velocity profiling. In *GeoManitoba, Winnipeg, Manitoba*. Canadian Geotechnical Conference.

Styler, M., Howie, J., and Woeller, D. (2013). Measuring down-hole shear waves from a vibrating perpetual source during Cone Penetration Testing. In *GeoMontreal, Montreal, Quebec*.

Thomann, T. G. and Hryciw, R. D. (1990). Laboratory measurement of small strain shear modulus under K_0 conditions. *Geotechnical Testing Journal*, 13(2):97–105.

Vaid, Y. (2009). personal communication.

Vaid, Y. P. and Negussey, D. (1984). A critical assessment of membrane penetration in the triaxial test. *Geotechnical Testing Journal*, 7(2):70–76.

Vaid, Y. P. and Negussey, D. (1988). Preparation of reconstituted sand specimens. *Advanced triaxial testing of soil and rock*, pages 405–417.

Velea, D., Shields, F., and Sabatier, J. (2000). Elastic wave velocities in partially saturated ottawa sand: experimental results and modeling. *Soil Science Society of America Journal*, 64(4):1226–1234.

Viana da Fonseca, A., Ferreira, C., and Fahey, M. (2009). A framework interpreting bender element tests, combining time-domain and frequency-domain methods. *Geotechnical Testing Journal*, 32(2):1.

Viggiani, G. and Atkinson, J. (1995). Interpretation of bender element tests. *Géotechnique*, 45:149.

Wang, Y., Lo, K., Yan, W., and Dong, X. (2007). Measurement biases in the bender element test. *Journal of Geotechnical and Geoenvironmental Engineering*, 133:564.

Wang, Y. and Mok, C. (2008). Mechanisms of small-strain shear-modulus anisotropy in soils. *Journal of Geotechnical and Geoenvironmental Engineering*, 134(10):1516–1530.

Wichtmann, T. and Triantafyllidis, T. (2013). Effect of uniformity coefficient on g/g max and damping ratio of uniform to well-graded quartz sands. *Journal of Geotechnical and Geoenvironmental Engineering*, 139(1):59–72.

Woods, R. (1994). Laboratory measurement of dynamic soil properties. *Dynamic Geotechnical Testing II: ASTM Special Technical Publication*, 1213:165–165.

Wride, C., Robertson, P., Biggar, K., Campanella, R., Hofmann, B., Hughes, J., Küpper, A., and Woeller, D. (2000). Interpretation of in situ test results from the canlex sites. *Canadian Geotechnical Journal*, 37(3):505–529.

Wroth, C. (1984). The interpretation of in situ soil tests. *Géotechnique*, 34(4):449–489.

Yamashita, S., Kawaguchi, T., Nakata, Y., Mikaml, T., Fujiwara, T., and Shibuya, S. (2009). Interpretation of international parallel test on the measurement of Gmax using bender elements. *Soils and Foundations*, 49(4):631–650.

Yimsiri, S. and Soga, K. (2000). Micromechanics-based stress-strain behaviour of soils at small strains. *Géotechnique*, 50(5):559–571.

Youn, J., Choo, Y., and Kim, D. (2008). Measurement of small-strain shear modulus gmax of dry and saturated sands by bender element, resonant column, and torsional shear tests. *Canadian Geotechnical Journal*, 45(10):1426–1438.

Yu, P. and Richart, F. (1984). Stress ratio effects on shear modulus of dry sands. *Journal of Geotechnical Engineering*, 110(3):331–345.

Appendix A

Triaxial apparatus preparation

The triaxial apparatus must be prepared prior to any testing program. This preparation includes cleaning, levelling, and saturating the apparatus. It includes calibrating the sensors, measuring the constants, and characterizing systematic errors between the sensors and the state of the specimen. The triaxial equipment needs to be maintained for reliable performance. The sensors should be re-calibrated each time the equipment is moved. The connections for each sensor into the signal conditioning and amplification box must be periodically checked, especially if a noisy signal is observed.

Fully saturated water pressure transducers are necessary for responsive and accurate volume measurements. The saturation of the system can be qualitatively checked very easily and quickly. This is accomplished by closing Valve 2 in Figure 3.3 and turning up the back pressure to around 300 kPa. Any bubbles in the system will compress and possibly dissolve into the pore fluid. Dissolved air in water increases the compressibility of the fluid. If the system is not saturated then a significant finite drop in the water level in the volumetric cylinders will occur. There are three primary reasons for a loss in saturation. First, due to testing specimens that are not fully saturated. Second, air will dissolve into the water at the water-air boundary in the cell pressure reservoir and differential pore water pressure volumetric

cylinders. This dissolved air will slowly dissipate through the water in the apparatus. Third, draining too much water out of the apparatus. This can occur when the specimen is dilating or if the system is accidentally opened to atmosphere with an applied back pressure. If the system is not saturated then the apparatus must be flushed with boiled(and cooled) de-aired water. A more difficult problem is finding and removing any air bubbles that may reside in the plumbing of the system. These are dislodged by cyclically draining and filling the system while opening and closing the valves.

The apparatus is designed so that leaks can be detected. This is accomplished by using the manual back pressure regulator to apply a pressure of at least 200 kPa to the system. Valve 11 in Figure 3.3 is then shut. If the pressure indicated by the pressure gage adjacent to Valve 11 drops then there is a leak in the system. Leaks may be detected by spraying a soapy-water solution onto the pressurized apparatus at potential leak locations.

A.1 Sensor calibrations

The triaxial sensors were calibrated using the triaxial data acquisition system. Calibrating the the sensors using the triaxial data acquisition system captures the measurement uncertainty due to the peripheral electronics and signal conditioning in the uncertainty of the calibration factor. The sensors were calibrated with points spread through-out the expected measurement range. This prevents the calibration factor from being biased to a small portion of the curve. The sensors were calibrated over a loading and unloading loop to capture any hysteresis. Each calibration was based on at least 12 data points. The uncertainty in the calibration factor decreases with diminishing returns for each additional calibration point.

Calibration points are obtained with measurements against a standard. The standard for the load call calibration was a set of dead weights. These weights were applied to the load cell using a hanging loading frame. The load cell was detached from the apparatus and placed on the corner of a table. The loading frame was balanced on top of the load cell and dead weights were added. THe upper range of the load cell calibration could not

be tested with this approach. The potential danger of knocking over this hanging apparatus must be acknowledged prior to calibrating.

The LVDT was calibrated using an accurate screw controlled plunger device. The LVDT was locked into this device and a screw controlled plunger displaced the LVDT arm. The full range of the LVDT arm position was measured. The calibration factor only applies over the linear portion of the LVDT response. Calibration data points outside this linear range were discarded from the calibration. Triaxial testing is only performed over the linear range of the LVDT.

The water pressure transducers were calibrated using a digital pressure indicator (DPI). This device was not directly attached to the pressure transducer swage connections. The DPI pressurizes air, while the pore pressure sensors measure water pressure. A small reservoir was used to transfer the air pressure to water pressure.

The differential pore water pressure transducer(DPWPT) was calibrated using a pipette to measure volume. The pipette used was one of the two volumetric cylinders in the apparatus. First an initial reading is taken with both cylinders open. Second, the large cylinder is shut and a measured volume of water is added to or removed from the pipette. Third, both cylinders and opened and permitted to equalize prior to taking the final reading.

The DPWPT must also be calibrated for elevation head in order for the subsequent calibration of the expanded membrane diameter. This was done using the graduated measurement tape attached to one of the volumetric cylinders.

The calibration factors are detailed in Table 3.4. The conditional standard deviations are included in Table 3.4. These values represent the standard deviation of the measurement for a given voltage. For example, with the LVDT this is the standard deviation of the change in height conditional on the measured LVDT voltage. Equation A.1 calculates the conditional standard deviation where n is the sample size in the calibration, σ_y is the standard deviation of the calibration standard displacements, and r_{xy}^2 is the squared correlation coefficient for the calibration. The conditional standard

deviation for the LVDT sensor is 0.00386 mm. The DPWPT calibration was performed twice and the results are combined in DPWPT*.

$$\sigma(units|volts) = \sqrt{\frac{n-1}{n-2}\sigma_y(1-r_{xy}^2)} \tag{A.1}$$

A.2 Apparatus constants

Reducing the sensor measurements to the properties of the specimen require the measurement of apparatus constants. The height of the specimen during specimen preparation is measured using a dial gage. This dial gage has a range of 20 mm, while the initial specimen height is between 125 and 132mm. To calculate the height of the specimen, the dial gage measurements are corrected with respect to a datum specimen height. This datum specimen is a solid metal cylinder with recesses to accommodate the bender elements. The height of this datum specimen was measured 12 times with a micrometer. It has a mean height of 127.0775 mm $\pm$ 0.00827 mm.

An effective stress is applied to the soil specimen during specimen preparation. This effective stress is sufficient for the specimen to be self-supporting while the triaxial chamber is constructed. The effective stress is added to the specimen by applying an 18 kPa vacuum pressure to the pore water. This change in effective stress from 0 to 18 kPa induces a volumetric deformation of the soil skeleton. To calculate the initial volume of the specimen, this volumetric change needs to be measured. The DPWPT cylinders can not be used for this step. A vacuum pressure should not be applied to the pore water pressure transducer. Therefore, another graduated bored cylinder was calibrated. This bored cylinder collects the volume of water ejected from the specimen voids during specimen preparation.

This bored glass cylinder is not a pipette. The gradations attached to the outside of this cylinder are a measuring tape. The calibration is then the volume of water per gradation, where each gradation corresponds to a centimetre in elevation head. This graduated cylinder was calibrated using the DPWPT volumetric calibration. The bored glass cylinders that measure changes in the specimen volume (see Figure 3.3) were filled with

de-aired water. They were then connected to the specimen preparation glass cylinder through a saturated swage tube. The water in the DPWPT volumetric cylinders were at a higher elevation head so that when the valve is opened water would flow into the specimen preparation cylinder. Small volumes of water were transferred and the gradations and DPWPT voltages were recorded. A total of 41 points were collected during four cycles of transferring water between the glass cylinders. The specimen preparation glass cylinder has a calibration factor of -0.487 $cm^3/grad$ with a conditional standard deviation of $\pm$ 0.012 cm^3. This standard deviation is conditional on the person performing the measurement, as the reading of the gradation for the meniscus of the water may be slightly subjective.

The calibrated volumetric cylinder measures the change in volume during specimen preparation. To calculate the specimen volume, the initial volume must be determined. The specimen is prepared within a membrane that is held open using a membrane expander. The initial specimen volume is calculated from the internal diameter of the expanded membrane and the initial specimen height measured during specimen preparation. The specimen volume and void ratio are very sensitive to the expanded membrane internal diameter.

An accurate measure of the average internal diameter of the expanded membrane is required. The DPWPT can be used to measure both the height of water and the volume of water. These two measures can be used to calculate the average internal diameter of the expanded membrane. Figure A.1 depicts the apparatus set up required and details the procedure to measure the internal diameter using the DPWPT. This resulted in an internal expanded membrane diameter of 63.877$\pm$0.046 mm.

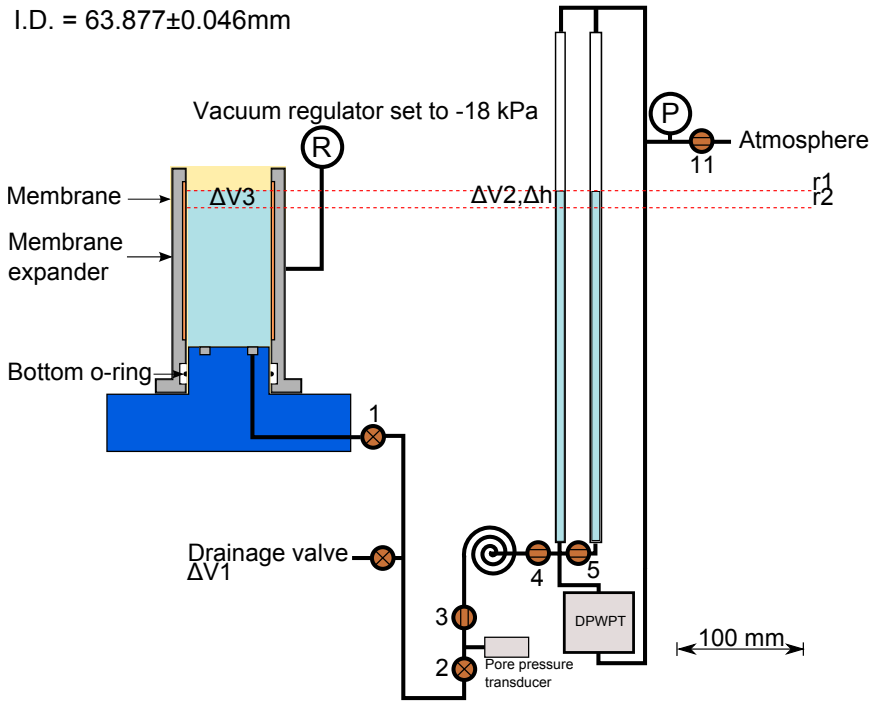

1. Open line (Valves 1 and 2) between expanded membrane and DWPWT and wait for elevation head to equalize
2. Record DPWPT voltage (r1)
3. Close the DPWPT Valve 2
4. Open drainage valve and drain a large volume of water (30-50mL) out of the expanded cavity
5. Close drainage valve
6. Record the weight of the discharged water and calculate the volume, ΔV1
7. Open DPWPT Valve 2 and wait for the elevation head to equalize
8. Record DPWPT voltage (r2)
9. Calculate volume of water drained out of the DPWPT cylinders from r1 and r2, ΔV2
10. Calculate the change in water height in the expanded membrane from r1 and r2, ΔH1
11. Calculate the change in water volume within the expanded membrane, ΔV3=ΔV1 - ΔV2
12. Calculate the average internal diameter of the expanded membrane from ΔV3 and ΔH1
13. Repeat until expanded membrane is drained

Figure A.1: Apparatus configuration to measure average internal expanded membrane diameter

A.3 Systematic error corrections

Systematic errors between the external sensor measurements and stress and deformation of the soil specimen need to be corrected. These include corrections for the axial stress from the ram friction, uplift, elastic membrane, and dead weight; for the radial stress from the elastic membrane, and for the volumetric strain from the membrane penetration into the specimen surface.

The measured axial stress at the centre of the specimen includes the effective weight of half of the soil, the weight of the top cap, downwards pressure on the top cap due to the chamber pressure minus the upwards pressure due to the pore water pressure, the measured applied load from the load cell minus any friction along the driving rod, and an applied load from the deformed elastic membrane. The weight of the top cap was measured using the laboratory scale and equals 0.4683 kg. The downward pressure on the top cap due to the chamber pressure acts on an area equal the cross sectional area of the specimen minus the cross sectional area of the driving rod attached to the top cap. The cross section area of the driving rod was measured 12 times with a micrometer and the mean diameter is 9.645 mm $\pm$ 0.0164 mm. This is the error in the estimate of the mean height based on an unbiased measurement. It is not the measurement error. The pore water pressure acting upwards applies over the cross section area of the specimen. The ram friction and elastic membrane corrections are not as simple.

The ram friction must be overcome by the driving rod to apply a load to the specimen. The ram friction can be measured in a pressurized triaxial chamber without a soil specimen. The triaxial chamber is placed in the triaxial apparatus, filled with water, and the chamber pressure lines are attached. The chamber was pressurized to 300 kPa, this is a typical pressure during a triaxial test, activates the friction reducer, and applies an uplift force. This uplift force is the chamber pressure times the cross section area of the driving rod, it will overcome the buoyant weight of the top cap. This will apply a load to the load cell. The constant strain stepper motor is used to slowly cycle the top cap upwards and downwards while recording the measured load cell readings. When the top cap is being driven downwards

the load cell is measuring the friction plus the uplift minus the top cap weight ($L_{down} = F+U-W$). When the top cap is being pulled upwards the load cell is measuring the uplift minus the friction minus the top cap weight ($L_{up} = -F+U-W$). The driving rod friction can be found by the difference in these two measurements, $L_{down}-L_{up} = (F+U-W)-(-F+U-W) = 2F$. Figure A.2 presents the measurements for this correction. The ram friction equals -0.0624 kg. Typical magnitudes for this correction are from -0.18 to -0.21 kPa for the axial stress. The negative sign means that the measurement by the load cell needs to be reduced, not that the rod friction is negative.

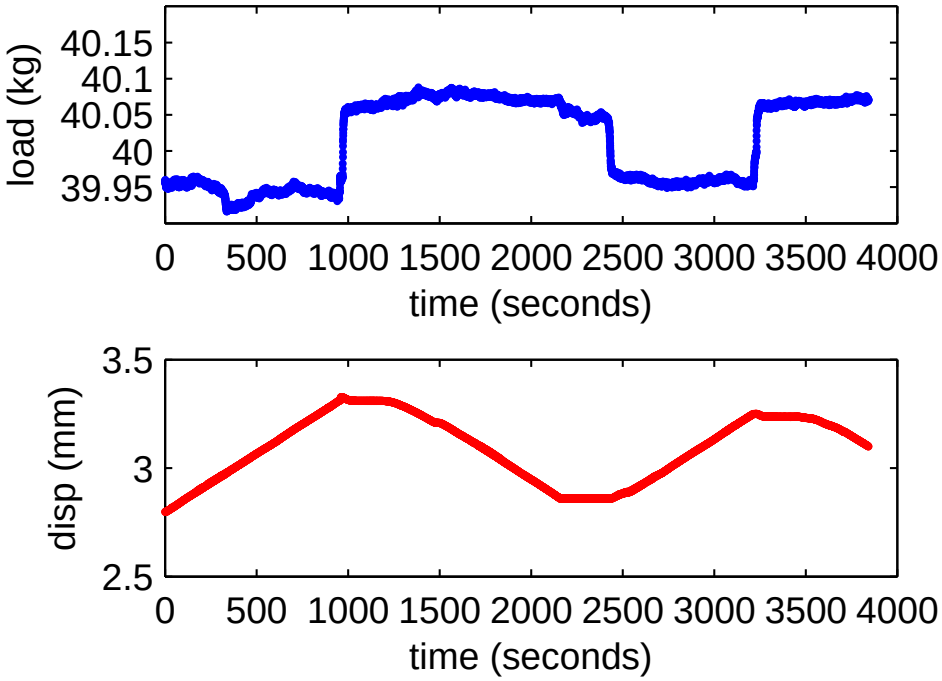

Figure A.2: Measuring the rod friction of -0.0624 kg

The triaxial specimen is enclosed in an elastic membrane. This elastic membrane is deformed from its unstretched state and will contribute to the axial and radial stresses experienced by the soil skeleton. The membrane is initially stretched over the membrane expander. Once it is snapped on to

the specimen it is already deformed and contributing to the axial and radial stress. The procedure for measuring the elastic properties of the membrane was presented by Bishop and Henkel (1957). The interpretation of these measurements was corrected by Kuerbis and Vaid (1990). The elastic properties for the membrane are determined by measuring the deformation to an applied stretching force. Two rods are inserted through the membrane. One rod is hung from a fixed point. A loading frame is attached to the other rod. Dead weight is added to the loading frame and the deformation of the membrane is measured. This membrane has an unstretched outer diameter of 61 mm and a wall thickness of 0.3 mm. The Young's modulus is 976 kPa. The contributions the membrane makes to the axial and radial stresses of the specimen are calculating from elastic shell theory. The equations for this correction are presented in Appendix C. Typical magnitudes for this correction are 0.17 kPa for the axial stress and 0.34 kPa for the radial stress.

The elastic membrane also affects the volumetric measurements. The elastic membrane will penetrate into the voids over the surface of the soil specimen. This penetration will increase with increasing radial effective stress. This penetration will result in an ejection of water from the specimen that does not correspond to a change in the volume of the void space. This ejected water will be measured by the DPWPT.

This effect has been quantified by comparing the volume change of multiple specimens under hydrostatic loading. Each of these specimens had a brass rod of varying diameter along the specimen axis. This results in a set of specimens with the same surface area, but different soil volumes. Vaid and Negussey (1984) disagreed with this approach, the inclusion of brass rods would influence the the developed volumetric strains in the soil. Vaid and Negussey (1984) assumed that soil behaved isotropically under hydrostatic unloading. They calculated the membrane penetration volume as the difference between the measured volume change during hydrostatic unloading and the isotropic volume change calculated from the axial strain. Alternatively, Bohac and Feda (1992) calculated the membrane penetration volume during K_0 consolidation by comparing the measured value to the calculated value assuming the radial strain was 0. Baldi and Nova (1984) presented an

equation resulting from an idealized analysis in terms of the diameter of the particles, the membrane properties, and the effective radial stress.

The hydrostatic unloading method presented by Vaid and Negussey (1984) was used to calculate the unit membrane penetration coefficient. Figure A.3 depicts one of the fifteen hydrostatic unloading loops used to calculate the membrane penetration coefficient. The value obtained 0.000326 is less than the value of 0.0021 used by Shozen (2001). Figure A.4 presents the unit membrane penetration volume against the logarithm of effective stress. For Fraser River Sand under a change in effective confining stress of 100 kPa, the measured unit penetration by the Vaid and Negussey (1984) method is 0.00065 cm^3 per square centimetre of specimen surface area. The Baldi and Nova (1984) simple analytical approach results in a comparable 0.0010 cm^3 per square centimetre of specimen surface area. Typical magnitudes for this correction are 0.18 cm^3, or 0.05 % volumetric strain.

Table A.1 details the measured constants for the UBC Triaxial testing of Fraser River Sand. This table includes standard deviation of the mean. The mean value is estimated from the set of measurements, it is not a constant. If an additional measurement was taken, then the mean value would change. The datum specimen was measured 12 times to result in a mean height of 127.0775 mm with a standard deviation of the mean of 0.00827 mm. This is the standard deviation of the mean value for the datum specimen height, it is not the standard deviation of the 12 measurements. The standard deviation of a mean for a normal distribution is calculated as the standard deviation of the sample size divided by the square root of the number of samples.

Table A.1 summarizes constants used in the reduction of the triaxial data. The n column is the number of measurements performed. These values are expected to be constants - to have a standard deviation of 0 if measured perfectly. Therefore, the standard deviation of the n measured samples is a result of the measurement procedure - not the measurand. The mean value of these n measurements is taken as the most likely point estimate for the constant. The standard deviation of the mean value is $s/\sqrt{n}$, where s is the standard deviation of n measurements.

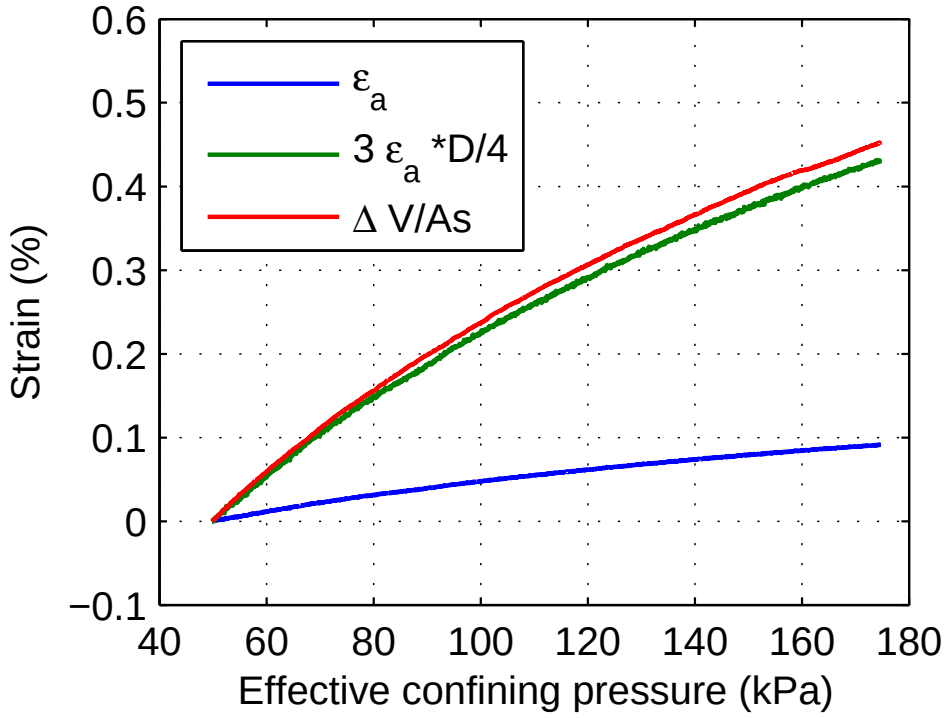

Figure A.3: Measured and calculated volumetric strains during hydrostatic unloading

Table A.1: Constants

Measurand	n	mean	stdev ($s/sqrt(n)$)
Datum specimen height	12	127.0775 mm	0.00827 mm
Driving rod diameter	12	9.645 mm	0.0164 mm
Top cap weight		0.4683	
Expanded membrane ID	6	63.8772 mm	0.0456
Unstretched membrane OD		61 mm	
Unstretched membrane thickness		0.3 mm	
Membrane Young's modulus		976 kPa	
Unit membrane penetration (cm^3/cm^2 per $\log(\sigma'_r$ kPa))	15	0.000326	0.000017
Ram friction		-0.0624 kg	

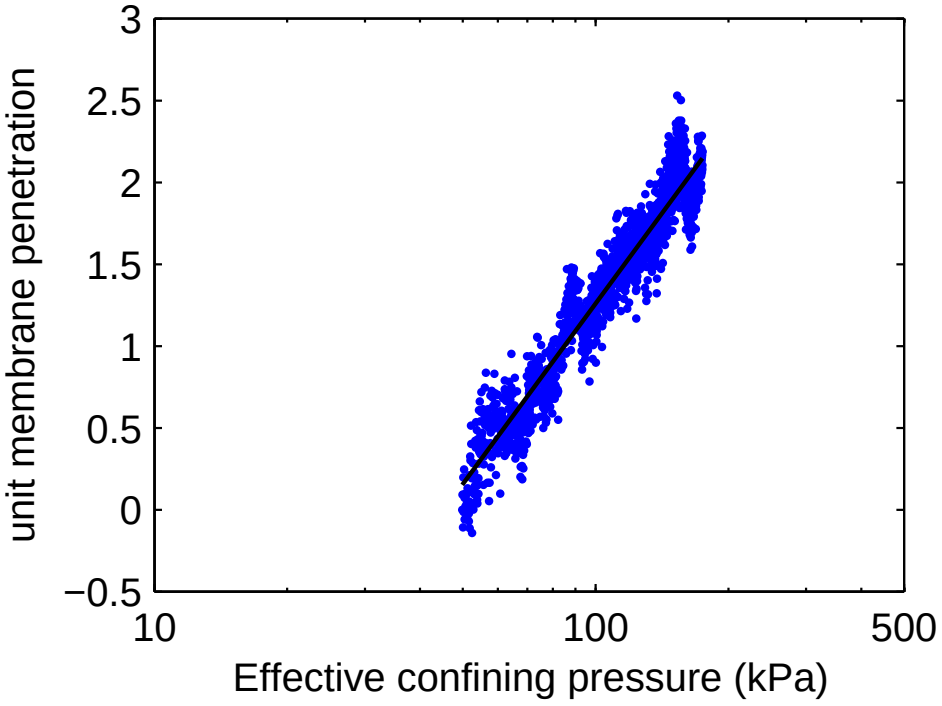

Figure A.4: Measured unit membrane penetration against effective confining pressure

Appendix B

Triaxial testing procedure

B.1 Sample preparation

Maintaining a fully saturated triaxial apparatus requires testing only saturated triaxial specimens. The procedure for testing fully saturated specimens begins with sample preparation. Each tested specimen is reconstituted from a prepared sample of Fraser River Sand. The particles larger than 2.362 mm are removed by dry sieving and particles finer than 75 μm are washed out by wet sieving. The Fraser River sand retained on the 75 μm sieve is oven dried then air cooled. This forms a bulk sample that is used to make multiple individual samples. De-aired water is added to individual samples of 590 to 600 grams of dry Fraser River Sand in pycnometer flasks. These samples are boiled for at least 30 minutes then stored under a vacuum. During periods when the vacuum source was broken the samples were re-boiled the day before testing and then sealed with a rubber stopper while still cooling. Prior to using a sample to reconstitute a specimen the sample flask is tilted approximately 30 degrees and rolled rapidly about its axis in an attempt to free any air bubbles. If no air bubbles are observed then the sample is used to create a specimen.

B.2 Specimen reconstitution procedure

There are a few preliminary steps prior to water pluviation of the sand specimen. The triaxial membranes do not arrive ready to use. They need to be marked in order to measure membrane deformations during specimen preparation. This is accomplished by inserting a piece of graph paper into the membrane cavity and tracing the lines with a ball point pen. Another preliminary step is to get a dial gauge reading of the datum specimen placed on to the base pedestal. This datum specimen has a known height (Table A.1). The difference between the datum specimen dial reading and the dial reading on the actual specimen can then be used to calculate the specimen height.

The water pluviation procedure described by Vaid and Negussey (1988) is used to create saturated triaxial specimens. Figure B.1 through Figure B.3 depict the creation of a specimen using water pluviation. These three figures highlight the main steps in the specimen preparation procedure.

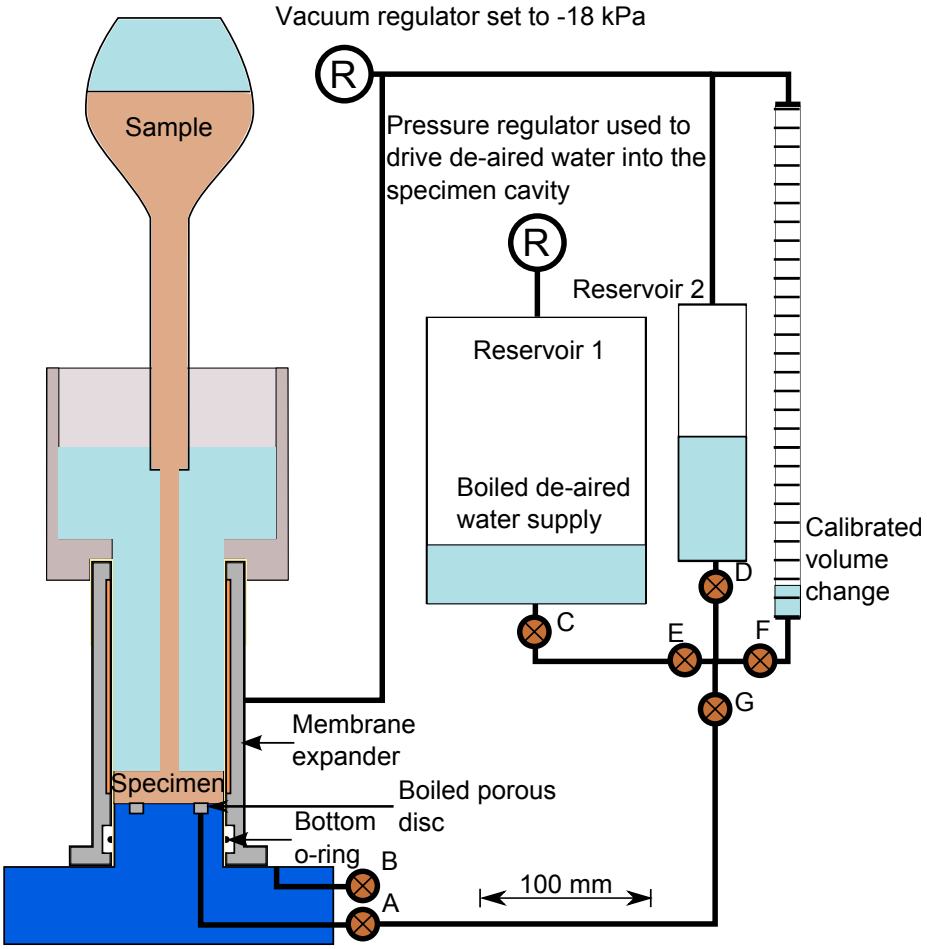

1. Jet de-aired water through base pedestal to dislodge bubbles (open C E G A)
2. Place membrane onto base pedestal, partly fill with de-aired water
3. Remove any air trapped between membrane and base pedestal
4. Place bottom o-ring
5. Attached membrane expander, stretch membrane over the lip
6. Apply 15-20 kPa vacuum to membrane expander
7. Place siphon chamber and fill cavity with de-aired water
8. Place boiled porous disc into the specimen cavity at at angle, drop into place
9. Fill sample flask with de-aired water
10. Block end of sample flask, invert, place end into specimen cavity
11. Wait for specimen deposition

Figure B.1: Specimen pluviation

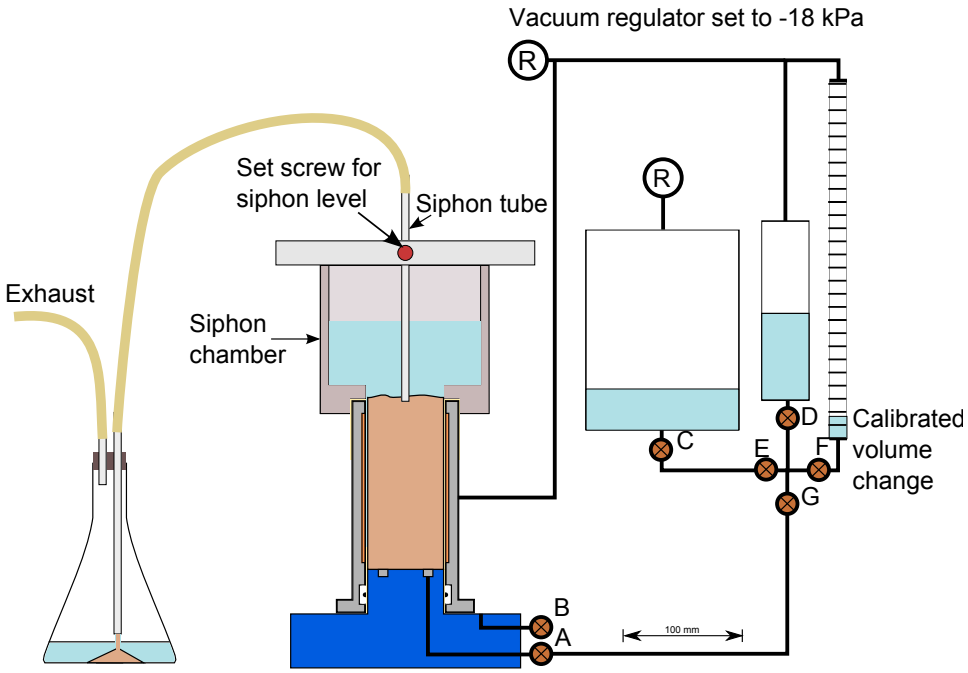

1. Place siphon tube end under the water in the siphon chamber
2. Attach a compressed red rubber ball hand pump on the exhaust
3. Release the hand pump to create a slight vaccum in the flask
4. Once the siphon is running remove the hand pump
5. Level the specimen top surface by moving the siphon
6. The specimen top surface should be 3-5mm below the membrane expander
7. The water level should be siphoned until it is just above the specimen
8. Remove the siphon chamber

Figure B.2: Specimen siphon

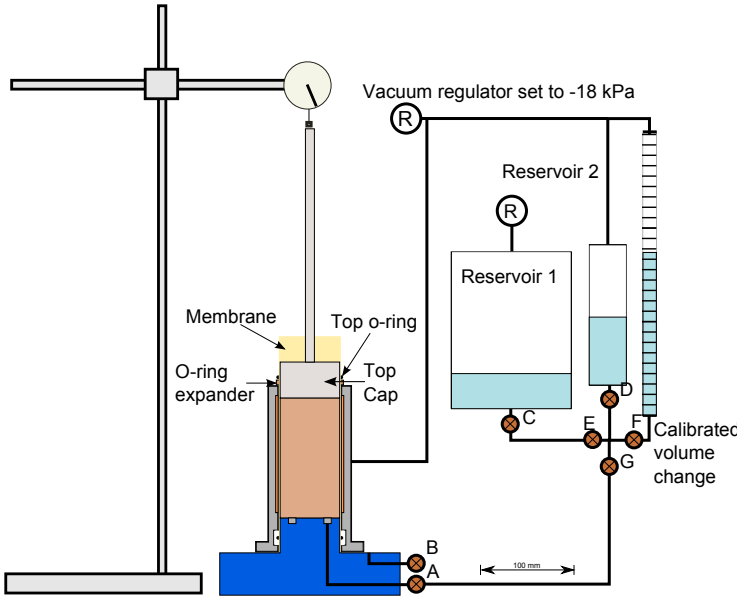

1. Place top o-rin expander onto membrane expander
2. Open Reservoir 2 to atmosphere and valves A,D,G
3. Brake the specimen surface water with the top cap at an angle
4. Place the top cap
5. Roll up the membrane off of the membrane expander
6. Level the top cap
7. Snap the top o-ring off of the o-ring expander
8. Level the top cap
9. Close valve D, attach graduated cylinder (GC) to 15-20 kPa vacuum
10. Record inital dial gauge reading and GC water level
11. Open valve F to apply a vacuum to the specimen pore water
12. Record dial gauge and GC
13. Remove membrane expander
14. Record dial gauge and GC
15. Measure axial membrane strain using a micrometer
16. Construct triaxial chamber and fill with water - the chamber must be vented to fill without pressuring
17. Measure final dial gauge reading
18. Add supply pressure to E/P regulators
19. Float the load cell by adding a downward load on the DAS and an upward load from the manual regulator
20. Place the triaxial chamber in the apparatus
21. Adjust the LVDT to have maximum linear range
22. Measure final GC reading
23. Shut valve A
24. Attach PWP and Chamber pressure lines
25. Apply a chamber pressure to 20 kPa
26. Open PWP transudcer to the specimen - record first PWP, it should be between 1 and 5 kPa

Figure B.3: Specimen preparation

B.3 Triaxial testing procedure

Once the specimen is in the apparatus the experiment proceeds in four sequential phases: back pressure saturation, consolidation, ageing, and shear.

Back pressure saturation serves two purposes: it provides an indication of the specimen saturation and it increases the saturation of the specimen. Back pressure saturation is performed by increasing the chamber pressure while drainage is closed. The increasing back pressure causes any air in the specimen or equipment to dissolve, which increases the saturation. B-values can be calculated during back pressure saturation steps of increasing hydrostatic pressure. If the deviator stress changes during back-pressure saturation then the change in the pore water pressure is due to both Skempton's A and B parameters. Increasing the hydrostatic pressure requires precise computer control of the axial load to maintain a σ_1/σ_3 ratio of 1.0. B-Values are calculated by increasing the hydrostatic pressure by 20 kPa, waiting two minutes, and measuring the resulting increase in pore water pressure. The B-Value is the ratio of the increase in pore pressure to the increase in hydrostatic pressure. In an incompressible specimen saturated with an incompressible fluid, the B-Value equals 1.0. An acceptable initial B-Value is in excess of 0.95 (Vaid, 2009). If the initial B-value is too low then the specimen will undergo unmeasured volumetric strains during back pressure saturation. This volumetric strain is a result of the compression of residual air in the pores of the specimen and the increased compressibility of aerated water. B-values in excess of 1.0 are indicative of a leaking membrane. Very low B-values can be measured due to a leak to atmosphere pressure at the bender element in the top cap or along the pore water pressure drainage line.

Back pressure saturation was performed until the pore water pressure exceeds 200 kPa. At this point Valve 2 is closed and Valve 3 is opened (see Figure 3.3). The back pressure regulator is adjusted to match the final pore water pressure measurement. Valve 2 is then opened. The specimen should not experience any volumetric strain when drainage is open. At this point the specimen is open to drainage and should have an effective stress

of approximately 20 kPa for both σ_1' and σ_3'. The bender element wires are then connected and tested prior to the start of consolidation.

Consolidation occurs in two sequential stages. First the axial stress is increased until the desired stress ratio is achieved. Then the computer controlled data acquisition system increases both the axial and radial stresses, maintaining the stress ratio, until the desired stress state is achieved. Consolidation is temporarily paused when discrete bender element testing is performed.

The age phase maintains the specimen boundary conditions for a specified amount of time. There are two ways to maintain the boundary conditions. One is to maintain the loads, the other is to maintain the stresses. The specimen experiences volumetric and axial creep strains during ageing. These strains change the cross sectional area of the specimen, resulting in a decreasing axial stress. This can be compensated for with small increases in the axial load. It is very challenging to maintain a stable ageing environment with a feedback control adjusting the loads on the specimen. Consequently, the second approach was adopted and the loads were maintained during ageing.

The shear phase loads the specimen to failure along a specified shear path. The equipment is capable of shearing along three different shear paths: conventional, constant p, and slope 0. The conventional shear path increases the axial load until the specimen fails. The constant p shear path maintains the mean stress ($\frac{\sigma_1+2\sigma_3}{3}$) while the deviator stress ($\sigma_1 - \sigma_3$) is increased. This requires increasing the axial load and decreasing the radial load simultaneously to maintain the mean stress. This was accomplished in a feedback loop that estimated the succeeding axial stress and adjusted the chamber pressure accordingly. The slope 0 shear path maintains a constant axial stress while the radial stress is decreased. The axial stress is a combination of the axial load and the cell pressure. As the computer controlled cell pressure is decreased, the axial load must be increased in order to maintain a constant axial stress.

The cell pressure is not adjusted during conventional shear paths. The axial load is increased until the specimen fails. The voltage to the chamber

pressure regulator is kept constant. As the specimen experiences volumetric changes the differential pore water pressure volumetric cylinders change in water elevation head. These changes are noticeable in the measured pore pressure during conventional shear paths. It is possible to compensate for these changes using the computer controlled cell pressure, but this approach was not taken in order to match conventional triaxial tests.

The equipment limits the extent of the shear phase. The differential pore water pressure transducer can only handle pore water volume changes that fit in the cylindrical tubes. The test must be stopped if the specimen contracts or dilates beyond this range. There is also an upper limit on the load cell and on the LVDTs. The LVDTs have a linear range that once exceeded the interpreted specimen heights are incorrect. The shear phase ends when the specimen fails or the equipment limitations are met.

Appendix C

Triaxial data reduction

The initial specimen height is calculated with Equation C.1, where d_f is the final dial reading, d_d is the datum dial reading, and $datum$ is the height of the datum specimen (see Table A.1).

$$h_0 = d_f - d_d + datum \tag{C.1}$$

Equation C.2 is for the height of the unstretched membrane covering the surface area of the specimen. It is calculated from $d_3 - d_d + datum$, the height of the specimen after the membrane expander has been removed, and ε_{ma}, the measured membrane axial strain. The measured membrane axial strain is based on the distortion of markings drawn onto the membrane.

$$h_{m0} = (d_3 - d_d + datum) * (1 + \varepsilon_{ma}) \tag{C.2}$$

The initial specimen volume is calculated with Equation C.3. In this equation Δv is the measured change in volume using the calibrated glass cylinder (see Table 3.4). This change in volume is taken off of the volume calculated with the expanded membrane diameter v_X (see Table A.1). The volume of the specimen when it is within the expanded membrane is based on the diameter of the expanded membrane and the height of the specimen h_X when it is in the expanded membrane. The height of the specimen within the membrane expander is found with the first dial reading and datum dial.

$$
\begin{aligned}
h_X &= d_i - d_d + datum \\
v_X &= \pi r^2 * h_X \\
\Delta V &= gc_i - gc_f \\
v_0 &= \Delta v + v_X
\end{aligned} \tag{C.3}
$$

The initial void ratio of the specimen is calculated with Equation C.4, where G is the specific gravity of the material, ρ_w is the density of water in g/cm^3, v_0 is the total volume in cm^3, and m_d is the dry mass in grams. This equation assumes that the specimen is fully saturated.

$$
e_0 = \frac{G_S * \rho_w * v_0}{m_d} - 1 \tag{C.4}
$$

The height of the specimen during the test is calculated with Equation C.5. The height is the initial height plus the change in height measured with the LVDT sensor. The change in height is calculated form the LVDT calibration factor (see Table 3.4) and $\Delta volts$, which is the change in volts from the zero to current reading. The pore water pressure, chamber pressure, load cell, and measured change in volume are all calculated with similar equations.

$$
h = h_0 + C_{lvdt} * (\Delta volts) \tag{C.5}
$$

The volume of the specimen is calculated with Equation C.6, where v_m is the membrane penetration volume. As the membrane penetrates into the specimen due to the confining pressure it causes water to be drained from the specimen without a corresponding volume loss of the soil skeleton. This systematic error must be corrected to calculate the volume of the soil skeleton.

$$
v = v_0 + C_{dpwpt} * (\Delta volts) - v_m \tag{C.6}
$$

Equation C.7 is used to calculate the membrane penetration volume. The membrane penetration constant, m_p, depends on the membrane and soil particles, and is in Table A.1. The circumferential surface area of the

specimen is $\pi * d * h$, where d is the diameter of the specimen.

$$v_m = m_p * (\pi * d * h) * log_{10}(cell - pwp) \tag{C.7}$$

Equation C.8 is for the diameter of the specimen. Note that a dependency-circle has been created, the diameter equation(Equation C.8) requires the specimen volume (Equation C.6) and the specimen volume equation requires the diameter(through the membrane penetration Equation C.7). The solution taken to this problem was to use the previous time steps membrane penetration value to estimate the volume and diameter - then calculate the volume and membrane penetration with these estimates. This solution also assumes that there is no membrane penetration in the first time step - when the confining pressures are low.

$$d = 2\sqrt{\frac{v}{h\pi}} \tag{C.8}$$

Equation C.9 is the axial strain in the membrane at any point during the test based on the specimen height (Equation C.5) and initial membrane height (Equation C.2).

$$\varepsilon_{ma} = \frac{(h_{m0} - h)}{h_{m0}} \tag{C.9}$$

Equation C.10 is the radial strain experienced by the membrane, where d_m is the unstretched membrane diameter (see Table A.1).

$$\varepsilon_{mr} = \frac{d_m - d}{d_m} \tag{C.10}$$

Equation C.11 is the volumetric strain of the membrane cavity.

$$\varepsilon_{mv} = \varepsilon_{ma} + 2 * \varepsilon_{mr} \tag{C.11}$$

Equation C.12 is the radial stress contribution on the specimen due to the deformed elastic membrane, where E_m is the Young's modulus of the membrane and t_m is the thickness of the membrane shell (see Table A.1). Equation C.13 is the axial stress contribution on the specimen due to the

deformed elastic membrane.

$$\sigma_{mr} = \frac{-4E_m t_m (2 + \varepsilon_{mv} + \varepsilon_{ma})\varepsilon_{mv}}{3d_m(2 - \varepsilon_{mv}) + \varepsilon_{ma}} \tag{C.12}$$

$$\sigma_{ma} = \frac{-4E_m t_m (2 + \varepsilon_{mv} + \varepsilon_{ma})(3\varepsilon_{ma} + epsilon_{mv})}{3d_m(2 - \varepsilon_{mv}) + \varepsilon_{ma}} \tag{C.13}$$

Equation C.14 is the effective radial stress acting on the specimen. The stresses in this equation are all acting on the cylindrical surface area of the specimen.

$$\sigma'_r = cell - pwp + \sigma_{mr} \tag{C.14}$$

Equation C.15 is the cross sectional area of the specimen.

$$a_c = \pi \left(\frac{d}{2}\right)^2 \tag{C.15}$$

Equation C.16 is the downward axial pressure applied by the combination of chamber pressure downwards on the top cap and pore water pressure upwards. The chamber pressure exerts over an area of $(a_c - a_r)$ where a_c is the cross section area from Equation C.15 and a_r is the area of the driving rod (see Table A.1).

$$\sigma_c = \frac{cell(a_c - a_r) - pwp(a_c)}{a_c} \tag{C.16}$$

Equation C.17 is the effective axial stress on the specimen, where the load cell, mass, ram friction, and dry weight are all in kilograms. When multiplied by gravity ($9.81\ m/s^2$) the result is newtons, which are then divided by 1000 to get kilo-newtons.

$$\sigma'_a = \frac{(loadCell + 0.5w_d + capMass + ramFriction) * \frac{9.81}{1000} + a_c\sigma_{ma} + a_c\sigma_c}{a_c} \tag{C.17}$$

Equation C.18 through Equation C.21 calculate the axial strain, volumetric strain, radial strain, and shear strain from reference height h_r and volume v_r in percent. The reference height and volume may be taken as the

initial specimen properties or from the start of a phase of testing (consolidation, age, shear).

$$\varepsilon_a = \frac{h_r - h}{h_r} * 100 \tag{C.18}$$

$$\varepsilon_v = \frac{v_r - v}{v_r} * 100 \tag{C.19}$$

$$\varepsilon_r = \frac{\varepsilon_v - \varepsilon_a}{2} \tag{C.20}$$

$$\varepsilon_q = \frac{2}{3}(\varepsilon_a - \varepsilon_r) \tag{C.21}$$

Equations C.22 and C.23 are the deviator stress and mean stress.

$$q = \sigma'_a - \sigma'_r \tag{C.22}$$

$$p' = \frac{\sigma'_a + 2\sigma'_r}{3} \tag{C.23}$$

Equation C.24 calculates the secant shear modulus. In this equation ε_q is divided by 100 if it is in percent. Note that the units of G_{sec} will be the same units as q, so it is often divided by 1000 to get MPa.

$$G_{sec} = \frac{\Delta q}{3\varepsilon_q/100} \tag{C.24}$$

Appendix D

Triaxial Results

This appendix contains results from this investigation as well as Shozen (2001) and Lam (2003). The past results from Shozen (2001) and Lam (2003) were complemented with the empirical G_0 equation in order to build a larger empirical dataset for drawing conclusions on the shape of the G_{sec}/G_0 normalized stiffness curves.

D.1 Results from this study

D.1.1 Summarized creep strains

A certain amount of creep strain will occur with out without increasing the shear stress. When the shear phase occurs after short age durations, the magnitude of the continued creep strains are comparable to the observable small-strain measurements. Uncorrected, this will decrease the measured G_{sec} over small strains and make it difficult to compare the stiffness between different age durations. This effect can be corrected by projecting the developed creep strains during ageing through the shear phase. These projected creep deformations are subtracted from the axial and volumetric displacements prior to calculating ϵ_q and G_{sec}. For specimens that have undergone over 100 minutes of ageing, this correction becomes negligible (Lam, 2003; Shozen, 2001).

To correct for continued creep strains after short age durations, the creep strain rates need to be characterized. After consolidation the applied axial load and chamber pressure are kept constant for an age phase of up to 1000 minutes. Creep strains occur during this phase - a continued deformation of the specimen without a significant change in the imposed effective stress state. During ageing, the data acquisition system maintains constant axial load and chamber pressure to avoid instability. The imposed boundary condition constants are maintained by applying a constant voltage to the two electronic pressure regulators. Soil creep will change the dimensions of the soil specimen. Creep strains that result in radial contraction or extension change the cross-section area of the specimen. This changes the calculated stress for a constant axial load. Contractive volumetric strains will increase the water head measured with the DPWPT sensor. This slightly increases the back pressure, and therefore reduces both the radial and axial effective stress.

Despite efforts to maintain stability during ageing, sensor drift was observed in some experiments. The creep strains were very small -e.g. from 0.008mm to 0.088mm of axial displacement per log-cycle of age time. Any sensor drift often completely obscured the magnitude of the creep strains. Loss of stability was found to be related to the environmental conditions. Many tests were not affected and stability was maintained throughout ageing. To quantify the log-linear creep strain behaviour the median of the tabulated creep strain rates for the full dataset were calculated. This metric is not sensitive to outliers that may have occurred due to sensor drift during ageing. Table D.1 and Table D.2 provide the median value of developed creep strains for loose specimens for age times up to 1000 minutes.

The developed creep strains quickly, but not immediately, become linear on a log-time scale. The medians of the log-linear slopes are detailed in Table D.3. This table is the amount of creep strain per log cycle of time for each tested stress ratio. The axial creep strains increase with increasing stress ratio. The volumetric strains increase, but are not as sensitive to stress ratio. The radial and shear strains are derived from the calculated axial and volumetric strains. The radial strains decrease with stress ratio

Table D.1: Developed axial creep strains (%) for loose specimens with $\sigma'_r = 100$ kPa

Developed axial creep strains (%)						
	Stress ratio (increasing axial stress)					
Minutes	1.0	1.6	2.0	2.1	2.5	2.8
1	0.01	0.01	0.03	0.03	0.05	0.07
10	0.01	0.03	0.07	0.06	0.09	0.14
100	0.02	0.04	0.10	0.09	0.14	0.21
1000	0.02	0.05	0.14	0.12	0.19	0.28

Table D.2: Developed volumetric (%) creep strains for loose specimens with $\sigma'_r = 100$ kPa

Developed volumetric creep strains (%)						
	Stress ratio (increasing mean stress)					
Minutes	1.0	1.6	2.0	2.1	2.5	2.8
1	0.03	0.02	0.04	0.03	0.04	0.04
10	0.05	0.05	0.07	0.06	0.08	0.07
100	0.08	0.07	0.11	0.10	0.12	0.11
1000	0.10	0.09	0.15	0.13	0.16	0.14

through a transition from compression to extension at K_0. The magnitude of the creep shear strains increase with stress ratio.

Table D.3: Developed creep strains (%) per log-cycle of age time for loose specimens with $\sigma'_r = 100$ kPa

	Stress ratio					
	1.0	1.6	2.0	2.1	2.5	2.8
$\epsilon_a\%$	0.006	0.013	0.035	0.029	0.046	0.071
$\epsilon_v\%$	0.026	0.023	0.037	0.032	0.041	0.036
$\epsilon_r\%$	0.010	0.005	0.001	0.002	-0.003	-0.017
$\epsilon_q\%$	-0.003	0.005	0.022	0.018	0.033	0.059

The values listed in Table D.3 were used to perform creep-strain corrections for calculating G_{sec}.

D.1.2 Triaxial results

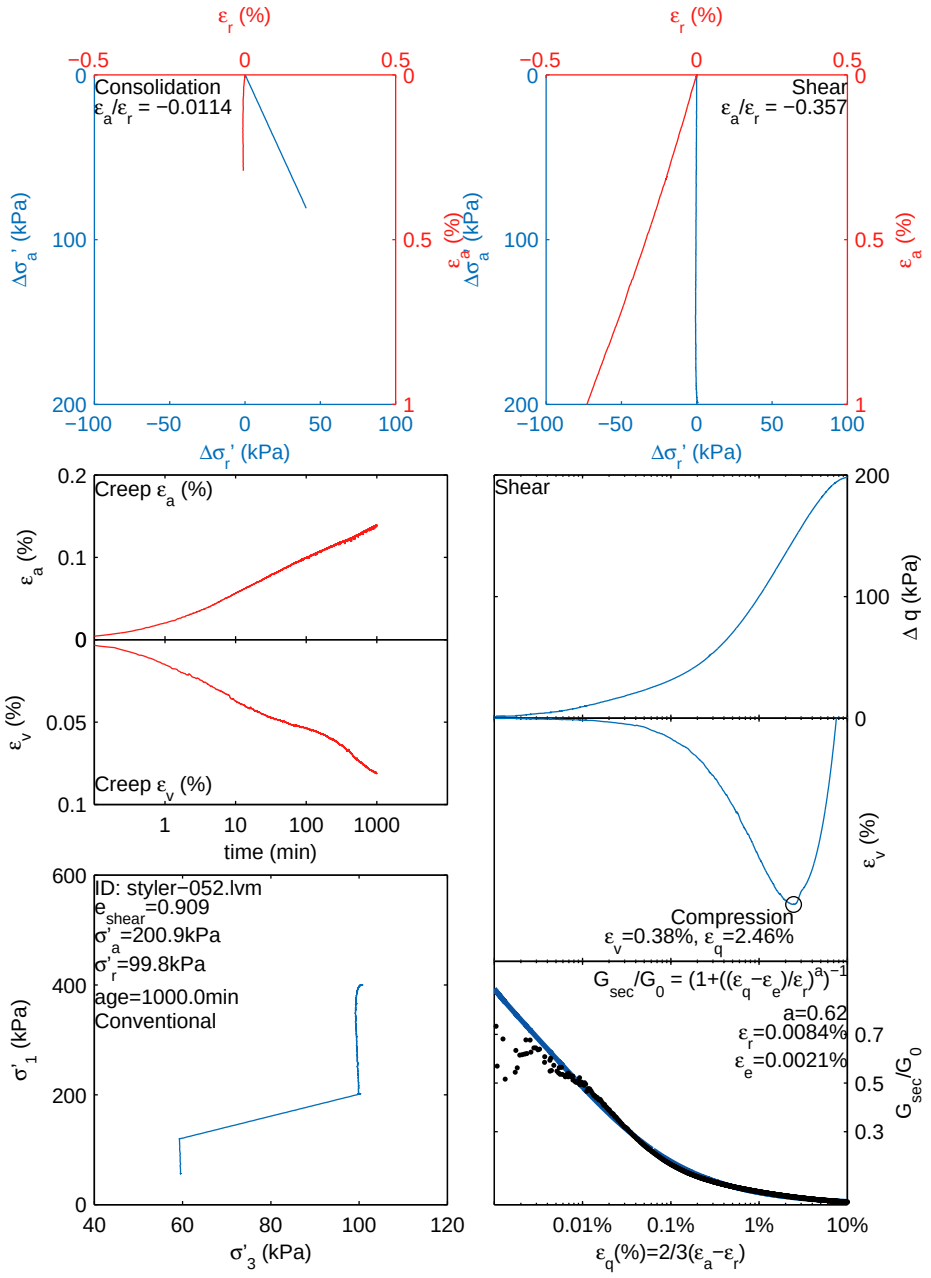

Figure D.1: Styler-052.lvm: σ_a = 200.9 kPa, σ_r = 99.8 kPa, age=1000.0 min, Stress path=C

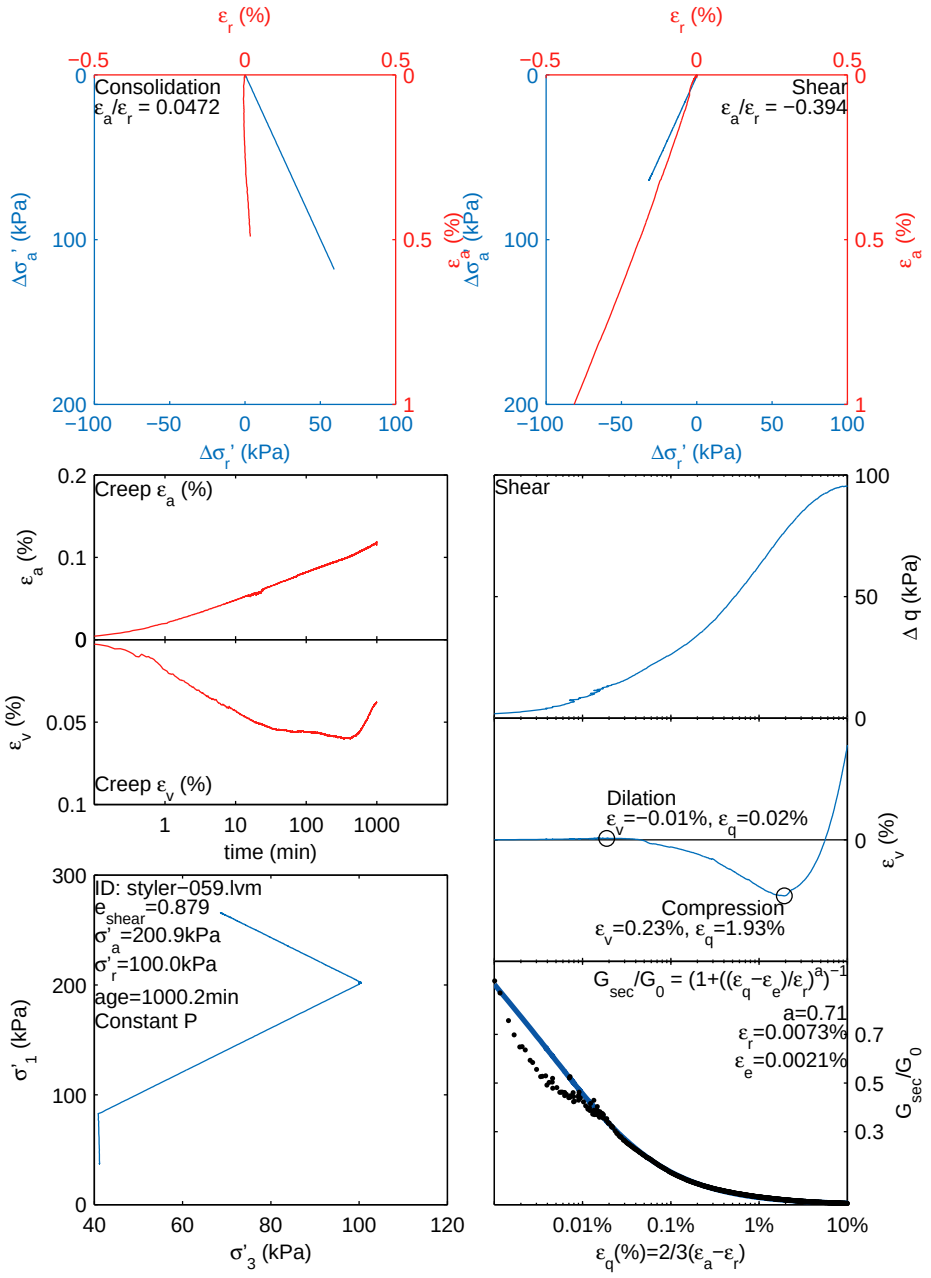

Figure D.2: Styler-059.lvm: $\sigma_a = 200.9$ kPa, $\sigma_r = 100.0$ kPa, age=1000.2 min, Stress path=P

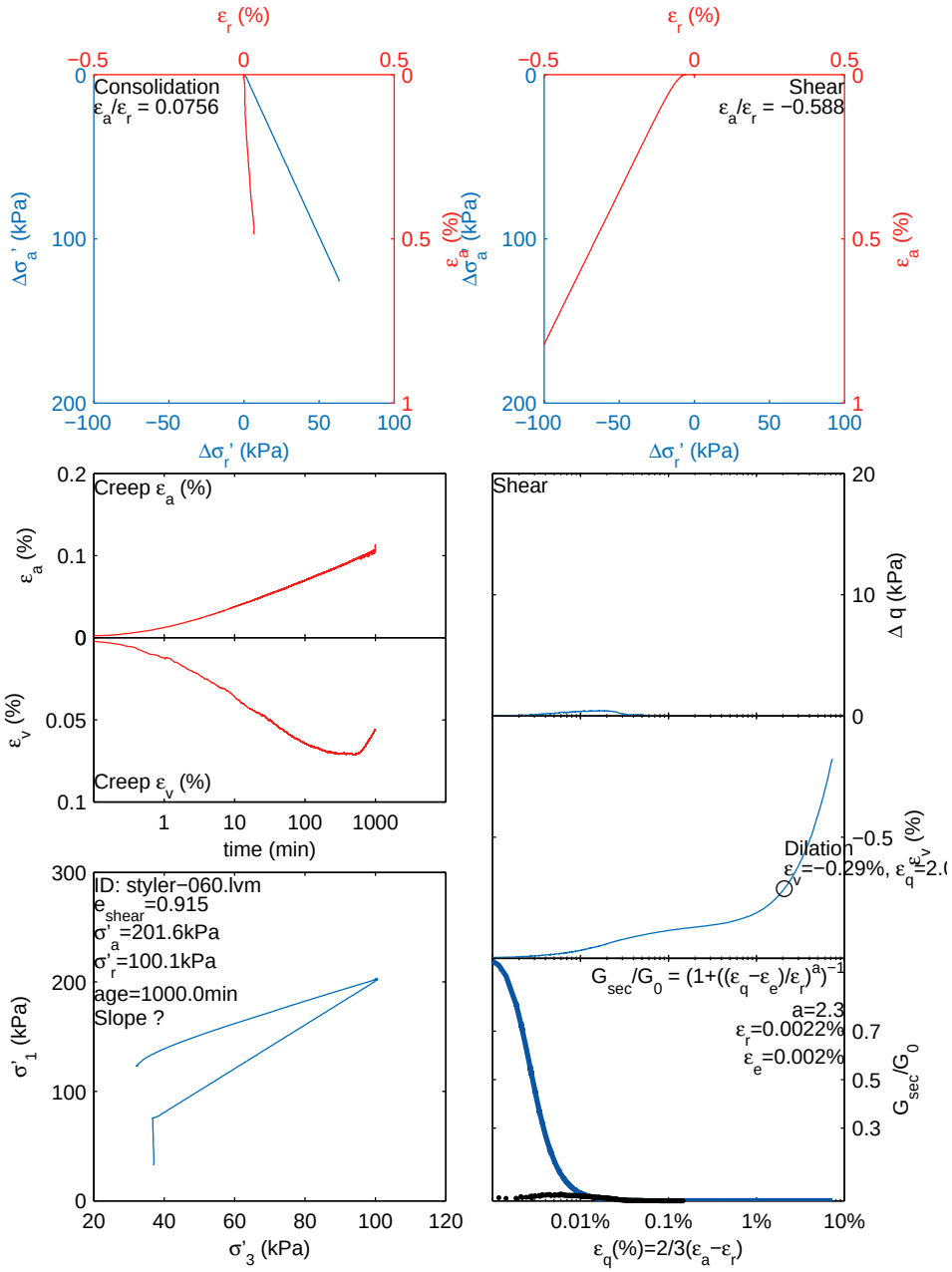

Figure D.3: Styler-060.lvm: $\sigma_a = 201.6$ kPa, $\sigma_r = 100.1$ kPa, age=1000.0 min, Stress path=?

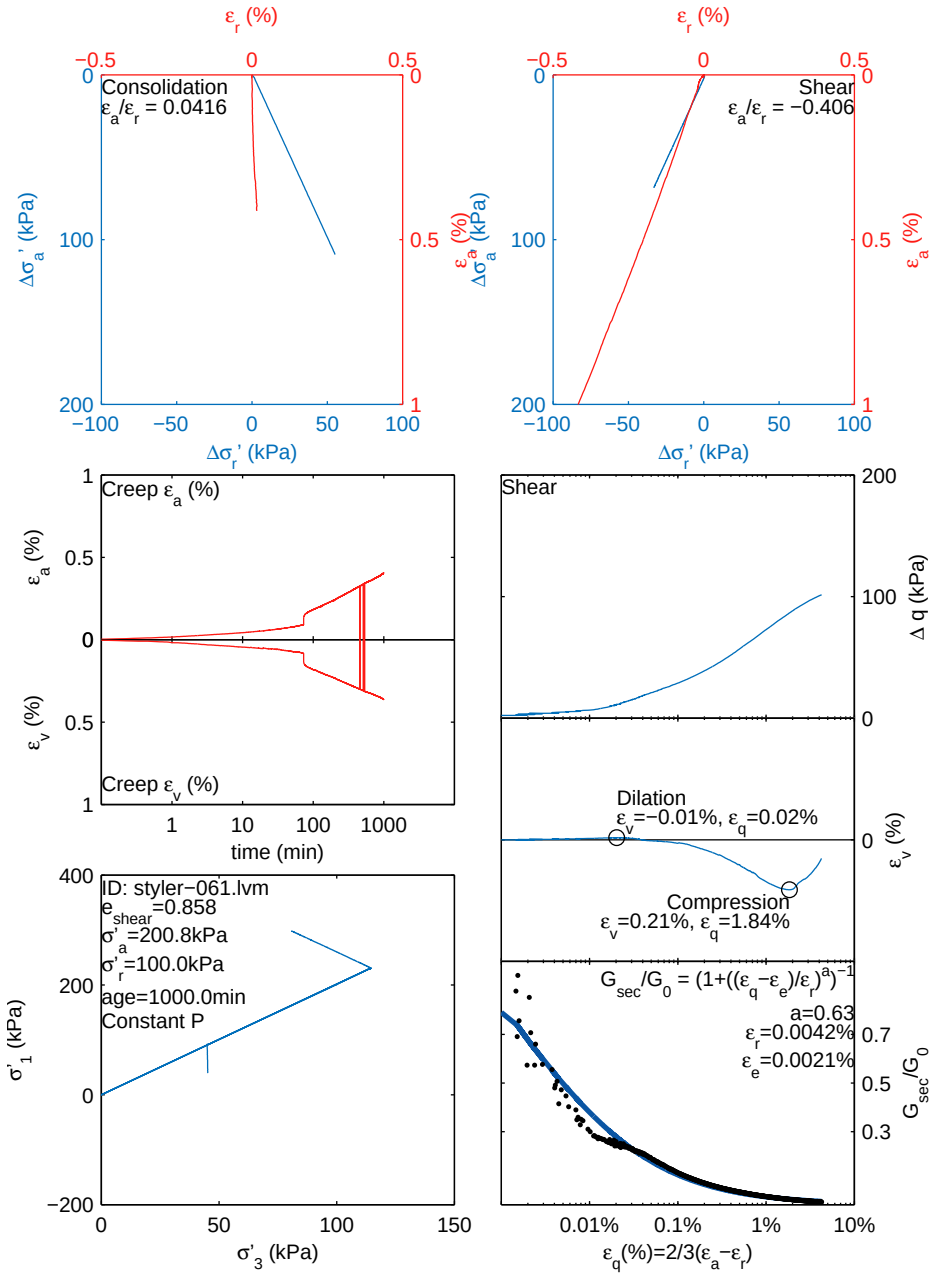

Figure D.4: Styler-061.lvm: σ_a = 200.8 kPa, σ_r = 100.0 kPa, age=1000.0 min, Stress path=P

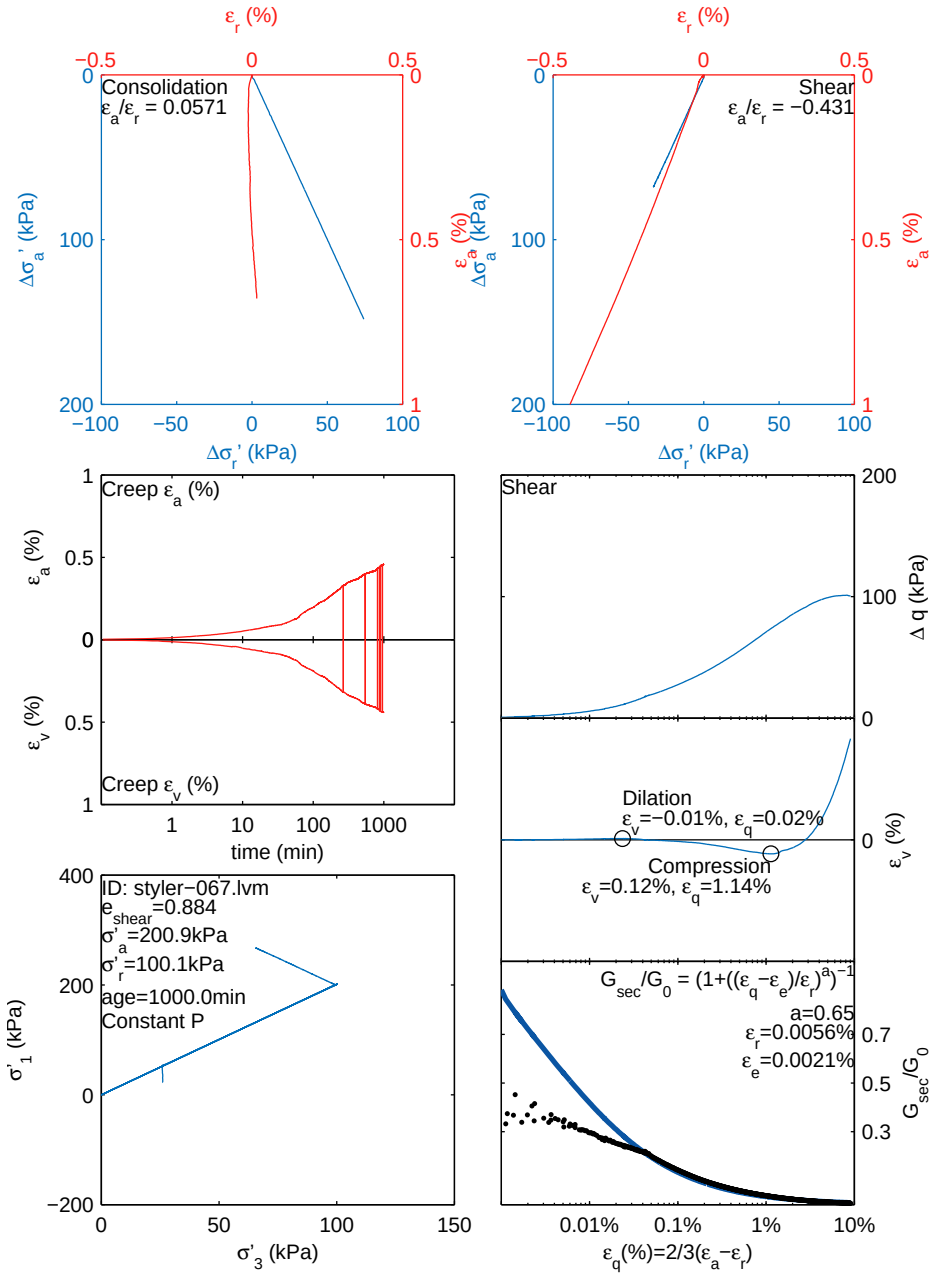

Figure D.5: Styler-067.lvm: σ_a = 200.9 kPa, σ_r = 100.1 kPa, age=1000.0 min, Stress path=P

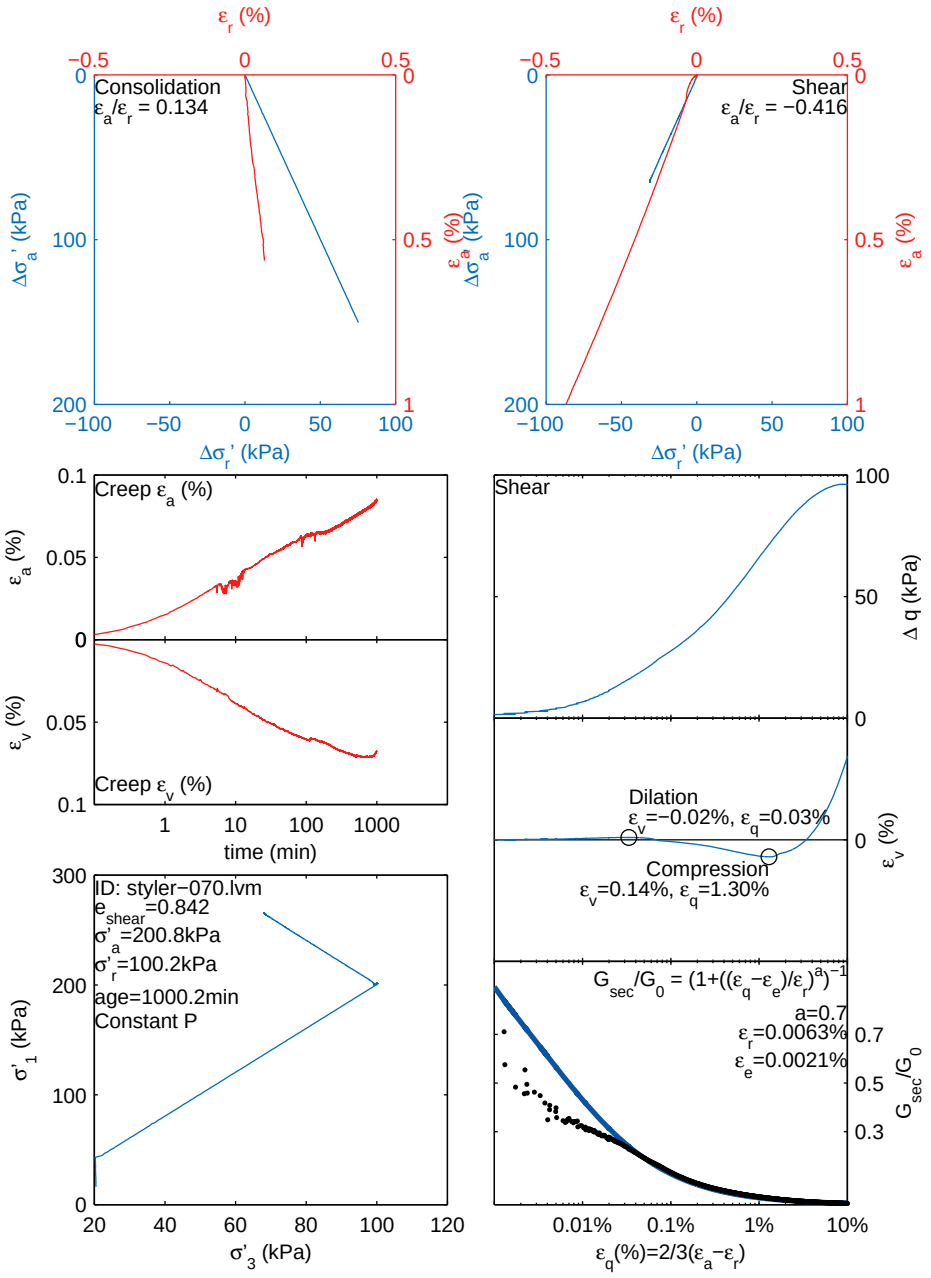

Figure D.6: Styler-070.lvm: $\sigma_a = 200.8$ kPa, $\sigma_r = 100.2$ kPa, age=1000.2 min, Stress path=P

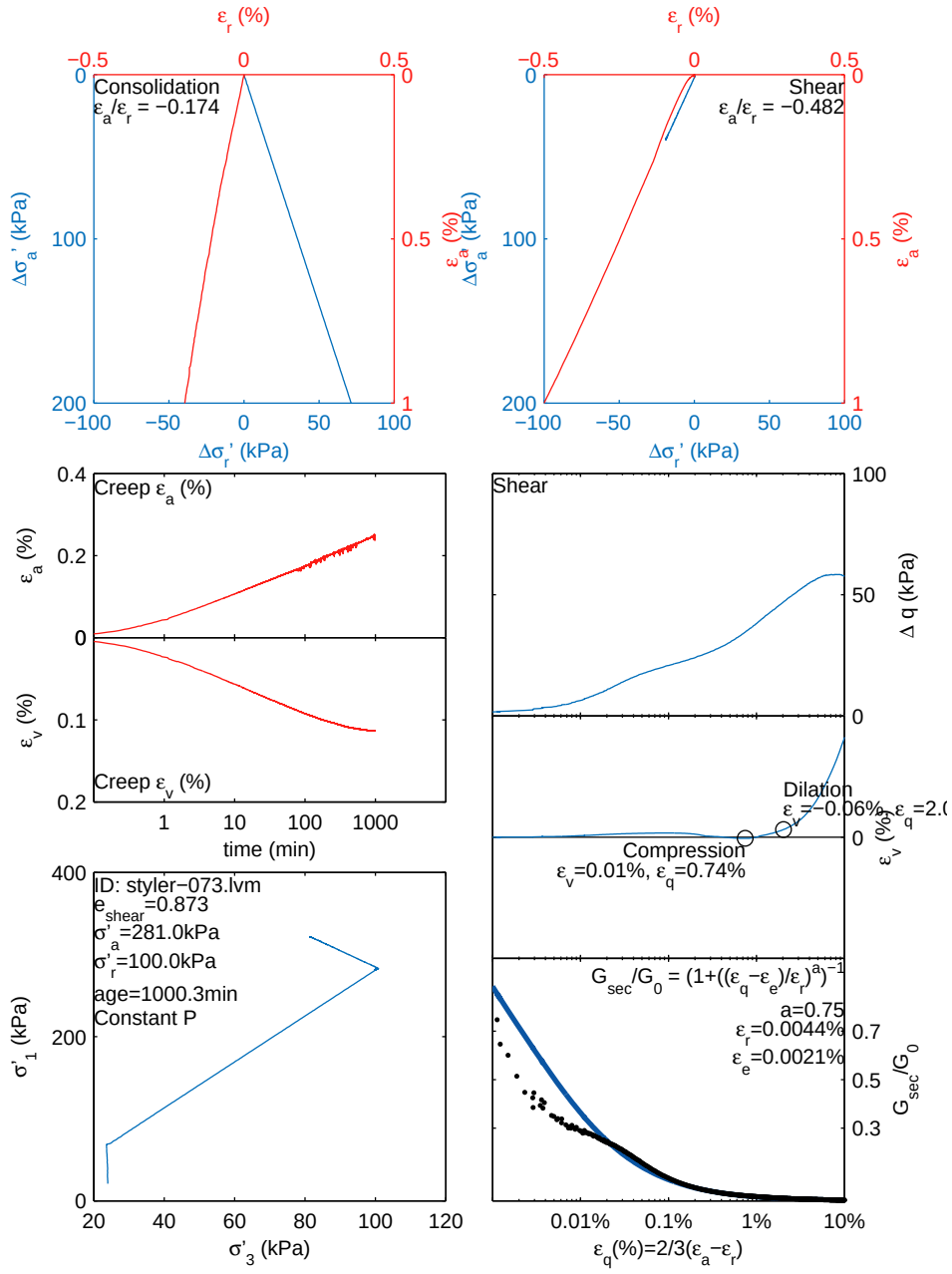

Figure D.7: Styler-073.lvm: σ_a = 281.0 kPa, σ_r = 100.0 kPa, age=1000.3 min, Stress path=P

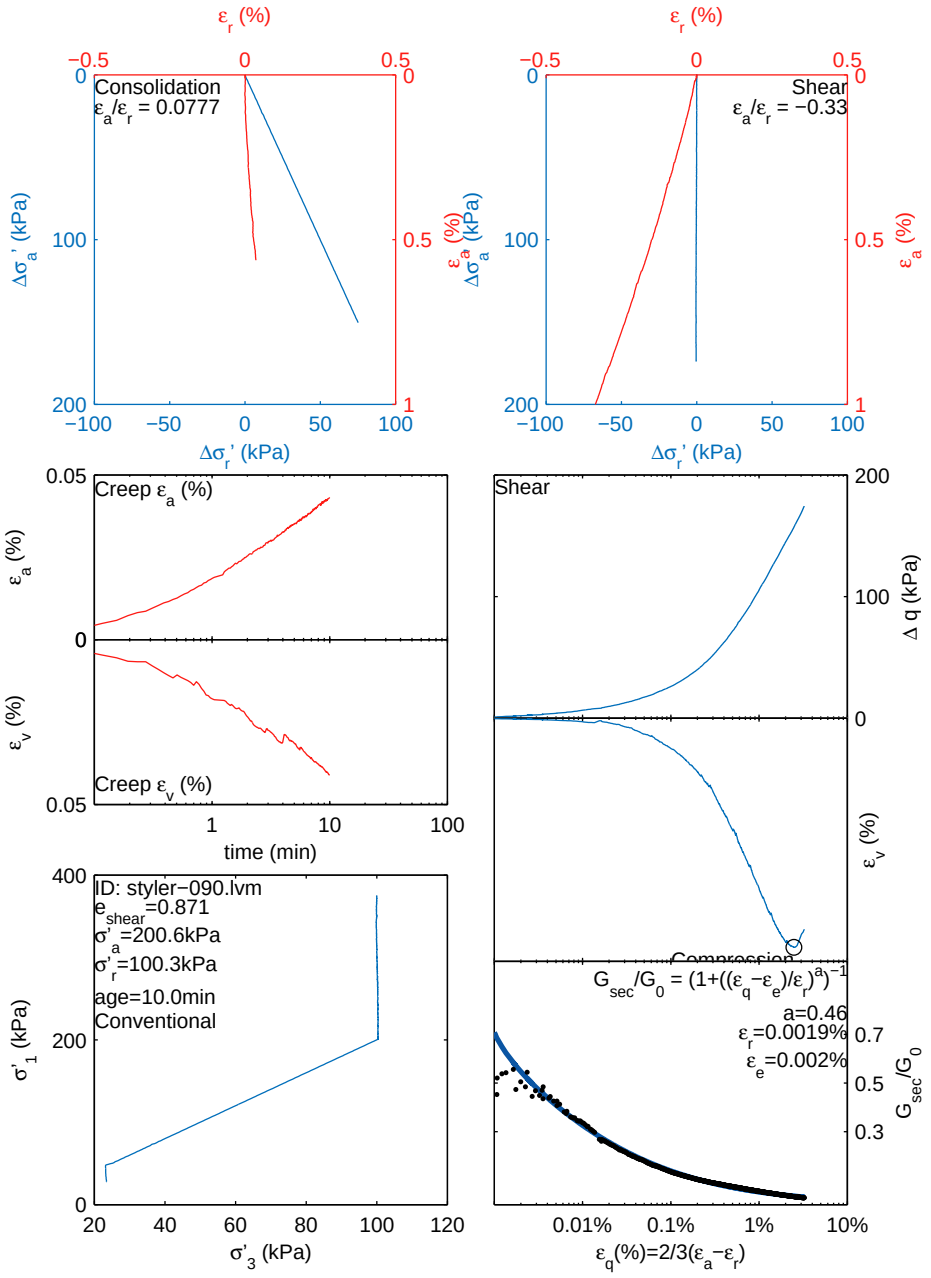

Figure D.8: Styler-090.lvm: σ_a = 200.6 kPa, σ_r = 100.3 kPa, age=10.0 min, Stress path=C

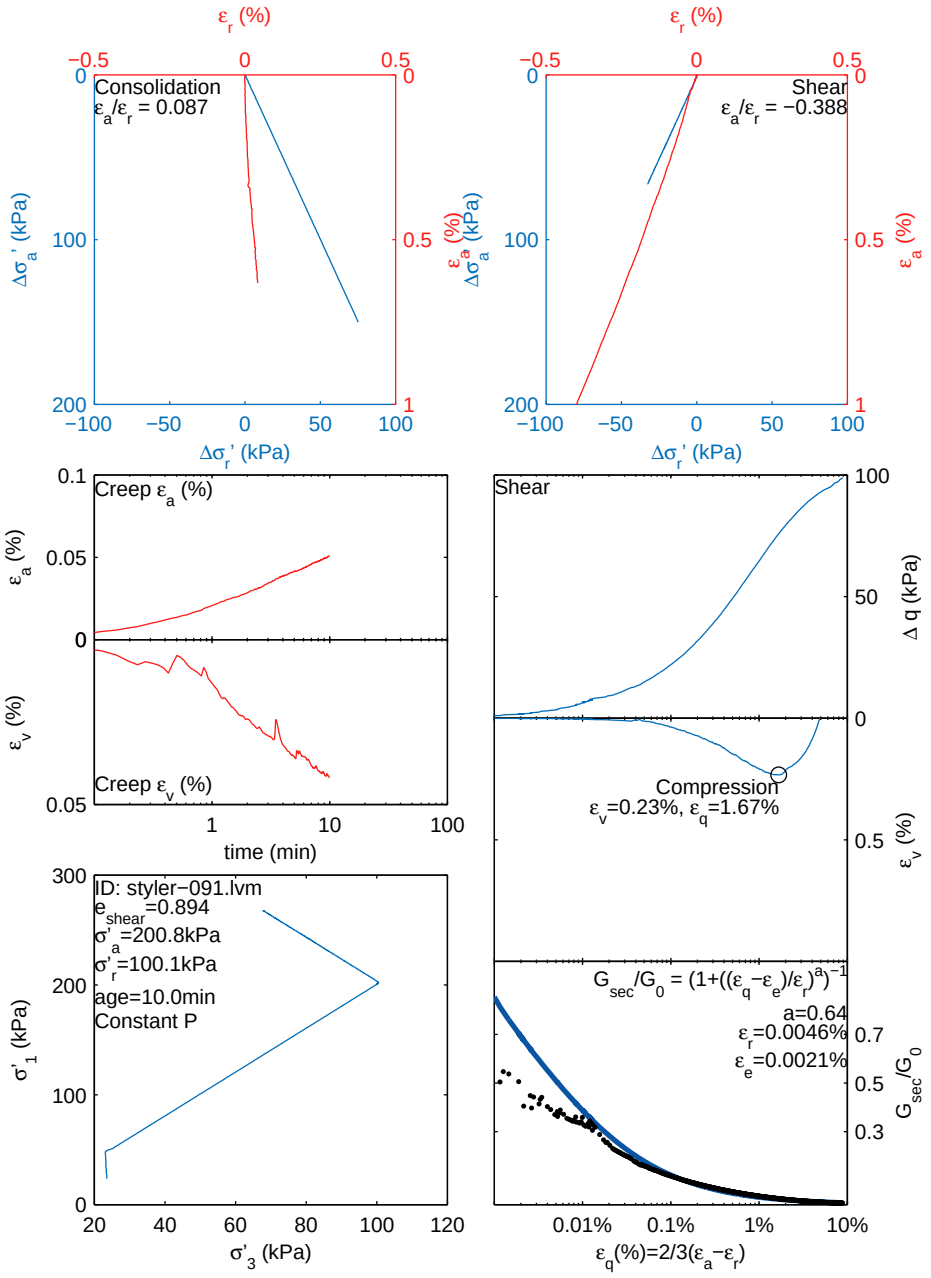

Figure D.9: Styler-091.lvm: σ_a = 200.8 kPa, σ_r = 100.1 kPa, age=10.0 min, Stress path=P

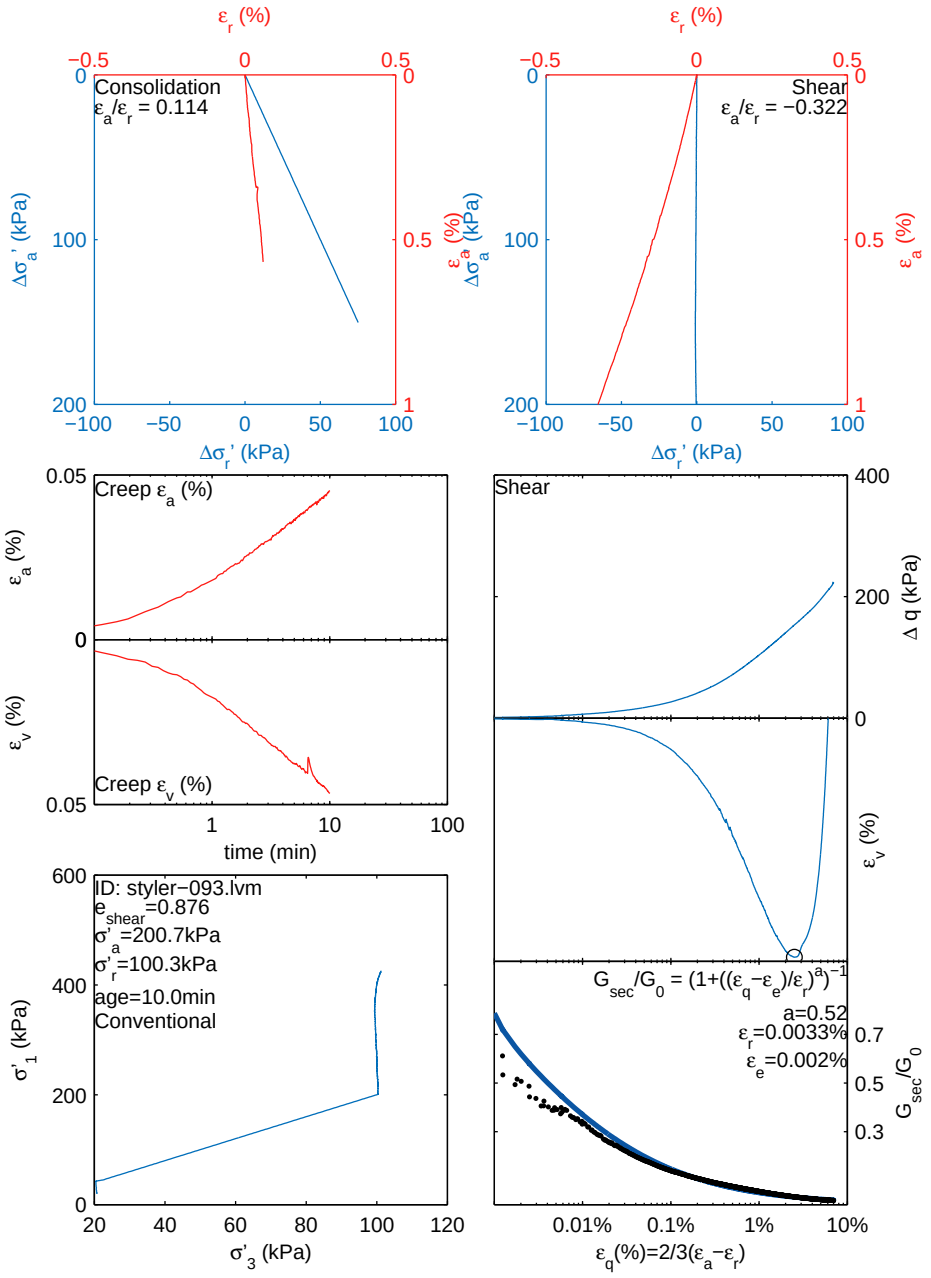

Figure D.10: Styler-093.lvm: σ_a = 200.7 kPa, σ_r = 100.3 kPa, age=10.0 min, Stress path=C

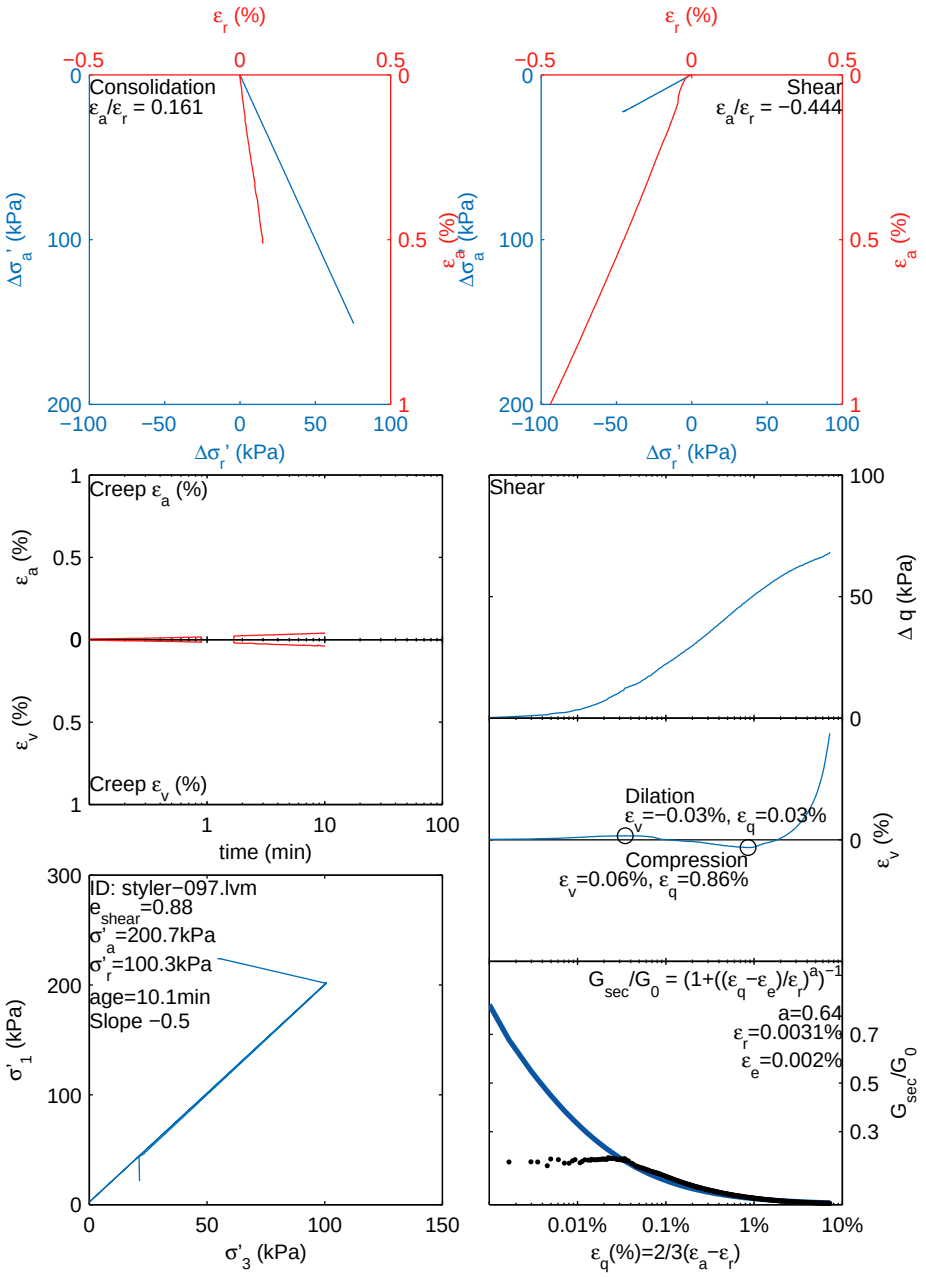

Figure D.11: Styler-097.lvm: σ_a = 200.7 kPa, σ_r = 100.3 kPa, age=10.1 min, Stress path=-0.5

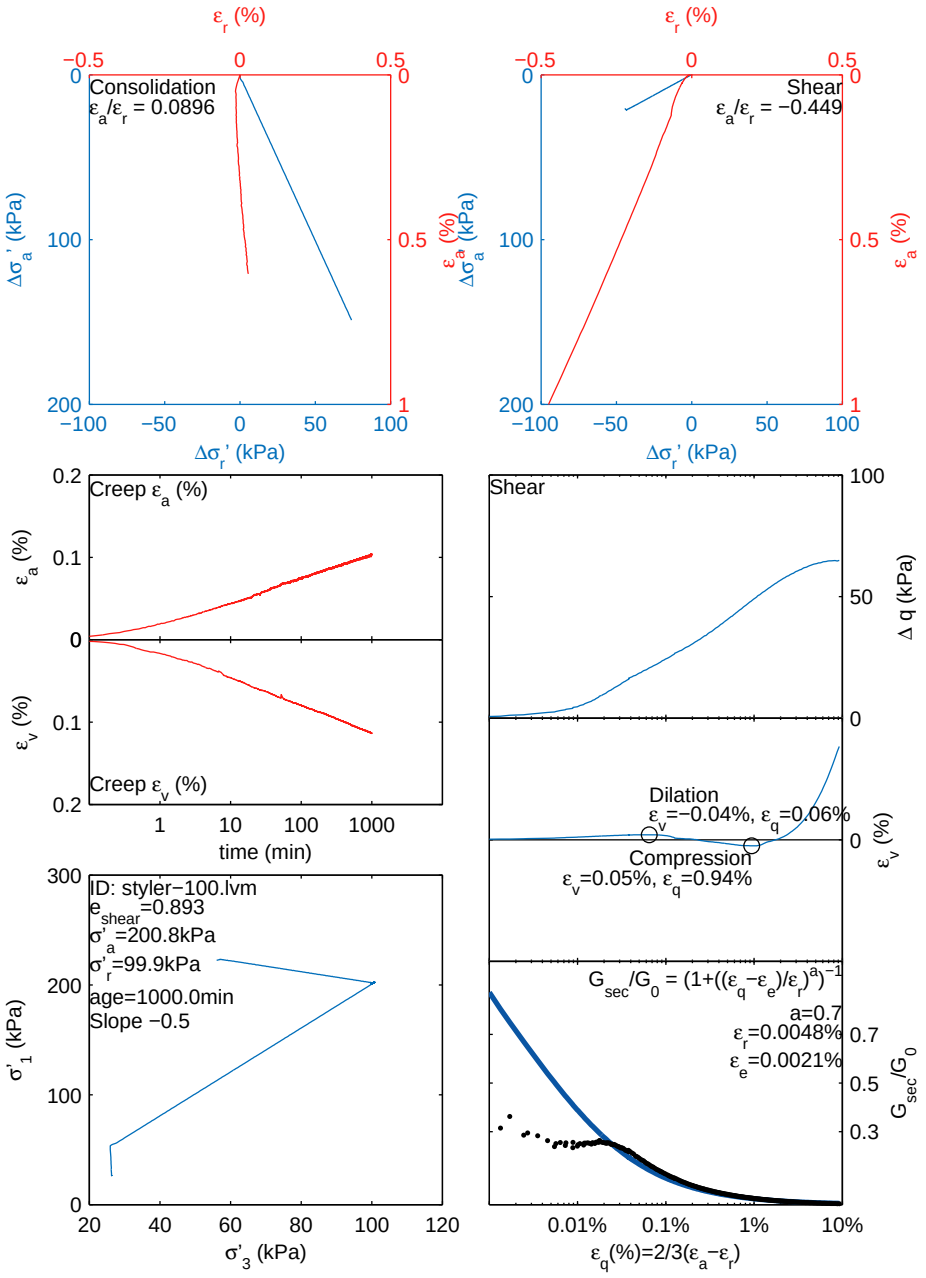

Figure D.12: Styler-100.lvm: σ_a = 200.8 kPa, σ_r = 99.9 kPa, age=1000.0 min, Stress path=-0.5

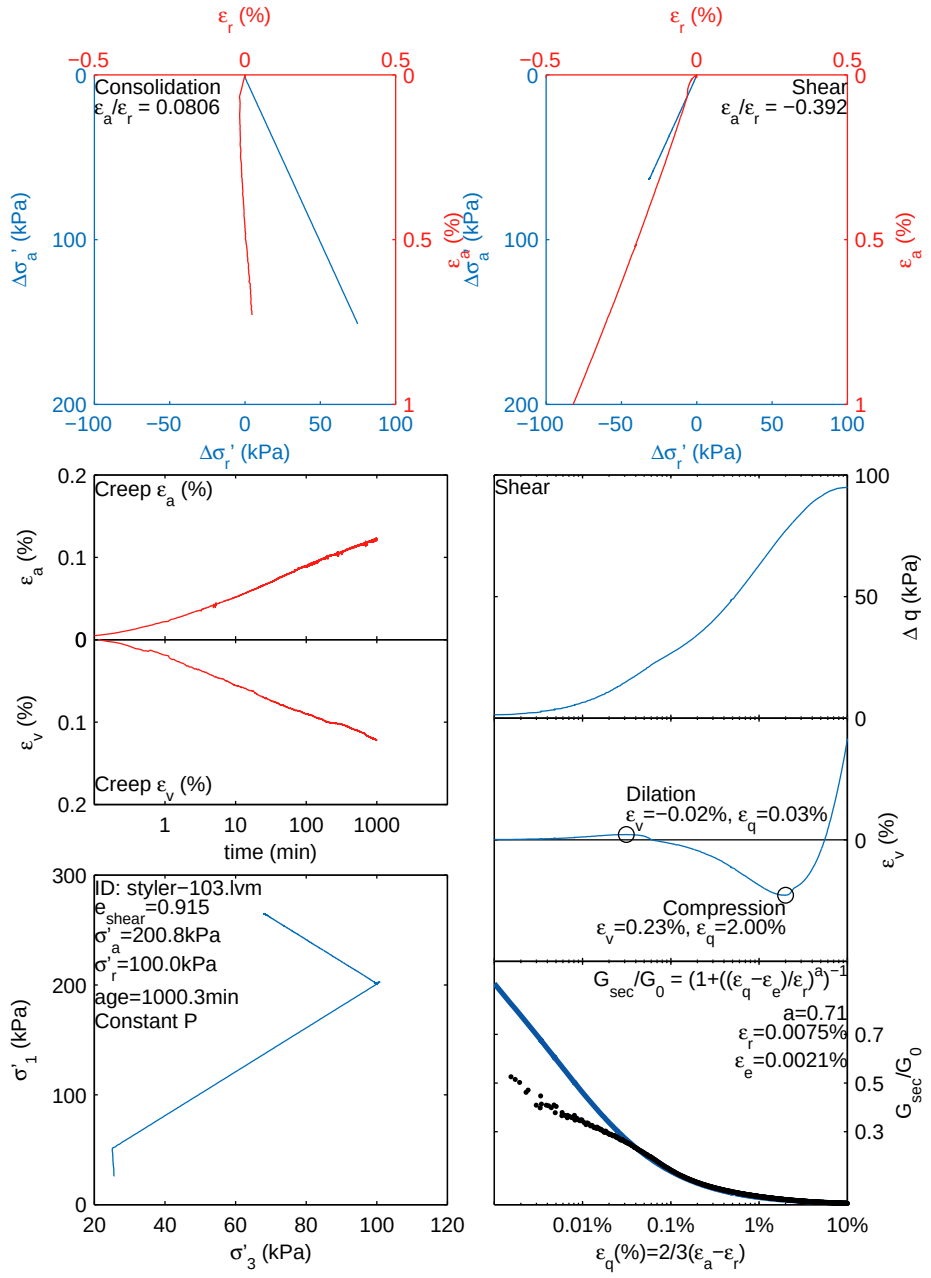

Figure D.13: Styler-103.lvm: σ_a = 200.8 kPa, σ_r = 100.0 kPa, age=1000.3 min, Stress path=P

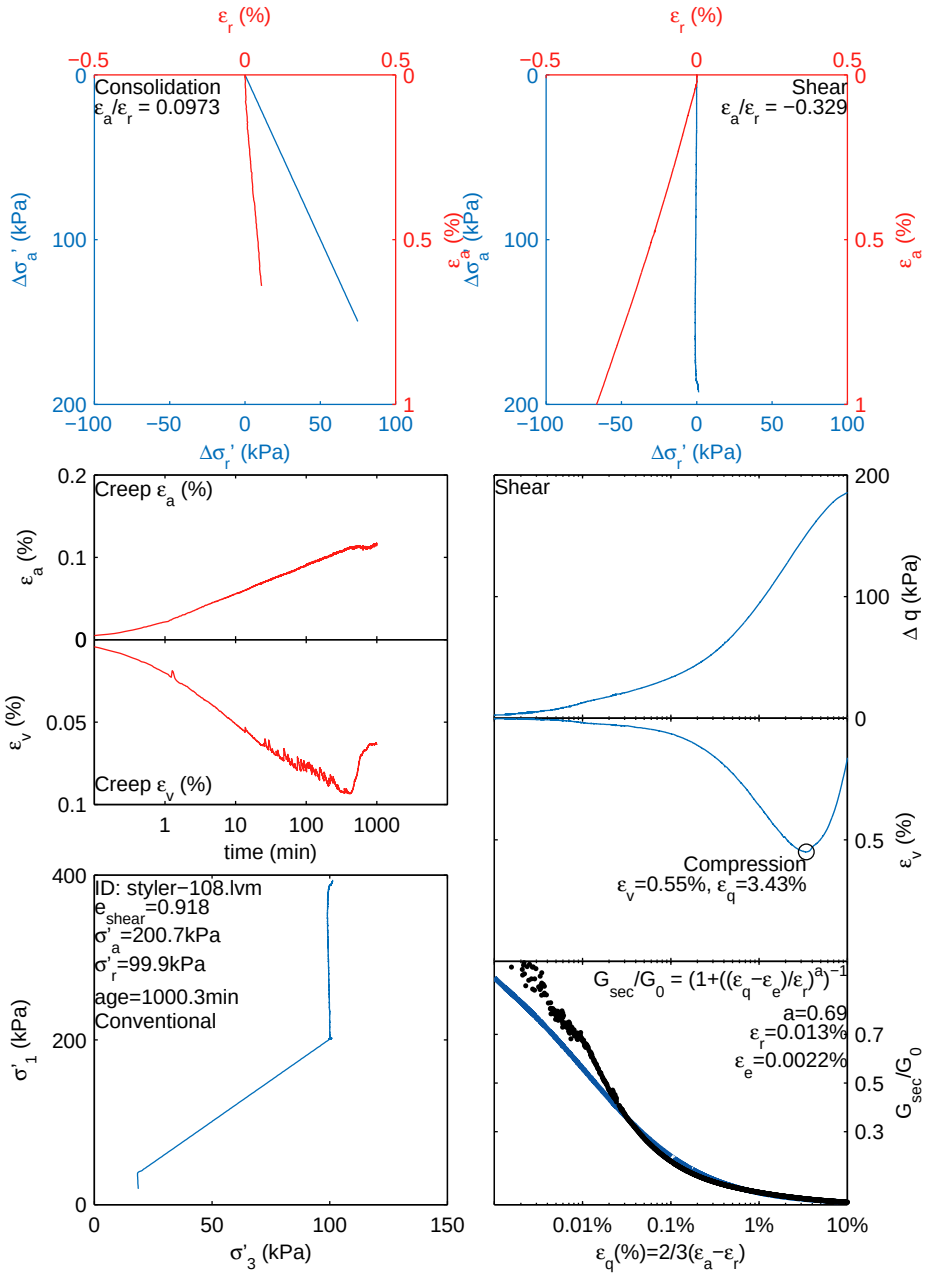

Figure D.14: Styler-108.lvm: σ_a = 200.7 kPa, σ_r = 99.9 kPa, age=1000.3 min, Stress path=C

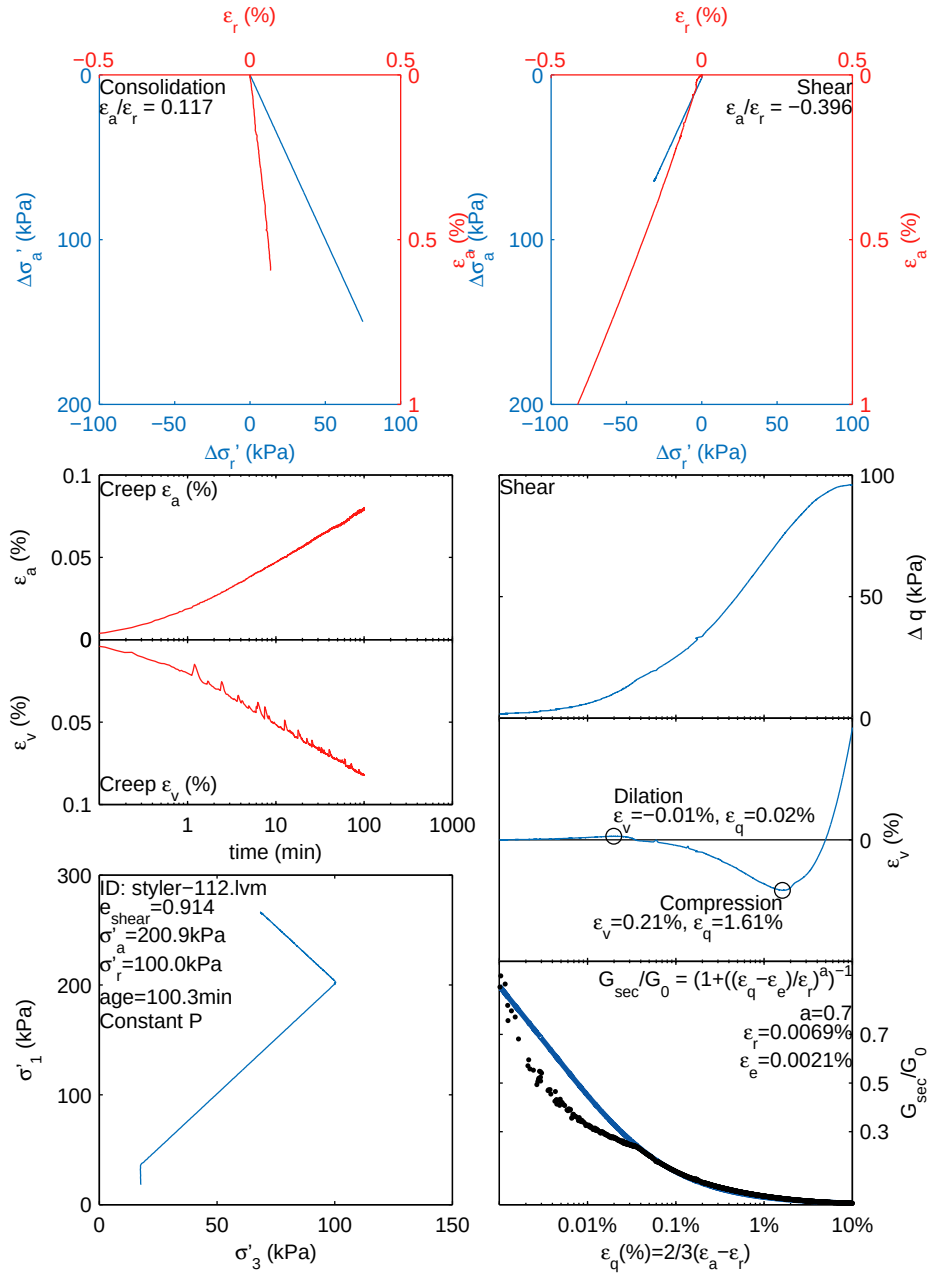

Figure D.15: Styler-112.lvm: σ_a = 200.9 kPa, σ_r = 100.0 kPa, age=100.3 min, Stress path=P

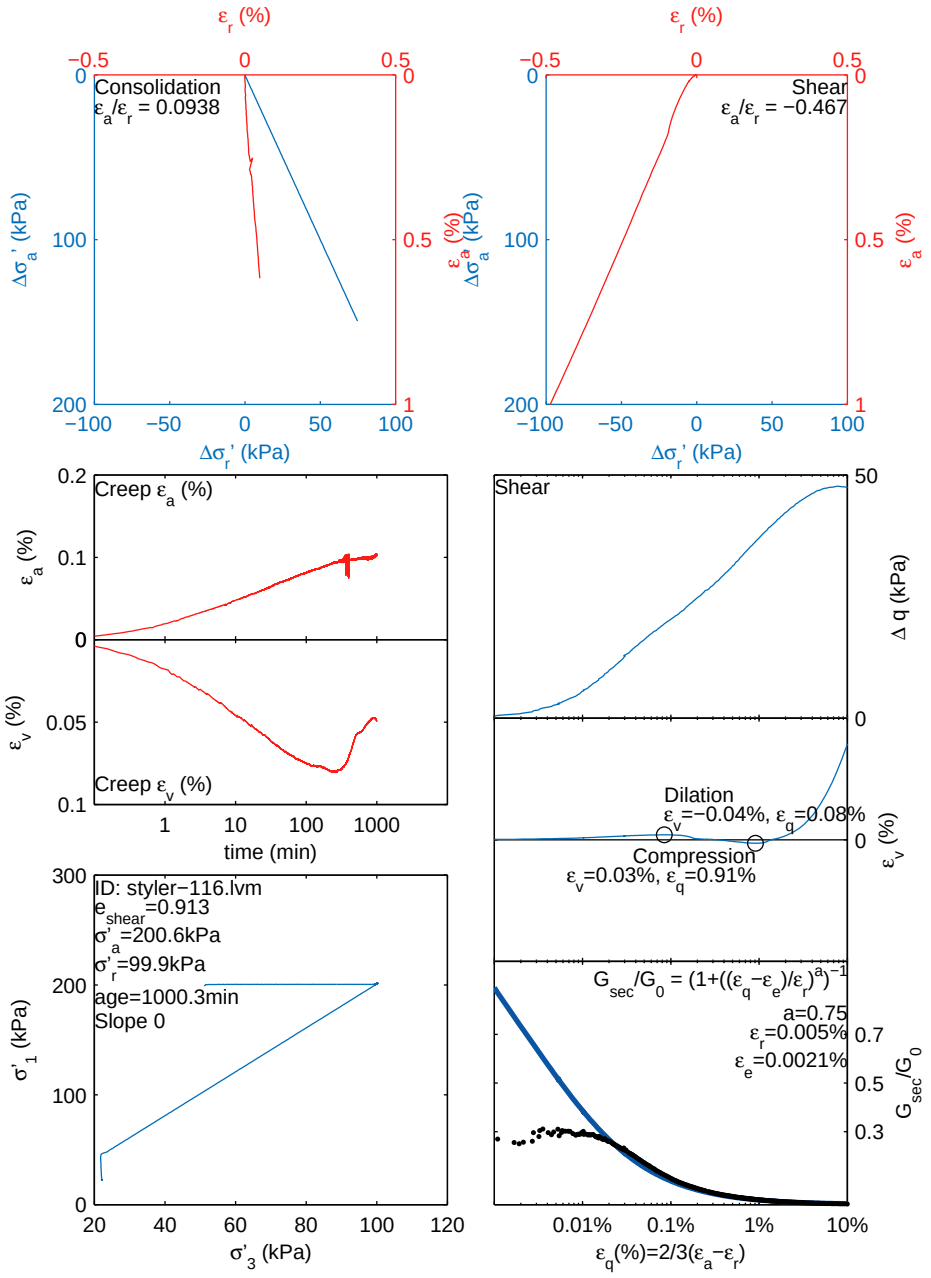

Figure D.16: Styler-116.lvm: σ_a = 200.6 kPa, σ_r = 99.9 kPa, age=1000.3 min, Stress path=0

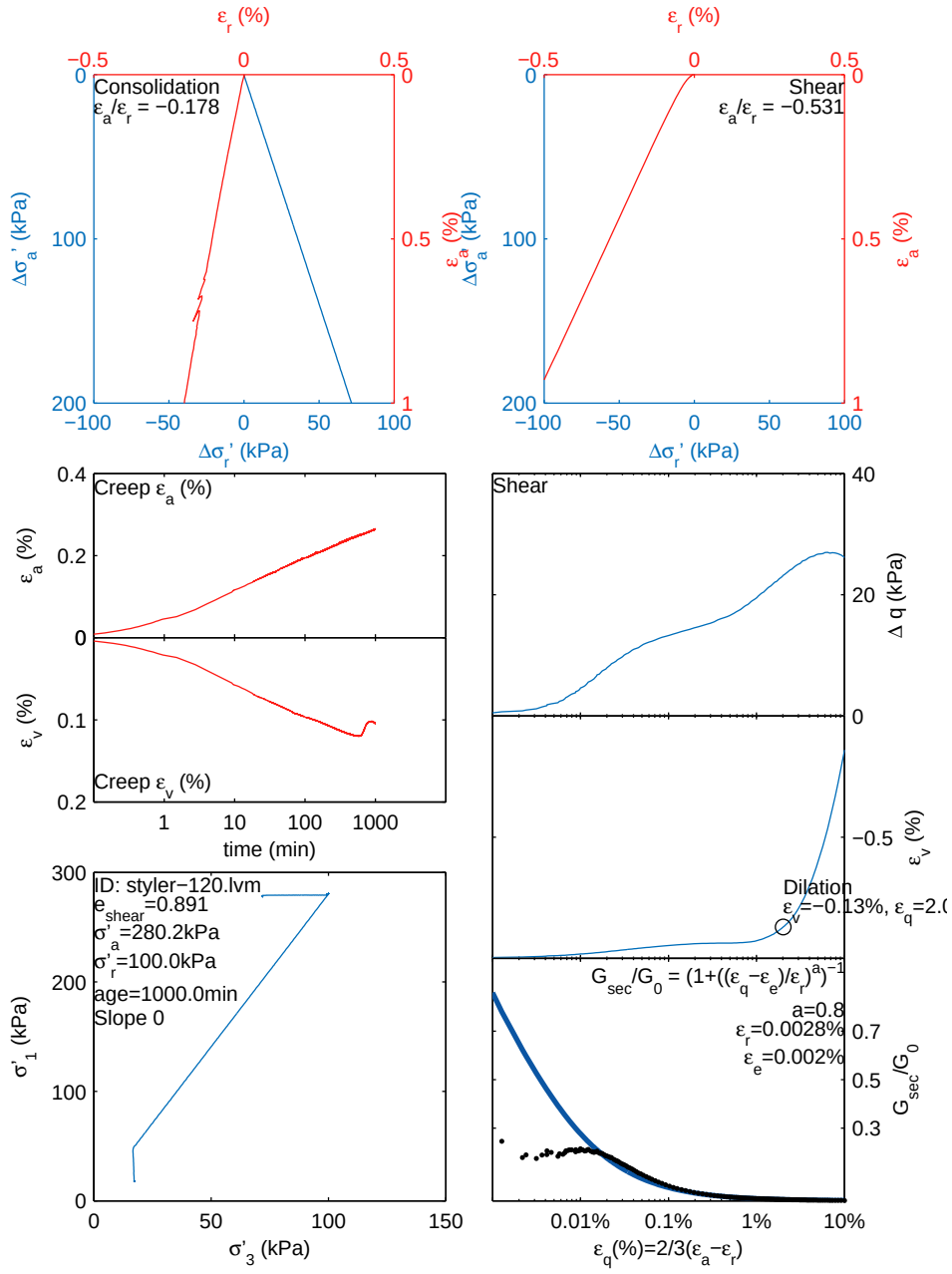

Figure D.17: Styler-120.lvm: $\sigma_a = 280.2$ kPa, $\sigma_r = 100.0$ kPa, age=1000.0 min, Stress path=0

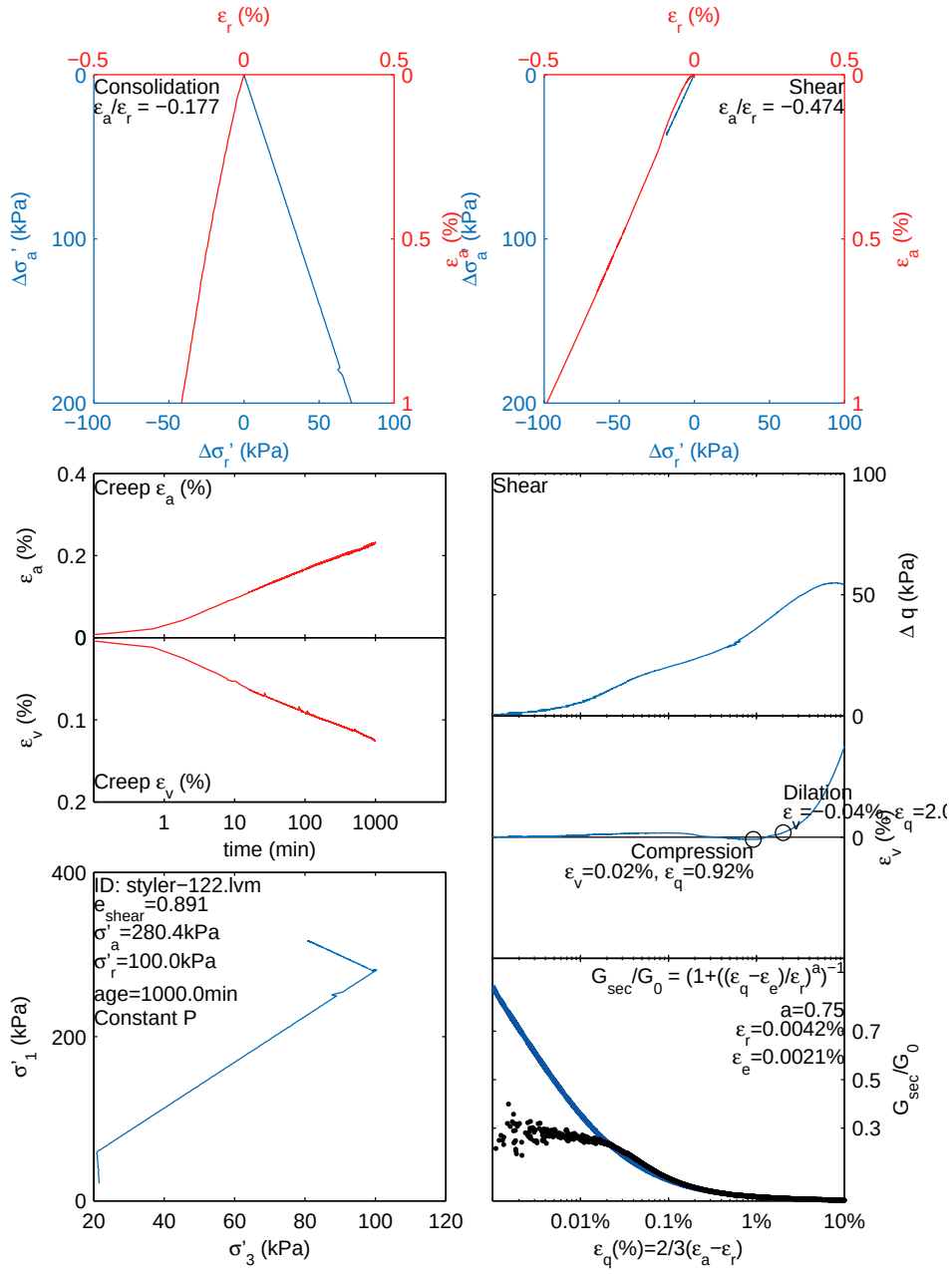

Figure D.18: Styler-122.lvm: σ_a = 280.4 kPa, σ_r = 100.0 kPa, age=1000.0 min, Stress path=P

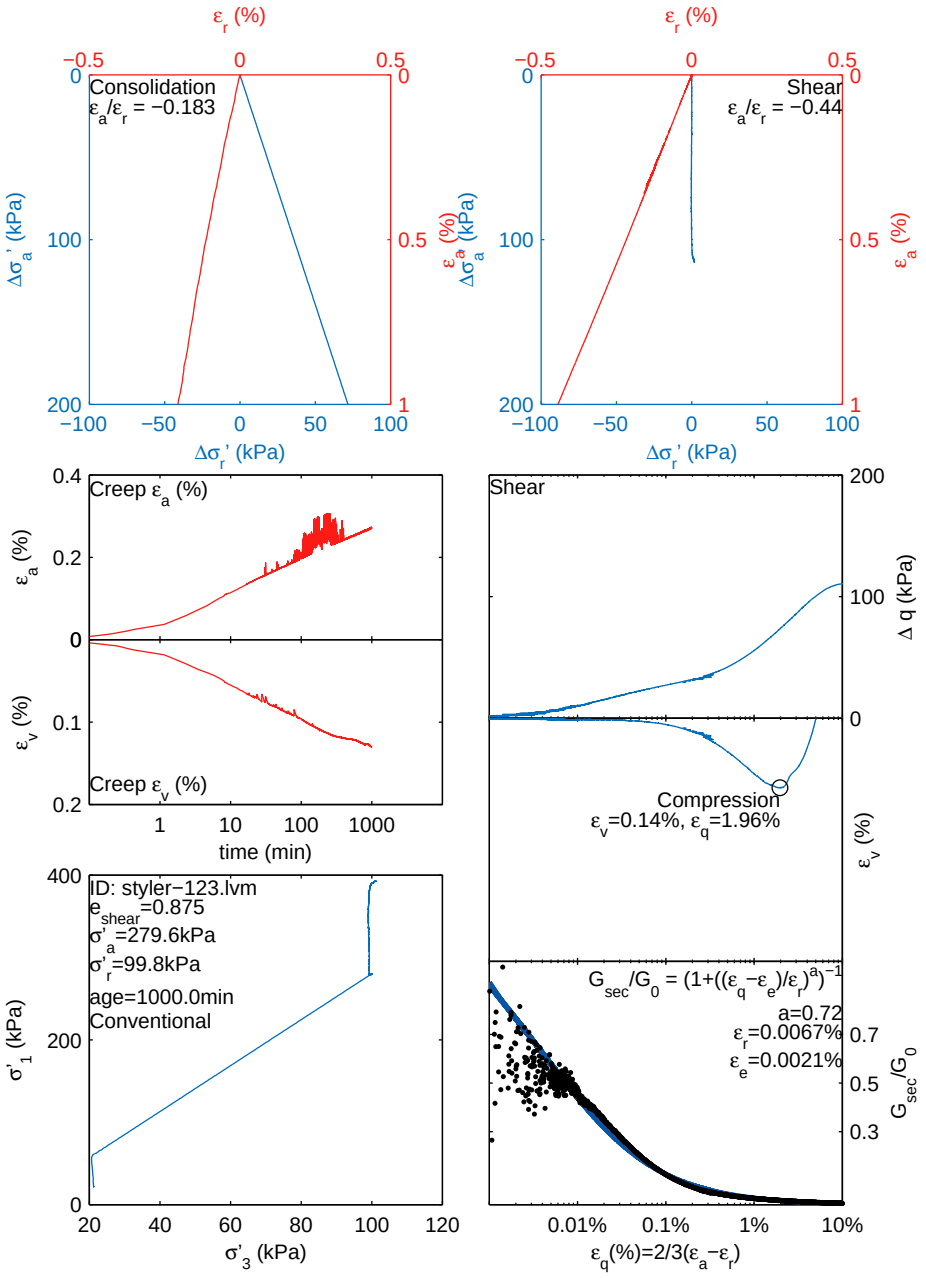

Figure D.19: Styler-123.lvm: σ_a = 279.6 kPa, σ_r = 99.8 kPa, age=1000.0 min, Stress path=C

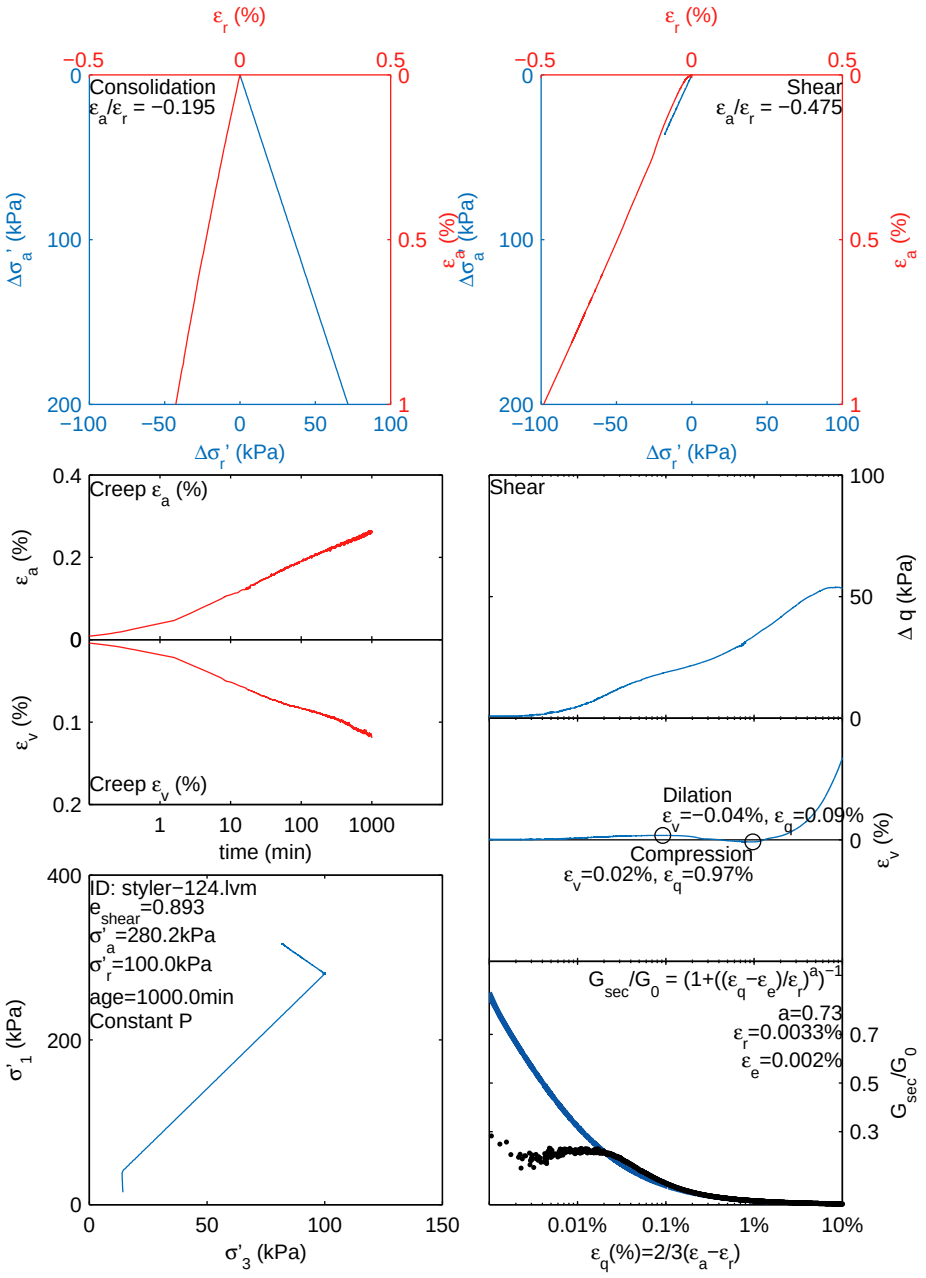

Figure D.20: Styler-124.lvm: σ_a = 280.2 kPa, σ_r = 100.0 kPa, age=1000.0 min, Stress path=P

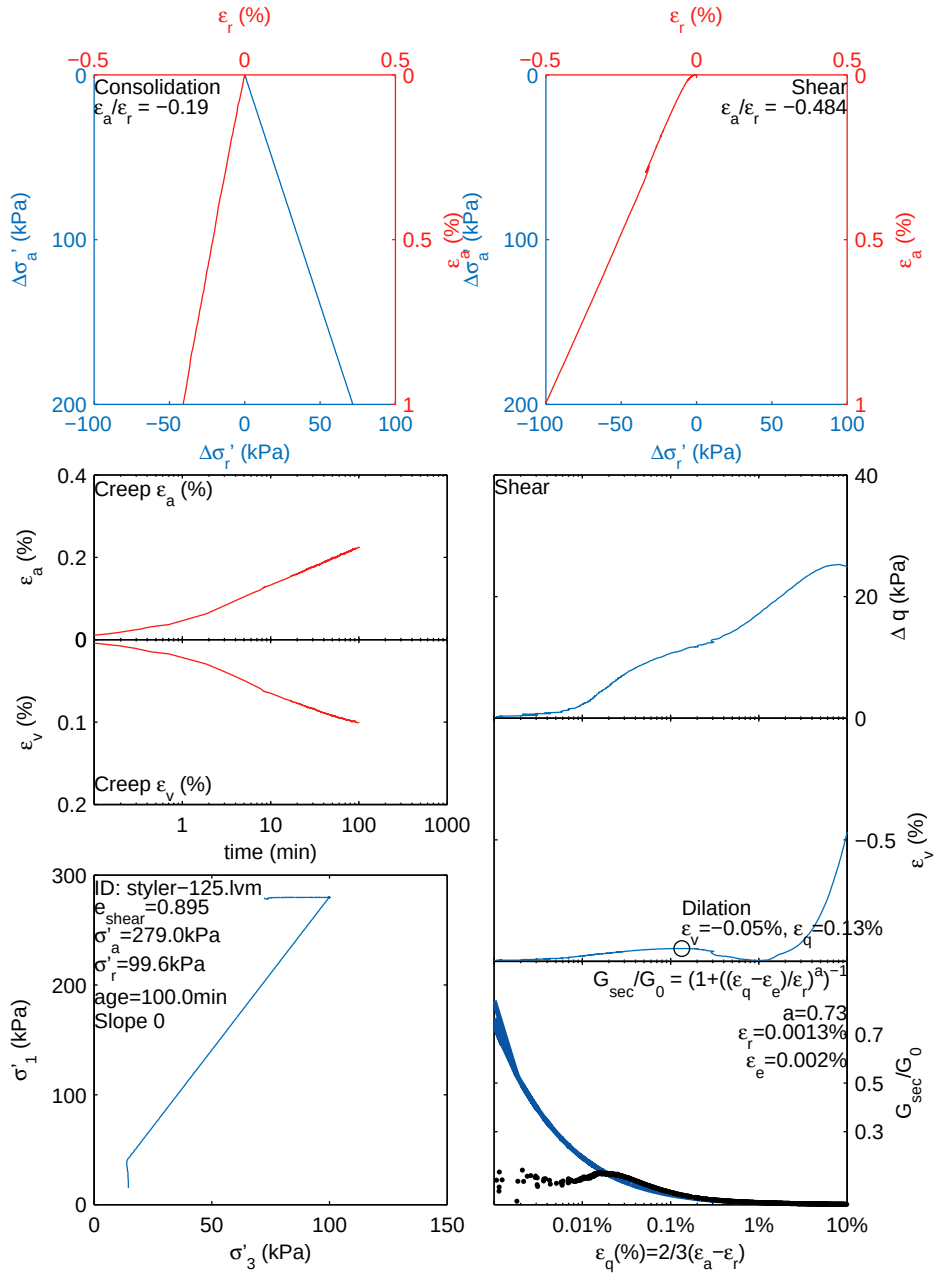

Figure D.21: Styler-125.lvm: σ_a = 279.0 kPa, σ_r = 99.6 kPa, age=100.0 min, Stress path=0

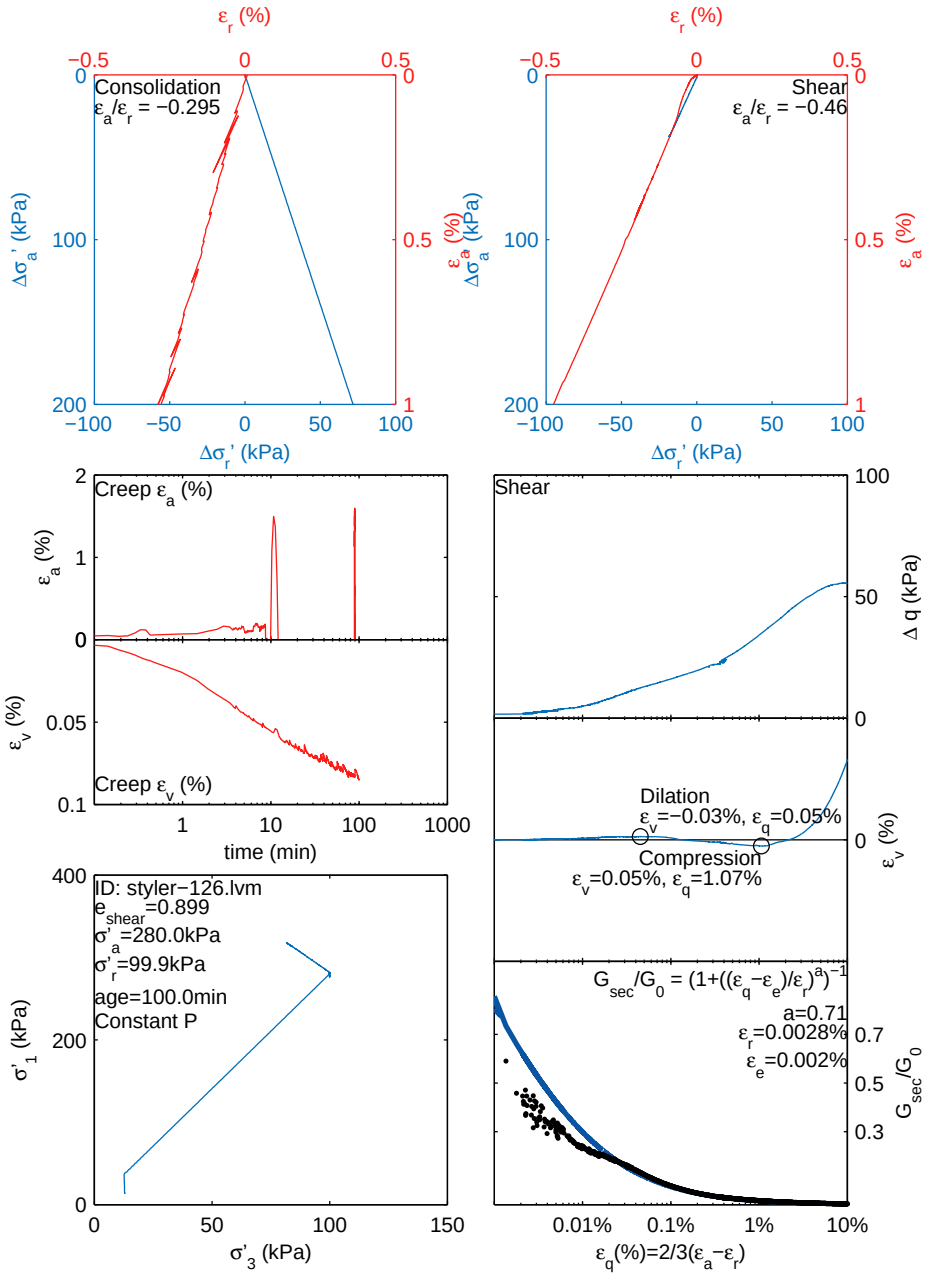

Figure D.22: Styler-126.lvm: σ_a = 280.0 kPa, σ_r = 99.9 kPa, age=100.0 min, Stress path=P

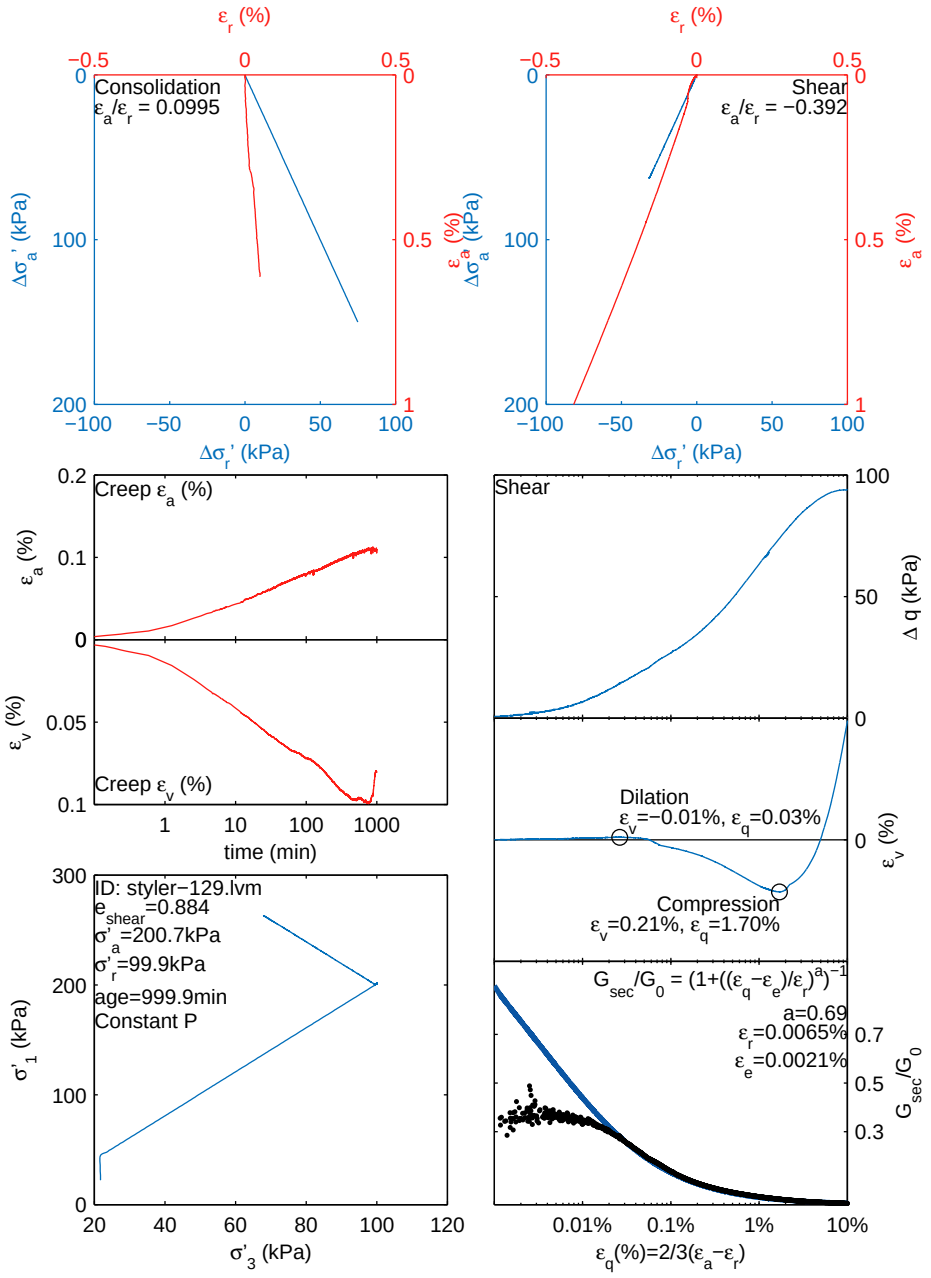

Figure D.23: Styler-129.lvm: σ_a = 200.7 kPa, σ_r = 99.9 kPa, age=999.9 min, Stress path=P

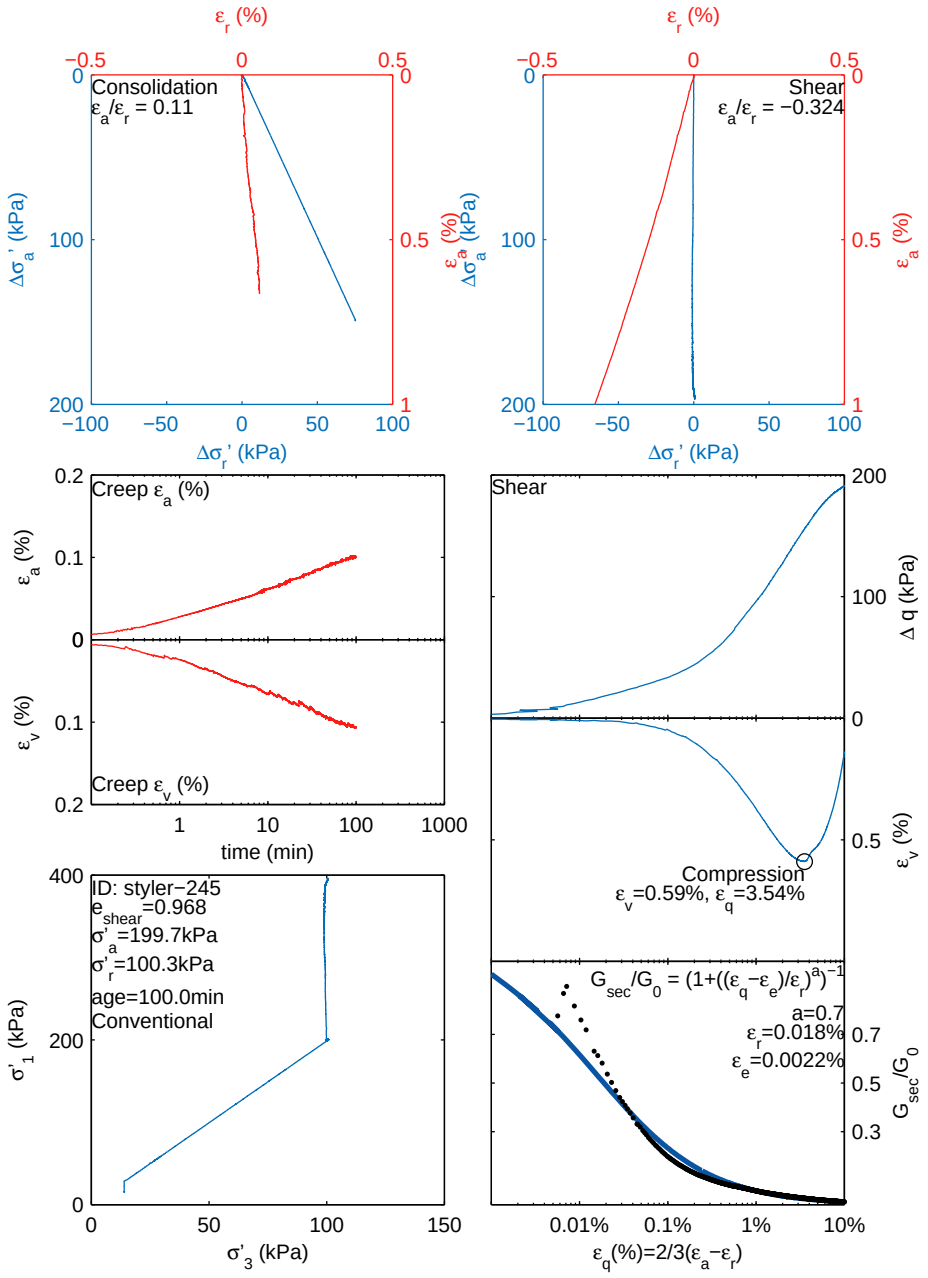

Figure D.24: Styler-245: $\sigma_a = 199.7$ kPa, $\sigma_r = 100.3$ kPa, age=100.0 min, Stress path=C

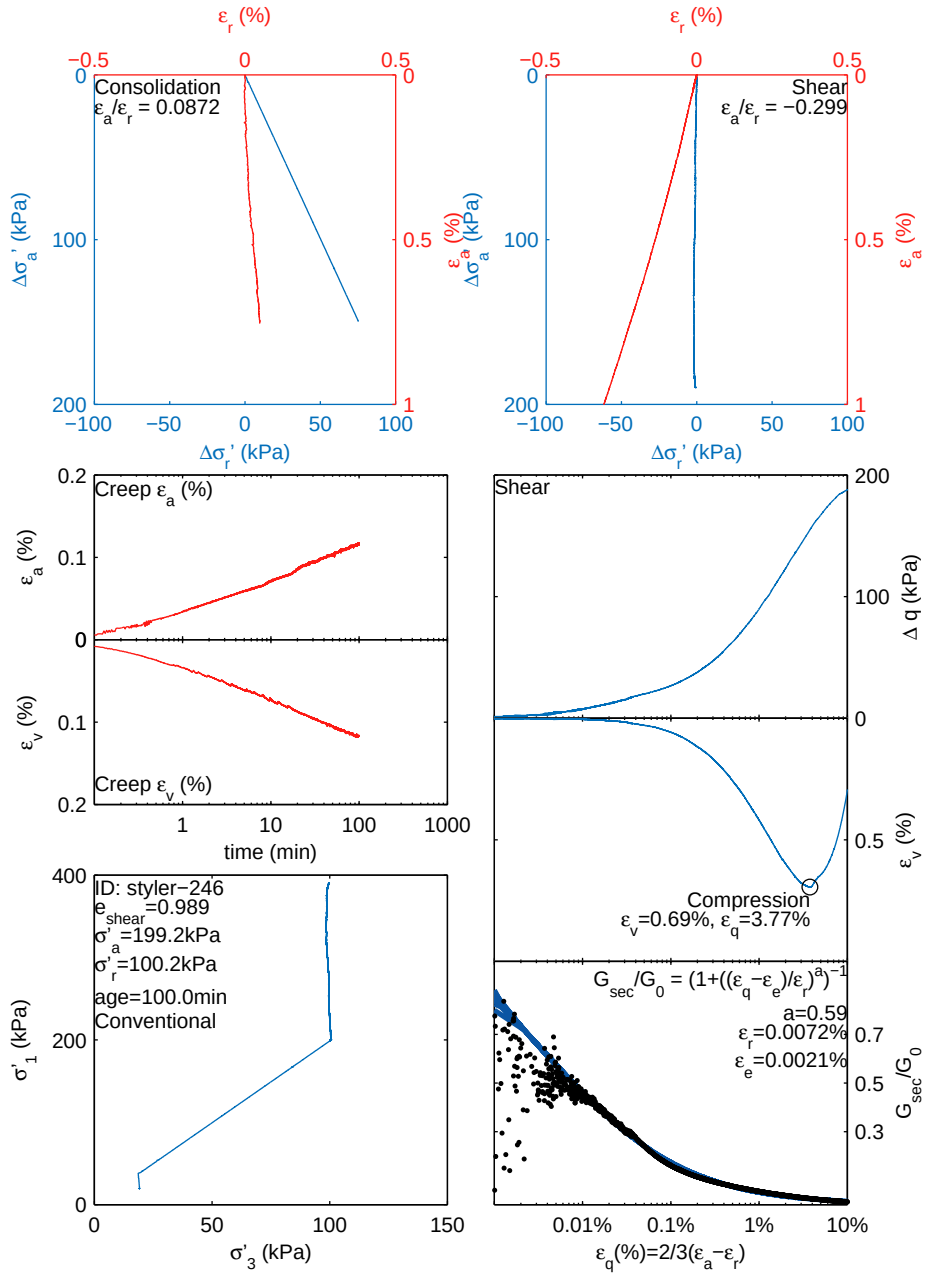

Figure D.25: Styler-246: $\sigma_a = 199.2$ kPa, $\sigma_r = 100.2$ kPa, age=100.0 min, Stress path=C

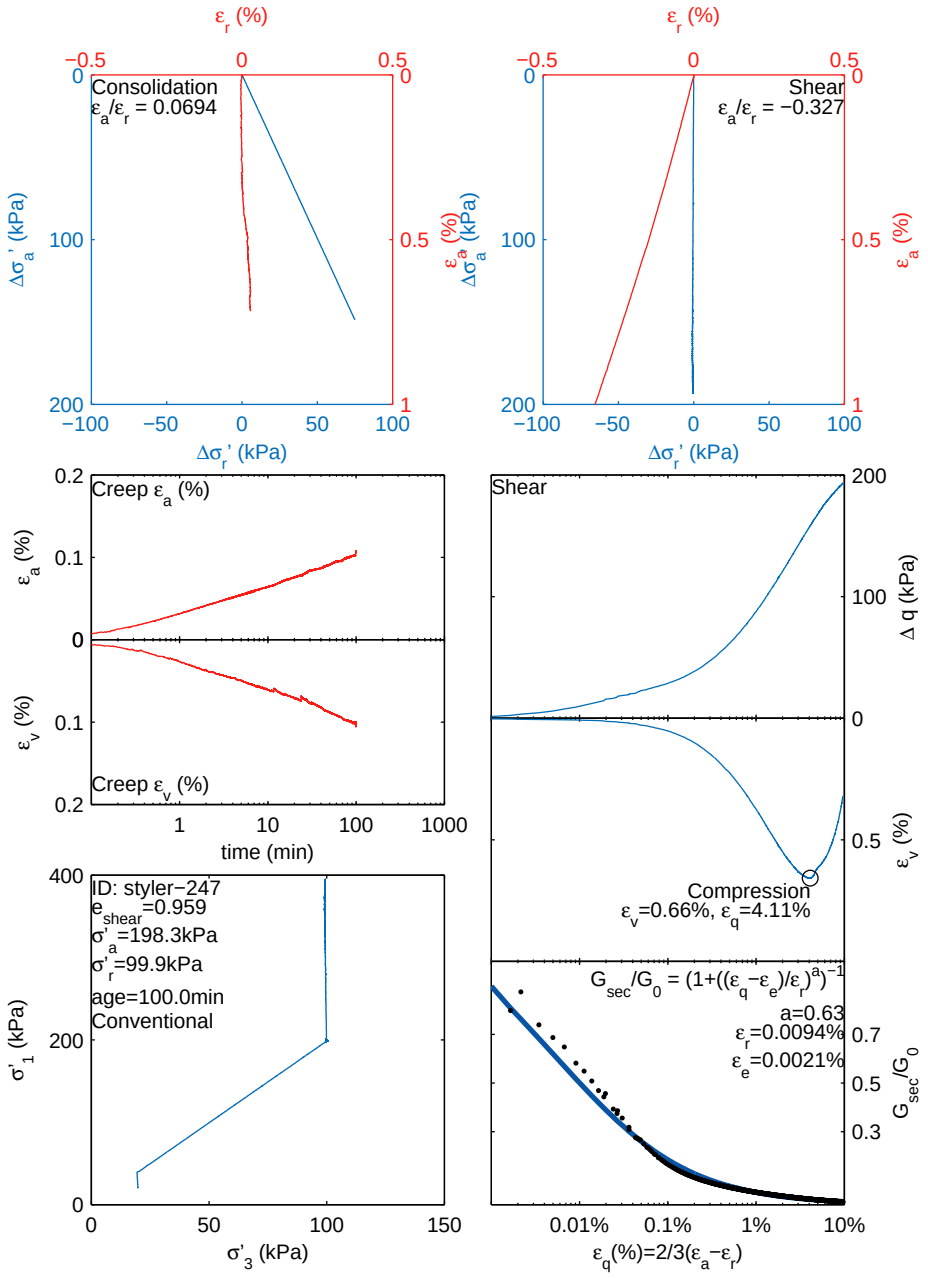

Figure D.26: Styler-247: σ_a = 198.3 kPa, σ_r = 99.9 kPa, age=100.0 min, Stress path=C

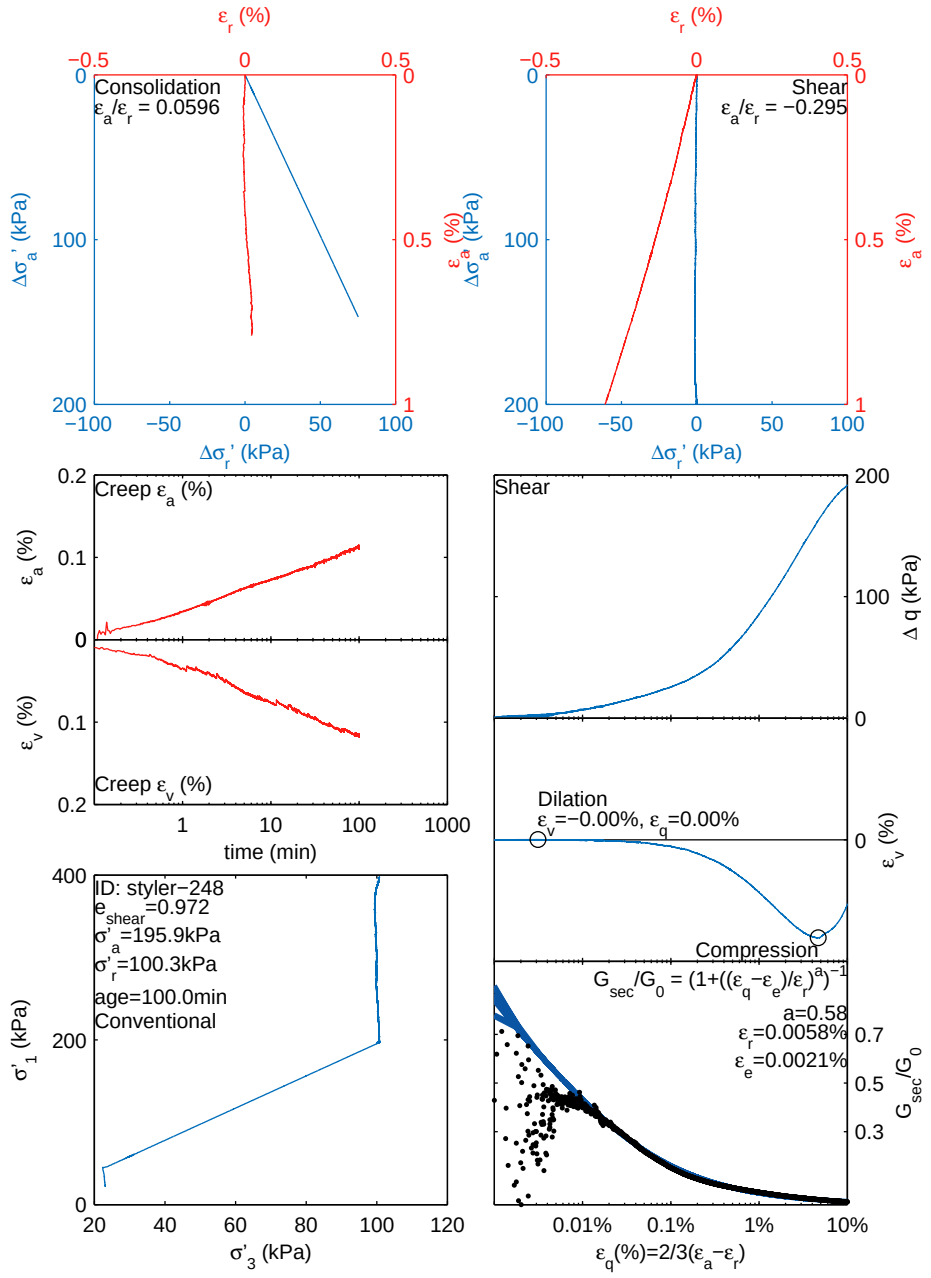

Figure D.27: Styler-248: $\sigma_a = 195.9$ kPa, $\sigma_r = 100.3$ kPa, age=100.0 min, Stress path=C

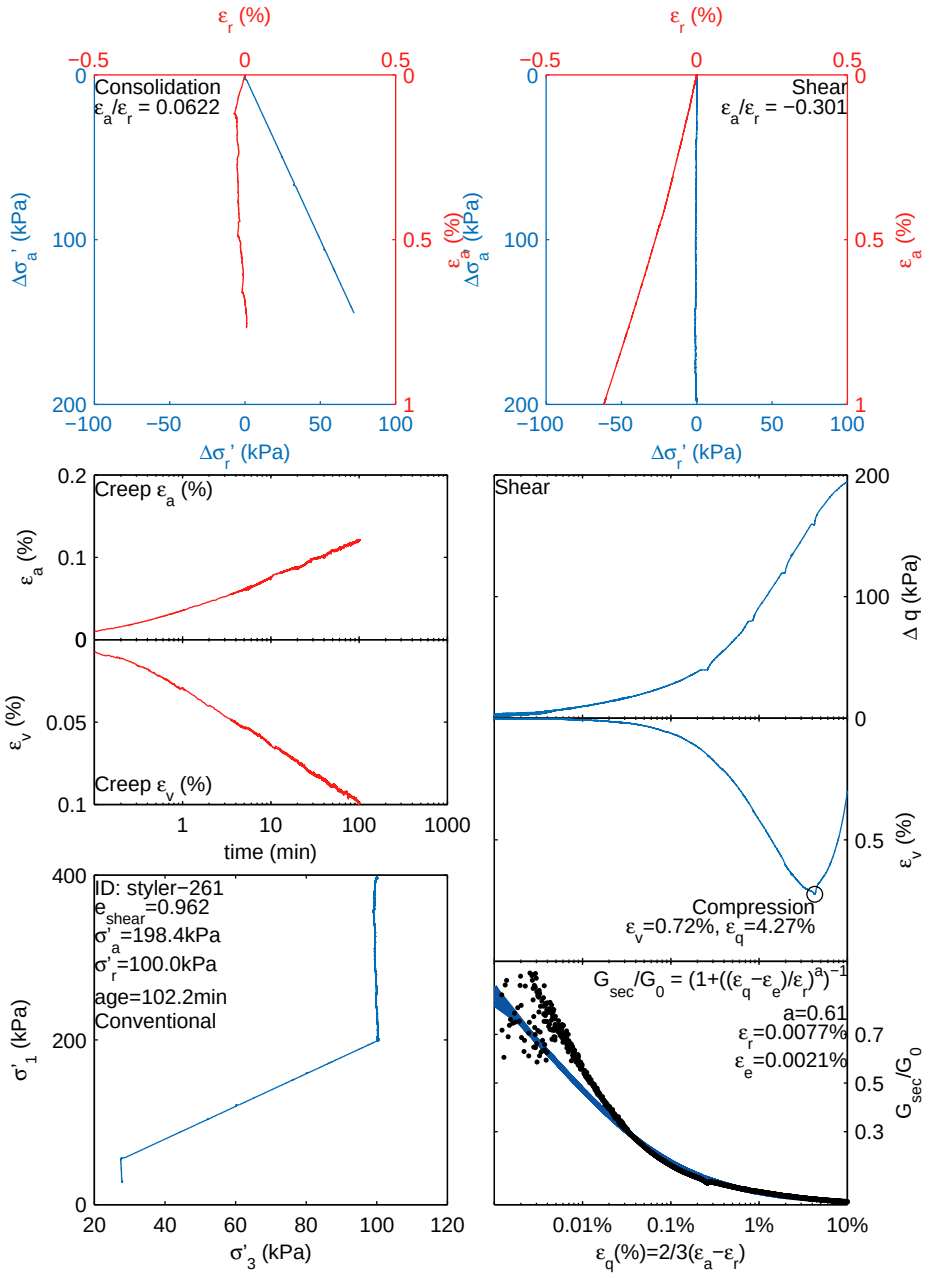

Figure D.28: Styler-261: $\sigma_a = 198.4$ kPa, $\sigma_r = 100.0$ kPa, age=102.2 min, Stress path=C

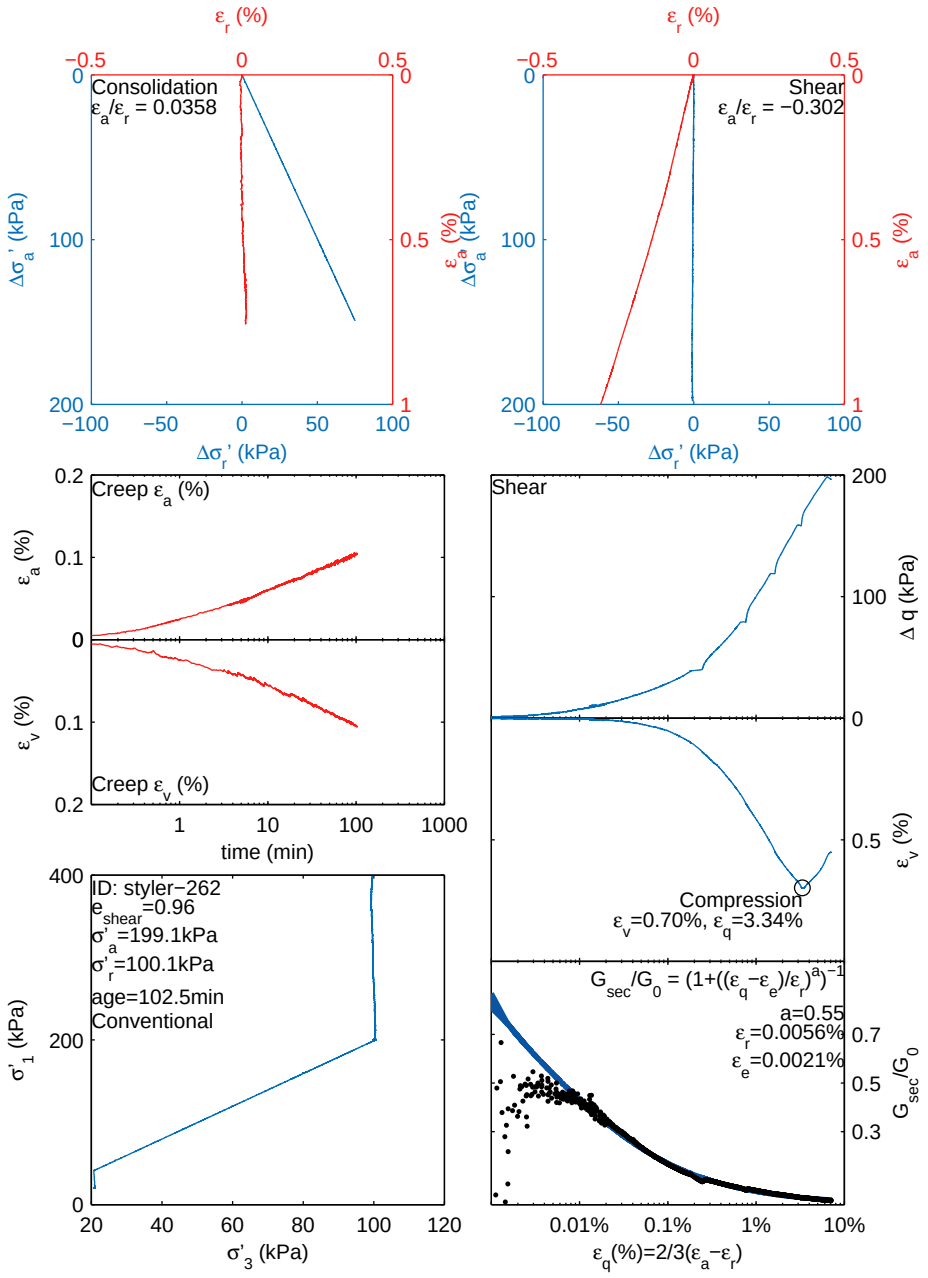

Figure D.29: Styler-262: $\sigma_a = 199.1$ kPa, $\sigma_r = 100.1$ kPa, age=102.5 min, Stress path=C

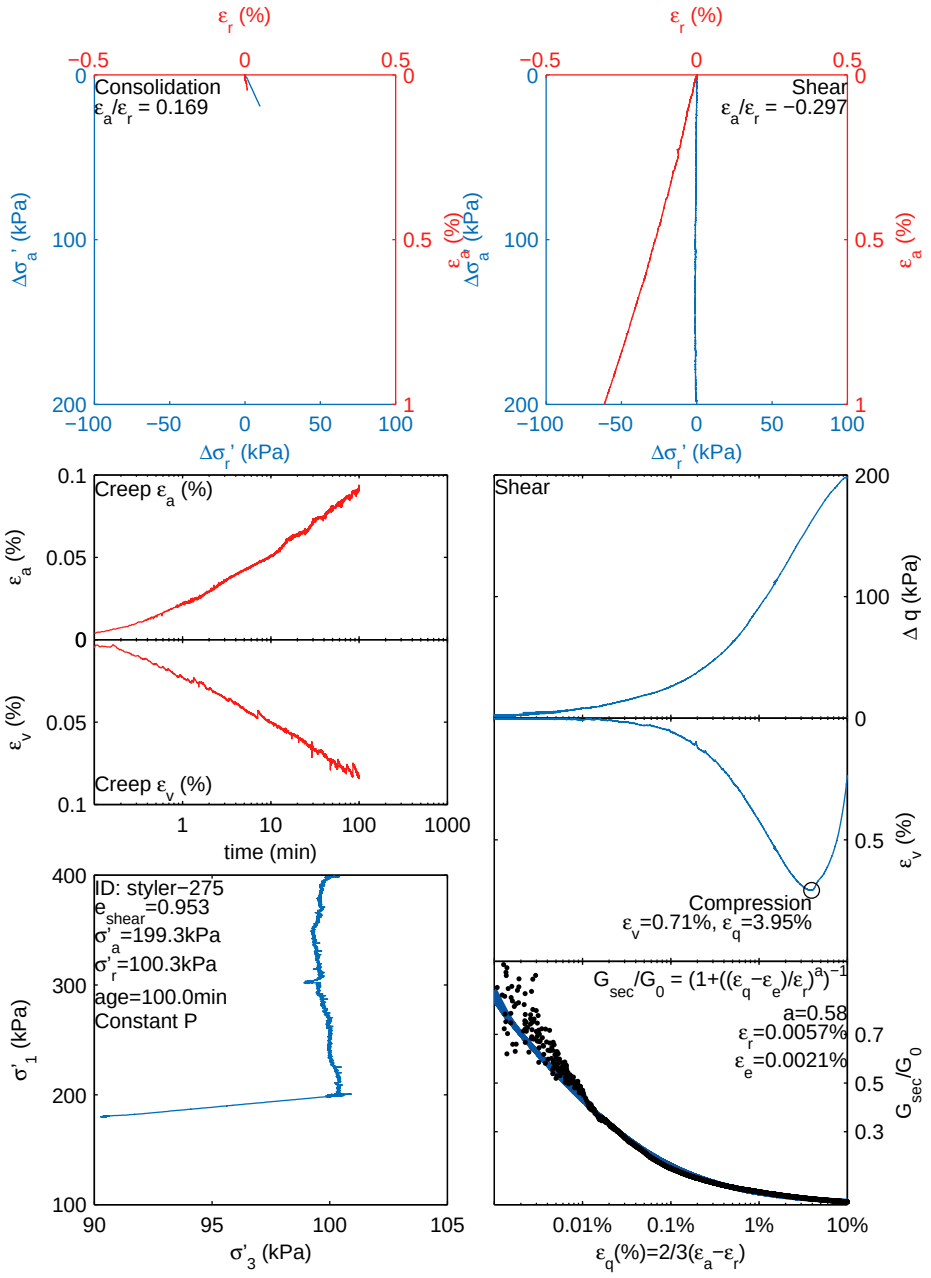

Figure D.30: Styler-275: $\sigma_a = 199.3$ kPa, $\sigma_r = 100.3$ kPa, age=100.0 min, Stress path=P

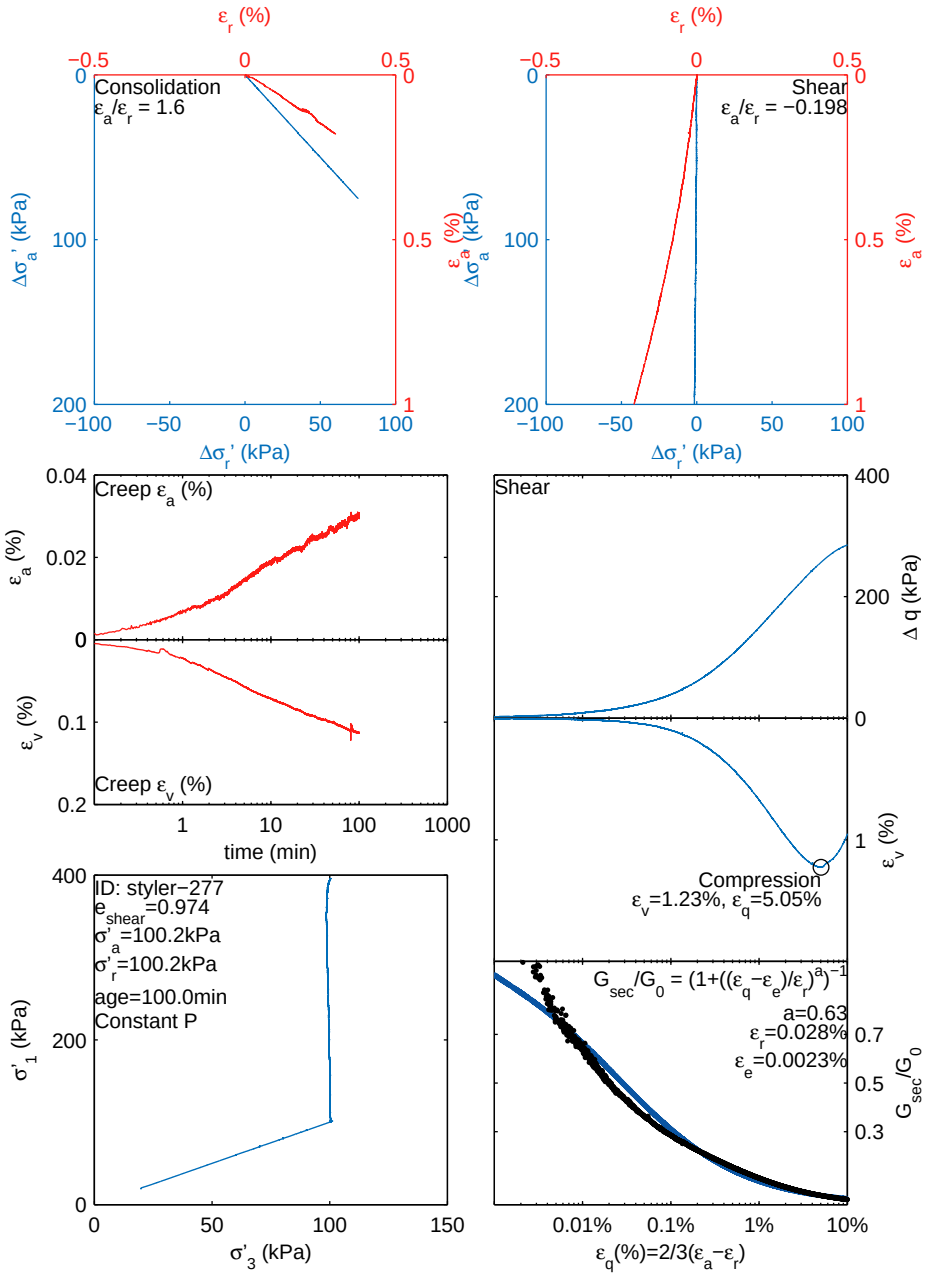

Figure D.31: Styler-277: $\sigma_a = 100.2$ kPa, $\sigma_r = 100.2$ kPa, age=100.0 min, Stress path=P

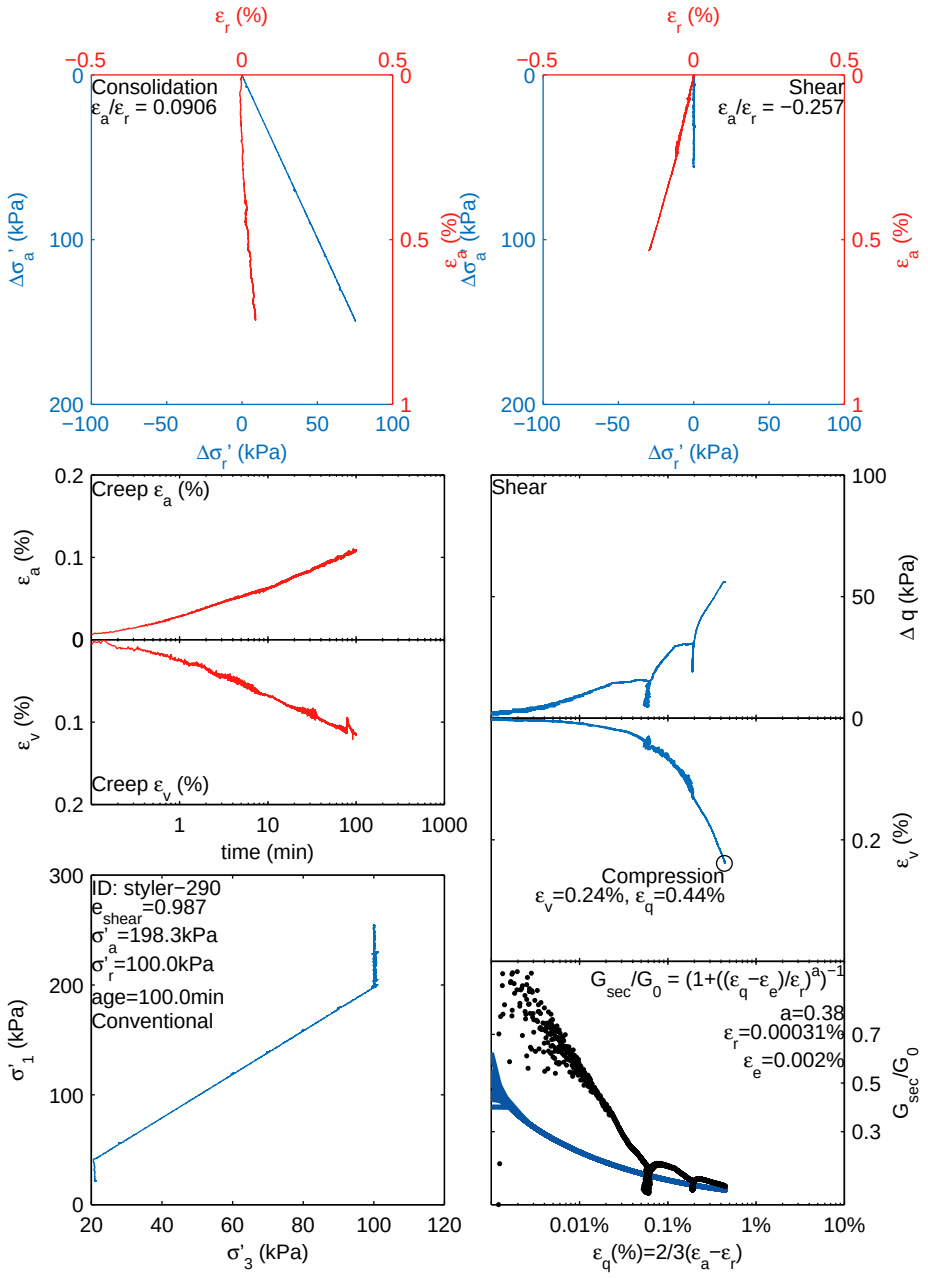

Figure D.32: Styler-290: $\sigma_a = 198.3$ kPa, $\sigma_r = 100.0$ kPa, age=100.0 min, Stress path=C

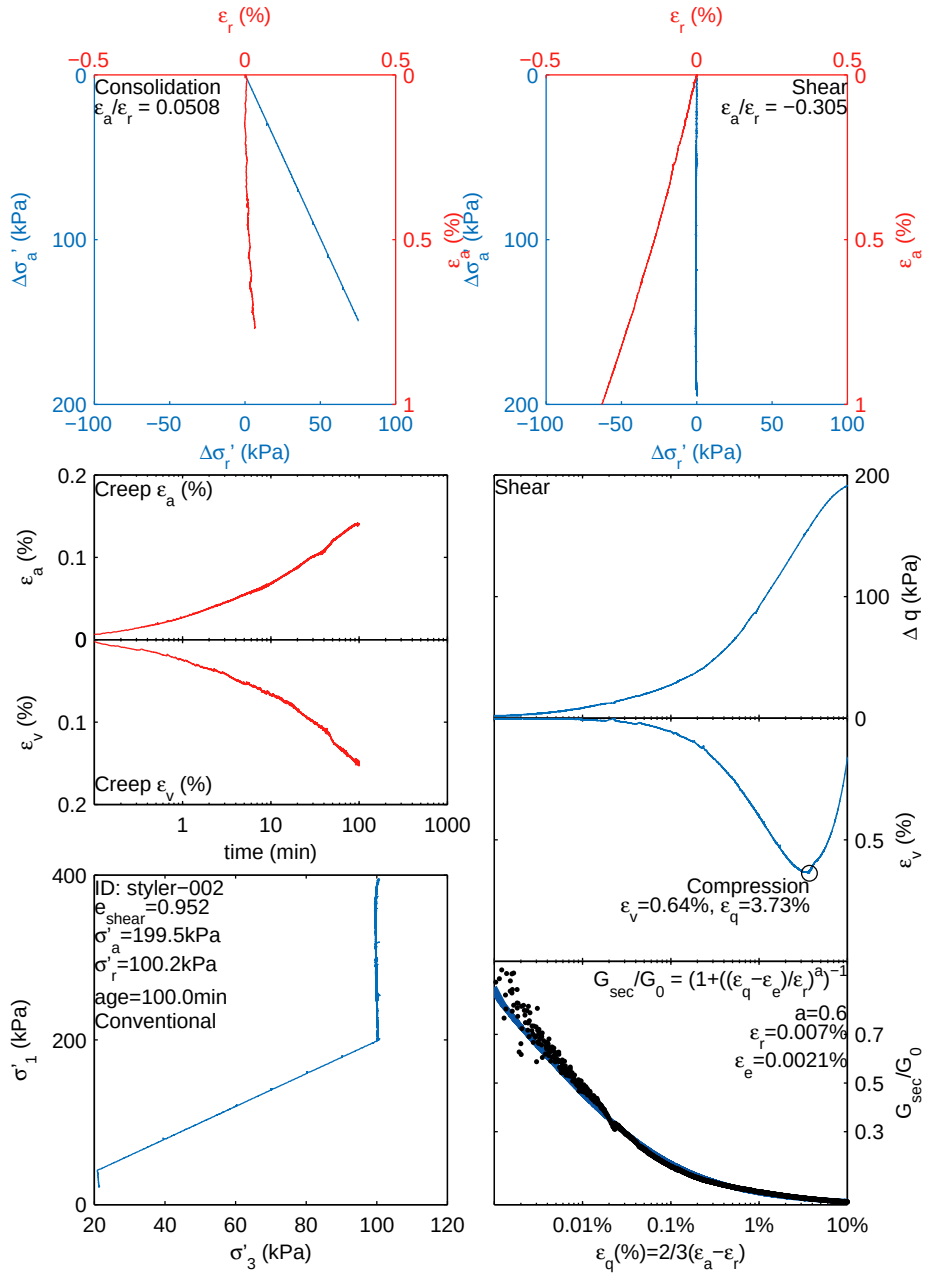

Figure D.33: Styler-002: $\sigma_a = 199.5$ kPa, $\sigma_r = 100.2$ kPa, age=100.0 min, Stress path=C

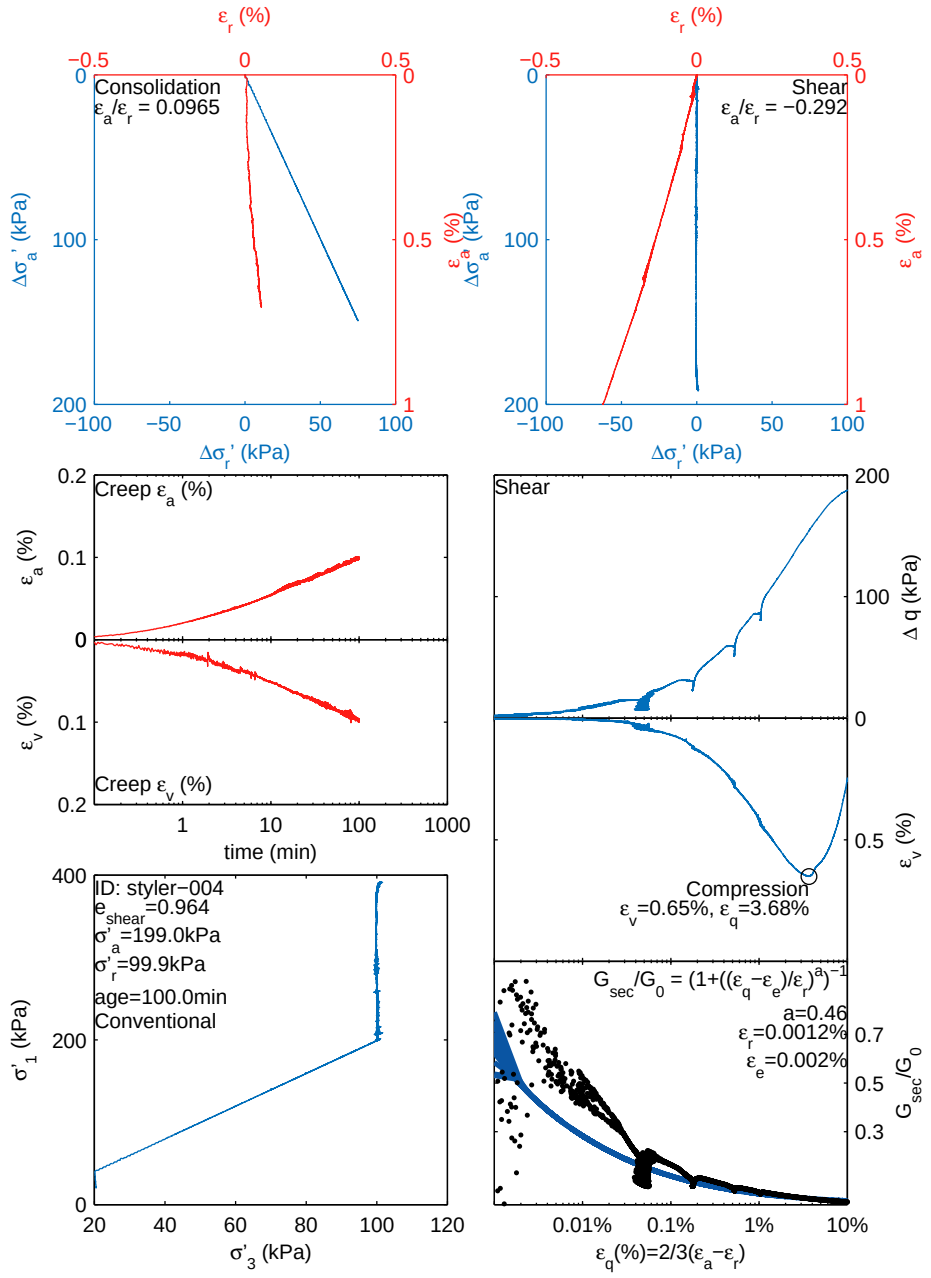

Figure D.34: Styler-004: σ_a = 199.0 kPa, σ_r = 99.9 kPa, age=100.0 min, Stress path=C

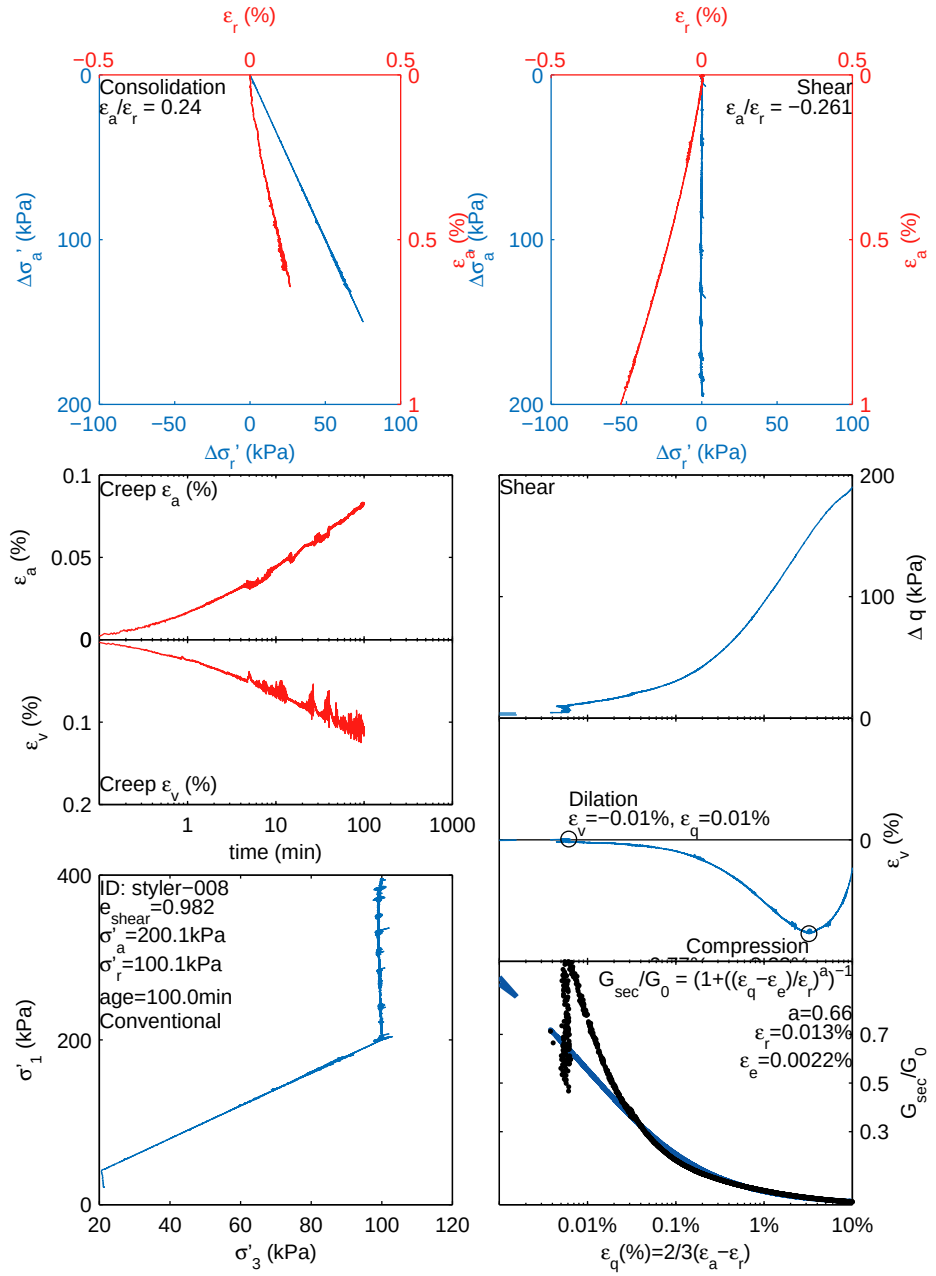

Figure D.35: Styler-008: $\sigma_a = 200.1$ kPa, $\sigma_r = 100.1$ kPa, age=100.0 min, Stress path=C

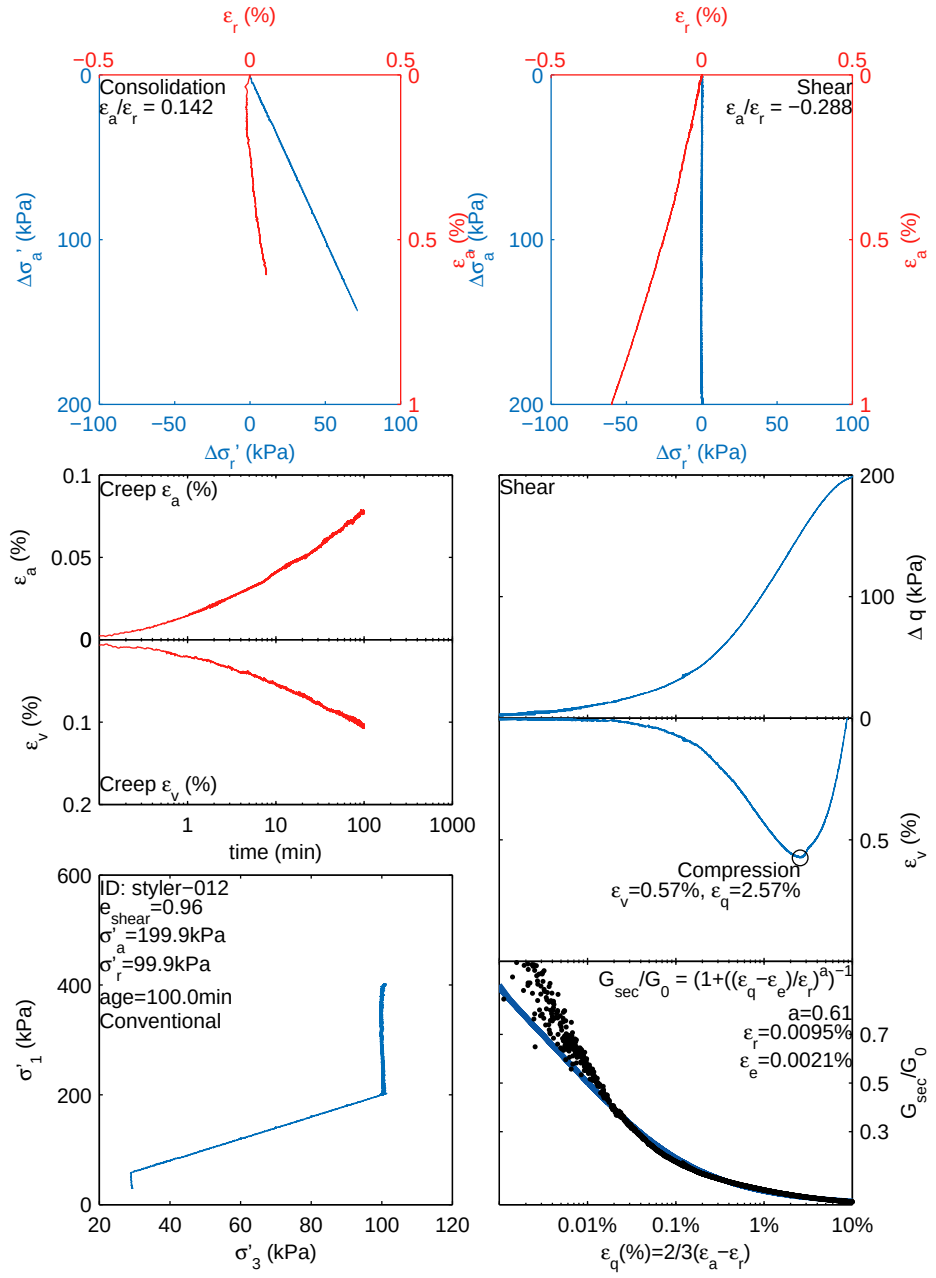

Figure D.36: Styler-012: σ_a = 199.9 kPa, σ_r = 99.9 kPa, age=100.0 min, Stress path=C

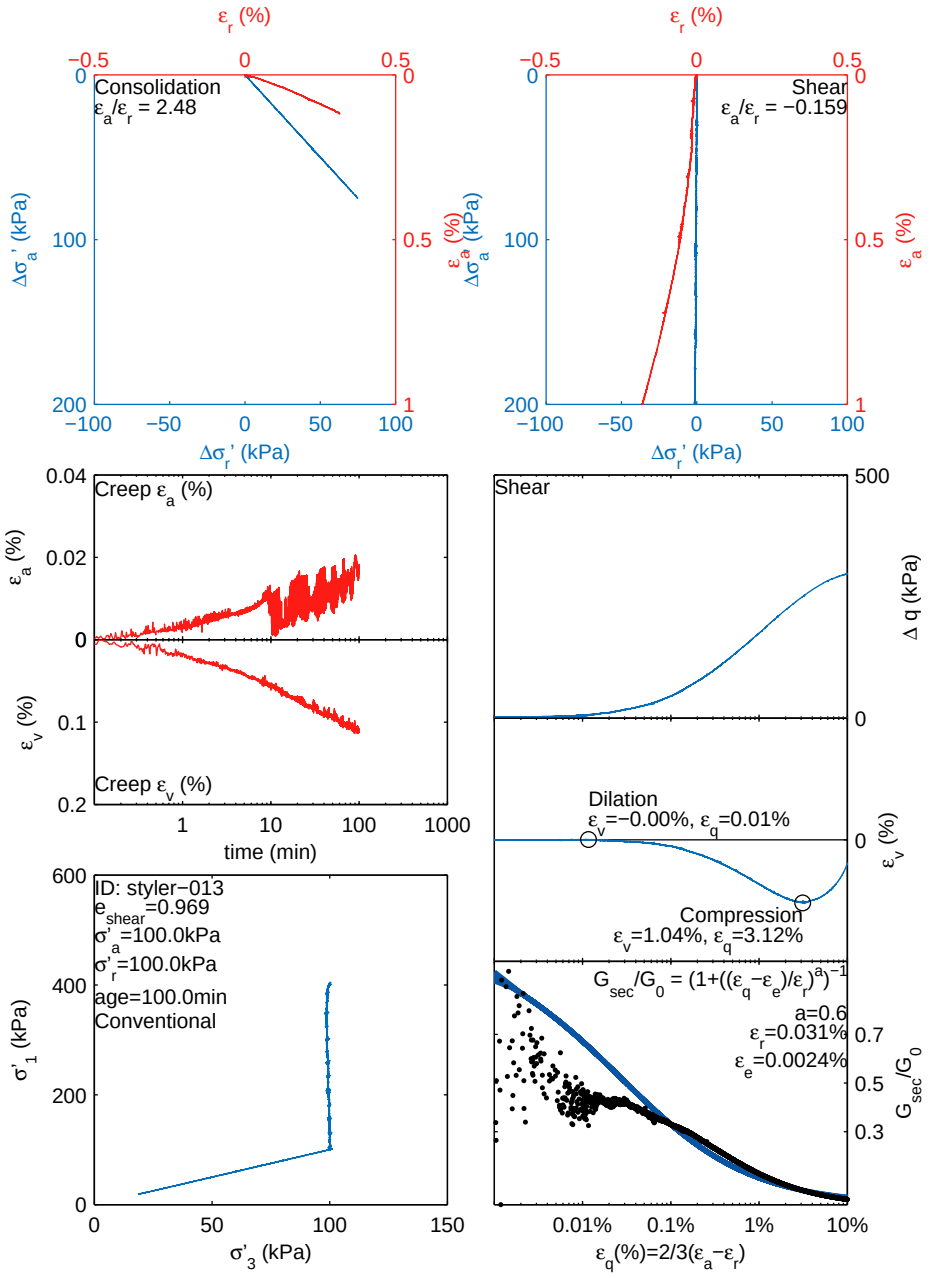

Figure D.37: Styler-013: $\sigma_a = 100.0$ kPa, $\sigma_r = 100.0$ kPa, age=100.0 min, Stress path=C

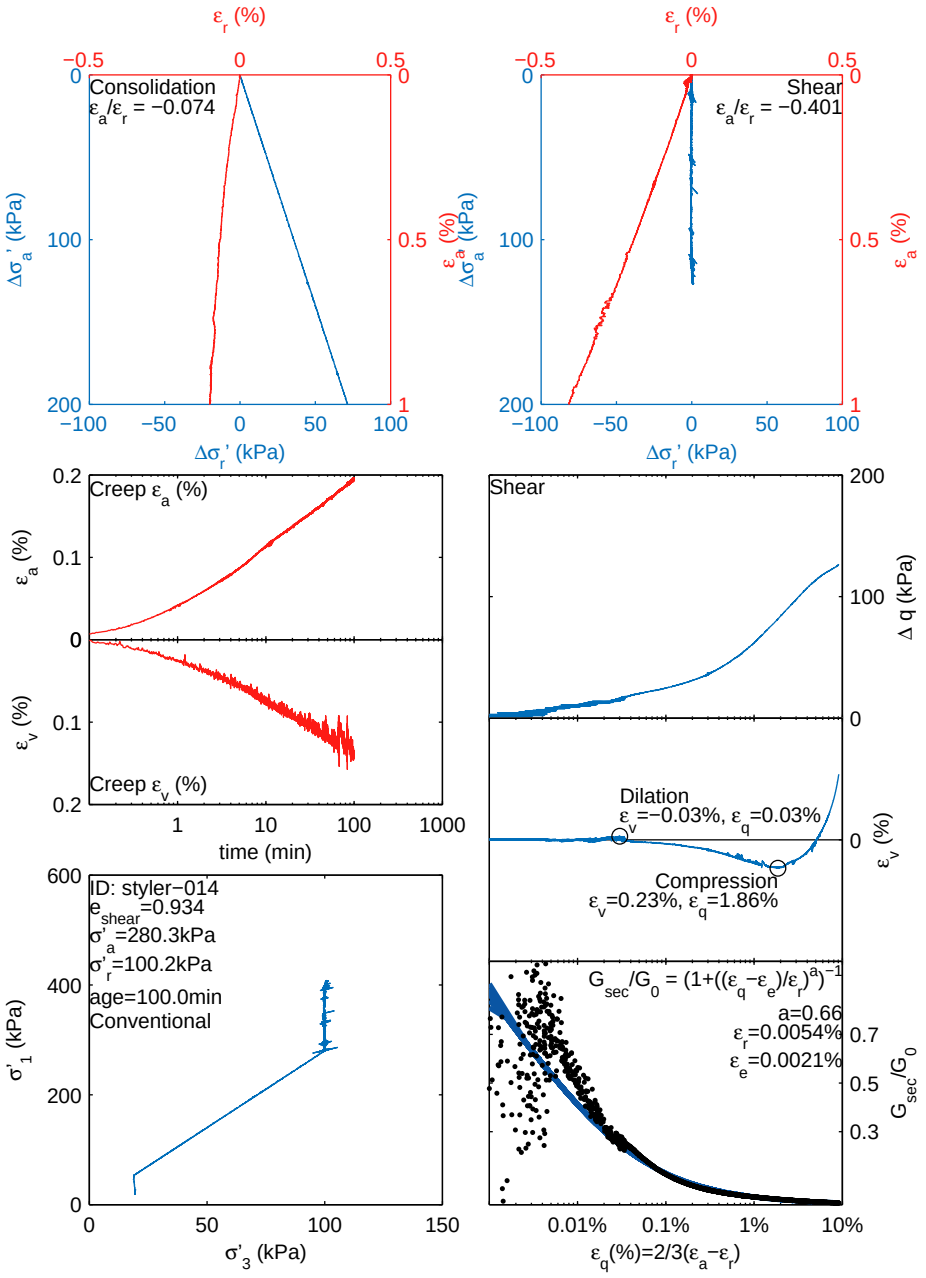

Figure D.38: Styler-014: $\sigma_a = 280.3$ kPa, $\sigma_r = 100.2$ kPa, age=100.0 min, Stress path=C

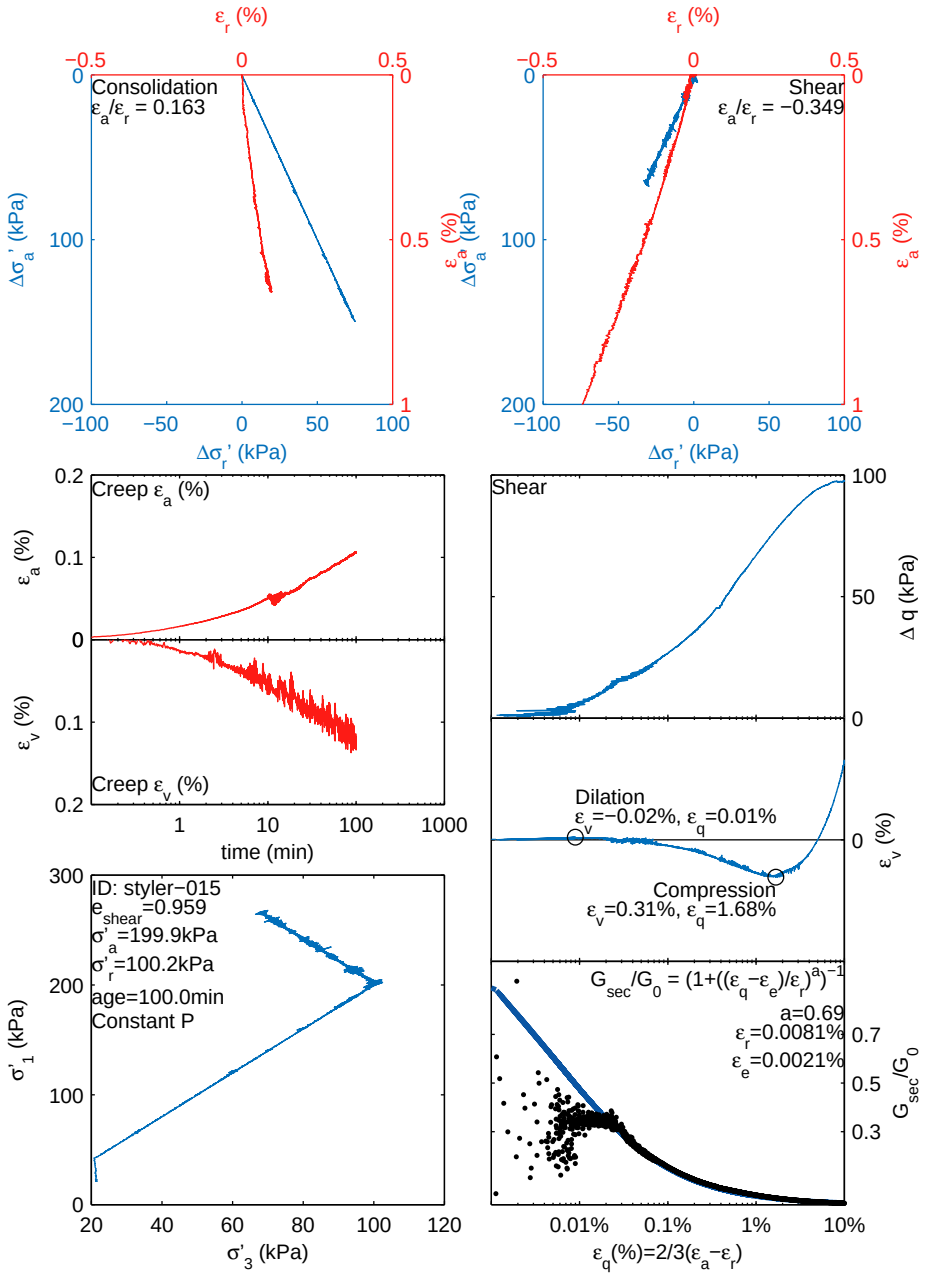

Figure D.39: Styler-015: $\sigma_a = 199.9$ kPa, $\sigma_r = 100.2$ kPa, age=100.0 min, Stress path=P

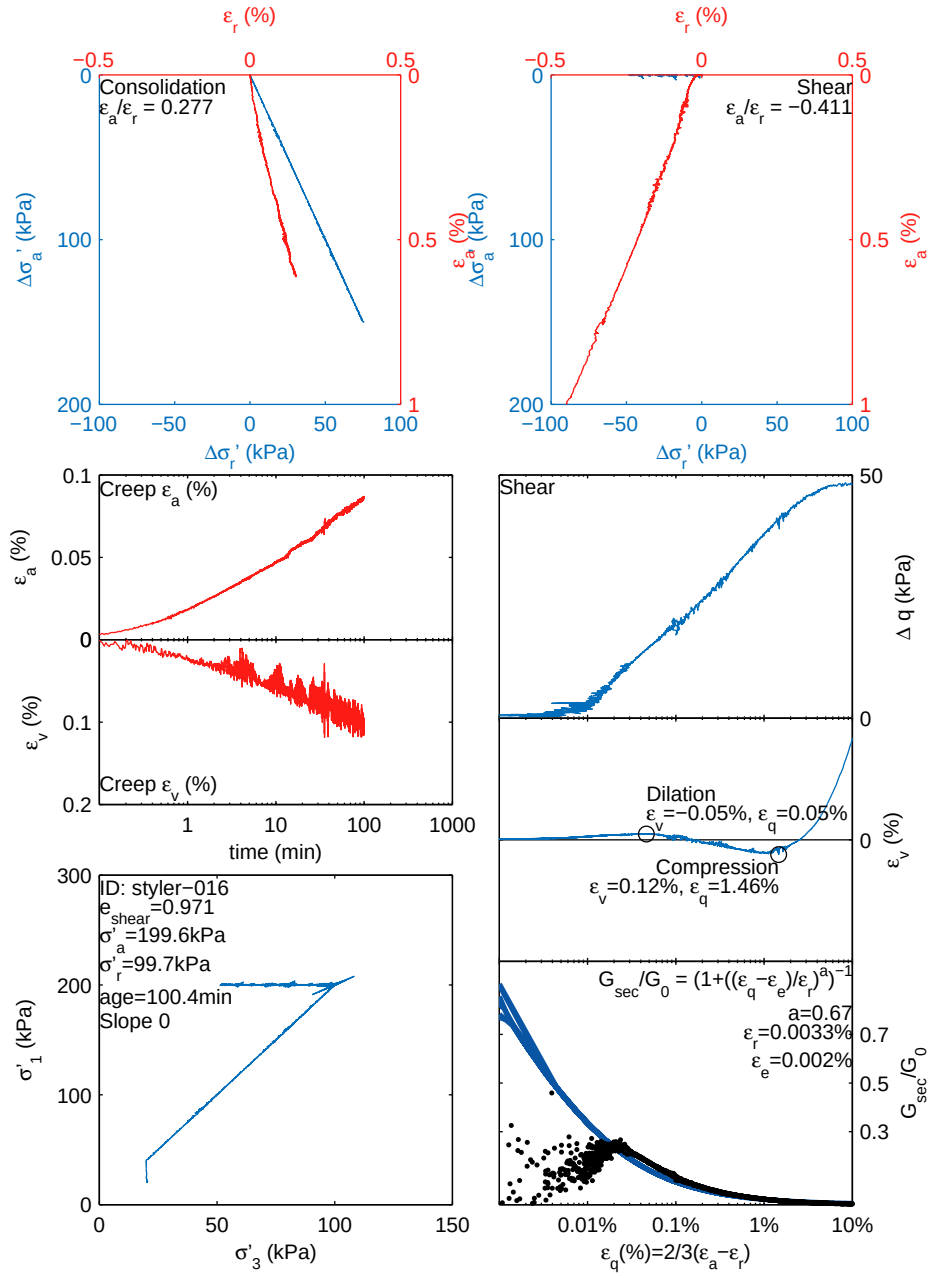

Figure D.40: Styler-016: σ_a = 199.6 kPa, σ_r = 99.7 kPa, age=100.4 min, Stress path=0

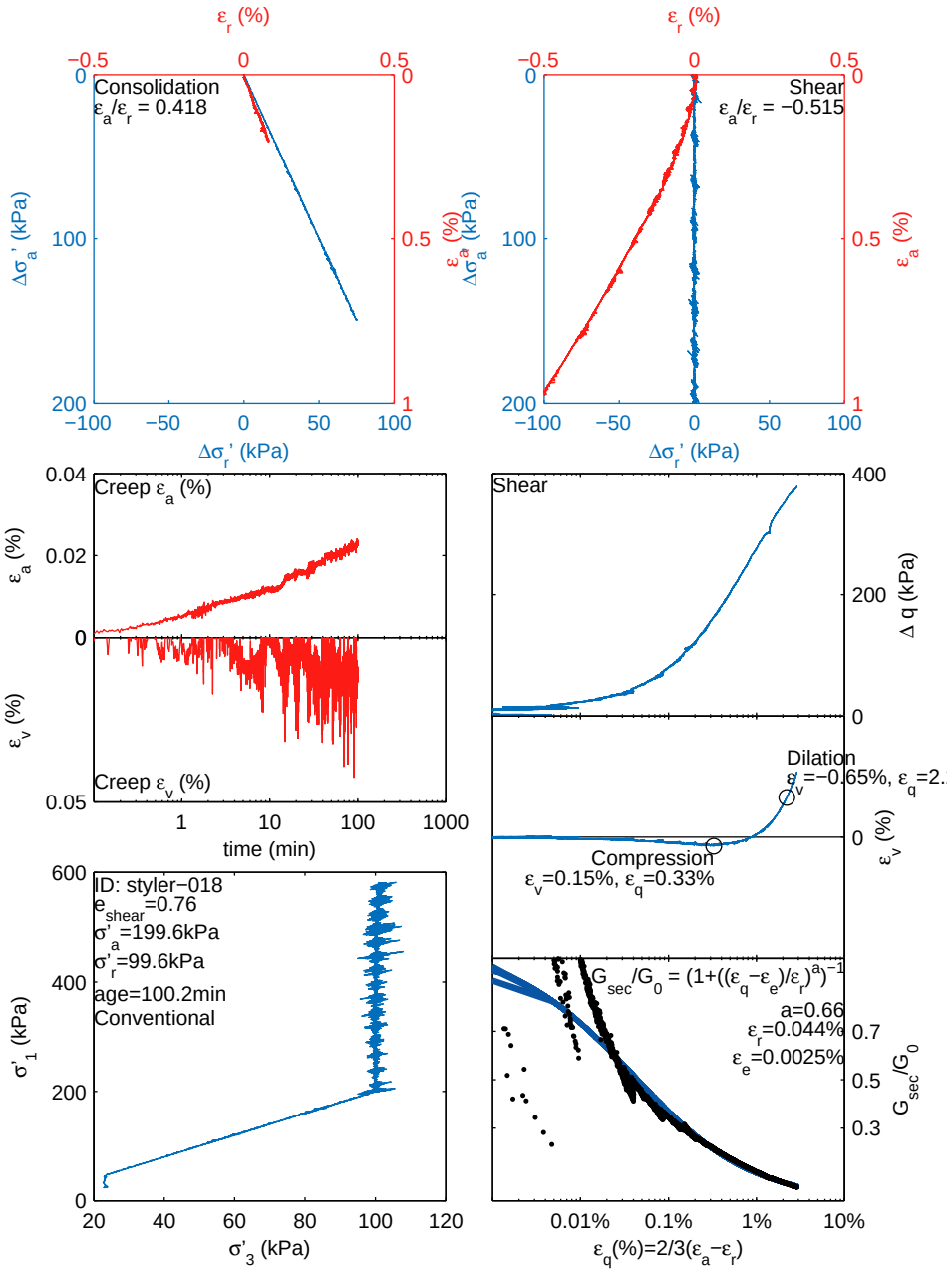

Figure D.41: Styler-018: σ_a = 199.6 kPa, σ_r = 99.6 kPa, age=100.2 min, Stress path=C

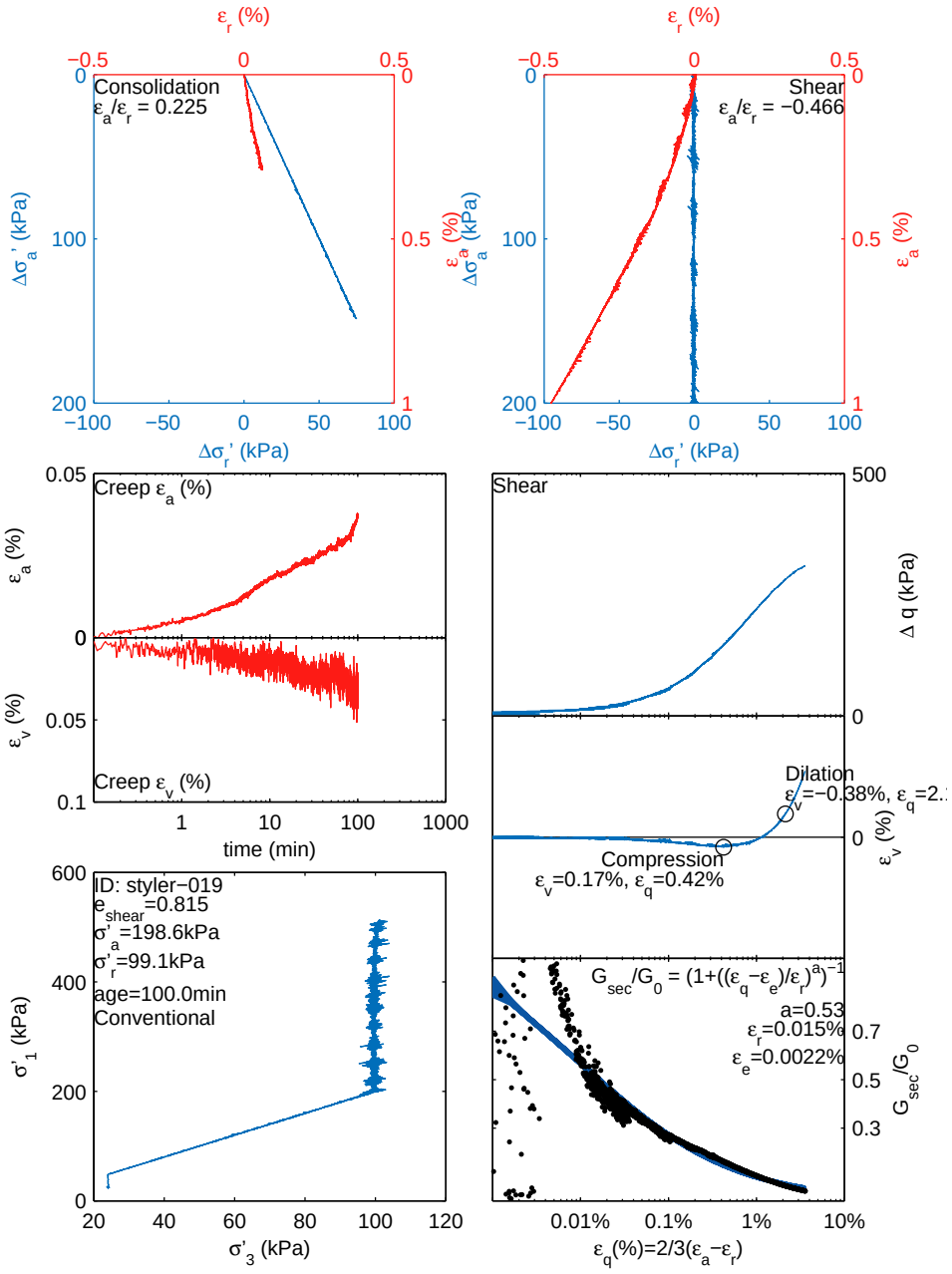

Figure D.42: Styler-019: σ_a = 198.6 kPa, σ_r = 99.1 kPa, age=100.0 min, Stress path=C

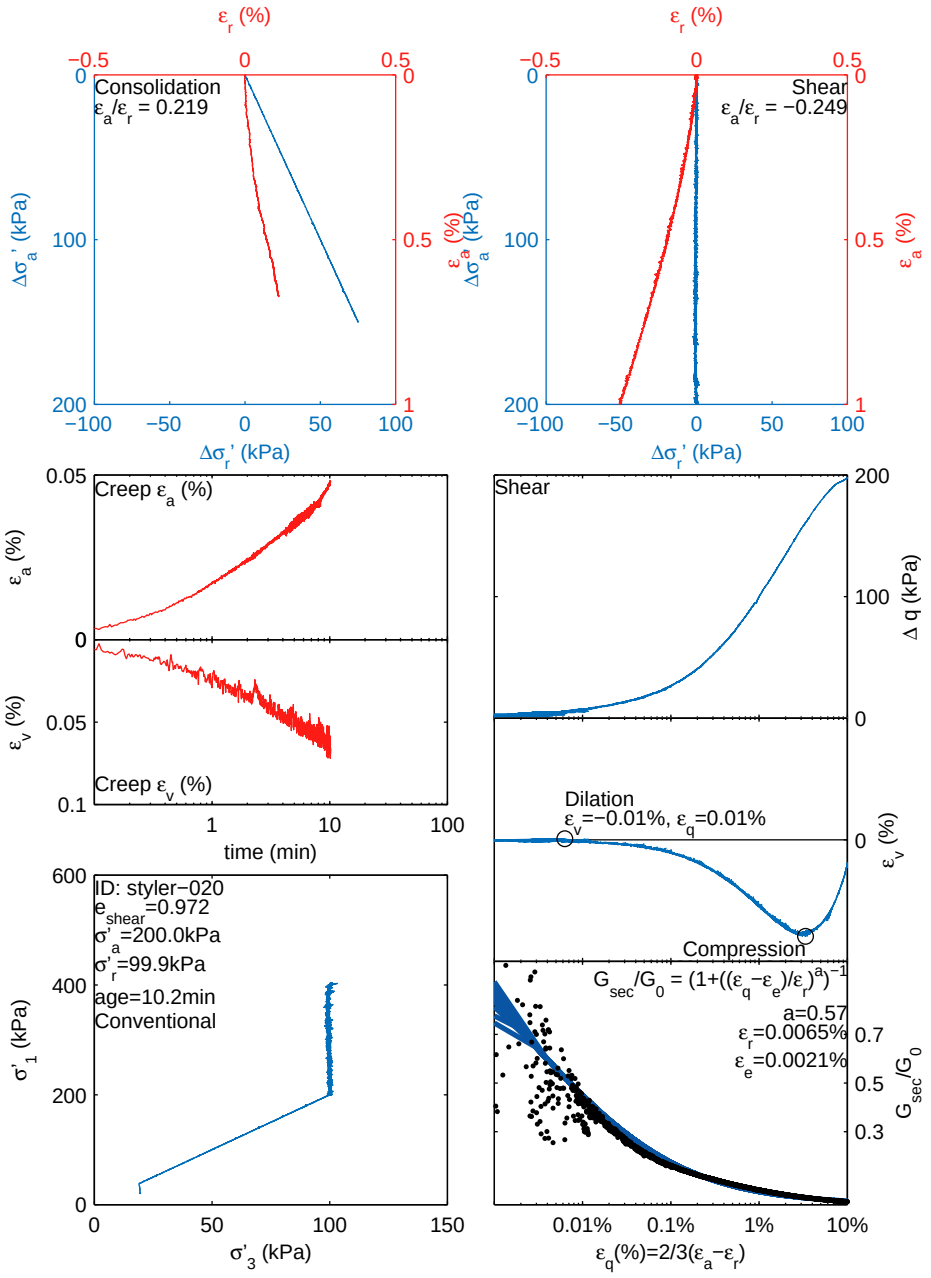

Figure D.43: Styler-020: σ_a = 200.0 kPa, σ_r = 99.9 kPa, age=10.2 min, Stress path=C

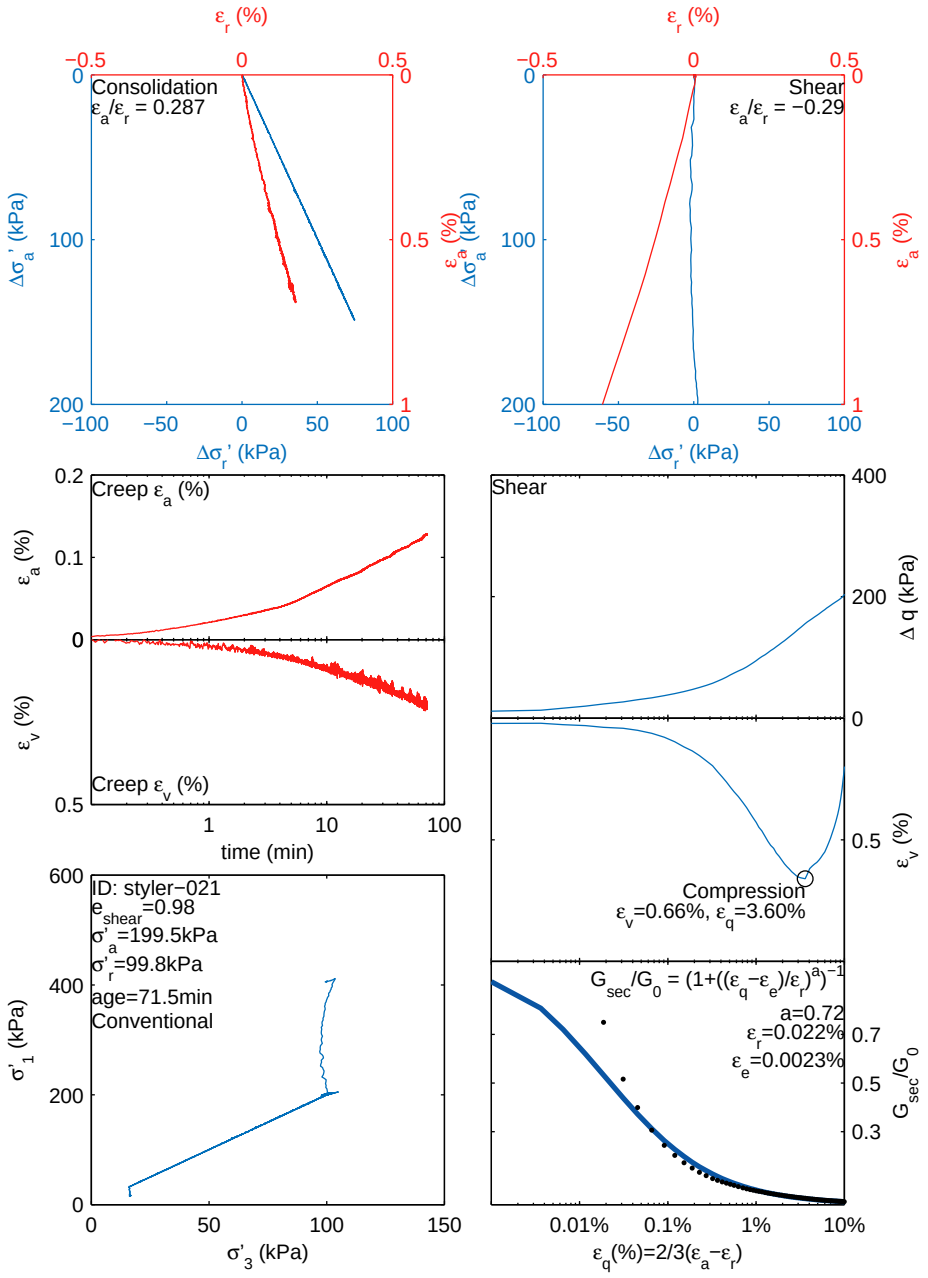

Figure D.44: Styler-021: σ_a = 199.5 kPa, σ_r = 99.8 kPa, age=71.5 min, Stress path=C

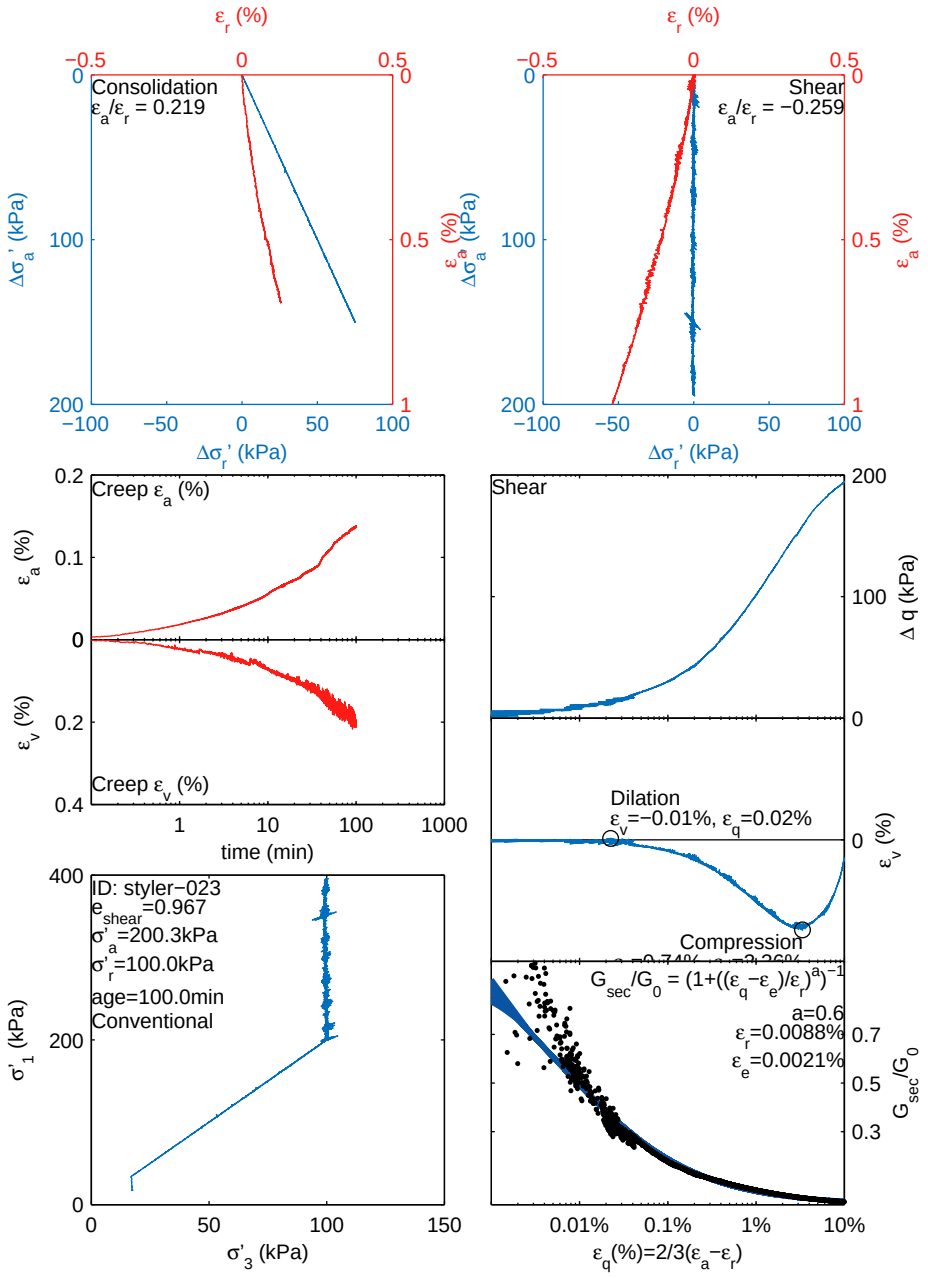

Figure D.45: Styler-023: $\sigma_a = 200.3$ kPa, $\sigma_r = 100.0$ kPa, age=100.0 min, Stress path=C

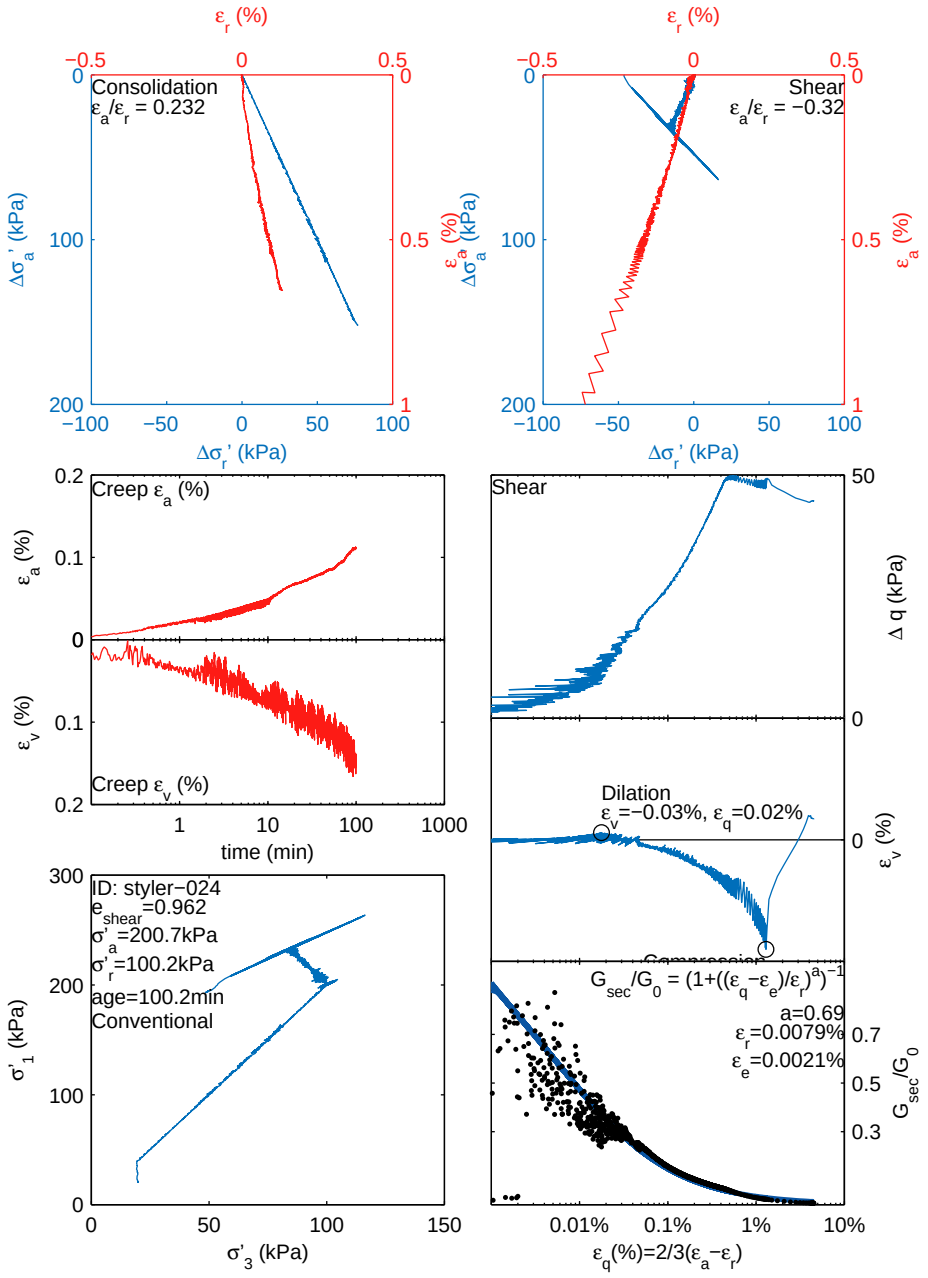

Figure D.46: Styler-024: $\sigma_a = 200.7$ kPa, $\sigma_r = 100.2$ kPa, age=100.2 min, Stress path=C

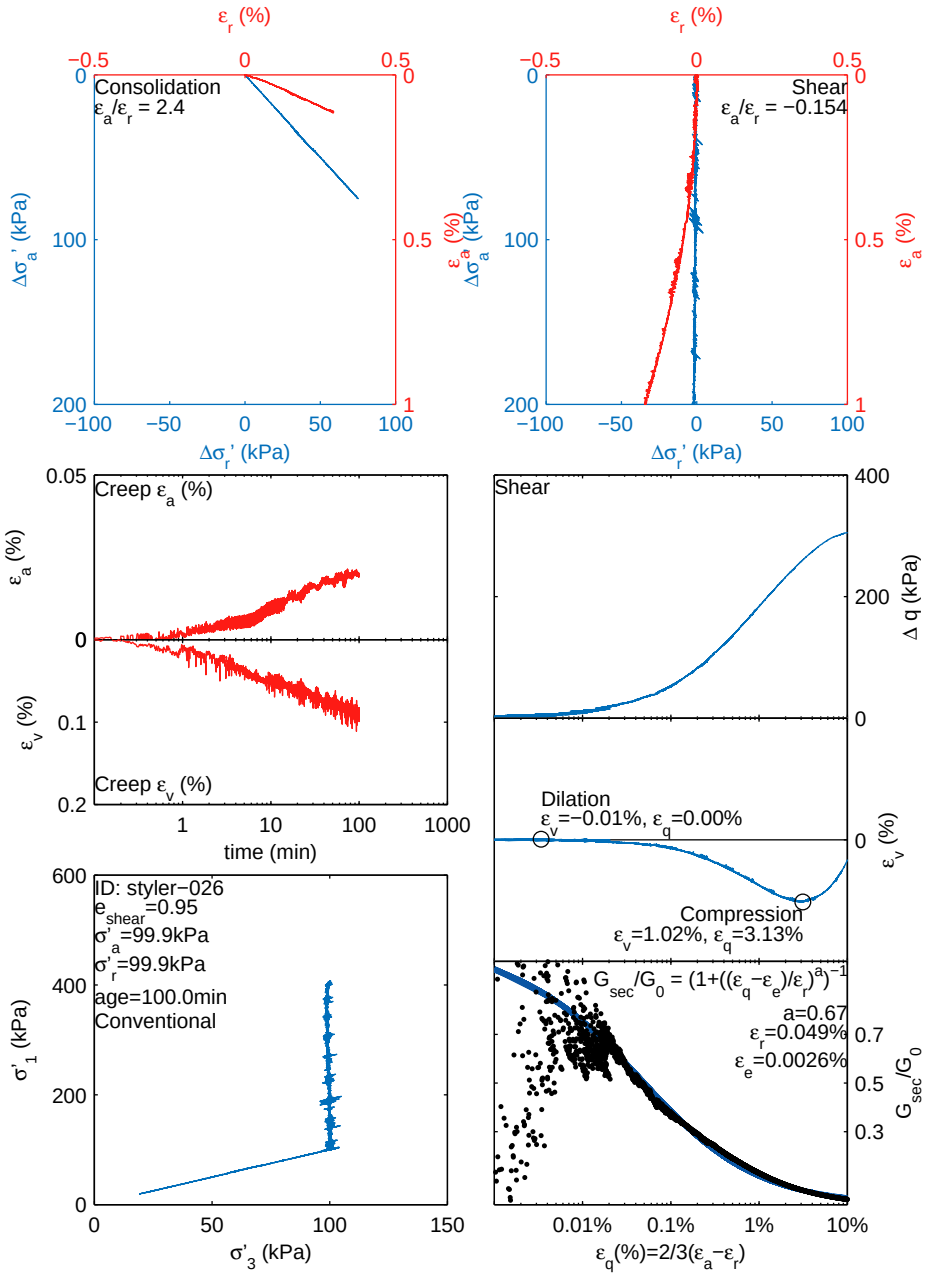

Figure D.47: Styler-026: σ_a = 99.9 kPa, σ_r = 99.9 kPa, age=100.0 min, Stress path=C

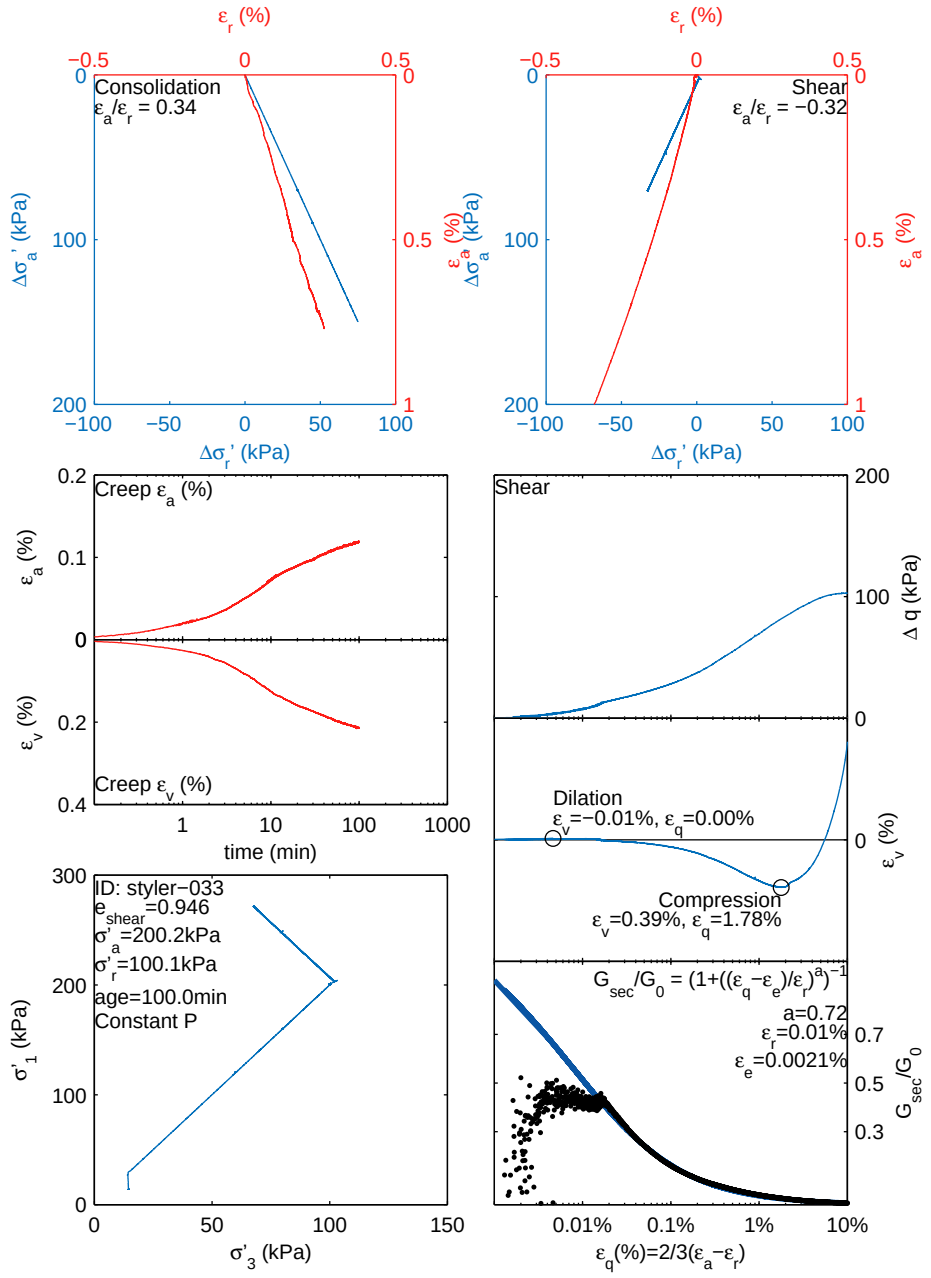

Figure D.48: Styler-033: $\sigma_a = 200.2$ kPa, $\sigma_r = 100.1$ kPa, age=100.0 min, Stress path=P

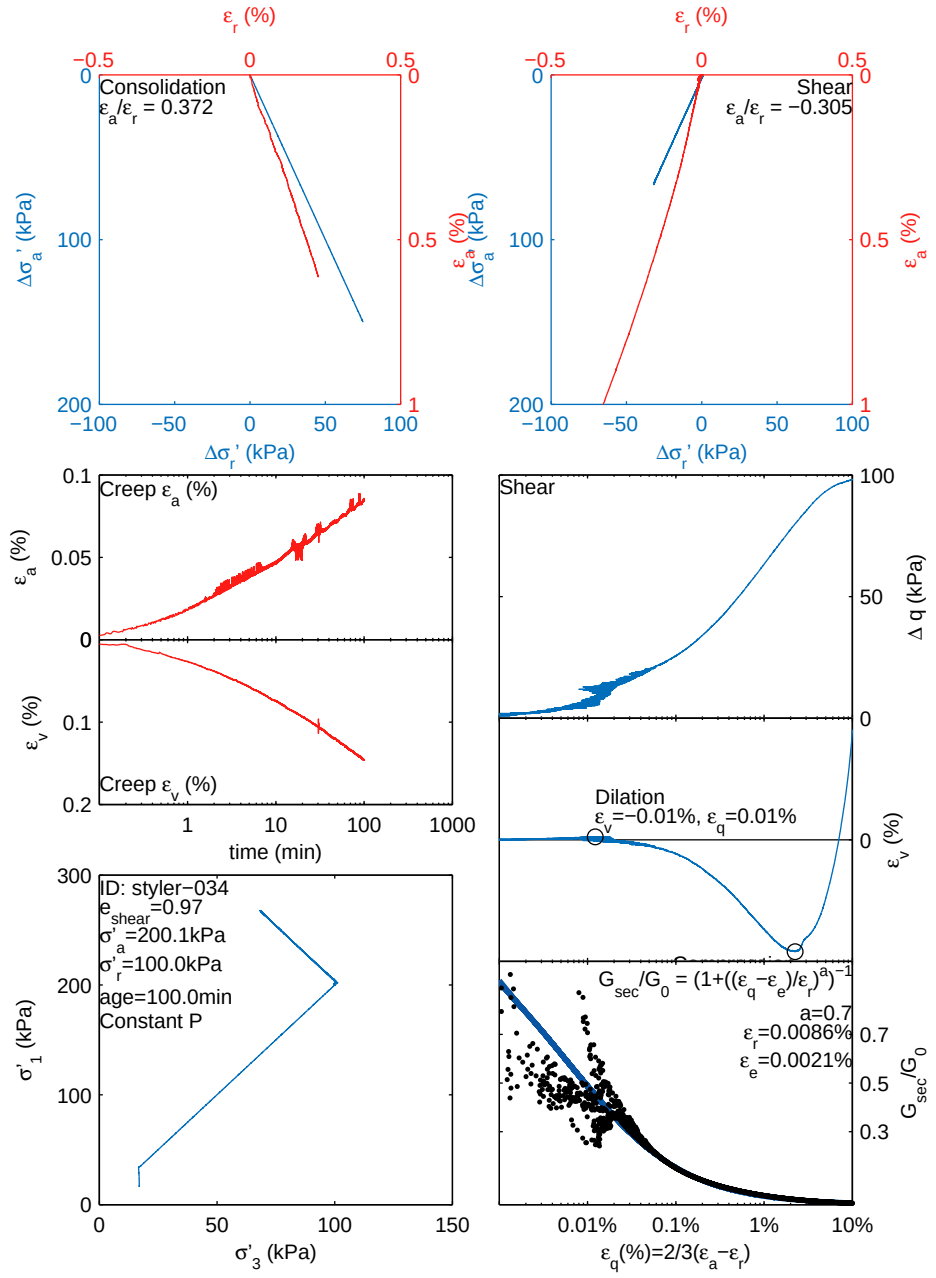

Figure D.49: Styler-034: $\sigma_a = 200.1$ kPa, $\sigma_r = 100.0$ kPa, age=100.0 min, Stress path=P

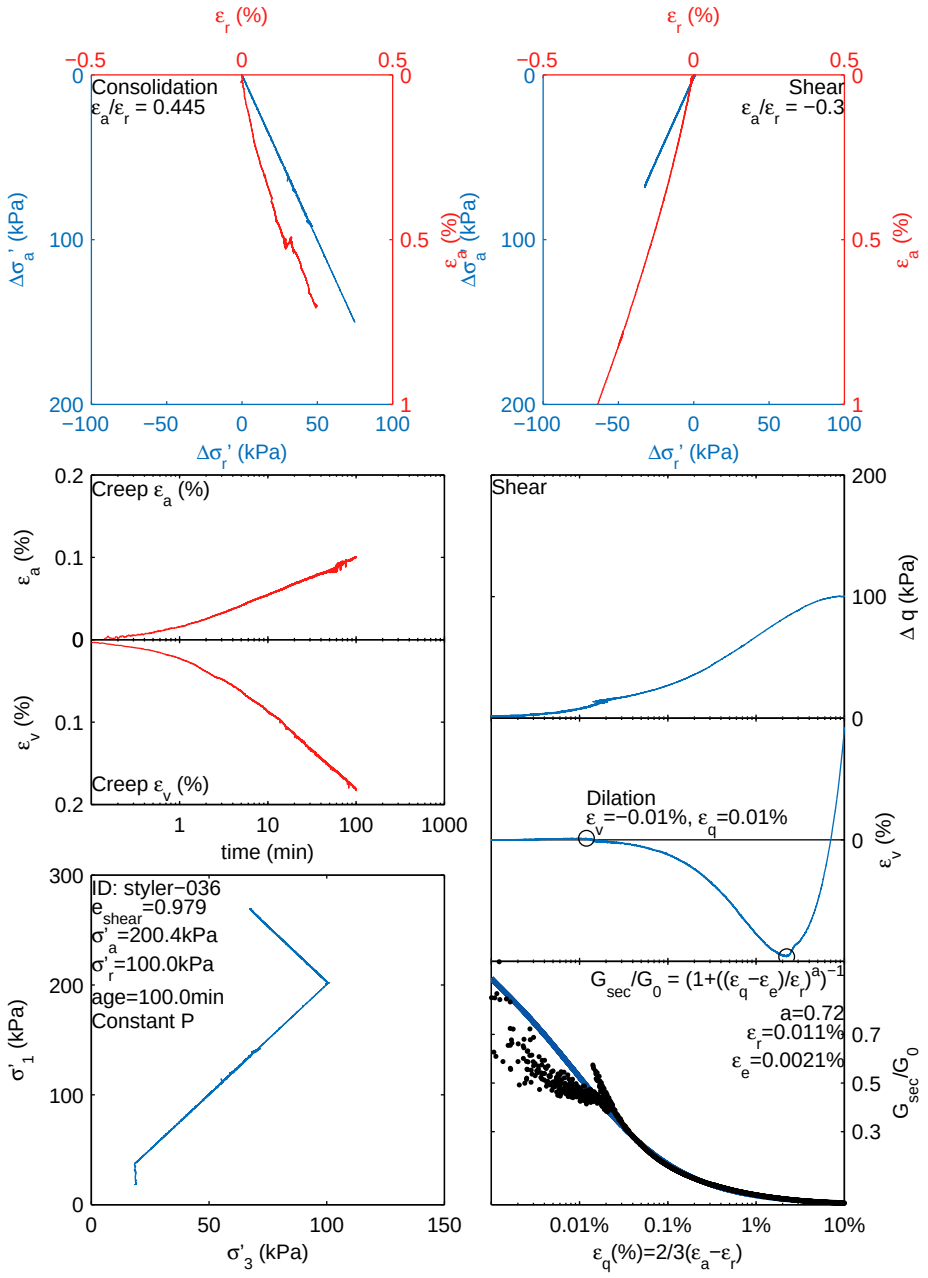

Figure D.50: Styler-036: $\sigma_a = 200.4$ kPa, $\sigma_r = 100.0$ kPa, age=100.0 min, Stress path=P

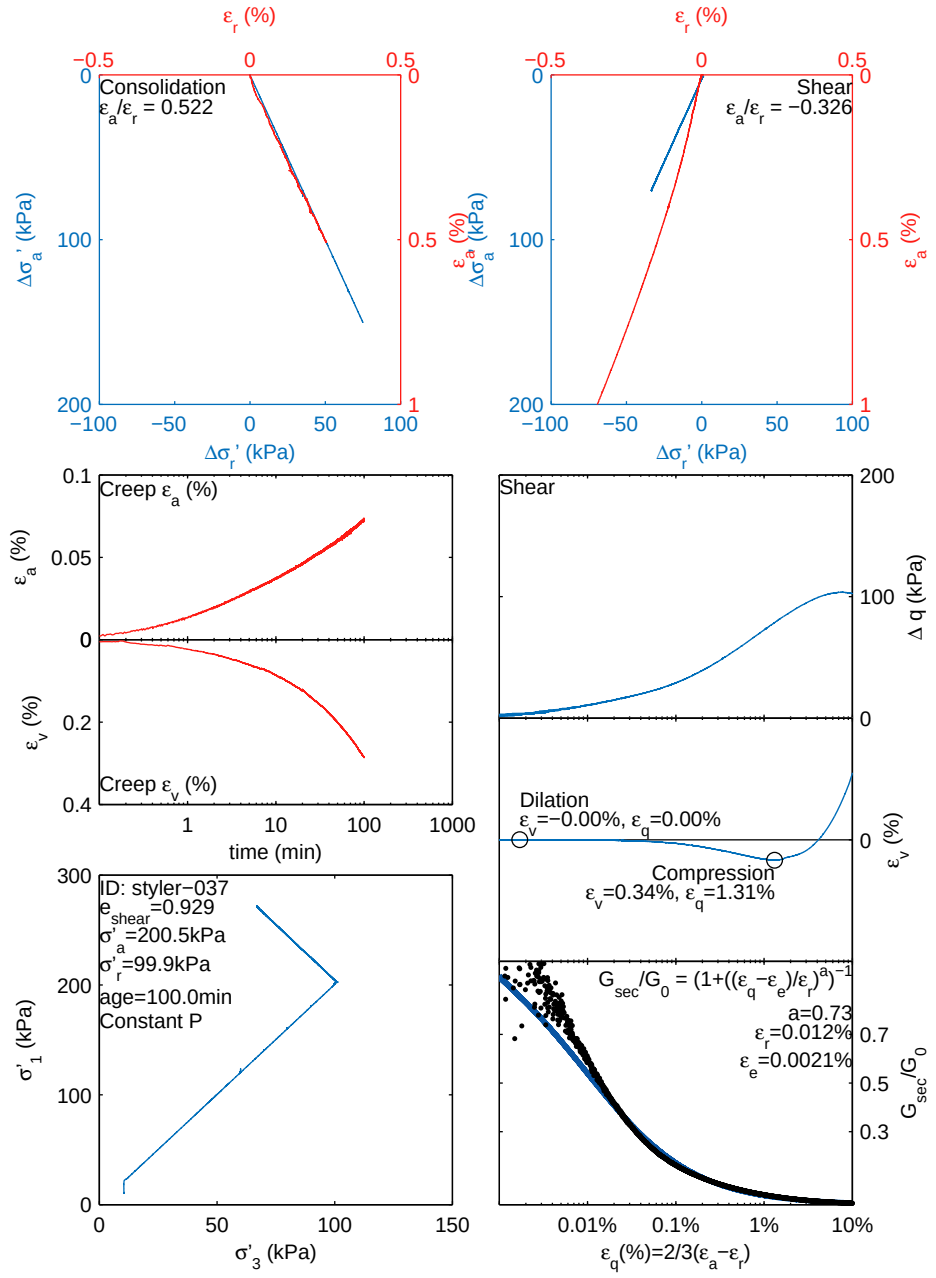

Figure D.51: Styler-037: σ_a = 200.5 kPa, σ_r = 99.9 kPa, age=100.0 min, Stress path=P

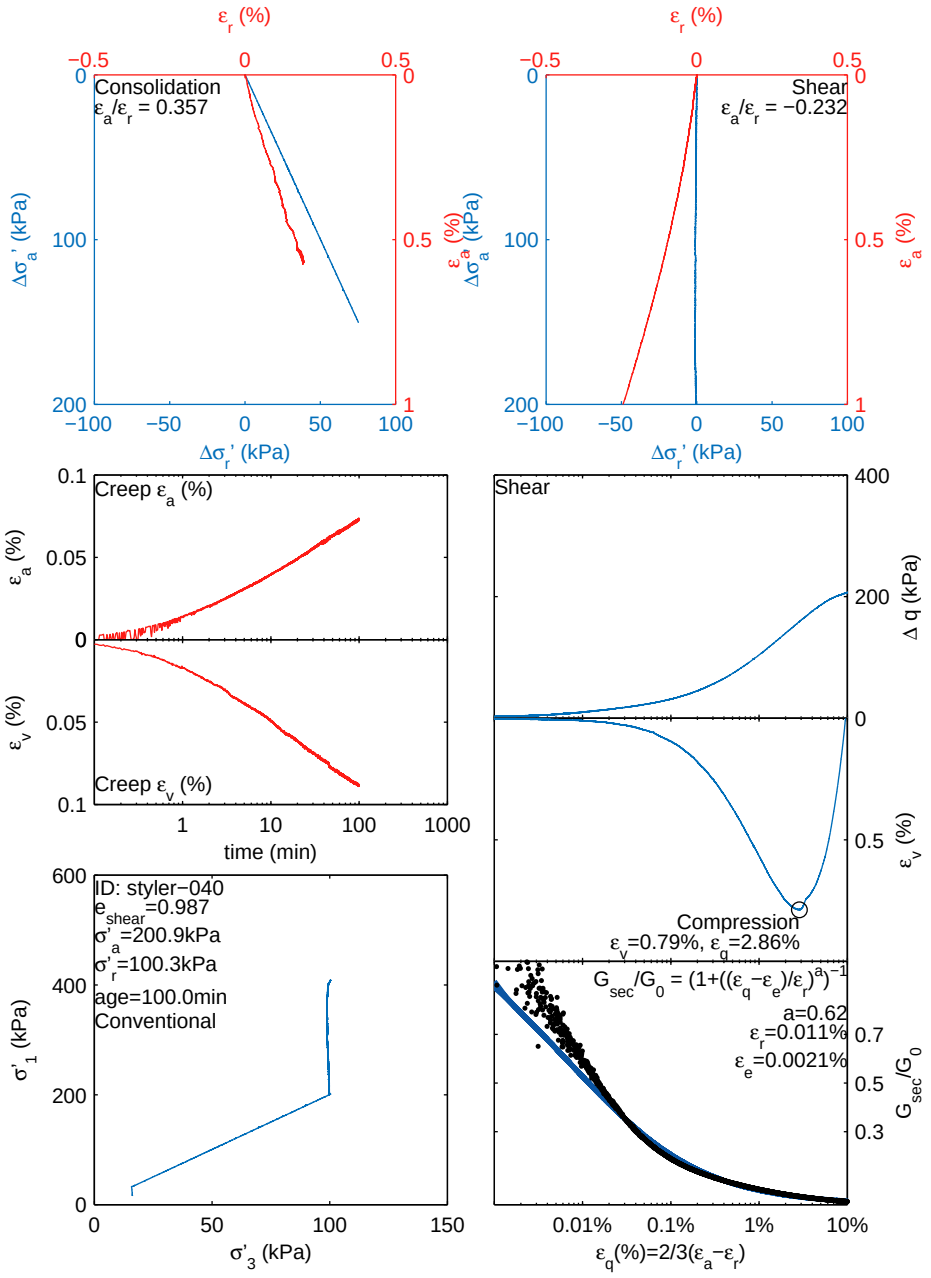

Figure D.52: Styler-040: $\sigma_a = 200.9$ kPa, $\sigma_r = 100.3$ kPa, age=100.0 min, Stress path=C

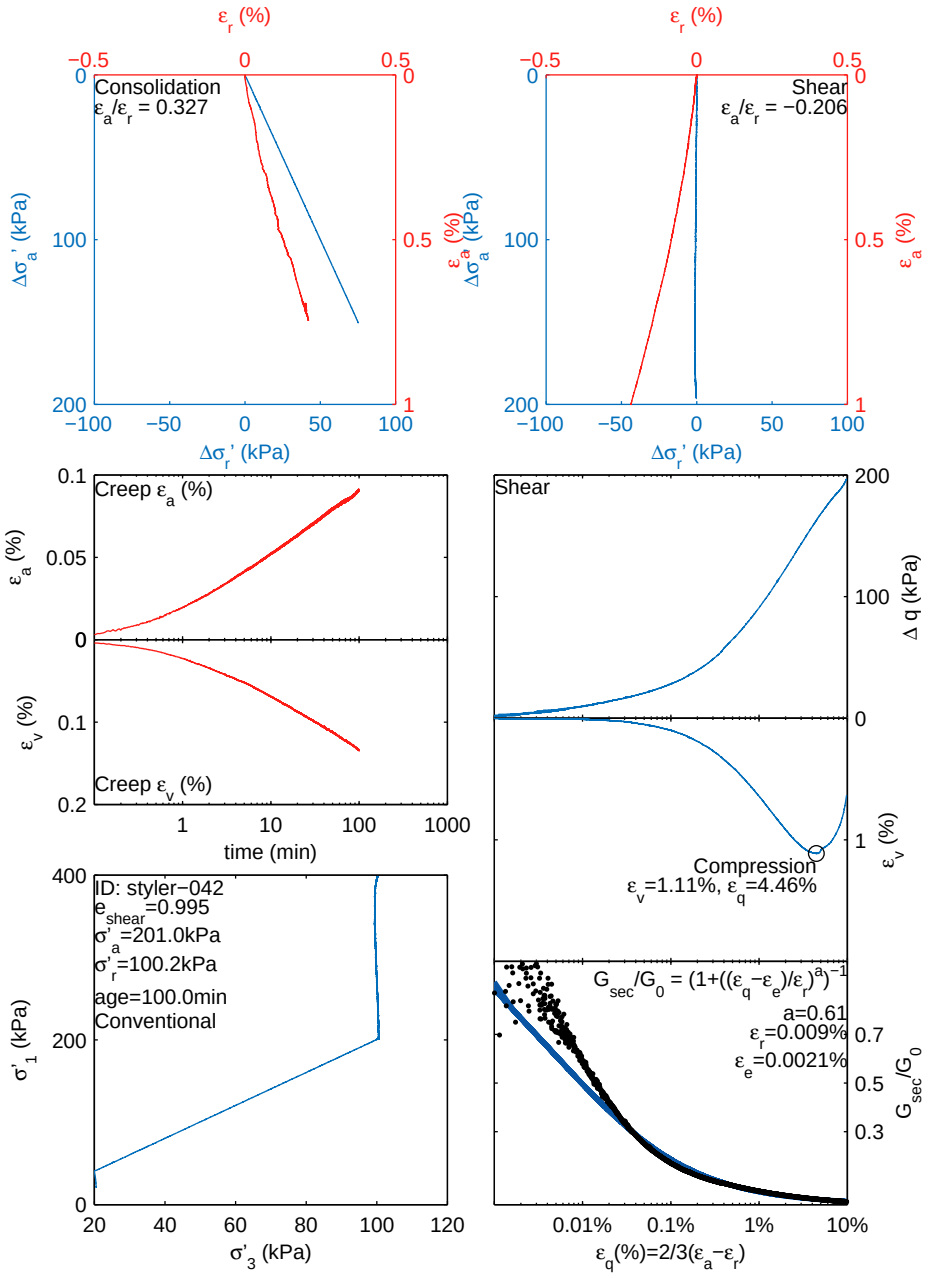

Figure D.53: Styler-042: $\sigma_a = 201.0$ kPa, $\sigma_r = 100.2$ kPa, age=100.0 min, Stress path=C

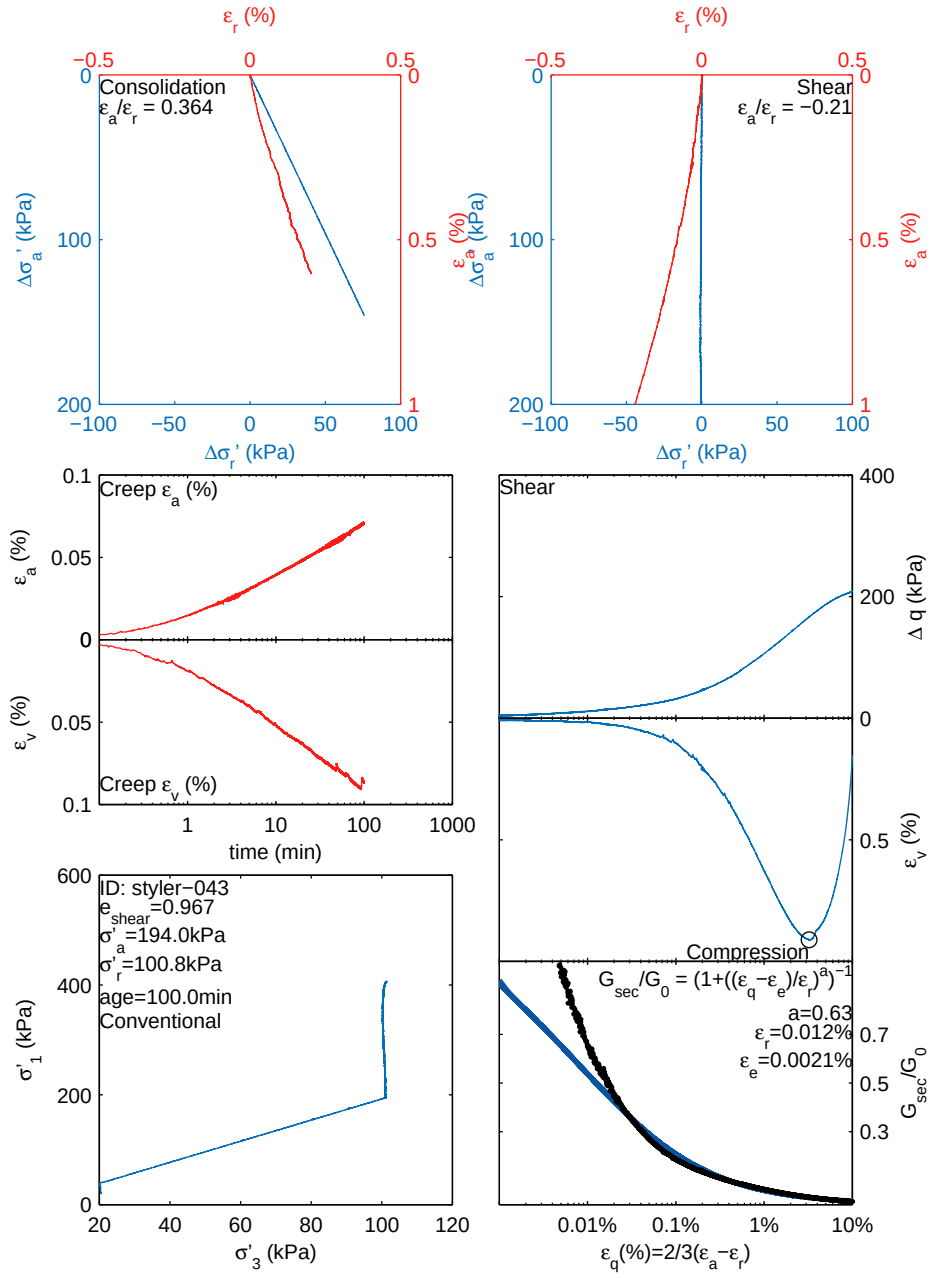

Figure D.54: Styler-043: $\sigma_a = 194.0$ kPa, $\sigma_r = 100.8$ kPa, age=100.0 min, Stress path=C

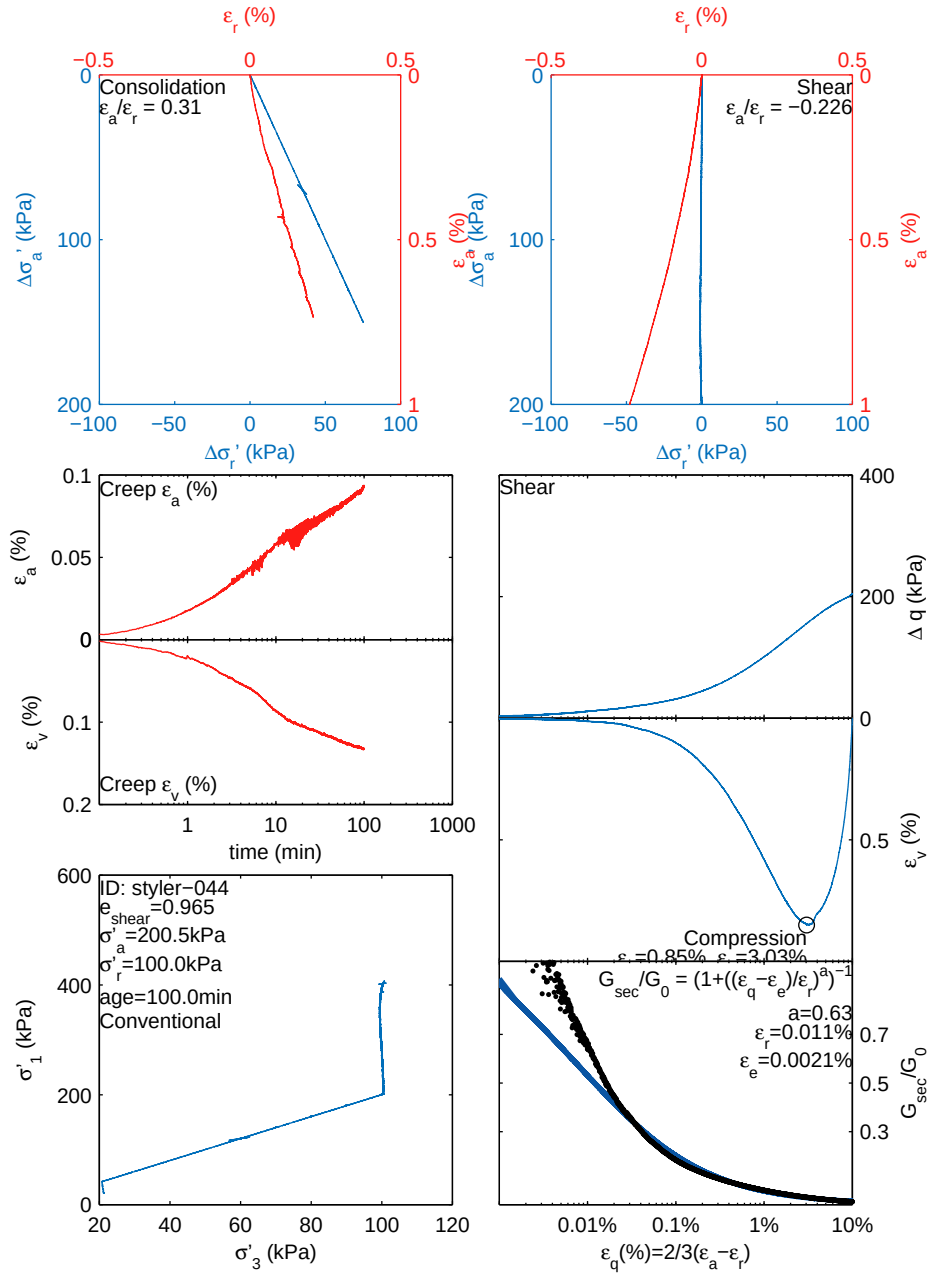

Figure D.55: Styler-044: $\sigma_a = 200.5$ kPa, $\sigma_r = 100.0$ kPa, age=100.0 min, Stress path=C

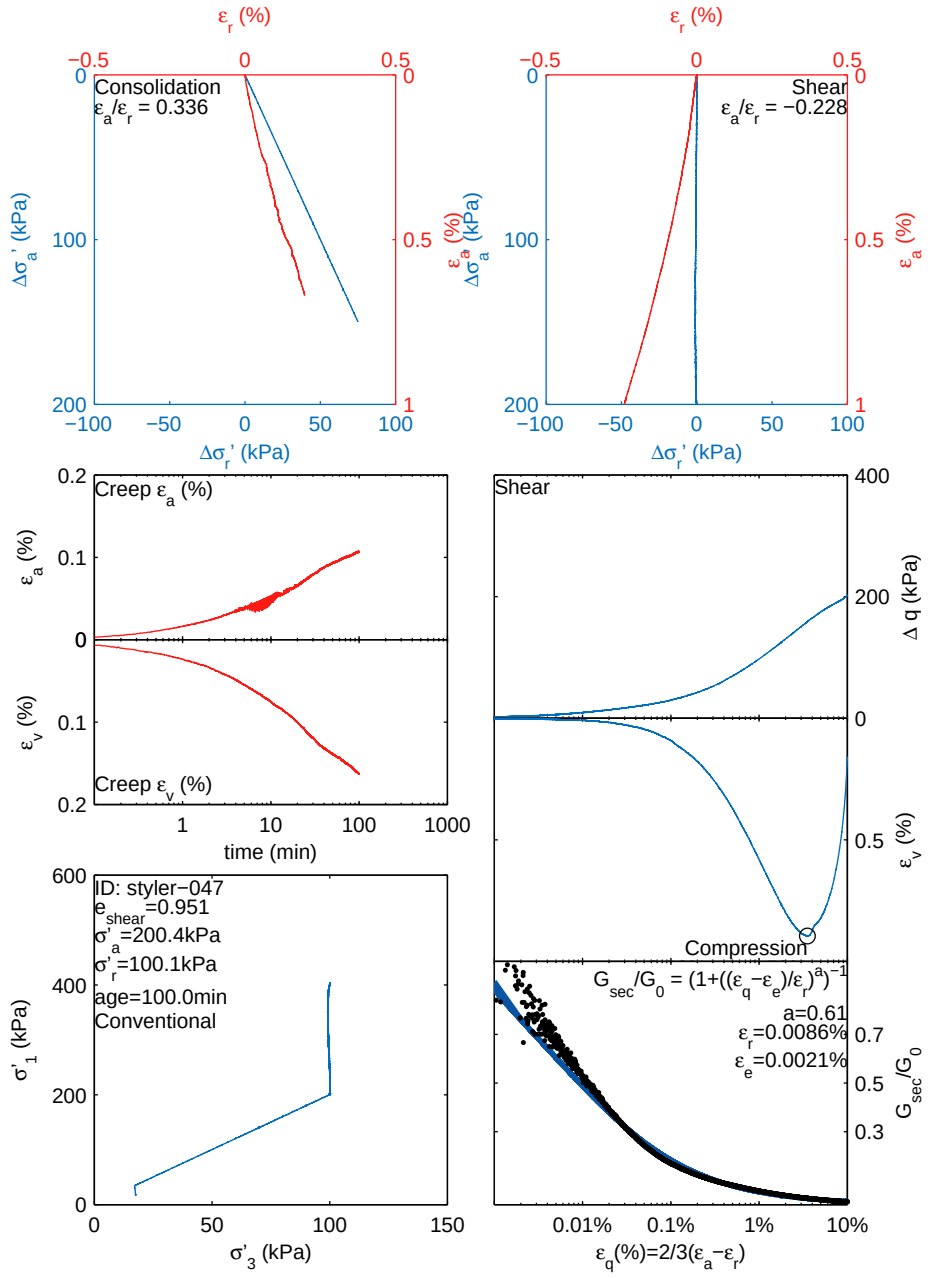

Figure D.56: Styler-047: $\sigma_a = 200.4$ kPa, $\sigma_r = 100.1$ kPa, age=100.0 min, Stress path=C

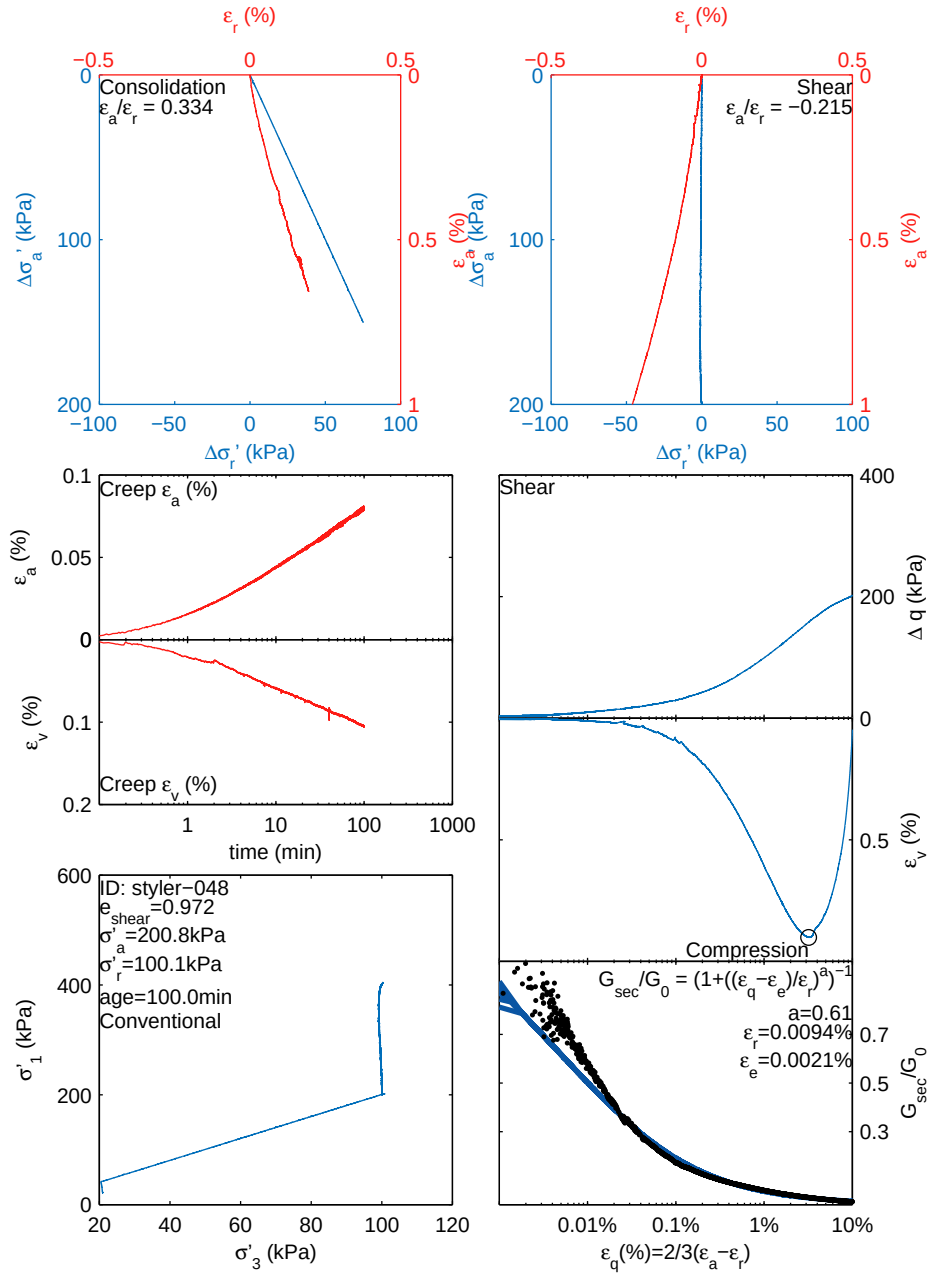

Figure D.57: Styler-048: $\sigma_a = 200.8$ kPa, $\sigma_r = 100.1$ kPa, age=100.0 min, Stress path=C

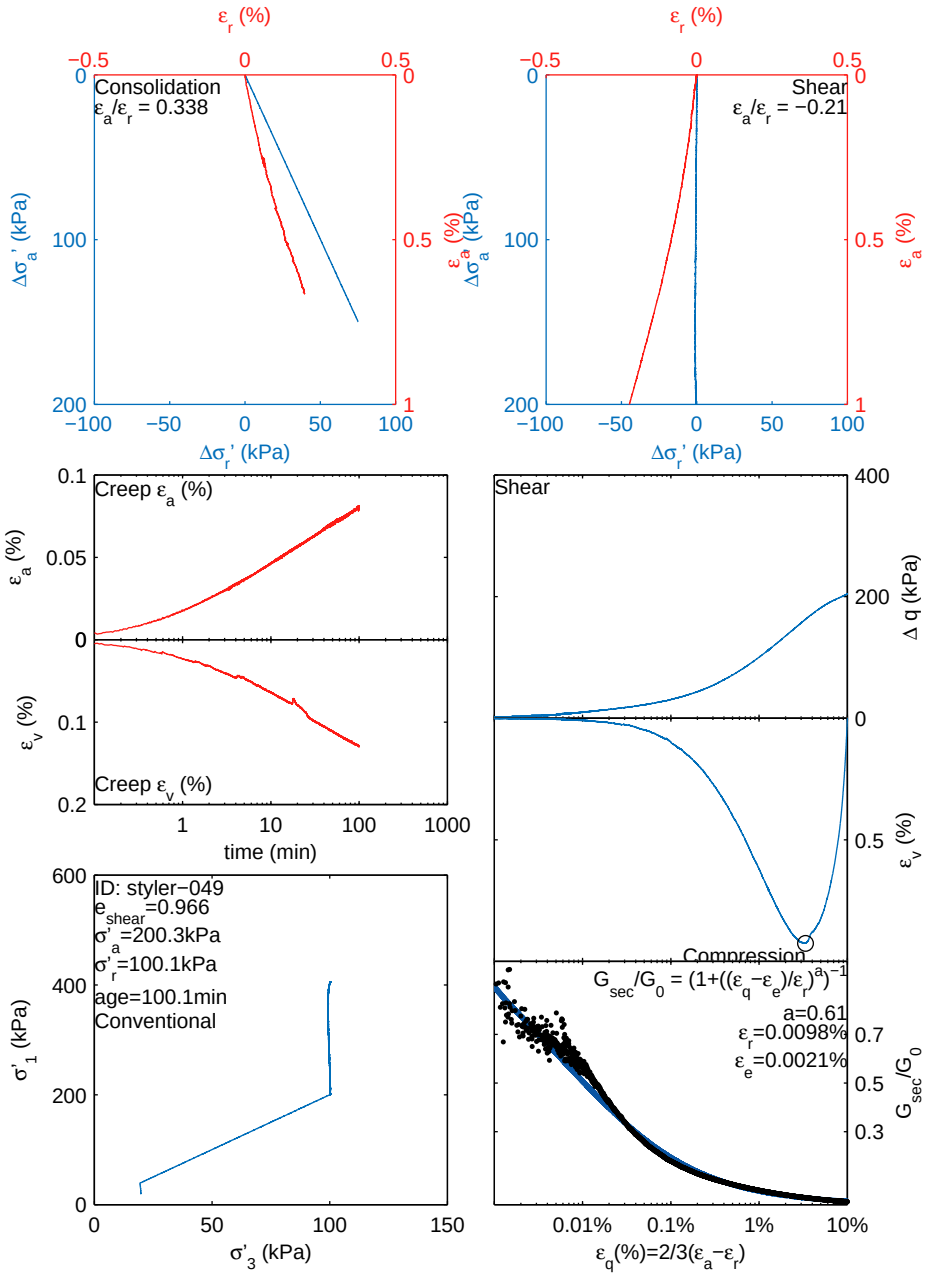

Figure D.58: Styler-049: $\sigma_a = 200.3$ kPa, $\sigma_r = 100.1$ kPa, age=100.1 min, Stress path=C

D.2 Results from Lam (2003)

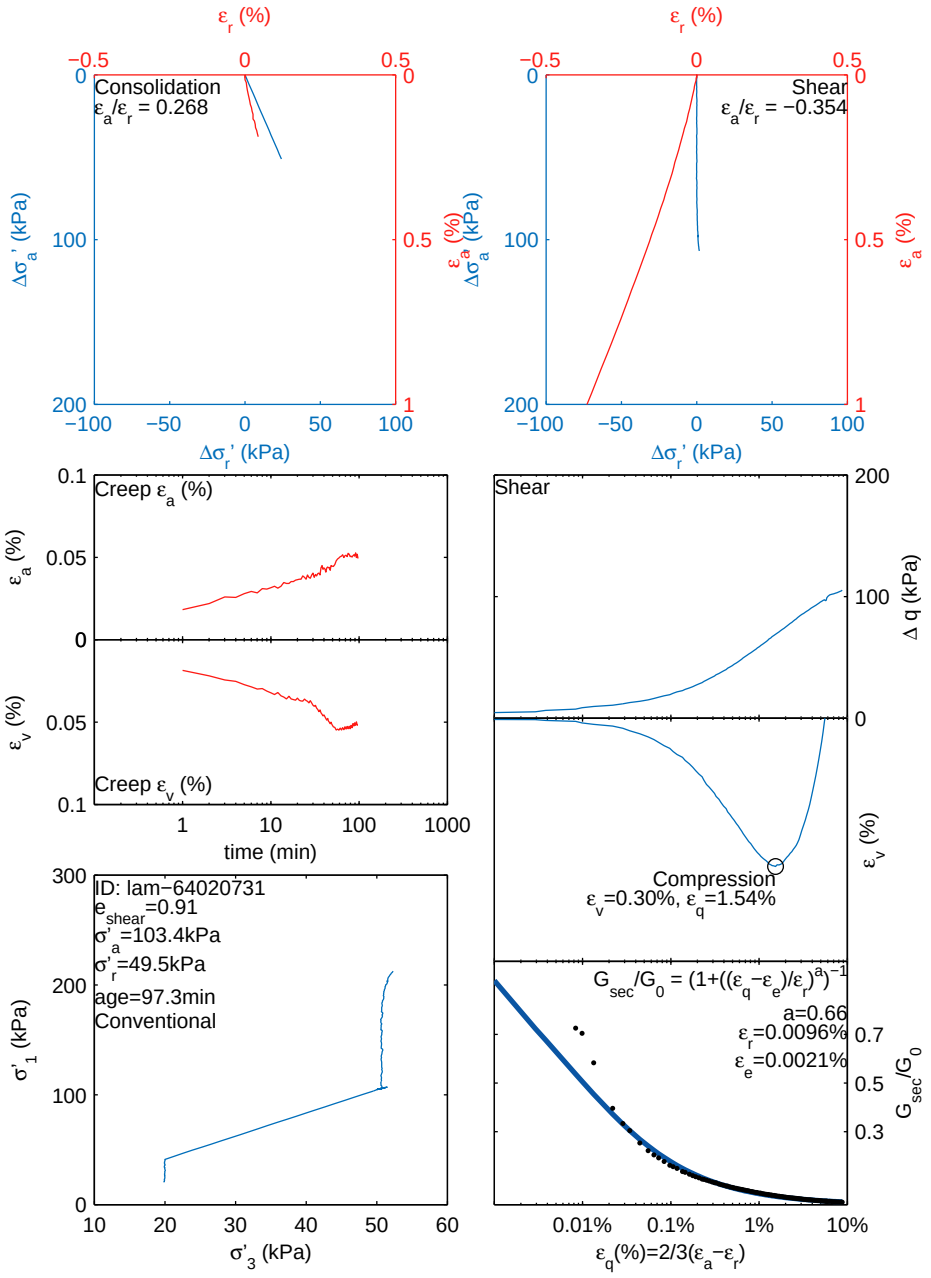

Figure D.59: Lam-64020731: σ_a = 103.4 kPa, σ_r = 49.5 kPa, age=97.3 min, Stress path=C

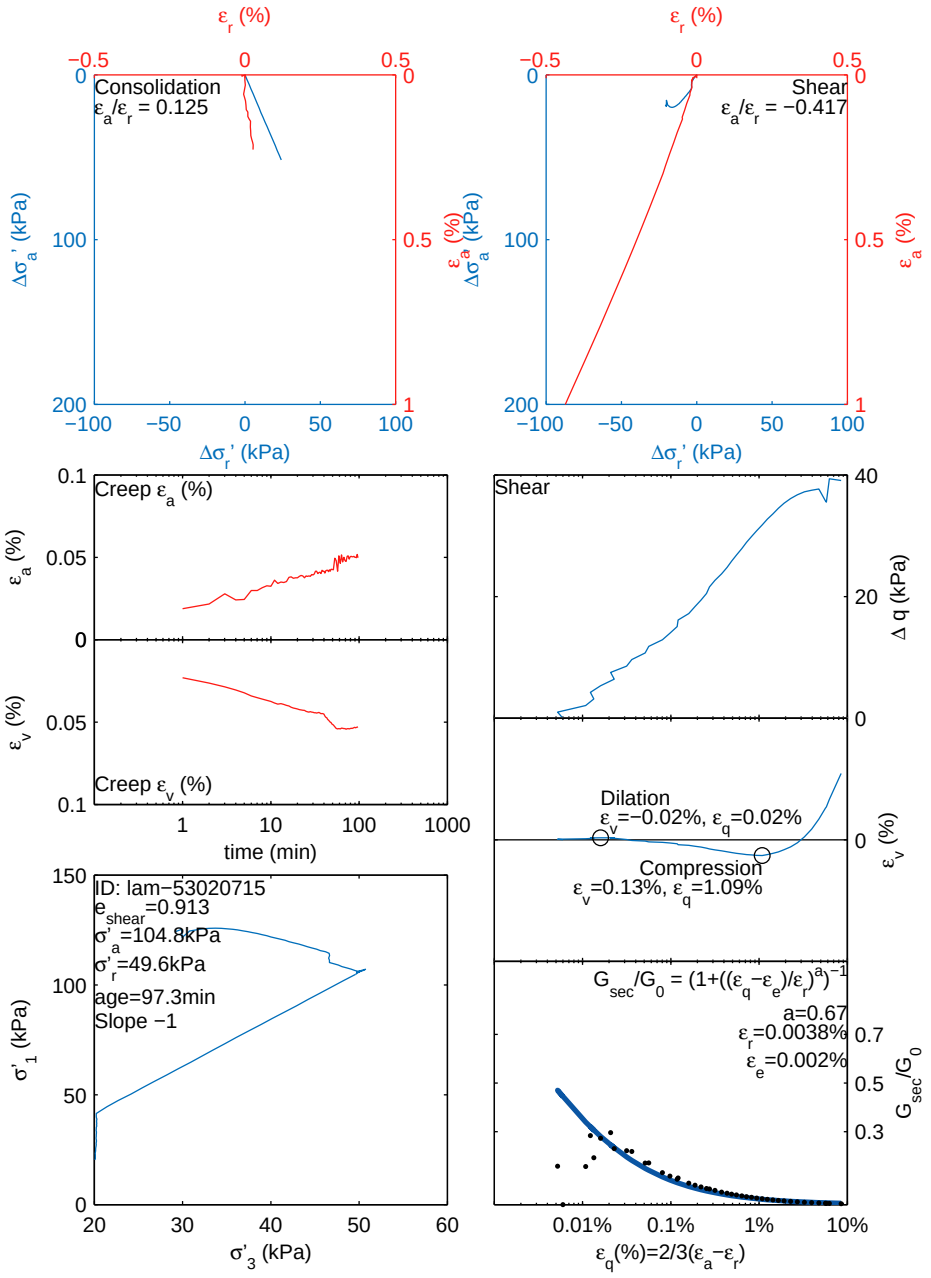

Figure D.60: Lam-53020715: σ_a = 104.8 kPa, σ_r = 49.6 kPa, age=97.3 min, Stress path=-1

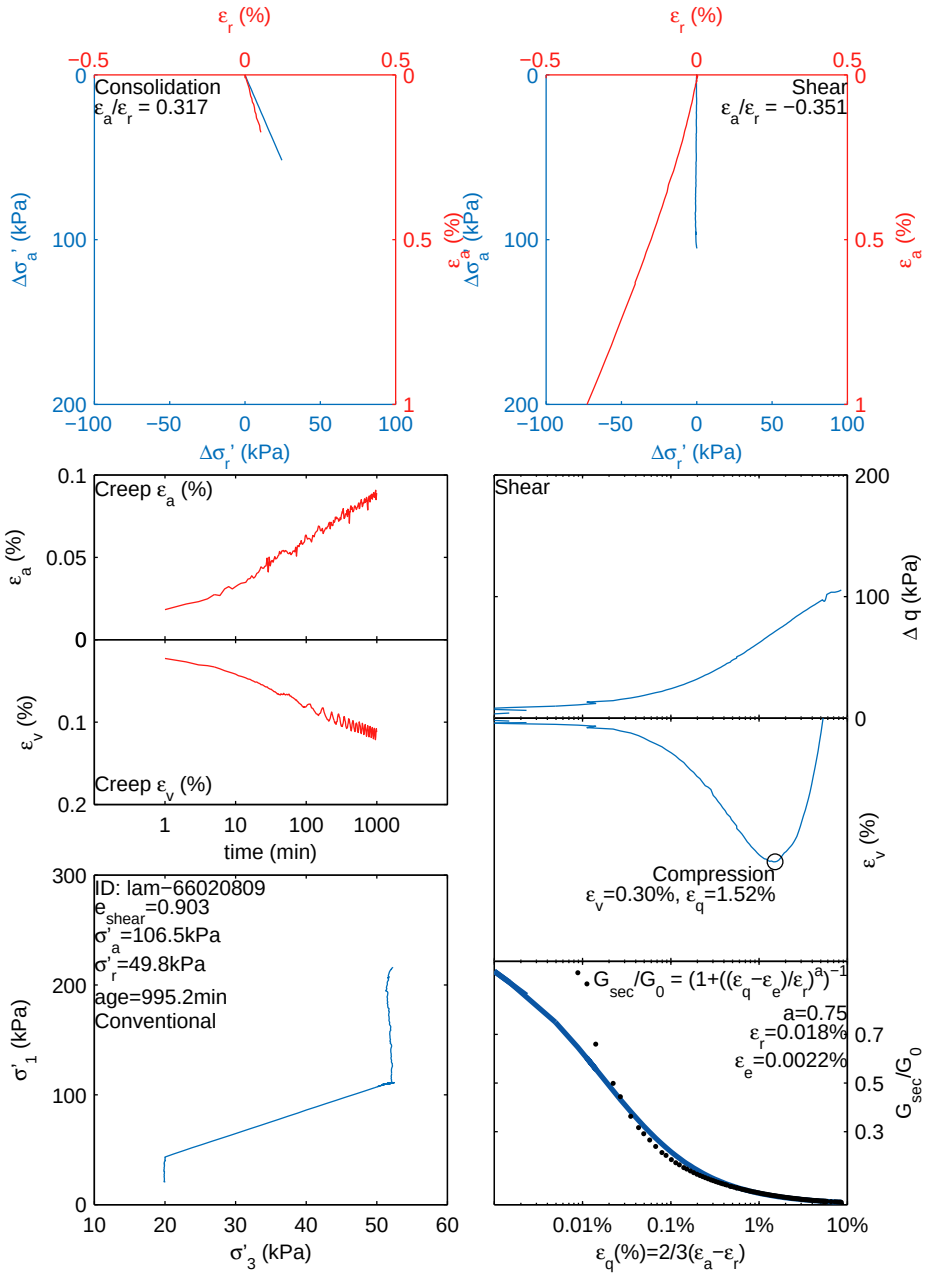

Figure D.61: Lam-66020809: σ_a = 106.5 kPa, σ_r = 49.8 kPa, age=995.2 min, Stress path=C

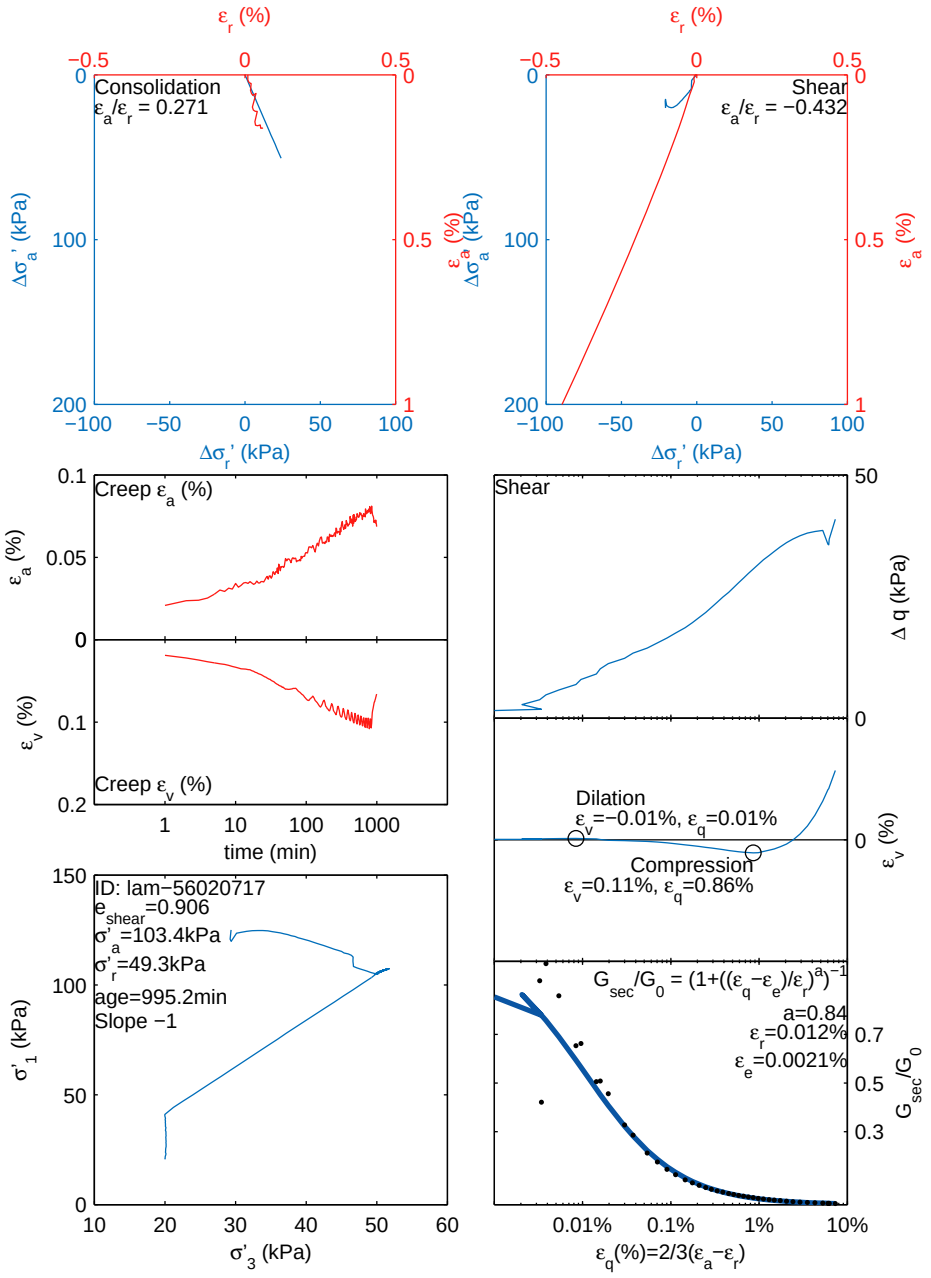

Figure D.62: Lam-56020717: σ_a = 103.4 kPa, σ_r = 49.3 kPa, age=995.2 min, Stress path=-1

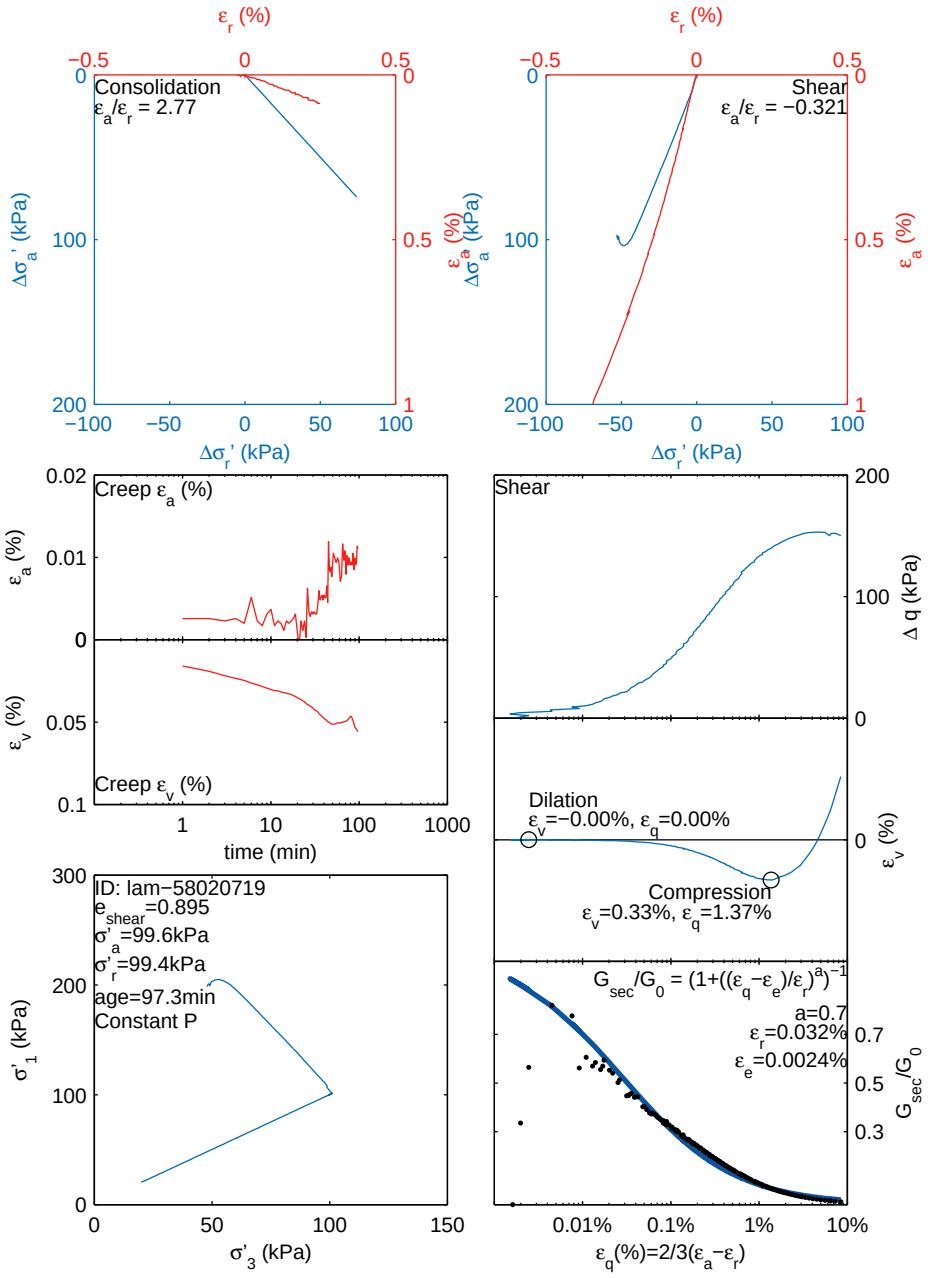

Figure D.63: Lam-58020719: $\sigma_a = 99.6$ kPa, $\sigma_r = 99.4$ kPa, age=97.3 min, Stress path=P

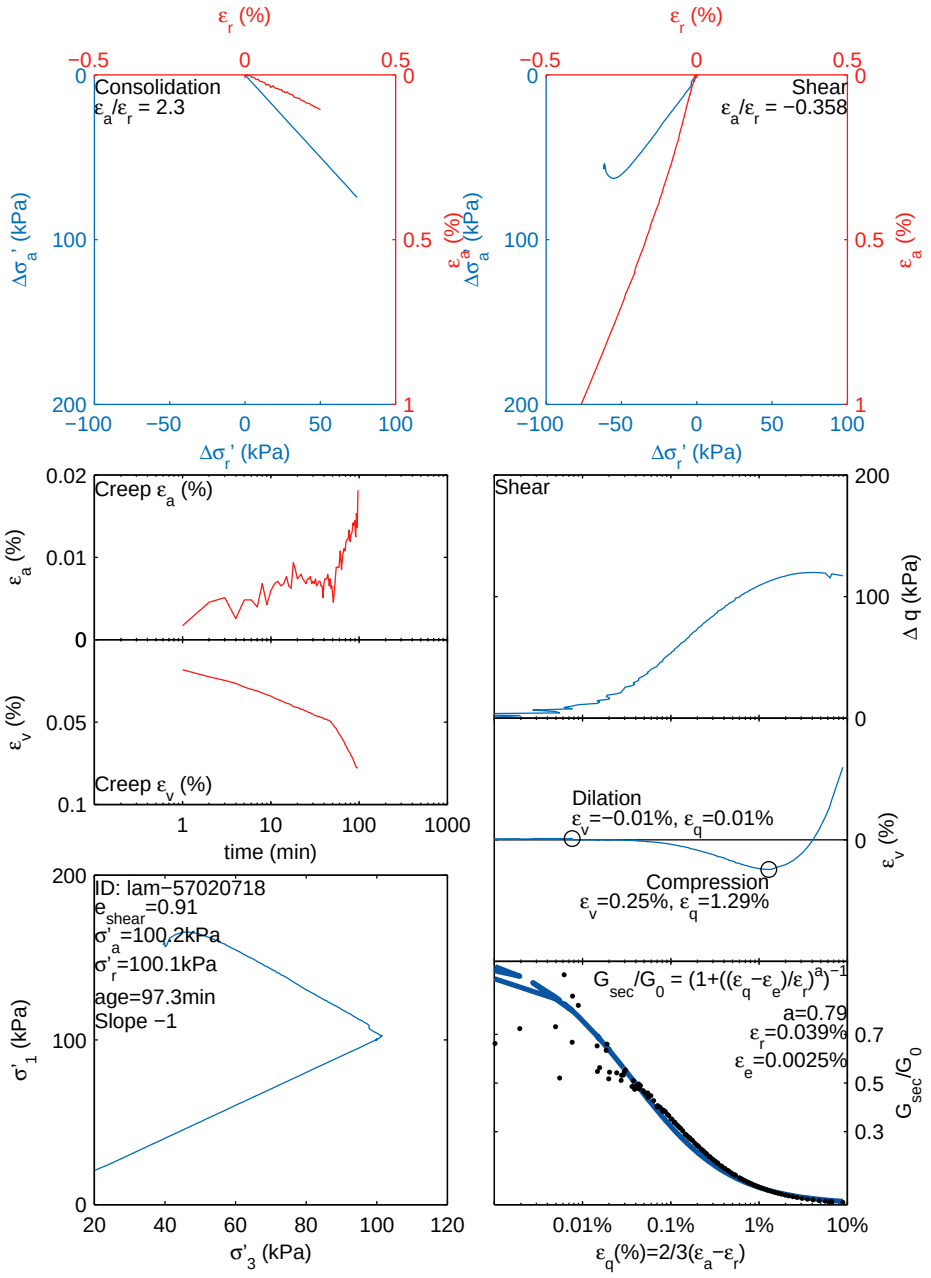

Figure D.64: Lam-57020718: σ_a = 100.2 kPa, σ_r = 100.1 kPa, age=97.3 min, Stress path=-1

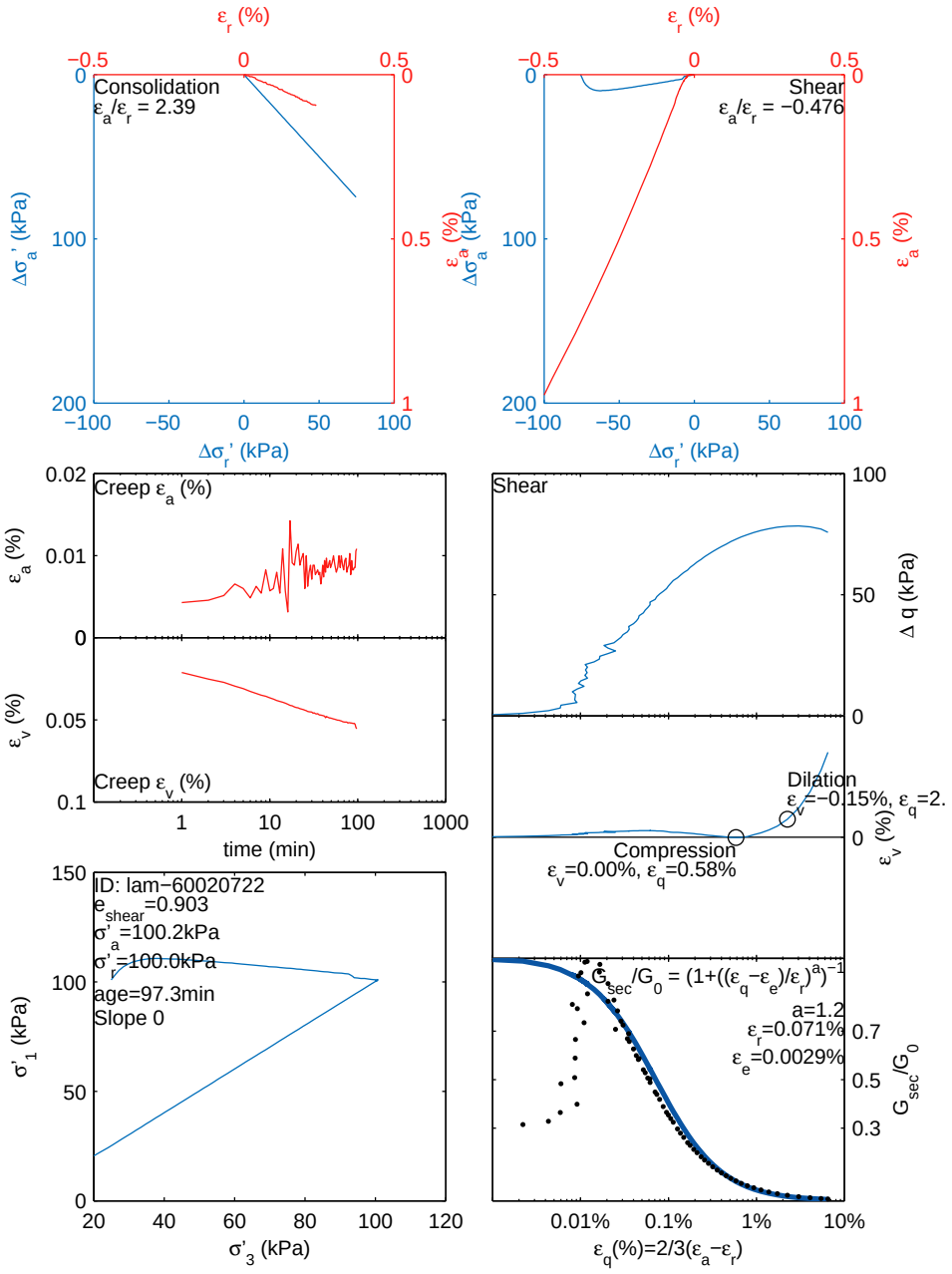

Figure D.65: Lam-60020722: σ_a = 100.2 kPa, σ_r = 100.0 kPa, age=97.3 min, Stress path=0

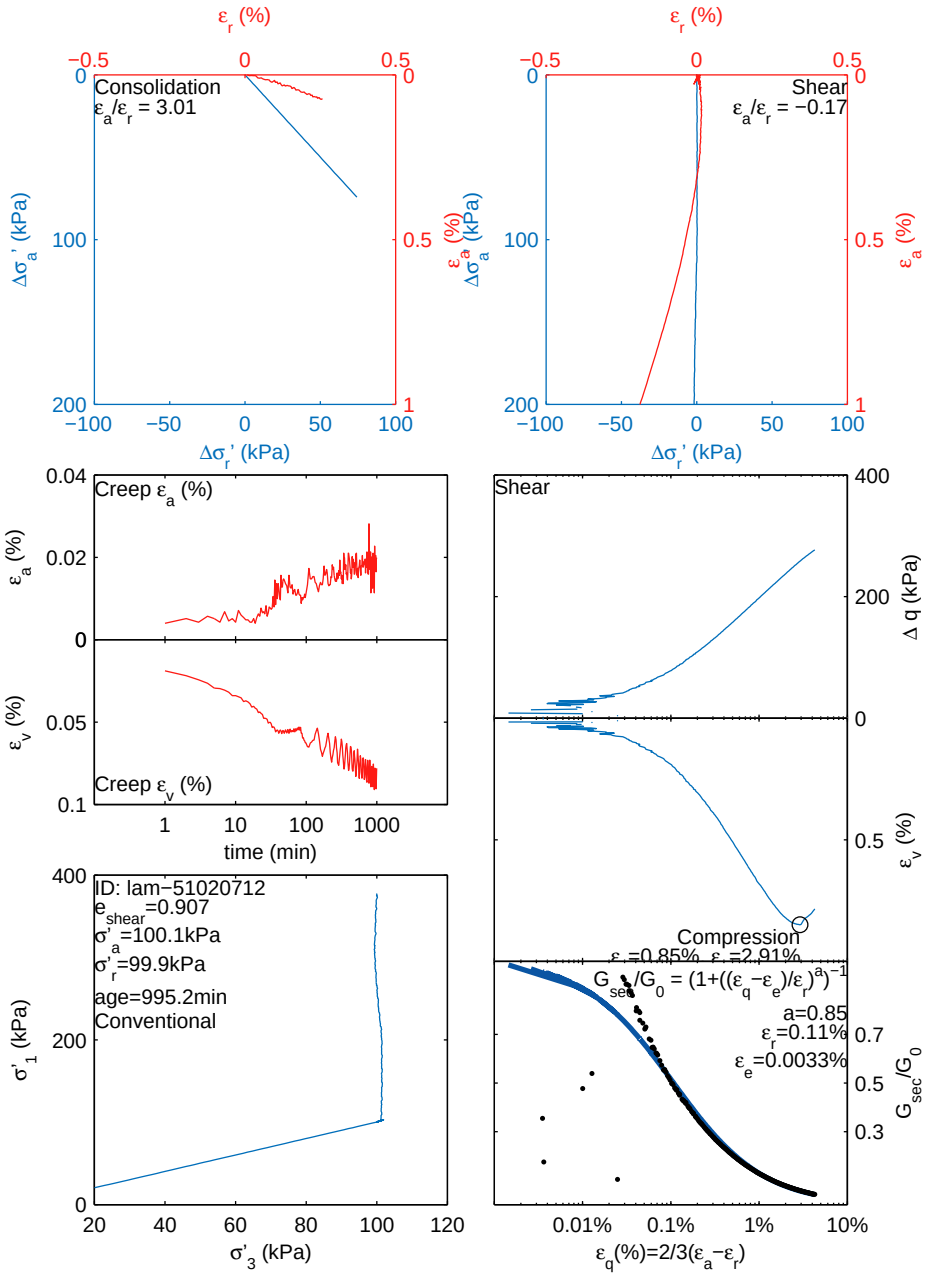

Figure D.66: Lam-51020712: σ_a = 100.1 kPa, σ_r = 99.9 kPa, age=995.2 min, Stress path=C

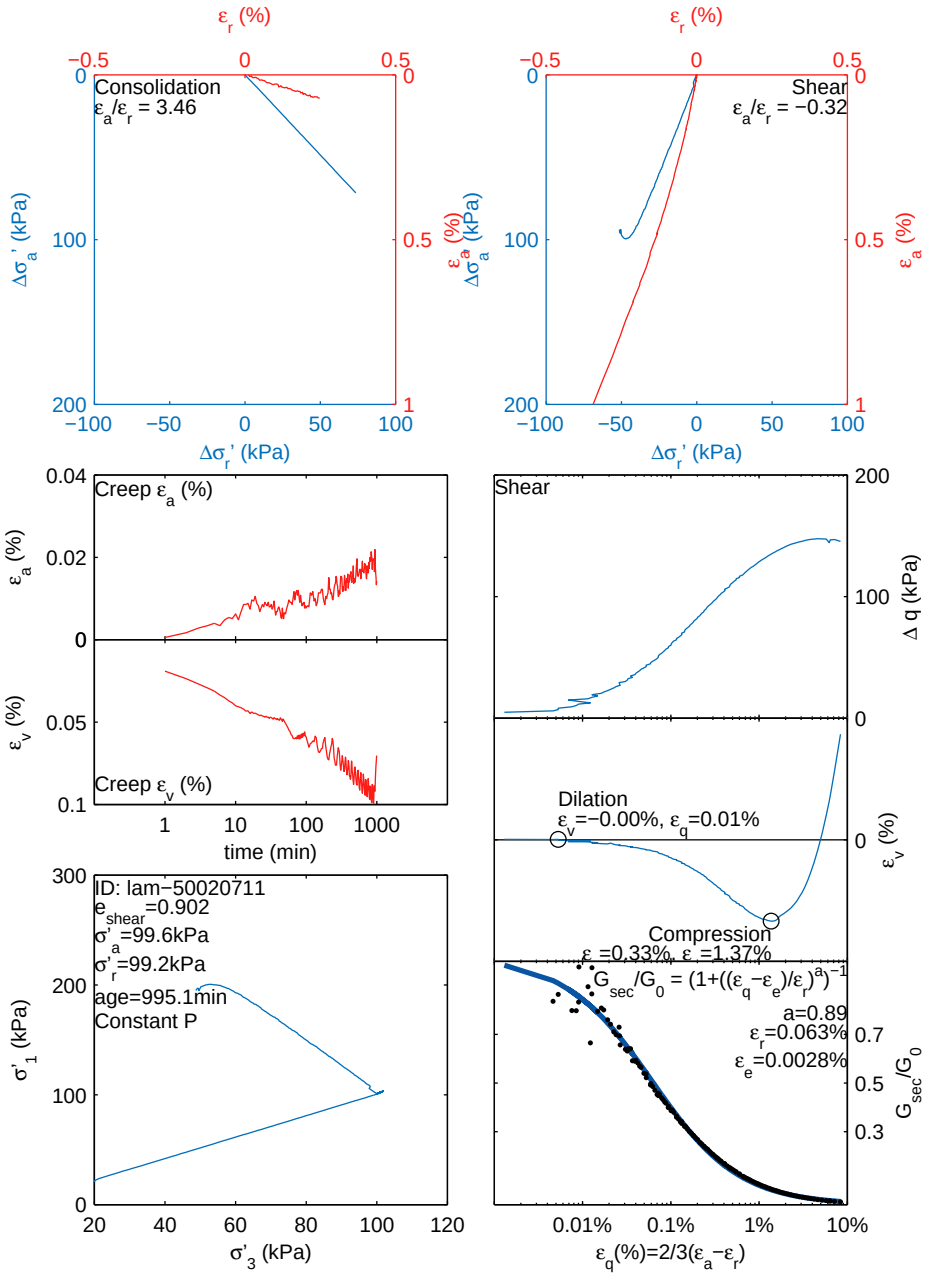

Figure D.67: Lam-50020711: σ_a = 99.6 kPa, σ_r = 99.2 kPa, age=995.1 min, Stress path=P

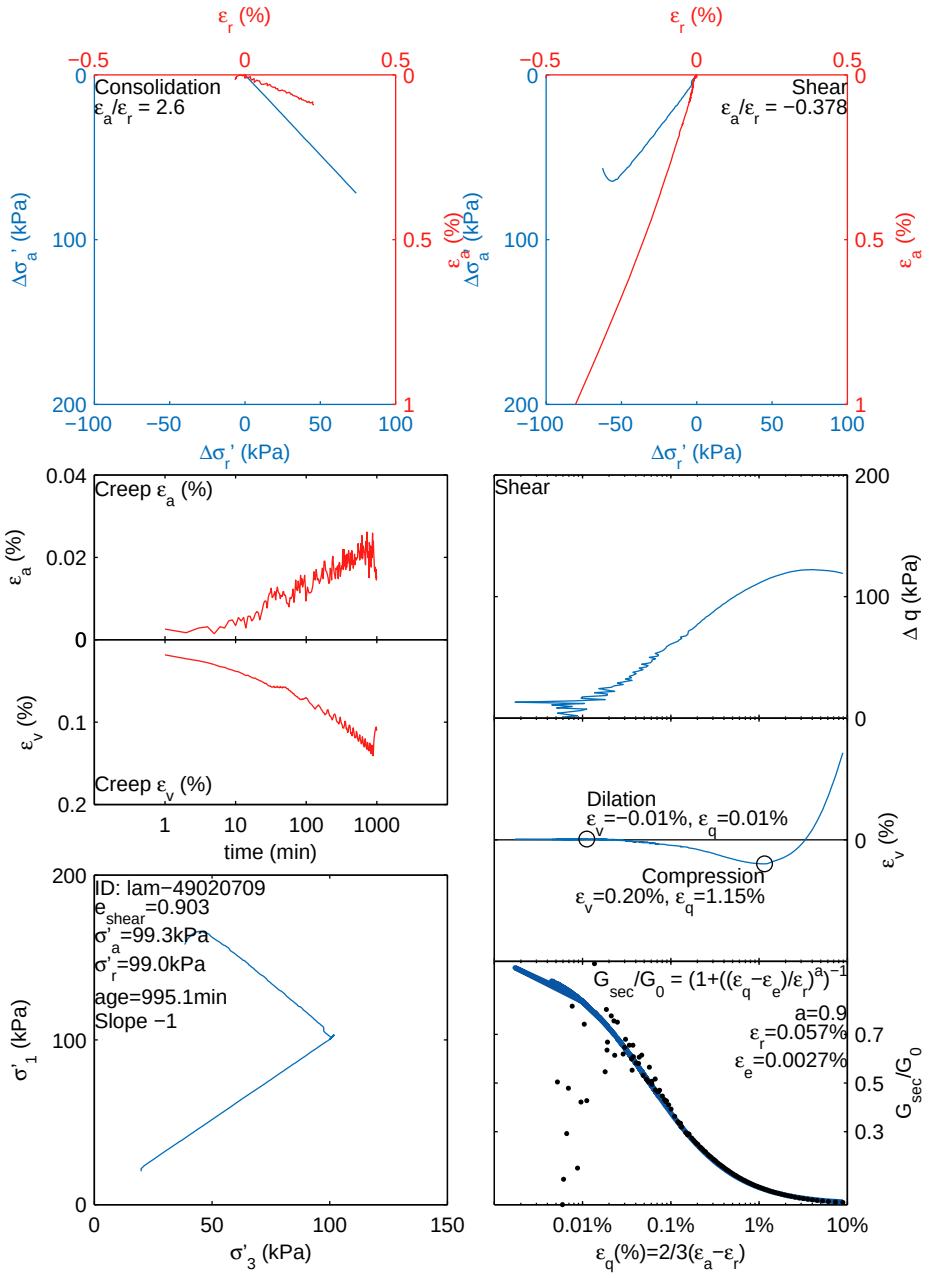

Figure D.68: Lam-49020709: σ_a = 99.3 kPa, σ_r = 99.0 kPa, age=995.1 min, Stress path=-1

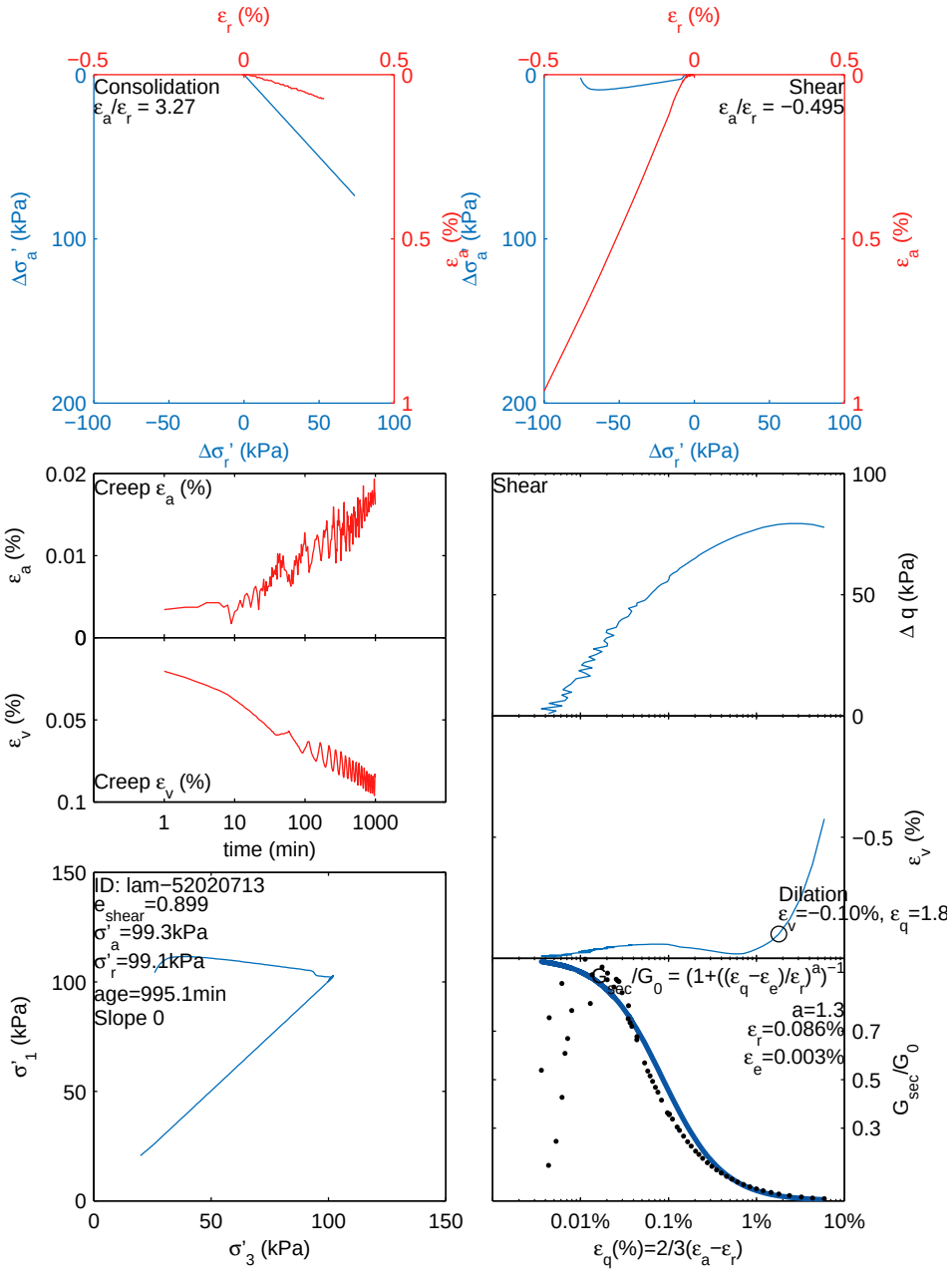

Figure D.69: Lam-52020713: σ_a = 99.3 kPa, σ_r = 99.1 kPa, age=995.1 min, Stress path=0

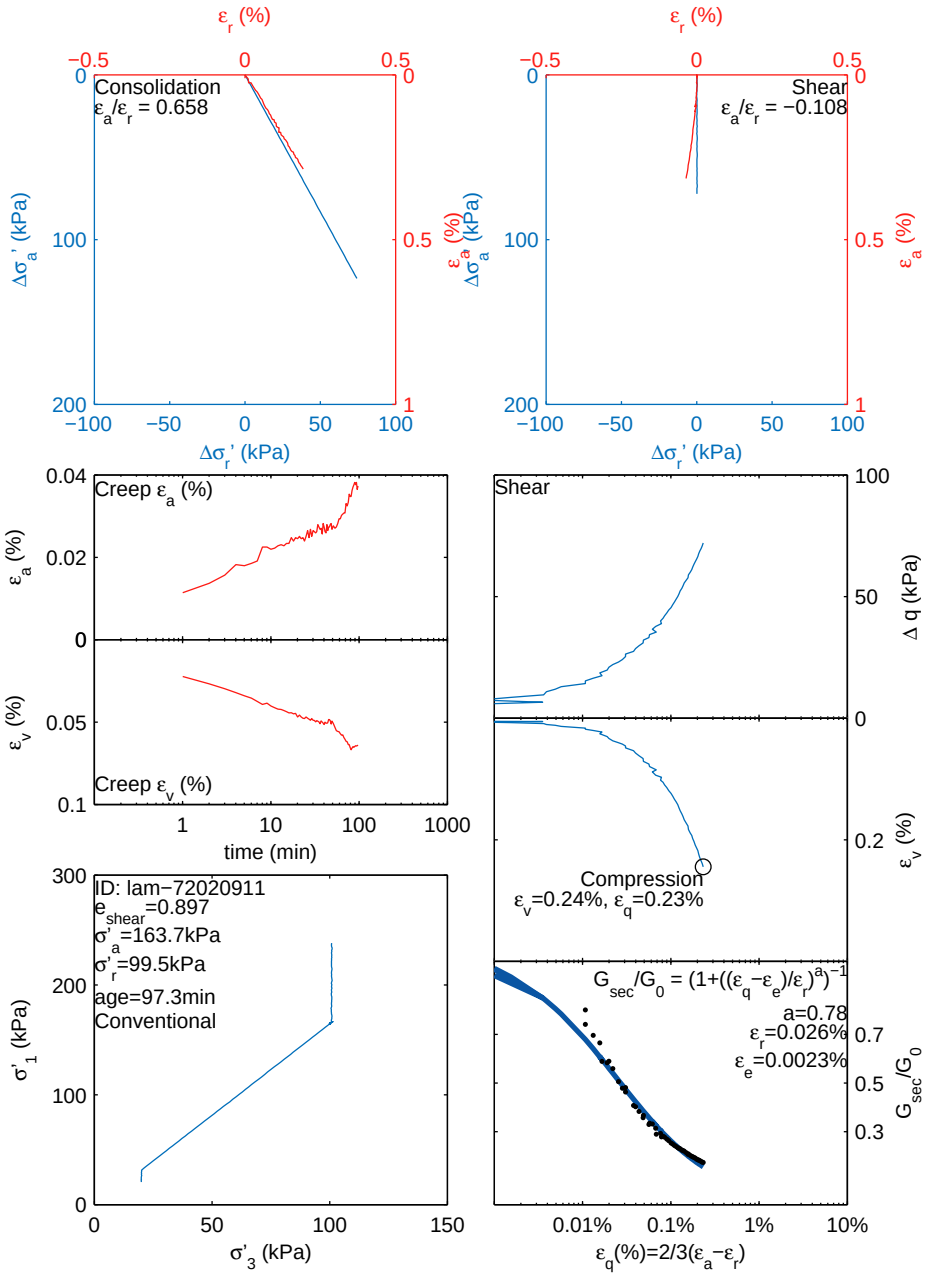

Figure D.70: Lam-72020911: σ_a = 163.7 kPa, σ_r = 99.5 kPa, age=97.3 min, Stress path=C

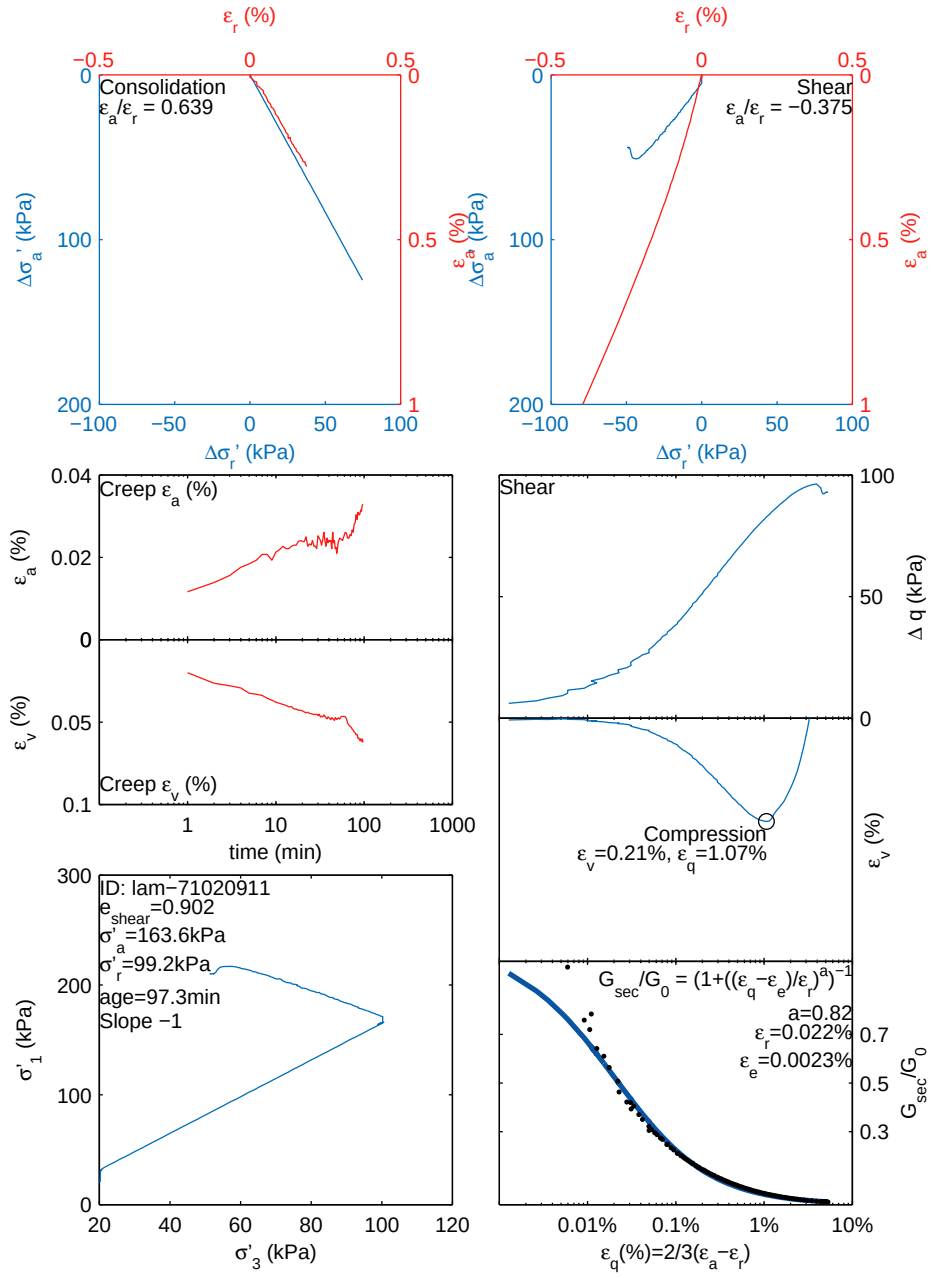

Figure D.71: Lam-71020911: σ_a = 163.6 kPa, σ_r = 99.2 kPa, age=97.3 min, Stress path=-1

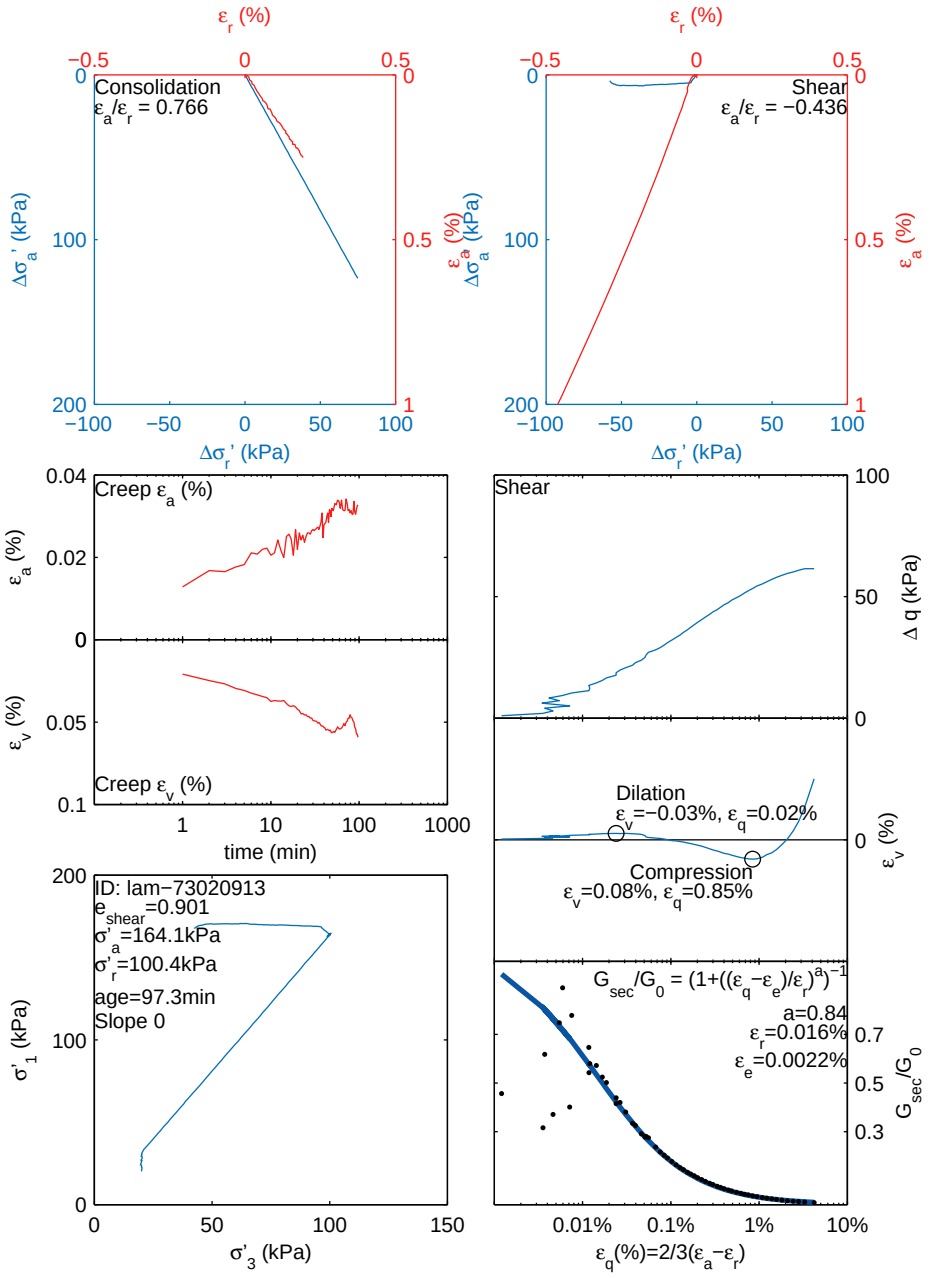

Figure D.72: Lam-73020913: σ_a = 164.1 kPa, σ_r = 100.4 kPa, age=97.3 min, Stress path=0

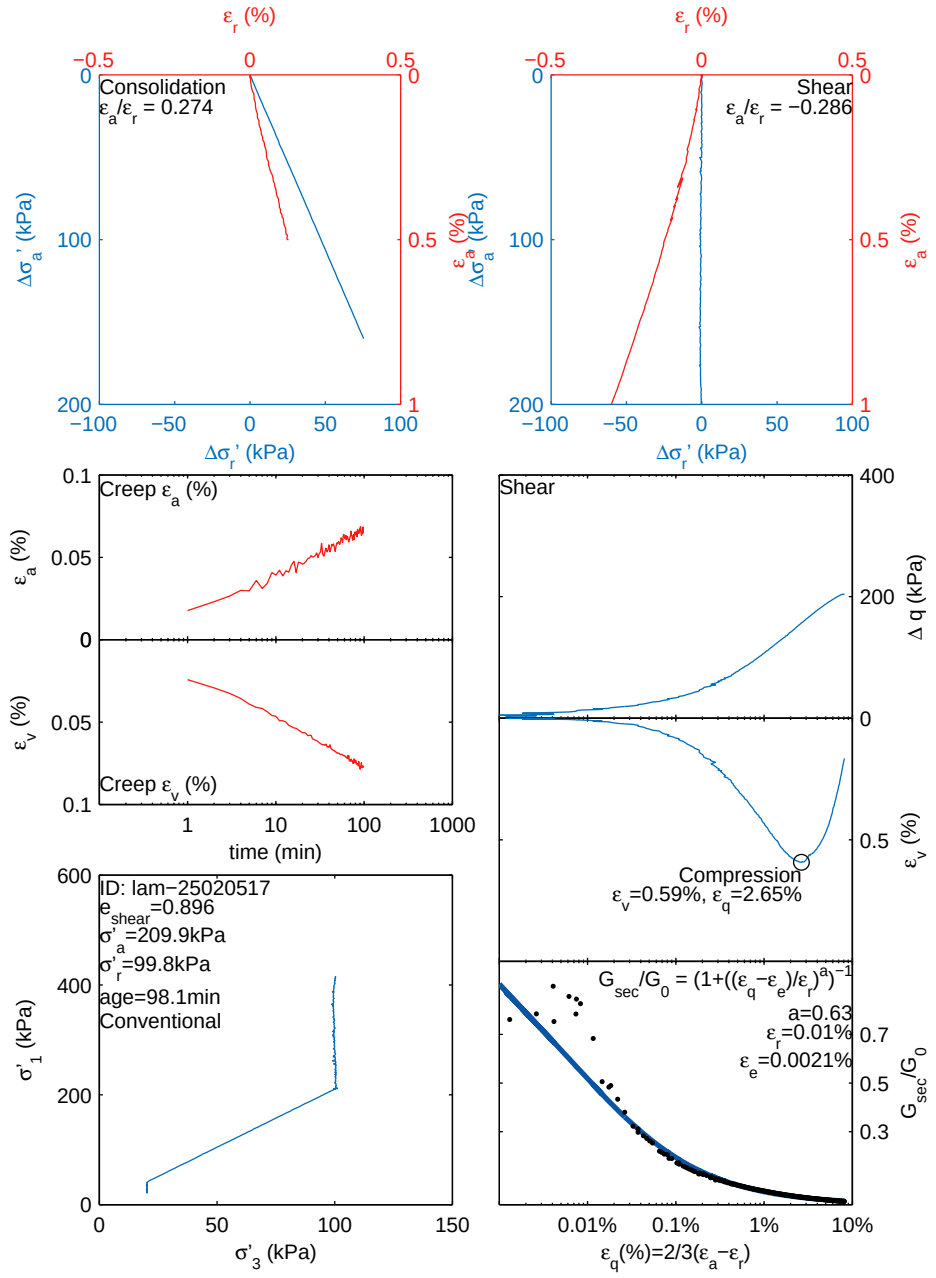

Figure D.73: Lam-25020517: σ_a = 209.9 kPa, σ_r = 99.8 kPa, age=98.1 min, Stress path=C

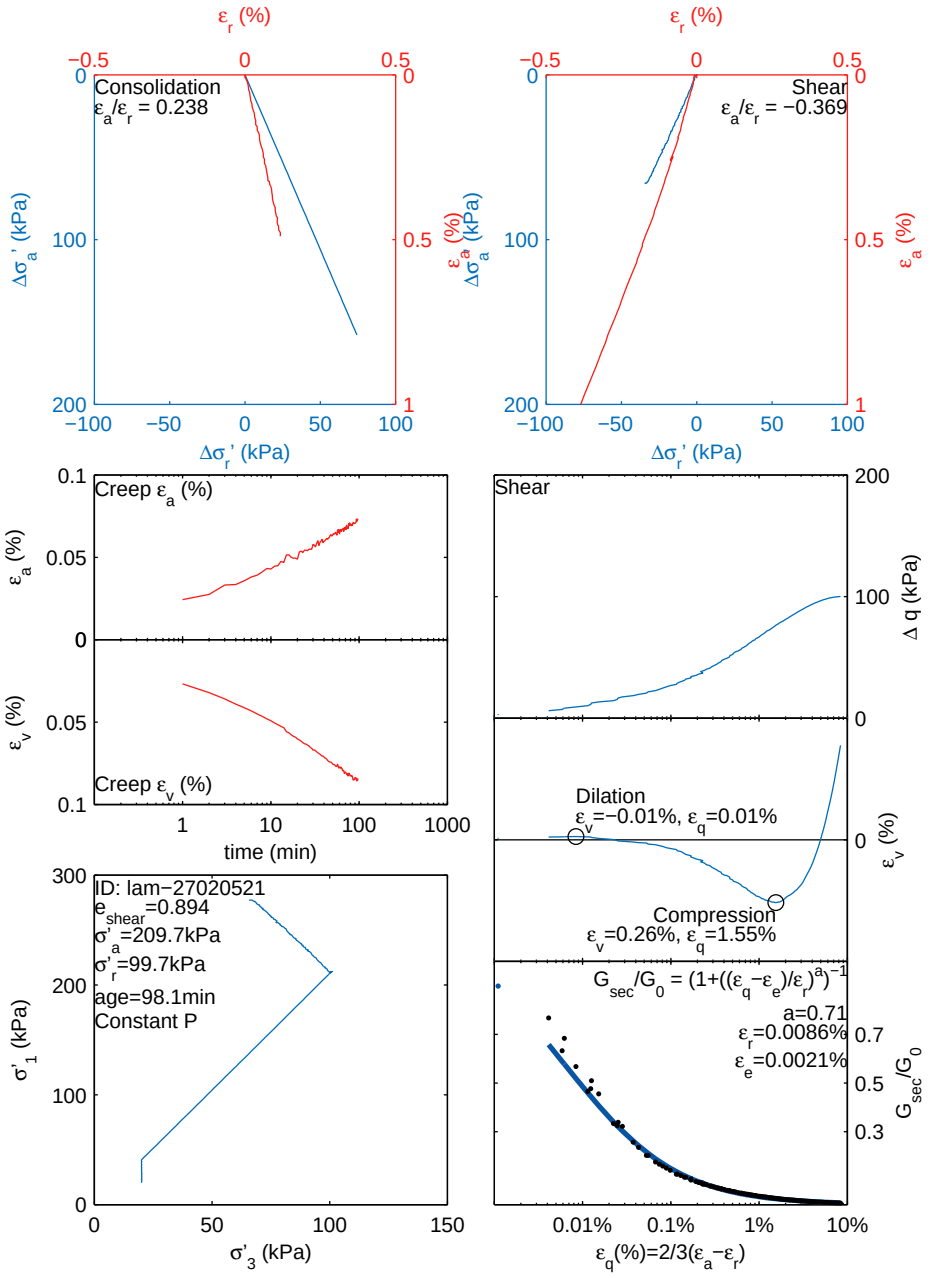

Figure D.74: Lam-27020521: σ_a = 209.7 kPa, σ_r = 99.7 kPa, age=98.1 min, Stress path=P

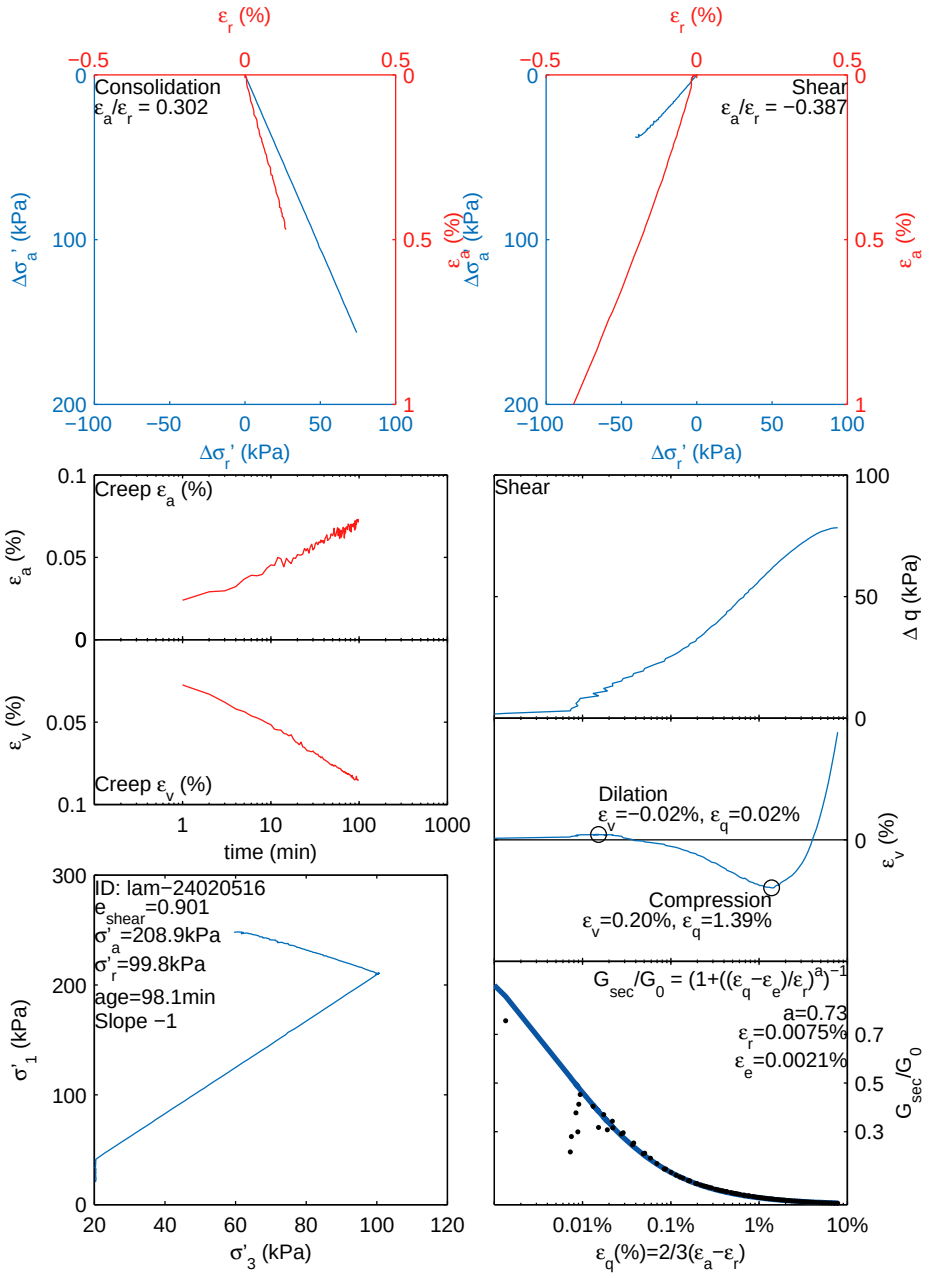

Figure D.75: Lam-24020516: σ_a = 208.9 kPa, σ_r = 99.8 kPa, age=98.1 min, Stress path=-1

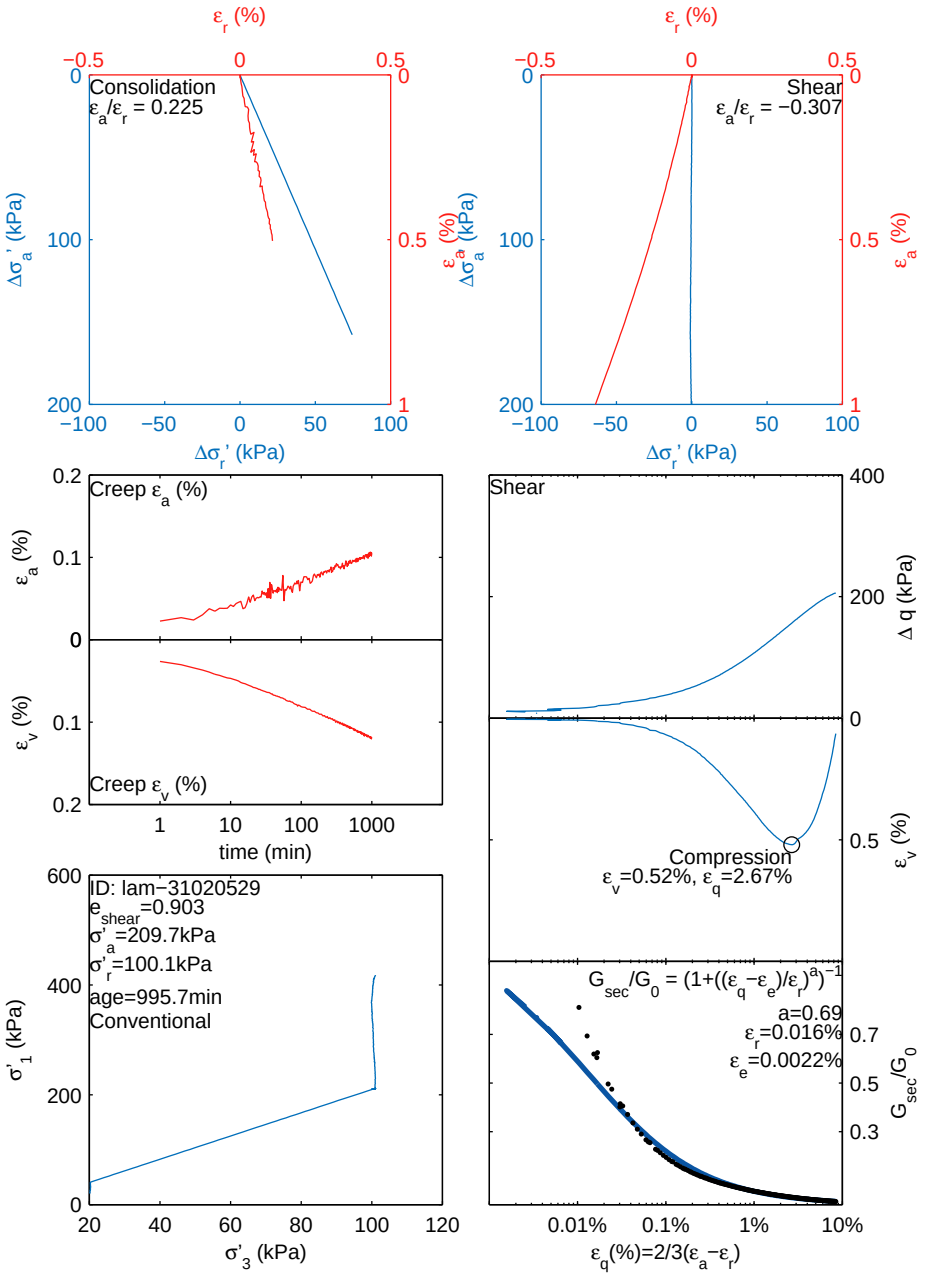

Figure D.76: Lam-31020529: σ_a = 209.7 kPa, σ_r = 100.1 kPa, age=995.7 min, Stress path=C

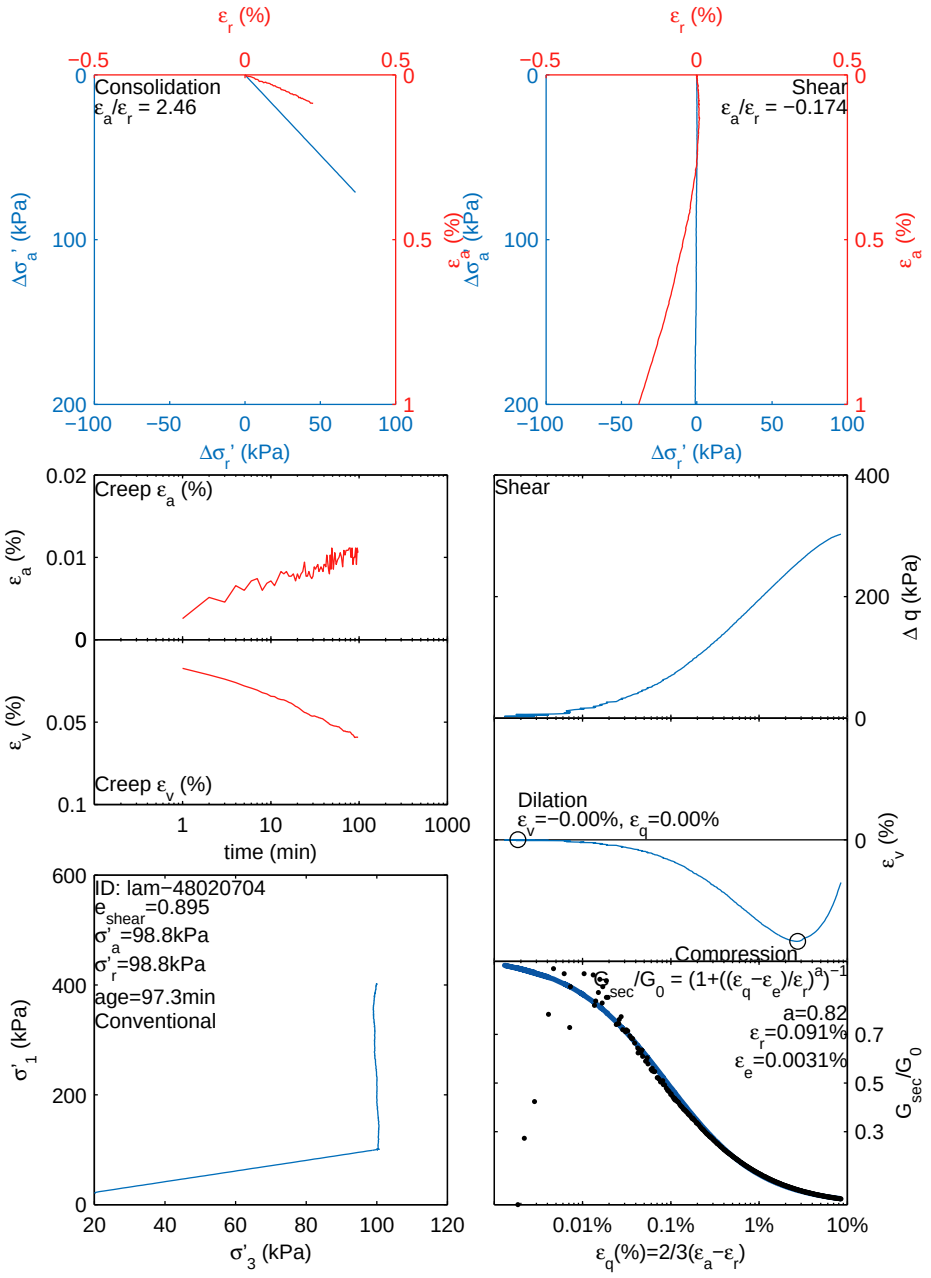

Figure D.77: Lam-48020704: $\sigma_a = 98.8$ kPa, $\sigma_r = 98.8$ kPa, age=97.3 min, Stress path=C

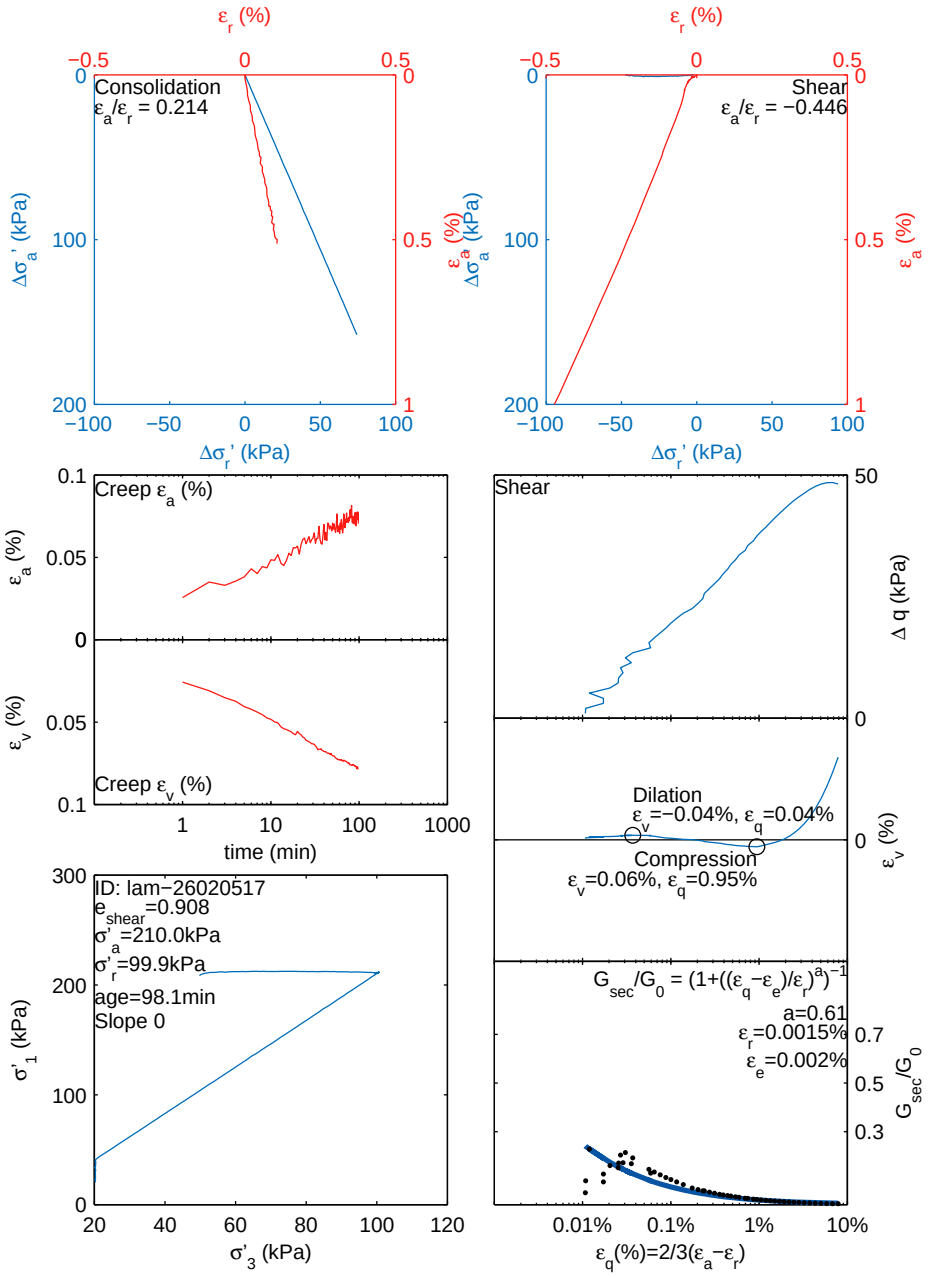

Figure D.78: Lam-26020517: σ_a = 210.0 kPa, σ_r = 99.9 kPa, age=98.1 min, Stress path=0

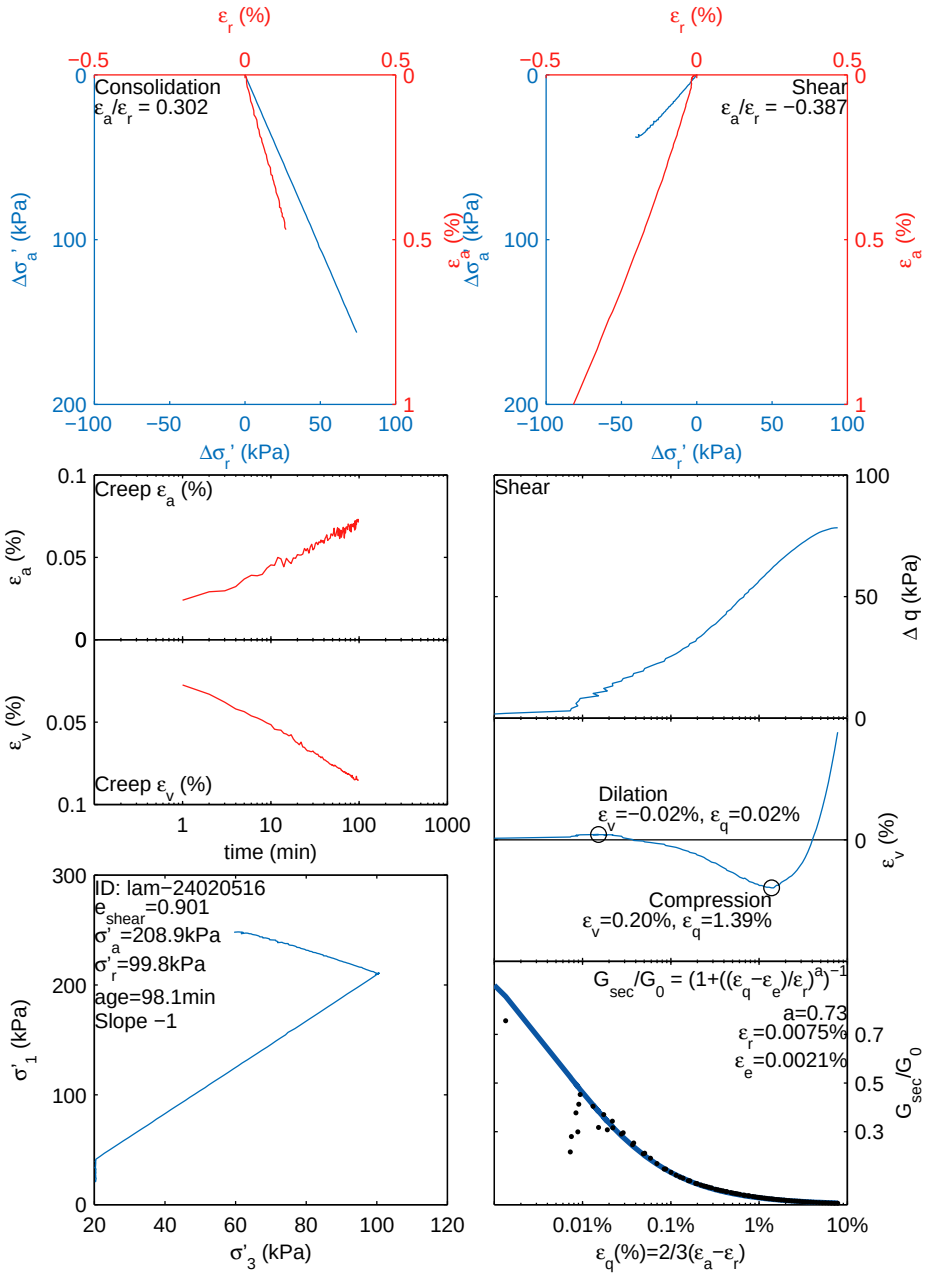

Figure D.79: Lam-24020516: σ_a = 208.9 kPa, σ_r = 99.8 kPa, age=98.1 min, Stress path=-1

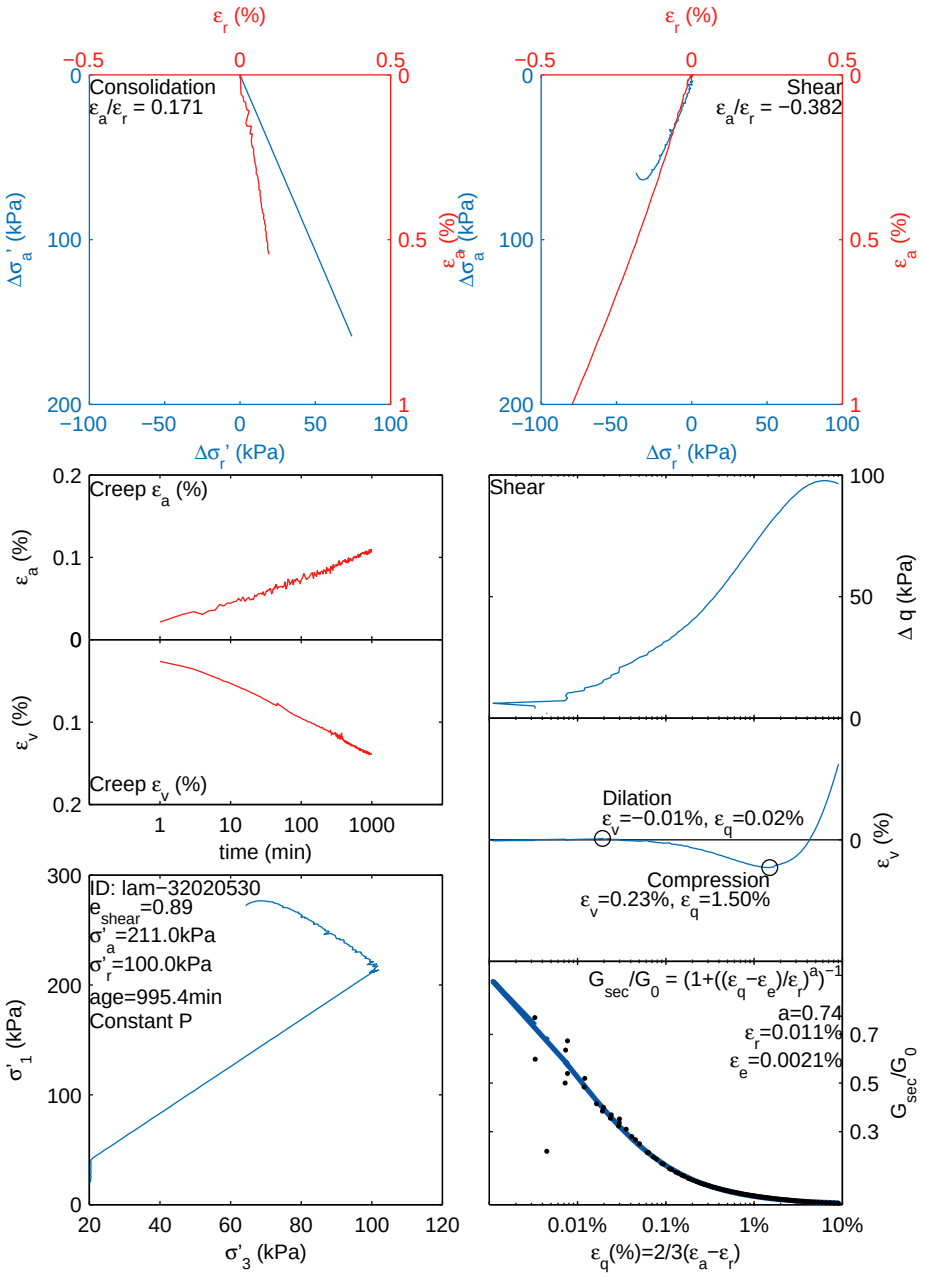

Figure D.80: Lam-32020530: σ_a = 211.0 kPa, σ_r = 100.0 kPa, age=995.4 min, Stress path=P

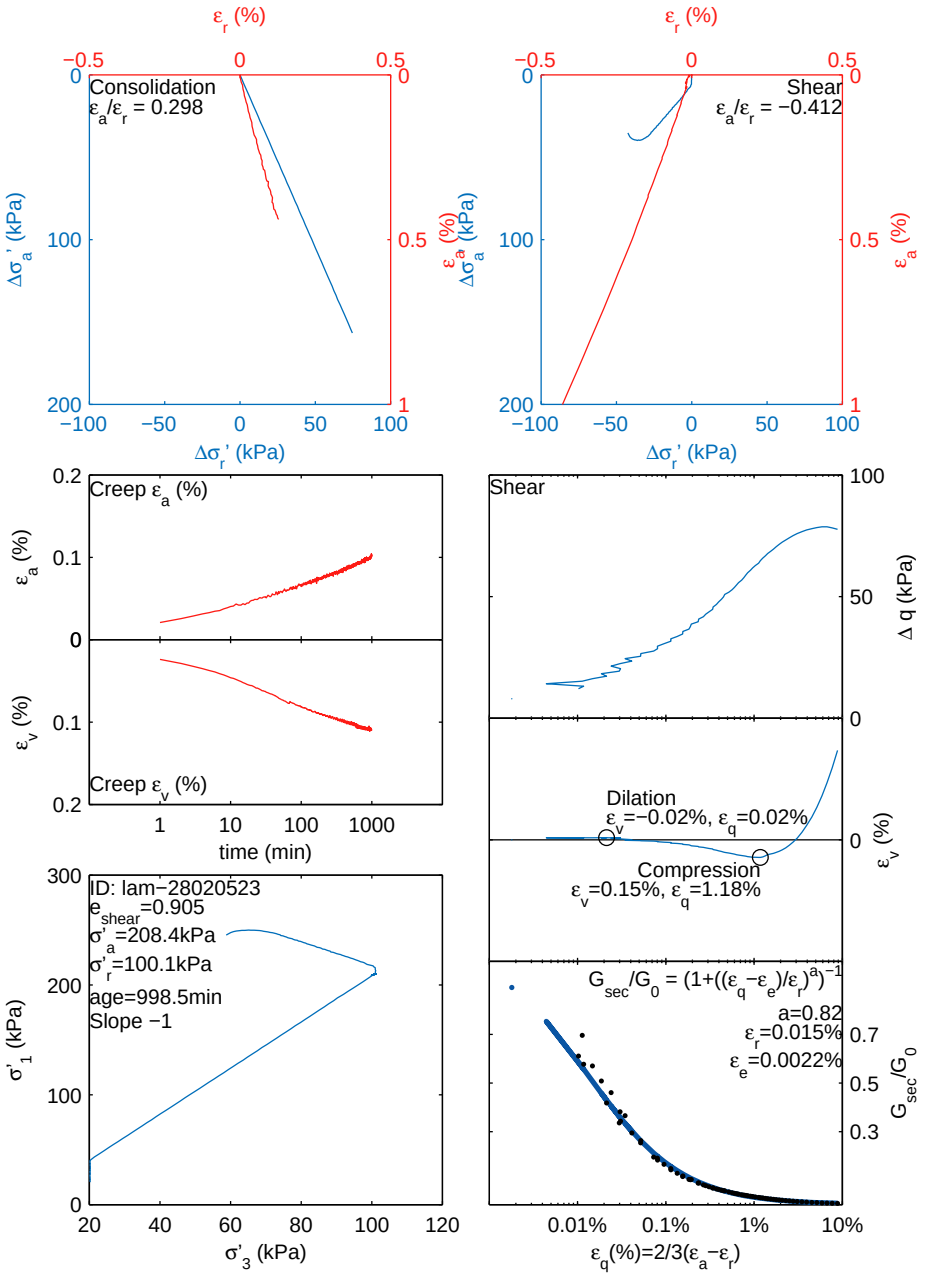

Figure D.81: Lam-28020523: σ_a = 208.4 kPa, σ_r = 100.1 kPa, age=998.5 min, Stress path=-1

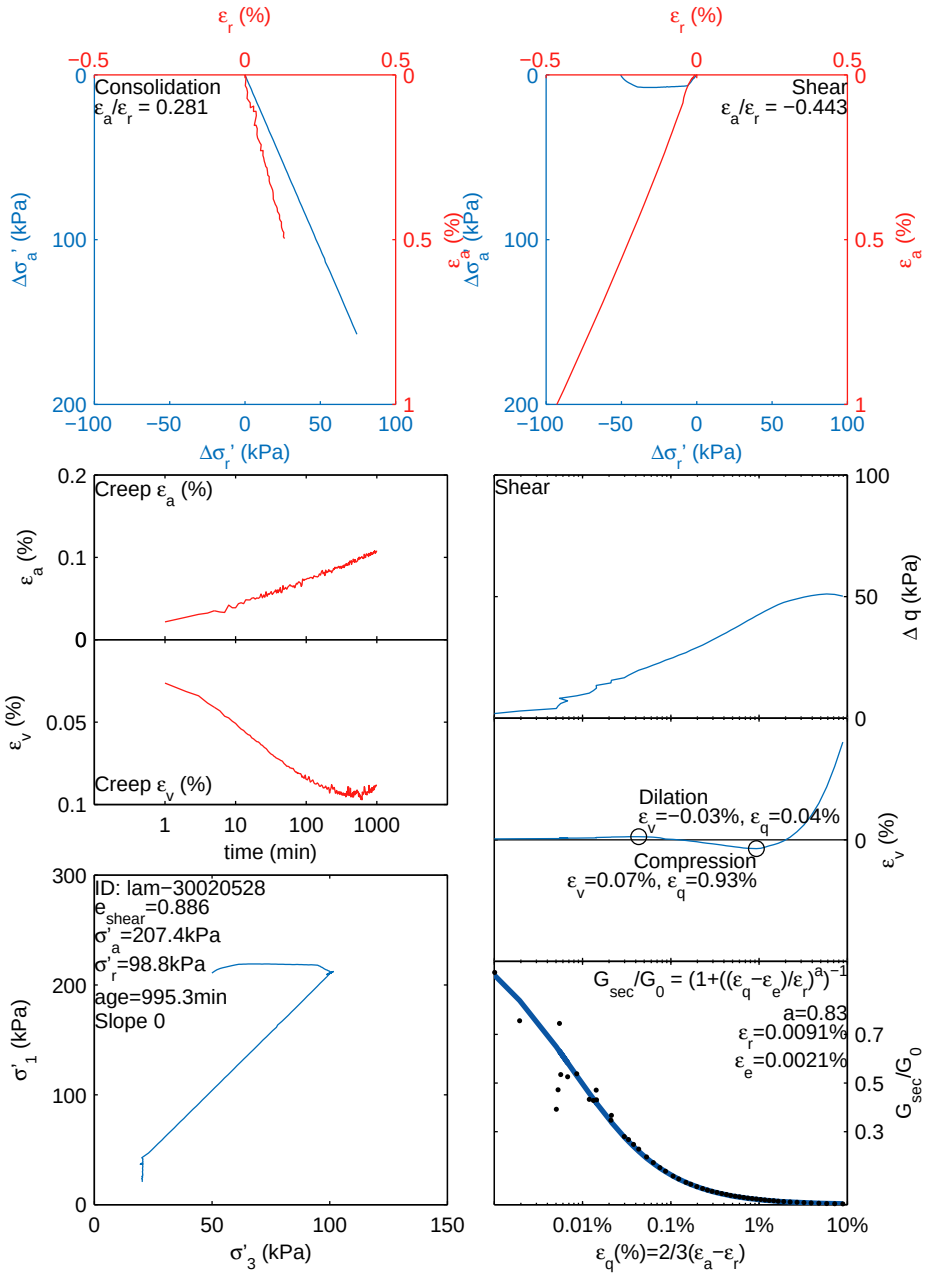

Figure D.82: Lam-30020528: σ_a = 207.4 kPa, σ_r = 98.8 kPa, age=995.3 min, Stress path=0

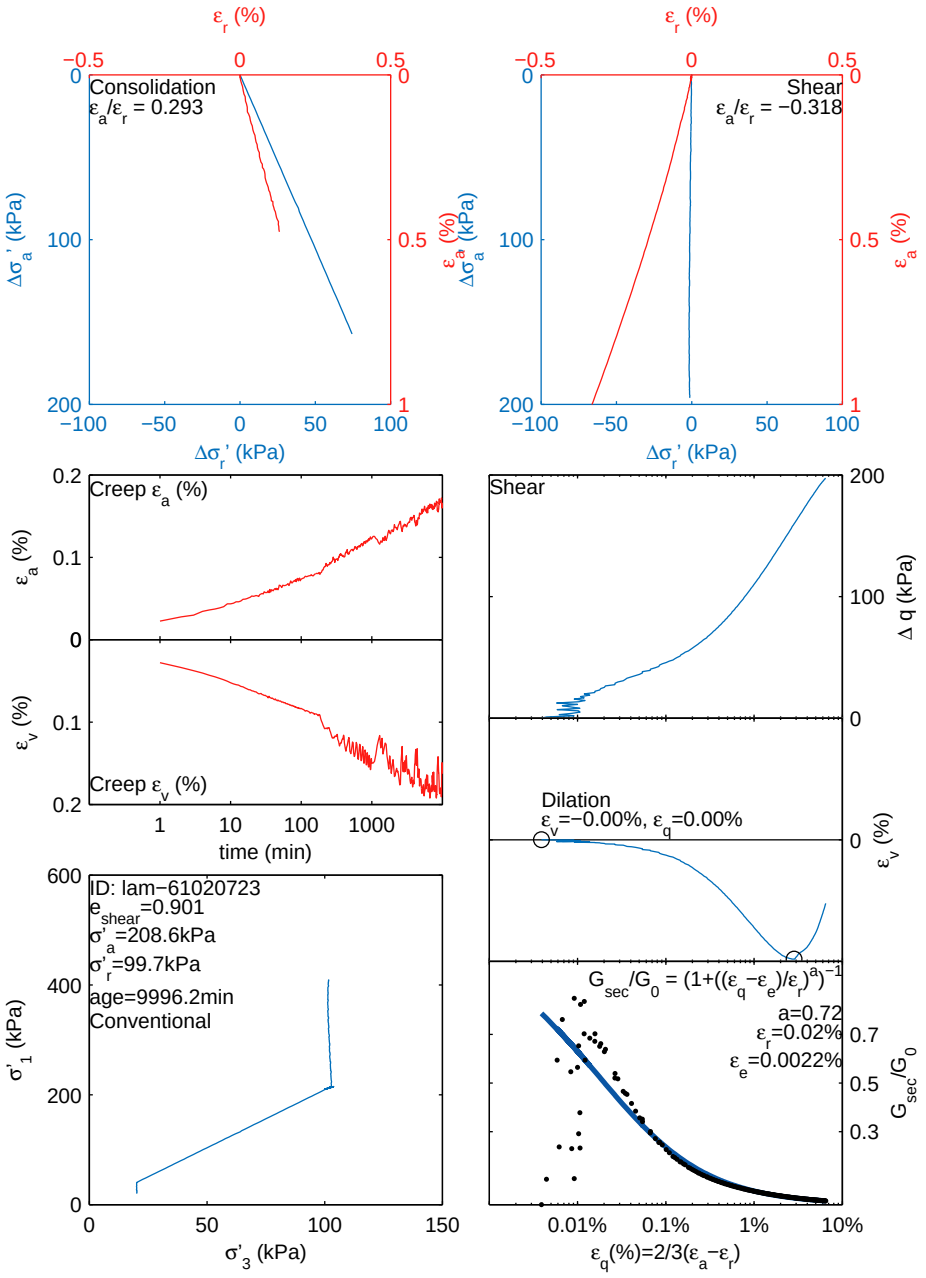

Figure D.83: Lam-61020723: σ_a = 208.6 kPa, σ_r = 99.7 kPa, age=9996.2 min, Stress path=C

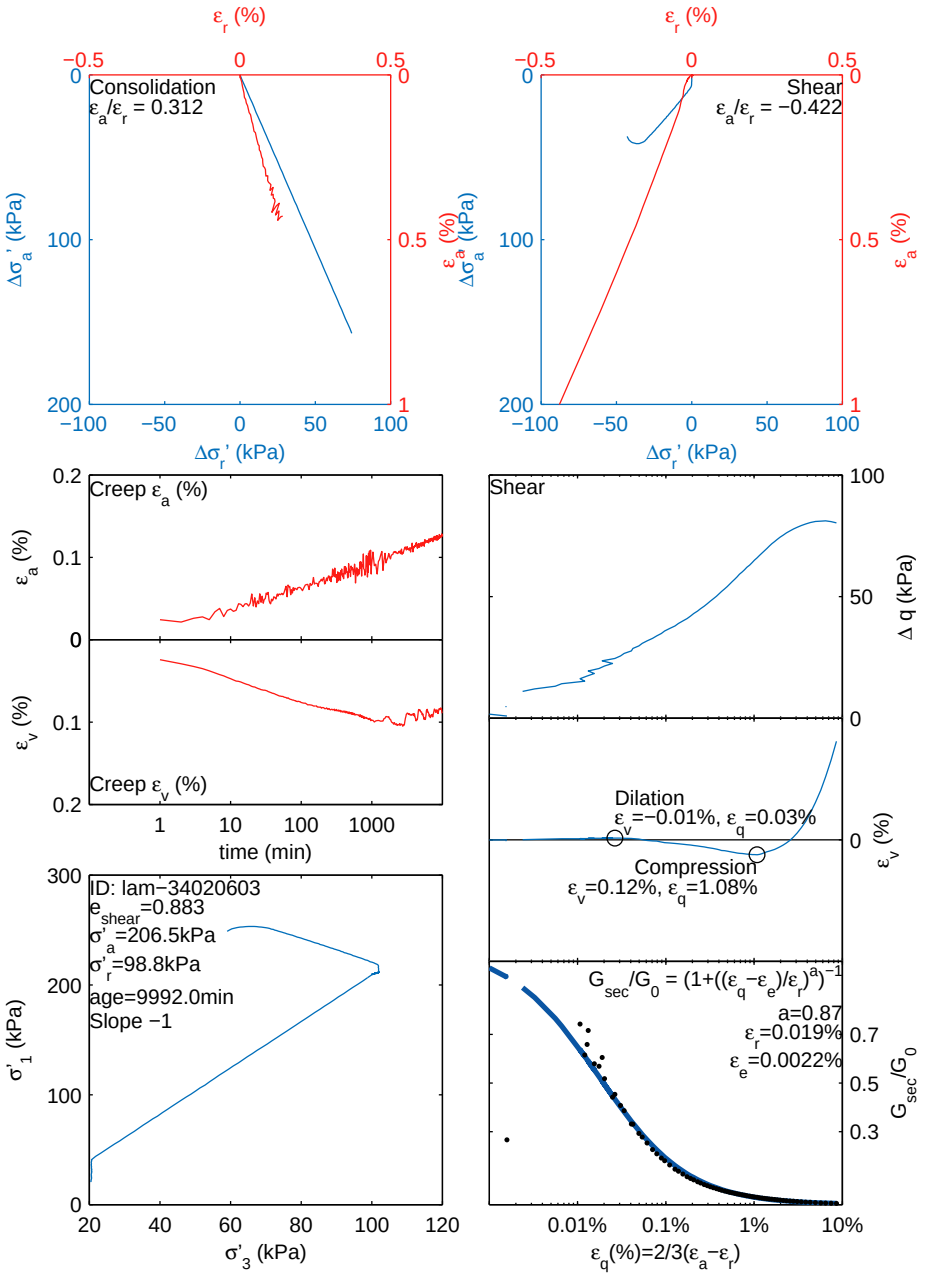

Figure D.84: Lam-34020603: σ_a = 206.5 kPa, σ_r = 98.8 kPa, age=9992.0 min, Stress path=-1

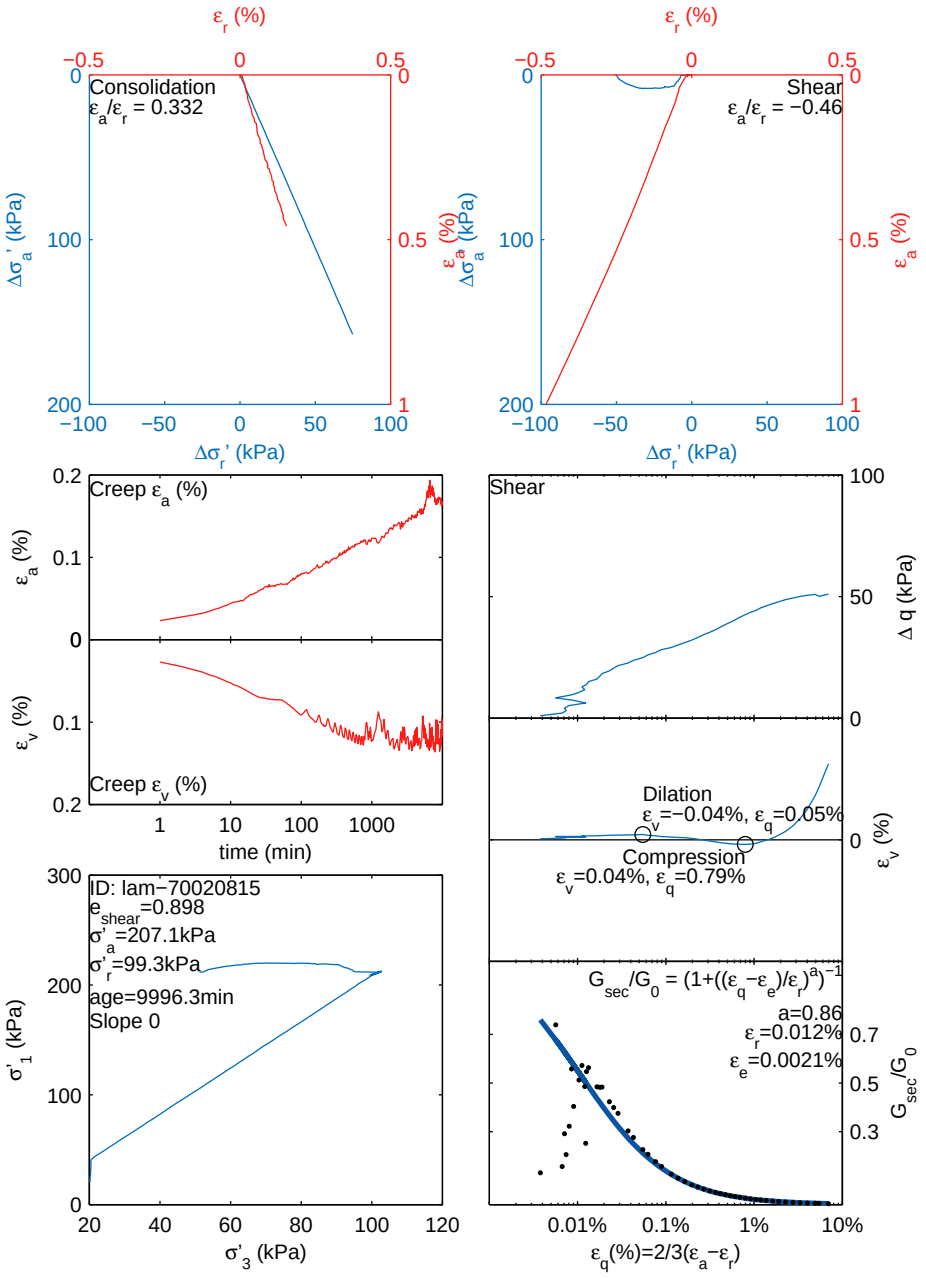

Figure D.85: Lam-70020815: σ_a = 207.1 kPa, σ_r = 99.3 kPa, age=9996.3 min, Stress path=0

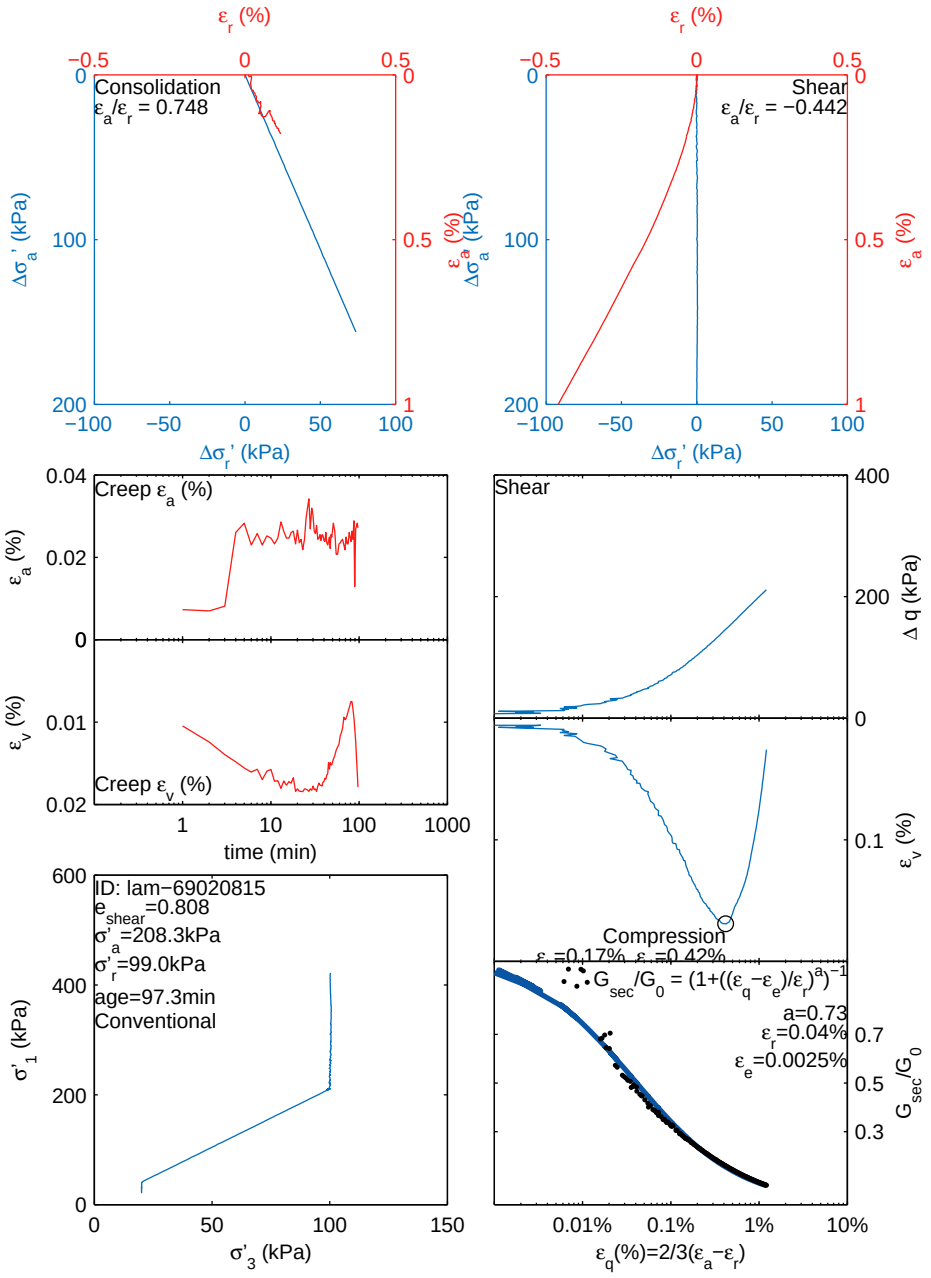

Figure D.86: Lam-69020815: σ_a = 208.3 kPa, σ_r = 99.0 kPa, age=97.3 min, Stress path=C

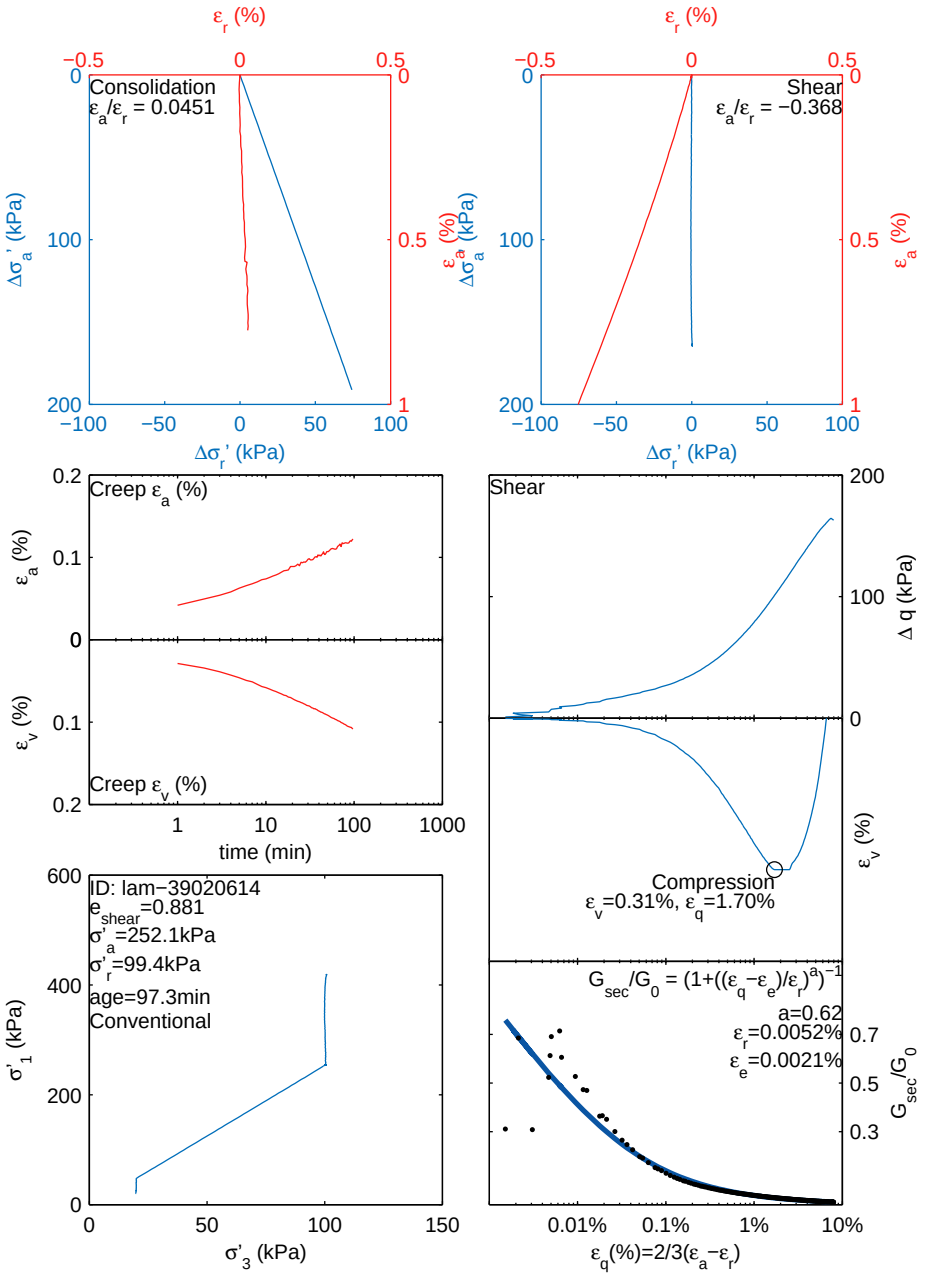

Figure D.87: Lam-39020614: σ_a = 252.1 kPa, σ_r = 99.4 kPa, age=97.3 min, Stress path=C

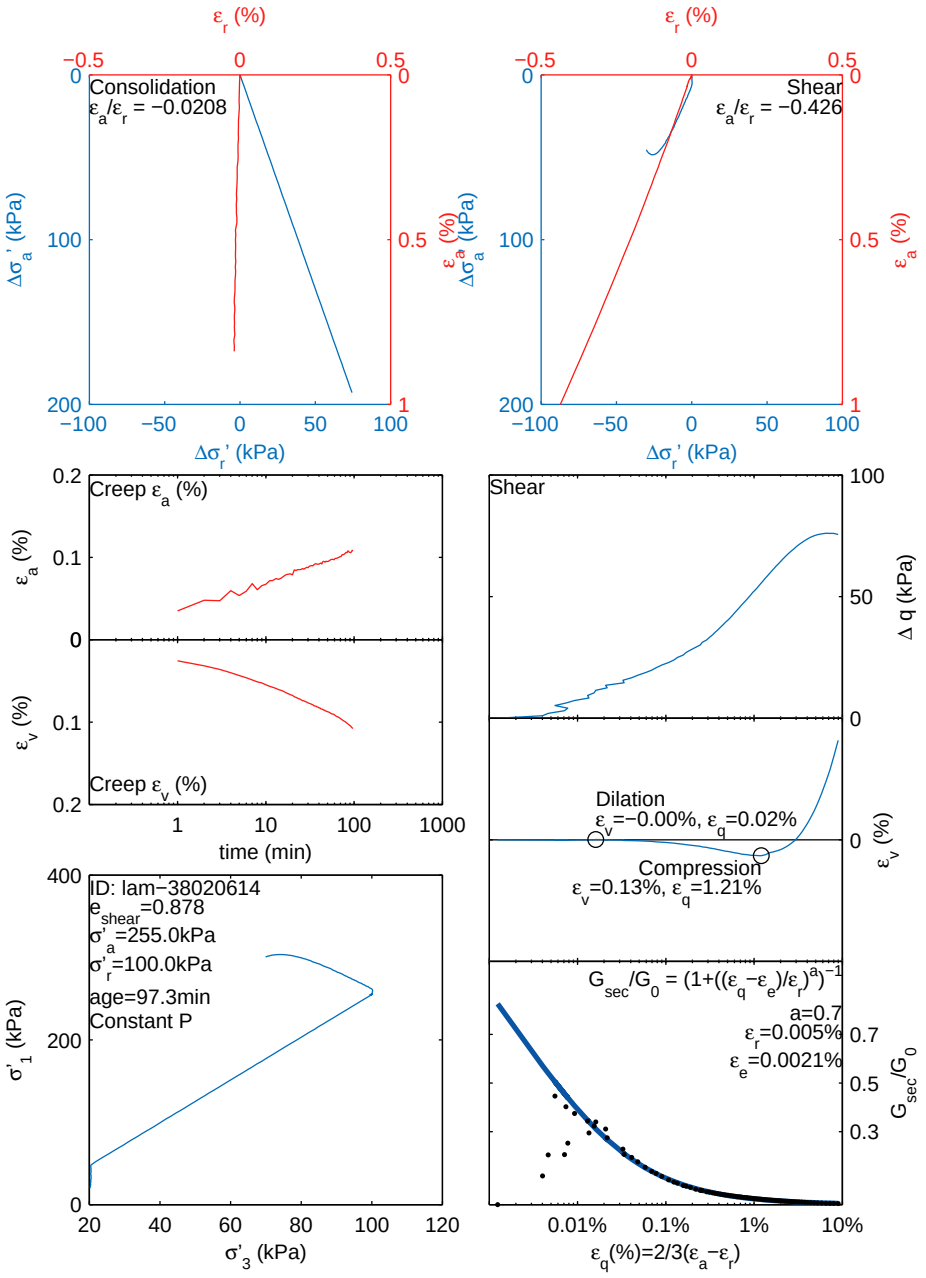

Figure D.88: Lam-38020614: σ_a = 255.0 kPa, σ_r = 100.0 kPa, age=97.3 min, Stress path=P

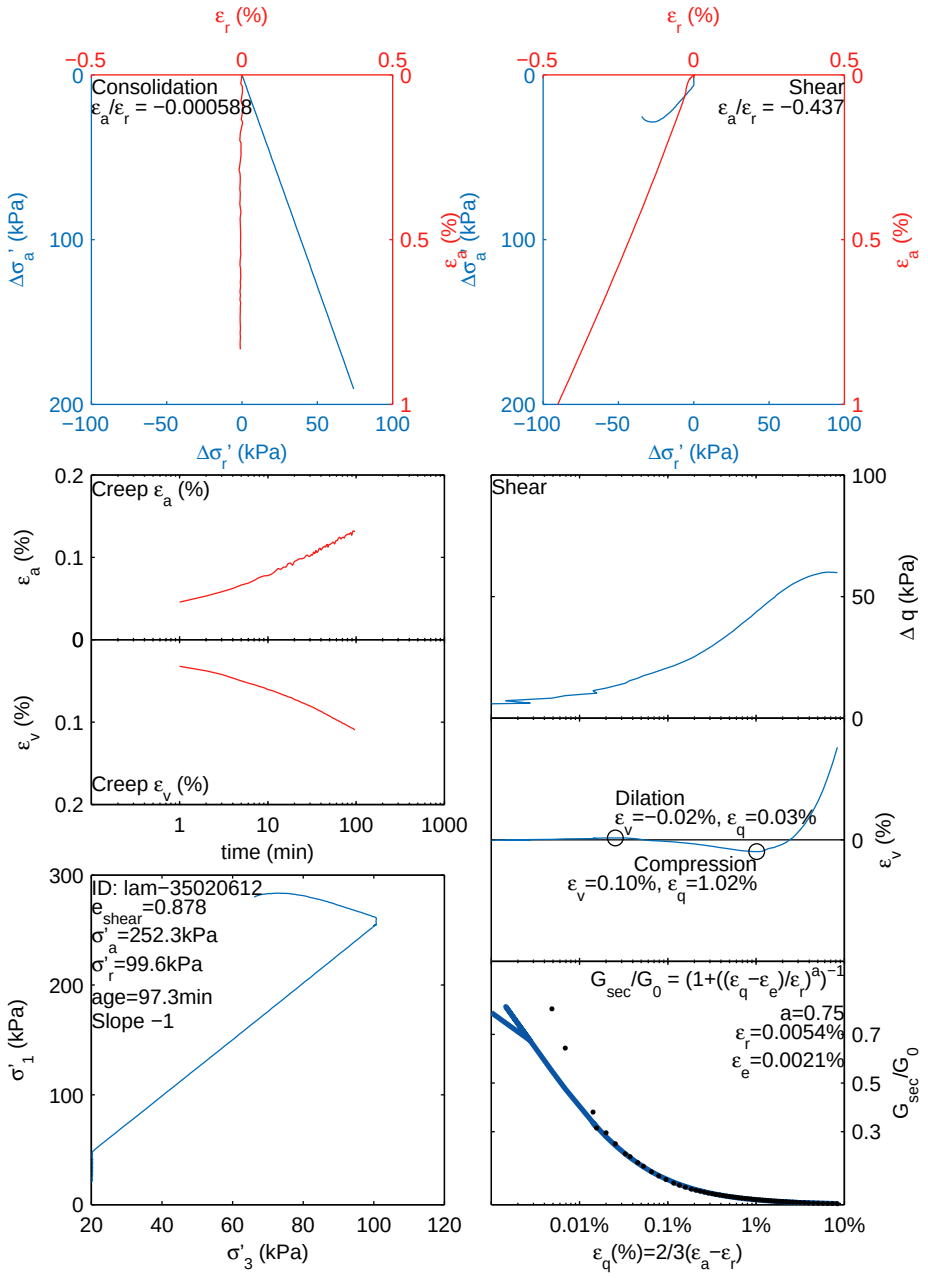

Figure D.89: Lam-35020612: σ_a = 252.3 kPa, σ_r = 99.6 kPa, age=97.3 min, Stress path=-1

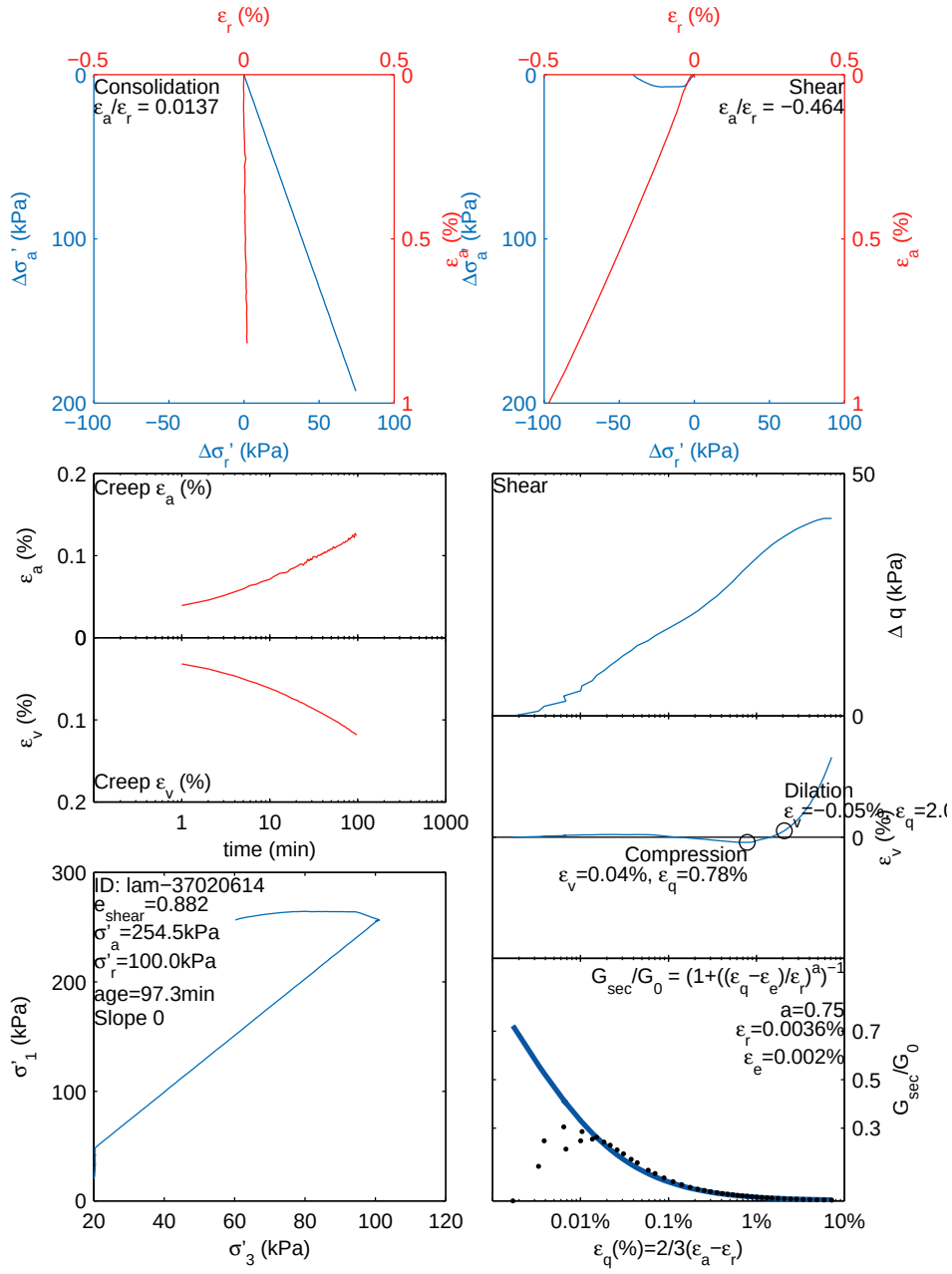

Figure D.90: Lam-37020614: σ_a = 254.5 kPa, σ_r = 100.0 kPa, age=97.3 min, Stress path=0

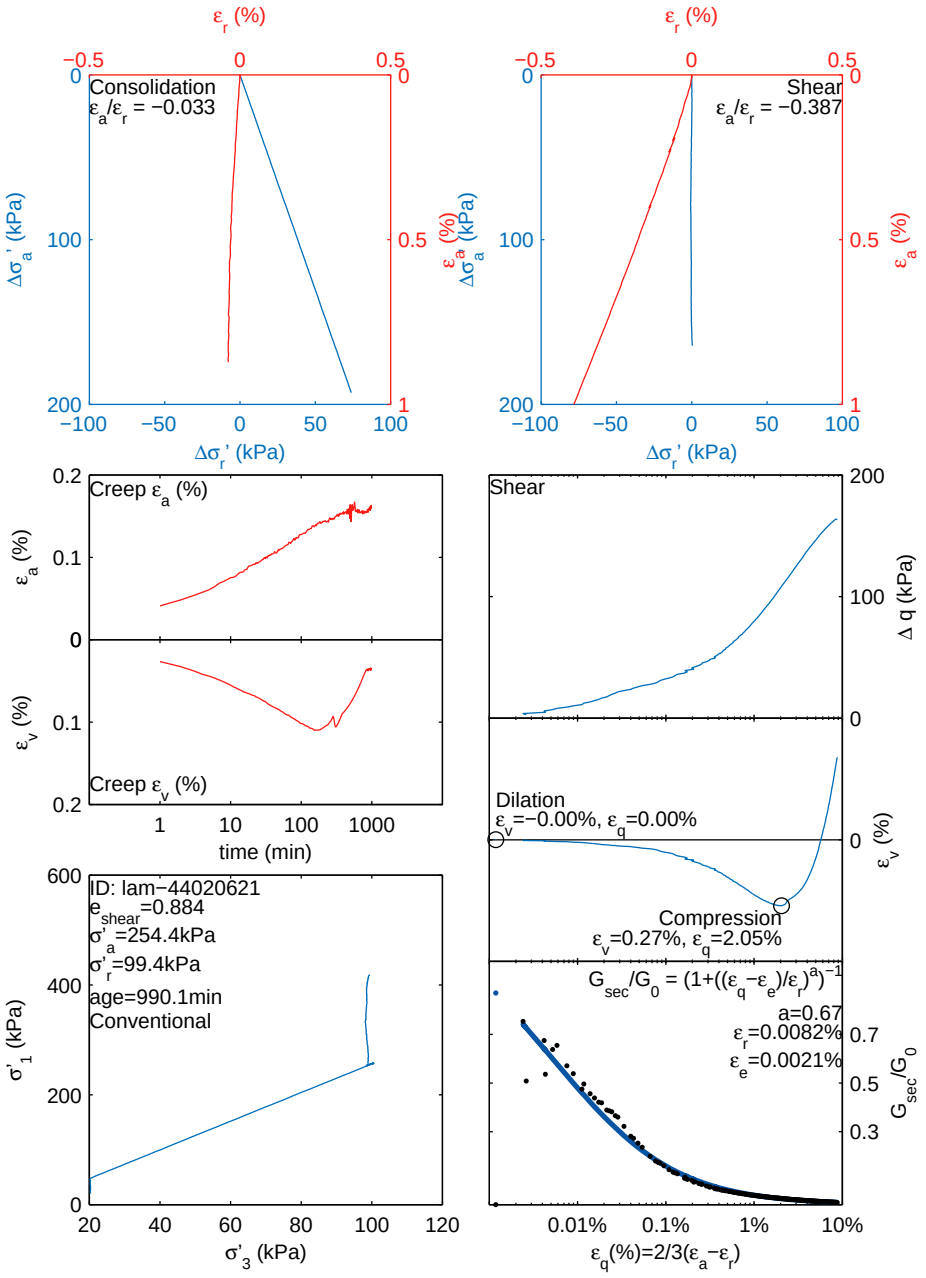

Figure D.91: Lam-44020621: σ_a = 254.4 kPa, σ_r = 99.4 kPa, age=990.1 min, Stress path=C

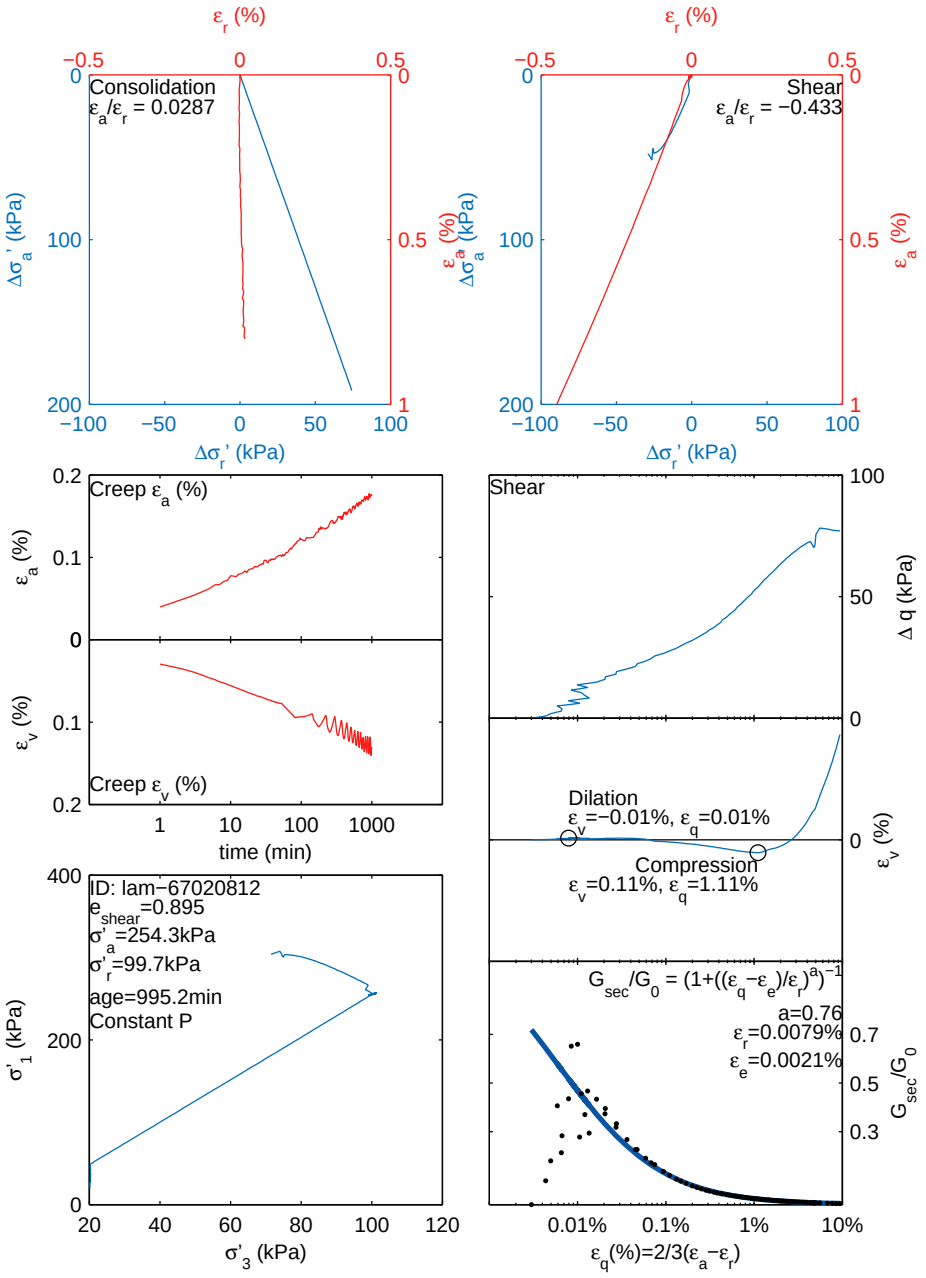

Figure D.92: Lam-67020812: σ_a = 254.3 kPa, σ_r = 99.7 kPa, age=995.2 min, Stress path=P

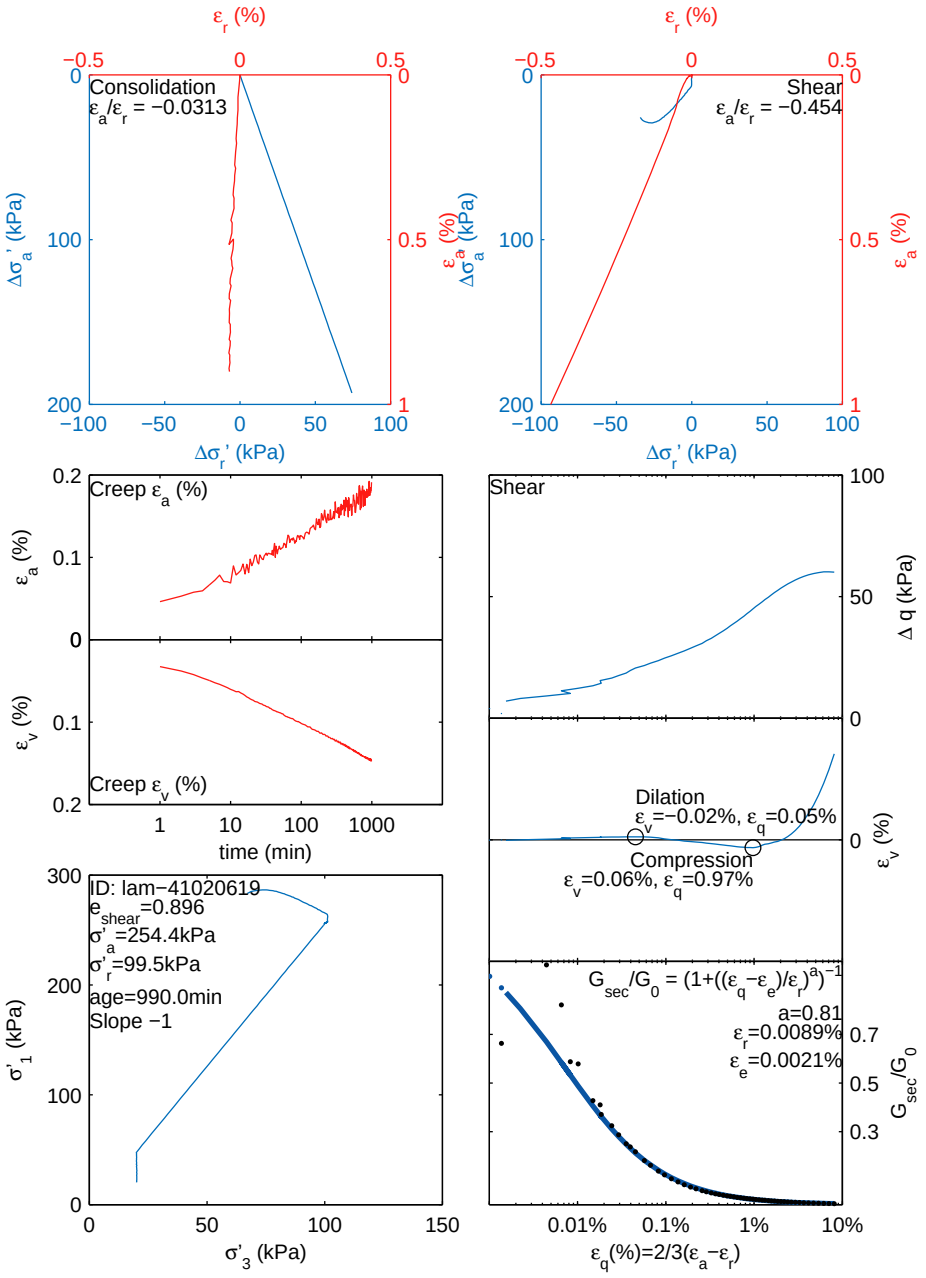

Figure D.93: Lam-41020619: σ_a = 254.4 kPa, σ_r = 99.5 kPa, age=990.0 min, Stress path=-1

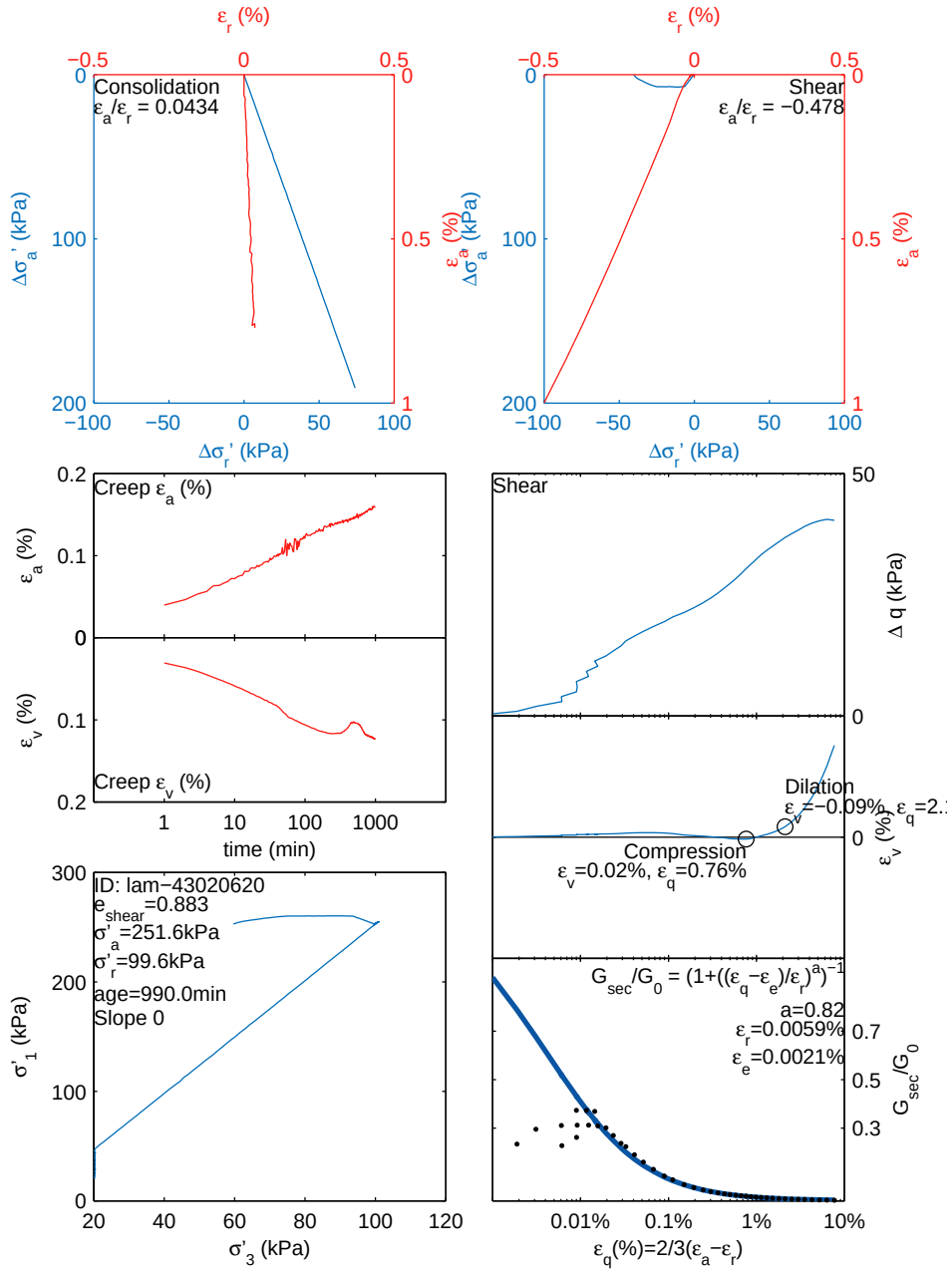

Figure D.94: Lam-43020620: σ_a = 251.6 kPa, σ_r = 99.6 kPa, age=990.0 min, Stress path=0

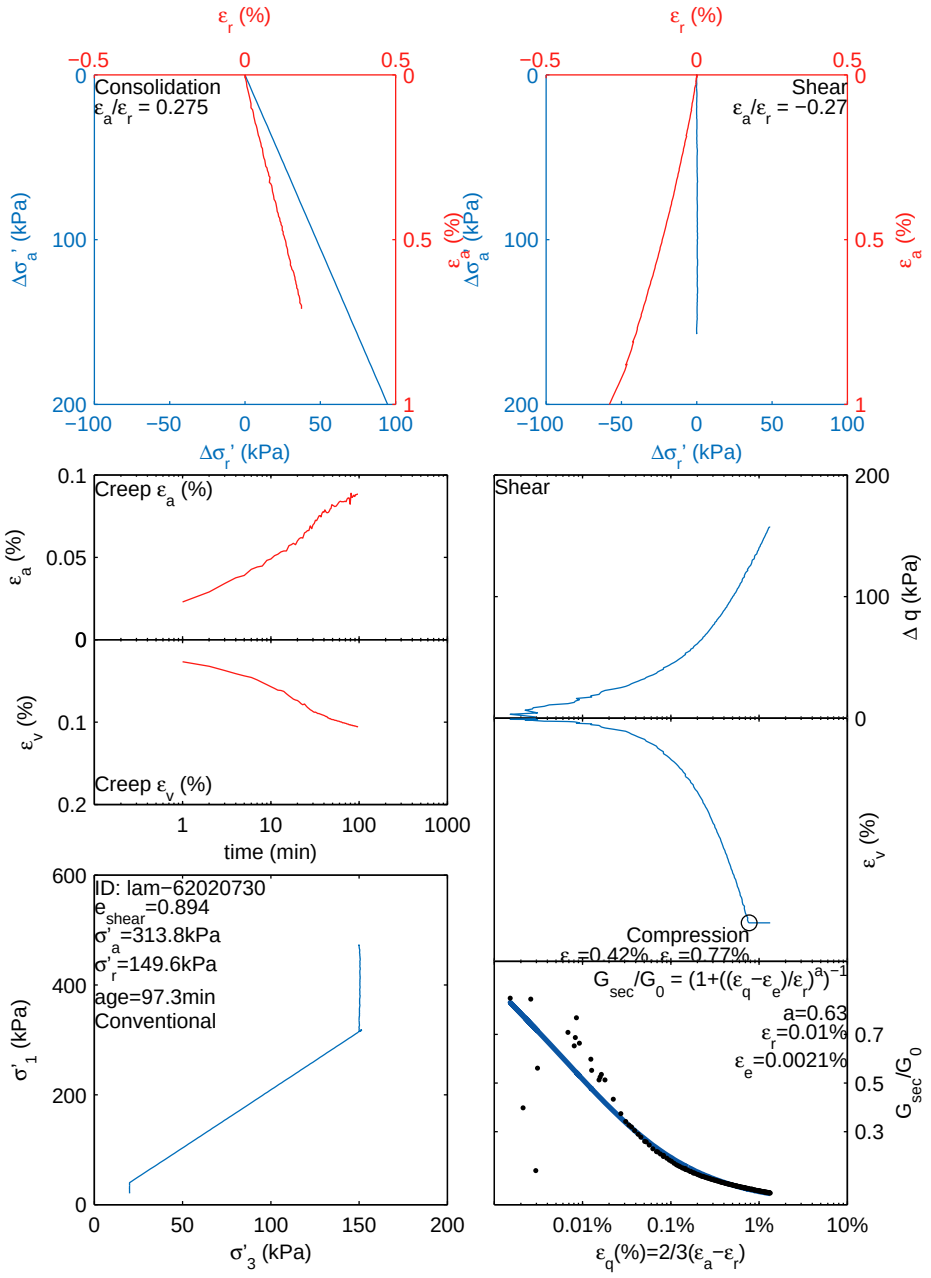

Figure D.95: Lam-62020730: σ_a = 313.8 kPa, σ_r = 149.6 kPa, age=97.3 min, Stress path=C

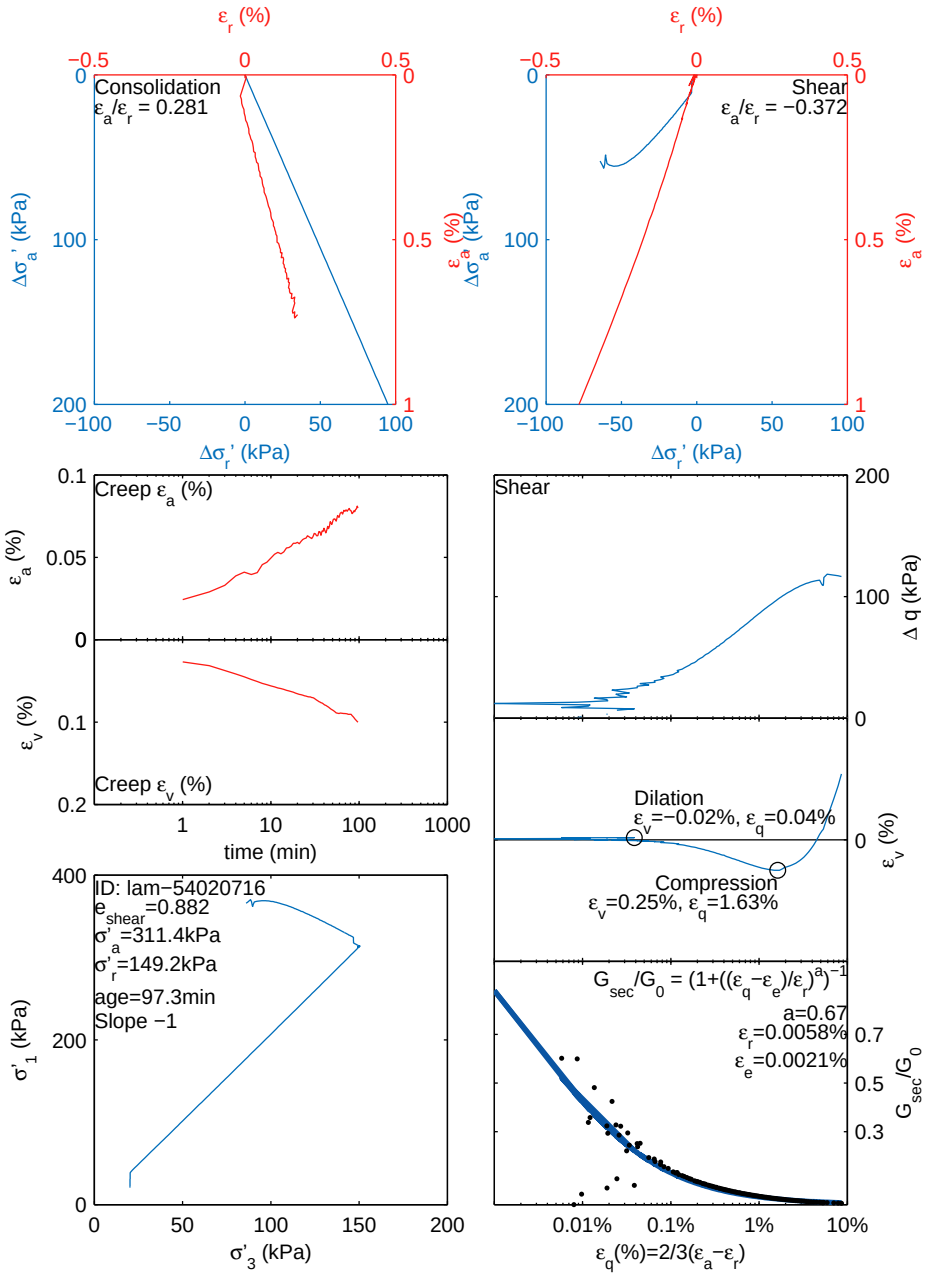

Figure D.96: Lam-54020716: σ_a = 311.4 kPa, σ_r = 149.2 kPa, age=97.3 min, Stress path=-1

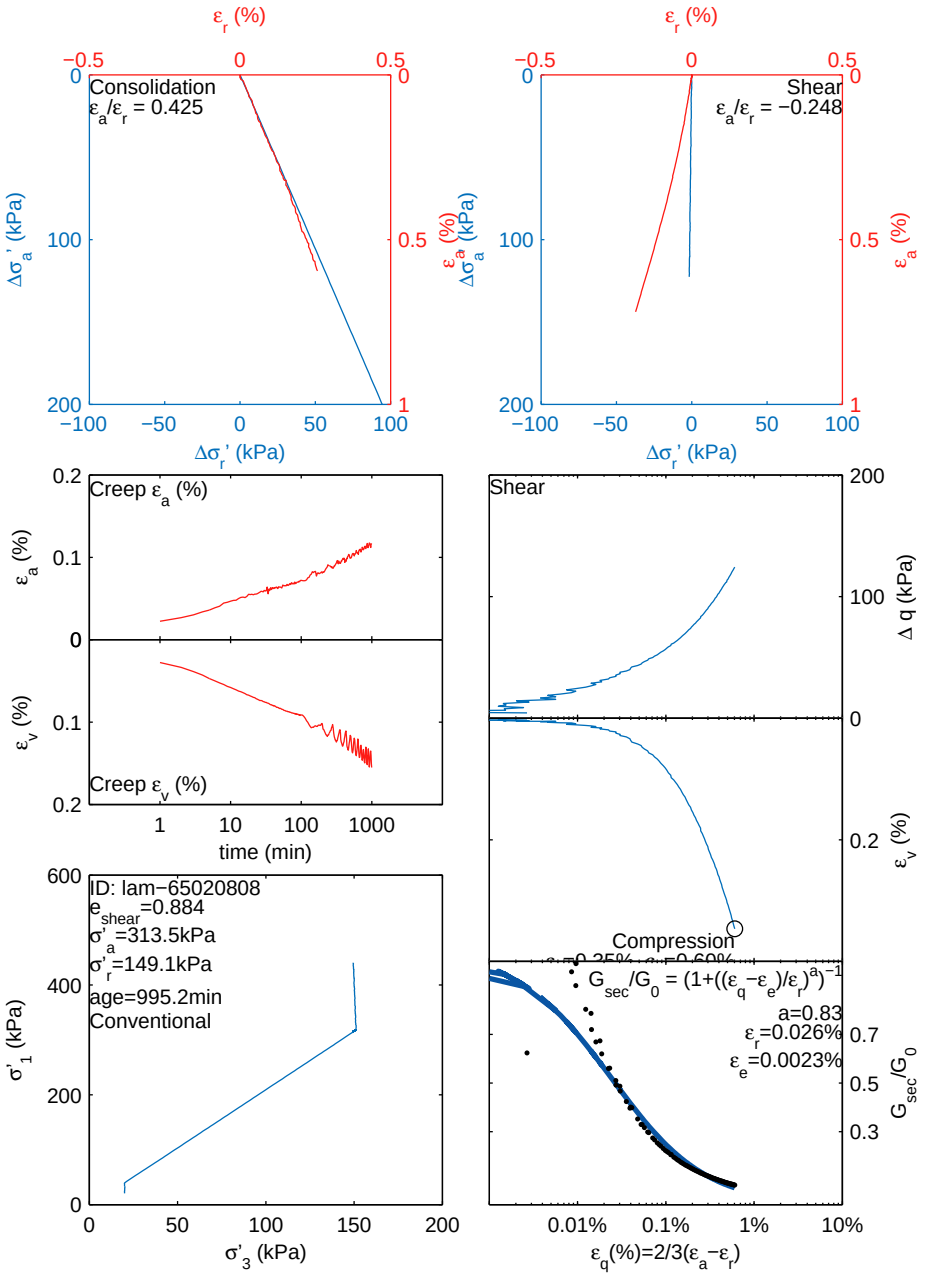

Figure D.97: Lam-65020808: σ_a = 313.5 kPa, σ_r = 149.1 kPa, age=995.2 min, Stress path=C

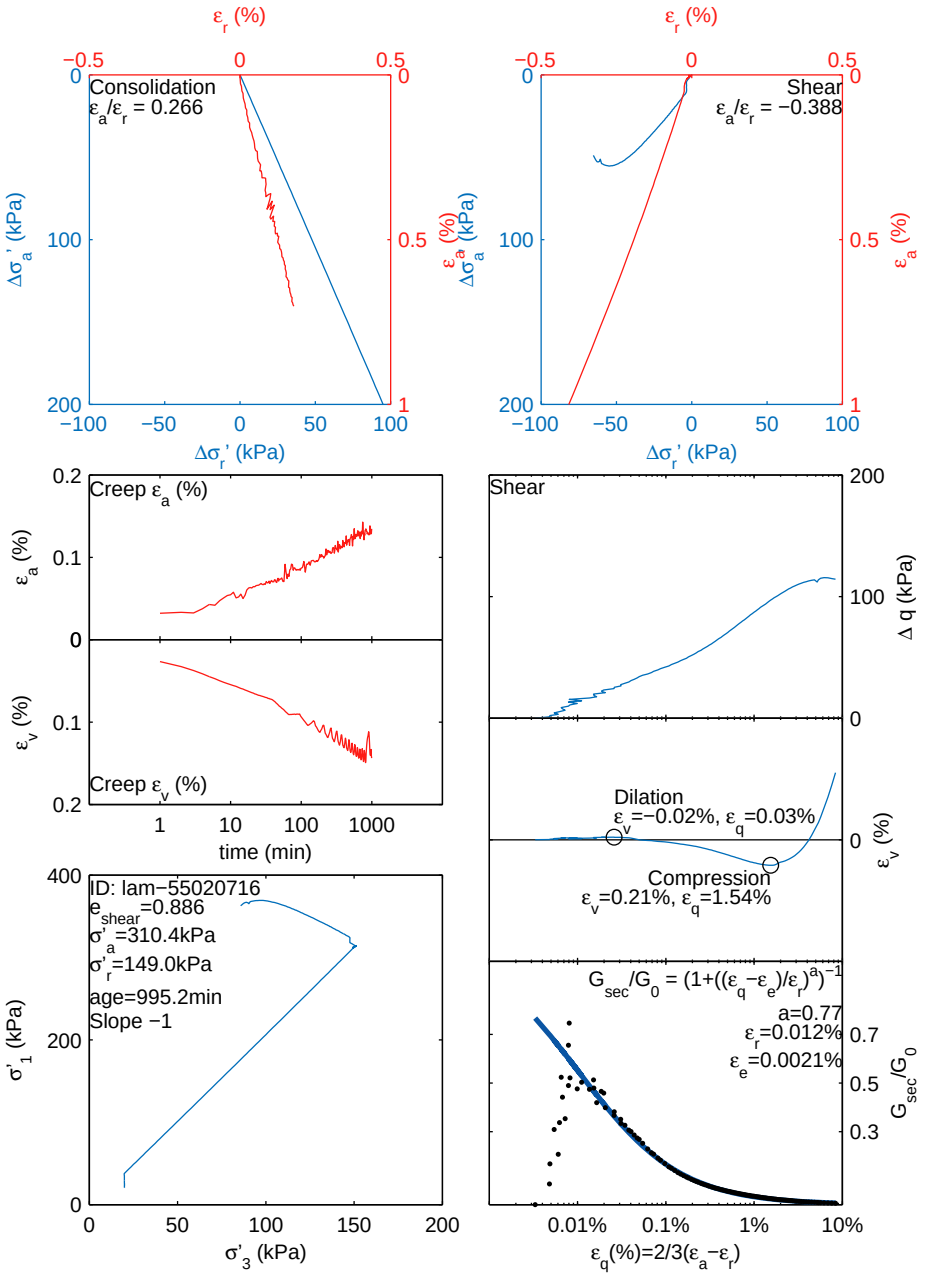

Figure D.98: Lam-55020716: σ_a = 310.4 kPa, σ_r = 149.0 kPa, age=995.2 min, Stress path=-1

D.3 Results from Shozen (2001)

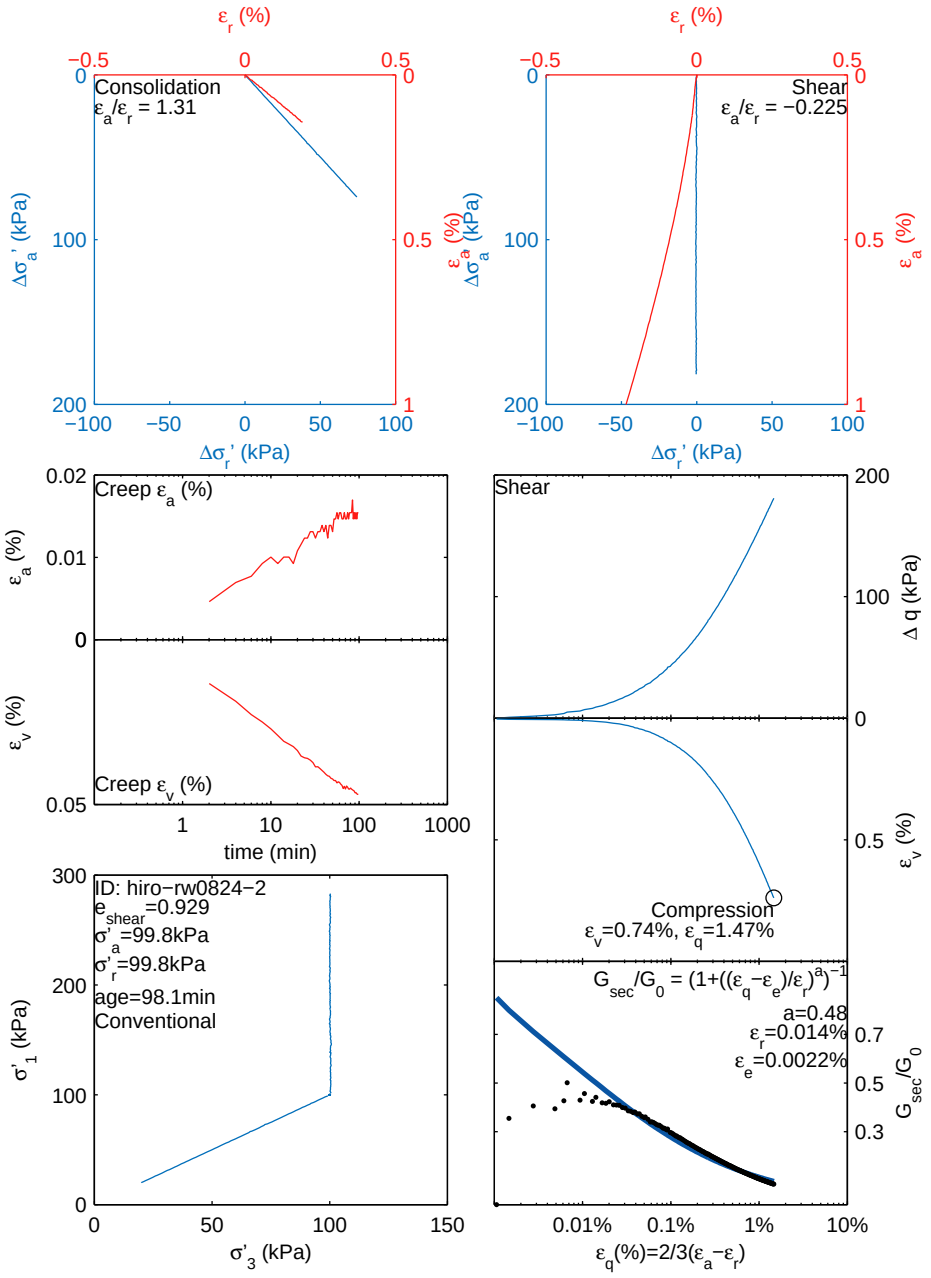

Figure D.99: Shozen-rw0824-2: σ_a = 99.8 kPa, σ_r = 99.8 kPa, age=98.1 min, Stress path=C

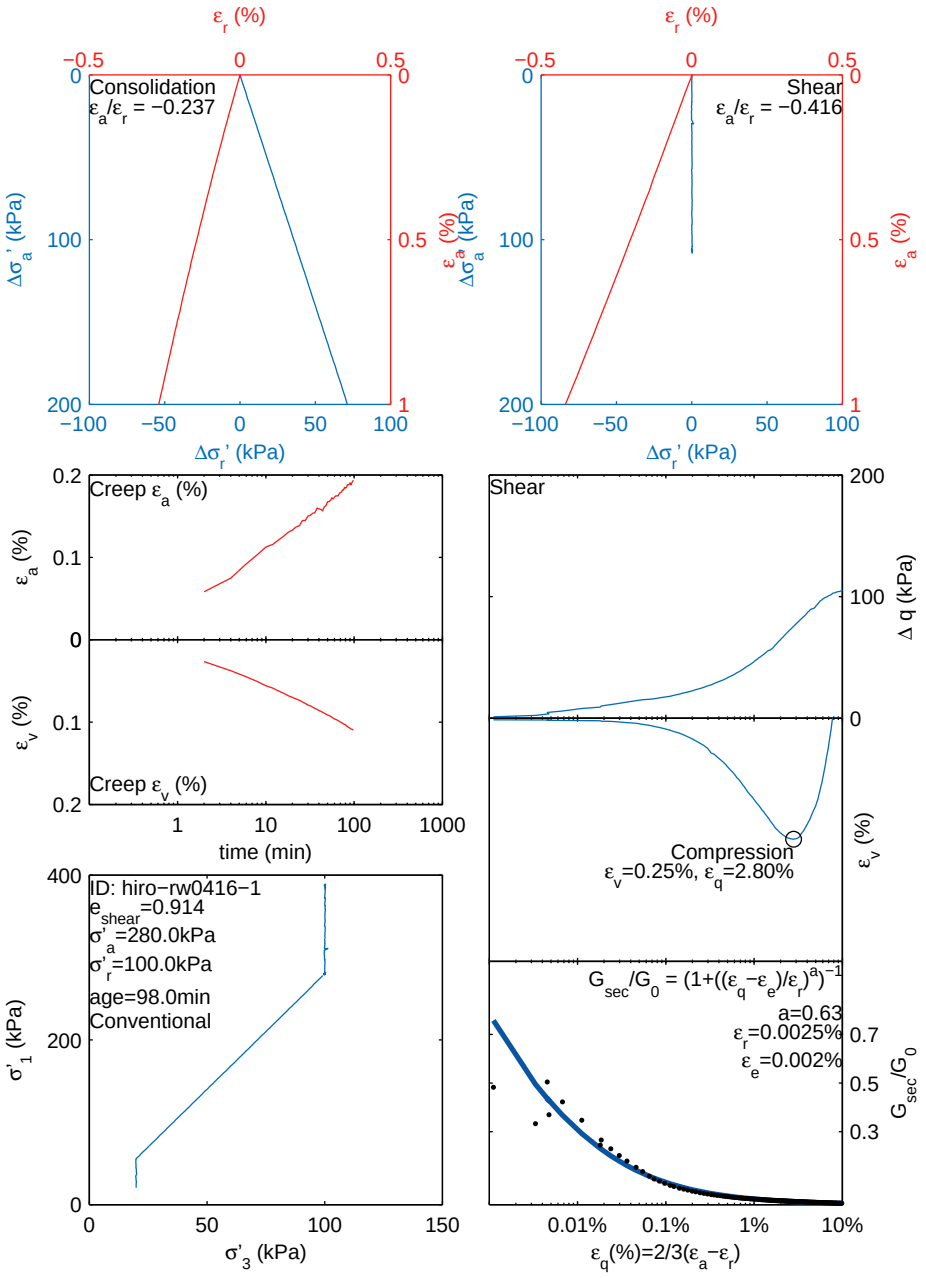

Figure D.100: Shozen-rw0416-1: σ_a = 280.0 kPa, σ_r = 100.0 kPa, age=98.0 min, Stress path=C

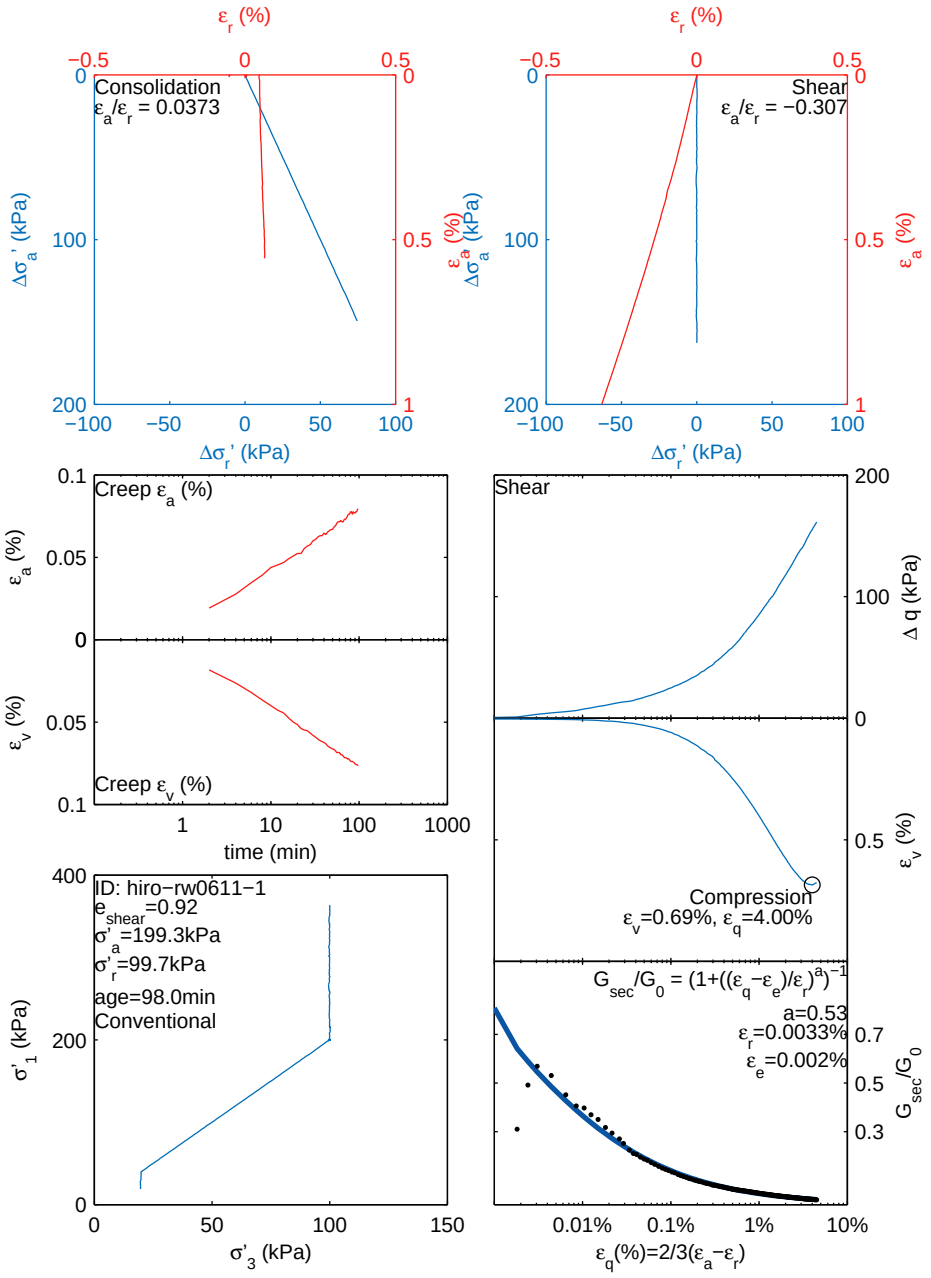

Figure D.101: Shozen-rw0611-1: σ_a = 199.3 kPa, σ_r = 99.7 kPa, age=98.0 min, Stress path=C

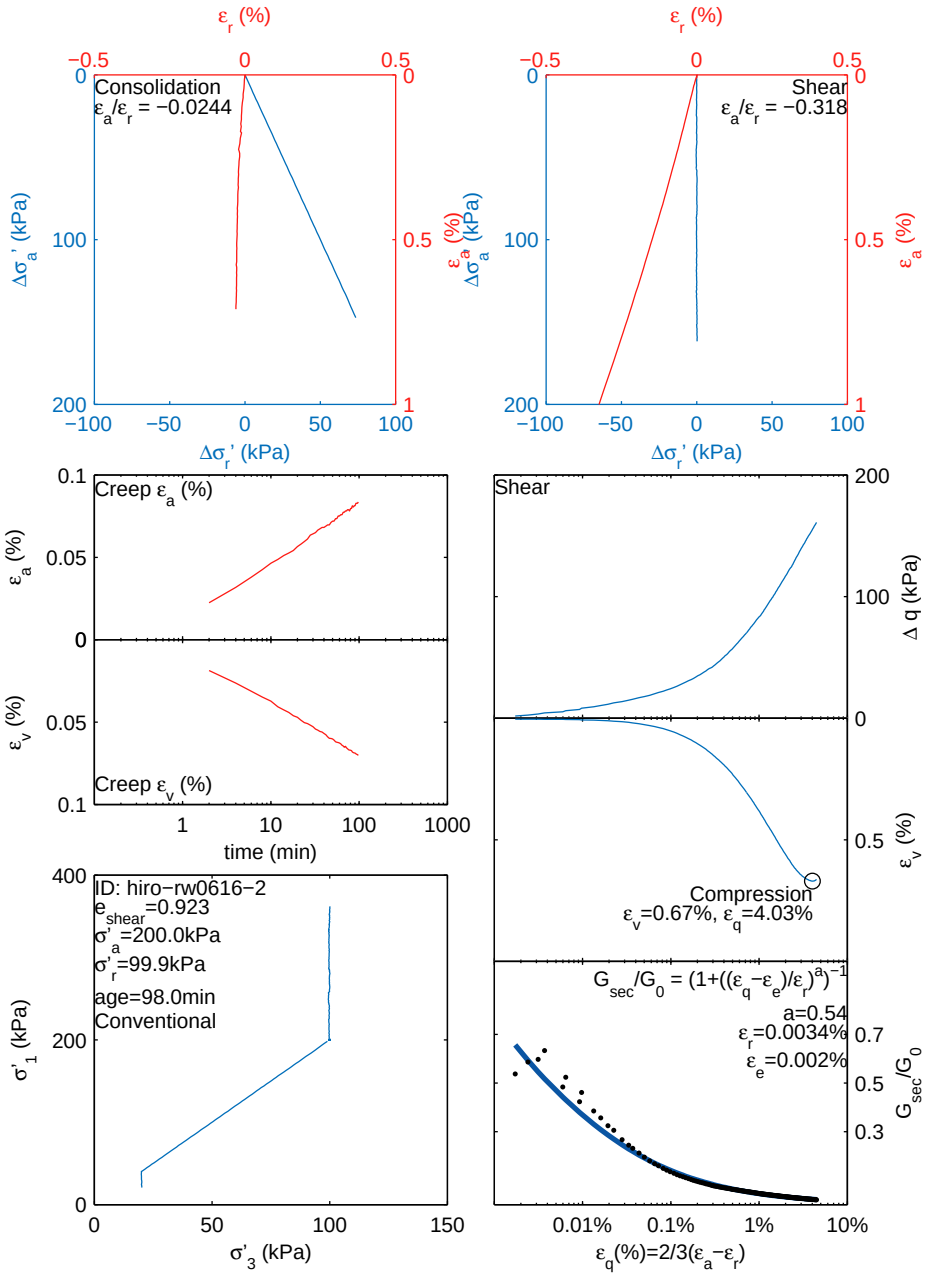

Figure D.102: Shozen-rw0616-2: σ_a = 200.0 kPa, σ_r = 99.9 kPa, age=98.0 min, Stress path=C

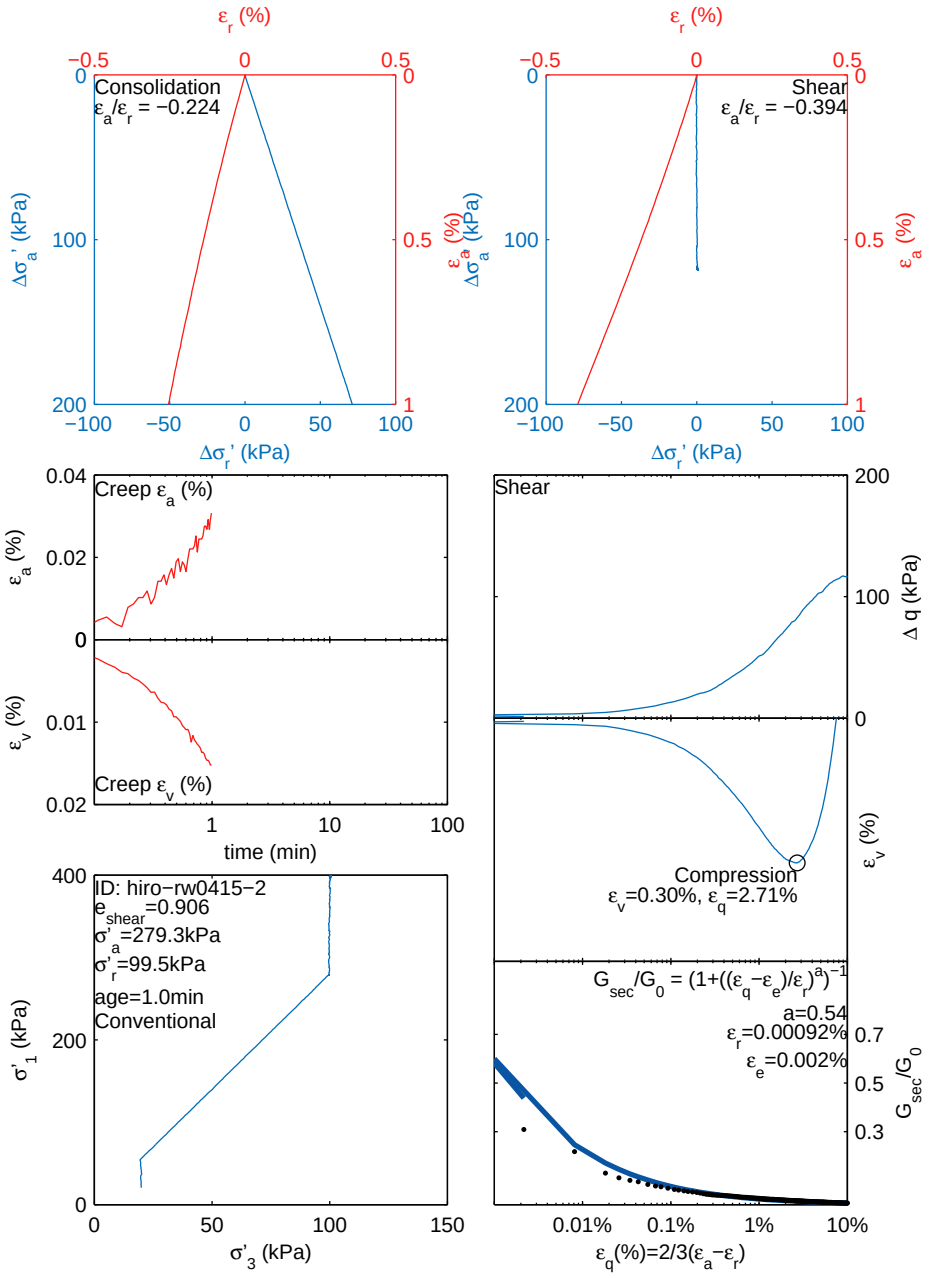

Figure D.103: Shozen-rw0415-2: σ_a = 279.3 kPa, σ_r = 99.5 kPa, age=1.0 min, Stress path=C

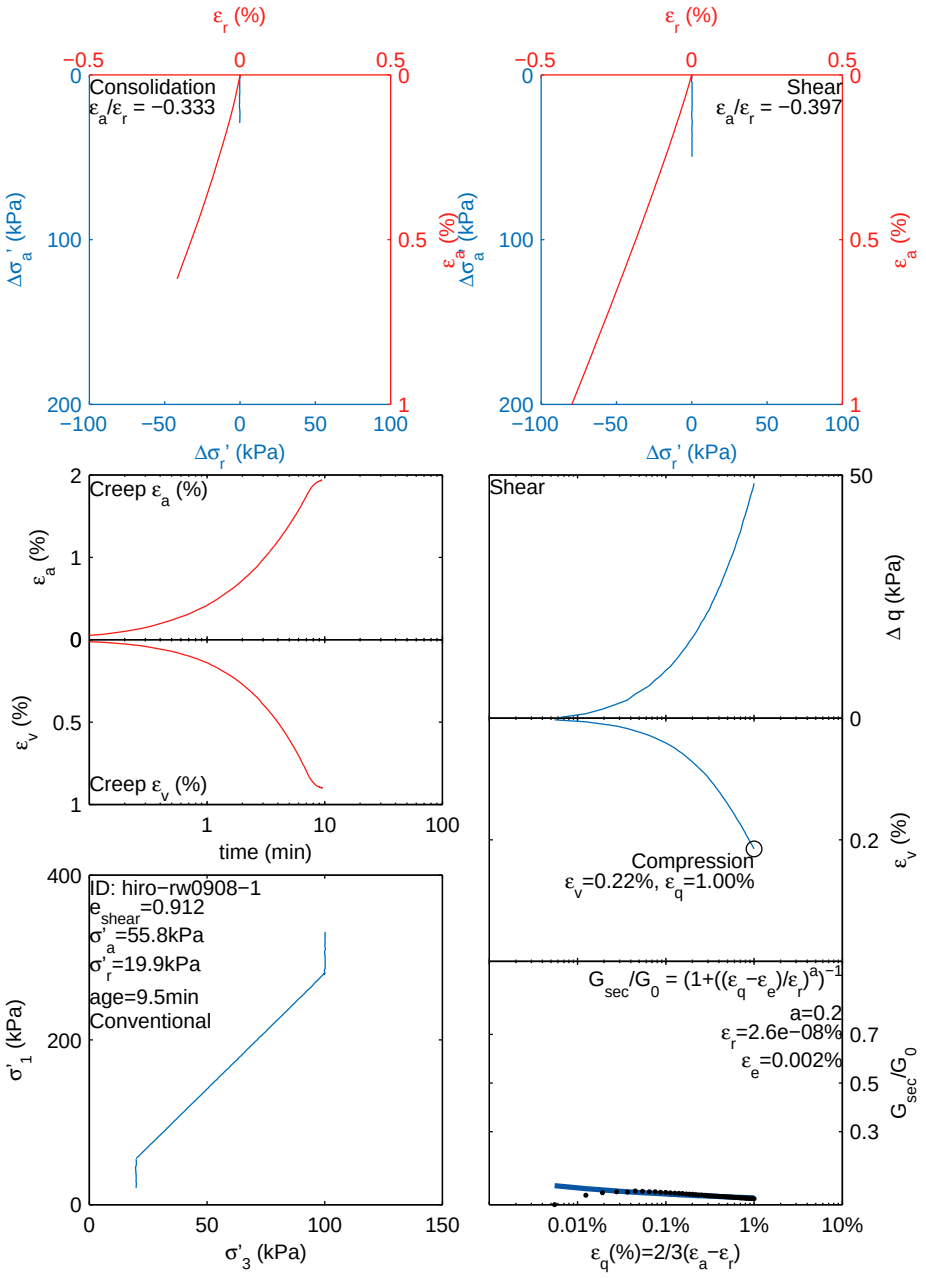

Figure D.104: Shozen-rw0908-1: σ_a = 55.8 kPa, σ_r = 19.9 kPa, age=9.5 min, Stress path=C

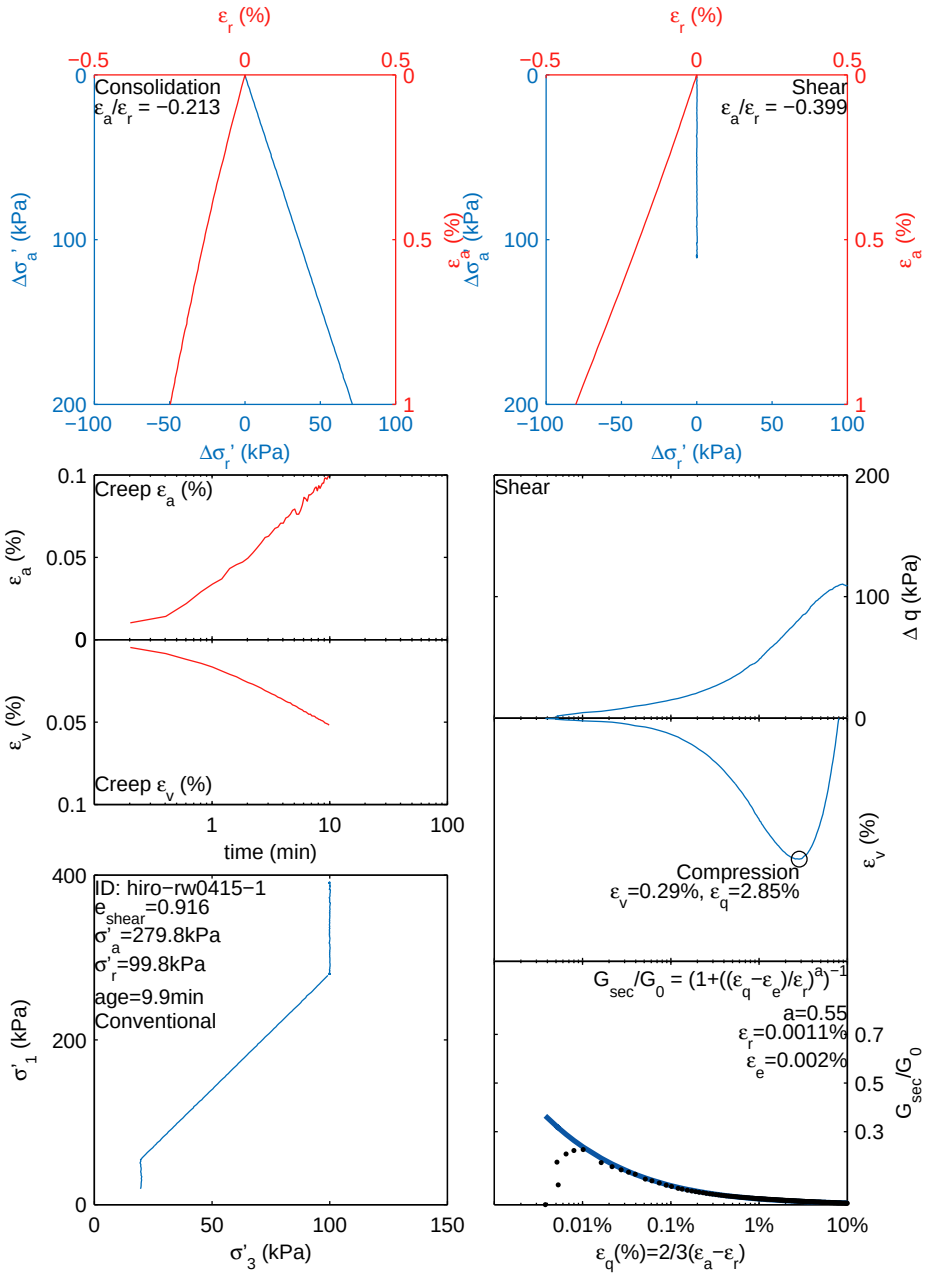

Figure D.105: Shozen-rw0415-1: σ_a = 279.8 kPa, σ_r = 99.8 kPa, age=9.9 min, Stress path=C

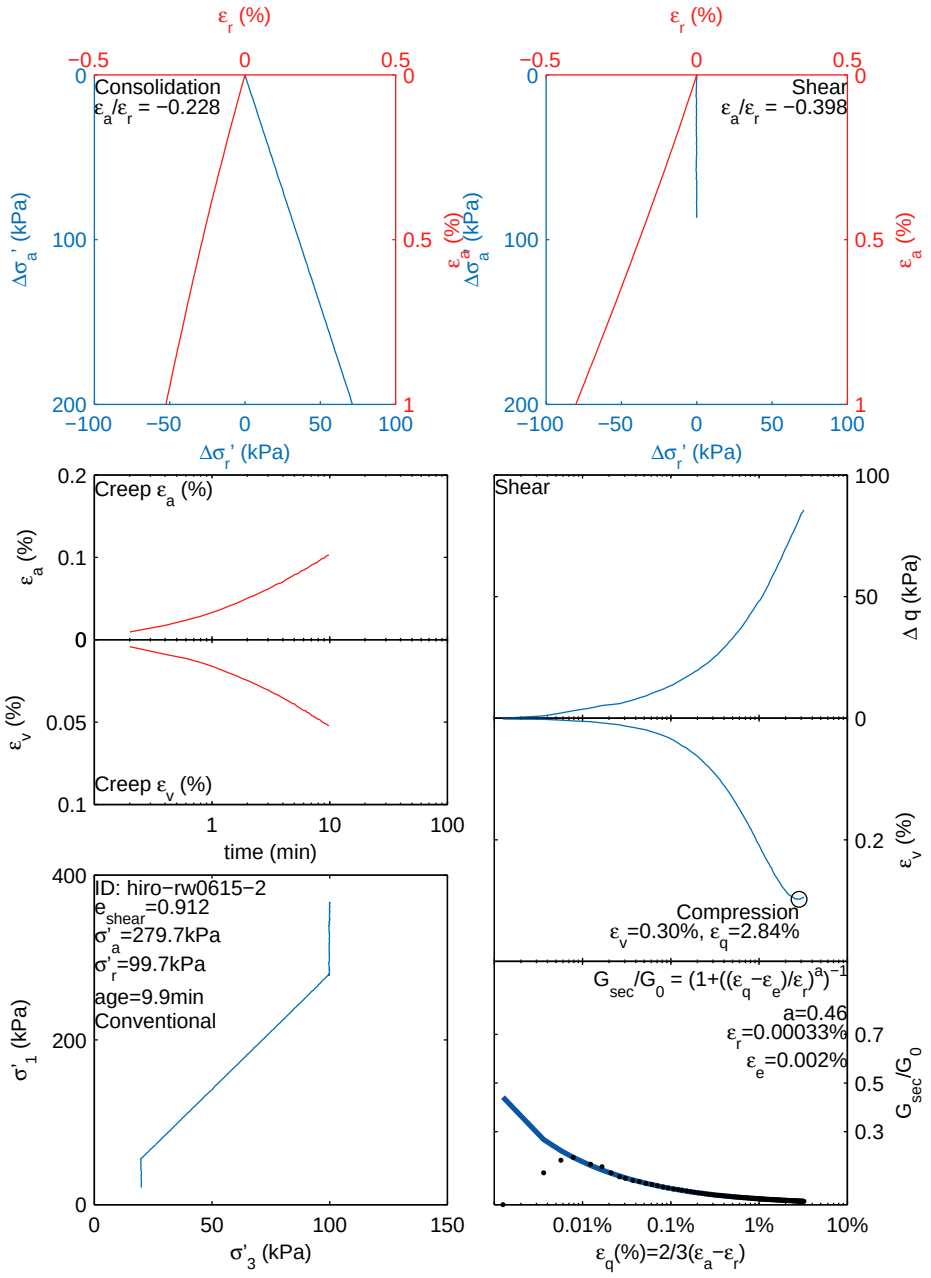

Figure D.106: Shozen-rw0615-2: σ_a = 279.7 kPa, σ_r = 99.7 kPa, age=9.9 min, Stress path=C

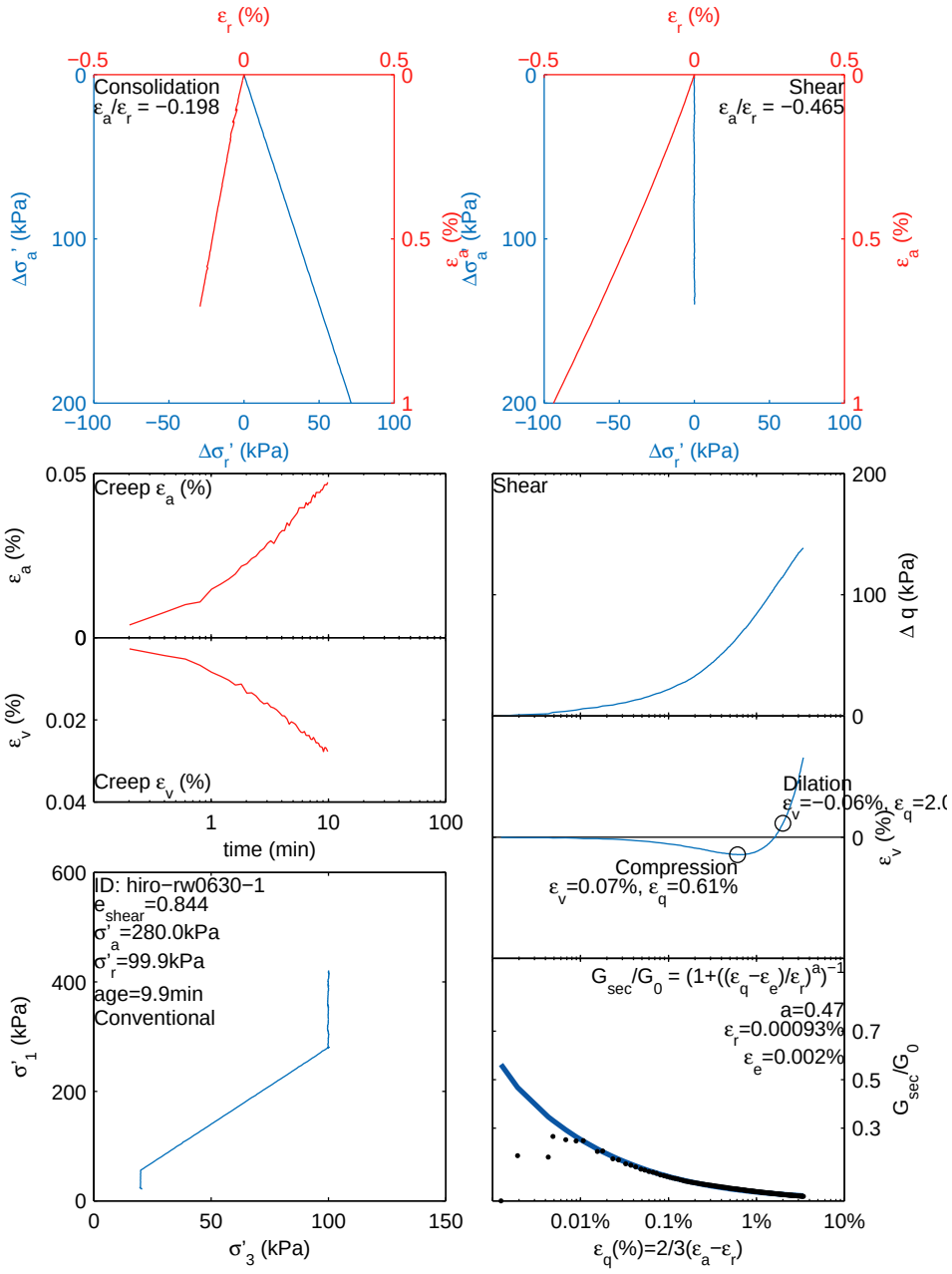

Figure D.107: Shozen-rw0630-1: σ_a = 280.0 kPa, σ_r = 99.9 kPa, age=9.9 min, Stress path=C

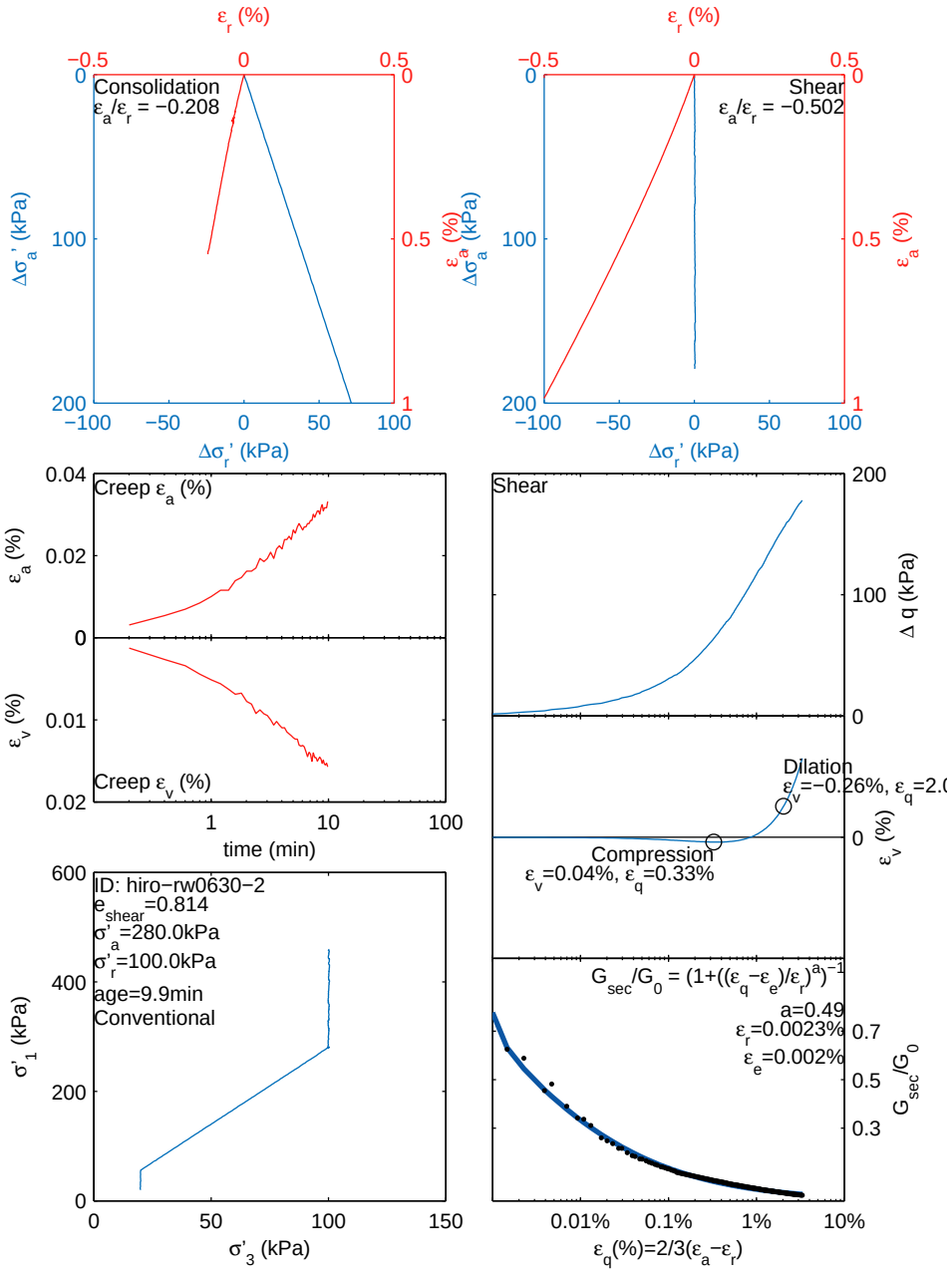

Figure D.108: Shozen-rw0630-2: σ_a = 280.0 kPa, σ_r = 100.0 kPa, age=9.9 min, Stress path=C

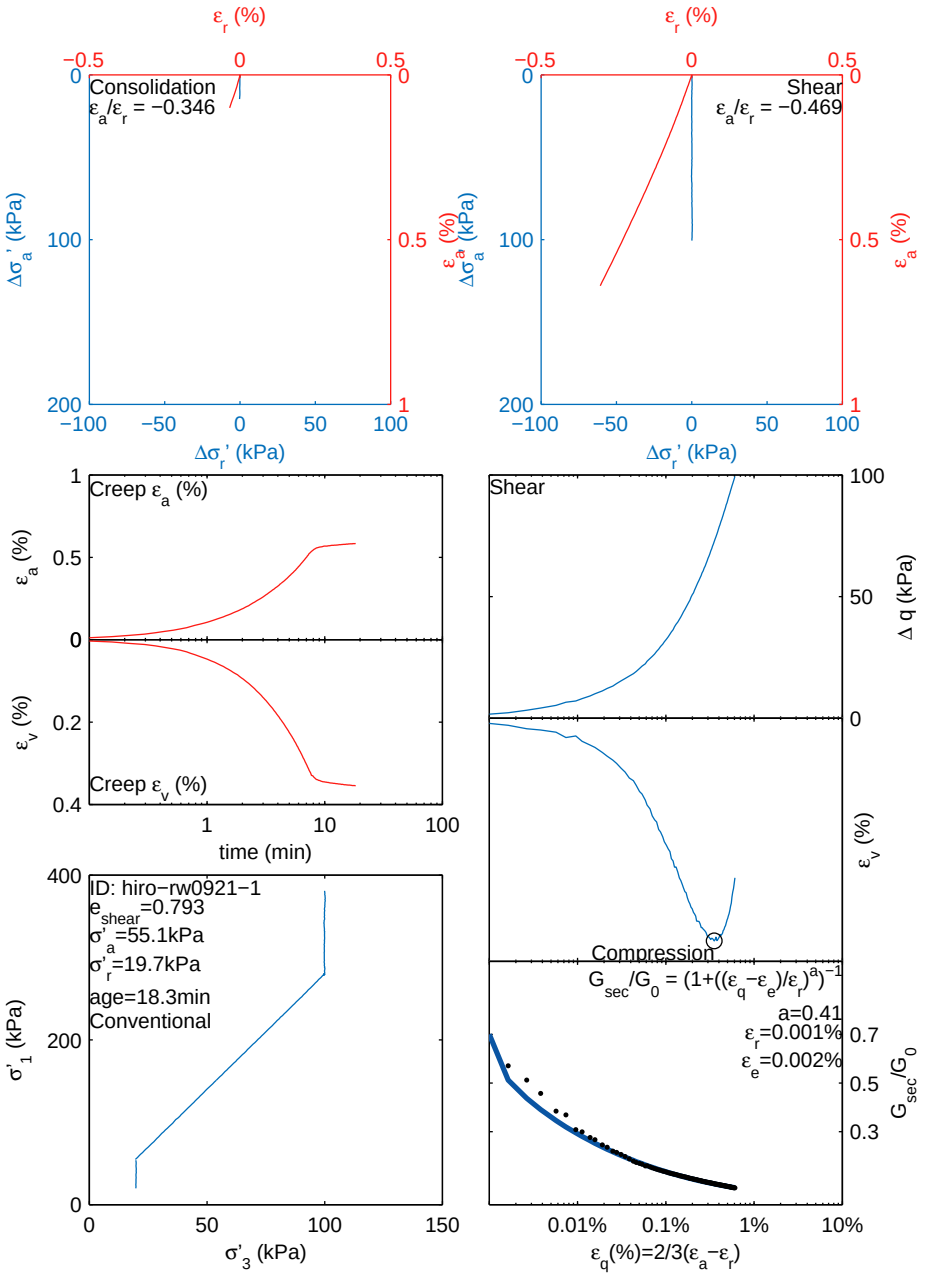

Figure D.109: Shozen-rw0921-1: σ_a = 55.1 kPa, σ_r = 19.7 kPa, age=18.3 min, Stress path=C

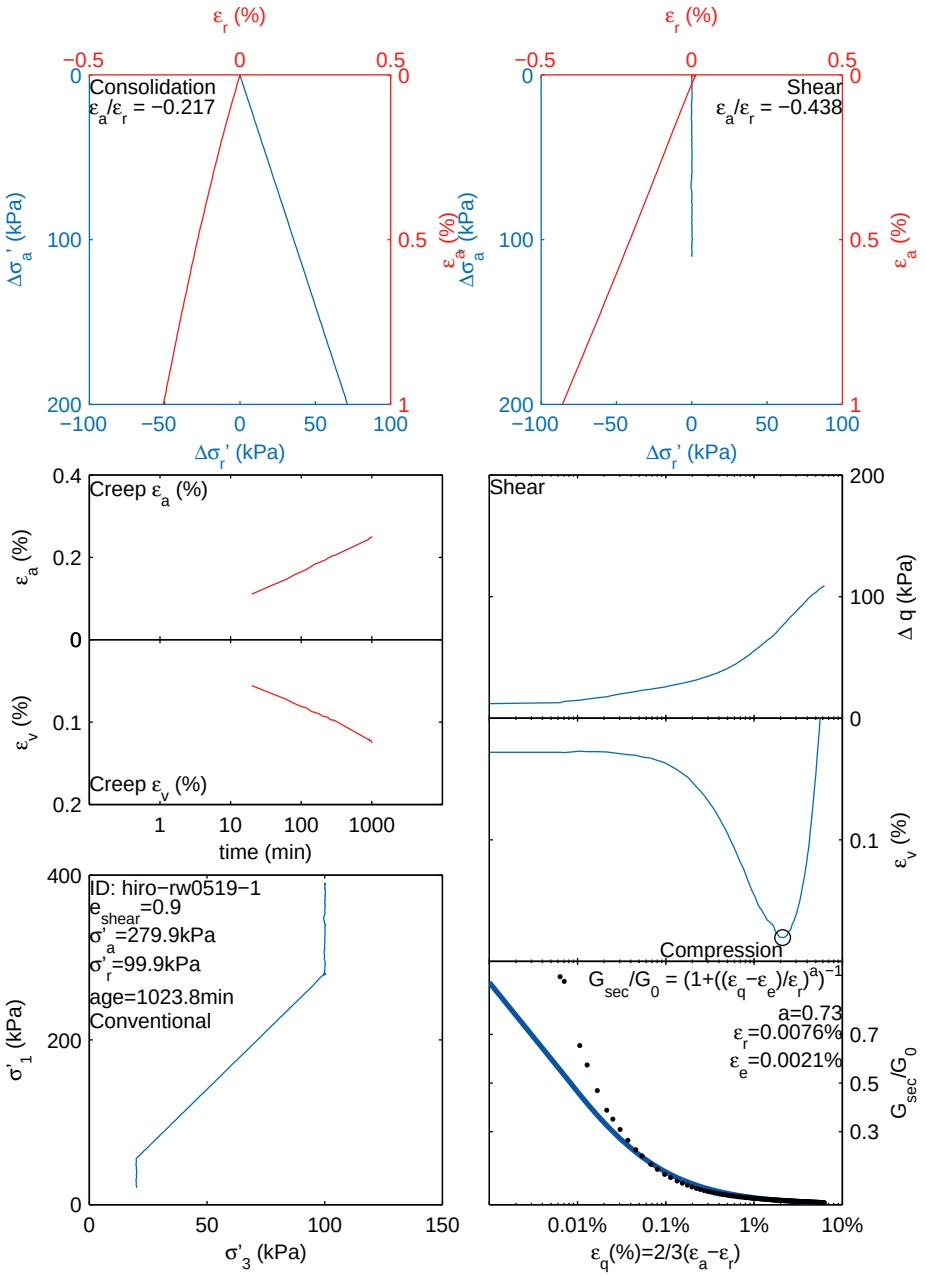

Figure D.110: Shozen-rw0519-1: σ_a = 279.9 kPa, σ_r = 99.9 kPa, age=1023.8 min, Stress path=C

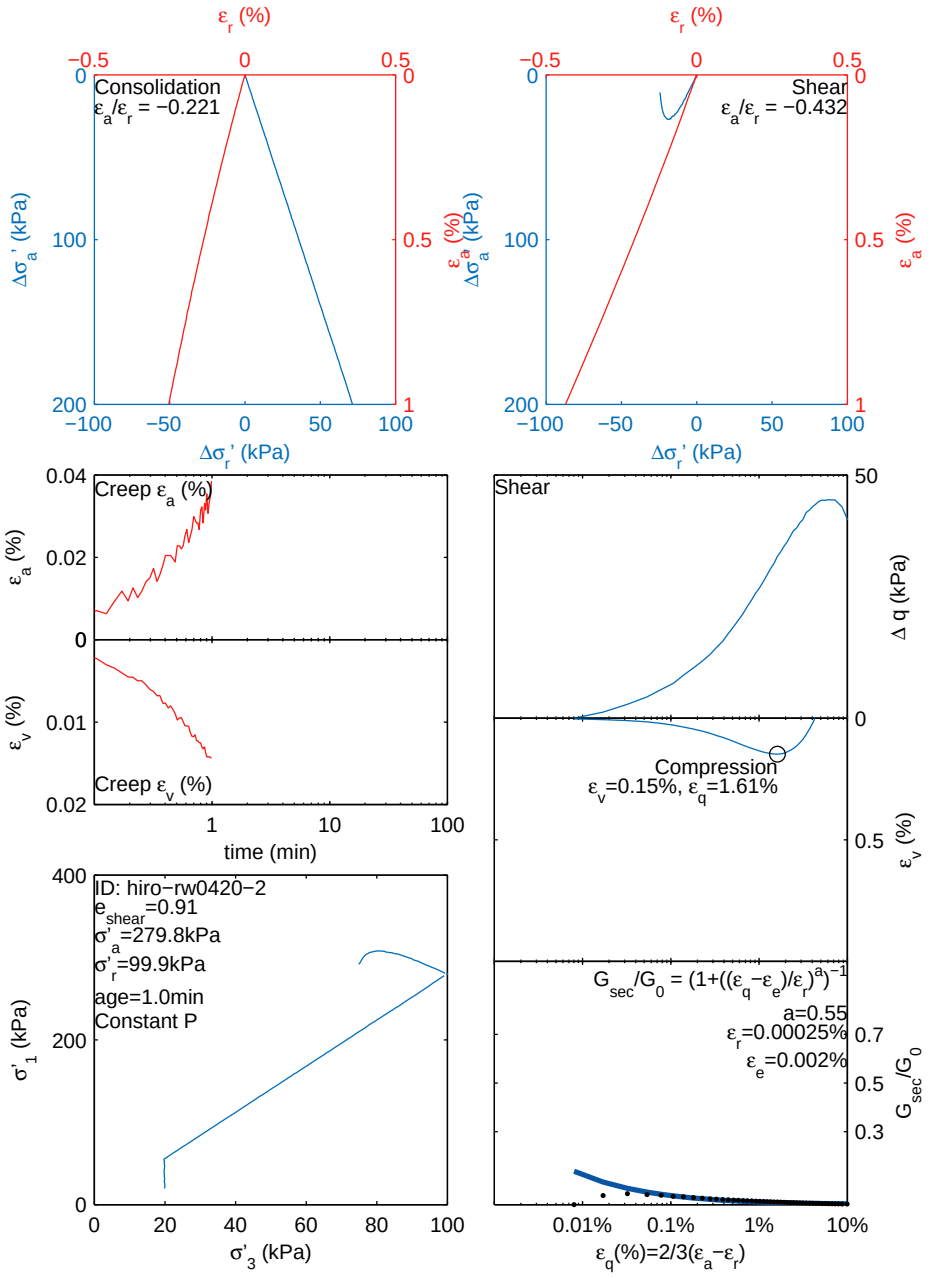

Figure D.111: Shozen-rw0420-2: σ_a = 279.8 kPa, σ_r = 99.9 kPa, age=1.0 min, Stress path=P

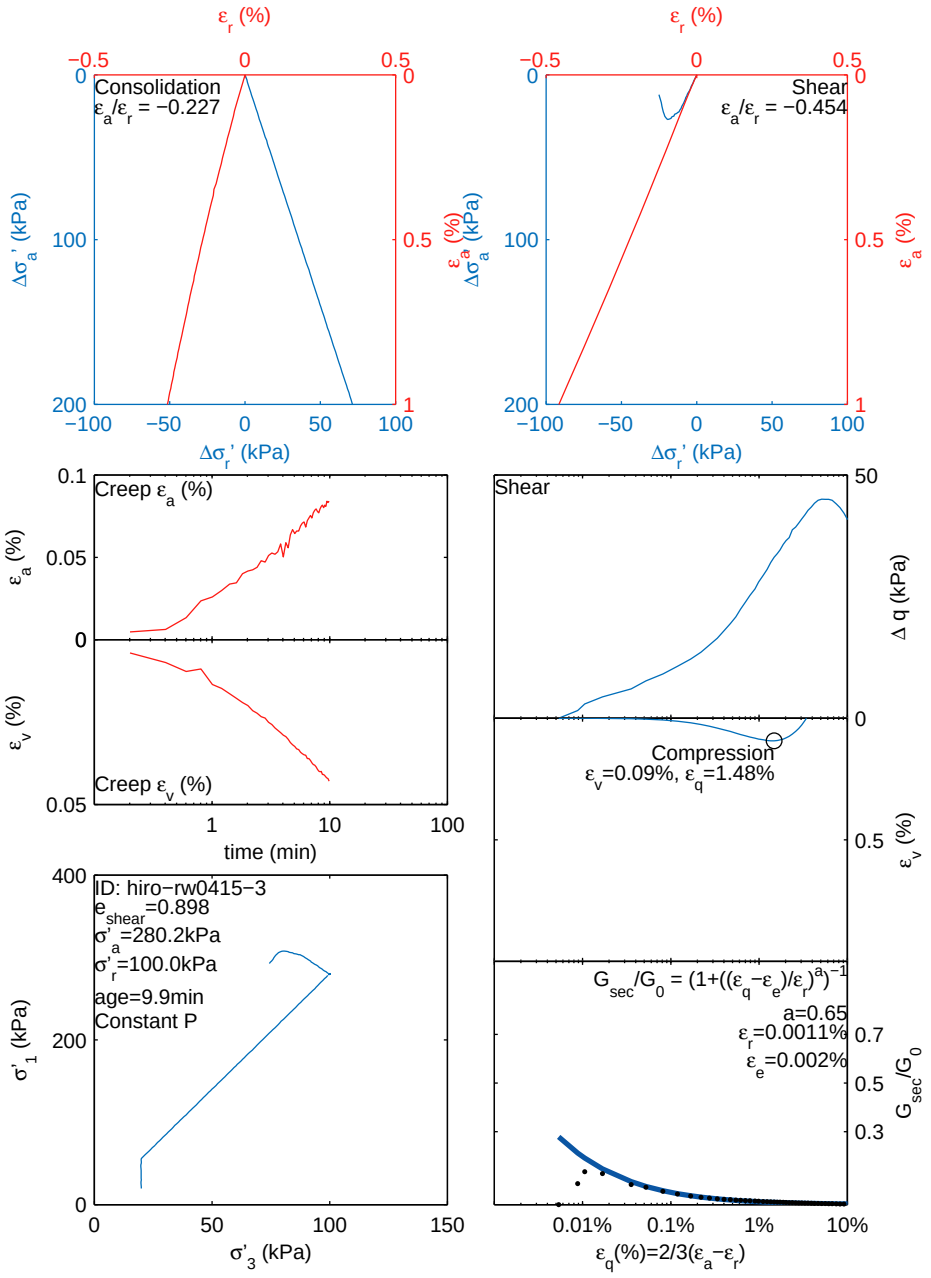

Figure D.112: Shozen-rw0415-3: σ_a = 280.2 kPa, σ_r = 100.0 kPa, age=9.9 min, Stress path=P

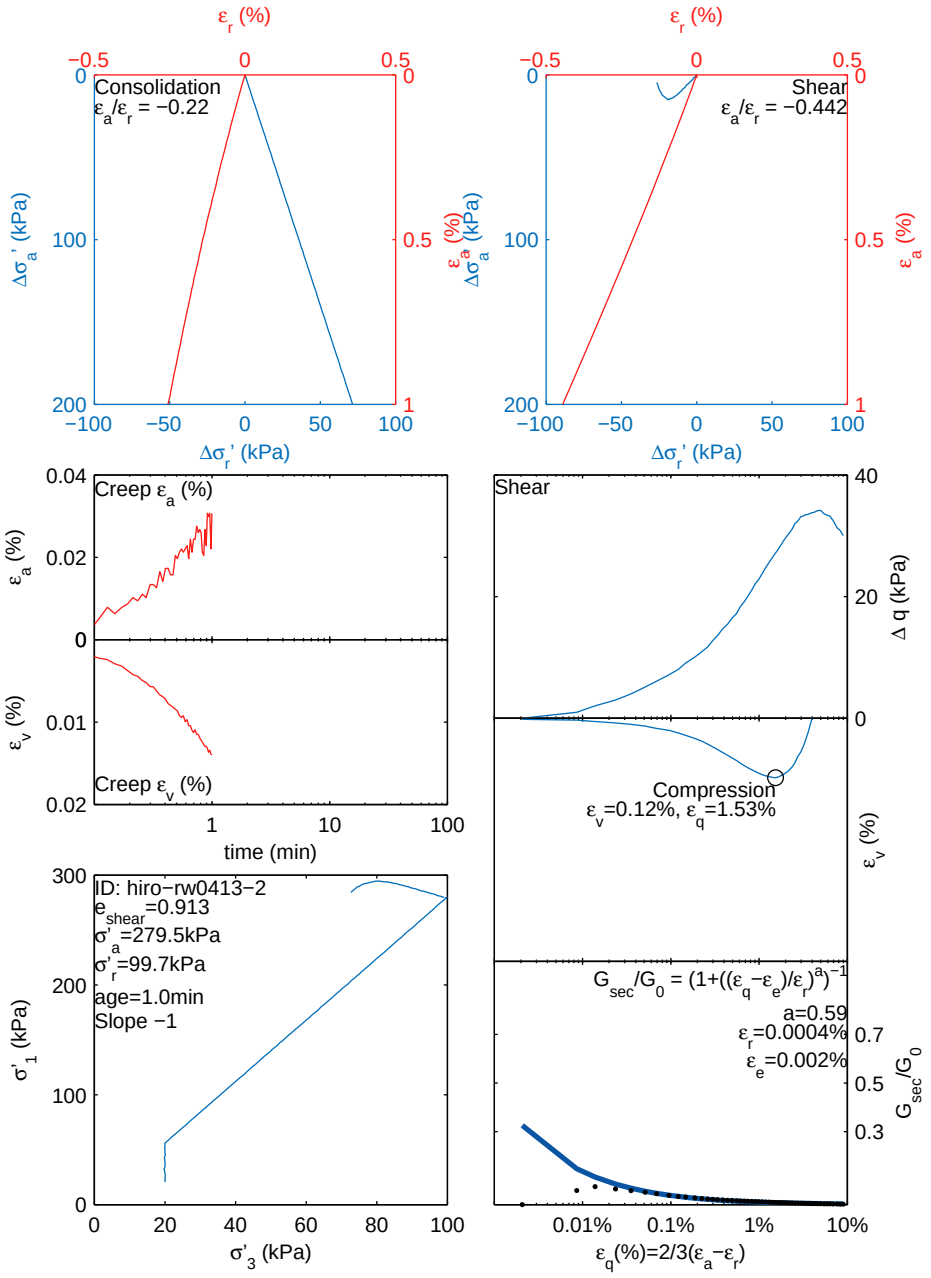

Figure D.113: Shozen-rw0413-2: σ_a = 279.5 kPa, σ_r = 99.7 kPa, age=1.0 min, Stress path=-1

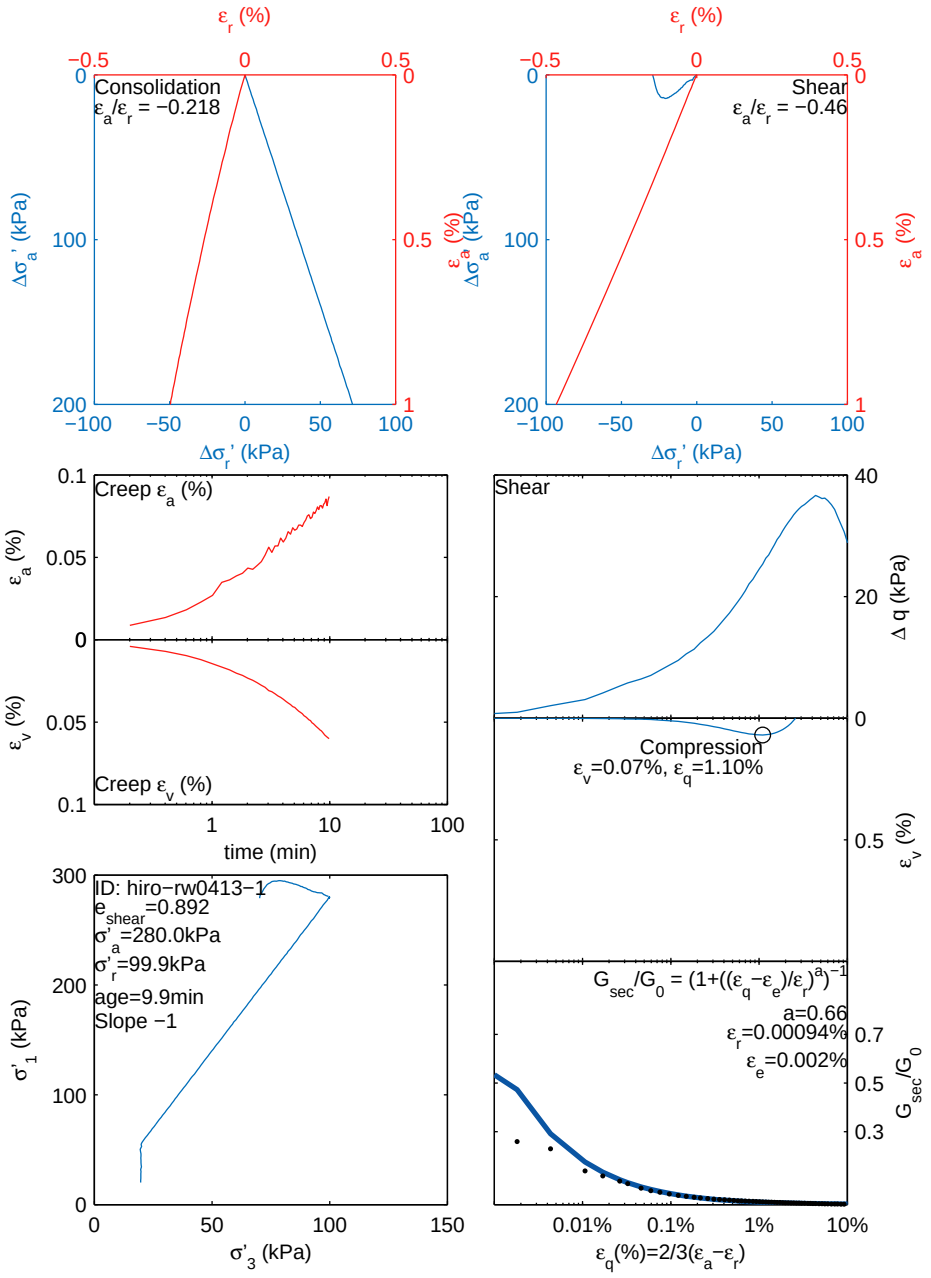

Figure D.114: Shozen-rw0413-1: σ_a = 280.0 kPa, σ_r = 99.9 kPa, age=9.9 min, Stress path=-1

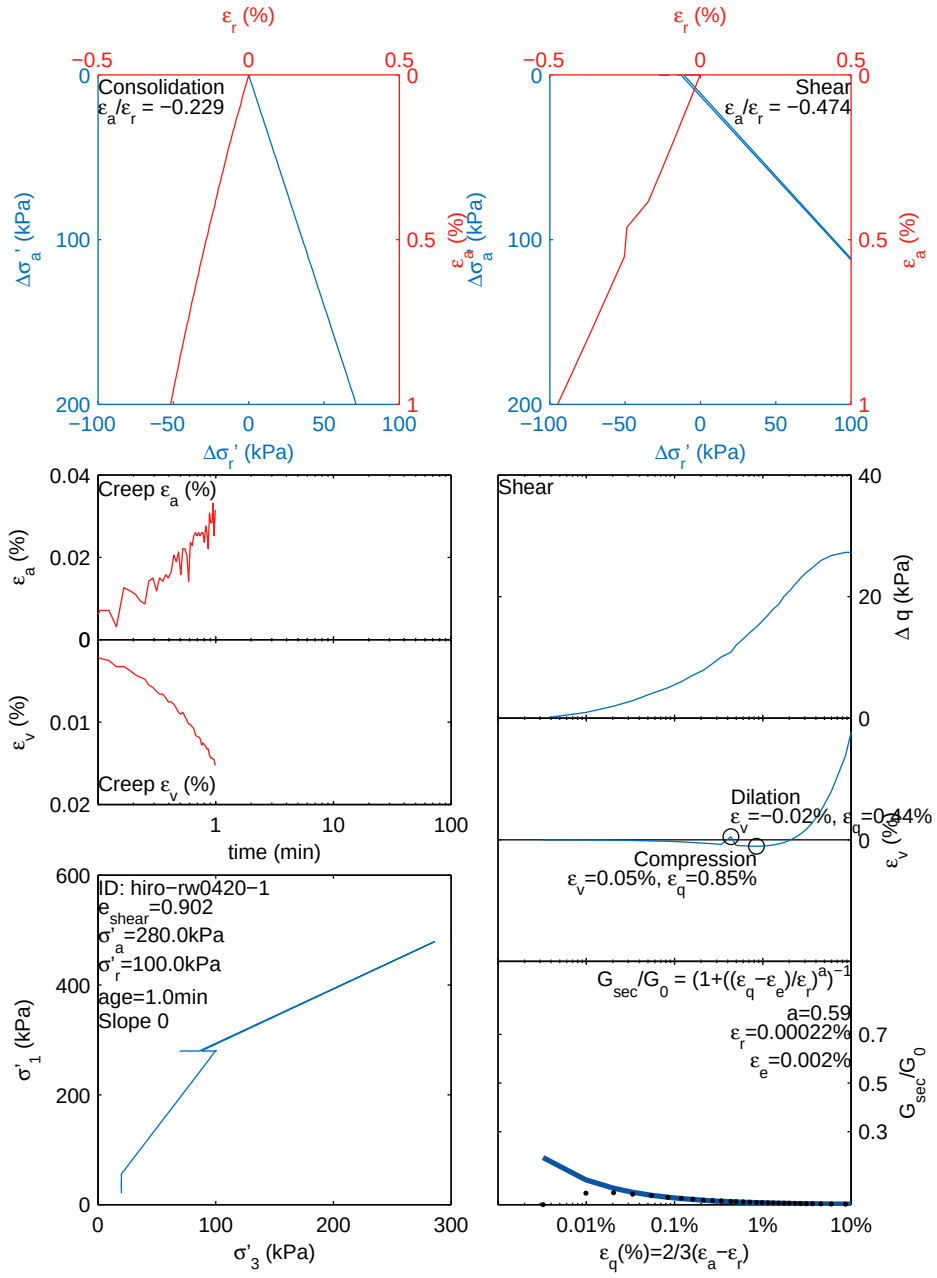

Figure D.115: Shozen-rw0420-1: σ_a = 280.0 kPa, σ_r = 100.0 kPa, age=1.0 min, Stress path=0

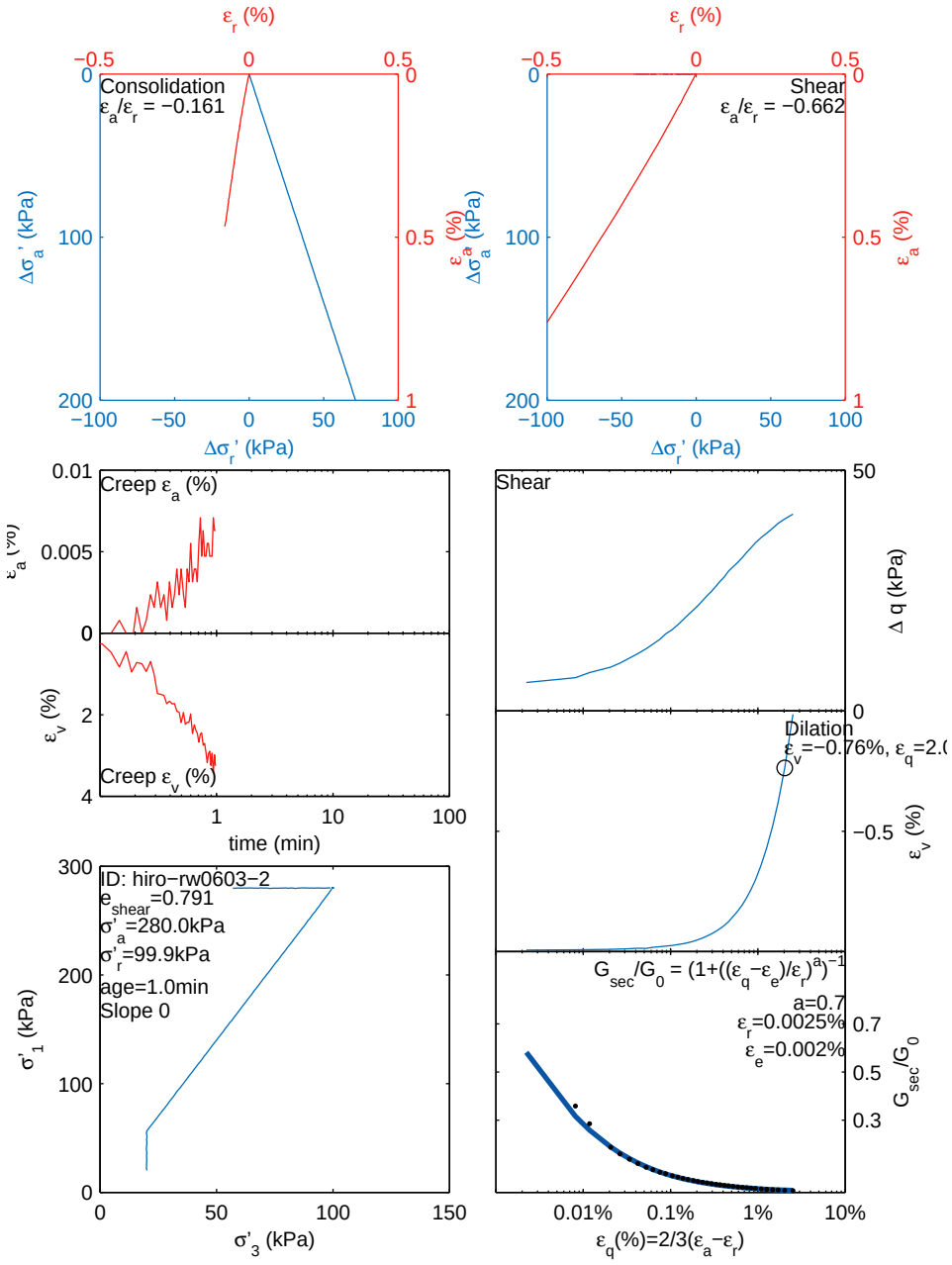

Figure D.116: Shozen-rw0603-2: σ_a = 280.0 kPa, σ_r = 99.9 kPa, age=1.0 min, Stress path=0

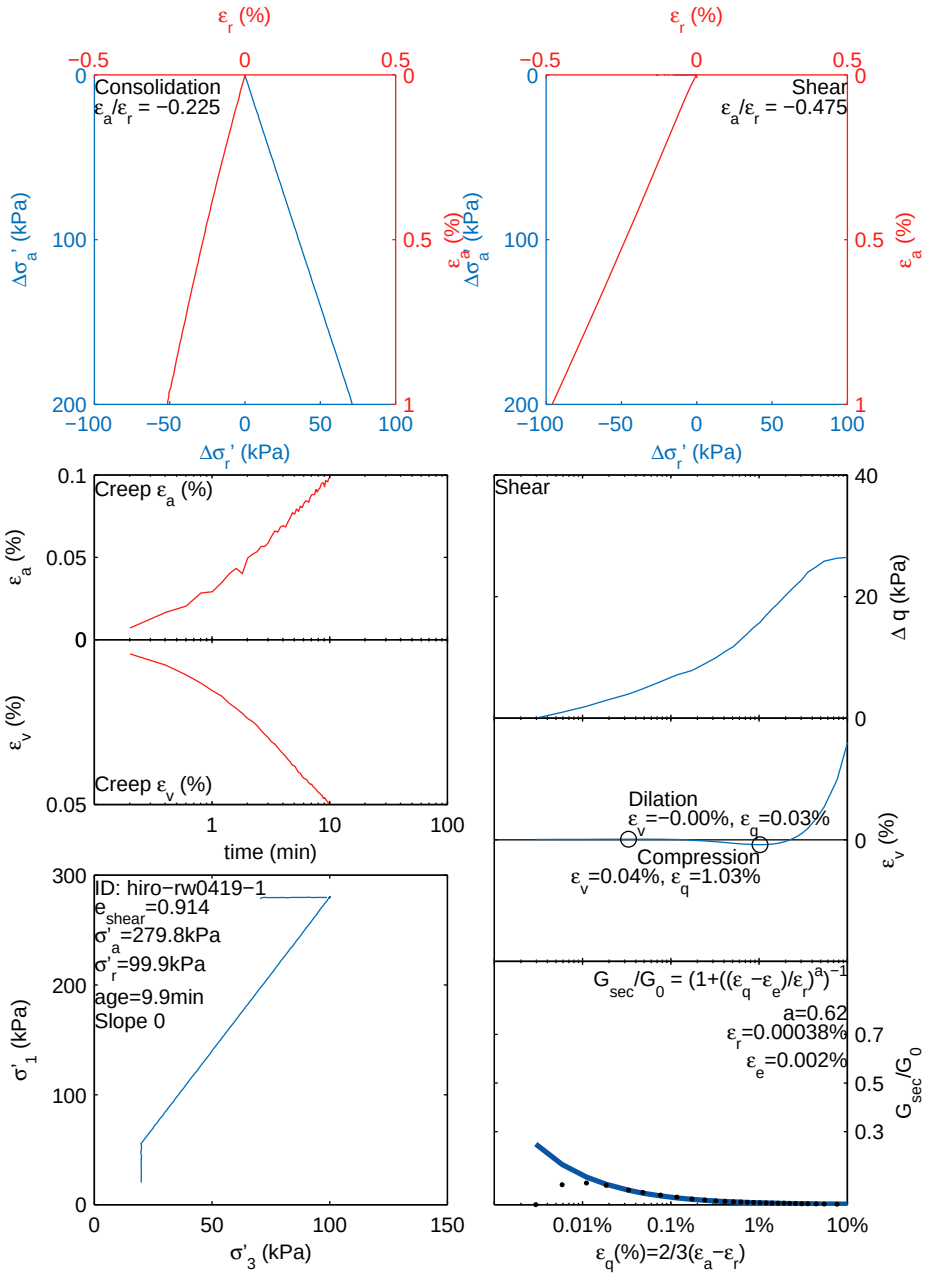

Figure D.117: Shozen-rw0419-1: σ_a = 279.8 kPa, σ_r = 99.9 kPa, age=9.9 min, Stress path=0

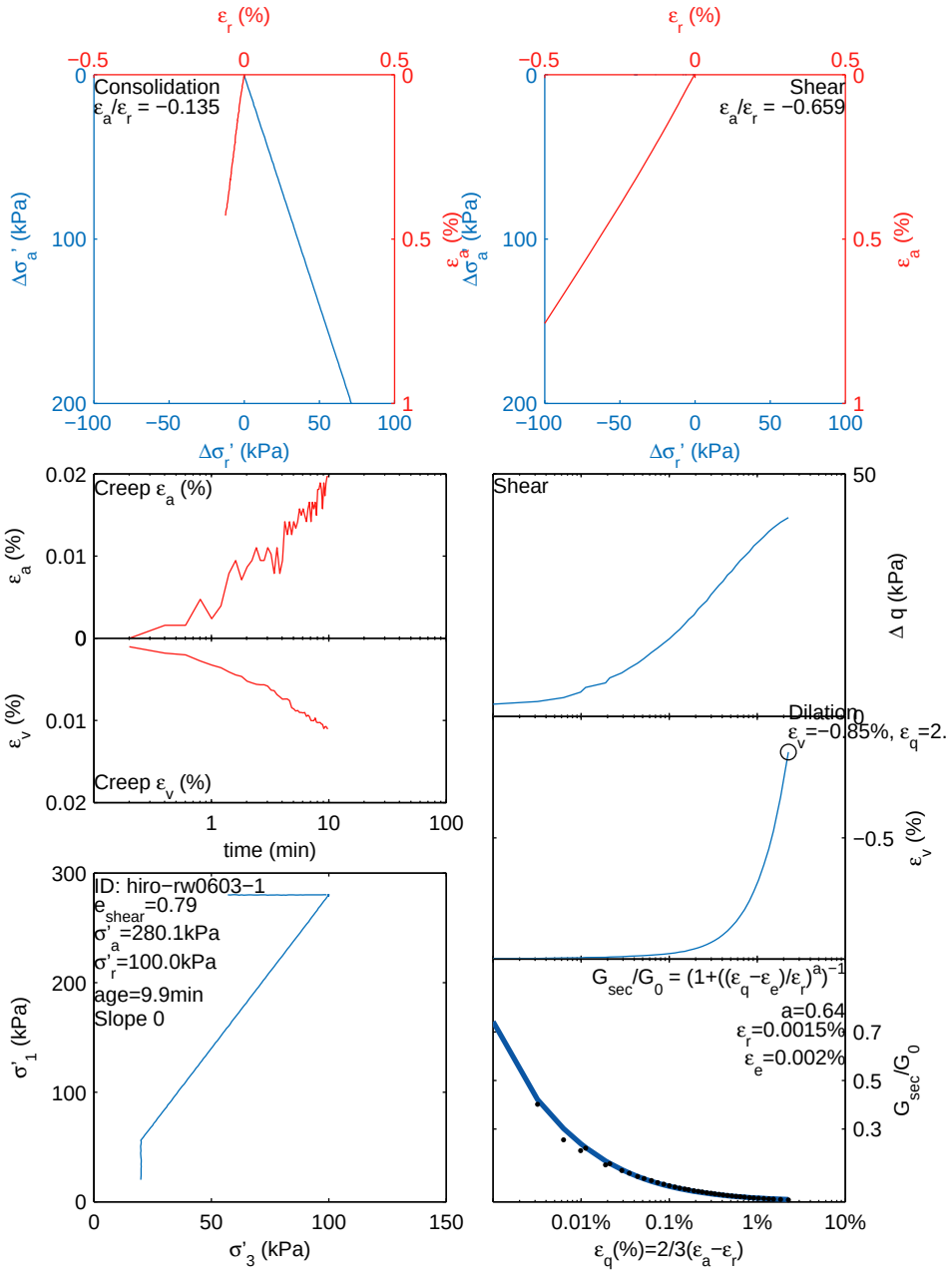

Figure D.118: Shozen-rw0603-1: σ_a = 280.1 kPa, σ_r = 100.0 kPa, age=9.9 min, Stress path=0

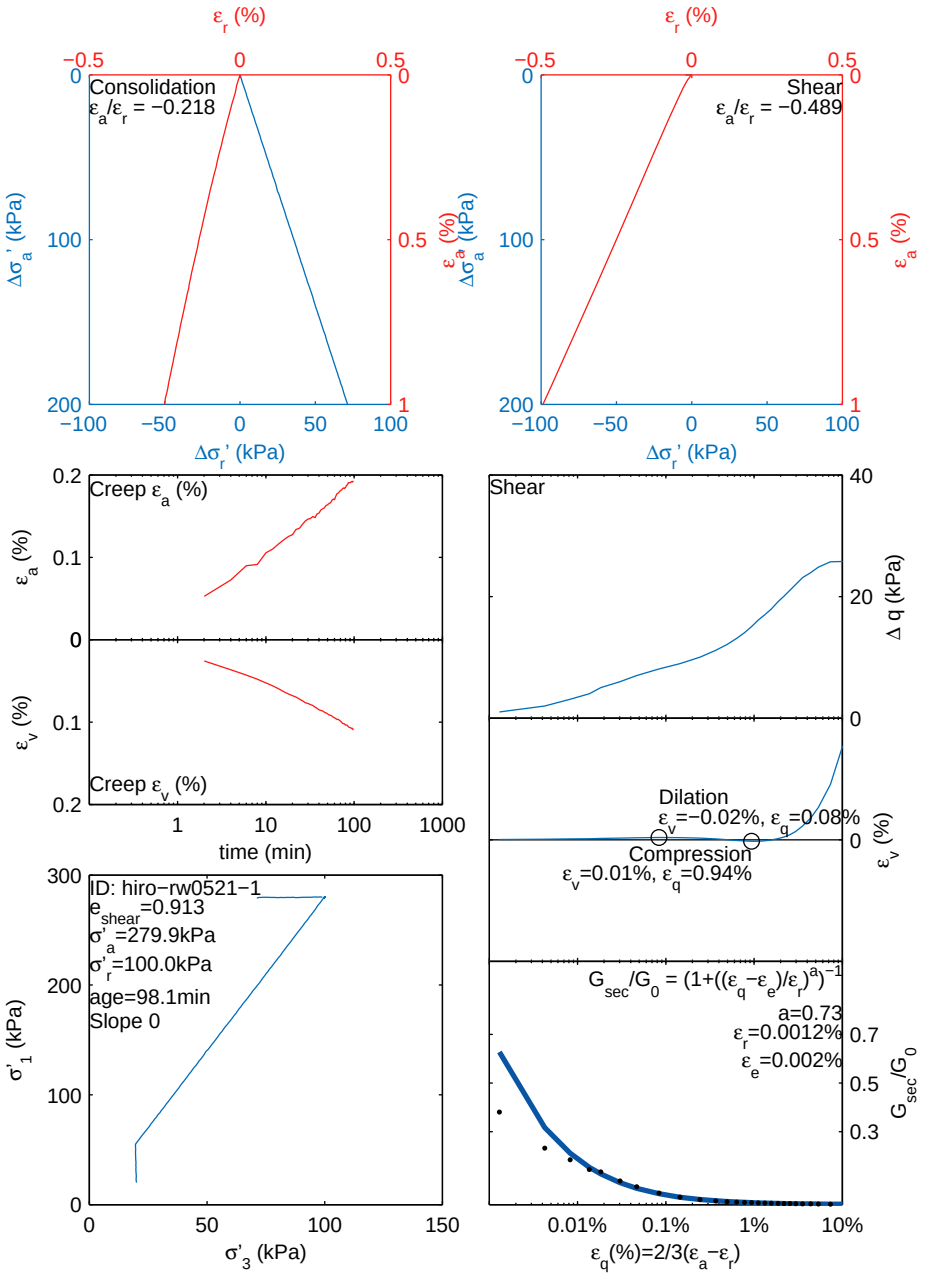

Figure D.119: Shozen-rw0521-1: σ_a = 279.9 kPa, σ_r = 100.0 kPa, age=98.1 min, Stress path=0

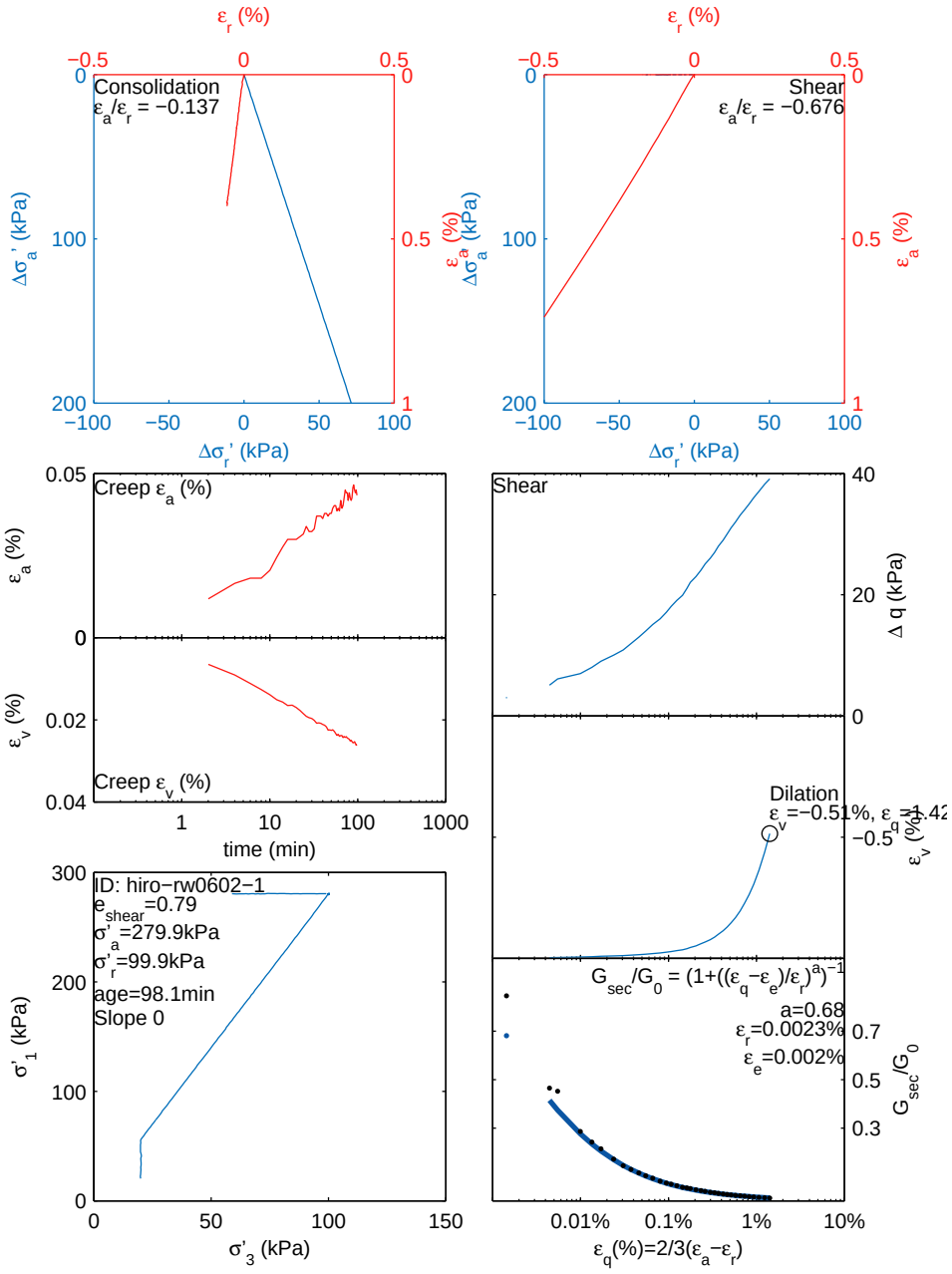

Figure D.120: Shozen-rw0602-1: σ_a = 279.9 kPa, σ_r = 99.9 kPa, age=98.1 min, Stress path=0

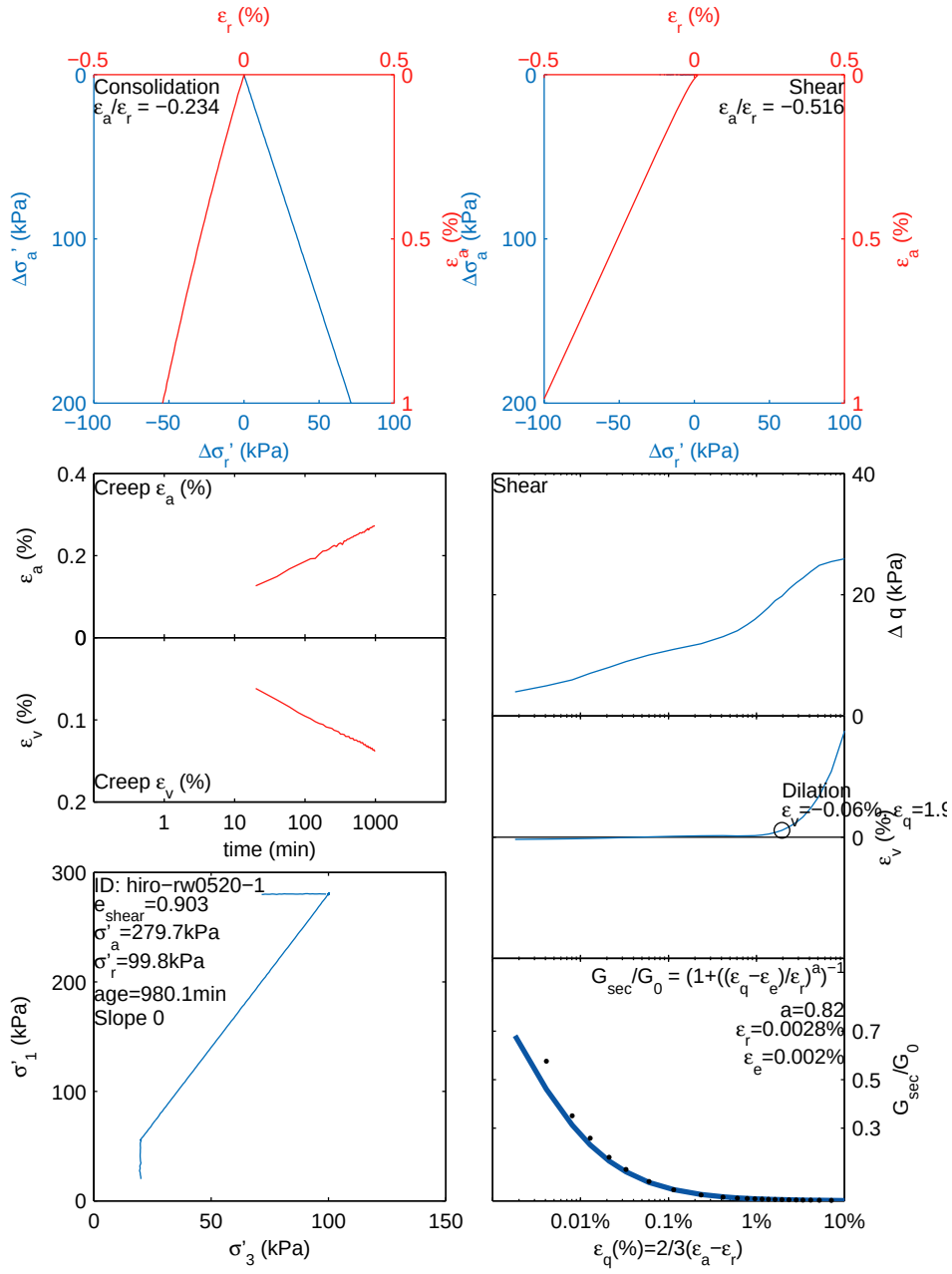

Figure D.121: Shozen-rw0520-1: $\sigma_a = 279.7$ kPa, $\sigma_r = 99.8$ kPa, age=980.1 min, Stress path=0

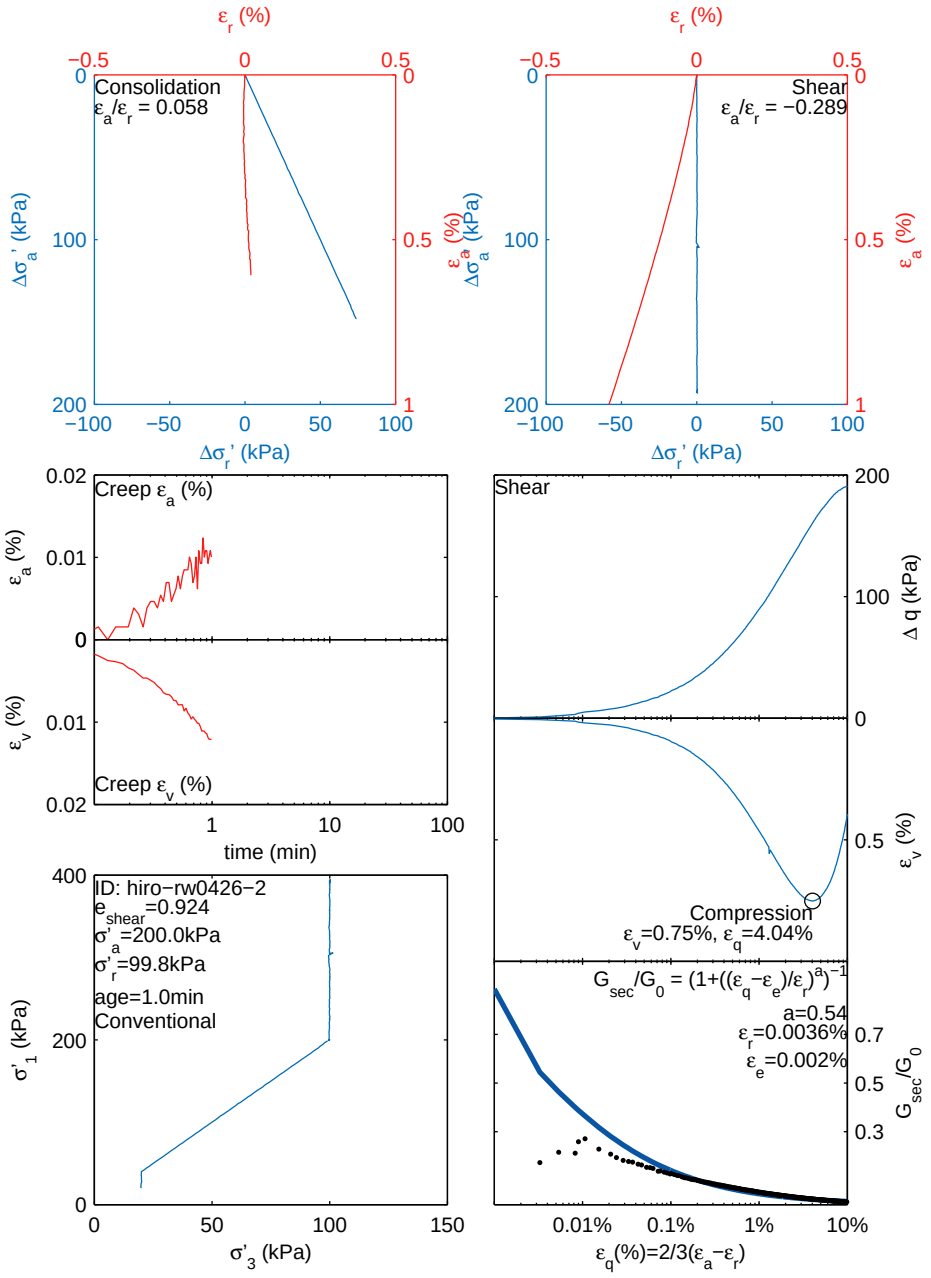

Figure D.122: Shozen-rw0426-2: σ_a = 200.0 kPa, σ_r = 99.8 kPa, age=1.0 min, Stress path=C

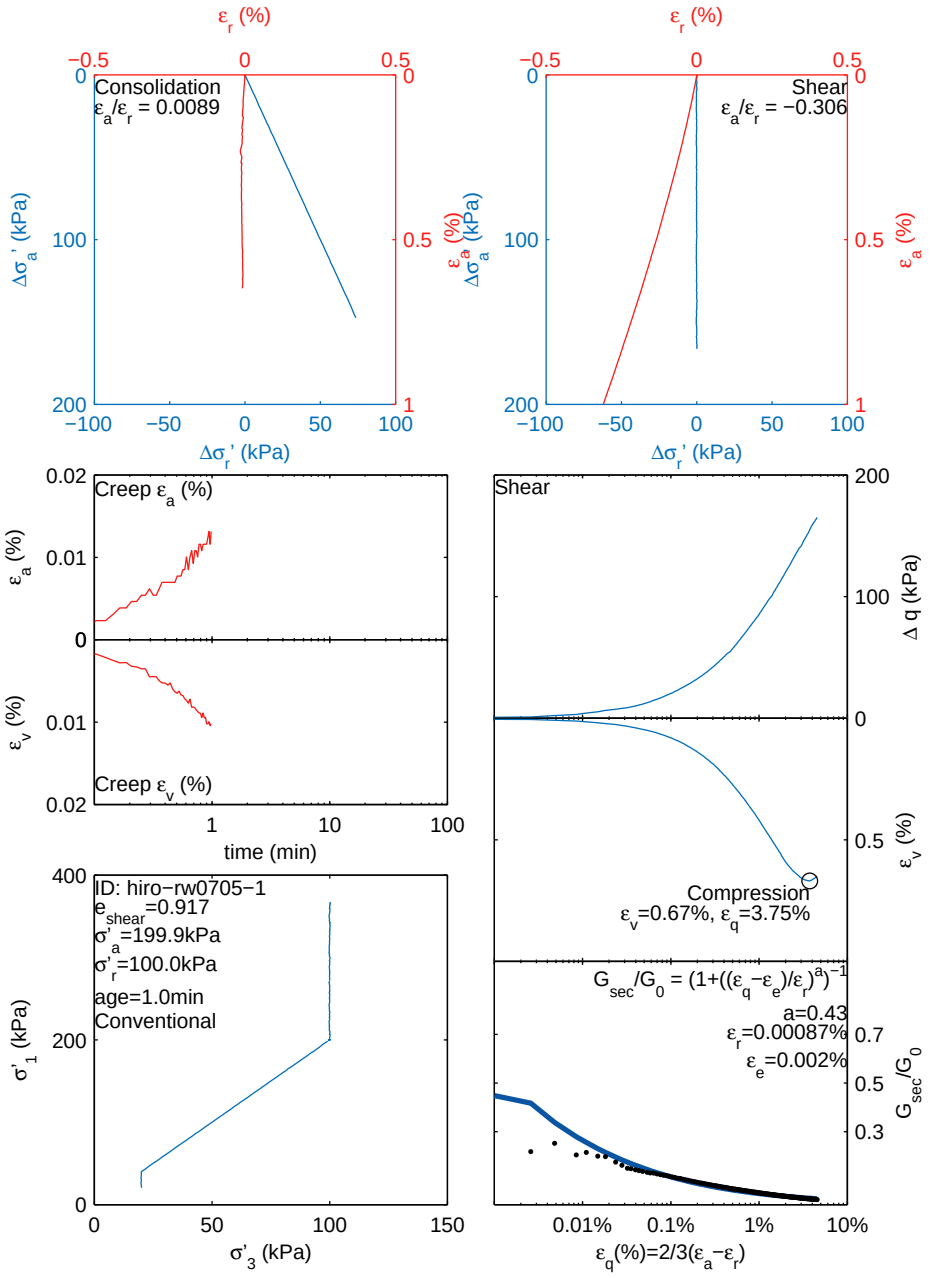

Figure D.123: Shozen-rw0705-1: σ_a = 199.9 kPa, σ_r = 100.0 kPa, age=1.0 min, Stress path=C

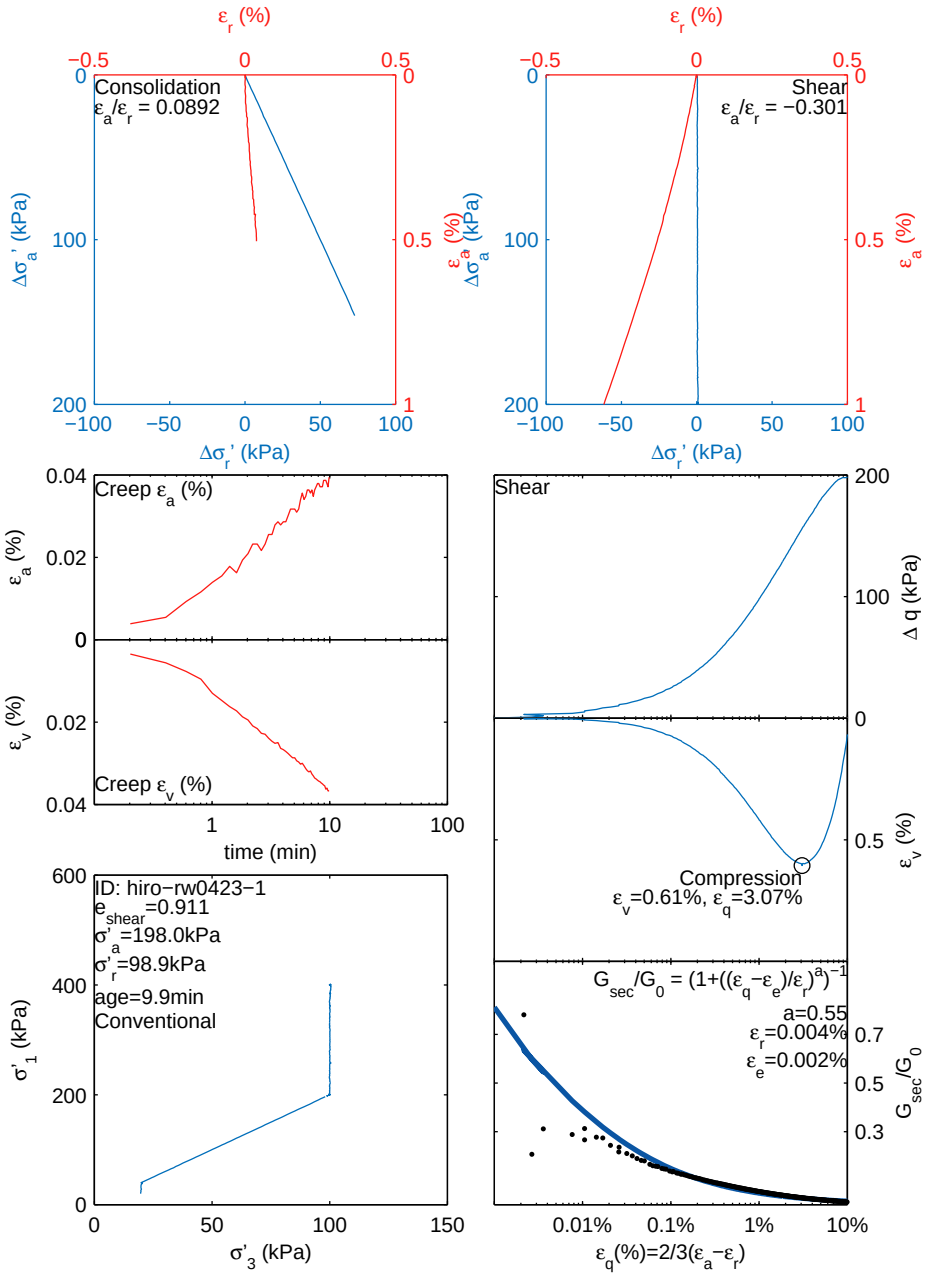

Figure D.124: Shozen-rw0423-1: σ_a = 198.0 kPa, σ_r = 98.9 kPa, age=9.9 min, Stress path=C

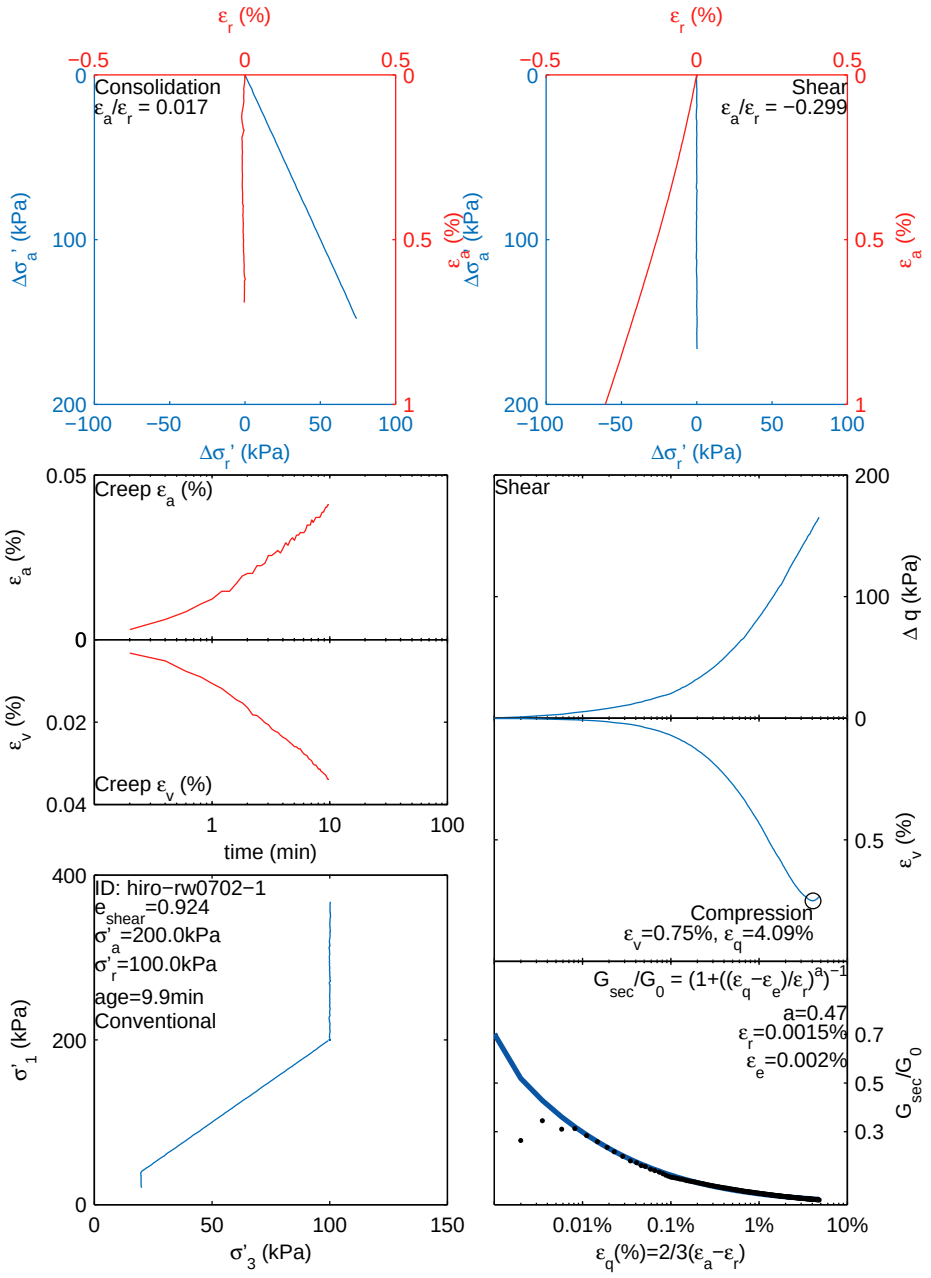

Figure D.125: Shozen-rw0702-1: σ_a = 200.0 kPa, σ_r = 100.0 kPa, age=9.9 min, Stress path=C

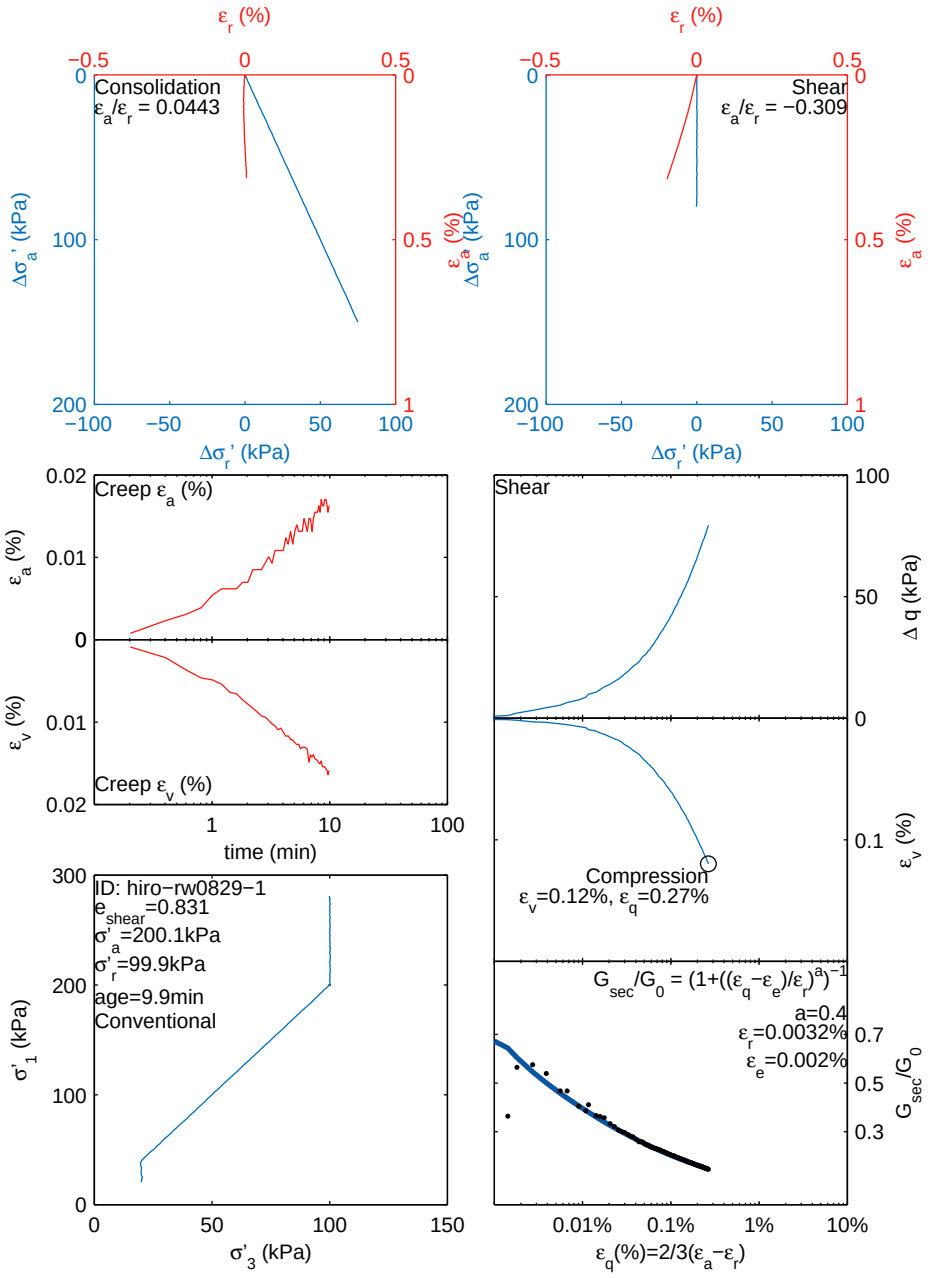

Figure D.126: Shozen-rw0829-1: σ_a = 200.1 kPa, σ_r = 99.9 kPa, age=9.9 min, Stress path=C

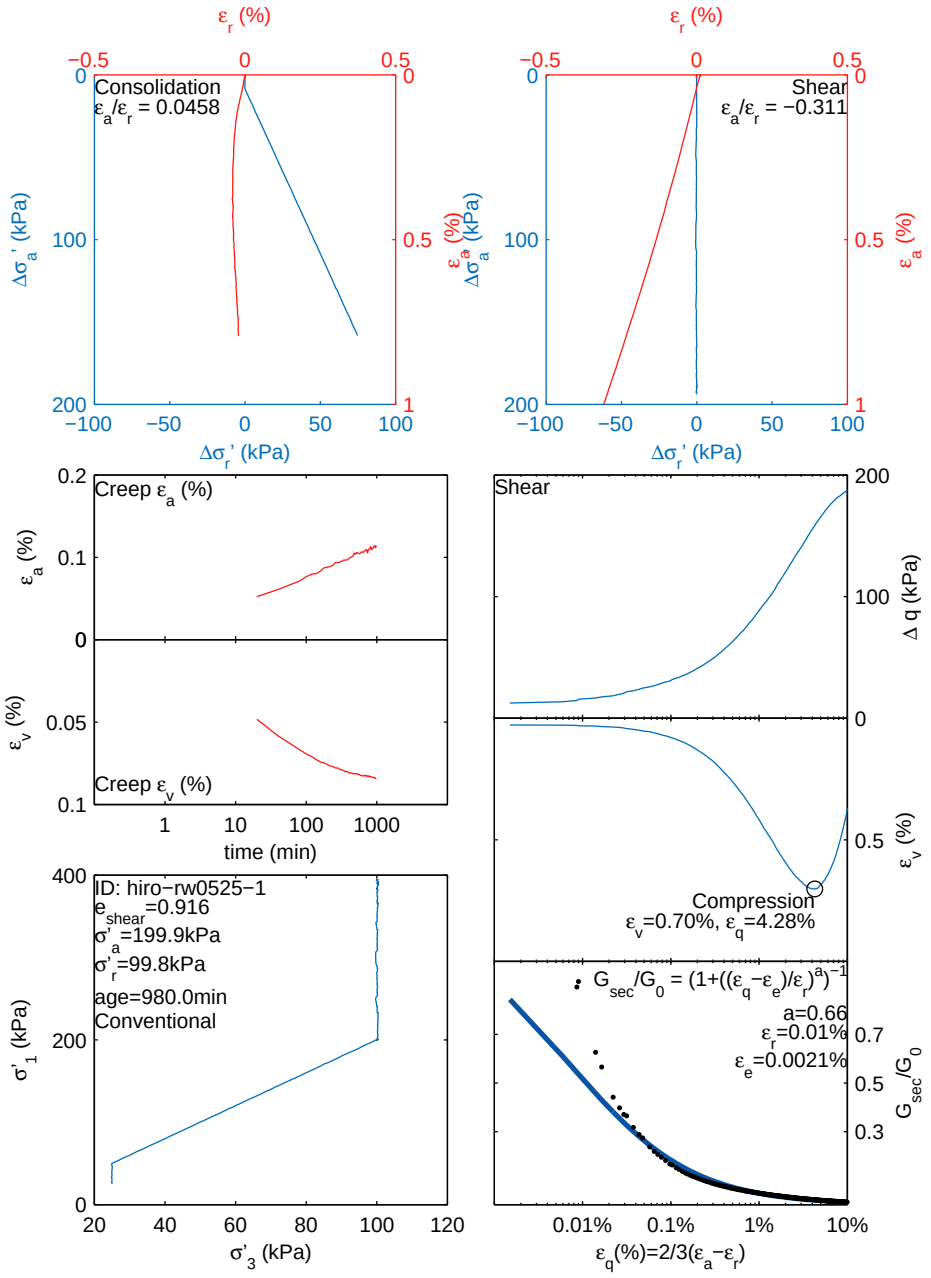

Figure D.127: Shozen-rw0525-1: σ_a = 199.9 kPa, σ_r = 99.8 kPa, age=980.0 min, Stress path=C

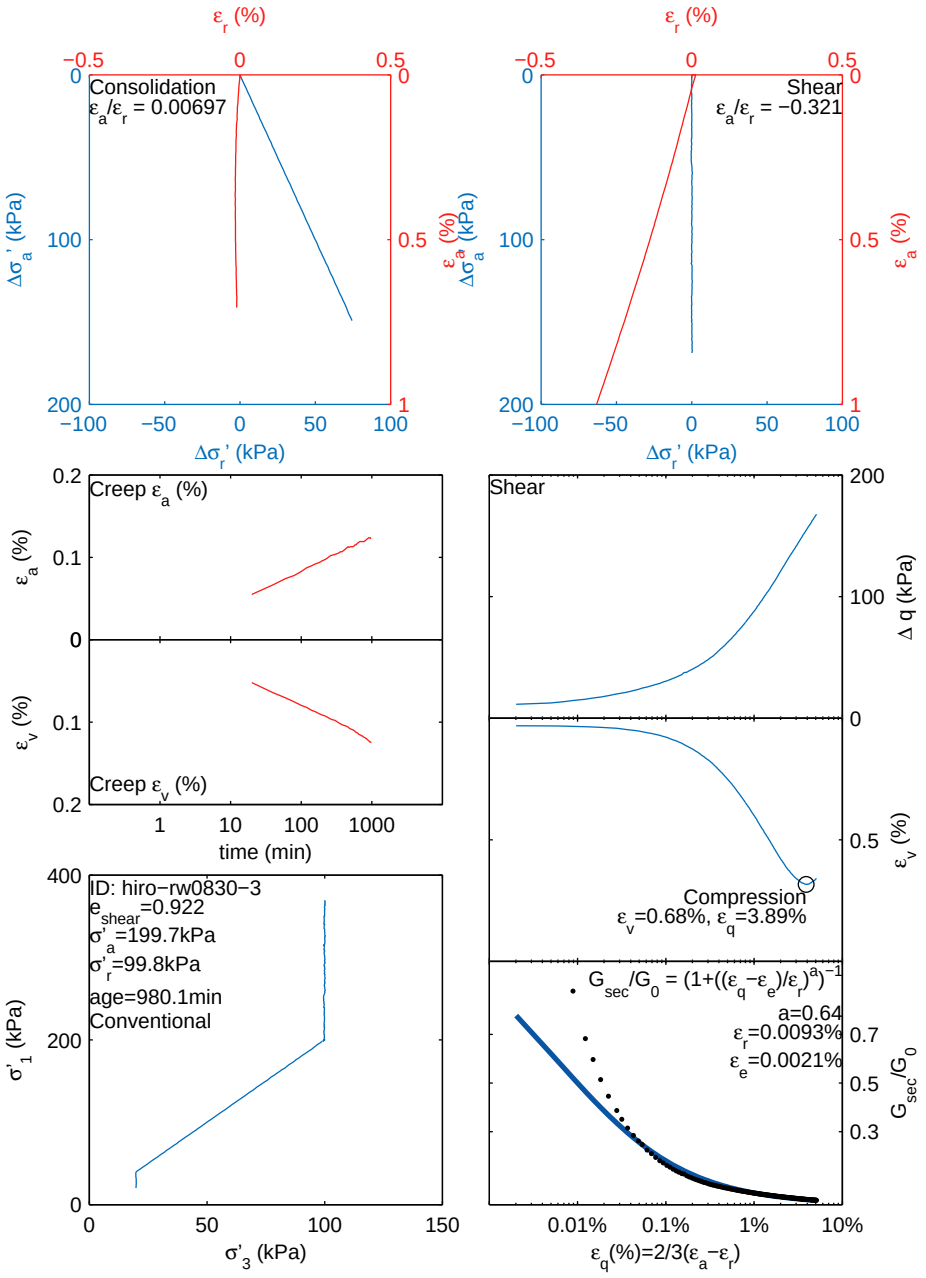

Figure D.128: Shozen-rw0830-3: σ_a = 199.7 kPa, σ_r = 99.8 kPa, age=980.1 min, Stress path=C

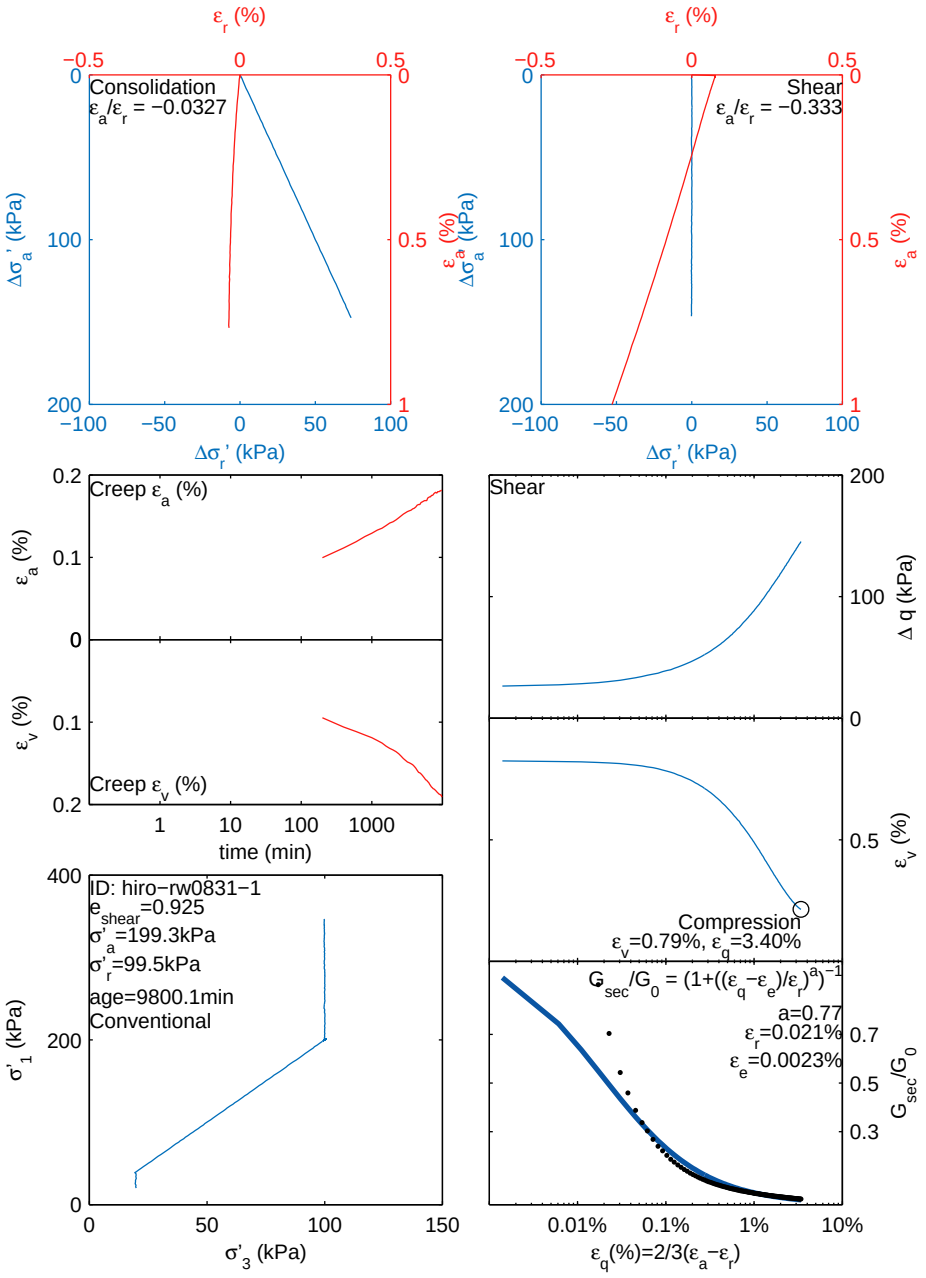

Figure D.129: Shozen-rw0831-1: σ_a = 199.3 kPa, σ_r = 99.5 kPa, age=9800.1 min, Stress path=C

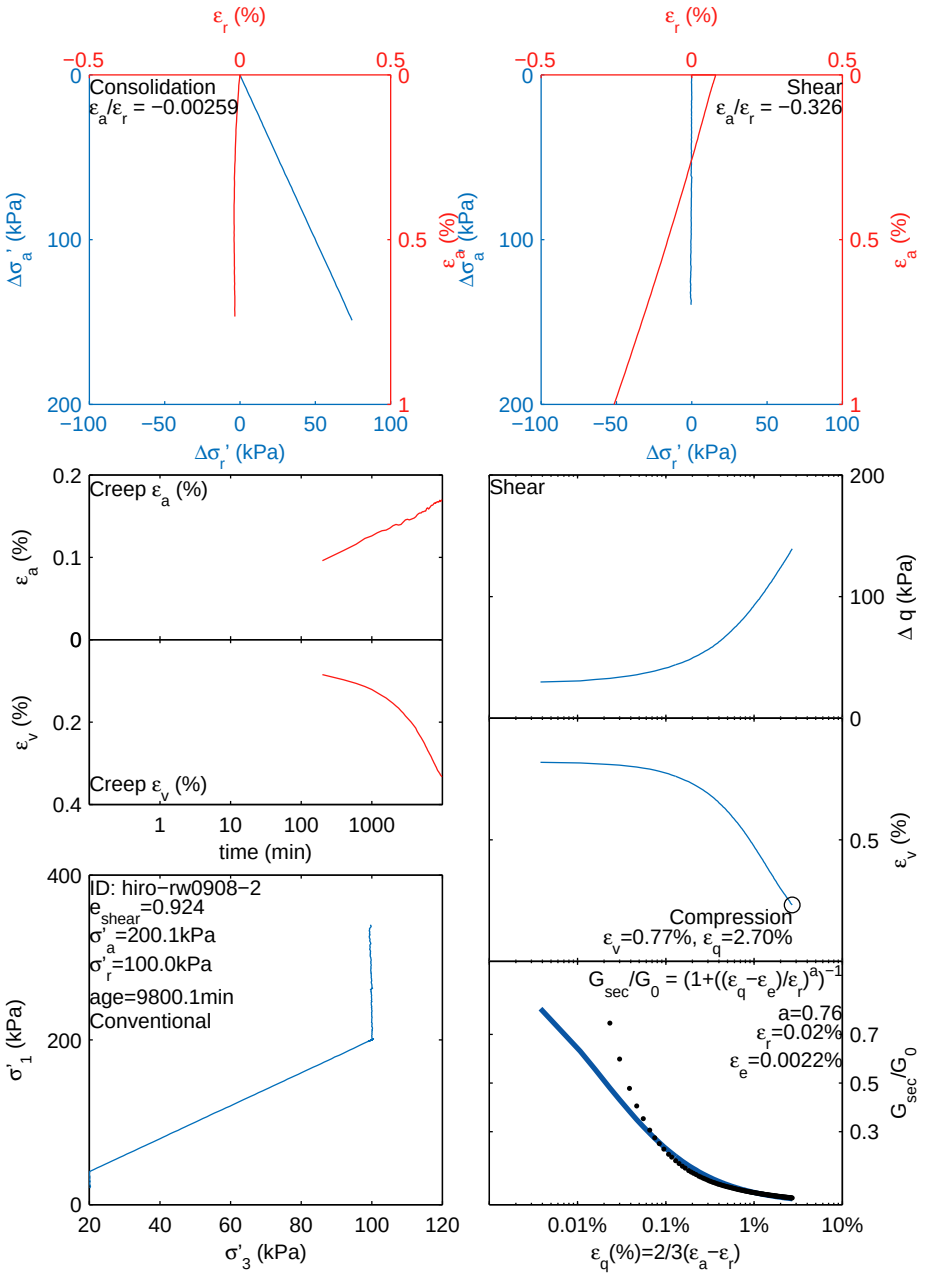

Figure D.130: Shozen-rw0908-2: σ_a = 200.1 kPa, σ_r = 100.0 kPa, age=9800.1 min, Stress path=C

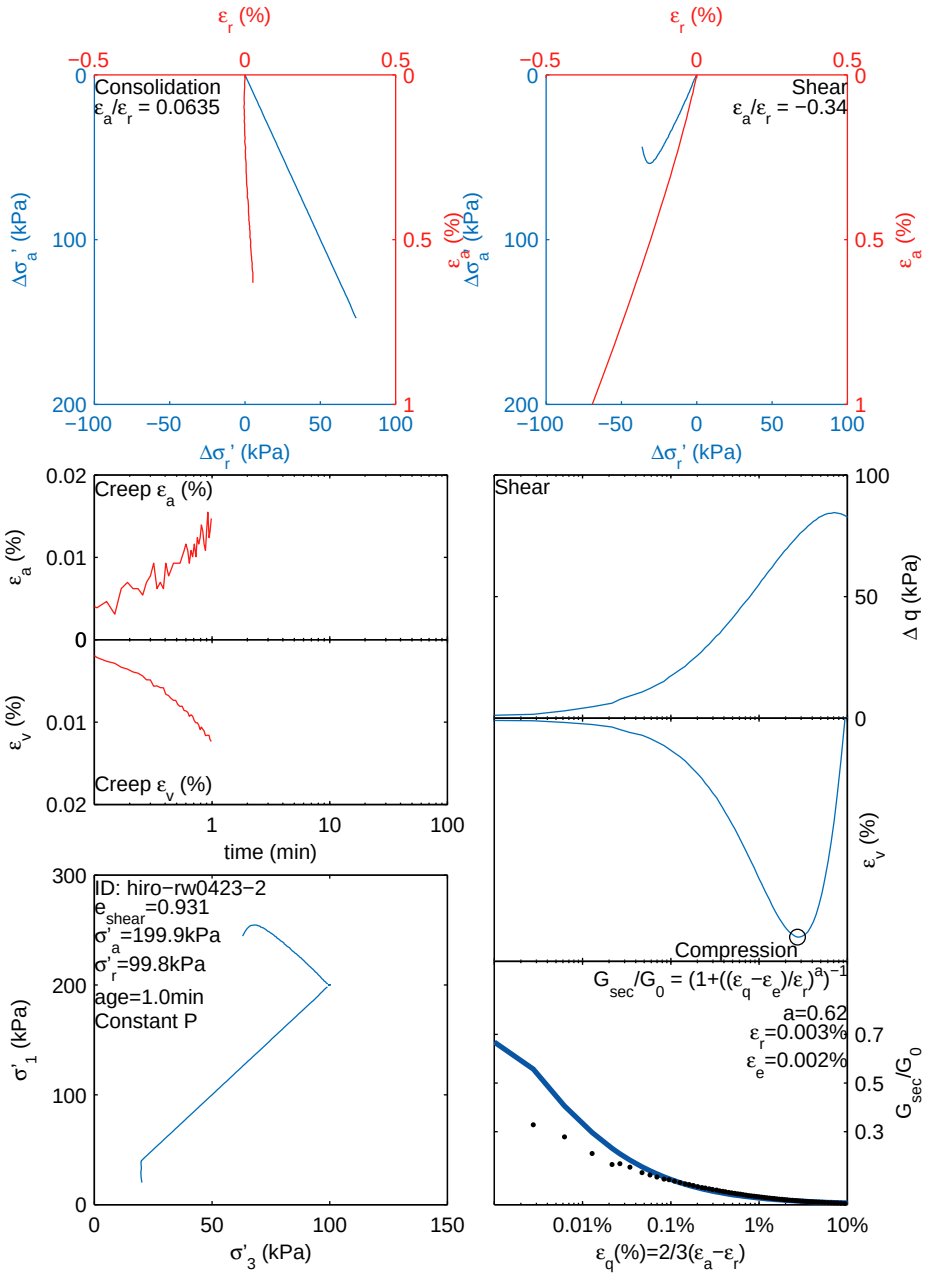

Figure D.131: Shozen-rw0423-2: σ_a = 199.9 kPa, σ_r = 99.8 kPa, age=1.0 min, Stress path=P

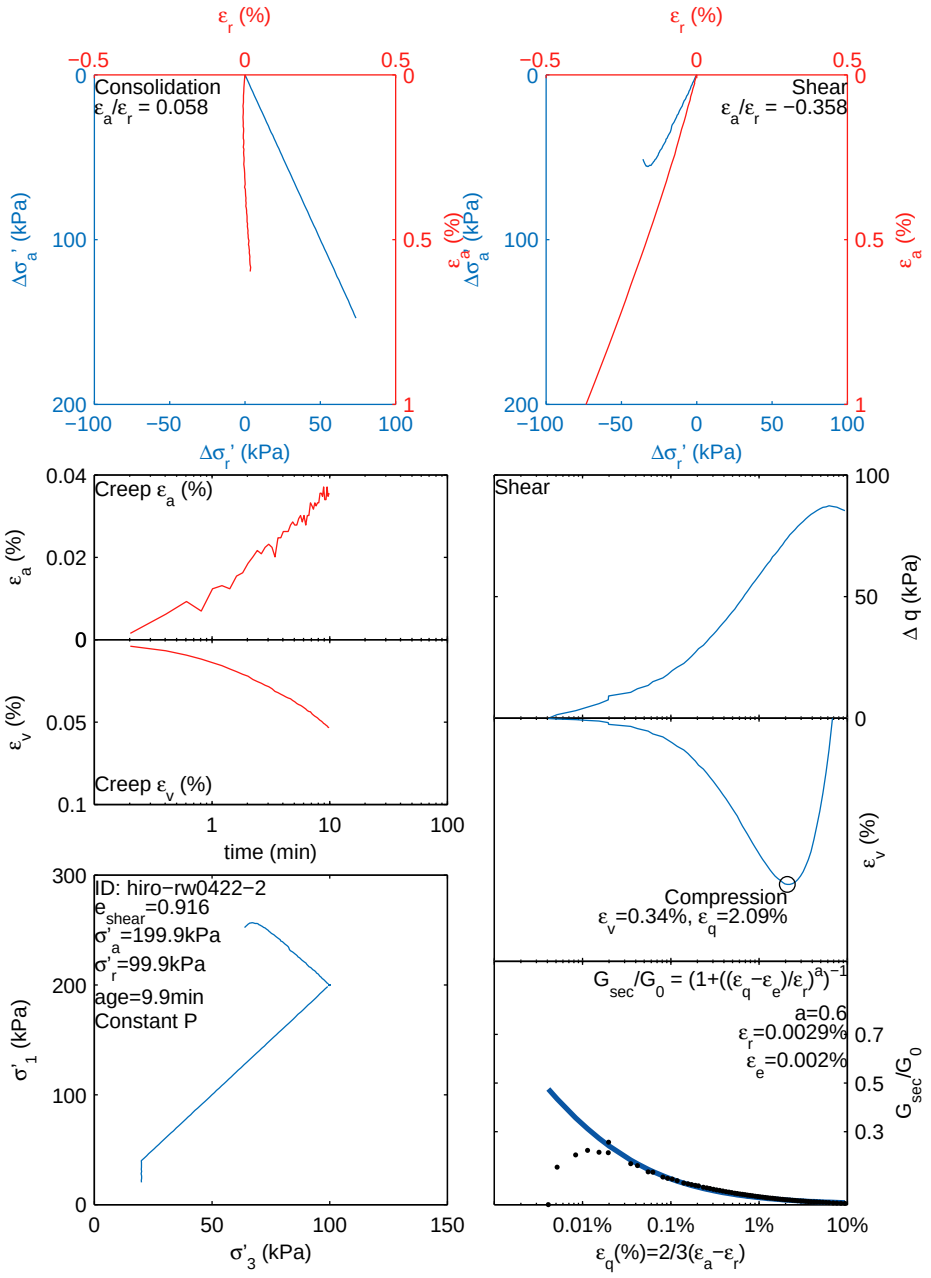

Figure D.132: Shozen-rw0422-2: σ_a = 199.9 kPa, σ_r = 99.9 kPa, age=9.9 min, Stress path=P

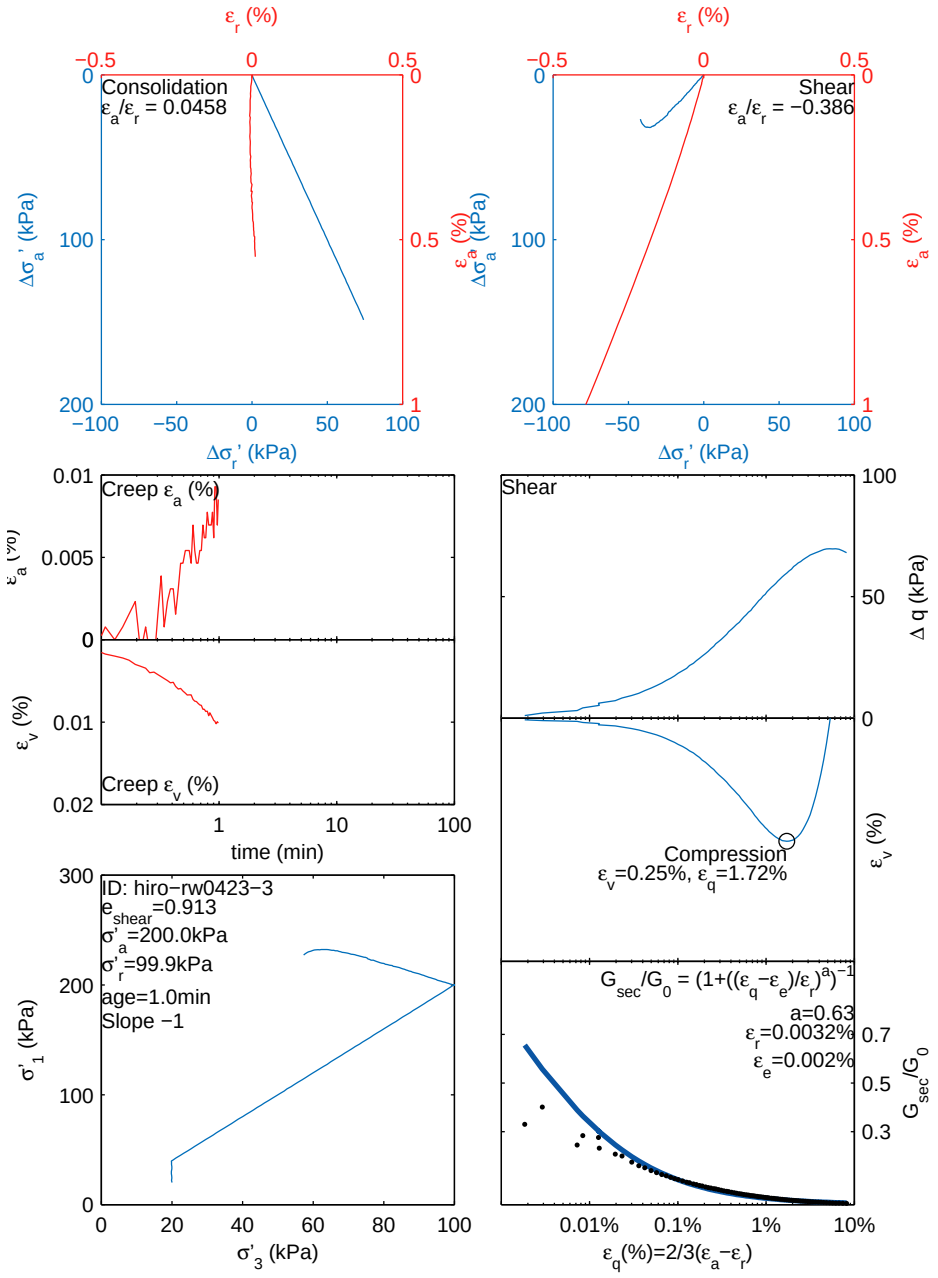

Figure D.133: Shozen-rw0423-3: σ_a = 200.0 kPa, σ_r = 99.9 kPa, age=1.0 min, Stress path=-1

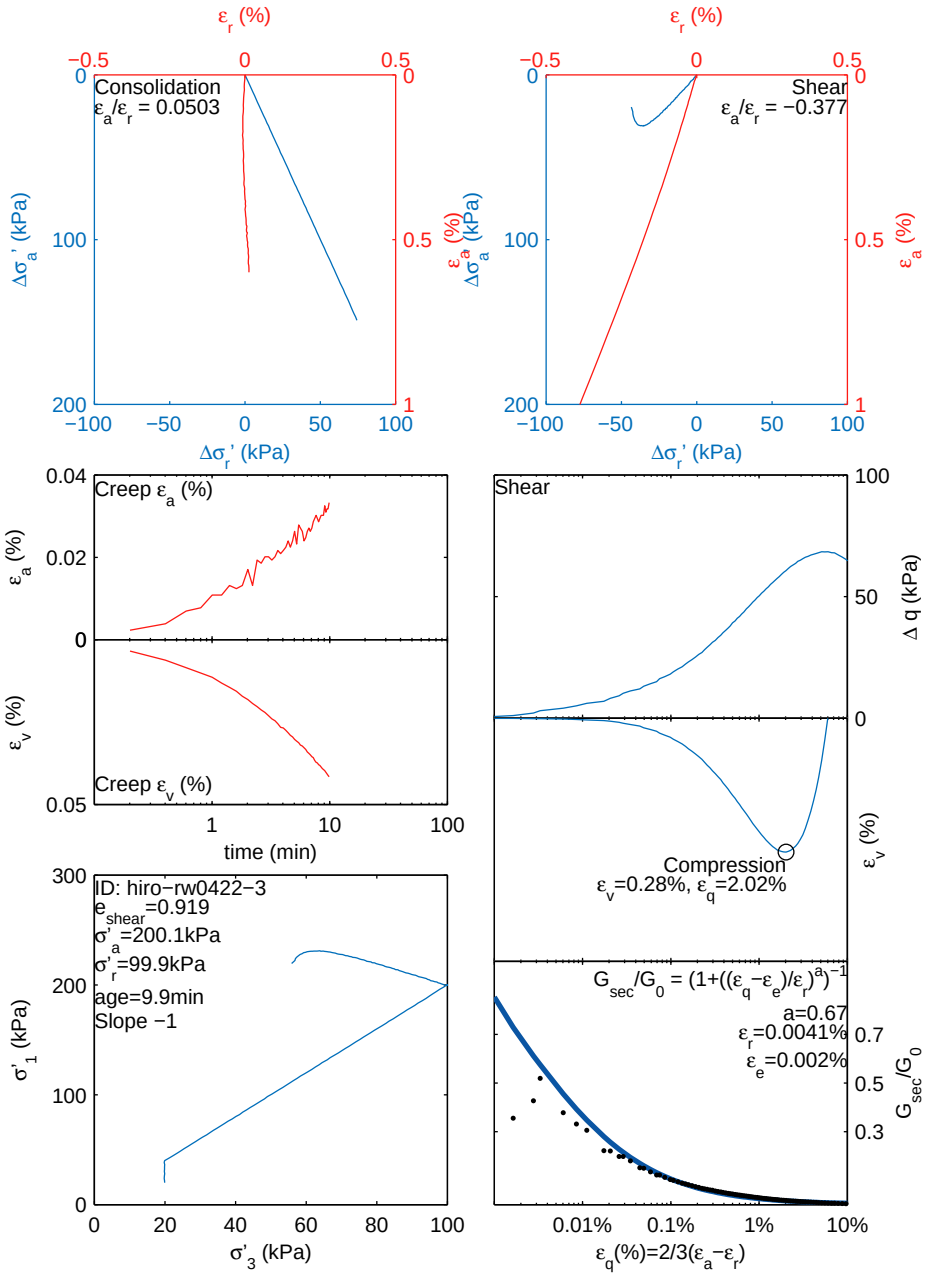

Figure D.134: Shozen-rw0422-3: σ_a = 200.1 kPa, σ_r = 99.9 kPa, age=9.9 min, Stress path=-1

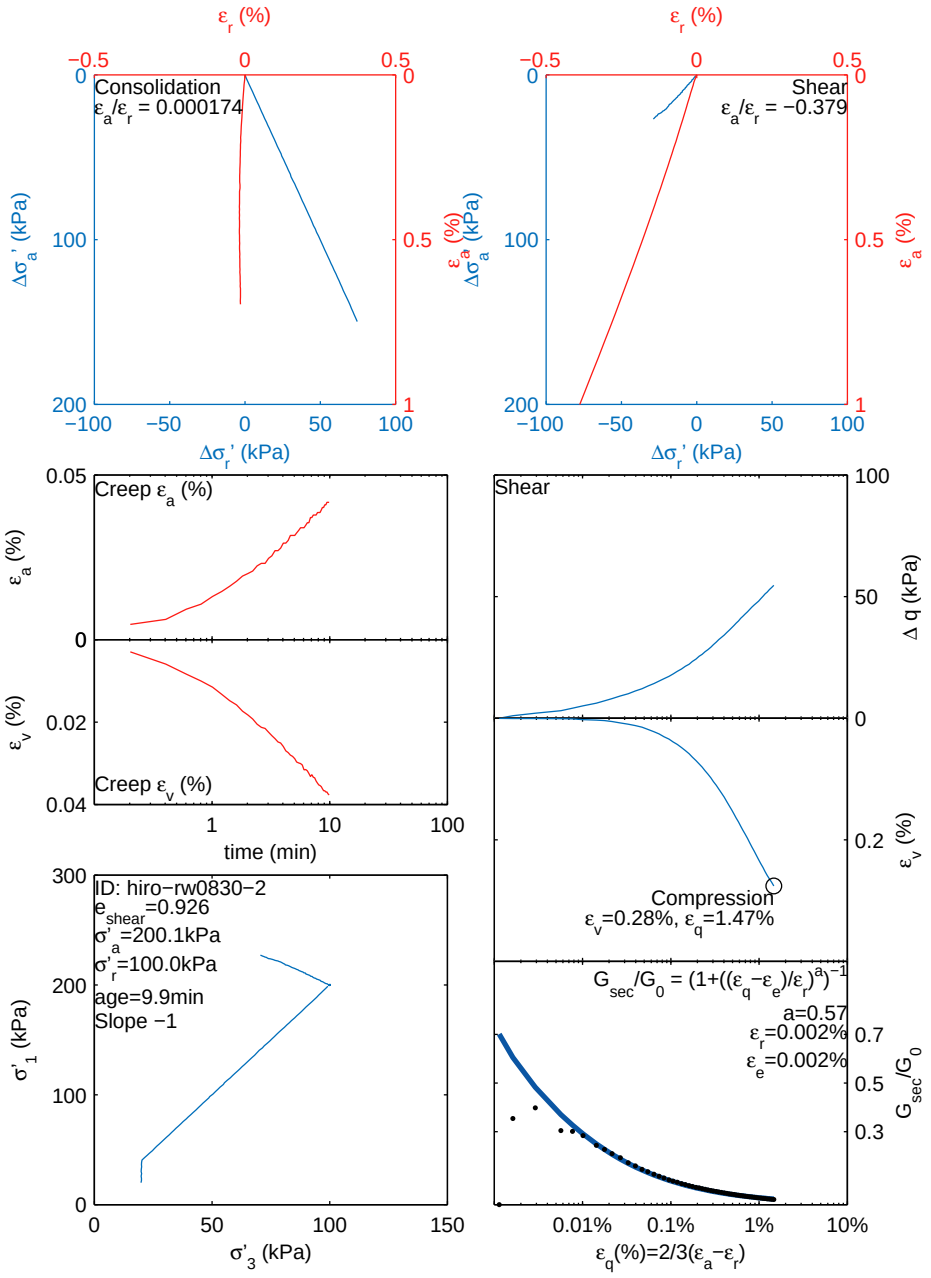

Figure D.135: Shozen-rw0830-2: σ_a = 200.1 kPa, σ_r = 100.0 kPa, age=9.9 min, Stress path=-1

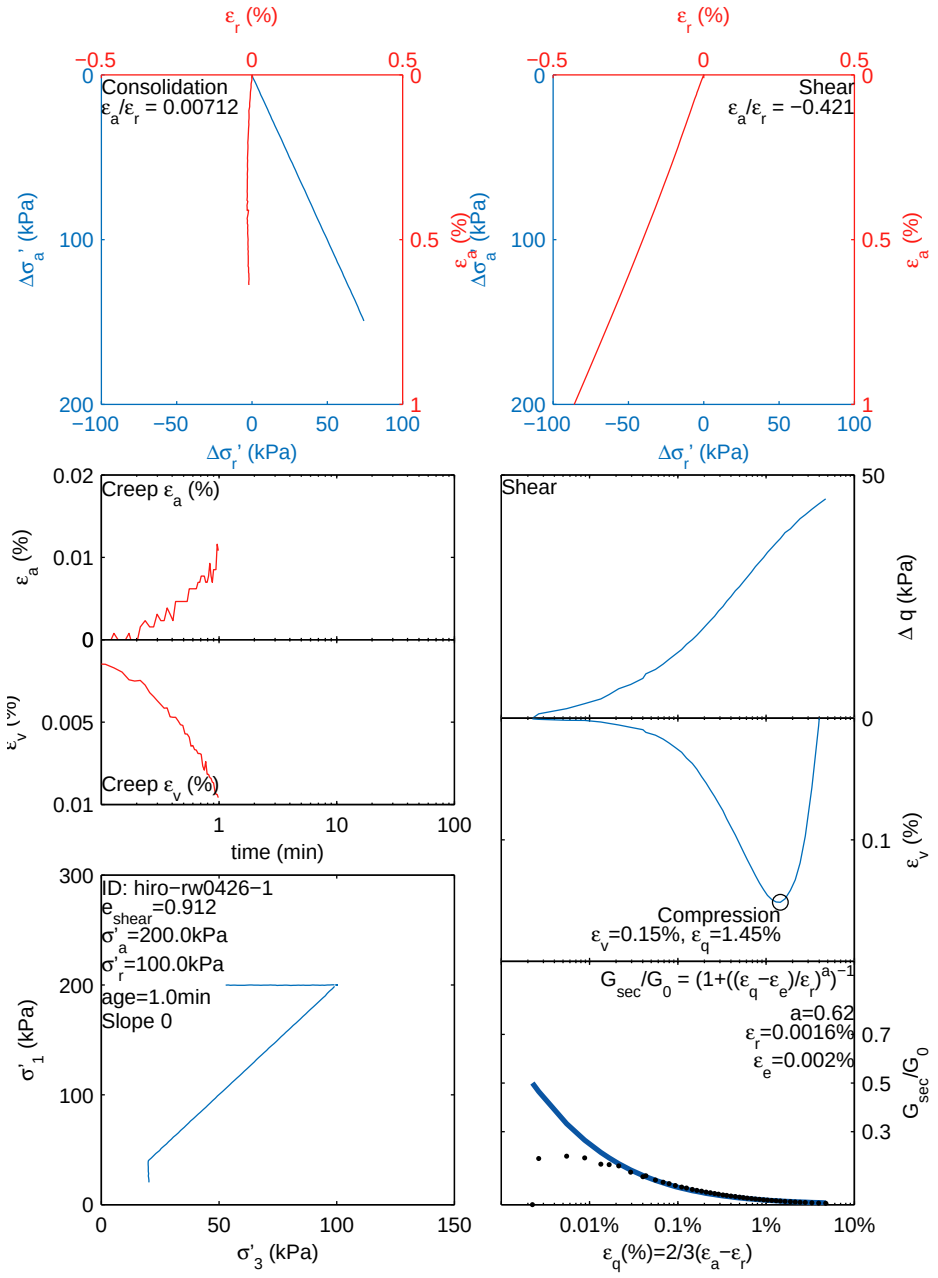

Figure D.136: Shozen-rw0426-1: σ_a = 200.0 kPa, σ_r = 100.0 kPa, age=1.0 min, Stress path=0

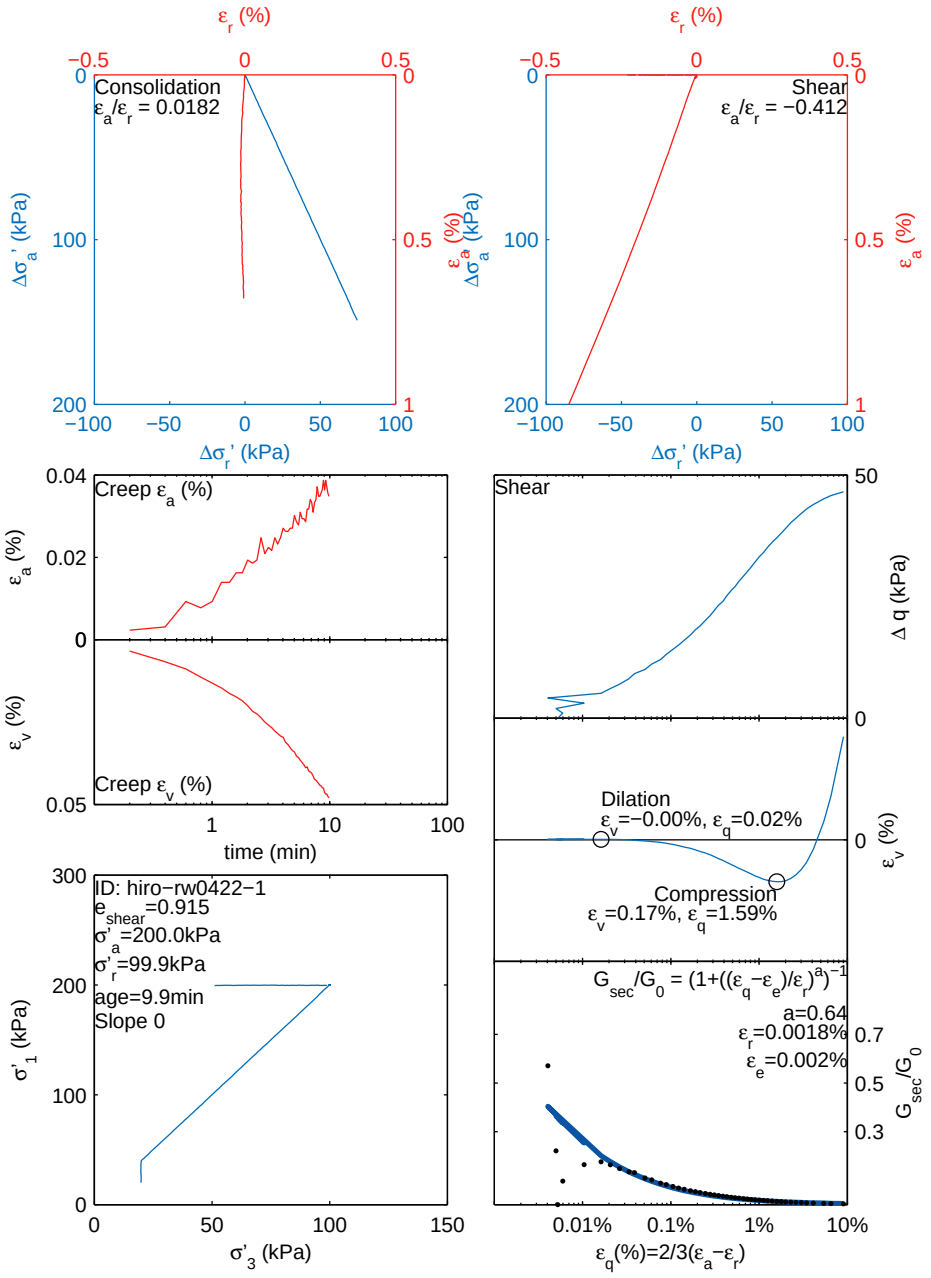

Figure D.137: Shozen-rw0422-1: σ_a = 200.0 kPa, σ_r = 99.9 kPa, age=9.9 min, Stress path=0

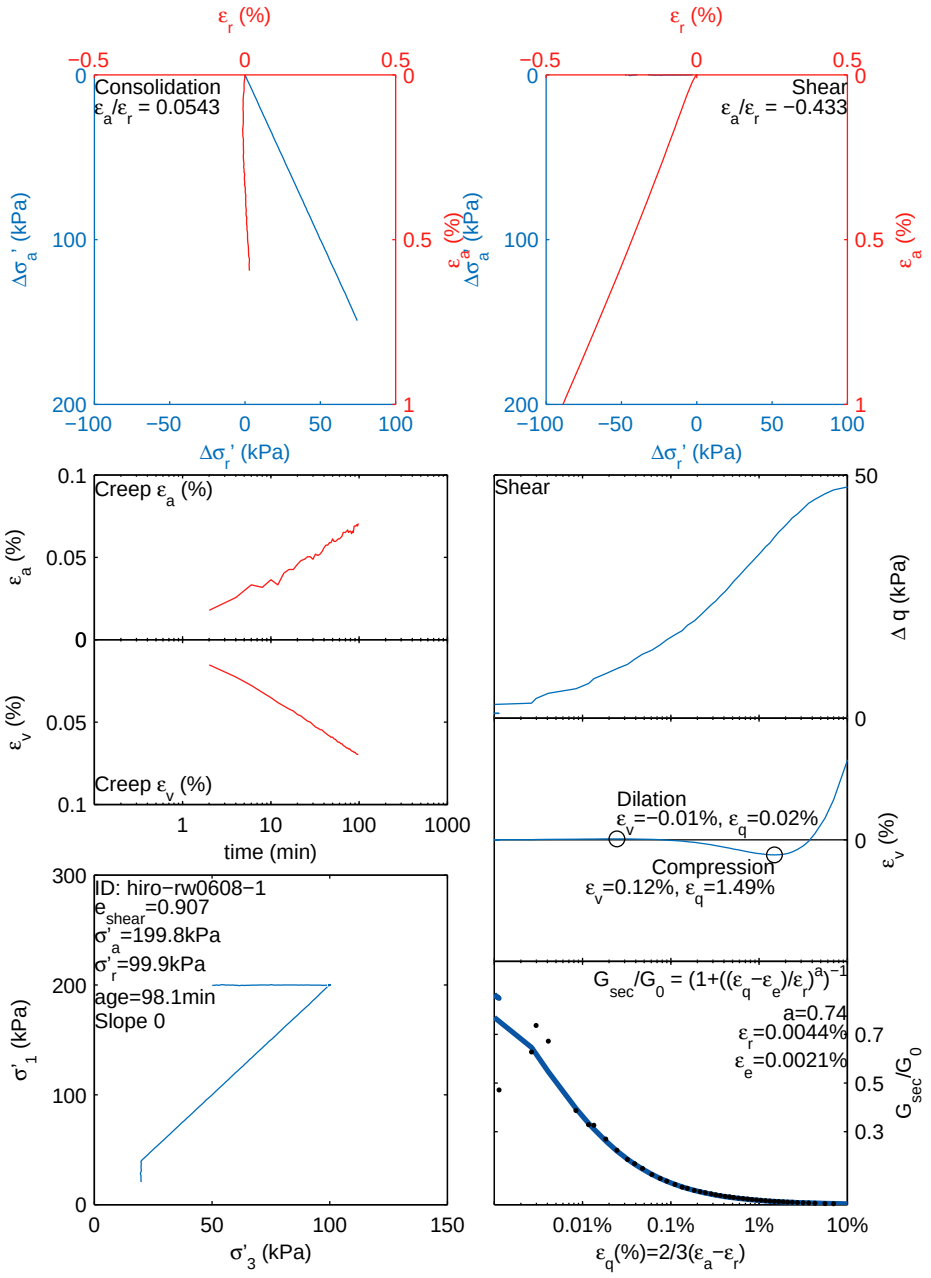

Figure D.138: Shozen-rw0608-1: σ_a = 199.8 kPa, σ_r = 99.9 kPa, age=98.1 min, Stress path=0

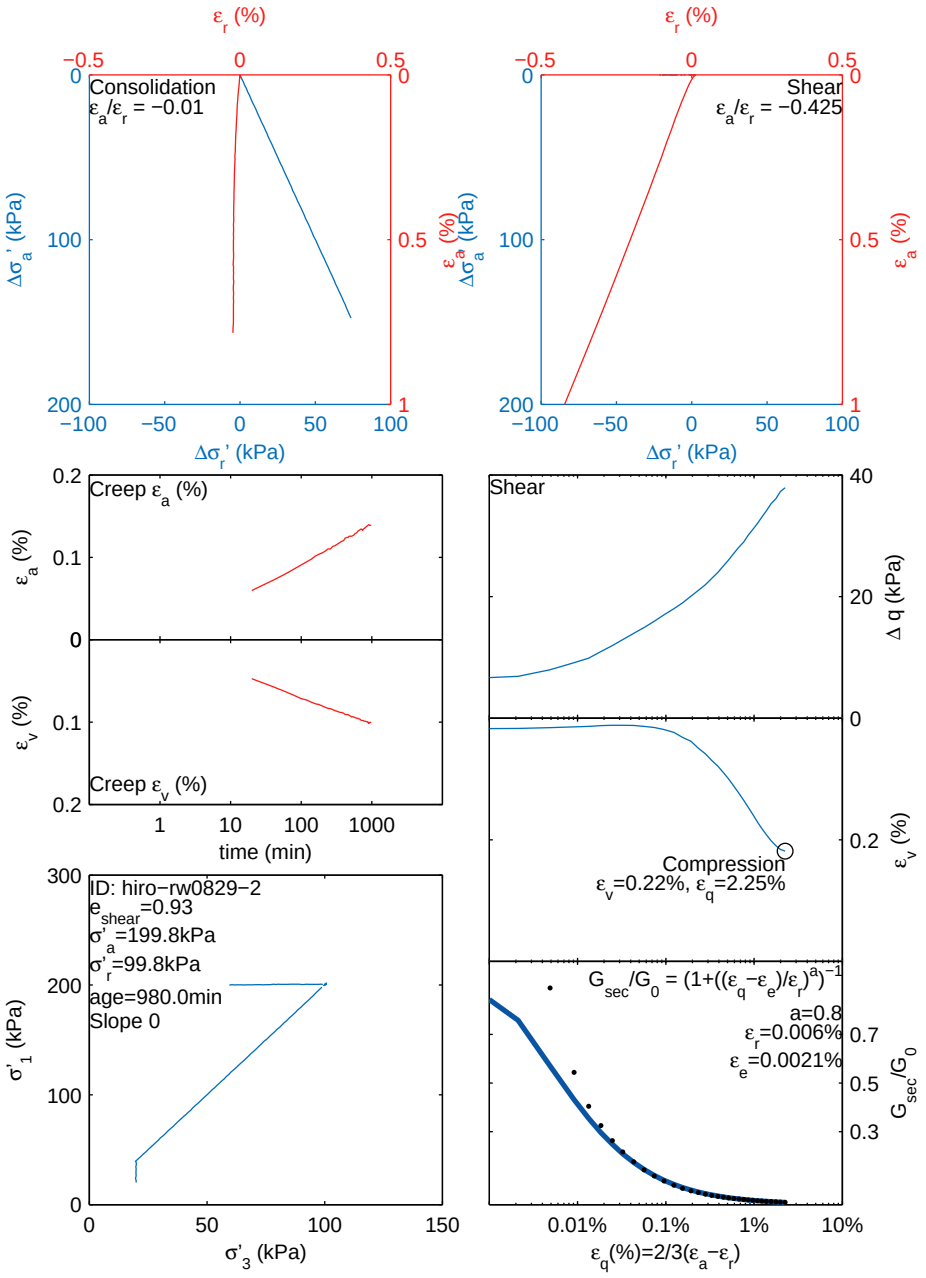

Figure D.139: Shozen-rw0829-2: σ_a = 199.8 kPa, σ_r = 99.8 kPa, age=980.0 min, Stress path=0

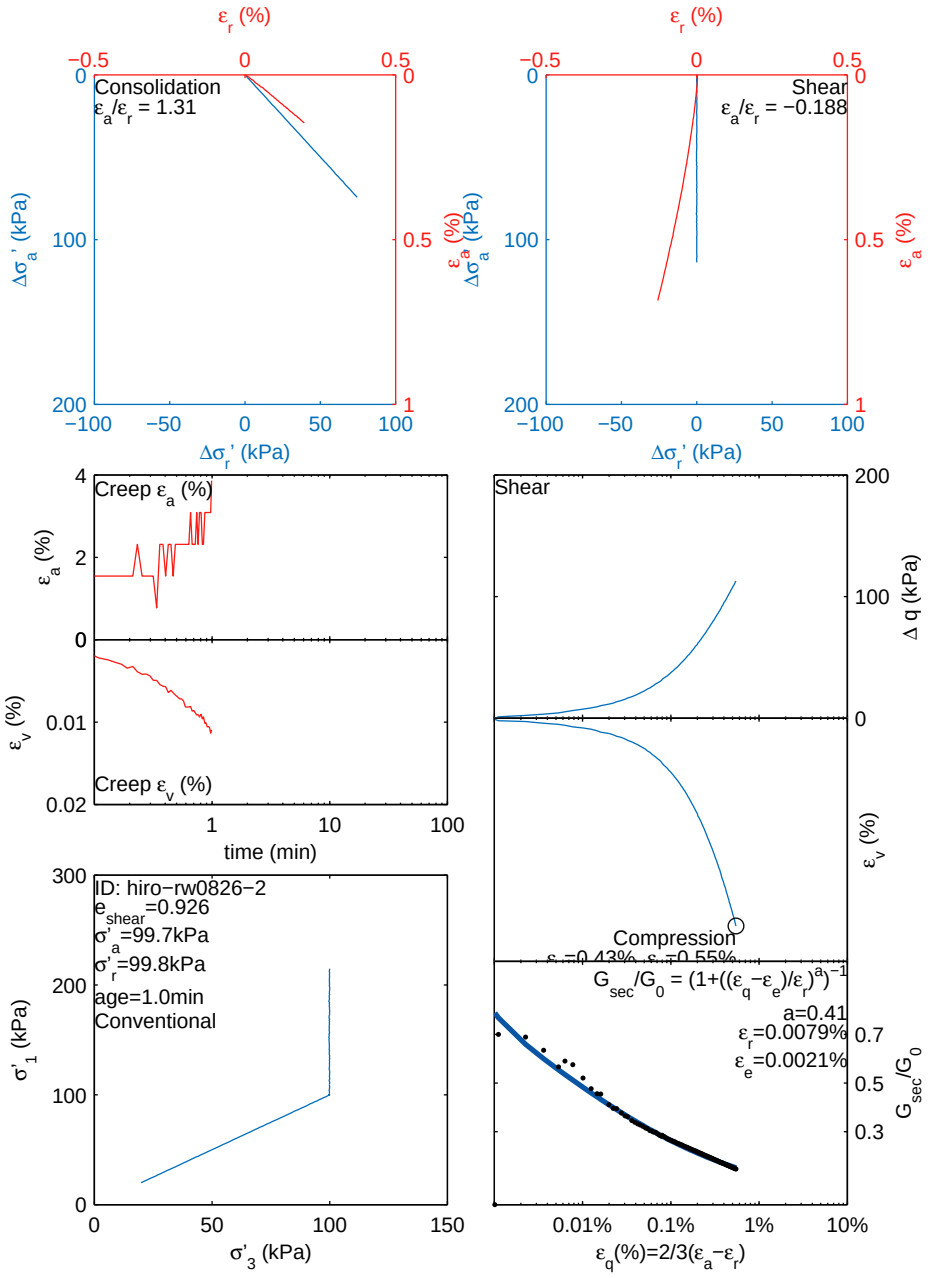

Figure D.140: Shozen-rw0826-2: σ_a = 99.7 kPa, σ_r = 99.8 kPa, age=1.0 min, Stress path=C

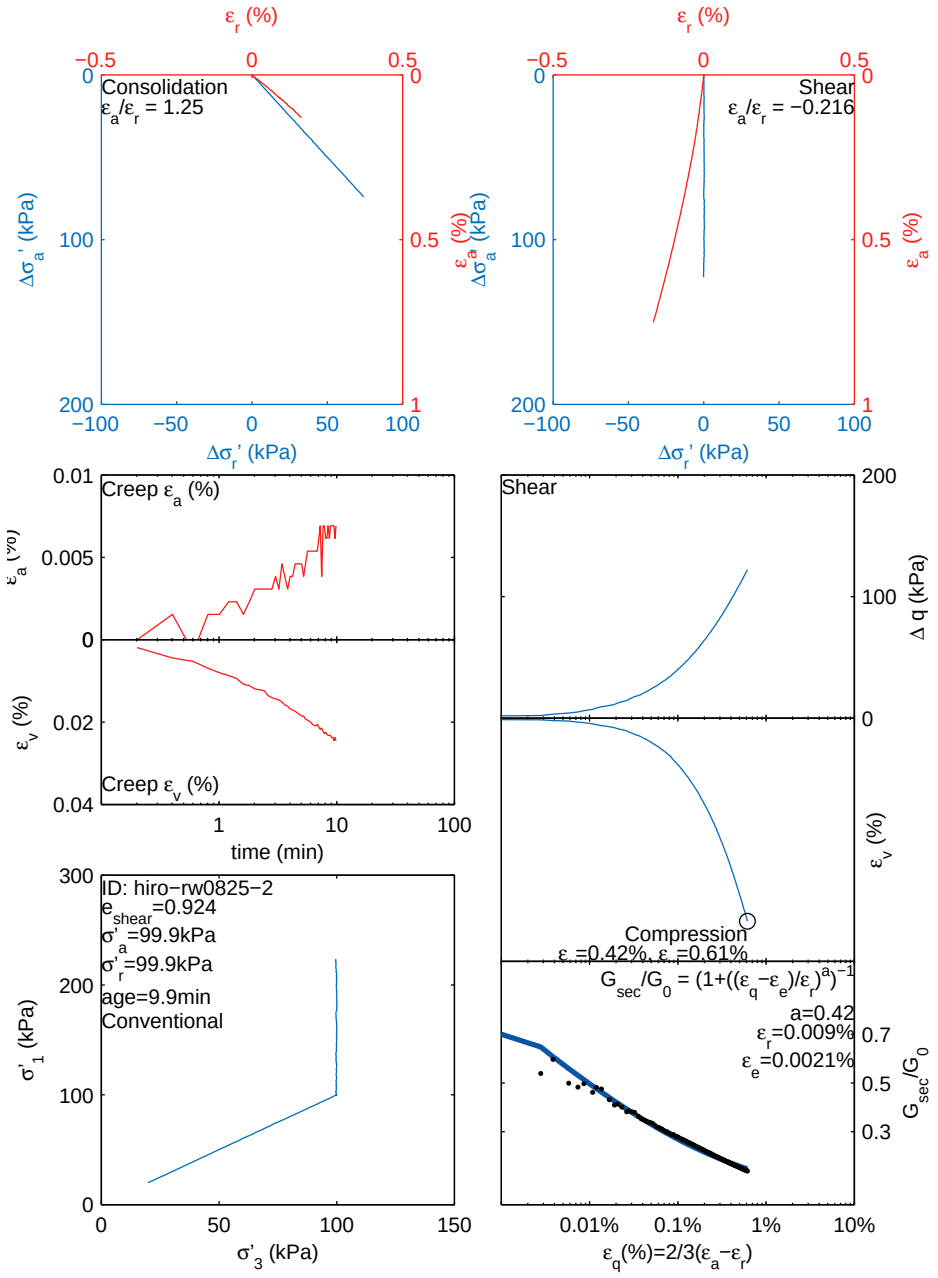

Figure D.141: Shozen-rw0825-2: σ_a = 99.9 kPa, σ_r = 99.9 kPa, age=9.9 min, Stress path=C

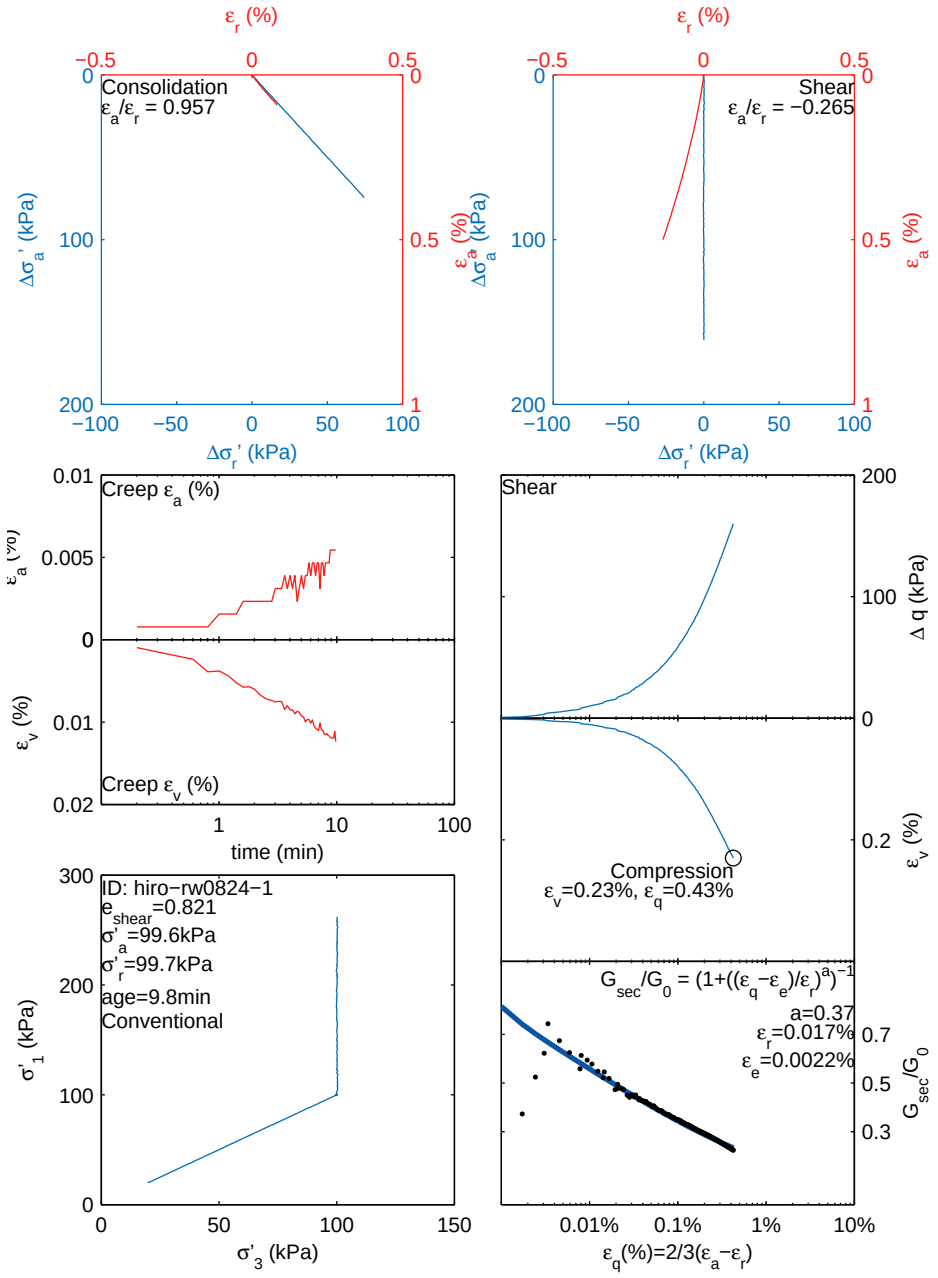

Figure D.142: Shozen-rw0824-1: σ_a = 99.6 kPa, σ_r = 99.7 kPa, age=9.8 min, Stress path=C

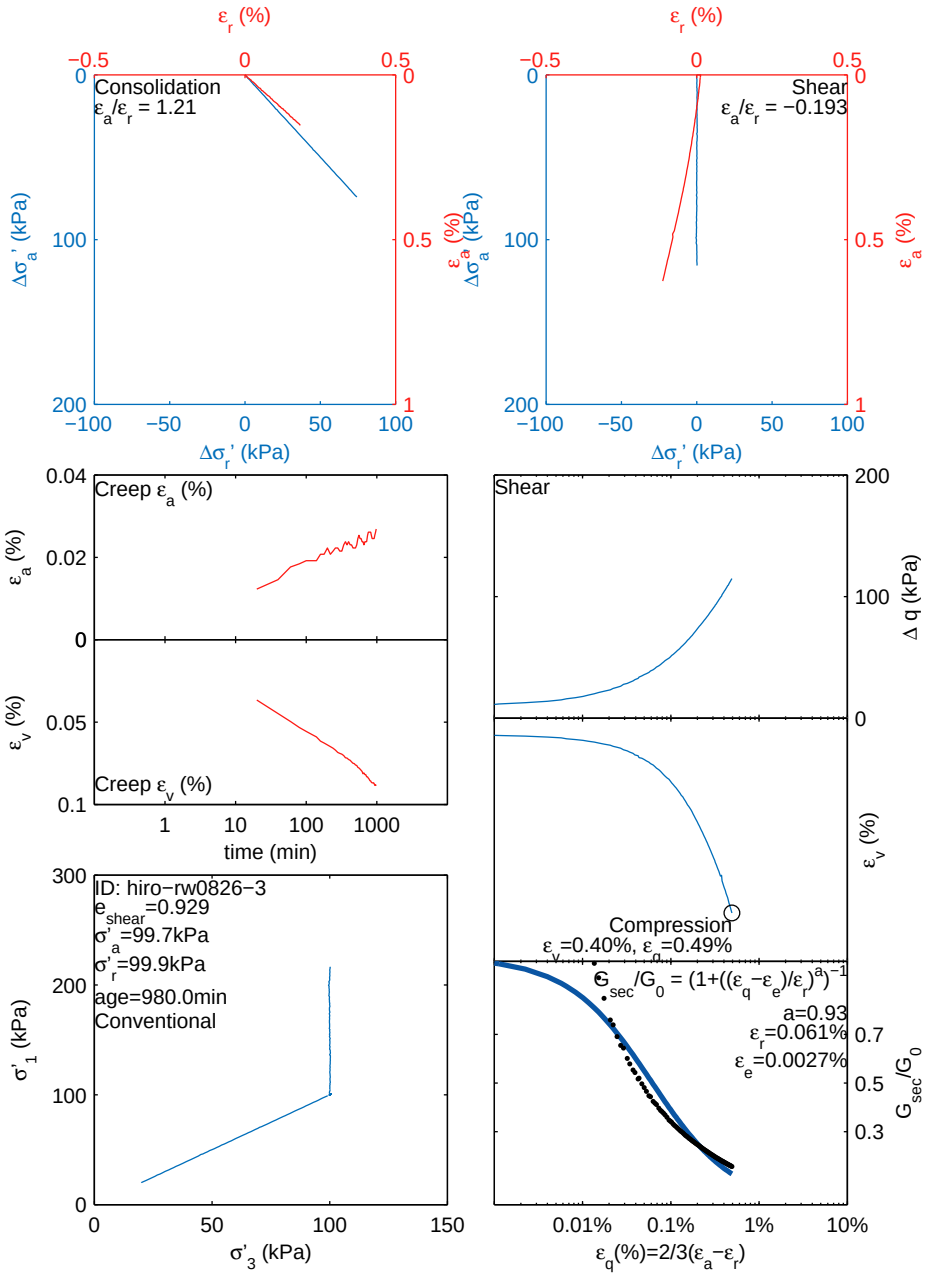

Figure D.143: Shozen-rw0826-3: σ_a = 99.7 kPa, σ_r = 99.9 kPa, age=980.0 min, Stress path=C

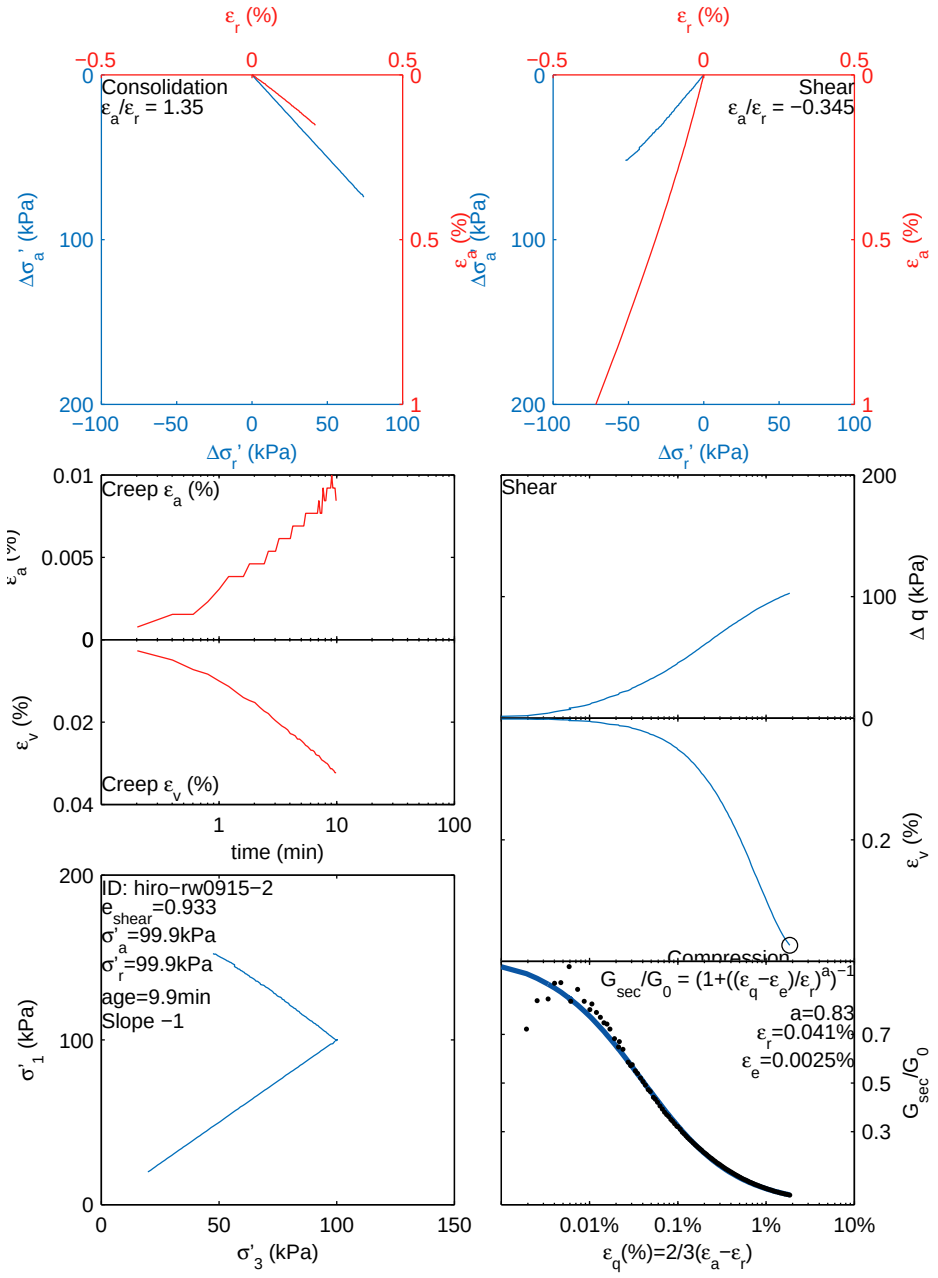

Figure D.144: Shozen-rw0915-2: σ_a = 99.9 kPa, σ_r = 99.9 kPa, age=9.9 min, Stress path=-1

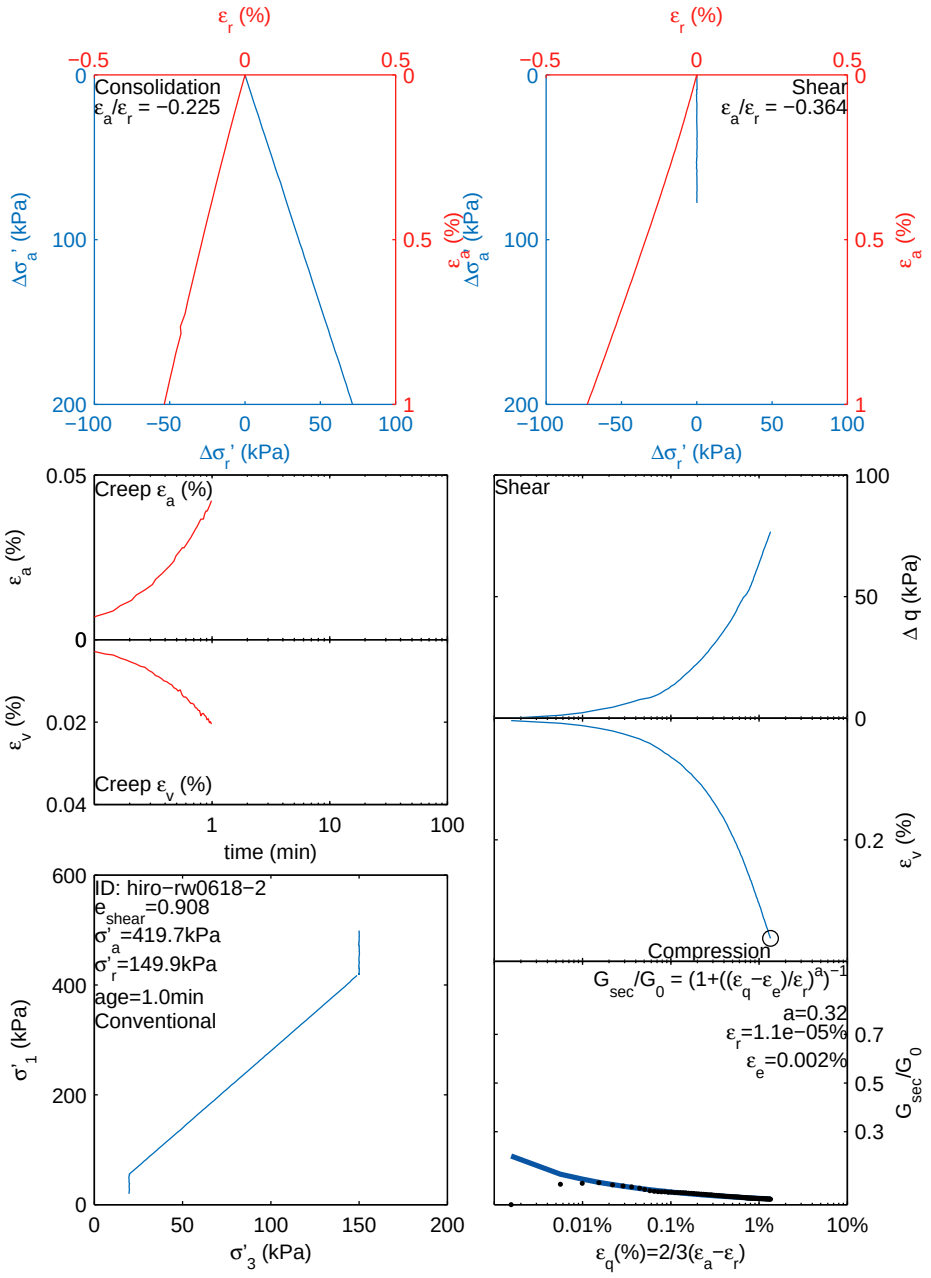

Figure D.145: Shozen-rw0618-2: σ_a = 419.7 kPa, σ_r = 149.9 kPa, age=1.0 min, Stress path=C

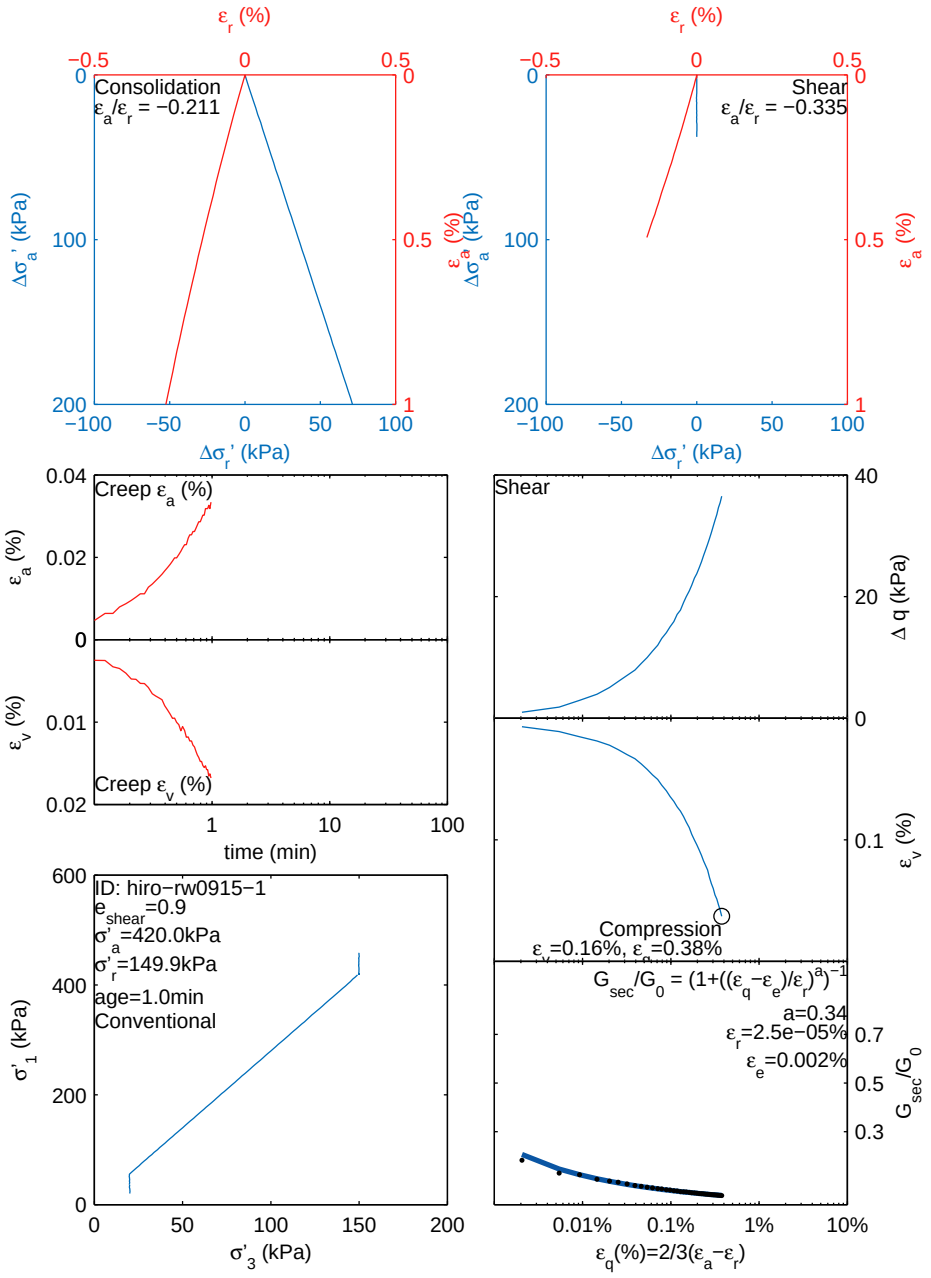

Figure D.146: Shozen-rw0915-1: σ_a = 420.0 kPa, σ_r = 149.9 kPa, age=1.0 min, Stress path=C

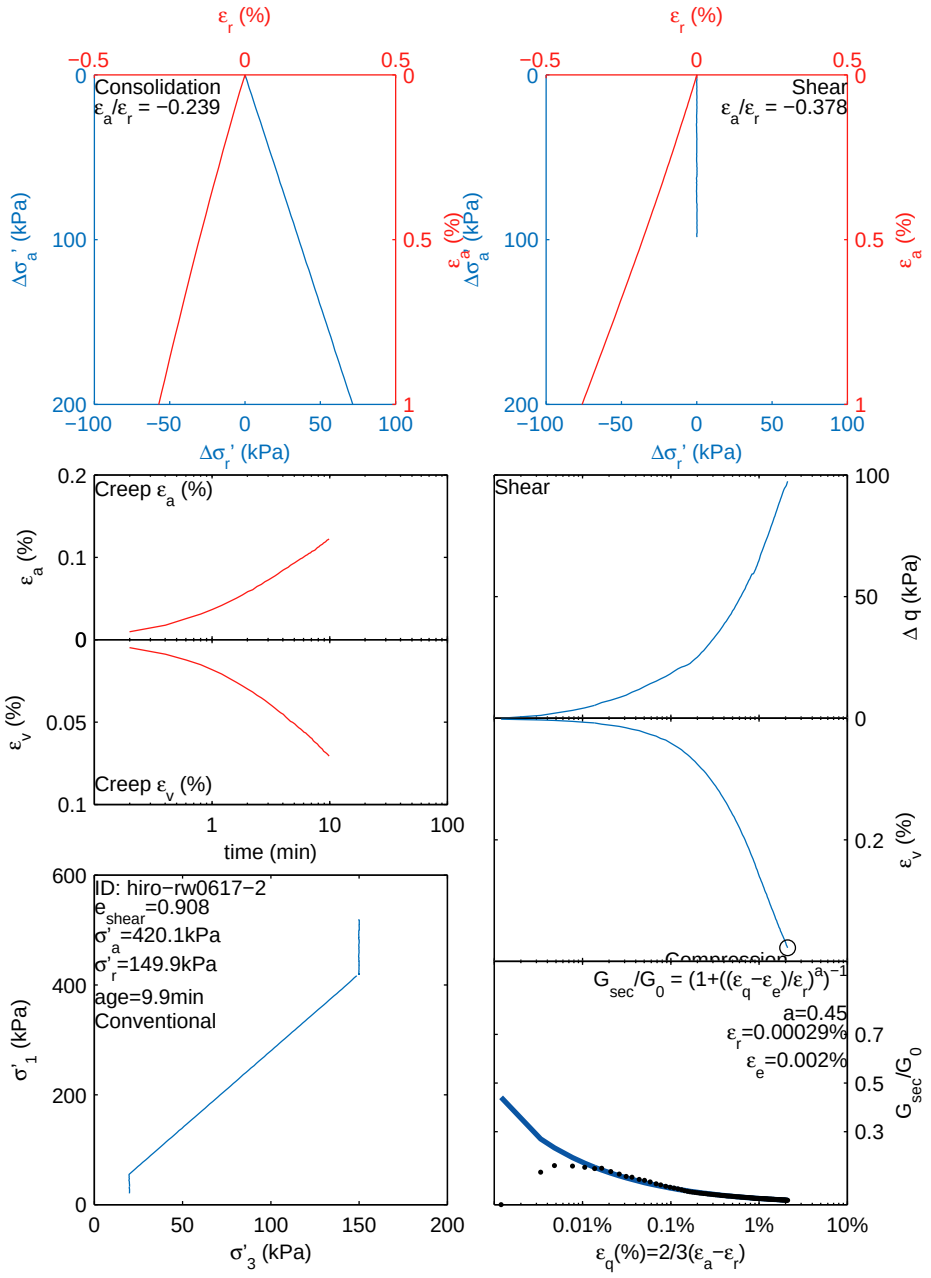

Figure D.147: Shozen-rw0617-2: σ_a = 420.1 kPa, σ_r = 149.9 kPa, age=9.9 min, Stress path=C

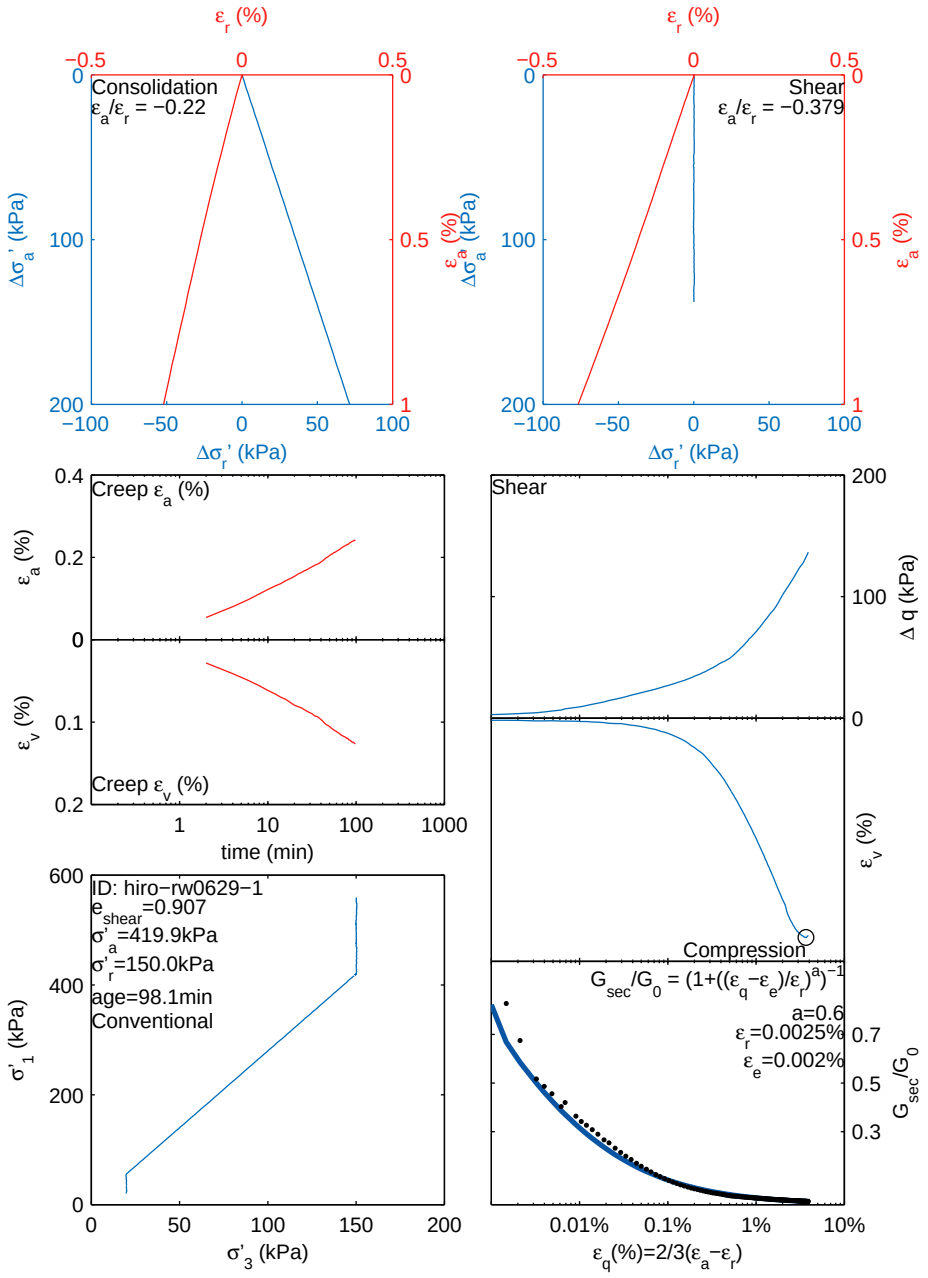

Figure D.148: Shozen-rw0629-1: σ_a = 419.9 kPa, σ_r = 150.0 kPa, age=98.1 min, Stress path=C

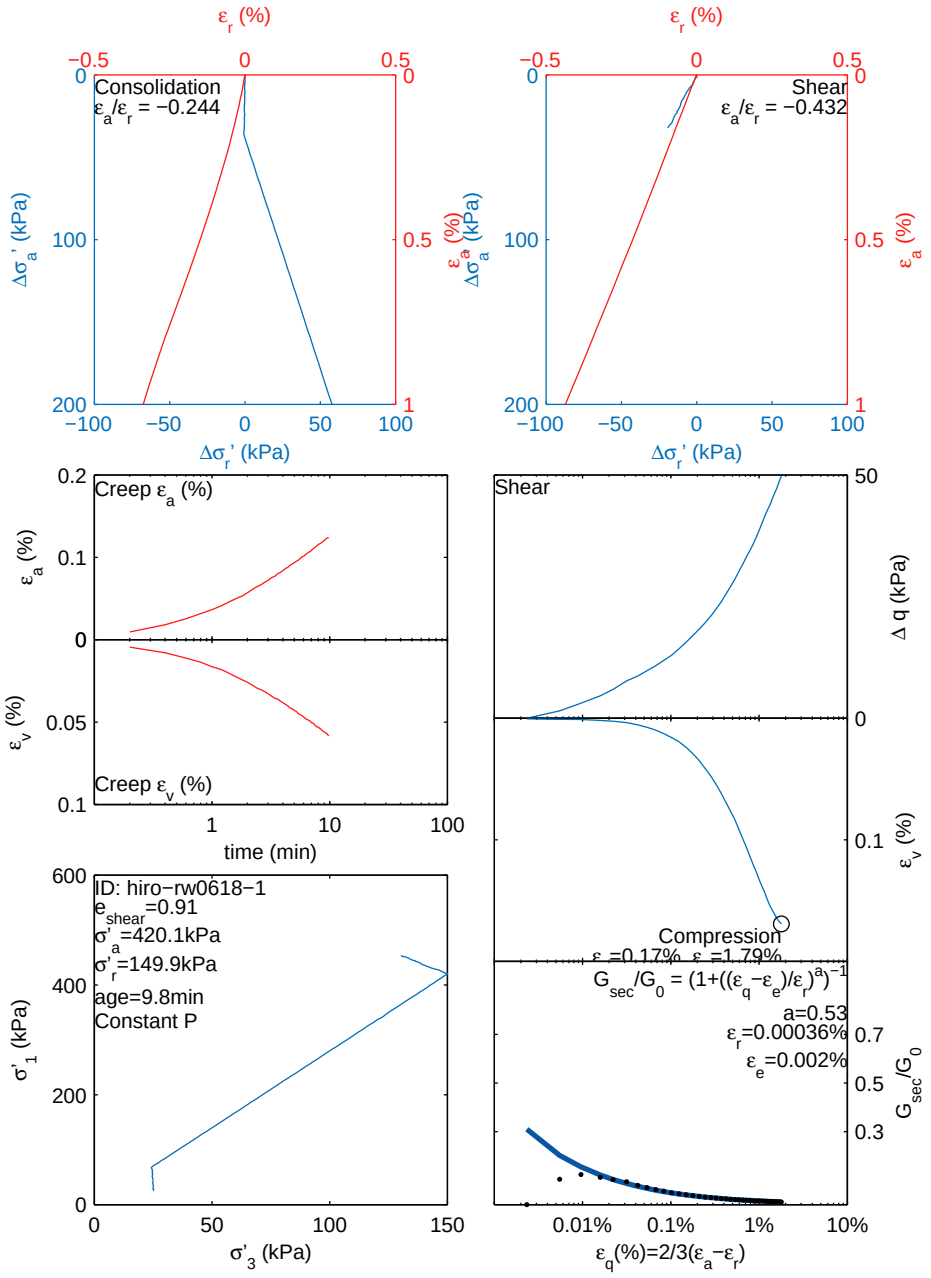

Figure D.149: Shozen-rw0618-1: σ_a = 420.1 kPa, σ_r = 149.9 kPa, age=9.8 min, Stress path=P

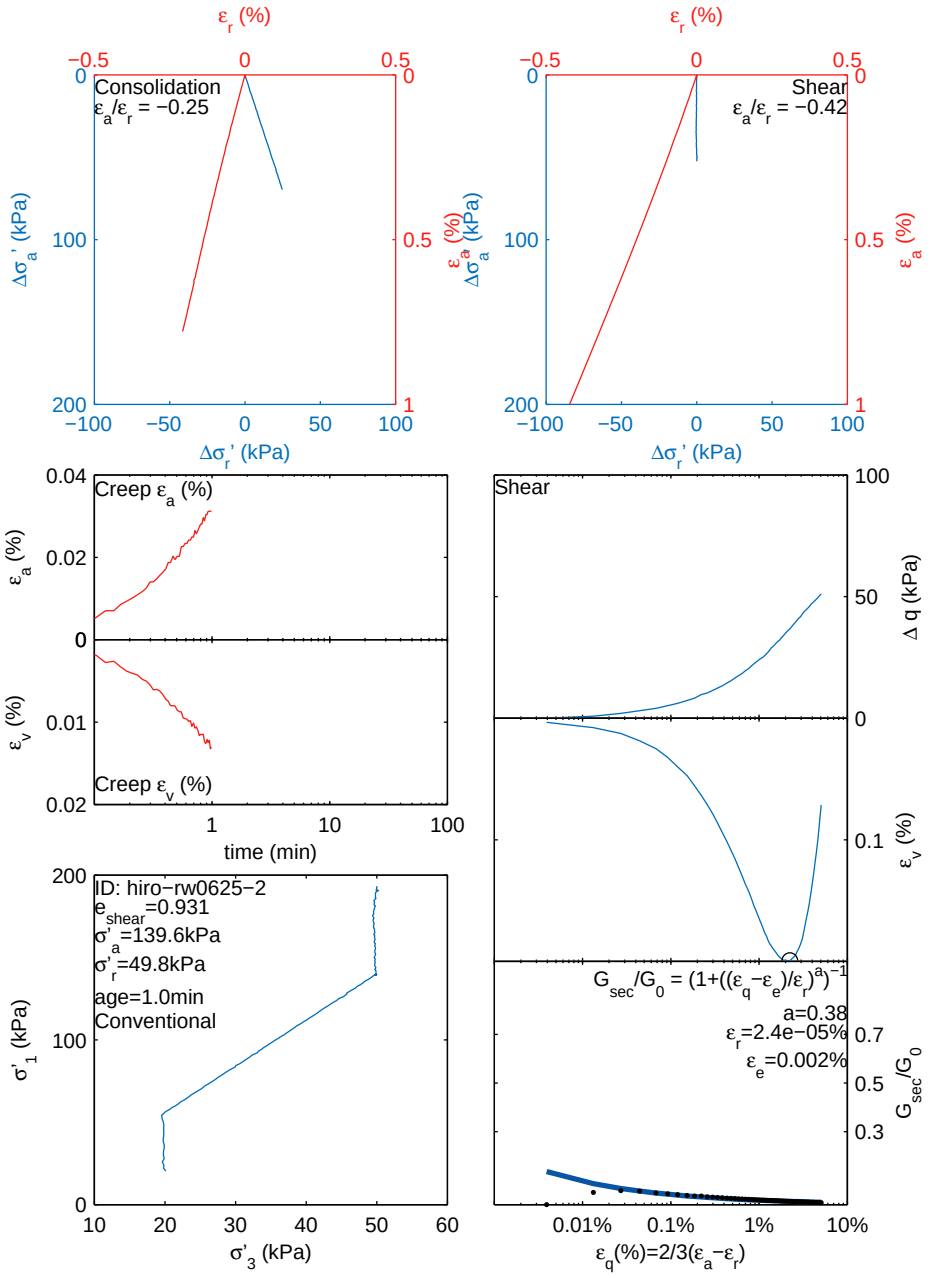

Figure D.150: Shozen-rw0625-2: σ_a = 139.6 kPa, σ_r = 49.8 kPa, age=1.0 min, Stress path=C

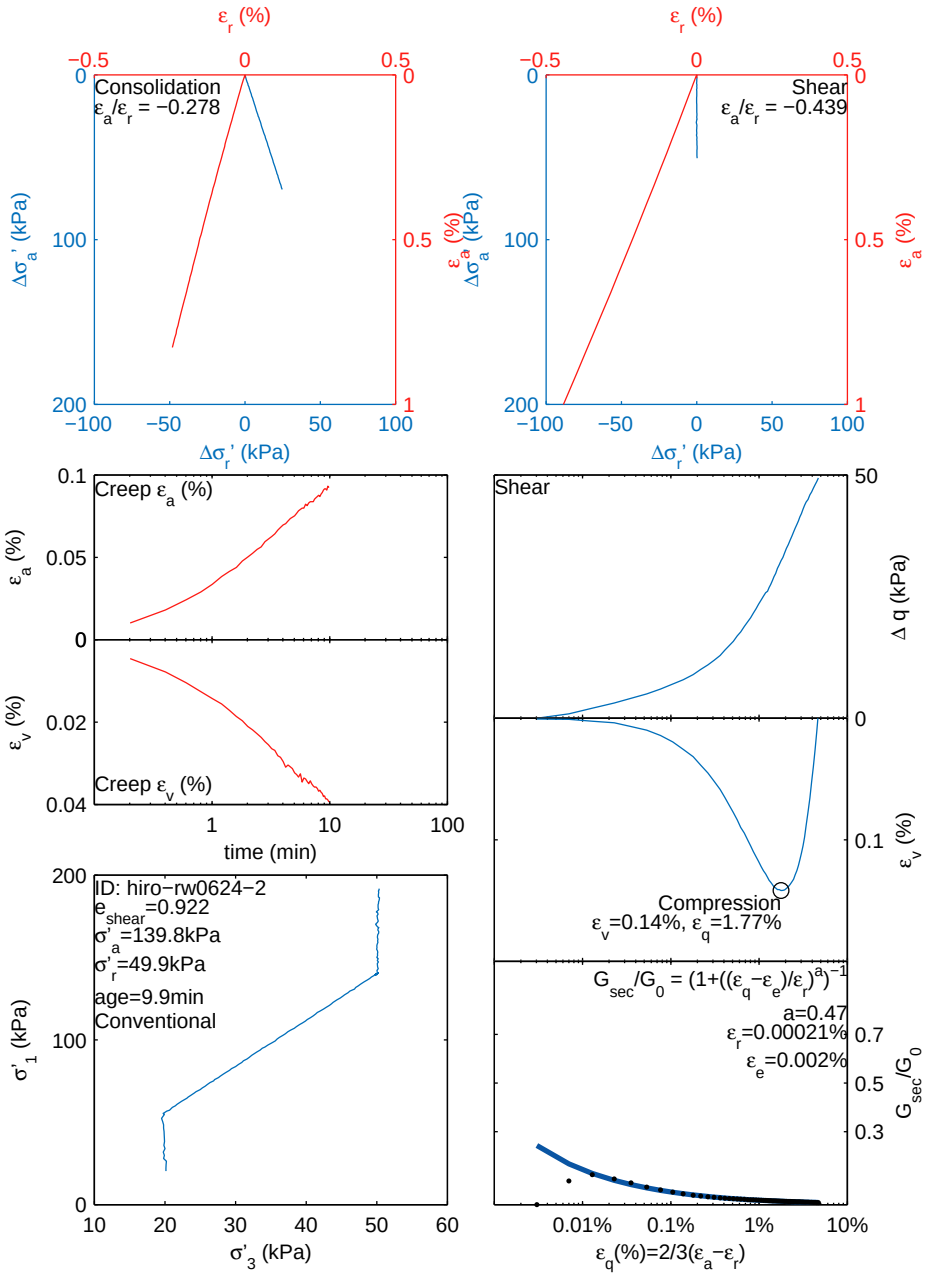

Figure D.151: Shozen-rw0624-2: σ_a = 139.8 kPa, σ_r = 49.9 kPa, age=9.9 min, Stress path=C

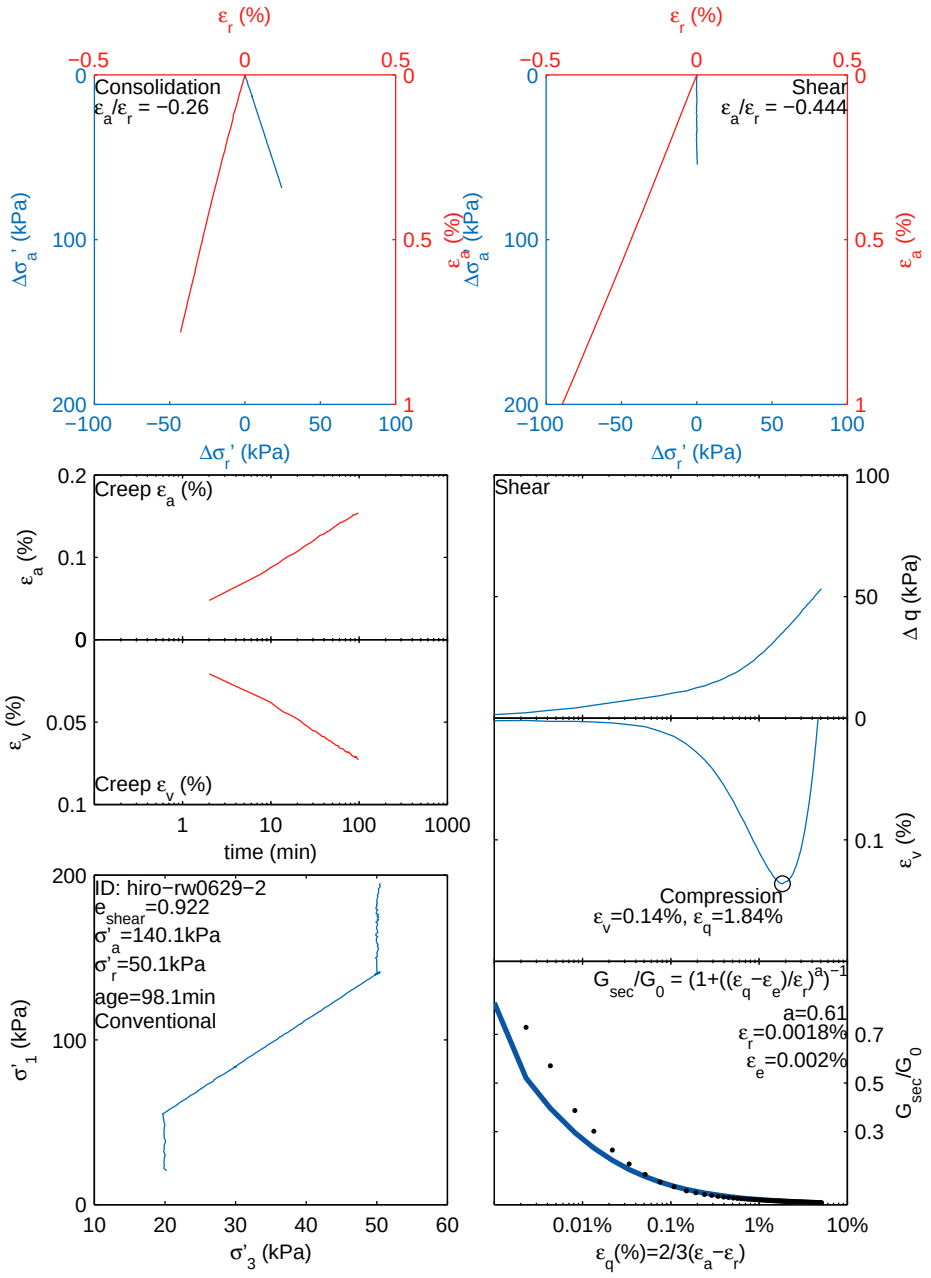

Figure D.152: Shozen-rw0629-2: σ_a = 140.1 kPa, σ_r = 50.1 kPa, age=98.1 min, Stress path=C